

DTIC FILE COPY

1

AD-A217 182

ANALYSIS OF GALE DATA  
FINAL REPORT  
SAIC 89/1746  
Contract No. N00014-86-C-2365  
DECEMBER 1989



*Science Applications International Corporation*  
An Employee-Owned Company

DTIC  
ELECTE  
JAN 25 1990  
S DCS D

DISTRIBUTION STATEMENT A  
Approved for public release  
Distribution Unlimited

90 01 23 036

**ANALYSIS OF GALE DATA**

**FINAL REPORT**

**SAIC 89/1746**

**DECEMBER 1989**

Submitted to:

Dr. Rangarao Madala  
Atmospheric Physics Branch  
Space Science Division  
Naval Research Laboratory  
Washington, DC 20375-5000

Prepared by:

Dr. Ellis Hyman  
with  
Drs. Keith Sashegyi and Darrell Strobel  
and  
Mr. John Hardgrove  
and Dr. Sethu Raman and Staff of  
North Carolina State University

Contract No. N00014-86-C-2365

For the period from  
August 11, 1986 to  
September 30, 1989

Accession For	
NTIS CRA&I	<input checked="checked" type="checkbox"/>
DTIC TAB	<input type="checkbox"/>
Unannounced	<input type="checkbox"/>
Justification	
By <i>per CB</i>	
Distribution /	
Availability Codes	
Dist	Avail and/or Special
A-1	

## TABLE OF CONTENTS

I.	DISCUSSION.....	1
II.	NUMERICAL CYCLONE CODE DEVELOPMENT AND SIMULATIONS .....	1
1.	Introduction.....	1
2.	Simulation of GALE Cases .....	2
3.	Initialization for GALE Data.....	4
4.	Analysis Scheme for Extra GALE Data .....	6
III.	NUMERICAL MODELING STUDIES OF THE MID-LATITUDE AND TROPICAL CYCLONE BY THE N.C. STATE UNIVERSITY .....	8
IV.	CHEMISTRY AND TRANSPORT MODELING IN THE MESOSPHERE .....	10
V.	SPACE SCIENCE ENGINEERING SUPPORT .....	11

## **I. DISCUSSION**

This report covers the period 11 August 1986 to 30 September 1989, and describes the work completed for contract N00014-86-C-2365, SAIC project #1-157-13-241. The work on numerical simulation of cyclone genesis was performed by SAIC staff on-site at NRL and via a subcontract to North Carolina State University by Dr. Sethu Raman and his graduate students. The space science engineering tasks were performed by SAIC staff on-site at NRL and the mesospheric simulations by our consultant, Dr. Darrell Strobel of Johns Hopkins University. In the following sections each of these efforts is described in some detail, with more complete detail provided in Appendices.

## **II. NUMERICAL CYCLONE CODE DEVELOPMENT AND SIMULATION**

### **1. Introduction**

The Limited Area Numerical Weather Prediction system at the Naval Research Laboratory (NRL) is being developed to accurately simulate and study the development of extratropical cyclones, which rapidly develop off the east coast of the U.S. and the North Atlantic Ocean. Data collected during the Genesis of Atlantic Lows Experiment (GALE) and the Experiment on Rapidly Intensifying Cyclones in Atlantic (ERICA) are being used for model simulations and studies and for testing of the software developed. SAIC has contributed extensively to the development of the NRL mesoscale numerical model for GALE, including analysis and initialization methods, and parameterization of sub-grid scale circulations and has used the NRL model for simulation studies. We have, also, assisted with the NRL east coast snowstorm study described in Section 2. SAIC has run simulations for the case of cold air damming and coastal front formation and the subsequent off-shore cyclogenesis during the second intensive observing period of GALE. This work is also described in Section 2. SAIC has developed software to read and unpack the special packed binary data for the analyses and forecasts on the National Meteorological Center (NMC) history tapes, and for the preprocessing of GALE data on the VAX computers at NRL. Copies were made of the NMC history tapes and archived by SAIC at NRL for the periods of the GALE and ERICA experiments. SAIC developed a dry convective



adjustment scheme to parameterize sub-grid scale dry convection and incorporated a Davies (1976) lateral boundary formulation for use in the model for the simulation of GALE storms. SAIC has worked with the NRL staff in the development of initialization schemes, including a vertical mode initialization scheme, and has extensively tested the schemes with analyses for the GALE period from the NMC. For use with the initialization procedures, the NRL solver for partial differential equations was also modified as described in a report by SAIC and discussed in Section 3. For the analysis of the GALE data, SAIC has developed an efficient analysis scheme based on the successive corrections method, to enhance the operational NMC analyses and has included an extensive quality control package. These efforts are described further in the following sections.

## 2. Simulation of GALE Cases

The basic numerical model developed at NRL is described in the technical report of Madala et al. (1987). A version of the model to be used for GALE studies, was used to study the east coast snowstorm of February 10-12, 1983 in the paper of Chang et al. provided in Appendix A and published in Mon. Wea. Rev. 117, 1768 (1989). The study demonstrated the feasibility of enhancing operational analyses with the original data soundings using the Barnes (1973) scheme, as adapted for the NRL model by Brehme (1987). Sensitivity of the forecasts of the snowstorm along the east coast to boundary conditions and physical processes were investigated in the study, details of which can be found in Appendix A. For this study, SAIC's software was used to unpack the initial data to be used for the analysis of Brehme (1987) and also used to process the NMC analyses, used for verification purposes. SAIC's dry convective adjustment software (see below) was also used. This model and modifications, which were to be used for the GALE simulations, was also presented at the 6th Extratropical Cyclone Workshop of the American Meteorological Society in Monterey, CA, June, 1987, entitled "A Model for the Simulation of Extratropical Cyclones During GALE," R.V. Madala, K. D. Sashegyi, and S.W. Chang.

In the papers by Sashegyi et al. (Appendices B, C, and D), simulations of the development of cold air damming and the coastal front and the subsequent offshore cyclogenesis for the case of the second Intensive

Observing Period (IOP#2) of GALE were carried out by SAIC using the NRL model. The simulations by SAIC showed that as the cold front moved off the east coast of the U.S., a strong low level temperature contrast was produced in the model in the first 36 hours of integration. This was caused by (1) the blocking by the Appalachian mountains of the north-easterly flow of cold air behind the front (cold air damming), (2) strong surface sensible heat fluxes over the Gulf Stream, and (3) a confluent flow along the western edge of the Gulf Stream enhancing the temperature gradient. In the simulation of the subsequent offshore cyclogenesis by Sashegyi et al. described in Appendix D the low level trough/coastal front moved inland with a weak low forming on the front and moving rapidly up the coast. A new cyclone then formed offshore of Cape Hatteras, in agreement with the operational analyses. Realistic precipitation patterns were developed in the model. Details of the simulations can be found in the papers by Sashegyi et al. in Appendices B, C, and D.

SAIC has developed software to read and unpack the special packed binary data for the analyses and forecasts on the NMC history tapes, and for the preprocessing of GALE data on the VAX computers at NRL. Copies were made of the NMC history tapes and archived by SAIC at NRL for the periods of the GALE and ERICA experiments. To extract the NMC analyses from the history tapes, extensive use is made of the VAX system service utilities for magnetic tape I/O.

SAIC developed a dry convective adjustment scheme, based on Manabe et al. (1965), to parameterize sub-grid scale dry convection for use in the model for the east coast snowstorm study of Chang et al. (1989) (see Appendix A) and for the simulation of GALE storms by Sashegyi et al. (Appendices B, C, and D). In the scheme, unstable lapse rates between adjacent layers are removed by lifting the air adiabatically to the next layer and exchanging the heat at constant pressure. This is continued to successively higher layers up to and including the first stable layer above the unstable lapse rate. In this way the temperature of the unstable layers and the first stable layer above are adjusted to a neutral lapse rate.

The single layer planetary boundary layer formulation of Chang (1981), which is based on similarity theory, was adapted for use by SAIC in the GALE model. In this formulation the surface fluxes of momentum, sensible heat and moisture are dependent on the stability as well as the wind speed.

Realistic surface fluxes were obtained by SAIC with the GALE simulation and described in the paper of Sashegyi et al. (1988) (Appendix D). The spatial gradients in the fluxes were sharper than with the constant drag coefficient formulation that had been used by SAIC in the earlier simulation of Sashegyi et al. (1987) (see Appendix C), bringing an improvement in the predicted model low level winds and temperatures in the cold air over the ocean.

A relaxation type of lateral boundary condition, following Davies(1976, 1983), in which the model variables are relaxed to specified boundary values of the variables, was developed and tested by SAIC for the NRL model. This scheme better simulated the propagation speed of fronts from the boundary region into the domain than the Perkey-Kreitzberg (1976) scheme in which tendencies are specified at the boundary. Tests by SAIC of the influence of the lateral boundaries of the model domain, nested grid, diffusion and the use of initial conditions initialized with the vertical mode scheme (described below) on the GALE simulation for IOP#2 are currently underway. Preliminary test simulations with the GALE case with the nested version of the model, being developed by Dr. R.V. Madala at NRL, were presented orally by SAIC at the International Conference on High Resolution Atmospheric Limited Area Modelling in August, 1989 in Oslo, Norway, entitled "The NRL Nested, Limited-Area Weather Prediction Model" by R. Madala, K. Sashegyi, and S. Chang.

### **3. Initialization for GALE Data**

Errors in the observations and analysis and inconsistencies of the data analysis with the physics, dynamics and numerics of the model give rise to inertial gravity wave oscillations in numerical integrations of a model. In the papers by Sashegyi et al. (1987) and Sashegyi and Madala (1988), provided in Appendices B and E respectively, SAIC showed that the split-explicit time integration scheme of Madala (1981), which is used in the NRL model, reduces the amplitude of the external gravity wave oscillations in the first three or four hours of integration. Oscillations in the vertical motion are not reduced, however. With an explicit centered difference scheme for time integration, however, the resulting high frequency oscillations seen in the surface pressure, can be as large 5 or 6 mb, for example. SAIC adopted a static non-linear initialization procedure to control the initial oscillations,

except for an initial adjustment of the vertical motion in the first five hours of integration. However, a small mean drift of about a mb in the surface pressure is produced by this scheme in the first twelve hours of integration. For further details refer to the papers in Appendices B and E.

SAIC has assisted with the development of a vertical mode initialization scheme, based on the work of Bourke and McGregor (1983), to remove these unwanted high frequency inertial gravity wave oscillations in the NRL model. The scheme provides a dynamically balanced velocity divergence field for the first three vertical modes of the model. It uses an iterative procedure to solve a system of linear Helmholtz equations, based on the model dynamical equations, to filter the high frequency gravity waves from the initial data used for the model. Only the external and the first two internal vertical modes are initialized. The procedure eliminates the unwanted high frequency gravity wave oscillations in the model integrations, and provides a dynamically balanced initial vertical motion field for the first three vertical modes of the model, thereby reducing the spin up time of disturbances in the model. The scheme also produces smaller changes to the initial mass and wind fields compared to the static initialization. Preliminary results with the scheme were described by SAIC in the paper by Sashegyi and Madala (1988) in the Numerical Weather Prediction Conference preprints volume (see Appendix E). A paper for publication is being prepared by Madala and Sashegyi. The results were presented orally by SAIC at the 2nd Storm Workshop on Regional Data Assimilation in Norman, OK in March, 1989 entitled "Vertical Normal Mode Initialization for the Naval Research Laboratory's Mesoscale Numerical Model," R.V. Madala and K.S. Sashegyi.

In a technical report to be submitted by Sashegyi and Madala the extensive testing of the vertical mode initialization scheme is described in detail by SAIC using NMC analyses for the GALE period. The convergence of the iterative procedure, used to obtain the initialized fields, was tested for different grids, and grid domains and model boundary conditions. For a large domain with a 2 x 1.5 degree grid covering the continental U.S, and little topography on the boundary, convergence of the scheme was rapid for the first three modes. Only three iterations were required before changes to the fields were small. For the GALE domain with a 0.5 degree grid, the sloping topography on the western boundary required specification of the

boundary divergence in the velocity field. In this case, the convergence of the divergence changes was slower for the third mode, but three iterations were still sufficient. The NRL model was integrated with uninitialized and initialized initial conditions for the two grids, using two different lateral boundary treatments. In the Davies (1976, 1983) lateral boundary treatment, model integrated variables are relaxed to prescribed boundary values in a boundary zone, while the Perkey-Kreitzberg (1976) scheme damps the model tendencies of the integrated variables. Boundary values or tendencies are obtained by interpolation from twelve hourly larger scale analysis fields, which have been further initialized for the cases of model integrations starting from initialized fields. For the large U.S. domain, smooth traces of surface pressure and vertical motion variation with time were produced for both treatments of the model lateral boundaries. The Perkey-Kreitzberg scheme produced some noise in the boundary zone however. For the U.S. domain, the values of the divergence in the boundary zones were small. However for the GALE domain, in which the divergence is substantial over the sloping topography along the western boundary and the grid separation was smaller, more noise was produced in the boundary zone for both cases. During the integrations, some small amplitude gravity wave oscillations of long period were present using the Perkey-Kreitzberg scheme, which were not present using the Davies scheme.

For use with the initialization procedures, the NRL solver for partial differential equations was also modified. In NRL Memorandum Report 6450 (1989) by Sashegyi and Madala, provided in Appendix F, the modifications of the Stabilized Error Vector Propagation method of solving elliptic partial differential equations are described. The code was modified to include cyclic boundary conditions, the case for a single block, and the merging of the code to handle any of the other boundary condition types, Dirichlet or Neumann (including four sided Neumann). For further details refer to the report by Sashegyi and Madala in Appendix F.

#### **4. Analysis Scheme for Extra GALE Data**

During the GALE and ERICA experiments, a large number of extra observations were collected using extra upper air soundings taken by balloon sondes and by dropwindsondes deployed from aircraft. An efficient analysis

scheme, based on a successive corrections technique for the interpolation of the observed data to the model grid, has been developed by SAIC to enhance the NMC operational analyses using the extra GALE data on the Cray supercomputer. The scheme includes an extensive quality control package, which discards bad data by using a buddy check of neighboring observations and fills data void regions with bogus null data (no change to first guess). The quality control prior to analysis allowed for the vectorizing of the analysis code and a dramatic reduction in the CPU time required to produce analyses.

In the analysis procedure for the GALE data, SAIC extensively modified Brehme's (1987) analysis, which adapted the successive corrections scheme of Barnes (1973) for the NRL model, to analyze the deviations from a first guess NMC analysis on a 1.5 degree latitude and longitude grid, consistent with the average upper air station spacing of 350 km. By analyzing the deviations, any large scale balance of the mass and wind fields which existed in the first guess analysis is retained, while maintaining the well defined wavelength response characteristics of the Barnes interpolation weights for the analysis of the deviations. The Barnes scheme uses two iterations of the analysis with the second pass using a smaller influence radius for the observations to update the smaller scales in the analysis, thereby rapidly converging to an accurate analysis. A third pass of the analysis scheme on a smaller 0.5 degree grid can be added in regions of higher observational density, such as in regions of drifting buoys or dropwindsondes. The Barnes successive corrections approach is very efficient compared to other more sophisticated analyses such as multivariate optimal interpolation, which are used for larger scale synoptic analysis at operational centers.

An important part of any analysis scheme of real data is testing for accuracy (or the quality control) of the data. Data which are inconsistent with the first guess and are not supported by neighboring observations or are of a scale too small to be resolved by the analysis scheme, will create fictitious features in any analysis. To handle the extra GALE observational data, SAIC has developed extensive quality control software for use with the analysis scheme. Similar to quality control procedures at operational weather centers, the upper air soundings are initially checked for hydrostatic consistency, and at each pressure level, data are checked for gross errors compared to the first guess analysis, a buddy check performed

to compare observations to near neighbors and the inconsistent observations removed. To prevent observations in regions of much higher than average observation density from having too much weight compared to areas of lower density during analysis, closely spaced observations are averaged and replaced by a single "super" observation. To prevent extrapolation of observations into data void areas during analysis, "bogus" null data deviations (from first guess values) are inserted at approximately the average station spacing in data void regions. Further, after the first pass of our analysis scheme, the data are again checked for inconsistency with the first pass analysis itself, and the inconsistent data (spikes) removed and the first pass repeated. A further advantage of the quality control, is that by removing bad and missing data prior to the analysis, our analysis code was able to be vectorized to run rapidly on a supercomputer.

### **III. NUMERICAL MODELING STUDIES OF THE MID-LATITUDE AND TROPICAL CYCLONE BY THE N.C. STATE UNIVERSITY**

Following are the principal results of the collaborative research between the North Carolina State University (NCSU) and SAIC in support of the program at NRL:

- (1) Incorporation of an interpolation scheme in the NRL limited area weather forecasting model for initial data.
- (2) Incorporation of improved graphics package in the model to assist in the analysis of model results.
- (3) Incorporation of Planetary Boundary Layer (PBL) parameterization schemes with improved physics and testing the sensitivity of the model results to these parameterizations using the Genesis of Atlantic Lows Experiment (GALE) data.
- (4) A study of the structure of the outflow jet of an idealized tropical cyclone using the NRL tropical cyclone model.
- (5) Study of the evolution of the Hurricane Florence (1988) (in progress).
- (6) Sensitivity of the results using the nested grid models in simulating orographically induced precipitation (in progress).

This work has resulted in three theses at NCSU on the M.S. level and one Ph.D. thesis, as follows:

- (1) A method of objective analysis for meteorological fields for use in numerical weather prediction model, K.A. Brehme, M.S. (1987).
- (2) Study of the seasonal migration of the ITCZ and the quasi-periodic oscillations in a simple monsoon system using an energy balance model, K.K. Alapati, MS (1988).
- (3) A numerical study of the structure of the outflow layer of a tropical cyclone using a primitive equation model, J.J. Shi, M.S. (1988).
- (4) Boundary layer parameterization for use in a limited area forecast model, T.R. Holt, Ph.D. (1989).

The M.S. Thesis by J.J. Shi was totally supported by this program and is reproduced here in Appendix G.

In addition, several journal publications resulted from this work, as follows:

- Holt, T. and S. Raman (1988): A review and comparative evaluation of multi-level boundary layer parameterization for first order and kinetic energy closure schemes, *Reviews of Geophysics*, 26, 761-780.
- Holt, T., S. Chang and S. Raman (1989): A numerical study of the coastal cyclongenesis in GALE IOP 2: Sensitivity to PBL parameterizations, *Monthly Weather Review* (in press).
- Gerber, H., S. Chang, and T. Holt (1989): Evolution of a marine boundary-layer Jet, *Journal of the Atmospheric Sciences*, 46, 1312-1326.
- Chang, S., K. Brehme, R. Madala, and K. Sashegyi (1989): A numerical study of the east coast snowstorm of 10-12 February 1983, *Monthly Weather Review*, 117, 1768-1778.
- Shi, J., S. Chang, and S. Raman (1989): A Numerical study of the outflow layer of tropical cyclones, submitted to *Monthly Weather Review*.
- Alapati, K. and S. Raman (1989): Study of the seasonal migration of the ITCZ and the quasi-periodic oscillations in a simple monsoon system using an energy balance model, *Meteorology and Atmospheric Physics* (in press).

Of the above publications, the paper by Holt and Raman (1988) appears here as Appendix H and the paper by Gerber, et al. is reproduced in Appendix I. The Chang, et al paper has already been described and is Appendix A. Finally, Appendix J provides the paper by Shi, et al.



#### IV. CHEMISTRY AND TRANSPORT MODELING IN THE MESOSPHERE

The focus of this research during the past three years has been on the analysis and interpretation of chemical species in the mesosphere that serve as tracers of atmospheric transport processes. In the first study ground-based microwave spectroscopy measurements of mesospheric CO and H<sub>2</sub>O vertical mixing ratio profiles were used to infer vertical mixing rates in the upper mesosphere. The CO and H<sub>2</sub>O data consistently implied vertical eddy diffusion coefficients in the 70-85 km region of  $K_{zz} < (1-2) \times 10^5 \text{ cm}^2 \text{ s}^{-1}$  during spring through summer at midlatitudes. The effect of chemical acceleration of vertical transport was investigated and found to be substantial for O and O<sub>3</sub> below the mesopause, but the divergences of their associated fluxes were modest, with at most a factor of 2 effect on the concentrations of O and O<sub>3</sub> for measured variability in gravity wave activity. A comparison of the vertical eddy diffusion coefficients for momentum stresses, constituent transport, and heat transport suggests that the eddy Prandtl number must be of order 10. For further details, see Appendix K entitled "Vertical Constituent Transport in the Mesosphere," by Strobel et al, published in the Journal of Geophysical Research **92**, 6691 (1987).

In a follow-up study with a much larger H<sub>2</sub>O mixing ratio data base, the low mesospheric  $K_{zz}$  values deduced from the vertical gradient of the microwave H<sub>2</sub>O measurements by Strobel et al. in the previous paper were confirmed for all seasons. In addition the data indicated that the H<sub>2</sub>O seasonal variation at mid-latitudes in the upper mesosphere is dominated by an annual component with low mixing ratios in winter and high mixing ratios in summer. This suggests that the vertical distribution of H<sub>2</sub>O in the upper mesosphere (up to 80 km) is controlled by advective rather than diffusive processes and points to the need for a 2D model of the middle atmospheric dynamics. This work is described in detail in Appendix L, which has been accepted for publication in the Journal of Geophysical Research.

More recently, a 1D photochemical model and a time dependent heat equation were used to study the response of mesospheric ozone concentration to short term solar UV flux variations. This study was motivated by the current deficiencies in our understanding of O<sub>3</sub> photochemistry in the mesosphere. We found that the magnitude of the computed ozone response to increased solar UV flux in the upper mesosphere (> 70 km) strongly coupled to the H<sub>2</sub>O abundance through the HO<sub>x</sub> catalytic cycle that removes O<sub>3</sub>. We concluded that a better theoretical description of the temperature response due to both chemical and dynamical effects is needed than was included in our model. The results of this work have been submitted (December 1989) for publication in the Journal of Geophysical Research entitled "A Model Study of the Response of Mesospheric Ozone to Short-Term Solar Ultraviolet Flux Variations," Summers, et al., which is included in Appendix M of this report.

In our pursuit of understanding O<sub>3</sub> photochemistry in the mesosphere an experimental and theoretical study of the diurnal variation of O<sub>3</sub> was carried out. A comparison of observed and theoretical O<sub>3</sub> mixing ratios suggests that the O<sub>3</sub> photolysis rate and diurnal variation was accurately modeled. However the observations did not provide a sensitive test of mesospheric chemistry controlling the abundance of odd oxygen. This work has been submitted for publication in the Journal of Geophysical Research and is included here as Appendix N.

## **V. SPACE SCIENCE ENGINEERING SUPPORT**

In support of the Upper Atmosphere Physics Branch of NRL's Space Science Division for the Space Shuttle Hitchhiker programs, UVLIM and MAHRS, SAIC performed various tasks that ranged from initial design concepts to fabrication of space flight hardware. At each phase, from conception to fabrication steps were taken to insure that NASA quality and safety requirements were carried out and documented.

The first task carried out was to update the current design for the payload controller and to incorporate those changes into the artwork that was then being done in house. Fabrication problems occurred due to the tight tolerances which were needed to correctly mate the payload controller board to an existing buffer card and the need to plot the artwork out on a

conventional plotter. These problems were overcome in a joint effort between SAIC and the board manufacturers by carefully matching the artwork between the two different boards.

With the fabrication of the payload controller subsystem of the UVLM project underway the next priority was the development of a power conditioning and distribution system and a stepper motor driver system. Special attention was required to adhere to the NASA specifications on interfacing with NASA Shuttle Power Systems. Filtering of noise, fuse protection, prevention of ground loops, redundancy of critical power paths, reliability of relays all needed to be built into the power distribution design from the initial design stages. Design concerns for the stepper motor included electrical isolation of the motors from the rest of the payload electronics and a power reducing circuit to control the duty cycle of the stepper motor.

Documentation in the form of reports, schematics, netlist, partlist, benchmarks, timing diagrams, mechanical drawings, memos, and test procedures was also generated and made available to all members of the project team. Schematics for all electronic subsystems were completed including wiring harness drawings which are critical to understanding the interconnections between all the electrical subsystems.

A successful electrical integration with NASA Hitchhiker equipment at Goddard Space Flight Center was also accomplished, assuring that all the power and communications lines were fully functional and that the software drivers written were downloading commands and data correctly. Other successful tests at Goddard included a mechanical integration with the Hitchhiker canister and a complete shake and vibration test. The preparation for these tests requires a considerable amount of preliminary work. In the case of electrical, all circuits must be tested to insure their correct location in their connector, their interconnections with other circuits and the creation of ground loops. The mechanical interface required close attention to details and tolerances. For the shake and vibration test we performed a mechanical stress analysis which required providing the mechanical drawings and the weights of the printed circuit cards including estimates of their center of gravity and material type.

With the UVLM project coming to an end the initial studies on the requirements for the MAHRS project began. The MAHRS payload is to be

integrated onto a German pallet called Astro-Spas. The electrical and mechanical interfaces were defined in the Astro-Spas system equipments specifications. This specification allowed us to determine the communication rates and power requirements for our payload. With the given restrictions on power and communication rates it then had to be determined if the MAHRS project could carry out its mission on the German Pallet Astro-Spas. Calculations on the processing speeds of the 80286 and the 68020 were performed in addition to data compression techniques using the TMS32C25. Along with processing speed, power consumption and board sizes were also then taken into consideration. A preliminary control system configuration was designed which included board sizes and their positions. The control systems box size and its location on the MAHRS payload was also determined.

Mechanical size and weight requirements were also defined and addressed by our preliminary study of the MAHRS payload system. While the MAHRS payload is of considerable size and mass it does appear that modification can be made to the existing design to reduce the weight and still maintain its structural integrity. The conclusion of the preliminary study showed that it will be possible to develop the MAHRS payload with the given restriction on power, weight, room and communication bandwidth. This effort was completed in August 1989.

Starting in August SAIC has been supporting the Radio and IR Astronomy Branch of NRL's Space Science Division. This entails development of an optical interferometer. This optical interferometer has its light-collecting components located at a number of separate and independent stations which together act as a unified system. These independent stations are called siderostats. Each siderostat must move with extreme accuracy and resolution. The control of these siderostats is SAIC's primary task on this project.

Other initial tasks were to gain overall familiarity with the project in the areas of servo control loops, optical interferometry, optical detectors, high precision rail tables and 2 axis optical mounts. Initial hardware tasks include the evaluation and troubleshooting of a servocontrol system prototype, manufactured by MFM Technology and the repair of an optical detector for a laser metrology system.

## REFERENCES

- Barnes, S.L., 1973: Mesoscale objective map analysis using weighted time-series observations. NOAA Technical Memorandum, ERL NSSL-62, Norman, OK, 60pp.
- Brehme, K., 1987: A method of objective analysis for meteorological fields for use in a numerical weather prediction model. Master's Thesis, Department of Marine, Earth and Atmospheric Sciences, North Carolina State University, Raleigh, N.C., 123pp.
- Bourke, W., and J.L. McGregor, 1983: A nonlinear vertical mode initialization scheme for a limited area prediction model. Mon. Wea. Rev., 111, 2285-2297.
- Chang, S.W., 1981: Test of a planetary boundary-layer parameterization based on a generalized similarity theory in tropical cyclone models. Mon. Wea. Rev., 109, 843-853.
- Davies, H.C., 1976: A lateral boundary formulation for multi-level prediction models. Quart. J. Roy. Meteor. Soc., 102, 405-418.
- Davies, H.C., 1983: Limitations of some common lateral boundary schemes used in regional NWP models. Mon. Wea. Rev., 111, 1002-1012.
- Madala, R.V., 1981: Efficient time integration schemes for atmosphere and ocean models. Finite Difference Techniques for Vectorized Fluid Dynamic Calculations, Chpt. 4, Springer-Verlag, pp 56-74.
- Madala, R.V., S.W. Chang, U.C. Mohanty, S.C. Madan, R.K. Paliwal, V.B. Sarin, T. Holt and S. Raman, 1987: Description of the Naval Research Laboratory Limited Area Dynamical Weather Prediction Model. NRL Technical Report No. 5992, Washington, D.C., 131pp.

Manabe, S., J. Smagorinsky, and R.F. Strickler, 1965: Simulated climatology of a general circulation model with a hydrologic cycle. Mon. Wea. Rev., 93, 769-798.

Perkey, D.J., and C.W. Kreitzberg, 1976: A time-dependent lateral boundary scheme for limited-area primitive equation models. Mon. Wea. Rev., 104, 744-755.

## **APPENDIX A**

### **A Numerical Study of the East Coast Snowstorm of 10-12 February 1983**

## A Numerical Study of the East Coast Snowstorm of 10–12 February 1983

SIMON CHANG

*Naval Research Laboratory, Washington, D.C.*

KATHERINE BREHME

*North Carolina State University, Raleigh, North Carolina*

RANGARAO MADALA

*Naval Research Laboratory, Washington, D.C.*

KEITH SASHEGYI

*Science Applications International Corp., McLean, Virginia*

(Manuscript received 28 June 1988, in final form 14 February 1989)

### ABSTRACT

A numerical study of the East Coast snowstorm of 10–12 February 1983 has been conducted with the NRL mesoscale model. The three-dimensional, hydrostatic, primitive equation model has  $91 \times 51$  horizontal grid points with a half degree resolution in a verification domain of  $100^\circ\text{W}$  to  $60^\circ\text{W}$  and  $25^\circ\text{N}$  to  $45^\circ\text{N}$ . There are ten layers in the vertical of equal  $\sigma (=p/p_s)$  thickness. The model uses a split-explicit method for temporal integration and a second-order accurate spatial finite differencing. Model physics include precipitation on the resolvable scale and parameterized boundary layer and cumulus convection.

The NMC 2.5 degree hemispheric analyses are used as the basic dataset (called NMC analysis hereafter). Because significant details in the initial conditions contained in the original rawinsonde observations may have been smoothed out by the NMC analysis algorithm, the analyses are also altered to provide a closer fit to the rawinsonde data. Original rawinsonde data are used in this enhancement of the NMC analyses (called enhanced). Forecasts are made from both the NMC analysis and the enhanced analyses to determine whether the enhancement can improve the forecasts. The Barnes analysis scheme with parameters suitable for reducing the short wavelength noise on the model grid scale is used to enhance the NMC analyses with the original soundings. Three types of lateral boundary treatments—constant, tendency damping, and temporal relaxation boundary conditions—are tested and compared. Results from forecast experiments show that the boundary treatment has a great impact on the model performance. The constant boundary condition produces an unusable forecast after 12 h as judged by the S1 scores, while the relaxation boundary condition produces an excellent forecast. The enhancement of the initial conditions has a negligible effect on predictions when reasonable boundary updates are used for the snowstorm case. The enhanced dataset produces a slightly better but still useless forecast when constant boundary conditions are used.

Numerical experiments have also been conducted to test the sensitivity of the cyclogenesis to physical processes by suppressing one or more physical processes in the model. It is found that the evaporation from the ocean modulates the location and amount of precipitation. Without the evaporation, the intensity of the cyclone remains the same but the center stays on the coast instead of staying off shore. The track of the snowstorm is such that the sensible heating from the ocean dampens the development of the cyclone by reducing the low-level baroclinicity. Without the sensible heating, the minimum surface pressure of the cyclone is 11 mb lower. The latent heating is found to be important for this case in which the maximum heating rate is  $15^\circ\text{--}20^\circ\text{C/day}$ . When latent heating is suppressed, the cyclone translates at a much reduced rate and its central pressure is 10 mb higher after two days of simulation. These results from the sensitivity tests are of course case-dependent.

### 1. Introduction

The wintertime cyclone of 10–12 February 1983 developed from a weak low pressure center over eastern Texas and produced heavy snowfalls in almost every

major city along the East Coast. The heavy snow associated with this cyclone extended from western North Carolina to Boston, creating traffic disruptions, urban dislocation and general economic losses. The synoptic situation during the period of 10–12 February 1983 has been described in detail by Sanders and Bosart (1985a,b) and Bosart and Sanders (1986). They pointed out many meteorologically interesting aspects of the snowstorm, such as the narrow snow bands,

*Corresponding author address:* Dr. Simon W. Chang, Atmospheric Physics Branch, Code 4110, Naval Research Laboratory, Washington, D.C. 20375.



moist symmetric stability, and the intense singular gravity wave.

During the period of 00Z of 10 and 12 February 1983, the low pressure system originated in Texas-Louisiana, underwent a reorganization off the Georgia-Florida coast and developed into a well-organized cyclone off Cape Hatteras. More significant deepening occurred after 00Z of 12 February 1983. The purpose of conducting a numerical simulation study of the snowstorm, concentrating on the period of 10-12 February 1983, is twofold. First, we would like to find out whether the early organizing stage of an eventually intensifying cyclone can reasonably be simulated or predicted by the NRL mesoscale prediction model. Current operational numerical models still have difficulty in predicting the timing and location of the early phase of the cyclogenesis. Specifically, it is of great interest to find how to best treat the initial data and boundary conditions to produce better forecasts. Second, it is important to isolate the contribution of various physical processes, such as sensible heating and latent heating, to the cyclogenesis and heavy snowfalls. The snowstorm case of 10-12 February 1983 is ideal because it has attracted much attention and it was carefully documented by Sanders and Bosart.

The NRL mesoscale prediction model is used to conduct the numerical experiment. As described in detail in Madala et al. (1987), the model uses primitive equations with a quasi-hydrostatic assumption and a  $\sigma$  vertical coordinate. It uses a Barnes objective analysis scheme (Barnes 1973; Koch et al. 1981), and a nonlinear, nondivergent balanced initialization. The parameterized physics in the model include convective precipitation, grid-scale precipitation, surface drag and exchanges of sensible and latent heats, convective adjustment and internal diffusion. In all, the NRL mesoscale model is quite similar to many other operational or research mesoscale models. Some differences in the model, however, warrant a discussion later in the paper.

The organization of the paper is as follows. In section 2, the synoptic situation of the snowstorm will be discussed briefly. Data source and method of analysis will be presented in section 3. The NRL mesoscale model will be introduced in section 4. In section 5, results of numerical experiments on the effects of initial-field enhancement and boundary-condition treatment will be presented. The relative importance of some physical processes will be discussed in section 6.

## 2. Data source and methods of analysis

The basic dataset is the National Meteorological Center's (NMC) 2.5-degree resolution, gridded hemispheric analyses provided every 12 h from 00Z 10 February 1983 (02/10/00Z) to 00Z 12 February 1983 (02/12/00Z). The analyses of geopotential, temperature, and the  $u$  and  $v$  wind components are on isobaric surfaces at the standard pressure levels. Relative-hu-

midity analyses are available on levels between 300 and 1000 mb. A subset of this dataset bounded by 15°N and 55°N, 110°W and 50°W, is used for this study. It is suspected that the NMC 2.5 degree analyses may necessarily contain some smoothing and that meteorological signals at small scale are sometimes not properly assimilated. Therefore, in addition to the NMC 2.5 degree analyses, original rawinsonde data are obtained from the National Climate Data Center (NCDC). The original rawinsonde data are used for the "enhancement" of analyses. It is hoped that the enhancement is capable of retaining some of these smoothed-out signals. The enhancement is done with the bilinear back interpolation to the locations of the rawinsonde observations and with the computation of residues. Because our main interest is not to test the effects of additional data but a reanalysis (or enhancement) of the same original data, no additional data, such as satellite or aircraft data, are included.

A modified Barnes objective analysis scheme (Koch et al. 1981; Koch 1983; Harms 1985; Brehme 1987), a two-step successive corrections method using Gaussian weighting (Barnes 1973), is used for the analysis. Each value on the grid of the 2.5 degree NMC analysis is treated as an observation. Many constants in the modified Barnes analysis scheme are selected subjectively (Brehme 1987) so that the divergence fields computed from the wind analyses are meteorologically meaningful. The enhancement is accomplished in the second step of the standard Barnes analysis procedure, which involves a bilinear back-interpolation of the first guess field to the locations of the original rawinsonde observations and a computation of residues between the first guess and the rawinsonde observations. This is followed by the correction of the first guess field with the obtained residues.

## 3. Synoptic situation

The rawinsonde enhanced analyses of 1000 and 500 mb surfaces at 02/10/00Z (mm/dd/hh), 02/11/00Z and 02/12/00Z are shown in Figs. 1, 2 and 3. At 02/10/00Z, the sea level pressure shows that a weak low with a central pressure of 1005 mb is located on the Louisiana coast. There is a pressure ridge extending from the Great Lakes region to the Atlantic Ocean east of the Florida peninsula. An occluded surface low with a minimum pressure of 988 mb is located to the northeast of Nova Scotia. Strong northwesterlies associated with the surface pressure gradient occupy most of the western Atlantic Ocean between 30° and 50°N, with strong cold advection over the ocean. The 500 mb analysis features mostly zonal thermal and height fields except for the short-wave trough over eastern Texas and Oklahoma.

During the period around 02/11/00Z, multiple low pressure centers form over southern Georgia. After 02/11/06Z, the low center located offshore of Georgia

as-  
North  
urban  
optic  
1983  
Bosart  
They  
spect  
ands,

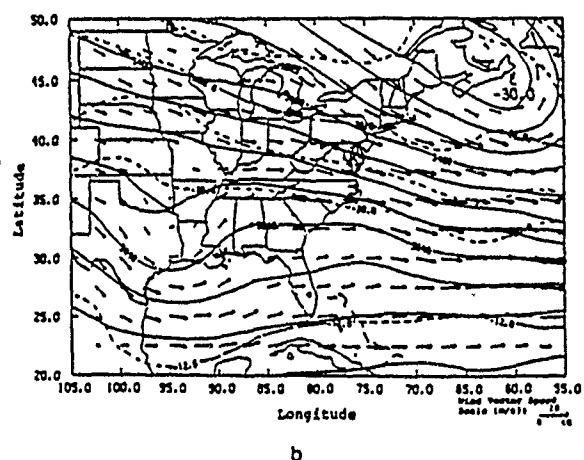
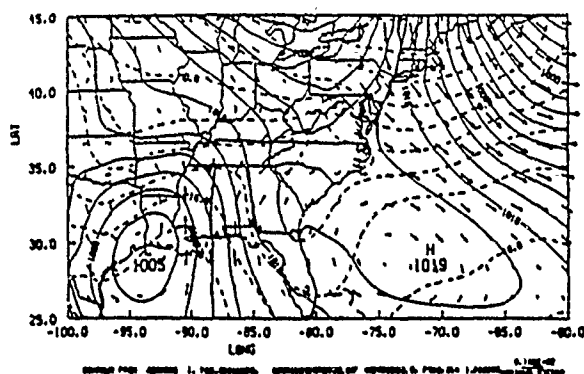


FIG. 1. (a) Rawinsonde enhanced sea level pressure (solid lines, every 2 mb), 1000-mb temperature (dashed line, every 4°C) and 1000-mb wind vector for 1983/02/10/00Z. (b) Rawinsonde enhanced geopotential height (solid lines, every 60 m), temperature (dashed lines, every 4°C) and wind vector (max. 38.4 m s<sup>-1</sup>) at 500 mb level for 1983/02/10/00Z.

reintensifies and eventually organizes into the low center off Cape Hatteras at 02/12/00Z. Due to the 2.5 degree resolution of the NMC analyses and the equally coarse rawinsonde station spacings in the enhanced analyses, the multiple centers are not resolved. The enhanced analyses at 02/11/00Z in Fig. 2 show that the surface low over eastern Texas has moved into the southeastern United States with one center of 1004 mb located in southern Georgia. The isotherms start to pack over the mid-Atlantic states at this time and strong onshore surface winds start to organize along the coast of the Carolinas. The 500 mb trough has moved into Tennessee and Alabama with southwesterly flow along the eastern seaboard. At this time, heavy precipitation is occurring over Georgia and the Carolinas. Precipitation is in the form of snow in the higher elevations of North Carolina and from Virginia to New Jersey.

By 02/12/00Z, a well-organized cyclone has formed approximately 500 km east of Cape Hatteras. The central pressure of 1003 mb is not particularly low, but

the tight isobars north of the storm have generated strong onshore flow from Virginia to New England. Heavy snowfalls occur along the coast and at the major East Coast cities from Richmond to Boston. The 500 mb trough is located over western Pennsylvania. The surface low later passed 300 km offshore of New England.

For more detailed synoptic description of the snow-storm case, readers can refer to Sanders and Bosart (1985a,b).

#### 4. The NRL mesoscale model

The model used for our study is the NRL mesoscale numerical prediction model. The model equations and numerical technique are documented in Madala et al. (1987). Only a brief description of the model is given here.

##### a. The governing equations

The governing primitive equations are in surface-pressure-weighted flux form written for curvilinear horizontal coordinates. The vertical coordinate is  $\sigma$

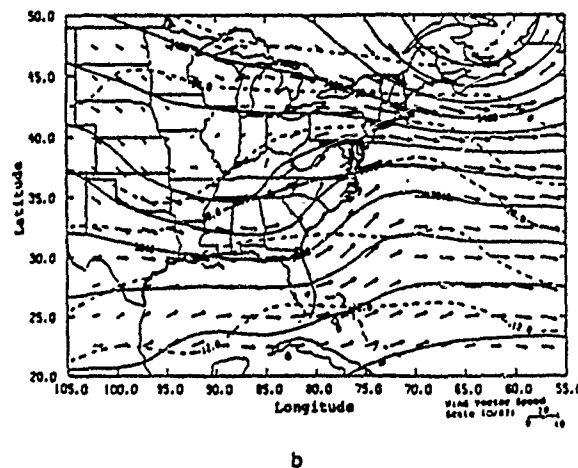
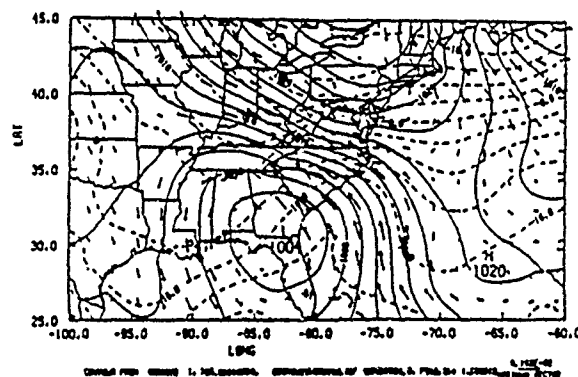


FIG. 2. (a) Same as Fig. 1a, except for 1983/02/11/00Z. (b) Same as Fig. 1b, except for 1983/02/11/00Z.

erated  
igland.  
major  
he 500  
a. The  
f New

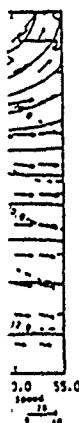
snow-  
Bosart

oscale  
ns and  
a et al.  
s given

urface-  
ilinear  
te is  $\sigma$



0 -50.0



0Z

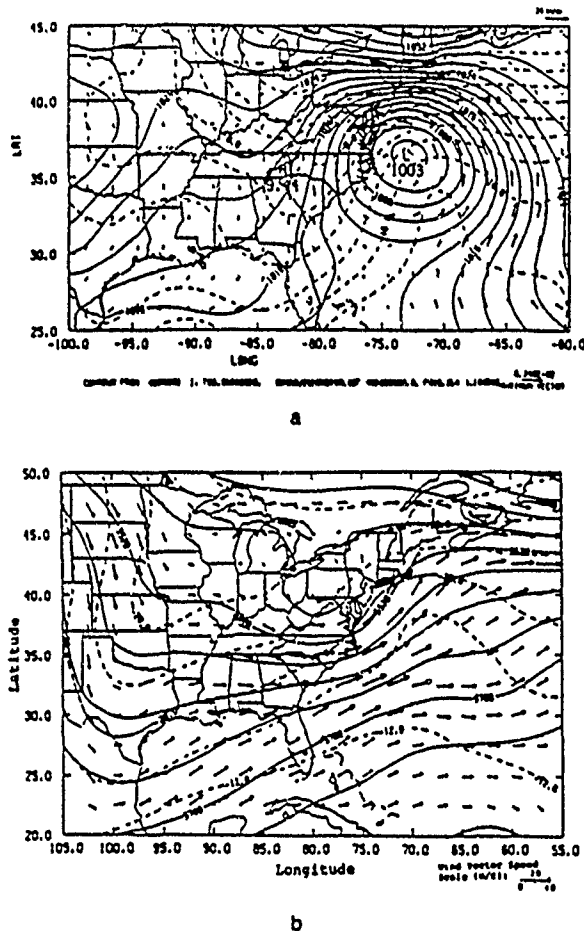


FIG. 3. (a) Same as Fig. 1a, except for 1983/02/12/00Z.  
(b) Same as Fig. 1b, except for 1983/02/12/00Z.

( $= p/p_s$ ) (Phillips 1957). The hydrostatic assumption is used.

### b. Parameterized physics

The model physics include dry convective adjustment, latent heat released in nonconvective clouds, a parameterized planetary boundary layer, convective precipitation and internal diffusion. The atmospheric radiative transfer processes are not considered in the model due to its computational complexity and the short integration range of 48 h.

Precipitation from convective clouds is parameterized with a modified Kuo scheme (Kuo 1974; Anthes 1977). Convective precipitation occurs when low-level moisture convergence exists in a convectively unstable environment. The partitioning of the latent heating and moistening, or the  $b$  factor, is determined by the column mean relative humidity. The vertical distribution of the heating is proportional to the temperature difference between the pseudoadiabatic and the environment.

Nonconvective precipitation occurs when saturation is reached on the resolvable scale. The Clausius-Clapeyron equation is used to compute the excess moisture and the isobaric heating. Depending on the height where the saturation occurs, a part of the excess moisture is assumed to precipitate into the lower model layers and to reevaporate. The remainder of the excess precipitates to the surface.

Dry convective adjustment is activated when the static energy of a layer exceeds that of the adjacent higher layer. The adjustment results in a slightly stable lapse rate while the total static energy is conserved. The adjustment can take place over several layers.

A second-order horizontal diffusion with a constant coefficient of  $4.0 \times 10^8 \text{ cm}^2 \text{ s}^{-2}$  is used in the model to suppress the computational instabilities. This yields approximately a value of 0.004 for the nondimensional diffusion coefficient  $K_H \Delta t / (\Delta x)^2$ . The small diffusion (Klemp and Lilly 1978; Anthes and Warner 1978) enables the model solution to remain nearly undamped; but some diffusion is needed in the model, no matter how small  $K_H$  is, to prevent the growth of the nonlinear instability which may deteriorate the solution after long integrations. In addition, the horizontal diffusion of temperature and mixing ratio on  $\sigma$  surfaces over mountainous terrain includes vertical diffusion. In the model, the diffusion operator  $K_H \nabla^2$  operates on the deviations of the temperature and mixing ratio from those of the standard atmosphere at the same pressure. Therefore, the horizontal diffusions of temperature and mixing ratio do not contain diffusion in the vertical direction.

For the coarse vertical resolution in the lower troposphere in the current version of the model, a bulk PBL parameterization described in Chang (1981) is most expedient. In order to provide the most clear-cut difference in our no-sensible-heating and no-evaporation experiments, constant exchange and drag coefficients are applied. The drag coefficient is 0.003 over the land and 0.0015 over the ocean. The exchange coefficients for sensible and latent heat are 0 over the land and 0.002 over the ocean. By not allowing sensible and latent heats over the land, the important diurnal variations are precluded from the simulations. This is only justifiable because our main interest in this comparison study is the differences between various experiments. The monthly mean sea surface temperature (Reynolds 1982) is used, which gives a weak signature of the Gulf Stream. The terrain at each model grid point is defined as the mean terrain height within a half degree box based on the Navy's 10 minute data.

### c. Numerics

The finite difference form of the governing equations is of second-order accuracy in space. A split-explicit scheme (Madala 1978) with the Brown and Campana (1978) filter is used for temporal integration. In this

scheme, the natural (or eigen) modes of the numerical model are obtained from the linearized governing equations. The spectral equations corresponding to the eigenmodes are integrated with different time intervals. The eigenmodes are then combined at the long interval to compute the nonlinear advection and physics. The method allows a time interval equal to four times that of a conventional leapfrog scheme.

The C grid (Arakawa and Lamb 1977) in the model has a "uniform" resolution of  $\frac{1}{2}$  degree in longitude and latitude. It is known that the impact of lateral boundaries increases with time in the limited-area forecast (e.g., Orlanski and Katzfey 1987). A rather small domain of 20 degrees latitude and 40 degrees longitude is selected for this study to test the lateral boundary updating technique without costly long-time integration. The interior of the model covers a domain of  $100^{\circ}\text{W}$  to  $60^{\circ}\text{W}$  and  $25^{\circ}\text{N}$  to  $45^{\circ}\text{N}$ . There are five extra points on each boundary for the boundary condition treatment. The model has ten vertical layers with a uniform thickness of  $\Delta\sigma = 0.1$ . There are a total of  $91 \times 51 \times 10$  grid points in the model.

#### d. Boundary conditions

One of the uncertainties in a limited-area model most difficult to resolve is the treatment of the lateral boundaries. Most of the known lateral boundary conditions for the limited area model are mathematically ill-posed. Most boundary treatments are engineering efforts which involve overspecifications of boundary parameters. The available techniques include a variety of blending of tendency damping, smoothing, and relaxation (Shapiro 1970; Perkey and Kreitzberg 1976; Baumhefner and Perkey 1982; Davies and Turner 1977; Orlanski and Katzfey 1987). It is generally agreed that the benefit of higher resolution in the limited area model can be offset by the improper treatment of the boundaries.

Many current limited area models try to minimize the impact of boundary conditions by employing large domains. The purpose of our tests of the boundary treatment is to determine the timing and the degree of deterioration of the model performance due to various boundary treatments. This task can be accomplished economically with a model that has a relatively small domain. Once the best boundary treatment is found, the deterioration of the forecasts in the interior of the model can be further reduced by expansion to a large domain. For our tests, a small domain of 20 degrees latitude and 40 degrees longitude is chosen for the model. Three fundamentally different treatments are tested:

- (i) A constant boundary condition. The initial boundary values are used throughout the integration. This resembles, to a certain degree, a scenario of a total failure of a large scale-forecast in an operational center.
- (ii) A damping of the tendency. The tendencies of

all dependent variables within five grid lengths of the boundaries are replaced by (Perkey and Kreitzberg 1976):

$$\frac{\delta X}{\delta t} = (1 - \alpha) \left( \frac{\delta X}{\delta t} \right)_m + \alpha \left( \frac{\delta X}{\delta t} \right)_L, \quad (1)$$

where  $X$  represents the dependent variables,  $(\delta X/\delta t)_m$  represents the tendencies as computed by the model, and  $(\delta X/\delta t)_L$  represents the large-scale tendencies. The weighting parameter  $\alpha$  is a linearly varying constant between 0.2 (at the fifth point from the boundary) and 1.0 (at the boundary). In this study, the large-scale tendencies are obtained from analyses at 12 h intervals. This resembles a scenario in an operational forecast in which the large scale prediction of tendencies is perfect. In the above, the tendencies are held unchanged during the 12 h interval.

(iii) A temporal relaxation. In this scheme, the values within five grid lengths of the boundaries are relaxed toward the large-scale analyses by:

$$\frac{\delta X}{\delta t} = (1 - \alpha) \left( \frac{\delta X}{\delta t} \right)_m + \lambda (X_0 - X), \quad (2)$$

where the parameter  $\lambda$  is the relaxation frequency and the large scale values  $X_0$  are from analyses at 12 h intervals. It is through the last term on the right-hand side of (2) that the forecast fields  $X$  are relaxed toward the analyzed 12, 24, 36 and 48 h values.

#### 5. Forecast experiments with various initial analyses, initializations and boundary conditions

A total of nine numerical experiments have been conducted using different combinations of initial analyses and boundary conditions. The characteristics of all the experiments are summarized in Table 1, along with the 48 h forecast root-mean-square (rms) errors and S1 scores (see Appendix for definition). The two initial analyses tested are the NMC 2.5 degree analysis only and the analysis enhanced with the original rawinsonde observations. The analysis procedure used to produce the two analyses has been discussed in section 3. The three different boundary conditions tested, constant boundary conditions, a tendency-damping method, and the relaxation method, are discussed in section 4. In supplementary numerical experiments, the effect of the initialization procedure is studied by comparing the predictions made with initialized and analyzed (unbalanced) fields. It is found that the prediction started from unbalanced fields contains initial oscillations of the surface pressure with a magnitude of several mbs. These oscillations dissipate in the first 12 h of the forecast, however, due to the damping of the high frequency gravity waves by the split-explicit time integration scheme (Sashegyi and Madala 1988). The initialized and analyzed (unbalanced) predictions are not noticeably different in terms of 24 and 48 h

TABLE 1. 48 h forecast statistics. (PK represents Perkey and Kreitzberg (1976). Exps. 5-9 use relaxation boundary where  $\lambda$  is the relaxation coefficient and  $f$  the Coriolis frequency. The rms errors for temperature, wind and height are for 500-mb level.)

Expt	Initial data	Boundary treatment	$P_1$ (mb)	Rms errors			S1 score
				Temperature (°C)	Wind	Height (m)	
1	NMC	constant	12.5	3.9	16.7	79	101
2	enhance	constant	12.8	3.8	16.4	78	84
3	NMC	PK	4.1	1.9	7.2	52	54
4	enhance	PK	5.9	2.7	9.0	55	60
5	enhance	$\lambda = 10(1 - \alpha)f$	2.8	2.0	7.7	48	47
6	enhance	$\lambda = 5(1 - \alpha)f$	2.8	2.0	7.7	50	46
7	enhance	$\lambda = 2f$	2.7	2.0	7.5	51	44
8	enhance	$\lambda = f$	2.6	2.0	7.5	51	43
9	NMC	$\lambda = f$	2.2	1.8	7.1	49	29

performance statistics. The performance statistics listed in Table 1 are pertinent for the unbalanced initial fields, i.e., forecasts start from unbalanced fields, using unbalanced boundary values and compared with unbalanced analyses.

It is obvious that the worst 48 h predictions among the nine experiments are produced with constant boundary conditions (exps. 1 and 2). The forecasts produced in exps. 1 and 2 (not shown) are not realistic at all, with low center located way south of the verification location. The best prediction starts from the NMC analysis using a relaxation boundary condition with a relaxation factor of  $f$  (exp. 9). It is common knowledge that a prediction with an S1 score (see Appendix) of 30 is a nearly perfect prediction while a prediction with an S1 score of 80 is almost useless (Anthes 1983). When the time-dependent boundary conditions are used, either using the Perkey-Kreitzberg method or the relaxation method, the S1 scores improved dramatically. The boundary effects are considerable in this model with a relatively small domain and for this case with strong pressure tendencies along the boundaries. Therefore, the updating of the boundary values by any method results in an improvement of the prediction. The 48 h S1 scores for exps. 3 through 9 are at least 24 points less than that of exp. 2. In exps. 3 and 4, where the Perkey and Kreitzberg (1976) type boundary-value blending is used, useful forecasts are generated with S1 scores of 54 and 60 respectively. The rms errors in both experiments are also significantly lower than the constant-boundary experiments. Here with the Perkey and Kreitzberg boundary treatment, the forecast made from NMC analysis (exp. 3) is even slightly better than that from the enhanced analysis (exp. 4).

The relaxation boundary condition is used in exps. 5-8 with different relaxation coefficients. The 48 h error statistics are very similar among the four forecasts; but the strongest relaxation produces unrealistically large gradients normal to the southern boundaries, which, in turn, produces precipitation bands along the southern boundary. Therefore, exp. 8 with  $\lambda = f$  is judged

the best among the five experiments starting from the enhanced analysis. Davies and Turner (1977) argued that the relaxation boundary treatment retards the phase speed of meteorologically important waves less than the Perkey-Kreitzberg treatment. Here we are dealing with a complex real data case, however, Davies and Turner's acclaim is still borne out by the forecast statistics.

As for the usefulness of the enhanced dataset, there seems to be no clear-cut conclusion among the experiments. For example, a comparison between exps. 8 and 9 may indicate a negative impact of the enhanced analysis, contrary to the positive impact that may be inferred from the comparison between exps. 1 and 2. Here, the enhanced analysis in exp. 8 produces an inferior prediction in terms of rms error and S1 score to the more smoothed NMC analysis. The latter produces a very low 48 h S1 score of 29. The lack of impact of the rawinsonde-data enhancement on the 24 and 48 h forecast, either positive or negative, turns out to be a common behavior of many mesoscale forecast systems (e.g., Orlanski and Katzfey 1987; NCAR 1988) with comparable horizontal resolutions as our model. Small and subtle differences between the forecasts made from the NMC and enhanced analyses are mostly masked by the boundary conditions and model-produced atmospheric structures.

## 6. The control experiment

Experiment 9 is the best forecast and will serve as the control experiment to test various physical processes. Figures 4 and 5 show the 500 mb and surface forecasts at 24 and 48 h, valid for 2/11/00Z and 01/12/00Z, respectively. At 24 h, the model seems to have developed two low pressure areas, one located over the Florida Panhandle and the other, just off the eastern Florida coast. This is in contrast to the analysis in Fig. 2a, which shows one low center at the Georgia/Florida border due to the coarse resolution of the analyses. The strong north-south temperature gradient from Cape Hatteras to Long Island is well simulated. The





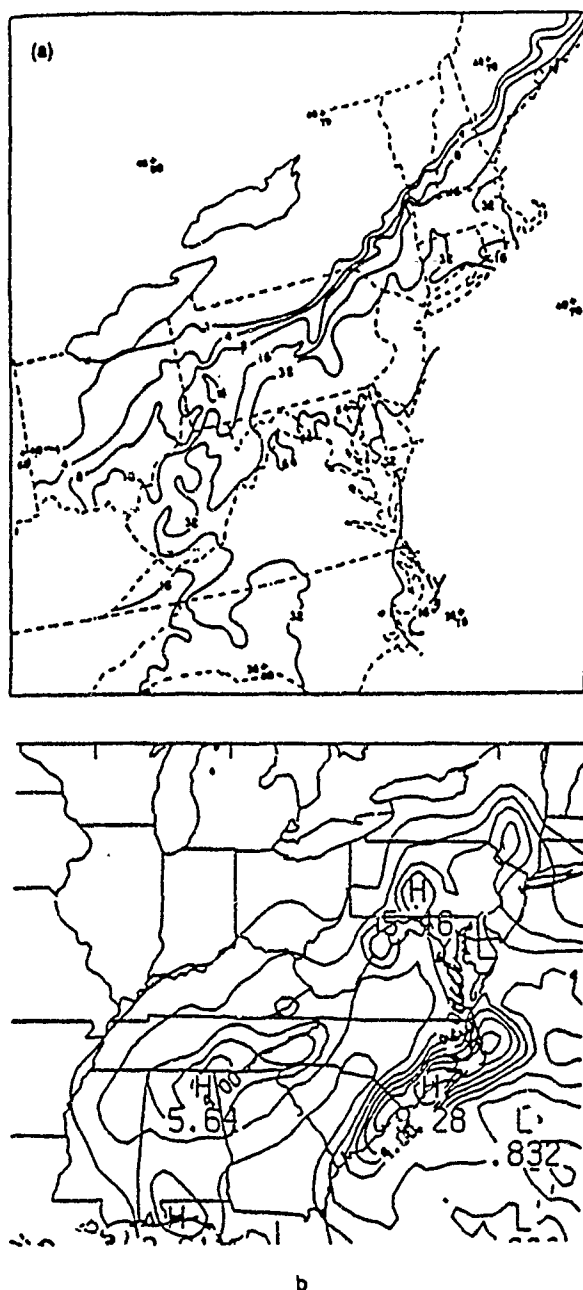


FIG. 6. (a) Total rain and/or equivalent liquid depth of frozen precipitation (mm) 10-12 Feb. 1983 (Sanders and Bosart 1985a). (b) Model forecast 48 h accumulated precipitation amount (cm) valid for 02/12/00Z.

02/12/00Z. Except for the heavy precipitation band near the southern boundary, which is probably due to the boundary treatment discussed earlier, the predicted heavy precipitation mainly occurs along the Appalachian range and along the Carolina coast, where the terrain lifting and the frictional induced convergence are the strongest. Regions of maximum precipitation in western Maryland, eastern West Virginia and south-

east Pennsylvania are pinpointed in the forecast. Unfortunately, the predicted precipitation along the Carolina coast and over the ocean cannot be verified by Fig. 6a. In their numerical study of the Presidents' Day cyclone, which had a similar storm track to the present case, Orlanski and Katzfey (1987) showed a similar precipitation pattern along the Carolina coast.

In all, the East Coast snowstorm of 10-12 February 1983, seems to have been realistically simulated by exp. 9, in spite of relatively simple physical parameterizations. To investigate the contribution of various physical processes that contribute to the cyclogenesis, three additional numerical experiments are conducted, in which one or more of the physical processes are suppressed in each experiment.

## 7. Sensitivity to physical processes

### a. Effects of evaporation

To test the effect of evaporation, expt. NOE is conducted in which the evaporation from the ocean is suppressed. Figures 7 and 8 show the 48 h (valid for 2/12/00Z) surface prediction and precipitation amount. The surface low in exp. NOE is located in Maryland Eastern Shore with a minimum pressure of 1001 mb. The concentration of the isotherms to the north and south of the low center fits the description of a cold/warm front coinciding with the coastline. The most striking difference in the precipitation pattern is the absence of precipitation along the coast and over the ocean that is evident in the control (exp. 9). The maximum precipitation along the Appalachian ridges, however, is higher than the control due to the more landward location of the low pressure center and intrusion of the moist onshore easterly flow. These suggest for this case that the evaporation has great influence on the location and pattern of precipitation although it does not greatly affect the intensity of the cyclone. Without the evaporation from the ocean to provide enough convective instability over the ocean, the low pressure remains close to the coast where the sea-land

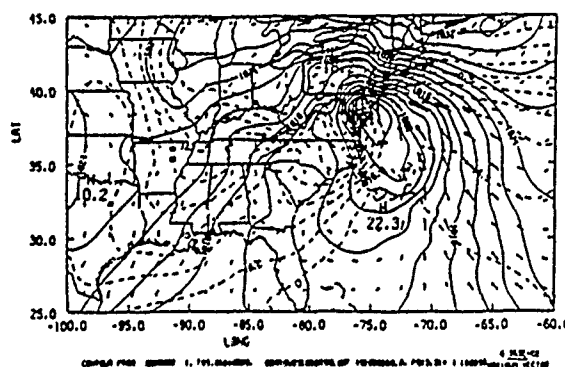


FIG. 7. 48 h surface forecast valid for 2/12/00Z for exp. NOE (no evaporation).

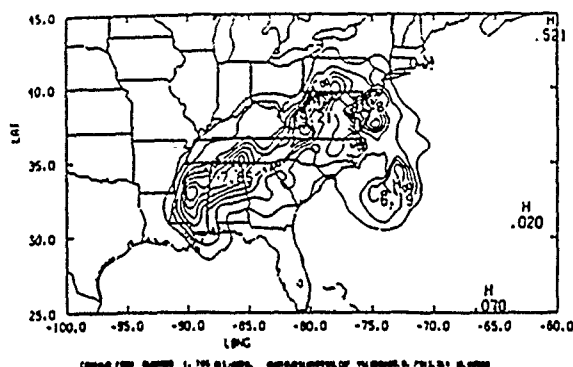


FIG. 8. 48 h accumulated total precipitation for exp. NOE.

temperature contrast provides the strongest baroclinicity for growth.

#### b. Effects of sensible heating

When the sensible heating from the ocean is suppressed in exp. NOS, the central pressure of the cyclone deepens to 990 mb at 48 h (Fig. 9). The location is only slightly to the north of that in the control. The cold air outbreak to the west and southwest of the cyclone is much stronger than the control and advances well into the Atlantic Ocean over the Gulf Stream. Therefore, the cyclogenesis in NOS is more vigorous than that of control expt. 9 as the low pressure centers in both cases move offshore. Also, the area to the southwest of the low pressure with strong temperature gradients in NOS (Fig. 9) is much larger than that in the control (Fig. 5a). It is apparent for this storm, the sensible heating, which is mainly from the Gulf Stream, occurs mostly in the cold sector of the cyclone after 02/11/00Z as the low center moves from Georgia to offshore of Virginia. Therefore, the sensible heating acts to decrease the low-level baroclinicity and reduce the strength of the cyclogenesis. The warm sector to the east of the low center in NOS is warmer than the control, due to the stronger northward advection in the more intense cyclone of the warmer, low-latitude air.

The damping effect of the sensible heating on the East Coast cyclogenesis has also been found by others, such as Danard and Ellenton (1980) and Nuss and Anthes (1987). The sensible heating, however, can contribute positively to the cyclogenesis if its horizontal distribution is in phase with the lower tropospheric temperature distribution. By evaluating operational forecasts of 29 rapidly deepening cyclones over the western Atlantic Ocean, Davis and Emanuel (1988) concluded that the latent and sensible heating from the ocean can, in the mean, enhance the explosive cyclogenesis. Chen and Dell'Osso (1987) found that the surface energy fluxes are important in coastal cyclogenesis. The surface fluxes, however, had no impact on an explosive cyclogenesis in Eastern Pacific (Kuo and Reed 1988). It is apparent that the relative loca-

tions of the maximum surface fluxes and the cyclone are crucial in determining the positive or negative contribution of the surface fluxes to the development of the cyclone.

The precipitation pattern in exp. NOS (not shown) differs from the control experiment in that the precipitation is more concentrated along the coastal baroclinic zone. In exp. NOS, the moist easterlies north of the cyclone turn more sharply due to the strong pressure gradient, becoming northerlies west of the cyclone center. Thus, the precipitation over the Appalachian Mountains is reduced.

#### c. The effect of latent heating

Experiment NOL is conducted with the latent heating suppressed, including both the convective heating and the large scale heating. As shown by the 48 h surface forecast in Fig. 10, the latent heating has a significant effect on the development of the cyclone. At 48 h, the surface low is located just off the South Carolina coast with a central pressure of 1011 mb. The cyclone in this case has a slower speed and is 10 mb higher than that of the control. Accordingly, the latent heating in our control exp. must be responsible for a 10 mb deepening. Nuss and Anthes (1987) found a 4 mb difference when latent heating was suppressed, whereas a 13 mb difference was found in Orlanski and Katzfey (1987). In our control experiment, the maximum heating rate between 24–48 h is  $15^{\circ}\text{--}20^{\circ}\text{C day}^{-1}$ , which is stronger than the rate of  $5^{\circ}\text{C day}^{-1}$  in Nuss and Anthes (1987) but approaches the  $25^{\circ}\text{C day}^{-1}$  found in the western Pacific explosive cyclogenesis case of Liu and Elsberry (1987). Our 10 mb difference between the control and exp. NOL is thus very reasonable. Without latent heating, the temperature gradient in front of the midlevel trough and the steering current cannot be maintained, resulting in a slower translating speed of the cyclone. The importance of latent heating in intensifying the surface low, in maintaining the upper-level jet, and in the vertical coupling within the cyclone has also been found in many recent numerical studies of marine cyclogenesis (e.g., Chen and

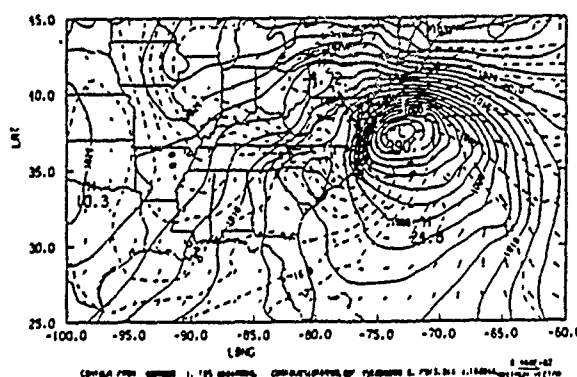


FIG. 9. Same as Fig. 7, except for exp. NOS (no sensible heat).



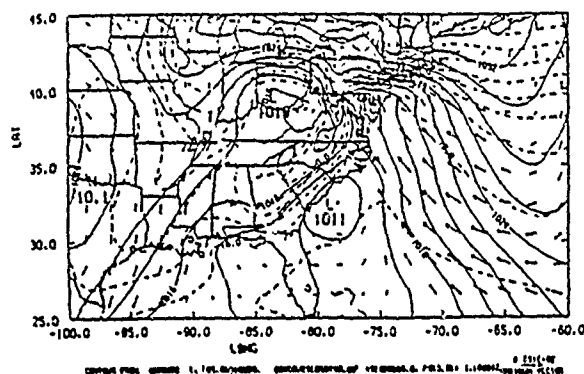


FIG. 10. Same as Fig. 7 except for exp. NOL (no latent heat).

Dell'Osso 1987; Chang et al. 1987; Kuo and Reed 1988; Pauley and Smith 1988).

## 8. Discussion

The forecast experiments presented here have been conducted with the NRL mesoscale model. In terms of parameterized physics, resolution, and domain size, the model is intentionally made to be rather conservative so that the results are more trackable and model-independent. The results from the experiments with differing boundary conditions confirm that the boundary treatment is of great importance in the mesoscale model prediction. Regardless of the method of updating, the predictions with boundary updating are much improved compared to the nonupdating cases, exps. 1 and 2. The effect of the enhanced analyses is not clear-cut: with boundary updating, NMC produces better forecasts, but without updating, the enhanced analysis yields a better forecast. It is perhaps because the snowstorm develops from instabilities that are already embedded in the large-scale environment that additional details in the description of the initial state are not needed. Also, our experimentation may be hindered by the fact that the NMC analyses already contain the original rawinsonde observations, although there are significant statistical differences between the NMC and the enhanced analyses (Brehme 1987). Thus it would be useful to test if "additional" data, that are not included in the basic dataset, can improve model performance. Efforts are now being undertaken to conduct such study using the GALE dataset.

The sensible and latent heating from the warmer Atlantic Ocean can enhance or dampen the development of the cyclone depending on the phasing. The evaporation supplies moisture for convection over the ocean. Without the available moisture over the ocean, the cyclone develops on the coastline where the sea-land temperature contrast provides the greatest low-level baroclinicity. The sensible heating for this 10–12 February 1983 snowstorm dampens the development of the cyclone while it undoubtedly reduces the low-level stability. The track of the snowstorm is such that

the sensible heating warms up the cold sector, which decreases the thermal advection and vertical motion in the baroclinic zone. As a result, the model cyclone is 11 mb deeper in the absence of sensible heating. In the megalopolitan snowstorm of 10–12 February 1983, latent heating apparently has an important contribution. Without the release of latent heating, the cyclone is weaker and becomes disassociated from the upper-level flow.

**Acknowledgments.** We thank Professor Frederick Sanders for a critical review of the manuscript and many helpful suggestions. The research is supported by the Accelerated Research Initiative "Heavy Weather at Sea" program of the Naval Research Laboratory. The second author was also partially supported by NSF Grant ATM 83-11812.

## APPENDIX

### S1 Score

S1 score, perhaps the most commonly used measure of forecast skill in mesoscale or synoptic scale models, is defined as (Teweles and Wobus 1954; Anthes 1983):

$$S1 = 100 \frac{\sum |e_G|}{\sum |G_L|},$$

where  $e_G$  is the error of the forecast pressure difference, and  $G_L$  is the maximum of either the observed or forecast pressure difference between two points. The summation is over all or selected model grid points or observations in the verification domain. In this paper, the S1 scores are summation over model grid points, excluding the five-point boundary zone along each lateral boundary.

## REFERENCES

- Anthes, R. A., 1977: A cumulus parameterization scheme utilizing a one-dimensional cloud model. *Mon. Wea. Rev.*, 105, 270–286.
- , 1983: Regional models of the atmosphere in middle latitudes. *Mon. Wea. Rev.*, 111, 1306–1335.
- , and T. T. Warner, 1978: Development of hydrodynamic models suitable for air pollution and other meteorological studies. *Mon. Wea. Rev.*, 106, 1045–1078.
- Arakawa, A., and V. R. Lamb, 1977: Computational design of the basic dynamic process of the UCLA general circulation model. *Methods in Computational Physics*, Vol. 17, Academic Press, 173–265.
- Barnes, S. L., 1973: Mesoscale objective map analysis using weighted time-series observations. NOAA Tech. Memo., ERL NSSL-62, Norman, OK, 60 pp.
- Baumhefner, D. P., and D. J. Perkey, 1982: Evaluation of lateral boundary errors in a limited-domain model. *Tellus*, 34, 409–428.
- Bosart, L. F., and F. Sanders, 1986: Mesoscale structure in the megalopolitan snowstorm of 11–12 February 1983. Part III: A large amplitude gravity wave. *J. Atmos. Sci.*, 43, 924–939.
- Brehme, K. A., 1987: A method of objective analysis for meteorological fields for use in a numerical weather prediction model. M.S. thesis, Department of Marine, Earth and Atmospheric Sciences, North Carolina State University, Raleigh, NC, 123 pp.

- Brown, J. A., Jr., and K. A. Campana, 1978: An economical time differencing system for numerical weather prediction. *Mon. Wea. Rev.*, 106, 1125-1136.
- Chang, C. B., D. J. Perkey and W.-D. Chen, 1987: Observed dynamic structure of an intense oceanic cyclone. *Mon. Wea. Rev.*, 115, 1127-1139.
- Chang, S. W., 1981: Test of a planetary boundary layer parameterization based on a generalized similarity theory in tropical cyclone models. *Mon. Wea. Rev.*, 109, 843-853.
- Chen, S.-J., and L. Dell'Osso, 1987: A numerical case study of east Asian coastal cyclogenesis. *Mon. Wea. Rev.*, 115, 477-487.
- Danard, M. B., and G. E. Ellenton, 1980: Physical influences on east coast cyclogenesis. *Atmosphere-Ocean*, 18, 65-82.
- Davies, H. C., and R. E. Turner, 1977: Updating prediction models by dynamical relaxation: an examination of the technique. *Quart. J. Roy. Soc.*, 103, 225-245.
- Davis, C. A., and K. A. Emanuel, 1988: Observational evidence for the influence of surface heat fluxes on rapid maritime cyclogenesis. *Mon. Wea. Rev.*, 116, 2649-2659.
- Harms, D. E., 1985: Application of an objective analysis scheme to mesoscale observational network design. M.S. thesis, North Carolina State University, Raleigh, NC, 91 pp.
- Klemp, J. B., and D. K. Lilly, 1978: Numerical simulation of hydrostatic mountain waves. *J. Atmos. Sci.*, 35, 78-107.
- Koch, S. E., 1983: An interactive Barnes objective scheme for use with satellite and conventional data. *J. Climate Appl. Meteor.*, 22, 1487-1503.
- , M. des Jardins and P. J. Kocin, 1981: The Gempak Barnes objective analysis scheme. NASA Tech. Memo. 83851, NASA/GLAS, Greenbelt, MD, 56 pp.
- Kuo, H. L., 1974: Further studies of the parameterization of the influence of cumulus convection on large scale flow. *J. Atmos. Sci.*, 31, 1232-1240.
- Kuo, Y.-H., and R. Reed, 1988: Numerical simulation of an explosively deepening cyclone in the Eastern Pacific. *Mon. Wea. Rev.*, 116, 2081-2105.
- Liu, C.-S., and R. L. Elsberry, 1987: Heat budgets of analyses and forecasts of an explosively deepening maritime cyclone. *Mon. Wea. Rev.*, 115, 1809-1824.
- Madala, R. V., 1978: Efficient time integration scheme for atmosphere and ocean models. *Finite-Difference Techniques for Vectorized Fluid Dynamics*. D. L. Book, Ed. Springer-Verlag, 56-70.
- , S. W. Chang, U. C. Mohanty, S. C. Madan, R. K. Paliwal, V. B. Sarin, T. Holt and S. Raman, 1987: Description of Naval Research Laboratory limited area dynamical weather prediction model. NRL Tech. Rep. 5992, Washington, D. C. 131 pp.
- NCAR, 1988: *Proc., Workshop on Limited Area Modeling Intercomparison*, Boulder, CO.
- Nuss, W. A., and R. A. Anthes, 1987: A numerical investigation of low-level processes in rapid cyclogenesis. *Mon. Wea. Rev.*, 115, 2728-2743.
- Orlanski, I., and J. J. Katzfey, 1987: The sensitivity of model simulations for a coastal cyclone. *Mon. Wea. Rev.*, 115, 2792-2821.
- Pauley, P. M., and P. J. Smith, 1988: Direct and indirect effects of latent heat release on a synoptic-scale wave system. *Mon. Wea. Rev.*, 116, 1209-1235.
- Perkey, D. J., and C. W. Kreitzberg, 1976: A time-dependent lateral boundary scheme for limited-area primitive equation model. *Mon. Wea. Rev.*, 104, 744-755.
- Phillips, N. A., 1957: A coordinate system having some special advantage for numerical forecasting. *J. Meteor.*, 14, 184-185.
- Reynolds, R. W., 1982: Monthly averaged sea surface temperature climatology. NOAA Tech. Rep. NWS-31, Washington, D.C.
- Sanders, F., and L. F. Bosart, 1985a: Mesoscale structure in the megalopolitan snowstorm of 11-12 February 1983. Part I: Frontogenetical forcing and symmetric instability. *J. Atmos. Sci.*, 42, 1050-1061.
- , and —, 1985b: Mesoscale structure in the megalopolitan snowstorm of 11-12 February 1983. Part II: Doppler radar study of the New England snowband. *J. Atmos. Sci.*, 42, 1398-1407.
- Sashegyi, K. D., and R. V. Madala, 1988: Initialization with the NRL mesoscale numerical model. Preprint, *Eighth Conference on Numerical Weather Prediction*, Baltimore, Amer. Meteor. Soc., 778-781.
- Shapiro, R., 1970: Smoothing, filtering, and boundary effects. *Rev. Geophys. Space Phys.* 8, 359-387.
- Teweles, S., and H. Wobus, 1954: Verification of prognostic charts. *Bull. Amer. Meteor. Soc.*, 35, 455-463.

## **APPENDIX B**

### **Preliminary Results from Real Data Experiments with the NRL Mesoscale Numerical Model**

## PRELIMINARY RESULTS FROM REAL DATA EXPERIMENTS WITH THE NRL MESOSCALE NUMERICAL MODEL

KEITH D. SASHEGYI

SIMON W. CHANG

RANGARAO V. MADALA

Science Applications Int. Corp.  
P.O. Box 1303, McLean, VA 22102

Atmospheric Physics Branch  
Naval Research Laboratory  
Washington, D.C. 20375

## ABSTRACT

The Naval Research Laboratory's Limited Area Weather Prediction model uses an efficient split-explicit scheme to integrate in time. The split-explicit scheme itself is shown to greatly reduce the amplitude of the unwanted external gravity wave oscillations in the first three to four hours of integration. A static non-linear initialization procedure provides a balanced initial state, except for an initial adjustment of the vertical motion in the first five hours of integration. Examples of model forecasts are shown for the cases of an explosive cyclogenesis on February 10-12, 1983 and for a cold-air damming and coastal front event of January 23-25, 1986 during GALE.

Keywords: Limited Area Numerical Weather Prediction, Split-explicit, Gravity Wave Oscillations, Dynamical and Non-linear Static Initialization, Forecast, GALE

from 22.5°S to 47.5°N in latitude and 102.5°W to 57.5°W in longitude. An enveloped topography is derived from the U.S. Navy's global 10 minute elevation data using the grid heights plus one standard deviation. Climatological 1 degree resolution mean sea surface temperatures from Reynolds (Ref. 7) for the month of interest are interpolated to the model grid. The model includes large scale precipitation and a cumulus parameterization using a modified Kuo scheme. Unstable lapse rates are removed by a dry convective adjustment scheme. The boundary layer is parameterized using a drag coefficient formulation. The boundary conditions of Perkey and Kreitzberg (Ref. 6) are used to update the large scale conditions at the horizontal boundaries during the integration of the model. A nudging technique or one way interaction technique is also being used to update the variables at the horizontal boundaries.

## 1.2 Analysis and Initialization

## 1. INTRODUCTION

A limited area numerical weather prediction system has been developed to study the development of extratropical cyclones, which occurred along the East coast of the U.S. during the Genesis of Atlantic Lows Experiment (GALE). The Naval Research Laboratory's primitive equations model (Ref. 5) uses sigma coordinates and incorporates topography and physical parameterizations of the boundary layer and precipitation processes. The model is integrated in time using the efficient split-explicit method (Ref. 4). A static non-linear initialization procedure provides a balanced initial state. The effect of the split-explicit scheme and the non-linear initialization procedure in reducing gravity wave oscillations in the model are presented. Real data experiments have been conducted with selected GALE and other cyclogenesis cases.

## 1.1 Model Description

In the horizontal, an Arakawa C grid is used with 0.5 degree resolution. The finite difference scheme is a second order quadratic conserving scheme. In the vertical, ten layers of equal  $\sigma$  thickness are used. The domain of the model is

A first guess analysis is provided by a National Meteorological Center (NMC) 2.5° hemispheric analysis. The NMC 2.5° resolution hemispheric analysis is interpolated to the horizontal model grid using cubic polynomial interpolation to provide a first guess analysis. Conventional observations and available supplementary observations (e.g. from GALE) are incorporated by Brehme (Ref. 2) using the Barnes (Ref. 1) scheme to enhance this first guess analysis.

The analyzed vorticity on pressure surfaces is used to first calculate the non-divergent component of the wind. A first guess of the surface pressure and temperature is found by interpolation to the model topography. The non-divergent wind is interpolated to the surface, and a consistent surface pressure is then derived from a non-linear balance, using the first guess surface temperature and pressure for the non-linear terms. The non-divergent wind, temperature and humidity are then interpolated to the model sigma levels and a static initialization of the mass field performed using the non-linear mass balance equation in sigma coordinates. A vertical mode initialization scheme following that of Bourke and McGregor (Ref. 3) is being adapted for use with our model.

### 1.3 Split-Explicit Time Integration

In the split-explicit method of Madala (Ref. 4), a centered difference scheme (except for diffusion which uses forward differencing) with a time step of 150 s, appropriate for the Rossby modes, is used to step the model variables once forward in time. Gravity wave amplitudes for the deviations of the divergence and the generalized geopotential on sigma surfaces  $\phi = p_s[\phi + RT^* - \phi^*]$  are integrated at a smaller time steps for the external (37.5 s) and the first two internal vertical modes (75 s and 150 s). The average of these deviations, over a interval of twice the large time step, is then used to correct the explicit computation of the variables. Besides providing a 4 to 5 times saving in computer time over explicit methods, the averaging of the lower gravity wave eigenmodes may be expected to act as a partial filter of the higher frequency gravity waves.

## 2. INITIALIZATION EXPERIMENTS

To test the effect of the non-divergent initialization and the split-explicit time integration scheme in reducing the unwanted high frequency oscillations in the model, the model is integrated with initialized and uninitialized data both with the split-explicit scheme described above and with an explicit time integration of 30 s. The NMC 2.5 degree hemispheric analysis for 12Z January 23, 1986 is used to start the integrations for these experiments. For the boundary conditions the Perkey and Kreitzberg scheme is used with twelve hour tendencies derived from initialized analyses. Time series of surface pressure and vertical motion  $\dot{\sigma}$  in sigma coordinates at selected

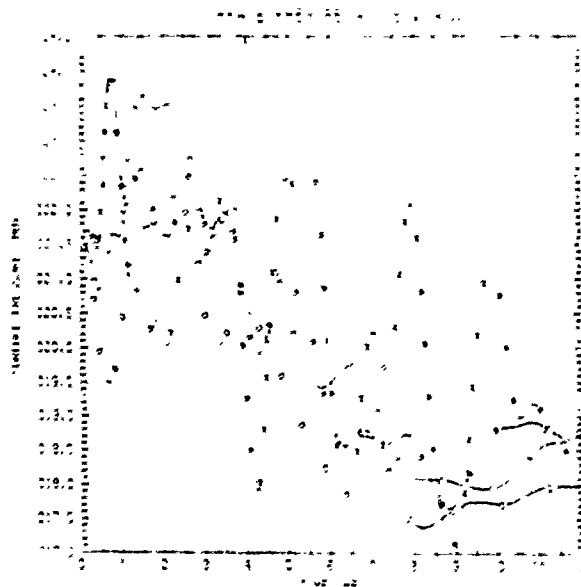


Figure 1. Time series of surface pressure in mb at a grid point at 35°N and 90°W during the first 12 hours of integration. Curves are for uninitialized initial conditions for an explicit integration in time (Curve A) and a split-explicit integration (Curve B); for split-explicit integrations with a non-divergent initial condition (Curve C) and a non-linear mass balance (Curve D).

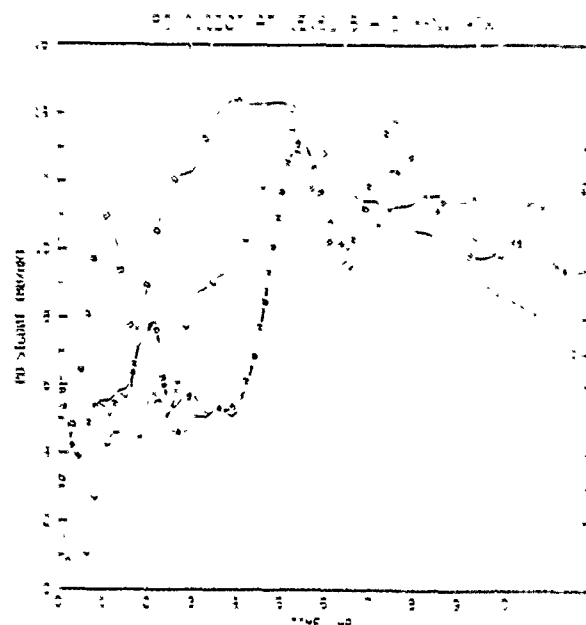


Figure 2. As in Figure 1 except for the vertical motion (in sigma coordinates) at  $\sigma = 0.5$  multiplied by a standard pressure  $p_0$  of 1000 mb. Units are in mb/hour.

points were compared for four experiments. In Figures 1 and 2 we compare time series for the first twelve hours of integration for surface pressure and for the vertical motion  $p_0\dot{\sigma}$  at level  $\sigma = 0.5$  for a grid point at 35°N and 90°W, where  $p_0 = 1000$  mb.

### 2.1 Explicit Integration

The model is integrated with a leapfrog scheme for 12 hours with a time step of 30 s. Oscillations of surface pressure of as much as 5 to 8 mb of amplitude and periods of 1 to 2 hours are observed in the first 12 hours of integration. Curve A in Figure 1 shows these typical oscillations. Curve A in Figure 2 shows the vertical motion  $p_0\dot{\sigma}$  at  $\sigma = 0.5$ . The curve shows a typical rapid adjustment (increase in this figure) between hours 4 to 6 of the integration with smaller oscillations of periods of 2 to 4 hours superimposed. The higher frequency oscillations in surface pressure are largely due to the barotropic external gravity mode while the adjustment and oscillations in  $\dot{\sigma}$  in the middle troposphere are largely due to the internal gravity modes.

### 2.2 Split-Explicit Integration

The model is integrated for 48 hours with the split-explicit scheme using a time step of 150 s for uninitialized data. For the first hour or so the oscillations in the surface pressure (Curve B in Figure 1) are the same as in the explicit integration. However the oscillations are strongly damped in the next three hours of integration. Little difference is noticed in Figure 2 in the variation of  $\dot{\sigma}$  at  $\sigma = 0.5$  between the explicit (Curve A) and split-explicit (Curve B) integrations. One can conclude that the split-explicit integration scheme acts as a dynamical initialization by greatly reducing the amplitude of the unwanted external gravity waves in the first three to four hours of integration.

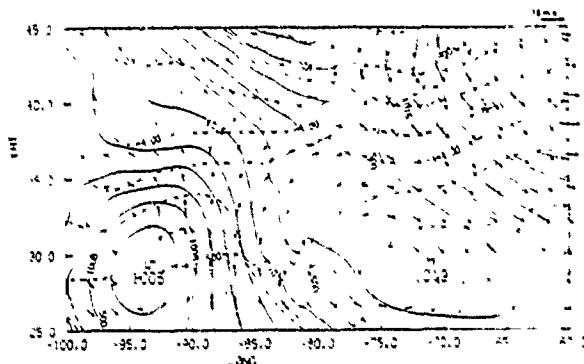


Figure 3. Sea level pressure in mb, 1000 mb wind and temperature ( $^{\circ}\text{C}$ ) for the initial conditions at 00Z February 10, 1983. The maximum vector is indicated by the labelled arrow in  $\text{m s}^{-1}$ .

In the next two experiments the effect of our current initialization procedure is assessed.

### 2.3 Non-divergent Wind

In the first part of our initialization procedure, the non-divergent wind and analyzed temperature are interpolated to the model sigma surfaces, using a balanced surface pressure. A 48 hour integration using the split-explicit scheme is then performed with this data. As shown by Curve C in Figure 1, the amplitude of the initial oscillations of the surface pressure are reduced to 2 to 3 mb and are largely damped out after 3 hours. The balancing of the initial surface pressure has produced a small shift in the initial value of the surface pressure compared to the uninitialized cases. Curve C in Figure 2 shows that the strong adjustment (increase) in the vertical motion  $\dot{\sigma}$  is still present in the first 6 hours and the superimposed higher frequency oscillations are only slightly reduced in amplitude. By removing the divergent component of the wind from the analyzed data the initial value of  $\dot{\sigma}$  is also reduced. On sigma surfaces over sloping topography a vertical shear of the non-divergent wind will introduce a non-zero value as will horizontal divergence introduced by errors caused by vertical interpolation. By largely removing the horizontal divergence we have essentially removed the external gravity mode after three hours of integration.

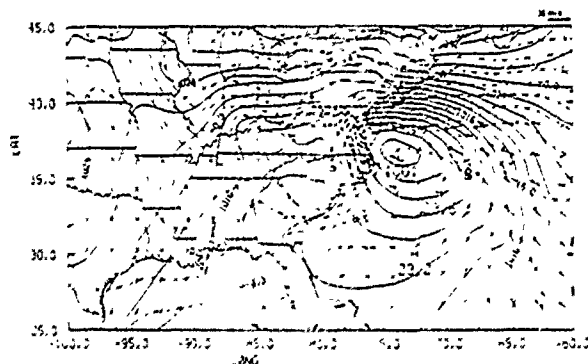


Figure 4. As in Fig. 3 but for 48 hour forecast.

### 2.4 Static Non-linear Mass Balance

In the last step of our initialization procedure we use the non-linear balance equation and derive a balanced geopotential and temperature field from the non-divergent wind field. A 48 hour integration was carried out using this fully initialized data. The oscillations shown in Curve D in the surface pressure are of the same amplitude as in the non-divergent case (Curve C) being damped after 3 hours of integration. The vertical motion shown in curve D still shows the rapid adjustment (increase) during the first 5 hours, but the higher frequency oscillations are much reduced in amplitude and mostly eliminated after 4 hours of integration. The non-linear balance of the mass field essentially removes the internal gravity waves except for the initial adjustment in the first 4 hours.

In all the three cases (B), (C) and (D) using the split-explicit scheme with uninitialized and initialized data, the 12 to 48 hour forecasts are very similar. Only in the case of the 12 hour explicit time integration with uninitialized data are high frequency oscillations in the surface pressure and vertical motion still substantial at 12 hours of integration, which can be seen to produce a marked difference in the 12 hour forecast.

## 3. SIMULATION OF EXPLOSIVE CYCLOGENESIS

We chose the example of the storm which occurred on 12 February, 1983 to test our prediction system. For our initial conditions we use the NMC 2.5 degree hemispheric analysis of 00Z 10 February, 1983, enhanced with the observed upper air data and surface marine data. The initial surface conditions are illustrated in Figure 3. The Figure shows a low along the Gulf coast. For the boundary conditions in this case, 12 hourly tendencies were derived from initialized NMC 2.5 degree analyses and a nudging technique used to update the boundary values during the integration. The resulting 48 hour forecast is shown in Figure 4, which shows a low which had developed along the east coast and intensified as it moved up the coast. The verification from the NMC analysis is shown in Figure 5. The position and intensity of the low has been well simulated and the strong easterly winds north of the low forecast by our model. With our limited area for integration, the forecasts are strongly dependent on the accuracy of the boundary values. With fixed boundary

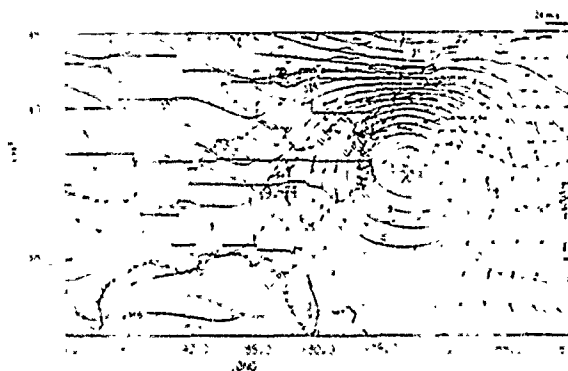


Figure 5. As in Fig. 3 but for a Verifying analysis at 00Z February 12, 1983.

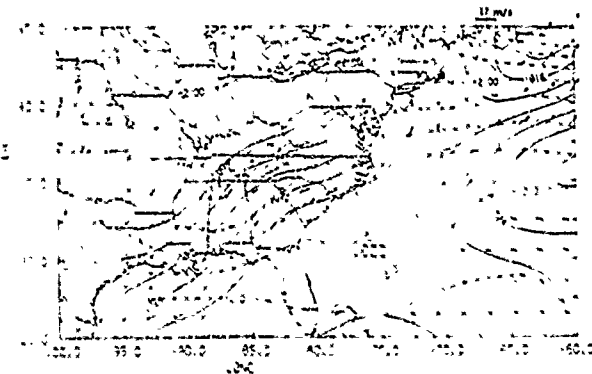


Figure 6. Sea-level pressure in mb, 1000 mb wind and temperature (°C) for initial conditions at 12Z January 23, 1986.

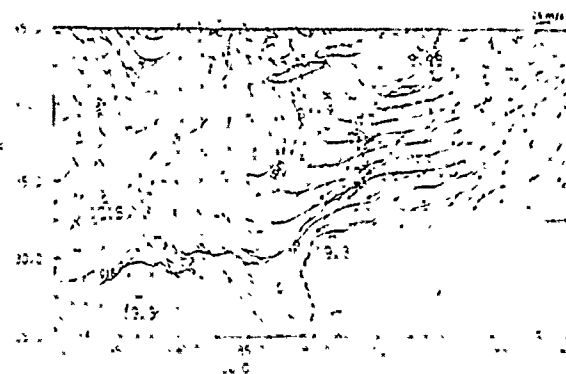


Figure 7. As in Fig. 4 but for a 36 hour forecast.

conditions, the initial low weakened with time moving on a eastward track and not up the coast.

#### 4. SIMULATION OF COLD AIR DAMMING, COASTAL FRONT

Successful simulations of the development of the coastal front and the cold air damming observed prior to the offshore cyclogenesis in the second Intensive Observing Period of GALE have been performed. The model has been initially integrated from the first guess analysis interpolated from the NMC 2.5° resolution analysis of 12Z, January 23. Perkey and Kreitzberg boundary conditions are used with 12 hourly tendencies obtained from initialized NMC analyses. Figure 6 shows the initial surface conditions. Despite the reduction of the initial temperature gradients with the use of a static initialization and the large scale analysis, the frontal strength is reproduced by the model after the first twelve hours of integration. With the further eastward movement of the front, a wedge of cold air develops between the Appalachians and the coast in a northerly low level flow behind the front. Convective and stable precipitation develops in the moist north easterly air that overflows the wedge of cold air. The cold wedge can be seen in Figure 7, which shows the 36 hour model forecast. After 36 hours of integration, a coastal front develops southwards from Cape Hatteras to offshore of the Carolinas, where the north-easterly flow meets the wedge of cold air. With further integration to 48 hours the precipitation strengthens offshore and the coastal front moves inland forming a trough.

#### 5. SUMMARY

The Naval Research Laboratory Limited Area Numerical Weather Prediction model uses the split-explicit scheme to integrate in time. The scheme has been shown to greatly reduce the amplitude of the unwanted external gravity wave oscillations in the first three to four hours of integration. The static non-linear initialization procedure further reduces the initial external and internal gravity wave oscillations, except for an initial adjustment of the vertical motion in the first five hours or less of integration. The model has successfully simulated the case of an explosive cyclogenesis on February 10-12, 1983 and the cold-air damming and coastal front event of January 23-25, 1986 during GALE.

#### 6. ACKNOWLEDGEMENTS

This research was supported by SPAWAR and NRL's basic research program.

#### 7. REFERENCES

1. Barnes S L 1973, Mesoscale objective map analysis using weighted time-series observations, NOAA Technical Memorandum ERL NSSL-62, Norman, OK, 60pp.
2. Brehme K 1987, A method of objective analysis for meteorological fields for use in a numerical weather prediction model, Master's Thesis, Department of Marine, Earth and Atmospheric Sciences, North Carolina State University, Raleigh, N.C.
3. Bourke W and J L McGregor 1983, A nonlinear vertical mode initialization scheme for a limited area prediction model, Mon. Wea. Rev. 111, 2285-2297.
4. Madala R V 1981, Efficient time integration schemes for atmosphere and ocean models, Finite Difference Techniques for Vectorized Fluid Dynamic Calculations, Chpt. 4, Springer-Verlag, pp 56-74.
5. Madala R V, S W Chang, U C Mohanty, S C Madan, R K Paliwal, V B Sarin, T Holt and S Raman 1987, Description of the Naval Research Laboratory Limited Area Dynamical Weather Prediction Model, NRL Technical Report No. 5992, Washington, D.C., 131pp.
6. Perkey D J and C W Kreitzberg 1976, A time-dependent lateral boundary scheme for limited-area primitive equation models, Mon. Wea. Rev. 104, 744-755.
7. Reynolds R W 1982, Monthly averaged sea surface temperature climatology, NOAA Technical Report NWS-31, Washington, D.C.

## **APPENDIX C**

### **A Numerical Study of the Development of an Extratropical Cyclone Off the East Coast of the U.S. During the GALE Experiment**



*Extended Abstracts, Third Conference on Mesoscale Processes, Vancouver, Canada, 21-26 August, 1987, Amer. Meteor. Soc. (August, 1987)*

A NUMERICAL STUDY OF THE DEVELOPMENT OF AN EXTRATROPICAL CYCLONE OFF THE EAST COAST OF THE U.S. DURING THE GALE EXPERIMENT.

Keith D. Sashegyi

Science Applications Int. Corp.  
McLean, Virginia

Rangarao V. Madala and Simon W. Chang

Naval Research Laboratory  
Washington, D.C.

1. INTRODUCTION

The Naval Research Laboratory's Mesoscale Weather Prediction Model is being used to study the development of an extratropical cyclone which occurred off the East coast of the U.S. during the second Intensive Observing Period (IOP) of the Genesis of Atlantic Lows Experiment (GALE) on January 23-29, 1986. The model is a three dimensional primitive equations model, incorporating topography and physical parameterizations of the boundary layer and precipitation processes (Madala et al., 1987). In the vertical, sigma coordinates are used while in the horizontal a staggered grid is used. The finite difference scheme is a second order quadratic conserving scheme. The model is integrated in time using the split-explicit method (Madala, 1981).

2. MODEL DESCRIPTION

The domain of the model is from 22.5°S to 47.5°N in latitude and 102.5°W to 57.5°W in longitude with a half a degree horizontal resolution. In the vertical, ten layers of equal  $\sigma$  thickness are used. An enveloped topography is derived from the U.S. Navy's global 10 minute elevation data by calculating the mean for each model grid square and adding one standard deviation. Climatological 1 degree resolution mean sea surface temperatures for January from Reynolds (1982) are interpolated to the model grid. The model includes large scale precipitation and a cumulus parameterization using a modified Kuo scheme. Unstable lapse rates are removed by a dry convective adjustment scheme. The boundary layer is parameterized using a drag coefficient formulation.

An NMC 2.5° resolution hemispheric analysis is interpolated to the horizontal model grid using cubic polynomial interpolation to provide a first guess analysis. Available observed GALE data will be analyzed in future using the Barnes (1973) scheme to enhance this first guess analysis following Brehme (1987). The non-divergent wind, temperature and humidity are then interpolated to the model sigma levels and a non-linear static initialization of the mass field performed. The Perkey and Kreitzberg (1976) boundary conditions are used to update the large scale conditions at the horizontal boundaries during the integration of the model. The large scale tendencies are obtained from initialized

NMC 2.5° resolution hemispheric analyses and are updated every twelve hours in the boundary region. The smaller scale interior waves produced by the model and propagating into the boundary region are absorbed by this technique.

3. MODEL SIMULATION

Successful simulations of the development of the coastal front and the cold air damming and the subsequent offshore cyclogenesis during the second IOP of GALE have been performed. The model has been initially integrated from the first guess analysis interpolated from the NMC 2.5° resolution analysis of 12Z, January 23. Figure 1 shows the initial conditions. Despite the reduction of the initial temperature gradients with the use of a static initialization and the large scale analysis, the frontal strength is reproduced by the model after the first twelve hours of integration. With the further eastward movement of the front, a wedge of cold air develops between the Appalachians and the coast in a northerly low level flow behind the front. Convective and stable precipitation develops in the moist easterly air that overflows the wedge of cold air. After 36 hours of integration, a coastal front develops southwards from Cape Hatteras to offshore of the Carolinas, where the north-easterly low-level flow meets the wedge of cold air. With the upper level wave and surface low approaching the coast from the west, the

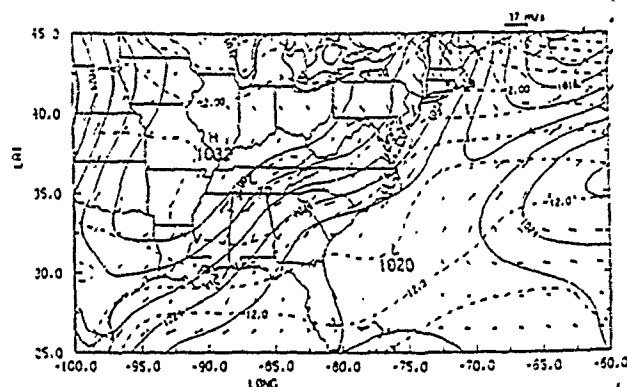


Fig. 1. Contours of sea level pressure every 2 mb, 1000 mb wind and temperature (every 2.5°C) for the initial conditions at 12Z January 23, 1986. The maximum vector is indicated by the labelled arrow.

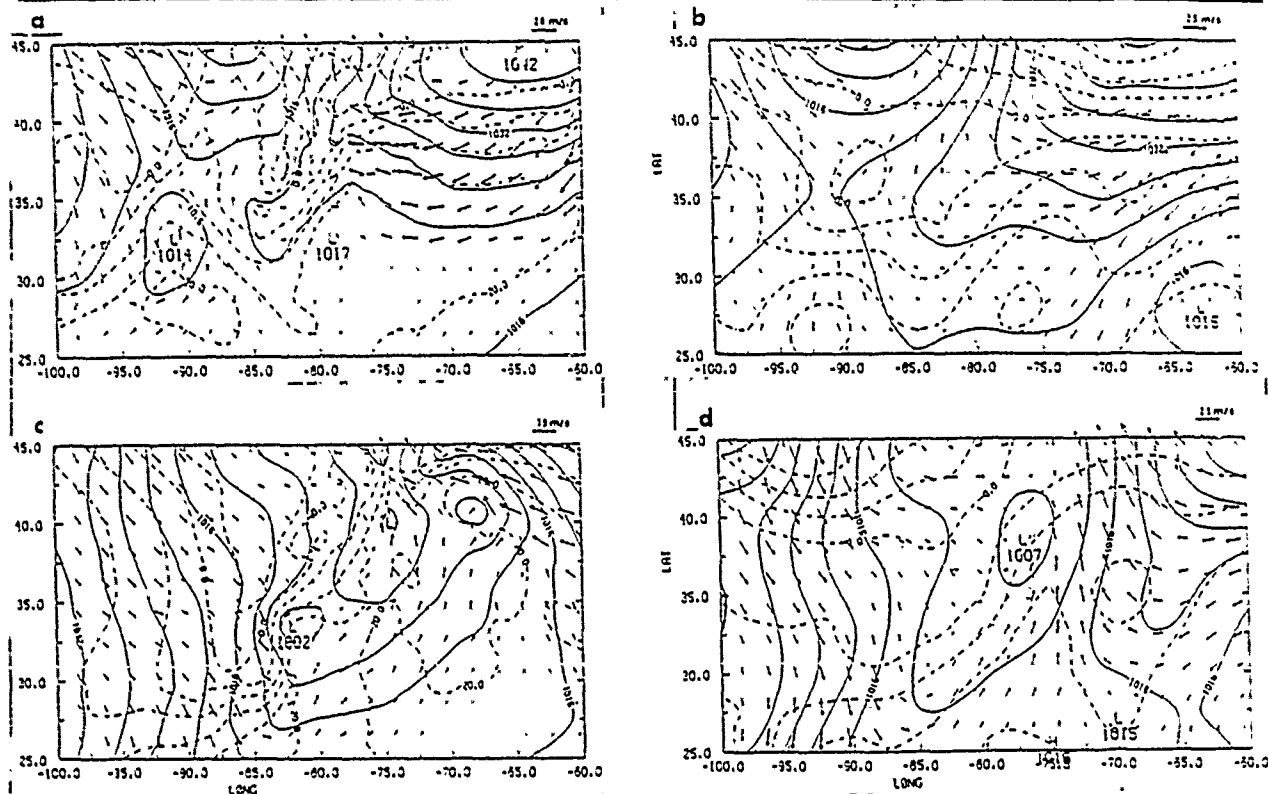


Fig. 2. Contours of sea level pressure every 4 mb, 1000 mb wind and temperature (every 5°C) for (a) 48 hour forecast, (b) analysis for 122 January 25, 1986, (c) 72 hour forecast and (d) analysis for 122 January 26, 1986.

precipitation strengths offshore and the coastal front moves inland forming a trough at 48 hours of integration (see Figure 2a). The large scale surface analysis at this time shown in Figure 2b does indicate a surface trough in the same position. In our model integration, a weak low forms at the southern end of the coastal front/trough and then moves rapidly northwards up the coast slowly deepening. By 72 hours this low can be found in Figure 2c along the N.J. coast in a position a little further north than the analysis shown in Figure 2d. In the 72 hour simulation, the low which approached from the west is found on the Georgia and North Carolina border, while the analysis shows a weaker area of low pressure. In the next 12 hours, a cyclone forms offshore moving off Cape Hatteras and deepening more rapidly as it moves north of Hatteras. This scenario of cyclogenesis is similar to that observed.

By updating the large scale flow at the model boundaries, using tendencies derived from initialized analyses, the major short wave event propagates smoothly in from the western boundary through the integration period and cyclogenesis occurs offshore as observed. However the strength of a weak short wave, which crossed the coastline at 12 hours of integration, did not deepen so that a reduced south easterly flow is found behind the first front. This may lead to the cold air damming to persist longer and be stronger than is observed. The influence of topography and sensible heating on the cold air damming, the coastal front and on the subsequent cyclogenesis offshore is being studied.

#### 4. REFERENCES

- Barnes, S.L., 1973: Mesoscale objective map analysis using weighted time-series observations. NOAA Technical Memorandum, ERL NSSL-62, Norman, OK, 60pp.
- Brehme, K., 1987: A method of objective analysis for meteorological fields for use in a numerical weather prediction model. Master's Thesis, Department of Marine, Earth and Atmospheric Sciences, North Carolina State University, Raleigh, N.C.
- Madala, R.V., 1981: Efficient time integration schemes for atmospheric and ocean models. Chpt. 4, Finite Difference Techniques for Vectorized Fluid Dynamic Calculations. Springer-Verlag, pp 56-74.
- Madala, R.V., S.W. Chang, U.C. Mohanty, S.C. Madan, R.K. Paliwal, V.B. Sarin, T. Holt and S. Raman, 1987: Description of the Naval Research Laboratory Limited Area Dynamical Weather Prediction Model. NRL Technical Report No. 5992, Washington, D.C., 131pp.
- Perkey, D.J., and C.W. Kreitzberg, 1976: A time-dependent lateral boundary scheme for limited-area primitive equation models. Mon. Wea. Rev., 104, 744-755.
- Reynolds, R.W., 1982: Monthly averaged sea surface temperature climatology. NOAA Technical Report NWS-31, Washington, D.C.

## **Appendix D**

### **A Numerical Simulation of the Development of an Extratropical Cyclone Off the East Coast of the U.S. During the GALE Experiment**

*Proceedings of GALE/CASP Workshop, Virginia Beach, Virginia, 2-6 November, 1987, GALE Project Office, National Center for Atmospheric Res. (February 1988)*

A NUMERICAL SIMULATION OF THE DEVELOPMENT OF AN EXTRATROPICAL CYCLONE  
OFF THE EAST COAST OF THE U.S. DURING THE GALE EXPERIMENT.

by

Keith D. Sashegyi

Science Applications Int. Corp.  
McLean, Virginia

Rangarao V. Madala and Simon W. Chang

Naval Research Laboratory  
Washington, D.C.

1. INTRODUCTION

The Naval Research Laboratory's Mesoscale Weather Prediction Model is being used to study the development of an extratropical cyclone which occurred off the East coast of the U.S. during the second Intensive Observing Period (IOP) of the Genesis of Atlantic Lows Experiment (GALE) on January 23-29, 1986. The model is a three dimensional primitive equations model, incorporating topography and physical parameterizations of the boundary layer and precipitation processes (Madala et al., 1987). In the vertical, sigma coordinates are used while in the horizontal a staggered grid is used. The finite difference scheme is a second order quadratic conserving scheme. The model is integrated in time using the split-explicit method (Madala, 1981).

2. MODEL DESCRIPTION

The domain of the model is from 22.5°S to 47.5°N in latitude and 102.5°W to 57.5°W in longitude with a half a degree horizontal resolution. In the vertical, ten layers of equal  $\sigma$  thickness are used. An enveloped topography is derived from the U.S. Navy's global 10 minute elevation data by calculating the mean for each model grid square and adding one standard deviation. Climatological 1 degree resolution mean sea surface temperatures for January from Reynolds (1982) are interpolated to the model grid. The model includes large scale precipitation and a cumulus parameterization using a modified Kuo scheme. Unstable lapse rates are removed by a dry convective adjustment scheme. The boundary layer is parameterized using a single layer with the fluxes of heat and momentum computed using a generalized similarity theory, in which the drag coefficients are stability dependent.

An NMC 2.5° resolution hemispheric analysis is interpolated to the horizontal model grid using cubic polynomial interpolation to provide a first guess analysis. Available observed GALE data will be analyzed in

future using the Barnes (1973) scheme to enhance this first guess analysis following Brehme (1987). The non-divergent wind, temperature and humidity are then interpolated to the model sigma levels. The Perkey and Kreitzberg (1976) boundary conditions are used to update the large scale conditions at the horizontal boundaries during the integration of the model. The large scale tendencies are obtained from NMC 2.5° resolution hemispheric analyses with the divergence removed. The tendencies are updated every twelve hours in the boundary region. The smaller scale interior waves produced by the model and propagating into the boundary region are absorbed by this technique.

### 3. MODEL SIMULATION

Successful simulations of the development of the coastal front and the cold air damming and the subsequent offshore cyclogenesis during the second IOP of GALE have been performed. The model has been initially integrated from a first guess analysis interpolated from the NMC 2.5° resolution analysis of 12Z, January 23. Figure 1a shows the initial conditions of a cold front moving off the east coast of the U.S.

With the further eastward movement of the front, a wedge of cold air can be seen to develop after 24 hours of integration (Figure 1b) between the Appalachians and the coast in a northerly low level flow behind the front. Comparing with the verifying surface analysis, shown in Figure 1c, we see that the simulated secondary low on the front has not deepened as much as was observed. The temperature gradient across the coastline of North Carolina and Virginia is further enhanced in the model simulation by large surface sensible heat fluxes of as much as  $391 \text{ watts m}^{-2}$  over the Gulf Stream (Figure 2a). Latent heat fluxes in the same region in the model are 2 to 3 times as large as the sensible heat fluxes. The model shows in Figure 2b a realistic pattern of precipitation in the secondary low and shows convective and stable precipitation developing off the coast in the moist easterly air that overflows the wedge of cold air. Satellite photographs do indicate convection offshore over the Gulf Stream on the afternoon of the 24th.

The cold wedge is well developed at 36 hours, as shown in Figure 2c. A developing coastal front is indicated in the figure by the confluent flow in a region of enhanced temperature gradient along the western edge of the Gulf Stream between the easterly flow across the Gulf Stream and the north easterly flow over the land. A trough has developed at the southern end of this "coastal front". The 2.5 degree hemispheric analysis (Figure 2d) cannot resolve such features. With the upper level wave and surface low approaching the coast from the west, the precipitation strengthens offshore and the coastal front moves inland forming a trough at 48 hours of integration (see Figure 3a). The large scale surface analysis at this time (shown in Figure 3b) does indicate a weak surface trough in a position from Cape Hatteras to offshore of the Carolinas.

With further integration of our model, a weak low forms at the southern end of the coastal front/trough and then moves rapidly northwards up the coast slowly deepening. By 72 hours this low can be found in Figure 3c north of New Jersey, in a position further north than in the analysis shown in Figure 3d. In the 72 hour simulation, the low, which approached from the west, is found on the Georgia and North Carolina border, close to the

observed position in the analysis but a little deeper in intensity. The precipitation pattern for 60-72 hours, shown in Figure 4a, has realistic magnitude and distribution. Qualitatively the bands followed those seen in the satellite cloud pictures. In the next 12 hours, a cyclone forms offshore moving off Cape Hatteras (Figure 4b) and deepening more rapidly as it moves north of Hatteras. This scenario of cyclogenesis is similar to that observed.

#### 4. SUMMARY

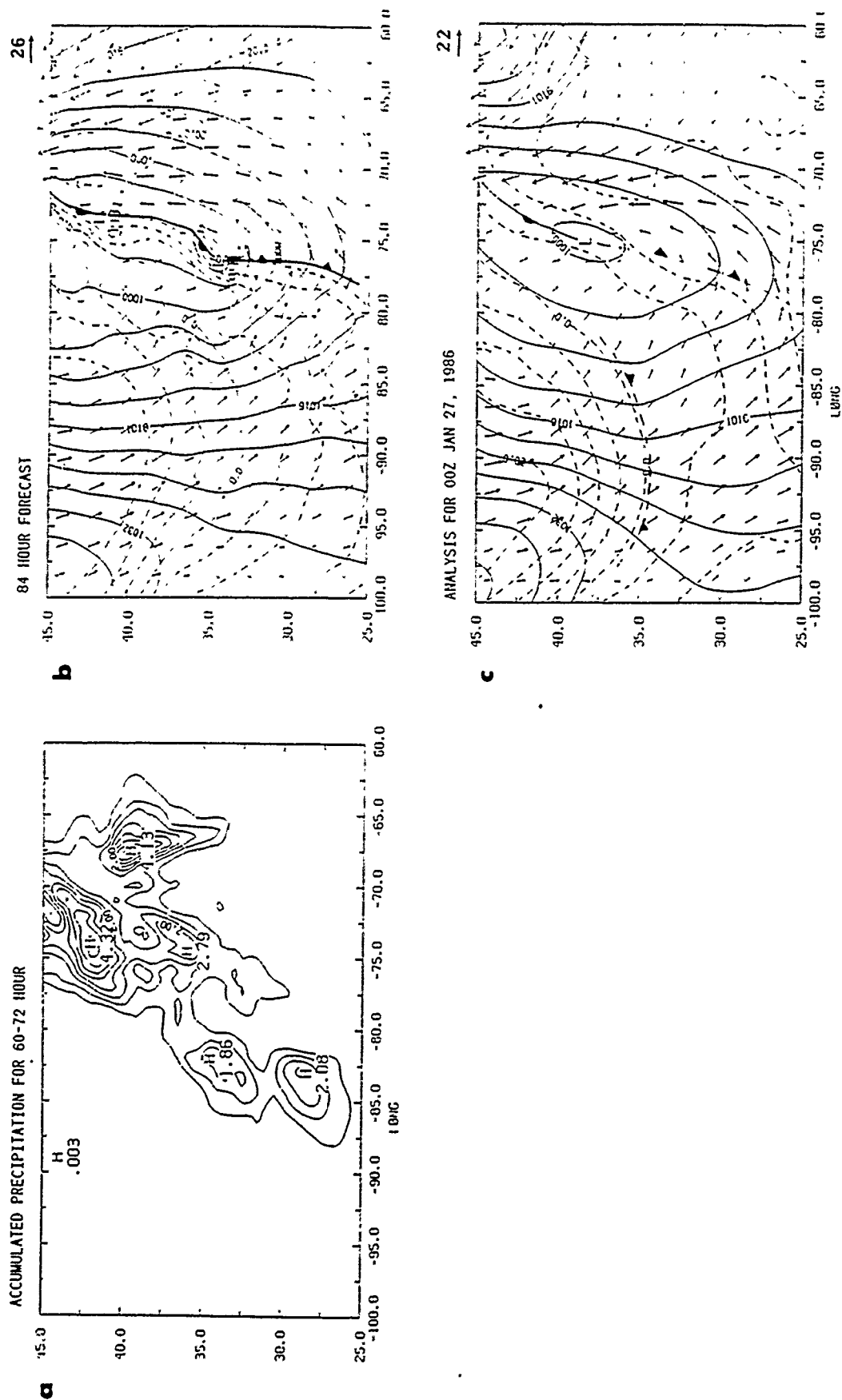
By updating the large scale flow at the model boundaries, using tendencies derived from initialized analyses, the major short wave event propagates smoothly in from the western boundary through the integration period and cyclogenesis occurs offshore as observed. However the strength of a weak short wave, which crossed the coastline at 12 hours of integration, did not deepen so that a reduced south easterly flow is found behind the first front. This may lead to the cold air damming to persist longer and be stronger than is observed. The coastal trough formed in the model moved inland sooner than observed with the result that the low, which formed at its southern end, moved up the coast earlier than observed. The influence of topography and sensible heating on the cold air damming, the coastal front and on the subsequent cyclogenesis offshore will be being studied in future.

#### 5. ACKNOWLEDGEMENTS

This research was supported by NRL's basic research program and by SPAWAR. Parts of this material have been presented at the 3rd Mesoscale Conference held August 21-26, 1987 in Vancouver, Canada and as a poster at the GALE/CASP workshop held November 2-6, 1987 in Virginia Beach, Virginia.

## 6. REFERENCES

- Barnes, S.L., 1973: Mesoscale objective map analysis using weighted time-series observations. NOAA Technical Memorandum, ERL SSL-62, Norman, OK, 60pp.
- Brehme, K.A., 1987: A method of objective analysis for meteorological fields for use in a numerical weather prediction model. Master's Thesis, Department of Marine, Earth and Atmospheric Sciences, North Carolina State University, Raleigh, N.C., 123pp.
- Madala, R.V., 1981: Efficient time integration schemes for atmospheric and ocean models. Chpt. 4, Finite Difference Techniques for Vectorized Fluid Dynamic Calculations. Springer-Verlag, pp 56-74.
- Madala, R.V., S.W. Chang, U.C. Mohanty, S.C. Madan, R.K. Paliwal, V.B. Sarin, T. Holt and S. Raman, 1987: Description of the Naval Research Laboratory Limited Area Dynamical Weather Prediction Model. NRL Technical Report No. 5992, Washington, D.C., 131pp.
- Perkey, D.J., and C.W. Kreitzberg, 1976: A time-dependent lateral boundary scheme for limited-area primitive equation models. Mon. Wea. Rev., 104, 744-755.
- Reynolds, R.W., 1982: Monthly averaged sea surface temperature climatology. NOAA Technical Report NWS-31, Washington, D.C.





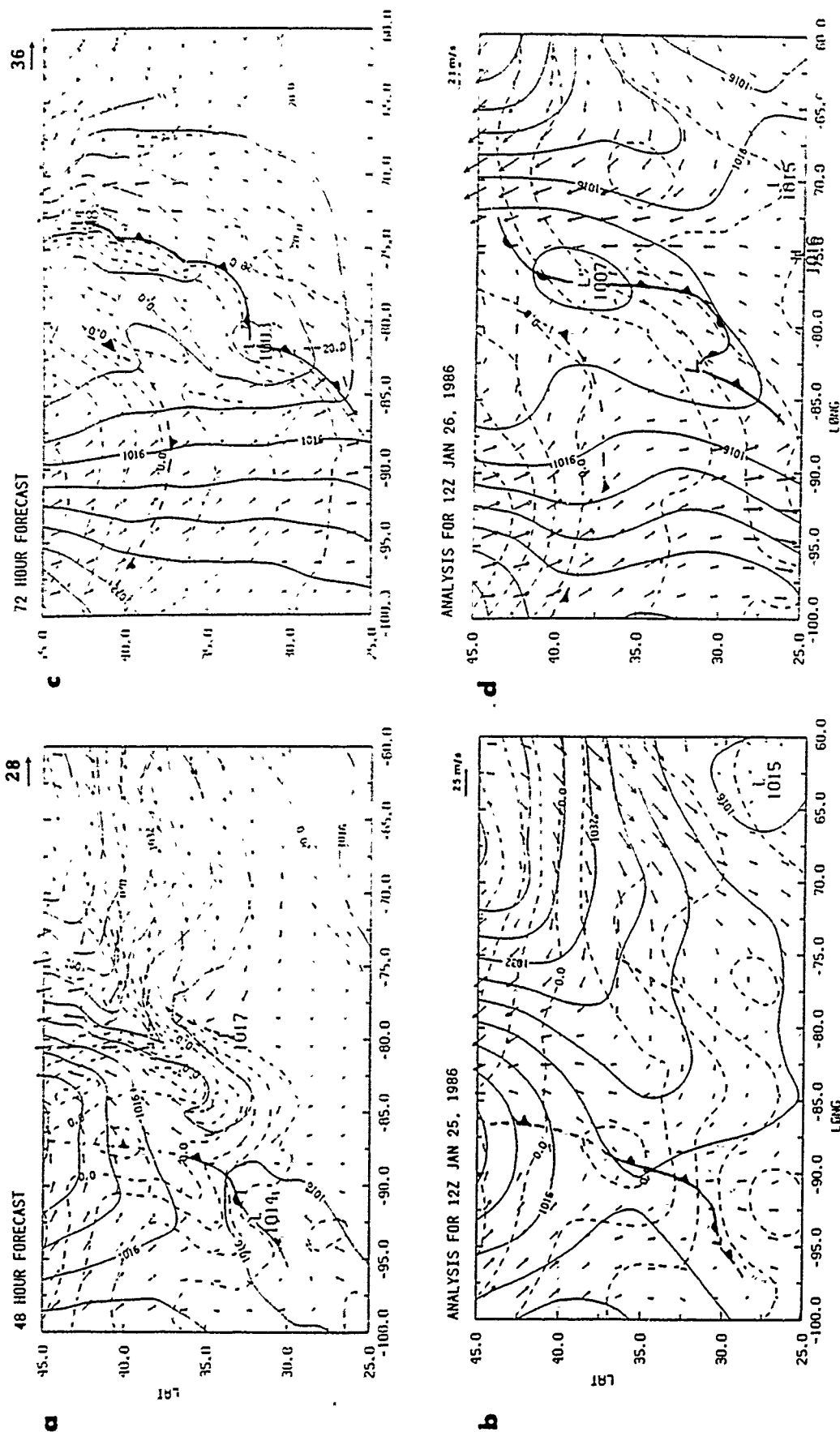


Fig. 3. Sea level pressure (contours every 4 mb), 1000 mb wind and temperature (every 5°C) for (a) 48 hour forecast, (b) NMC hemispheric analysis for 12Z January 25, 1986, (c) 72 hour forecast, and (d) NMC hemispheric analysis for 12Z January 26, 1986.

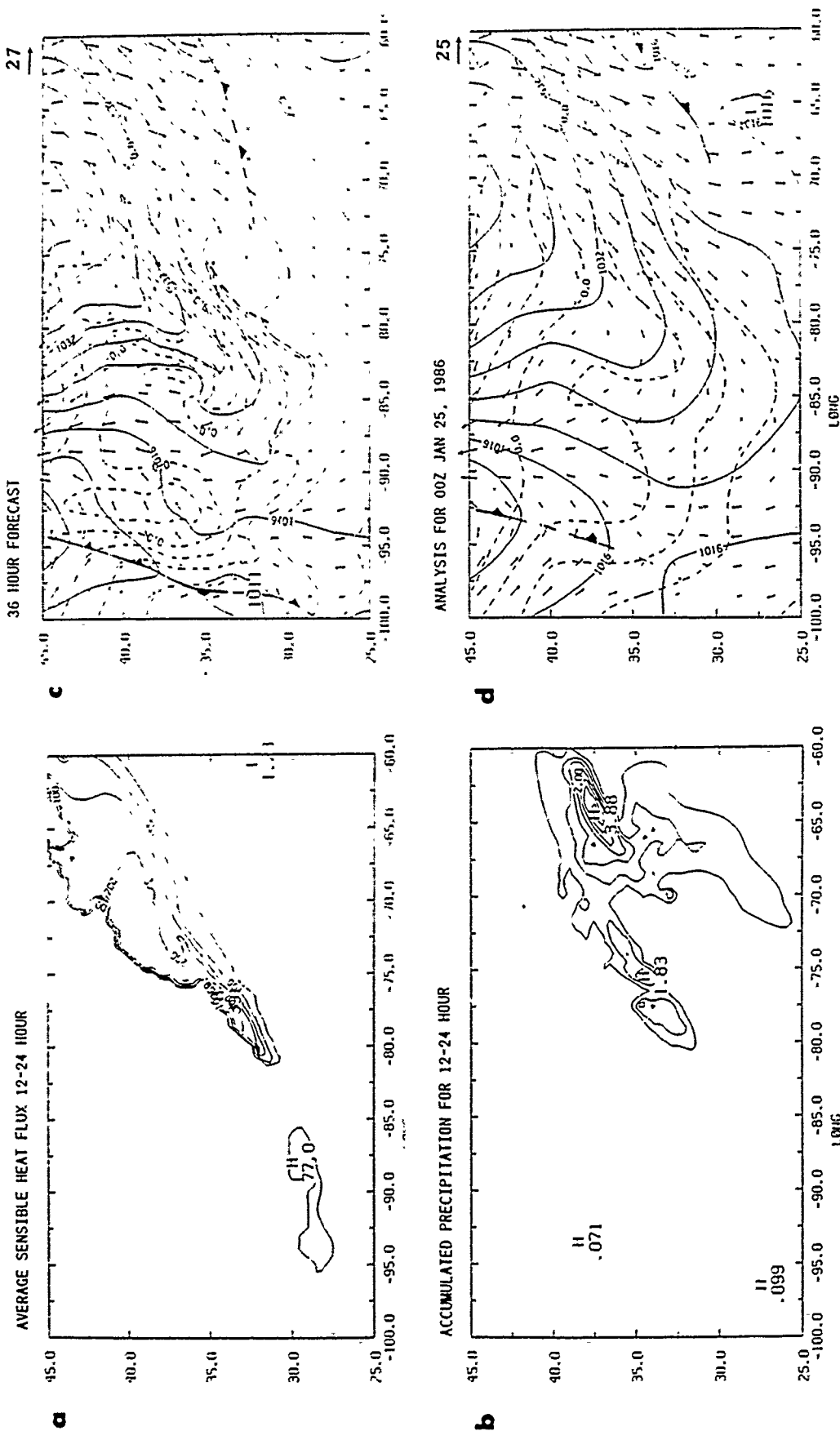


Fig. 2. (a) The average sensible heat flux ( $\text{watts m}^{-2}$ ) for 12 - 24 hours of integration and (b) the accumulated precipitation (cms) for 12 - 24 hours of integration, (c) sea level pressure (contours every 4 mb), 1000 mb wind and temperature (every 5°C) for a 36 hour forecast and for (d) the verifying NMC hemispheric analysis for 00Z January 25, 1986.

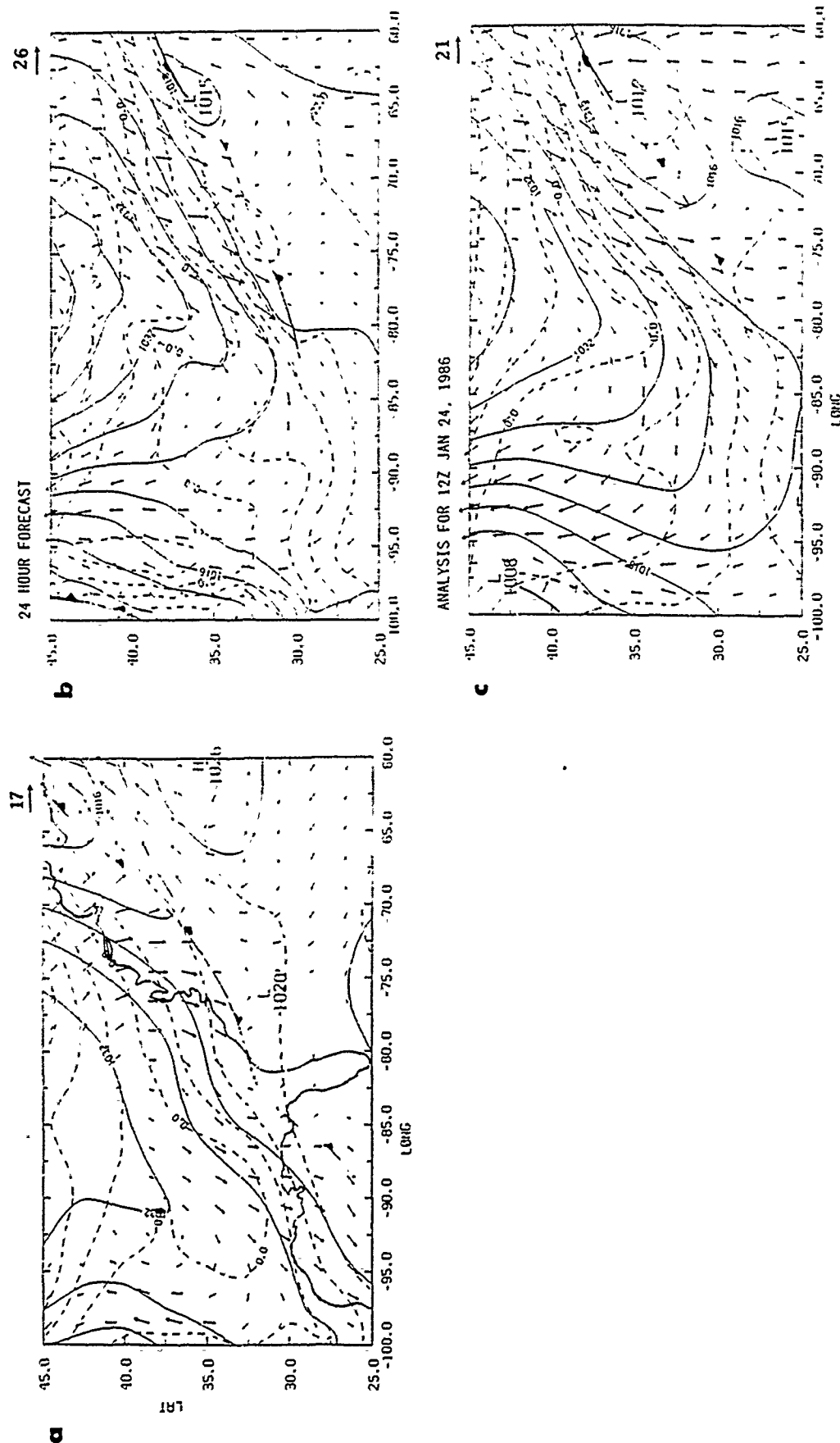


Fig. 1. Sea level pressure (contours every 4 mb), 1000 mb wind and temperature (every 5°C) for (a) the initial conditions at 12Z January 23, 1986; (b) for a 24 hour forecast and (c) the verifying NMC hemispheric analysis for 12Z January 24, 1986. The maximum vector is indicated by the labelled arrow (m s<sup>-1</sup>).

## **Appendix E**

### **Initialization Experiments with the NRL Mesoscale Numerical Model**

INITIALIZATION EXPERIMENTS WITH THE  
NRL MESOSCALE NUMERICAL MODEL

Keith D. Sashegyi

Science Applications Int. Corp.  
P.O. Box 1303  
McLean, Virginia 22102

Rangarao V. Madala

Atmospheric Physics Branch  
Naval Research Laboratory  
Washington, D.C. 20375

## 1. INTRODUCTION

Various initialization procedures have been tested for use with the Naval Research Laboratory's Limited Area Weather Prediction system. The system has been developed to study the development of extratropical cyclones, which occurred along the East coast of the U.S. during the Genesis of Atlantic Lows Experiment (GALE). The effect of the split-explicit scheme, used for integration in time, and various non-linear initialization procedures in reducing gravity wave oscillations in the model are presented. Preliminary results with a vertical mode initialization scheme are shown.

## 2. MODEL DESCRIPTION

The Naval Research Laboratory's primitive equations model (Madala et al., 1987) uses sigma coordinates and incorporates topography and physical parameterizations of the boundary layer and precipitation processes. The model is integrated in time using the efficient split-explicit method (Madala, 1981). In the horizontal, an Arakawa C grid is used with 0.5 degree resolution in latitude and longitude. The finite difference scheme is a second order quadratic conserving scheme. In the vertical, ten layers of equal  $\sigma$  thickness are used. An enveloped topography is derived from the U.S. Navy's global 10 minute elevation data using the average grid heights plus one standard deviation. Climatological 1 degree resolution mean sea surface temperatures from Reynolds (1982) for the month of interest are interpolated to the model grid. The model includes large scale precipitation and a cumulus parameterization using a modified Kuo scheme. Unstable lapse rates are removed by a dry convective adjustment scheme. The boundary layer is parameterized using a drag coefficient formulation. The boundary conditions of Perkey and Kreitzberg (1976) are used to update the large scale conditions at the horizontal boundaries during the integration of the model. An alternative nudging technique or one way interaction technique is also being used to update the variables at the horizontal boundaries.

### 2.1 Analysis

A first guess analysis is provided by a National Meteorological Center (NMC) 2.5° hemispheric analysis. The NMC 2.5° resolution

hemispheric analysis is interpolated to the horizontal model grid using cubic polynomial interpolation to provide a first guess analysis. Conventional observations and available supplementary observations (e.g. from GALE) are incorporated by Brehme (1987) using the Barnes (1973) successive corrections scheme to enhance this first guess analysis.

### 2.2 Split-Explicit Time Integration

In the split-explicit method of Madala (1981), a centered difference scheme (except for diffusion which uses forward differencing) with a time step of 150 s, appropriate for the Rossby modes, is used to step the model variables once forward in time. Gravity wave amplitudes for the deviations of the divergence and the pseudo-geopotential on sigma surfaces

$$\phi = p_s[\phi_s + RT^* - \phi^*]$$

are integrated at a smaller time steps for the external (37.5 s) and the first internal vertical mode (75 s). The average of these deviations, over a interval of twice the large time step, is then used to correct the explicit computation of the variables. Besides providing a 4 to 5 times saving in computer time over explicit methods, the averaging of the lower gravity wave eigenmodes may be expected to act as a partial filter of the higher frequency gravity waves.

## 3. EXPERIMENTS

To test the effect of the split-explicit time integration scheme in reducing the unwanted high frequency oscillations in the model, the model is integrated with uninitialized data both with the split-explicit scheme described above and with an explicit time integration of 30 s. Integrations with varying degrees of initialization are then compared in three other experiments. Time series of surface pressure and vertical motion  $\sigma$  in sigma coordinates at selected points were compared in the five experiments. The NMC 2.5 degree hemispheric analysis for 122 January 23, 1986 is used to start the integrations for each of the experiments. This is a case of a cold-air damming and coastal front event, which occurred from January 23-25, 1986, during GALE. The domain of the model is from 22.5°S to 47.5°N in latitude and 102.5°W to 57.5°W in longitude.

### 3.1 Uninitialized initial state with Explicit Integration

The model is integrated in time with a conventional leapfrog scheme for 12 hours with a time step of 30 s for uninitialized data. Oscillations of surface pressure of as much as 5 to 8 mb of amplitude and periods of 1 to 2 hours are observed in the first 12 hours of integration. Curve A in Figure 1 shows these typical oscillations in the surface pressure for a grid point at 35°N and 90°W. Curve A in Figure 2 shows the vertical motion  $p_0\dot{\sigma}$  at  $\sigma = 0.5$  for the same grid point, where  $p_0 = 1000$  mb. The curve A shows a typical rapid adjustment (increase in this figure) between hours 4 to 6 of the integration with smaller oscillations of periods of 2 to 4 hours superimposed. The higher frequency oscillations in surface pressure are largely due to the barotropic external gravity mode while the adjustment and oscillations in  $\dot{\sigma}$  in the middle troposphere are largely due to the internal gravity modes.

### 3.2 Uninitialized initial state with Split-Explicit Integration

The model is integrated for 48 hours with the split-explicit scheme using a time step of 150 s for uninitialized data. For the first hour or so the oscillations in the surface pressure (Curve B in Figure 1) are the same as in the explicit integration. However the oscillations are strongly damped in the next three hours of

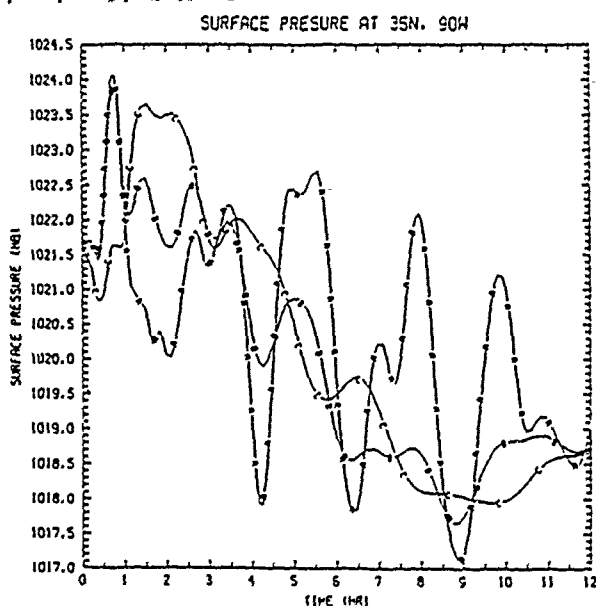


FIG. 1. Time series of surface pressure in mb at a grid point at 35°N and 90°W during the first 12 hours of integration. Curves are for uninitialized initial conditions for an explicit integration in time (Curve A) and a split-explicit integration (Curve B); for a split-explicit integration with a non-divergent initial condition (Curve C).

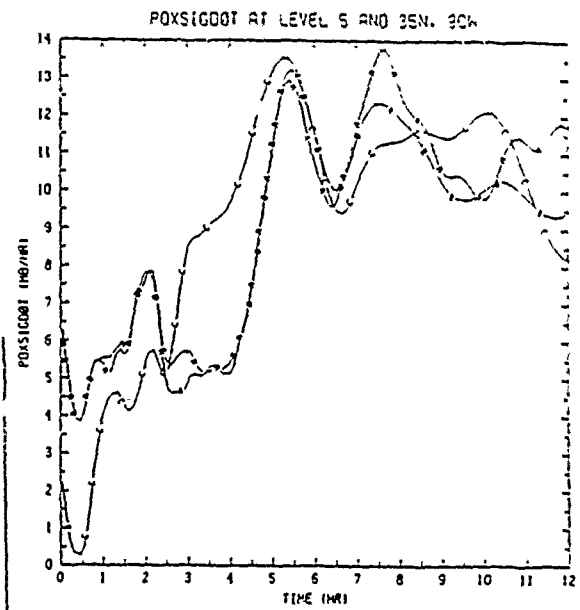


FIG. 2. As in Figure 1 except for the vertical motion (in sigma coordinates) at  $\sigma = 0.5$  multiplied by a standard pressure  $p_0$  of 1000 mb. Units are in mb/hour.

integration. Little difference is noticed in Figure 2 in the variation of  $\dot{\sigma}$  at  $\sigma = 0.5$  between the explicit (Curve A) and split-explicit (Curve B) integrations. One can conclude that the split-explicit integration scheme acts as a dynamical initialization by greatly reducing the amplitude of the unwanted external gravity waves in the first three to four hours of integration.

### 3.3 Non-divergent Initial State

The analyzed vorticity on pressure surfaces is used to first calculate the non-divergent component of the wind. A first guess of the surface pressure and temperature is found by interpolation to the model topography. The non-divergent wind, analyzed temperature and humidity are then interpolated to the model sigma levels. A 48 hour integration using the split-explicit scheme is then performed with this data. As shown by Curve C in Figure 1, the amplitude of the initial oscillations of the surface pressure are reduced to 2 to 3 mb and are largely damped out after 3 hours. Curve C in Figure 2 shows that the strong adjustment (increase) in the vertical motion  $\dot{\sigma}$  is still present in the first 6 hours and the superimposed higher frequency oscillations are only slightly reduced in amplitude. By removing the divergent component of the wind from the analyzed data the initial value of  $\dot{\sigma}$  is also reduced. On sigma surfaces over sloping topography, a vertical shear of the non-divergent wind will introduce divergence on the  $\sigma$  surfaces, as will errors caused by vertical interpolation. By largely removing the horizontal divergence we have essentially removed the external gravity mode after three hours of integration.

### 3.4 Static Non-linear Mass Balance

A static initialization of the mass field performed using the non-linear mass balance equation in sigma coordinates. The non-linear balance equation is used to derive a balanced geopotential and temperature field from the non-divergent wind field. A 48 hour integration was carried out using this fully initialized data. The oscillations in the surface pressure, shown in Curve D of Figure 3, are of the same amplitude as in the non-divergent case (Curve C in Figure 1), being damped after 3 hours of integration. However, a small mean drift of about a mb is seen to develop in the surface pressure (curve D) during the 12 hours of integration. The vertical motion shown in curve D of Figure 4 still shows the rapid adjustment (increase) during the first 5 hours, but the higher frequency oscillations are much reduced in amplitude and mostly eliminated after 4 hours of integration. The non-linear balance of the mass field essentially removes the internal gravity waves except for the initial adjustment in the first 4 hours.

### 3.5 Vertical Non-Linear Normal Mode Initialization

A vertical mode initialization scheme following that of Bourke and McGregor (1983) has been adapted for use with our model. The observed wind and temperature is first interpolated to the  $\sigma$  surfaces, and the non-divergent wind computed. An iterative procedure is then used to compute incremental changes to the pseudo-geopotential, divergence and vorticity for the first five

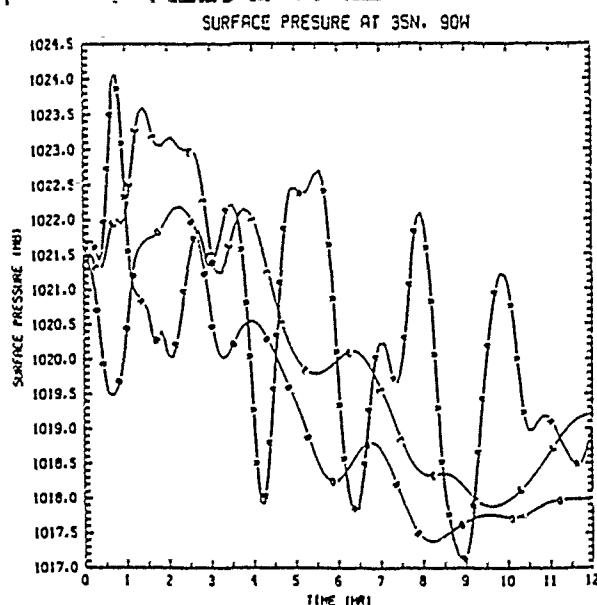


FIG. 3. Time series of surface pressure in mb at a grid point at 35°N and 90°W during the first 12 hours of integration. Curves are for uninitialized initial conditions for an explicit integration in time (Curve A); for split-explicit integrations with a non-linear mass balance (Curve D) and a vertical mode initialization (Curve E).

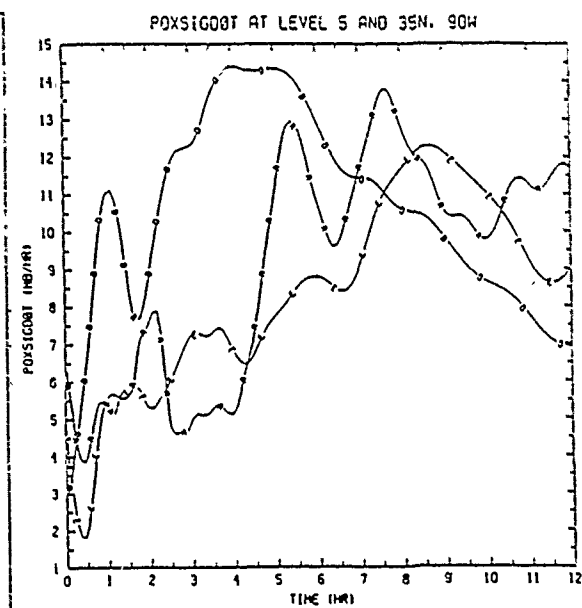


FIG. 4. As in Figure 3 except for the vertical motion (in sigma coordinates) at  $\sigma = 0.5$  multiplied by a standard pressure  $p_0$  of 1000 mb. Units are in mb/hour.

vertical modes. The surface pressure is not changed during the iterative procedure. Four iterations are found to be sufficient for the iterative scheme to converge. The oscillations in surface pressure, shown in curve E of Figure 3, are half a mb or less after the first hour of integration and no mean drift of the surface pressure is seen. Curve E in Figure 4 shows that the rapid initial adjustment has been removed, leaving a slower increase in the vertical motion with time. The procedure provides a balanced vertical motion field and produces smaller changes to the initial mass field, compared to the static initialization.

### 3.6 Model Forecasts

When using the split-explicit scheme with uninitialized or initialized data, the 12 to 48 hour forecasts are very similar. Only in the case of the 12 hour explicit time integration with uninitialized data are high frequency oscillations in the surface pressure and vertical motion still substantial after 12 hours of integration, producing noticeable differences in the 12 hour forecast.

## 4. SUMMARY

The Naval Research Laboratory Limited Area Numerical Weather Prediction model uses the split-explicit scheme to integrate in time. The scheme has been shown to greatly reduce the amplitude of the unwanted external gravity wave oscillations in the first three to four hours of integration. However, a typical rapid adjustment with superimposed oscillations occurs in the mid-troposphere vertical motion in the first 4 to 6 hours of integration. By interpolating the non-divergent wind and analyzed temperature to the model sigma surfaces, the amplitude of the

initial oscillations of the surface pressure are reduced to 2 to 3 mb and are largely damped out after 3 hours. Using the non-divergent wind and performing a static non-linear initialization of the mass field, provides a balanced initial state, except for a smooth initial adjustment of the vertical motion in the first five hours or less of integration and a small mean drift in the surface pressure. Initial tests with the vertical mode initialization procedure show promise to prevent gravity wave oscillations, without producing a mean drift in the surface pressure, and to provide a balanced vertical motion field. Smaller changes are produced to the initial mass field, compared to the static initialization. The various initialization procedures produce similar 12 to 48 hour forecasts.

#### ACKNOWLEDGEMENTS

This research was supported by SPANAR and NRL's basic research program.

#### REFERENCES

- Barnes, S.L., 1973: Mesoscale objective map analysis using weighted time-series observations. NOAA Technical Memorandum, ERL NSSL-62, Norman, OK, 60pp.
- Brehme, K., 1987: A method of objective analysis for meteorological fields for use in a numerical weather prediction model. Master's Thesis, Department of Marine, Earth and Atmospheric Sciences, North Carolina State University, Raleigh, N.C., 123pp.
- Bourke, W., and J.L. McGregor, 1983: A nonlinear vertical mode initialization scheme for a limited area prediction model. Mon. Wea. Rev., 111, 2285-2297.
- Madala, R.V., 1981: Efficient time integration schemes for atmosphere and ocean models. Fin. A Difference Techniques for Vectorized Fluid Dynamic Calculations, Chpt. 4, Springer-Verlag, pp 56-74.
- Madala, R.V., S.W. Chang, U.C. Mohanty, S.C. Madan, R.K. Paliwal, V.B. Sarin, T. Holt and S. Raman, 1987: Description of the Naval Research Laboratory Limited Area Dynamical Weather Prediction Model. NRL Technical Report No. 5992, Washington, D.C., 131pp.
- Perkey, D.J., and C.W. Kreitzberg, 1976: A time-dependent lateral boundary scheme for limited-area primitive equation models. Mon. Wea. Rev., 104, 744-755.
- Reynolds, R.W., 1982: Monthly averaged sea surface temperature climatology. NOAA Technical Report NWS-31, Washington, D.C.



## **APPENDIX F**

### **A User's Guide to the SEVP Solver: An Efficient Direct Solver for Elliptic Partial Differential Equations**

# Naval Research Laboratory

Washington, DC 20375-5000



NRL Memorandum Report 6450

## **A User's Guide to the SEVP Solver: An Efficient Direct Solver for Elliptic Partial Differential Equations**

KEITH D. SASHEGYI

*Science Applications International Corporation  
P.O. Box 1303, McLean, VA 22102*

RANGARAO V. MADALA

*Atmospheric Physics Branch  
Space Science Division*

April 13, 1989

SECURITY CLASSIFICATION OF THIS PAGE

REPORT DOCUMENTATION PAGE				Form Approved OMB No 0704-0188	
1a. REPORT SECURITY CLASSIFICATION <b>UNCLASSIFIED</b>			1b. RESTRICTIVE MARKINGS		
2a. SECURITY CLASSIFICATION AUTHORITY			3. DISTRIBUTION/AVAILABILITY OF REPORT Approved for public release; distribution unlimited.		
2b. DECLASSIFICATION/DOWNGRADING SCHEDULE			5. MONITORING ORGANIZATION REPORT NUMBER(S)		
4. PERFORMING ORGANIZATION REPORT NUMBER(S) NRL Memorandum Report 6450					
6a. NAME OF PERFORMING ORGANIZATION Naval Research Laboratory		6b. OFFICE SYMBOL (If applicable) Code 4110		7a. NAME OF MONITORING ORGANIZATION	
6c. ADDRESS (City, State, and ZIP Code) Washington, DC 20375-5000			7b. ADDRESS (City, State, and ZIP Code)		
8a. NAME OF FUNDING/SPONSORING ORGANIZATION Office of Naval Research		8b. OFFICE SYMBOL (If applicable)		9. PROCUREMENT INSTRUMENT IDENTIFICATION NUMBER	
8c. ADDRESS (City, State, and ZIP Code) Arlington, VA 22217			10. SOURCE OF FUNDING NUMBERS		
PROGRAM ELEMENT NO 61153N		PROJECT NO RR033-03-4A		TASK NO WORK UNIT ACCESSION NO DN156-046	
11. TITLE (Include Security Classification) A User's Guide to the SEVP Solver - An Efficient Direct Solver for Elliptic Partial Differential Equations					
12. PERSONAL AUTHOR(S) Sashegyi, * K.D. and Madala, R.V.					
13a. TYPE OF REPORT Interim		13b. TIME COVERED FROM _____ TO _____		14. DATE OF REPORT (Year, Month, Day) 1989 April 13	
15. PAGE COUNT 42					
16. SUPPLEMENTARY NOTATION *Science Applications International Corporation, McLean, VA 22102					
17. COSATI CODES			18. SUBJECT TERMS (Continue on reverse if necessary and identify by block number)		
FIELD	GROUP	SUB-GROUP	Numerical solution		
			Elliptic partial differential equations		
			Finite difference method Fortran subroutines		
19. ABSTRACT (Continue on reverse if necessary and identify by block number)					
<p>This technical report describes how to use the Stabilized Error Vector Propagation (SEVP) fortran subroutines, which have been developed at the Naval Research Laboratory, to solve an elliptic partial differential equation using finite difference methods. The SEVP method is an efficient direct method which can be used for separable and non-separable elliptic equations. The derivation of the finite difference equations and the use of Dirichlet, Neumann and periodic boundary conditions are demonstrated. The method and a test example are also described.</p>					
20. DISTRIBUTION/AVAILABILITY OF ABSTRACT <input checked="" type="checkbox"/> UNCLASSIFIED/UNLIMITED <input type="checkbox"/> SAME AS RPT <input type="checkbox"/> DTIC USERS			21. ABSTRACT SECURITY CLASSIFICATION <b>UNCLASSIFIED</b>		
22a. NAME OF RESPONSIBLE INDIVIDUAL R. Madala			22b. TELEPHONE (Include Area Code) (202) 767-2226		22c. OFFICE SYMBOL Code 4110

DD Form 1473, JUN 86

Previous editions are obsolete.

SECURITY CLASSIFICATION OF THIS PAGE

S/N 0102-LF-014-6603

## CONTENTS

1. Introduction .....	1
2. Subroutine SEVP .....	3
2.1 Description of arguments .....	4
3. Difference Approximation .....	8
3.1 Dirichlet boundary conditions .....	9
3.2 Neumann boundary conditions .....	10
3.3 Periodic boundary conditions .....	10
4. Solution Method .....	11
5. Description of SEVP subroutines .....	17
5.1 Initial Set-up, SEVP .....	17
5.2 The Preprocessor, BSM1 .....	19
5.3 The Solution, BSM2, BSM3 .....	21
6. Description of test example .....	24
6.1 Dirichlet boundary conditions in $y$ .....	25
6.2 Neumann boundary conditions in $y$ .....	27
7. References .....	30
Appendix. Listing of test programs .....	31
1. Test example with Dirichlet boundary condition .....	31
2. Test example with Neumann boundary condition .....	35

# A USER'S GUIDE TO THE SEVP SOLVER: AN EFFICIENT DIRECT SOLVER FOR ELLIPTIC PARTIAL DIFFERENTIAL EQUATIONS

## 1. INTRODUCTION

This report describes the Stabilized Error Vector Propagation (SEVP) fortran subroutines, which have been developed at the Naval Research Laboratory (NRL) for the solution of elliptic partial differential equations using finite difference methods. The SEVP subroutines have been used extensively with the NRL numerical weather prediction models. Since the code was first developed (Madala, 1978), various enhancements have been made. The code is now also being more widely used at NRL and at other research institutions and a users guide has therefore become necessary.

The SEVP method is an efficient direct method which is used to solve the finite difference approximation to an elliptic partial differential equation of the form

$$\begin{aligned} a(x,y) \frac{\partial^2 \phi}{\partial x^2} + b(x,y) \frac{\partial^2 \phi}{\partial y^2} + c(x,y) \frac{\partial \phi}{\partial x} \\ + d(x,y) \frac{\partial \phi}{\partial y} + e(x,y) \phi = f(x,y) \end{aligned}$$

in which  $a(x,y) b(x,y) > 0$  on a rectangular domain in some arbitrary  $x$  and  $y$  coordinate system. Grid points may be of variable spacing. The boundary conditions for  $\phi(x,y)$  can be Dirichlet, Neumann, periodic in one direction, or a mixed combination of these. The SEVP solver can be used for separable and non-separable elliptic equations.

Common examples of these elliptic partial differential equations are Poisson's equation  $\nabla^2 \phi = f$  in two dimensions and the special case when  $f \equiv 0$ , Laplace's equation in two dimensions. For the boundary conditions in each case, the value of  $\phi$  (Dirichlet boundary condition) or the normal derivative of  $\phi$  (Neumann boundary condition) are specified on each boundary. Poisson's equation, for example, arises in boundary value problems in which a stream function is used to solve for the motion of an incompressible fluid when the vorticity is given. A Poisson's equation is also encountered whenever a steady state potential distribution is produced in response to sources or

sinks of a quantity, where the rate of flow of the quantity is proportional to the gradient of the potential distribution.

As shown in Madala (1978), the SEVP method, which is based on the error vector propagation (EVP) method (Hirota, et al., 1970; for example), is much faster than successive over-relaxation (by 10 to 20 times) and uses an order of magnitude less storage space than the method of Lindzen and Kuo (1969). Unlike the EVP method, which was shown by McAvaney and Leslie (1972) to be unstable for more than 40 grid points in the marching direction, the SEVP method is stable for any number of grid points. The stabilization is accomplished by dividing the integration region into EVP stable overlapping blocks and imposing artificial boundaries between the blocks.

In this report, the form of the difference equation, boundary conditions and the subroutine arguments for the SEVP solver are first described. We then describe the derivation of the difference equation and boundary conditions from a two-dimensional, elliptic partial differential equation, defined on a rectangular grid. The following sections describe the stabilized error vector propagation method and each of the SEVP subroutines. In the initial set up in subroutine SEVP, the difference equations are modified for the boundary conditions. The sections on the preprocessor subroutine BSM1 and the solution subroutines BSM2, BSM3 may be skipped by the reader who is only interested in using the routines. As an example, Poisson's equation is solved in spherical coordinates on a domain on the surface of the earth bounded by constant latitude and longitude circles. Two test examples demonstrating the use of Dirichlet and Neumann boundary conditions in the y (marching) direction with periodic boundary conditions in x are described. A listing of the test programs is provided in the appendix.

## 2. SUBROUTINE SEVP

Subroutine SEVP solves a system of linear equations of the form

$$\begin{aligned} &AX(i,j)*X(i-1,j) + AY(i,j)*X(i,j-1) + BB(i,j)*X(i,j) \\ &\quad + CX(i,j)*X(i+1,j) + CY(i,j)*X(i,j+1) = F(i,j) \end{aligned} \quad (2.1)$$

for  $i = 2, \dots, M-1$  and  $j = 2, \dots, N-1$ .

with boundary conditions for  $j = 1$ ,  $j = N$ ,  $i = 1$  and  $i = M$  of the form

$$\begin{aligned} X(i,1) &= (1-A11)*X(i,1) + A11*(X(i,2) - F11(i)) \\ X(i,N) &= (1-A1N)*X(i,N) + A1N*(X(i,N-1) + F1N(i)) \quad \text{for } i = 1, \dots, M \\ \text{and} \\ X(1,j) &= (1-A21)*X(1,j) + A21*(X(2,j) - F21(j)) \\ X(M,j) &= (1-A2M)*X(M,j) + A2M*(X(M-1,j) + F2M(j)) \quad \text{for } j = 1, \dots, N \\ \text{or } X(1,j) &= X(M-1,j) \\ X(M,j) &= X(2,j) \quad \text{for } j = 1, \dots, N. \end{aligned} \quad (2.2)$$

These difference equations result from the discretization of elliptic partial differential equations of the form

$$\begin{aligned} a(x,y) \frac{\partial^2 \phi}{\partial x^2} + b(x,y) \frac{\partial^2 \phi}{\partial y^2} + c(x,y) \frac{\partial \phi}{\partial x} \\ + d(x,y) \frac{\partial \phi}{\partial y} + e(x,y) \phi = f(x,y) \end{aligned} \quad (2.3)$$

defined in a rectangular domain  $x_a < x < x_b$ ,  $y_a < y < y_b$  in which  $a(x,y) b(x,y) > 0$ , and the  $x$  and  $y$  represent some coordinate system. Grid points can be of variable spacing. Boundary conditions for  $\phi(x,y)$  may be Dirichlet or Neumann at the  $x$  and  $y$  boundaries  $x = x_a$ ,  $x = x_b$ ,  $y = y_a$ ,  $y = y_b$ ; or periodic in  $x$ ; or a mixed combination of these.

## 2.1 Description of Arguments

The SEVP subroutines are called by the statement

```
CALL SEVP(AX,AY,CX,CY,BB,RINV,RINV1,RCOR,NBSIZ2,IS,IE,INX,SUMF,  
DUMMY1,RTILDA,X,F,ERR,F11,F1N,F21,F2M,M,N,M1,N1,M2,N2,NBLK,  
NBLK1,B1,B2,A11,A1N,A21,A2M,ICY,TOL,IFLG)
```

where the arguments are as follows:

### ON INPUT

M

The number of points in the i direction, including the boundary.

M1 = M-1, M2 = M-2.

N

The number of points in the j (marching) direction, including the boundary.  
N must be larger than 4.

N1 = N-1, N2 = N-2.

NBLK

Represents the number of blocks in j (marching) direction. For N larger than 14,  $NBLK = (N+3)/9$  gives blocks of approximately 8 to 13 rows each. For N less than 11 but larger than 4, use  $NBLK = 1$ ; while for N between 11 and 14, one or two blocks may be used.

Note: For the case of Neumann boundary conditions at boundary  $j = N$  (i.e.  $A1N = 1$ ) and with NBLK larger than one, last block is fixed with 7 rows by SEVP solver, to allow for a more efficient convergence of the solution. In this case, use formula to calculate the number of blocks required for the first N-5 rows and then add one to get total number of blocks.

NBLK1

= NBLK-1, for NBLK greater than one.

= 1 for NBLK equal to one.

AX, AY, CX, CY, BB

Two-dimensional arrays of dimension M x N containing the coefficients of the difference equation.

X

Two-dimensional array that on input contains an initial guess for solution on interior points  $i = 2, \dots, M-1$ ,  $j = 2, \dots, N-1$ ; and for Dirichlet boundary conditions, contains the boundary values at the appropriate boundaries. Initial guess might be an average of the boundary values (for Dirichlet BC's) or a zero value (for Neumann BC's), for example.

F

Two-dimensional array of dimension M x N that specifies the forcing on the right hand side of the difference equation.



F11, F1N

One-dimensional arrays of length M that contain coefficients for the Neumann boundary conditions at the j boundaries.

F21, F2M

One-dimensional arrays of length N that contain coefficients for the Neumann boundary conditions at the i boundaries.

A11, A1N, A21, A2M

Real variables which take the value 0.0 for Dirichlet boundary conditions, and 1.0 for Neumann boundary conditions at their respective boundaries. A11 corresponds to  $j = 1$ , A1N to  $j = N$ , A21 to  $i = 1$ , and A2M to  $i = M$ . For periodic boundary conditions in i (with ICY = 1), A21 and A2M are zero.

ICY

= 1 for periodic boundary conditions in i.  
= 0, otherwise.

TOL

Error tolerance for SEVP solver.

IFLG

= 0 for first call of SEVP solver. Preprocessor, subroutine BSM1 called.  
= 1 for subsequent calls if coefficients AX, AY, CX, CY, BB of difference equation and the boundary condition type A11, A1N, A21, A2M, ICY do not change. Preprocessor is then skipped.

#### ON OUTPUT

X

Two-dimensional array of dimension M x N containing the solution.

ERR

Two-dimensional array of dimension M x N containing the residual error for the difference equation.

#### OUTPUT ARRAYS COMPUTED BY PREPROCESSOR

These arrays must not be destroyed if SEVP will be called again with IFLG = 1.

RINV

Three-dimensional array of dimension M2 x M2 x NBLK, containing two-dimensional M2 x M2 influence or residual matrices for the blocks. The first NBLK-1 influence matrices relate the solution error on the last interior row of each block to that on the second row of that block. The last two-dimensional matrix is a residual matrix relating the residual error computed on the last interior row to the solution error on the second row of the last block.

RINV1

Three-dimensional array of dimension M2 x M2 x NBLK1, containing NBLK-1 two-dimensional M2 x M2 influence matrices, which relate the solution error on the last two rows of each block, except the last.

### WORKING INTEGER ARRAYS

#### NBSIZ2

One-dimensional integer array of size NBLK, containing the number of interior rows in the j (marching) direction between the end boundaries of the blocks. The first block contains a total of NBSIZ2(1) + 2 rows, while the remaining blocks contain NBSIZ2() + 3 rows each.

#### IS, IE

One-dimensional integer arrays of size NBLK, defining the beginning and end row of each block, respectively.

#### INX

One-dimensional integer array of size M containing i indices.

### WORKING REAL ARRAYS

#### SUMF

One-dimensional array of size NBLK containing the sum of the absolute values of the forcing on the last interior row of each block.

#### RCOR

Two-dimensional array of dimension M x 3 containing set of three row vectors used for marching in j direction.

#### RTILDA

One-dimensional error vector of size M-2.

#### B1, B2

One-dimensional work arrays of size M-2.

#### DUMMY1

Two-dimensional work arrays of size M-2 x M-2.

### INTERNAL PARAMETERS IN SUBROUTINE SEVP

#### IOUT

To print residual errors after each iteration set iout=1, otherwise iout=0.

#### EPS

The machine precision of computer, used as a lower limit on the tolerance TOL. For the Cray with 64 bit words, single precision floating point words (with 48 bit mantissa) are precise to 14 decimal places or for a machine precision of about  $0.5 \times 10^{-14}$ .

#### MAXSIZ

Maximum number of points allowed in each block. For the precision of the Cray computer setting MAXSIZ = 15 ensures the solver converges rapidly to a solution.

IX, JX, JF

For 4-sided Neumann, or 2-sided Neumann with cyclic boundary conditions, a boundary value must be prescribed at point (IX, JX) for a solution to be obtained. JF is the nearest interior row to the prescribed boundary point (IX, JX). For boundary point IX=2, JX=1, the nearest interior row is JF=2.

PROGRAM LANGUAGE Fortran-77

PRECISION Single precision on 64 bit computer. For 32 bit computer, subroutines should be modified for double precision.

ORIGINATOR Rangarao V. Madala  
Naval Research Laboratory, Washington D.C. 20375

### 3. DIFFERENCE APPROXIMATION

In this section we show how the difference equation is derived from a two-dimensional elliptic partial differential equation. A two-dimensional elliptic equation of the form

$$\begin{aligned} a(x,y) \frac{\partial^2 \phi}{\partial x^2} + b(x,y) \frac{\partial^2 \phi}{\partial y^2} + c(x,y) \frac{\partial \phi}{\partial x} \\ + d(x,y) \frac{\partial \phi}{\partial y} + e(x,y) \phi = f(x,y) \end{aligned} \quad (3.1)$$

is assumed to be defined in a rectangular domain  $x_a < x < x_b$ , and  $y_a < y < y_b$ , where  $a(x,y) c(x,y) > 0$ , with boundary conditions specified at boundaries  $x=x_a$ ,  $x=x_b$ ,  $y=y_a$ , and  $y=y_b$ . Boundary conditions may be Dirichlet, Neumann in  $x$  and  $y$  or periodic in  $x$ .

As an illustration, we define a grid mesh of  $M$  by  $N$  points  $(x_i, y_j)$  with a grid spacing of constant  $\Delta x$  and  $\Delta y$ . However, variable grid spacing can be used, resulting in modification to the coefficients of the difference equation. A second order finite difference approximation of Eq. (3.1), using a five point stencil, is then

$$\begin{aligned} a_{i,j} \frac{\phi_{i+1,j} - 2\phi_{i,j} + \phi_{i-1,j}}{\Delta x^2} + b_{i,j} \frac{\phi_{i,j+1} - 2\phi_{i,j} + \phi_{i,j-1}}{\Delta y^2} \\ + c_{i,j} \frac{\phi_{i+1,j} - \phi_{i-1,j}}{2\Delta x} + d_{i,j} \frac{\phi_{i,j+1} - \phi_{i,j-1}}{2\Delta y} \\ + e_{i,j} \phi_{i,j} = f_{i,j} \end{aligned} \quad (3.2)$$

where  $\phi_{i,j} = \phi(x_i, y_j)$ ,

$f_{i,j} = f(x_i, y_j)$

and  $a_{i,j} = a(x_i, y_j)$ , etc.

By defining  $X(i,j) = \phi_{i,j}$  and

$$\begin{aligned}
AX(i,j) &= \frac{a_{i,j}}{\Delta x^2} - \frac{c_{i,j}}{2 \Delta x} \\
AY(i,j) &= \frac{b_{i,j}}{\Delta y^2} - \frac{d_{i,j}}{2 \Delta y} \\
CX(i,j) &= \frac{a_{i,j}}{\Delta x^2} + \frac{c_{i,j}}{2 \Delta x} \\
CY(i,j) &= \frac{b_{i,j}}{\Delta y^2} + \frac{d_{i,j}}{2 \Delta y} \\
BB(i,j) &= - \frac{2 a_{i,j}}{\Delta x^2} - \frac{2 b_{i,j}}{\Delta y^2} + e_{i,j} \\
F(i,j) &= f_{i,j}
\end{aligned} \tag{3.3}$$

Our difference equation (3.2) can then be written in the form

$$\begin{aligned}
AX(i,j)*X(i-1,j) + AY(i,j)*X(i,j-1) + BB(i,j)*X(i,j) \\
+ CX(i,j)*X(i+1,j) + CY(i,j)*X(i,j+1) = F(i,j)
\end{aligned} \tag{3.4}$$

for  $i = 2, \dots, M-1$  and  $j = 2, \dots, N-1$ .

We will now demonstrate the use of Neumann, Dirichlet and periodic boundary conditions in  $x$ .

### 3.1 Dirichlet Boundary Conditions

For Dirichlet boundary conditions in  $x$ , boundary values are given at  $x=x_a$  and  $x=x_b$

$$\phi(x_a, y) = p(y)$$

$$\text{and } \phi(x_b, y) = q(y) \text{ for } y_a \leq y \leq y_b$$

For our grid mesh, defining  $M$  points in  $x$  with

$$x_i = (i-1) \Delta x + x_a \text{ for } i = 1, \dots, M$$

where  $\Delta x = (x_b - x_a) / (M-1)$ , we have

$$\phi(1, j) = p_j$$

$$\phi(M, j) = q_j \text{ for } j = 1, \dots, N$$

By defining  $A_{21} = A_{2M} = 0.0$  and

$$X(1, j) = p_j \text{ and } X(M, j) = q_j \text{ for } j=1, \dots, N$$

our boundary conditions are in the appropriate form of Eq. (2.2).

### 3.2 Neumann Boundary Conditions

For Neumann boundary conditions in  $x$ , derivatives are specified at the boundaries  $x=x_a$  and  $x=x_b$

$$\frac{\partial \phi}{\partial x}(x_a, y) = u(y) \quad \text{and} \quad \frac{\partial \phi}{\partial x}(x_b, y) = v(y) \quad \text{for } y_a < y < y_b$$

For our grid mesh, we include two columns of fictitious points at  $x_a - \Delta x/2$  and  $x_b + \Delta x/2$ , and define our  $x$  grid points with a shift of  $\Delta x/2$ , so that

$$x_i = (i-1) \Delta x + x_a - \Delta x/2 \quad \text{for } i = 1, \dots, M$$

with  $\Delta x = (x_b - x_a)/(M-2)$ . Then using centered differences we have

$$\frac{\phi_{2,j} - \phi_{1,j}}{\Delta x} = u_j \quad \text{and} \quad \frac{\phi_{M,j} - \phi_{M-1,j}}{\Delta x} = v_j \quad \text{for } j = 2, \dots, N-1$$

By defining  $A21 = A2M = 1.0$ ,

$$F21(j) = \Delta x u_j, \quad \text{and} \quad F2M(j) = \Delta x v_j \quad \text{for } j = 2, \dots, N-1$$

we have our boundary conditions in the appropriate form of Eq. (2.2).

### 3.3 Periodic Boundary Conditions

Suppose that  $\phi$  is a periodic function in  $x$  with period  $L = x_b - x_a$  so that

$$\phi(x+x_b, y) = \phi(x+x_a, y)$$

With a column of points included at  $x=x_b+\Delta x$ , we define our grid mesh over a  $x$  domain of  $x_a \leq x \leq x_b+\Delta x$  so that

$$x_i = (i-1) \Delta x + x_a \quad \text{for } i = 1, \dots, M$$

with  $\Delta x = (x_b - x_a)/(M-2)$ . Then we have

$$\phi_{1,j} = \phi_{M-1,j} \quad \text{and} \quad \phi_{M,j} = \phi_{2,j} \quad \text{for } j = 1, \dots, N.$$

Setting  $ICY = 1$  with  $A21 = A2M = 0.0$  will give the boundary conditions

$$X(1,j) = X(M-1,j)$$

$$X(M,j) = X(2,j), \quad \text{for } j = 1, \dots, N$$

as required in Eq. (2.2).

#### 4. SOLUTION METHOD

The method is based on the error propagation method (EVP) or sweep out method (Hirota et al., 1970). In the EVP method, a forward sweep provides a particular solution, which is followed by a further forward sweep of the solution error and the correction of the solution. We demonstrate the method for the case of Dirichlet boundary conditions.

At the interior points, we start with an initial guess solution, which may be a constant value equal to the average of the boundary values, for example. Rearranging the difference equation (2.1) we can write

$$X(i,j+1) = [F(i,j) - AX(i,j)*X(i-1,j) - AY(i,j)*X(i,j-1) - BB(i,j)*X(i,j) - CX(i,j)*X(i+1,j)] / CY(i,j)$$

for  $i = 2, \dots, M-1$  and  $j = 2, \dots, N-1$ . (4.1)

A particular solution  $X_p(i,j)$  can be found by starting with the initial guess on the second row  $j = 2$  and marching Eq. (4.1) forward row by row to the end boundary  $j = N$ . The particular solution  $X_p(i)$  then satisfies the boundary conditions on three sides  $j = 1$ ,  $i = 1$ ,  $i = M$  but differs from the solution at the end boundary  $j = N$  by an error row vector defined by

$$\begin{aligned} \epsilon_N(i) &= X(i,N) - X_p(i,N) \\ &= X(i,N) - [F(i,N-1) - AX(i,N-1)*X_p(i-1,N-1) - AY(i,N-1)*X_p(i,N-2) \\ &\quad - BB(i,N-1)*X_p(i,N-1) - CX(i,N-1)*X_p(i+1,N-1)] / CY(i,N-1) \end{aligned}$$

for  $i = 2, \dots, M-1$ . (4.2)

A solution error  $X_h(i,j) = X(i,j) - X_p(i,j)$  can be defined which satisfies the homogeneous difference equation (Eq. (2.1) with  $F = 0$ ) with the homogeneous boundary conditions on the three sides

$$\begin{aligned} X_h(i,1) &= 0, \text{ for } i = 1, \dots, M \\ X_h(1,j) &= X_h(M,j) = 0 \text{ for } j = 1, \dots, N \end{aligned} \quad (4.3)$$

and a non-zero boundary value given by the solution error

$$X_h(i,N) = \epsilon_N(i) \text{ for } i = 2, \dots, M-1 \quad (4.4)$$

at the end boundary  $j = N$ . We can compute an influence matrix which relates the solution error on the last interior row to that on the second row. The solution error can then be obtained for the whole domain by marching forward from the second row and the particular solution corrected to give the solution.

To obtain the influence matrix we start with a unit row vector  $e_k$  defined on the second row. The unit row vector  $e_k$  has the  $k^{\text{th}}$  element unity and the

remaining elements zero. Marching the unit row vector forward, using the homogeneous difference equation, we obtain influence row vectors  $t_k$  on the last row  $j = N$ , defining the  $k^{\text{th}}$  row of our influence matrix  $T$ . Repeating the marching sequence for all the  $M-1$  unit row vectors defines a set of  $M-1$  influence row vectors, completing the influence matrix  $T$ . Using a linear combination of influence vectors and the principle of linear superposition, we can relate our error row vector  $\epsilon_N(i)$  (for the last row  $j = N$ ) to the error vector  $\epsilon_2(i)$  ( $= X_h(i,2)$ ) on the first interior row  $j = 2$ . That is, in matrix form using the influence matrix, we have

$$\epsilon_N = \epsilon_2 T \quad (4.5)$$

Therefore given the computed particular solution  $X_p(i,j)$  and the error vector  $\epsilon_N$  on the last row, the error vector can be computed on the first interior row,

$$\epsilon_2 = \epsilon_N T^{-1}. \quad (4.6)$$

Then marching the solution error forward provides the solution error throughout the whole domain, and, when combined with the particular solution, completes the solution.

The marching of the solution error can alternatively be conceptualized as follows. The error vector  $\epsilon_N$  at the end boundary  $j = N$  can be related to a residual vector  $\rho$  defined on the last interior row  $j=N-1$ . Rearranging Eq. (4.2), we have

$$\begin{aligned} & AX(i,N-1)*X_p(i-1,N-1) + AY(i,N-1)*X_p(i,N-2) + BB(i,N-1)*X_p(i,N-1) \\ & + CX(i,N-1)*X_p(i+1,N-1) + CY(i,N-1)*X(i,N) \\ & = F(i,N-1) + CY(i,N-1)*\epsilon_N(i) \end{aligned} \quad (4.7)$$

where we define the residual vector  $\rho$  on the last interior row  $j = N-1$  by

$$\rho(i) = CY(i,N-1)*\epsilon_N(i), \quad \text{for } i = 2, \dots, M-1. \quad (4.8)$$

The solution error can now be thought of satisfying the homogeneous boundary conditions on all sides and the homogeneous difference equation at all rows except at the last interior row. At the last row  $j=N-1$ , the solution satisfies the difference equation with a forcing function given by the residual  $\rho$ . By similarly marching the unit vectors forward, a set of residuals can be computed on the last interior row, defining a residual matrix  $R$  (Hirota, et al, 1970). The residual matrix then relates the solution error on the second row to the residual  $\rho$  defined on the last interior row.

$$\rho = \epsilon_2 R \quad (4.9)$$



The two equivalent views of the solution error are shown schematically below in Fig. 1.

Due to round-off errors in marching the particular solution forward and due to inaccuracies in the computed inverse  $T^{-1}$ , the error vector  $\epsilon_2$  computed on the second row using Eq. (4.6) is an approximation to the true error vector. Marching the error vector forward then and correcting the particular solution provides an approximate solution. Provided that the error vector is not too inaccurate, an improved solution can be found by recomputing a new error vector on the last row and repeating the above procedure. A number of iterations of the procedure are usually required to converge to an accurate solution.

#### SOLUTION ERROR

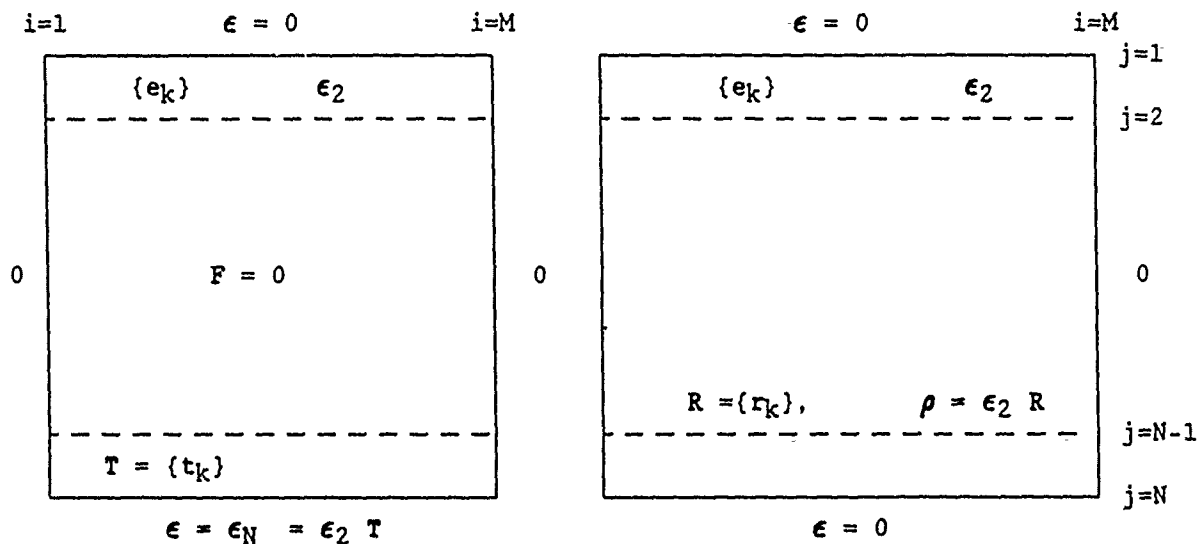


Fig. 1. The two equivalent views of the boundary conditions and forcing for the solution error. (a) Solution error satisfies homogeneous difference equation with a non zero boundary condition at  $j=N$  given by the error vector  $\epsilon_N$ . Influence matrix  $T$  found by marching set of unit vectors  $\{e_k\}$  to last row  $j = N$ . (b) Solution error satisfies homogeneous boundary conditions with non-zero line forcing function given by the residual  $\rho$  at  $j=N-1$ . Residual matrix  $R$  found by marching unit vectors  $\{e_k\}$  to last interior row  $j = N-1$  and computing residuals  $r_k$  on that row.

As pointed out by McAvaney and Leslie (1972), the residual matrix (or equivalently the influence matrix) is ill-conditioned, with the degree of ill-conditioning increasing rapidly with increasing number of points  $N$  in the marching direction. For large  $N$ , the inverse of the influence matrix may not be computed very accurately and for moderate round-off error any accuracy in the computed error vector may be lost. The iterative procedure then will not converge to a solution. The accuracy of the inverse therefore limits the number of points that can be effectively used in the marching and correction process. On the Cray computer with 64 bit words, this limit is about 20 points. The degree of ill-conditioning of the influence matrix, which leads to inaccuracies in the inverse, can be measured by a condition number defined by

$$\text{cond}(T) = \|T\| \|T^{-1}\| \quad (4.10)$$

where  $\|T\|$  and  $\|T^{-1}\|$  are matrix norms of the influence matrix and its inverse, respectively (see Dahlquist and Bjorck, 1974; for example). Then given an error  $\|\delta\epsilon_N\|$  in the error vector on the last row, an upper bound on the relative error of the computed error vector on the second row can be shown to be

$$\frac{\|\delta\epsilon_2\|}{\|\epsilon_2\|} \leq \text{cond}(T) \frac{\|\delta\epsilon_N\|}{\|\epsilon_N\|} \quad (4.11)$$

where the matrix and vector norms are defined in a consistent manner (see Dahlquist and Bjorck). For example, taking the case of a domain with 14 points in the marching  $j$  direction and 51 points in  $i$  direction the condition number is computed to be of order  $10^8$ . Then given an extreme case of a high relative round-off error of  $10^{-12}$  in the computed error vector  $\epsilon_N$  on the last row, when using single precision floating point numbers on the 64 bit Cray computer, we expect the computed error vector on the second row to have a precision of at least four significant figures (for a relative error of  $10^{-4}$ ). The iterative procedure will then converge to a solution.

To stabilize the EVP method for a large number of grid points, Madala (1978) divided the domain into a series of blocks in the marching direction. Adjacent blocks overlap in the marching direction so that the first and last two rows of adjacent blocks are common. To provide for a rapid convergence

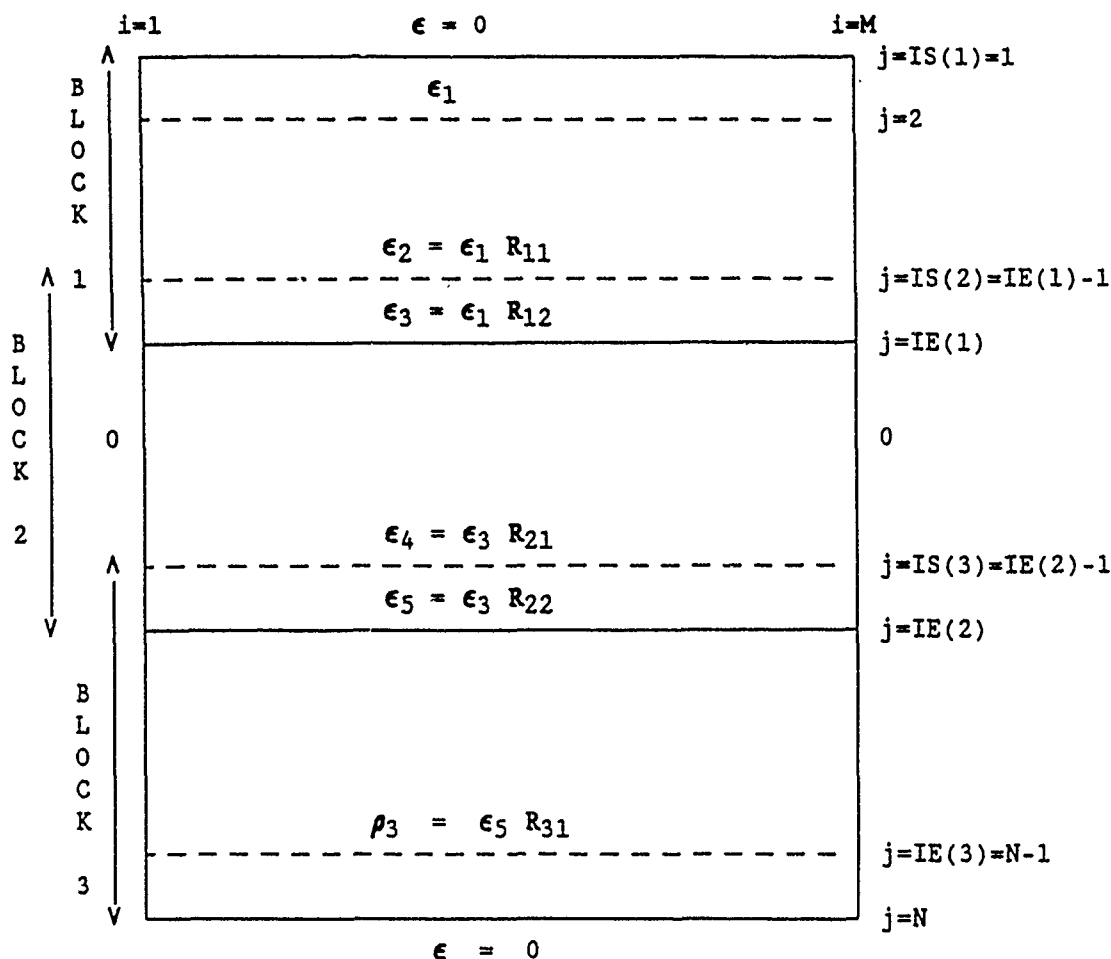


Fig. 2. The relationship between the error vectors  $\epsilon$  on various rows at the block boundaries and the residual error  $\rho_3$  on the next to the last row  $j=N-1$ , for the case of three blocks.  $R_{11}$ ,  $R_{12}$ ,  $R_{21}$ ,  $R_{22}$  are influence matrices and  $R_{31}$  is a residual matrix, defined on the rows shown.

of the iterative procedure, the number of points in each block is limited to less than 15 points.

In the preprocessor step,  $NBLK \times 2 - 1$  matrices are computed which relate the solution error on various boundary rows of each block. In Fig. 2, showing three blocks for example, the influence matrices  $R_{12}$ ,  $R_{11}$  for the first block relate the error vector  $\epsilon_1$  on the second row to the error vector  $\epsilon_3$  on the last row and to the error vector  $\epsilon_2$  on the next to the last row, respectively. Similar influence matrices  $R_{22}$ ,  $R_{21}$  are computed for the second block. For the

last block a residual matrix  $R_{31}$  relates the residual solution error  $\rho_3$  on the last interior row  $j=N-1$  to the error vector  $\epsilon_5$  on the second row of the last block.

In the forward sweep a particular solution is found by the marching and correction process above, satisfying the boundary conditions and the initial guess field on the interior block boundaries. The particular solution satisfies the forcing function at all points except on the last interior row, where the difference equation satisfies the forcing plus a residual  $\rho_3$ . In the backward sweep a solution error can be computed on the block boundaries and the first interior row from the residual  $\rho_3$  on the last interior row, using the residual and influence matrices defined for the blocks. By marching the solution error forward in each block the particular solution is then corrected to give the solution. The details of the stabilized error vector propagation method are described in the next chapter.

## 5. DESCRIPTION OF SEVP SUBROUTINES

### 5.1 Initial Set-up, SEVP

In the main subroutine SEVP, the block boundaries are first computed for the prescribed number of blocks and the difference equations are modified to accommodate boundary conditions which are not Dirichlet.

Fig. 2 shows the relationship of the block boundaries for the case of three overlapping blocks. The beginning and end rows of the blocks are defined by the one-dimensional arrays IS and IE, respectively. The integer array NBSIZ2, defining the number of interior rows between the end boundaries of the blocks, is computed for the prescribed number of blocks in subroutine BLKSIZ. The first block contains a total of  $NBSIZ2(1) + 2$  rows, while the remaining blocks contain  $NBSIZ2() + 3$  rows each. For the special case of Neumann boundary conditions at boundary  $j = N$  (i.e.  $AlN = 1$ ), the last block (third block in Fig. 2) is set with  $NBSIZ2() = 4$  by BLKSIZ (for a total of 7 rows for the block), to provide for a more efficient convergence of the solution.

For the case of cyclic boundary conditions we define an  $i$  index  $INX(i)$  by

$$\begin{aligned} INX(i) &= i \text{ for } i=2, \dots, M-1 \\ INX(1) &= M-1 \\ INX(M) &= 2 \end{aligned} \quad (5.1)$$

The difference equation (2.1) is then modified

$$\begin{aligned} &AX(i,j)*X(INX(i-1),j) + AY(i,j)*X(i,j-1) + BB(i,j)*X(i,j) \\ &+ CX(i,j)*X(INX(i+1),j) + CY(i,j)*X(i,j+1) = F(i,j) \end{aligned} \quad (5.2)$$

for  $i = 2, \dots, M-1$  and  $j = 2, \dots, N-1$ .

to provide for the cyclic boundary conditions at the boundaries  $i = 1$  and  $i = M$ ,

$$\begin{aligned} X(1,j) &= X(M-1,j) \\ X(M,j) &= X(2,j), \text{ for } j = 2, \dots, N-1. \end{aligned} \quad (5.3)$$

In the case of Neumann boundary conditions at the  $x$  boundaries  $i = 1$  and  $i = M$ , our boundary conditions are

$$\begin{aligned} X(1,j) &= X(2,j) - F21(j) \text{ and} \\ X(M,j) &= X(M-1,j) + F2M(j) \text{ for } j = 2, \dots, N-1. \end{aligned} \quad (5.4)$$

Now the difference equation at  $i = 2$  is

$$\begin{aligned} AX(2,j)*X(1,j) + AY(2,j)*X(2,j-1) + BB(2,j)*X(2,j) + CX(2,j)*X(3,j) \\ + CY(2,j)*X(2,j+1) = F(2,j) \end{aligned} \quad (5.5)$$

for  $j = 2, \dots, N-1$ .

Substituting our boundary condition Eq (5.4) for  $X(1,j)$  in Eq. (5.5) we have

$$\begin{aligned} AY(2,j)*X(2,j-1) + [BB(2,j) + AX(2,j)]*X(2,j) + CX(2,j)*X(3,j) \\ + CY(2,j)*X(2,j+1) = [F(2,j) + AX(2,j)*F21(j)] \end{aligned} \quad (5.6)$$

for  $j = 2, \dots, N-1$ .

By redefining our variables such that

$$\begin{aligned} X(1,j) &\rightarrow 0.0 \\ BB(2,j) &\rightarrow BB(2,j) + AX(2,j) \\ F(2,j) &\rightarrow F(2,j) + AX(2,j)*F21(j) \text{ for } j = 2, \dots, N-1 \end{aligned} \quad (5.7)$$

we can leave the form of the difference equation the same as for the case of Dirichlet boundary conditions. Similarly, by redefining

$$\begin{aligned} X(M,j) &\rightarrow 0.0 \\ BB(M-1,j) &\rightarrow BB(M-1,j) + CX(M-1,j) \\ F(M-1,j) &\rightarrow F(M-1,j) - CX(M-1,j)*F2M(j) \text{ for } j = 2, \dots, N-1 \end{aligned} \quad (5.8)$$

the form of the difference equation is maintained for  $i=M-1$ . We have essentially folded our boundary conditions into the difference equation, ostensibly replacing Neumann boundary conditions with Dirichlet boundary conditions with zero boundary values  $X(1,j) = X(M,j) = 0.0$  at the boundaries  $i = 1$  and  $i = M$ , respectively. Similar modifications are made for Neumann boundary conditions at the  $y$  boundaries,  $j = 1$  and  $j = N$ .

In the case of 4-sided Neumann boundary conditions or 2-sided Neumann with cyclic boundary conditions in  $x$ , the solution is indeterminate. For if  $\phi$  is a solution, then so is  $\phi + \kappa$ , where  $\kappa$  is an arbitrary constant. For the solver to obtain a solution, a boundary value must be prescribed at some chosen boundary point (IX, JX). For the most efficient convergence of the solution, it is recommended that a zero value be used in this case for the initial guess and for the constant value at the prescribed boundary point. For the nearest interior row  $j = JF$  to the prescribed boundary point, the boundary point  $X(IX, JX)$  and the coefficients  $BB(IX, JF)$  and the forcing  $F(IX, JF)$  in the difference equation are not modified by the SEVP subroutine. The boundary point initially chosen in SEVP is  $IX = 2$ ,  $JX = 1$ , with the nearest interior row being  $JF = 2$ .

For convenience, we further modify the difference equation for  $j=N-1$  to include the Dirichlet boundary condition at  $j=N$  in the forcing function. In this case the value  $X(i,N)$  of the solution variable is prescribed on the boundary  $j=N$ . The difference equation for  $j=N-1$  is

$$\begin{aligned} & AX(i,N-1)*X(i-1,N-1) + AY(i,N-1)*X(i,N-2) + BB(i,N-1)*X(i,N-1) \\ & + CX(i,N-1)*X(i+1,N-1) + CY(i,N-1)*X(i,N) = F(i,N-1) \end{aligned} \quad (5.9)$$

for  $i = 2, \dots, M-1$ ,

which we rearrange as

$$\begin{aligned} & AX(i,N-1)*X(i-1,N-1) + AY(i,N-1)*X(i,N-2) + BB(i,N-1)*X(i,N-1) \\ & + CX(i,N-1)*X(i+1,N-1) = F(i,N-1) - CY(i,N-1)*X(i,N) \end{aligned} \quad (5.10)$$

for  $i = 2, \dots, M-1$ .

By redefining our forcing function at  $j=N-1$  such that

$$F(i,N-1) \rightarrow F(i,N-1) - CY(i,N-1)*X(i,N) \text{ for } i = 2, \dots, M-1 \quad (5.11)$$

we can assume for convenience that  $X(i,N) = 0.0$  at the end boundary  $j = N$ .

## 5.2 The Preprocessor, BSM1

In the preprocessor, subroutine BSM1,  $NBLK \times 2 - 1$  matrices are computed which relate the solution error on various boundary rows of each block and the residual error on the last interior row  $j = N-1$ . The solution error satisfies homogeneous boundary conditions on all sides, and the homogeneous difference equation at all interior points except the last interior row  $j = N-1$ . On the last interior row the solution error is forced by a residual.

To obtain the influence matrices for the first block, the unit vector  $e_k$  (with the  $k^{th}$  element one) defined on the second row  $j = 2$ , is marched forward with homogeneous boundary conditions to compute row vectors on the last two rows of the block,  $j = IE(1)-1$ ,  $j = IE(1)$ . These define the  $k^{th}$  rows for two influence matrices (shown as  $R_{11}$  and  $R_{12}$  in Fig. 2) for the last two rows. Repeating the marching procedure for the other unit vectors completes the influence matrices  $R_{11}$  and  $R_{12}$ , which then relate the solution error vector  $\epsilon_1$  on the second row to the error vectors  $\epsilon_2$ ,  $\epsilon_3$  on the last two rows, respectively, so that

$$\epsilon_2 = \epsilon_1 R_{11} \quad (5.12)$$

and

$$\epsilon_3 = \epsilon_1 R_{12} \quad (5.13)$$

By matrix multiplication of the inverse of  $R_{11}$  times  $R_{12}$  a further influence matrix  $S_1$  can be obtained, which relates the solution error vector on the next to the last and the last rows of the first block. For by the elimination of  $\epsilon_1$  in Eqs. (5.12) and (5.13), we have

$$\epsilon_3 = \epsilon_2 R_{11}^{-1} R_{12} = \epsilon_2 S_1. \quad (5.14)$$

The inverse of the influence matrix  $S_1$  is computed using  $S_1^{-1} = R_{12}^{-1} R_{11}$ .

For the second block (and any other subsequent interior blocks), we again start with a unit vector defined on the second row of the block, but the vector on the first row is now defined by the  $k^{\text{th}}$  column of the inverse of the influence matrix  $S_1$  defined for the previous block. For if  $e_k$  is the unit vector, then the vector on the first row is given by  $e_k S_1^{-1}$ . Marching to the last row for each unit row vector, then defines the influence matrices  $R_{21}$  and  $R_{22}$  for the last two rows of the block. If error vectors  $\epsilon_3$ ,  $\epsilon_4$  and  $\epsilon_5$  represent the solution error on the second and last two rows of the block, respectively, then

$$\epsilon_4 = \epsilon_3 R_{21} \quad (5.15)$$

and

$$\epsilon_5 = \epsilon_3 R_{22} \quad (5.16)$$

An influence matrix  $S_2$  relating the solution error on the last two rows of the block is again defined so that

$$\epsilon_5 = \epsilon_4 S_2 \quad (5.17)$$

where  $S_2 = R_{21}^{-1} R_{22}$ , and its inverse also computed using  $S_2^{-1} = R_{22}^{-1} R_{21}$ .

For the last block (third block in Fig. 2), the unit vectors are marched to the next to last row and residuals computed, defining the rows of a residual matrix,  $R_{31}$ . The residual matrix then relates the residual solution error  $\rho$  on the last interior row  $j = N-1$  to the solution error  $\epsilon_5$  on the second row  $j = \text{IE}(2)$  of the last block, so that

$$\rho_3 = \epsilon_5 R_{31} \quad (5.18)$$



### 5.3 The Solution, BSM2, BSM3

In the forward sweep an approximate solution is found for each block, satisfying the boundary conditions and an initial guess field on the last row of each block. This particular solution satisfies the forcing function at all points except on the last interior row, where the difference equation satisfies the forcing plus a residual.

For the first block, we want to obtain the particular solution which satisfies an assigned initial guess value on the interior block boundary  $j = 1E(1)$ . The boundary values and the initial guess on the second row are used to march forward to the block boundary and the error  $\epsilon^p_3$  from the assigned guess value on the block boundary is computed. The required correction on the second row is then given by  $\epsilon^p_1 = \epsilon^p_3 R_{12}^{-1}$ , applying Eq. (5.13). By marching the error forward, the corrected particular solution is obtained. The process is repeated for several iterations to reduce the round off error.

For subsequent interior blocks, the particular solution on the first two rows of the block, which has been computed in the previous block, is similarly marched forward and corrected for the assigned initial guess value on the last row of this block. For the last block the particular solution from the previous block is marched to the last interior row  $j = N-1$  and a residual error  $\rho_3$  computed.

In the backward sweep, error vectors are computed on the block boundaries and the first interior row given the residual error on the last interior row, by using the residual and influence matrices defined for the blocks. The solution error can then be marched forward in each block and the particular solution corrected to give the solution.

For the case of three blocks, as shown in Fig. 3, we start the backward sweep with the residual error  $\rho_3$  given on the last interior row  $j = N-1$ . The error vectors  $\epsilon_4, \epsilon_5$  on the first two rows of the last block can then be computed using the residual matrix  $R_{31}$  and the influence matrix  $S_2$ , using

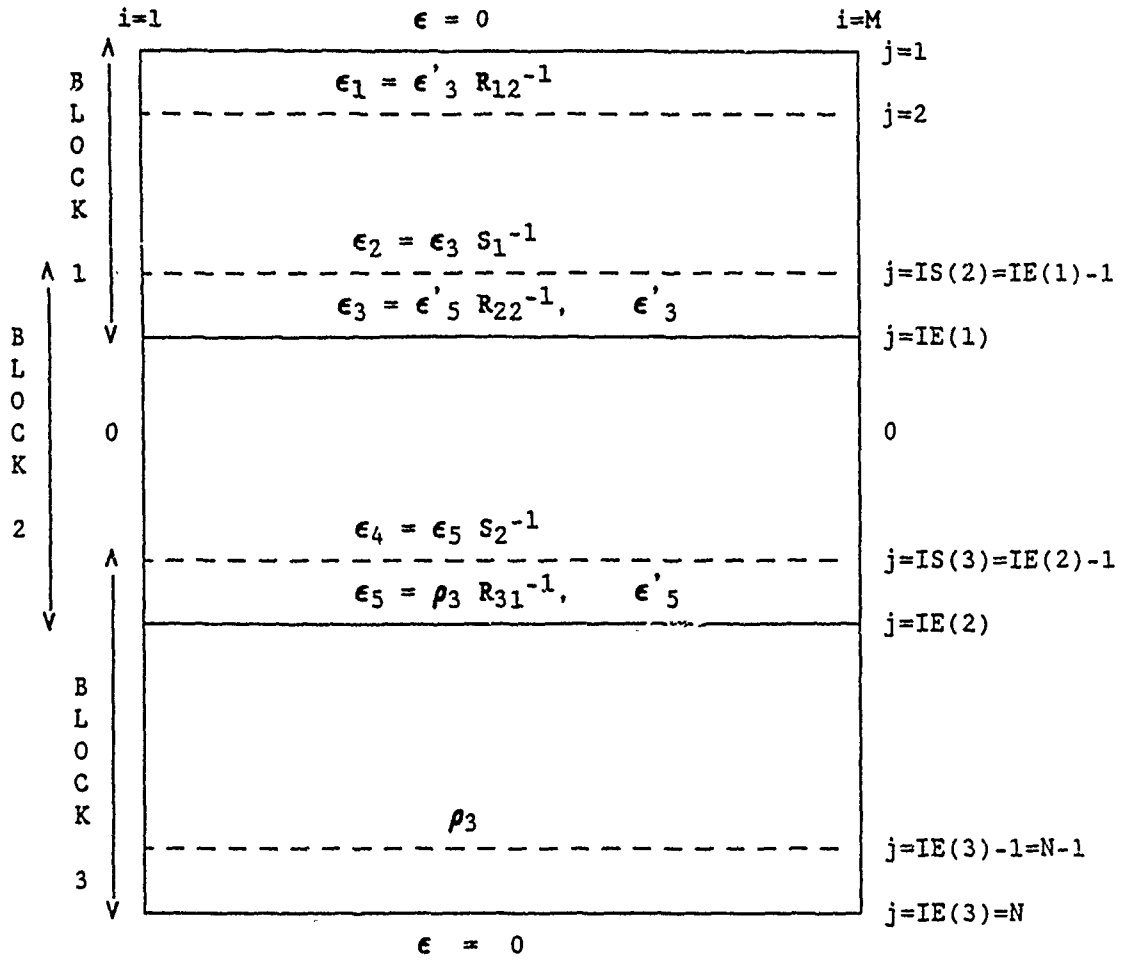


Fig. 3. The solution errors computed in the backward sweep of the blocks.  $\rho_3$  is the residual error on the row  $j=N-1$  and  $\epsilon$  represents the error vectors on the rows shown.

$$\epsilon_5 = \rho_3 R_{31}^{-1} \quad (5.19)$$

$$\epsilon_4 = \epsilon_5 S_2^{-1} \quad (5.20)$$

A forward marching of the solution error then corrects the solution in the last block. As before, several iterations are used to reduce round off error.

In the backward sweep of the remaining blocks, the particular solution is recomputed on the last row of each block and the solution error recomputed on the block boundary. For the second block in Fig. 3 for example, the error vector  $\epsilon'_5$  is recomputed by backing up three rows into the second block and

repeating a small segment of the forward sweep. The solution error is then obtained on the first two rows of the block using Eqs. (5.16) and (5.14),

$$\epsilon_3 = \epsilon'_5 R_{22}^{-1} \quad (5.21)$$

$$\epsilon_2 = \epsilon_3 S_1^{-1} \quad (5.22)$$

and the solution corrected throughout the block as above. For the first block the recomputed error vector  $\epsilon'_3$  on the last row provides the error vector  $\epsilon_1$  on the second row of the block by using Eq (5.13)

$$\epsilon_1 = \epsilon'_3 R_{12}^{-1} \quad (5.23)$$

and the solution corrected throughout the block.

With the correction of the solution in the first block the solution is complete. After the forward and backward sweep, the remaining residual error accumulates on the interior boundaries of the blocks. If necessary, the forward and backward sweep of the blocks is repeated for several iterations to reduce any remaining error.

## 6. DESCRIPTION OF TEST EXAMPLE

As an example we solve Poisson's equation  $\nabla^2 \phi = f$  in spherical coordinates in a rectangular domain on the surface of a spherical earth. We define transformed coordinates  $x$  and  $y$  by

$$x = r \lambda \text{ and } y = r \theta$$

where  $r = 6371$  km is the average radius of the earth,  $\theta$  and  $\lambda$  are the latitude and longitude, respectively in radians. In our coordinates, Poisson's equation is written

$$\frac{1}{h_x h_y} \left\{ \frac{\partial}{\partial x} \left[ \frac{h_y}{h_x} \frac{\partial \phi}{\partial x} \right] + \frac{\partial}{\partial y} \left[ \frac{h_x}{h_y} \frac{\partial \phi}{\partial y} \right] \right\} = f(x, y), \quad \begin{matrix} x_a < x < x_b \\ y_a < y < y_b \end{matrix} \quad (6.1)$$

where for our spherical coordinates the map factors  $h_x$  and  $h_y$  are

$$h_x = \cos \theta = \cos(y/r), \text{ and } h_y = 1.$$

For our rectangular domain we choose

$$x_a = 0 \text{ km}, x_b = 12,000 \text{ km}, y_a = 2,000 \text{ km and } y_b = 7,000 \text{ km}.$$

We want to force a wave solution on a zonal background field. An example of such a solution is given by

$$\phi(x, y) = 5.5 - 0.5 \tanh(y_p) + 0.5 \exp(-y_p^2) \cos \frac{2 \pi x}{L} \quad (6.2)$$

$$\text{where } y_p = \frac{y - y_c}{y_w}$$

and  $L = x_b - x_a = 12,000$  km,  $y_c = 4,500$  km,  $y_w = 1,500$  km. By applying Eq. (6.1), the appropriate forcing function for this solution is then

$$f(x, y) = \frac{1}{2 y_w^2} \left[ 2 \tanh(y_p) + \frac{y_w}{r} \tan\left(\frac{y}{r}\right) \right] \text{sech}^2(y_p) + \frac{1}{y_w^2} \left[ 2 y_p^2 + \frac{y_w}{r} \tan\left(\frac{y}{r}\right) y_p - c \right] \exp(-y_p^2) \cos\left(\frac{2 \pi x}{L}\right) \quad (6.3)$$

$$\text{where } c = 1 + \frac{2 \pi^2 y_w^2}{L^2 \cos^2\left(\frac{y}{r}\right)}$$

### 6.1 Dirichlet Boundary Conditions in y

Our boundary conditions are taken as periodic in x such that

$$\phi(x+x_b, y) = \phi(x+x_a, y)$$

and in this first case we treat Dirichlet boundary conditions at the y boundaries, specifying the values of  $\phi$  at  $y = y_a$  and  $y = y_b$ . That is

$$\begin{aligned}\phi(x, y_a) &= 5.9655 + 0.0311 \cos \frac{2\pi x}{L} \\ \phi(x, y_b) &= 5.0344 + 0.0311 \cos \frac{2\pi x}{L}\end{aligned}\tag{6.4}$$

We define a grid of  $M = 82$  by  $N = 51$  points  $(x_i, y_j)$  adding an extra column of points at  $x=x_b+\Delta x$  for the cyclic boundary conditions. The grid is then

$$\begin{aligned}x_i &= (i-1) \Delta x + x_a \text{ for } i = 1, \dots, M \\ y_j &= (j-1) \Delta y + y_a \text{ for } j = 1, \dots, N\end{aligned}\tag{6.5}$$

with  $\Delta x = (x_b - x_a)/(M-2) = 150$  km and  $\Delta y = (y_b - y_a)/(N-1) = 100$  km

Our Poisson's equation (6.1) can now be written in finite difference form as

$$\begin{aligned}\frac{1}{h_{xj} h_{yj} \Delta x} \left\{ \frac{h_{yj} [\phi_{i+1,j} - \phi_{i,j}]}{h_{xj} \Delta x} - \frac{h_{yj} [\phi_{i,j} - \phi_{i-1,j}]}{h_{xj} \Delta x} \right\} + \\ \frac{1}{h_{xj} h_{yj} \Delta y} \left\{ \frac{h_{xj+\frac{1}{2}} [\phi_{i,j+1} - \phi_{i,j}]}{h_{yj+\frac{1}{2}} \Delta y} - \frac{h_{xj-\frac{1}{2}} [\phi_{i,j} - \phi_{i,j-1}]}{h_{yj-\frac{1}{2}} \Delta y} \right\} \\ = f_{i,j}\end{aligned}\tag{6.6}$$

where  $h_{xj+\frac{1}{2}} = (h_{xj+1} + h_{xj})/2$  and with the boundary conditions (6.4)

$$\begin{aligned}
\phi_{i,1} &= 5.9655 + 0.0311 \cos \frac{2\pi x_i}{L} \\
\phi_{i,N} &= 5.0344 + 0.0311 \cos \frac{2\pi x_i}{L} \\
\text{and } \phi_{1,j} &= \phi_{M-1,j} \\
\phi_{M,j} &= \phi_{2,j}
\end{aligned} \tag{6.7}$$

The difference equation (6.6) can further be written as

$$\begin{aligned}
& [\phi_{i+1,j} - 2\phi_{i,j} + \phi_{i-1,j}] + \\
& \frac{h_{xj} \Delta x^2}{h_{yj} \Delta y^2} \left[ \frac{h_{xj+\frac{1}{2}} [\phi_{i,j+1} - \phi_{i,j}]}{h_{yj+\frac{1}{2}}} - \frac{h_{xj-\frac{1}{2}} [\phi_{i,j} - \phi_{i,j-1}]}{h_{yj-\frac{1}{2}}} \right] \\
& = h_{xj}^2 \Delta x^2 f_{i,j}
\end{aligned} \tag{6.7}$$

Setting  $\text{PHI}(i,j) = \phi_{i,j}$  and defining the coefficients in the form for the difference equation (2.1) we have for  $i = 2, \dots, M-1$  and  $j = 2, \dots, N-1$

$$\text{AX}(i,j) = 1.$$

$$\text{CX}(i,j) = 1.$$

$$\begin{aligned}
\text{AY}(i,j) &= \frac{h_{xj} (h_{xj} + h_{xj-1}) \Delta x^2}{h_{yj} (h_{yj} + h_{yj-1}) \Delta y^2} \\
\text{CY}(i,j) &= \frac{h_{xj} (h_{xj+1} + h_{xj}) \Delta x^2}{h_{yj} (h_{yj+1} + h_{yj}) \Delta y^2}
\end{aligned} \tag{6.8}$$

$$\text{BB}(i,j) = -2 - \text{AY}(i,j) - \text{CY}(i,j)$$

$$\text{F}(i,j) = h_{xj}^2 \Delta x^2 f_{i,j}$$

For our boundary conditions we have for  $i = 1, \dots, M$

$$\begin{aligned}
\text{PHI}(i,1) &= 5.9655 + 0.0311 \cos \frac{2 \pi x_i}{L} & \text{with } A_{11} &= 0.0 \\
\text{PHI}(i,N) &= 5.0344 + 0.0311 \cos \frac{2 \pi x_i}{L} & \text{with } A_{1N} &= 0.0
\end{aligned}
\tag{6.9}$$

and  $\text{ICY} = 0$ ,  $A_{21} = A_{2M} = 0.0$  giving

$$\text{PHI}(1,j) = \text{PHI}(M-1,j) \text{ and } \text{PHI}(M,j) = \text{PHI}(2,j) \tag{6.10}$$

As a first guess in the interior of the domain, we initially set PHI to the average of the boundary values at  $y = y_a$  and  $y = y_b$ , giving

$$\text{PHI}(i,j) = 5.5 \text{ for } i = 2, \dots, M-1 \text{ and } j = 2, \dots, N-1. \tag{6.11}$$

With a call to SEVP, the solution and the residual error are computed. The residual error gives the difference between the forcing and the discrete Laplacian of the computed solution. The maximum of the absolute values of the residual errors, divided by the maximum forcing is then computed and printed. A normalized discretization error is also computed by taking the maximum value of the absolute differences between the exact analytic solution Eq. (6.2) and the computed solution and dividing by the maximum value of the exact solution. With the Cray computer, the following values are printed:

Maximum residual error (normalized by maximum forcing) =  $5.9805 \times 10^{-11}$   
Maximum discretization error (normalized by maximum value of exact solution)  
=  $8.3005 \times 10^{-5}$ .

## 6.2 Neumann Boundary Conditions in y

Our boundary conditions are again taken as periodic in  $x$  such that

$$\phi(x+x_b, y) = \phi(x+x_a, y)$$

but in this case we treat Neumann boundary conditions at the  $y$  boundaries, specifying the values of the normal gradient of  $\phi$  at  $y = y_a$  and  $y = y_b$ . From our definition of  $\phi$  the  $y$ -gradient of  $\phi$  at the boundaries  $y = y_a$  and  $y = y_b$  is

$$\begin{aligned}\frac{\partial \phi}{\partial y}(x, y_a) &= \frac{-1}{2 y_w} \operatorname{sech}^2 y_{pa} - \frac{y_{pa}}{y_w} \exp(-y_{pa}^2) \cos \frac{2 \pi x}{L} \\ \frac{\partial \phi}{\partial y}(x, y_b) &= \frac{-1}{2 y_w} \operatorname{sech}^2 y_{pb} - \frac{y_{pb}}{y_w} \exp(-y_{pb}^2) \cos \frac{2 \pi x}{L}\end{aligned}\quad (6.12)$$

$$\text{where } y_{pa} = \frac{y_a - y_c}{y_w} \quad \text{and} \quad y_{pb} = \frac{y_b - y_c}{y_w}$$

We define a grid of  $M = 82$  by  $N = 53$  points  $(x_i, y_j)$  adding an extra column of points at  $x = x_b + \Delta x$  for the cyclic boundary conditions and two rows of points at  $y = y_a - \Delta y/2$  and  $y = y_b + \Delta y/2$  for the Neumann boundary conditions. The grid is then

$$\begin{aligned}x_i &= (i-1) \Delta x + x_a \quad \text{for } i = 1, \dots, M \\ y_j &= (j-1) \Delta y + y_a - \Delta y/2 \quad \text{for } j = 1, \dots, N\end{aligned}\quad (6.13)$$

with  $\Delta x = (x_b - x_a)/(M-2) = 150$  km and  $\Delta y = (y_b - y_a)/(N-2) = 100$  km.

Setting  $\text{PHI}(i, j) = \phi_{i, j}$ , the coefficients for the difference equation are defined by Eq. (6.8) as in the case of Dirichlet boundary conditions, but with the map factors computed for the new grid. For our boundary conditions we define

$$\begin{aligned}\text{Fl1}(i) &= \left[ \frac{-1}{2 y_w} \operatorname{sech}^2 y_{pa} - \frac{y_{pa}}{y_w} \exp(-y_{pa}^2) \cos \frac{2 \pi x_i}{L} \right] \Delta y \\ \text{FlN}(i) &= \left[ \frac{-1}{2 y_w} \operatorname{sech}^2 y_{pb} - \frac{y_{pb}}{y_w} \exp(-y_{pb}^2) \cos \frac{2 \pi x_i}{L} \right] \Delta y\end{aligned}\quad (6.14)$$

with  $\text{Al1} = 1.0$  and  $\text{AlN} = 1.0$

and  $\text{ICY} = 0$ ,  $\text{A21} = \text{A2M} = 0.0$  giving

$$\text{PHI}(1, j) = \text{PHI}(M-1, j) \quad \text{and} \quad \text{PHI}(M, j) = \text{PHI}(2, j) \quad (6.15)$$

With the boundary conditions as given, the solution is indeterminate. To obtain a unique solution, we require a value for the solution at a selected point chosen on the boundary (preset as  $i = 2, j = 1$  in the SEVP solver). For the most efficient convergence of the solver we use a zero value for PHI at this point and as the first guess, defining



$$\text{PHI}(i,j) = 0.0 \quad \text{for } i = 1, \dots, M \text{ and } j = 1, \dots, N. \quad (6.16)$$

With a call to SEVP, the solution and the residual error are computed. The residual error gives the difference between the forcing and the discrete Laplacian of the computed solution. The maximum of the absolute values of the residual errors, divided by the maximum forcing is then computed and printed. A normalized discretization error is also computed by taking the maximum value of the absolute differences between the exact analytic solution and the computed solution and dividing by the maximum value of the exact solution. With the Cray computer, the following values are printed:

[illegible]

## 7. REFERENCES

- Dahlquist, G., and A. Bjorck, 1974: Numerical Methods. Translated by N. Anderson, Prentice-Hall, 175-177.
- Hirota, I., T. Tokioka and M. Nishiguchi, 1970: A direct solution of Poisson's equation by generalized sweep-out method. J. Meteor. Soc. Japan, 48, 161-167.
- Lindzen, R.S., and H-L. Kuo, 1969: A reliable method for the numerical integration of a large class of ordinary and partial differential equations. Mon. Wea. Rev., 97, 732-734.
- Madala, R.V., 1978: An efficient direct solver for separable and non-separable elliptic equations. Mon. Wea. Rev., 106, 1735-1741.
- Madala, R.V., 1981: Solution of Elliptic Equations. Finite Difference Techniques for Vectorized Fluid Dynamic Calculations. D. Book, Ed., Chap. 7, Springer-Verlag, 117-135.
- McAvaney, B.J., and L.M. Leslie, 1972: Comments on "A direct solution of Poisson's equation by generalized sweep-out method. J. Meteor. Soc. Japan, 50, 136-137.

# APPENDIX: LISTING OF TEST PROGRAMS

## 1. Test Example with Dirichlet Boundary Condition

```

PROGRAM DRIVR1

C
C   This program uses SEVP to solve Poisson's equation
C       LAPLACIAN OF PHI = F
C   with cyclic boundary conditions in x and Dirichlet
C   boundary conditions in y.
C
PARAMETER (M=82, N=51)
PARAMETER (NBLK=(N+3)/9, NBLK1=NBLK-1)
PARAMETER (M1=M-1, M2=M-2, N1=N-1, N2=N-2)
PARAMETER (MN=M*N)
DIMENSION AX(M,N), AY(M,N), CX(M,N), CY(M,N), BB(M,N),
1 RINV(M2,M2,NBLK), RINV1(M2,M2,NBLK1), RCOR(M,3), RTILDA(M2),
2 NBSIZ2(NBLK), IS(NBLK), IE(NBLK), SUMF(NBLK), IXNDX(M),
3 DUMMY(M2,M2), B1(M2), B2(M2)
DIMENSION F(M,N), PHI(M,N), ERR(M,N)
DIMENSION F11(M), F1N(M), F21(N), F2M(N)
DIMENSION X(M), Y(N), YP1(N), YP2(N)
DIMENSION HXU(N), HXV(N1), HYU(N), HYV(N1)
DIMENSION AA(N), AC(N), CC(N)
DIMENSION T1(N), T2(N), T3(N), T4(N)
DIMENSION DUM3(M,N)
C SET COEFFICIENTS OF DIFFERENCE EQUATION AND BOUNDARY CONDITIONS TO
C ZERO INITIALLY
DATA AX/MN*0.0/, CX/MN*0.0/, AY/MN*0.0/, CX/MN*0.0/, BB/MN*0.0/,
1 F/MN*0.0/, F11/M*0.0/, F1N/M*0.0/, F21/N*0.0/, F2M/N*0.0/
C
PI = 4.0*ATAN(1.0)
AR = 6371.
XL = 12000.0
YL = 5000.0
C
C DEFINE GRID
DELX = XL/FLOAT(M-2)
DELY = YL/FLOAT(N-1)
PRINT 990, DELX, DELY
990 FORMAT(1H, 5HDELX=, 1PE13.5, 5X, 5HDELY=, 1PE13.5)
DO 5 J=1, N
Y(J)=DELY*FLOAT(J-1)+2000.
5 CONTINUE
DO 6 I=1, M
X(I)=DELX*FLOAT(I-1)
6 CONTINUE
DELXSQ=DELX*DELX
DELYSQ=DELY*DELY
C DEFINE MAP FACTORS
DO 10 J=1, N
HXU(J)=COS(Y(J)/AR)
HYU(J)=1.0
10 CONTINUE

```

```

      DO 20 J=1,N1
      HXV(J)=0.5*(HXU(J)+HXU(J+1))
      HYV(J)=1.0
20  CONTINUE
C
C  DEFINE FORCING FUNCTION
      XC= 0.0
      YC = 4500.0
      YW = 1500.0
      C1=YW/AR
      C2=1./(YW*YW)
      C3=2.*PI*PI*(YW/XL)*(YW/XL)
      DO 60 J=1,N
      YP1(J)=(Y(J)-YC)/YW
      YP2(J) = Y(J)/AR
60  CONTINUE
      DO 61 J=1,N
      T1(J) = TANH(YP1(J))
      T2(J) = EXP(-YP1(J)*YP1(J))
61  CONTINUE
      DO 62 J=1,N
      CSQ=COS(YP2(J))*CC ( T2(J))
      T3(J)=2.*T1(J)+C1* YP2(J))
      T4(J)= 2.*YP1(J)*YP1(J) - 1.0 + C1*YP1(J)*TAN(YP2(J))
1    C3/CSQ
62  CONTINUE
C  FORCING FUNCTION DEFINED AT INTERIOR POINTS OF DOMAIN ONLY
      DO 65 J=2,N-1
      DO 65 I=2,M-1
      F(I,J) = 0.5*C2*T3(J)*(1.-T1(J)*T1(J))
1    + C2*T4(J)*T2(J)*COS(2.*PI*(X(I)-XC)/XL)
65  CONTINUE
C
C
C  DIRICHLET BOUNDARY CONDITIONS IN Y
      A11 = 0.0
      A1N = 0.0
      DO 100 I=1,M
      PHI(I,1)=5.5-0.5*T1(1)+0.5*T2(1)*COS(2.*PI*(X(I)-XC)/XL)
      PHI(I,N)=5.5-0.5*T1(N)+0.5*T2(N)*COS(2.*PI*(X(I)-XC)/XL)
100  CONTINUE
C
C  FOR DIRICHLET B.C. INITIALLY SET PHI IN INTERIOR TO AVERAGE
C  OF BOUNDARY VALUES
      AVPH = 0.0
      DO 110 I=2,M1
      AVPH = AVPH+PHI(I,1)+PHI(I,N)
110  CONTINUE
      AVPH=AVPH/FLOAT(2*(M-2))
      DO 120 J=2,N1
      DO 120 I=2,M1
      PHI(I,J)= AVPH
120  CONTINUE
C  FOR CYCLIC BOUNDARY CONDITIONS

```

```

        ICYC = 1
        A21 = 0.0
        A2M = 0.0
        DO 130 J=1,M
            PHI(1,J) = PHI(M-1,J)
            PHI(M,J) = PHI(2,J)
130 CONTINUE
C
C DEFINE COEFFICIENTS ON L.H.S. OF DIFFERENCE EQUATION.
C COEFFICIENTS DEFINED IN INTERIOR OF DOMAIN ONLY.
        DO 25 J=2,N-1
            AA(J)=(HXU(J)*HXV(J-1))/(HYV(J-1)*HYU(J))*(DELXSQ/DELYSQ)
            CC(J)=(HXU(J)*HXV(J))/(HYV(J)*HYU(J))*(DELXSQ/DELYSQ)
            AC(J)=-AA(J)-CC(J)
25 CONTINUE
        DO 165 I = 2,M-1
        DO 165 J = 2,N-1
            AX(I,J) = 1.0
            CX(I,J) = 1.0
            AY(I,J) = AA(J)
            CY(I,J) = CC(J)
            BB(I,J) = AC(J)-2.0
165 CONTINUE
C DEFINE R.H.S. OF DIFFERENCE EQUATION, SCALING FORCING FUNCTION
        DO 170 J=2,N-1
        DO 170 I=2,M-1
            CON = HXU(J)*HXU(J)*DELXSQ
            F(I,J) = F(I,J)*CON
170 CONTINUE
            FMAX = 0.
        DO 305 J=2,N-1
        DO 305 I=2,M-1
            FMAX = AMAX1(FMAX,ABS(F(I,J)))
305 CONTINUE
C
C
C TOLERANCE FOR SOLVER
        TOL = 1.0E-8
C
        IFLG = 1
        CALL SEVP(AX,AY,CX,CY,BB,RINV,RINV1,RCOR,NBSIZ2,IS,IE,IXNDX,
1SUMF,DUMMY,RTILDA,PHI,F,ERR,F11,F1N,F21,F2M,M,N,M1,N1,M2,N2,
2NBLK,NBLK1,B1,B2,A11,A1N,A21,A2M,ICYC,TOL,IFLG)
C
        PRINT 710
        PRINT 711, NBSIZ2
710 FORMAT(1X,'BLOCK SIZE GIVEN BY NBSIZ2(1)+2 (1ST BLOCK) OR',
1 ' NBSIZ2()+3 (OTHER BLOCKS)'/,1X,' NBSIZ2: ')
711 FORMAT(1X,10I4)
C
C RESIDUAL ERROR OF LAPLACIAN
        ERMAX=0.0
        DO 750 I=2,M1
        DO 750 J=2,N1

```

```

    ERMAX = AMAX1(ERMAX,ABS(ERR(I,J)/FMAX))
750 CONTINUE
    PRINT 751, ERMAX
751 FORMAT(1X,' MAXIMUM RESIDUAL ERROR [(FORCING - LAPLACTIAN)/MAX',
1 ' FORCING ] = ',1PE12.4)
C
C DISCRETIZATION ERROR
    PMAX = 0.
    DO 3000 J=1,N
    DO 3000 I=1,M
        PHIX= 5.5-0.5*T1(J)
1 + 0.5*T2(J)*COS(2.*PI*(X(I)-XC)/XL)
        PMAX = AMAX1(PMAX,ABS(PHIX))
        DUM3(I,J)=PHI(I,J)-PHIX
3000 CONTINUE
    DSMAX=0.0
    DO 3007 I=2,M1
    DO 3007 J=2,N1
        DSMAX = AMAX1(DSMAX,ABS(DUM3(I,J)/PMAX))
3007 CONTINUE
    PRINT 732, DSMAX
732 FORMAT(1X,' MAXIMUM DISCRETIZATION ERROR [(COMPUTED - ANALYTIC',
1 ' PHI)/MAX ANALYTIC PHI] = ',1PE12.4)
C
600 CONTINUE
    END

```

## 2. Test Example with Neumann Boundary Condition

```

PROGRAM DRVR2
C
C   This program uses SEVP to solve Poisson's equation
C   LAPLACIAN OF PHI = F
C   with Neumann boundary conditions in y
C   and Cyclic boundary conditions in x
C
  PARAMETER (M=82, N=53)
  PARAMETER (NBLK=1+(N-5+3)/9, NBLK1=NBLK-1)
  PARAMETER (M1=M-1, M2=M-2, N1=N-1, N2=N-2)
  PARAMETER (MN=M*N)
  DIMENSION AX(M,N),AY(M,N),CX(M,N),CY(M,N),BB(M,N),
1  RINV(M2,M2,NBLK),RINV1(M2,M2,NBLK1),RCOR(M,3),RTILDA(M2),
2  NBSIZ2(NBLK),IS(NBLK),IE(NBLK),SUMF(NBLK),IXNDX(M),
3  DUMMY(M2,M2),B1(M2),B2(M2)
  DIMENSION F(M,N),PHI(M,N),ERR(M,N)
  DIMENSION F11(M),F1N(M),F21(N),F2M(N)
  DIMENSION X(M),Y(N),YP1(N),YP2(N)
  DIMENSION HXU(N),HXV(N1),HYU(N),HYV(N1)
  DIMENSION AA(N),AC(N),CC(N)
  DIMENSION T1(N),T2(N),T3(N),T4(N)
  DIMENSION DUM3(M,N)
C SET COEFFICIENTS OF DIFFERENCE EQUATION AND BOUNDARY CONDITIONS
C TO ZERO INITIALLY.
  DATA AX/MN*0.0/,CX/MN*0.0/,AY/MN*0.0/,CY/MN*0.0/,BB/MN*0.0/,
1  F/MN*0.0/,F11/M*0.0/,F1N/M*0.0/,F21/N*0.0/,F2M/N*0.0/
C
  PI = 4.0*ATAN(1.0)
  AR = 6371.
  XL = 12000.0
  YL = 5000.0
C
C DEFINE GRID
  DELX = XL/FLOAT(M-2)
  DELY = YL/FLOAT(N-3)
  PRINT 990,DELX,DELY
990 FORMAT(1H ,5HDELX=,1PE13.5,5X,5HDELY=,1PE13.5)
  DO 5 J=1,N
    Y(J)=DELY*(FLOAT(J-1)-0.5) + 2000.0
5  CONTINUE
  DO 6 I=1,M
    X(I)=DELX*FLOAT(I-1)
6  CONTINUE
  DELXSQ=DELX*DELX
  DELYSQ=DELY*DELY
C
C DEFINE MAP FACTORS
  DO 10 J=1,N
    HXU(J)=COS(Y(J)/AR)
    HYU(J)=1.0
10 CONTINUE
  DO 20 J=1,N1

```

```

      HXV(J)=0.5*(HXU(J)+HXU(J+1))
      HYV(J)=1.0
20  CONTINUE
C
C  DEFINE FORCING FUNCTION
      XC= 0.0
      YC = 4500.0
      YW = 1500.0
      C1=YW/AR
      C2=1./(YW*YW)
      C3=2.*PI*PI*(YW/XL)*(YW/XL)
      DO 60 J=1,N
      YP1(J)=(Y(J)-YC)/YW
      YP2(J) = Y(J)/AR
60  CONTINUE
      DO 61 J=1,N
      T1(J) = TANH(YP1(J))
      T2(J) = EXP(-YP1(J)*YP1(J))
61  CONTINUE
      DO 62 J=1,N
      CSQ=COS(YP2(J))*COS(YP2(J))
      T3(J)=2.*T1(J)+C1*TAN(YP2(J))
      T4(J)= 2.*YP1(J)*YP1(J) - 1.0 + C1*YP1(J)*TAN(YP2(J))
      1 - C3/CSQ
62  CONTINUE
C  FORCING FUNCTION ONLY DEFINED IN INTERIOR OF DOMAIN.
      DO 65 J=2,N-1
      DO 65 I=2,M-1
      F(I,J) = 0.5*C2*T3(J)*(1.-T1(J)*T1(J))
      1 + C2*T4(J)*T2(J)*COS(2.*PI*(X(I)-XC)/XL)
65  CONTINUE
C
C
C  NEUMANN BOUNDARY CONDITIONS IN Y
      A11 = 1.0
      A1N = 1.0
      Y11 = (Y(1)+(DELY/2.0)-YC)/YW
      Y1N = (Y(N)-(DELY/2.0)-YC)/YW
      T11 = TANH(Y11)
      T1N = TANH(Y1N)
      T21 = EXP(-Y11*Y11)
      T2N = EXP(-Y1N*Y1N)
      DO 150 I = 2,M-1
      F11(I) = - (DELY/YW)*( 0.5*(1.0-T11*T11)
      1 +Y11*T21*COS(2.*PI*(X(I)-XC)/XL) )
      F1N(I) = - (DELY/YW)*( 0.5*(1.0-T1N*T1N)
      1 +Y1N*T2N*COS(2.*PI*(X(I)-XC)/XL) )
150  CONTINUE
C  CYCLIC BOUNDARY CONDITIONS IN X
      ICYC = 1
      A21 = 0.0
      A2M = 0.0
C
C  FOR INDETERMINATE NEUMANN BOUNDARY CONDITIONS, A BOUNDARY VALUE

```



C MUST BE PROVIDED AT A SINGLE BOUNDARY POINT (IX,JX) FOR THE SOLVER TO  
 C OBTAIN A SOLUTION. THE BOUNDARY POINT SELECTED IN SEVP IS IX=2, JX=1.  
 C FOR THE EFFICIENT CONVERGENCE OF THE SOLUTION, WE USE A ZERO VALUE  
 C FOR THE SINGLE BOUNDARY POINT AND AS THE FIRST GUESS.

C

DO 120 J=1,N  
 DO 120 I=1,M  
 PHI(I,J)= 0.0

120 CONTINUE

C

C DEFINE COEFFICIENTS ON L.H.S. OF DIFFERENCE EQUATION.

C COEFFICIENTS DEFINED IN INTERIOR OF DOMAIN ONLY.

DO 25 J=2,N-1  
 AA(J)=((HXU(J)\*HXV(J-1))/(HYV(J-1)\*HYU(J)))\*(DELXSQ/DELYSQ)  
 CC(J)=((HXU(J)\*HXV(J))/(HYV(J)\*HYU(J)))\*(DELXSQ/DELYSQ)  
 AC(J)=-AA(J)-CC(J)

25 CONTINUE

DO 165 I = 2,M-1  
 DO 165 J = 2,N-1  
 AX(I,J) = 1.0  
 CX(I,J) = 1.0  
 AY(I,J) = AA(J)  
 CY(I,J) = CC(J)  
 BB(I,J) = AC(J)-2.0

165 CONTINUE

C DEFINE R.H.S. OF DIFFERENCE EQUATION, SCALING FORCING

DO 170 J=2,N-1  
 DO 170 I=2,M-1  
 CON = HXU(J)\*HXU(J)\*DELXSQ  
 F(I,J) = F(I,J)\*CON

170 CONTINUE

FMAX = 0.  
 DO 305 J=2,N-1  
 DO 305 I=2,M-1  
 FMAX = AMAX1(FMAX,ABS(F(I,J)))

305 CONTINUE

C

C

C TOLERANCE FOR SOLVER

TOL = 1.0E-8

C

IFLG = 1  
 CALL SEVP(AX,AY,CX,CY,BB,RINV,RINV1,RCOR,NBSIZ2,IS,IE,IXNDX,  
 1SUMF,DUMMY,RTILDA,PHI,F,ERR,F11,F1N,F21,F2M,M,N,M1,N1,M2,N2,  
 2NBLK,NBLK1,B1,B2,A11,A1N,A21,A2M,ICYC,TOL,IFLG)

C

PRINT 710

710 FORMAT(1X,'BLOCK SIZE GIVEN BY NBSIZ2(1)+2 (1ST BLOCK) OR',  
 1 ' NBSIZ2()+3 (OTHER BLOCKS)'/,1X,' NBSIZ2' )

PRINT 711, NBSIZ2

711 FORMAT(1X,10I4)

C

C RESIDUAL ERROR OF LAPLACIAN

FNORM=FMAX

```

    ERMAX=0.0
    DO 750 I=2,M1
    DO 750 J=2,N1
    ERMAX = AMAX1(ERMAX,ABS(ERR(I,J)/FNORM))
750 CONTINUE
    PRINT 751, ERMAX
751 FORMAT(1X, ' MAXIMUM RESIDUAL ERROR [(FORCING - LAPLACIAN)/MAX',
1 ' FORCING ] = ',1PE12.4)
C
C DIFFERENCE AT PRESCRIBED BOUNDARY POINT (IX,JX)
    PHI21=5.5-0.5*T1(1)+0.5*T2(1)*COS(2.*PI*(X(2)-XC)/XL)
    PDIFF = PHI21 - PHI(2,1)
C DISCRETIZATION ERROR
    PMAX = 0.
    DO 3000 J=1,N
    DO 3000 I=1,M
    PHIX= 5.5-0.5*T1(J)
1 + 0.5*T2(J)*COS(2.*PI*(X(I)-XC)/XL)
    DUM3(I,J)=PHI(I,J)-PHIX+PDIFF
    PMAX = AMAX1(PMAX,ABS(PHIX))
3000 CONTINUE
    PNORM = PMAX
    DSMAX=0.0
    DO 3007 I=2,M1
    DO 3007 J=2,N1
    DSMAX = AMAX1(DSMAX,ABS(DUM3(I,J)/PNORM))
3007 CONTINUE
    PRINT 732, DSMAX
732 FORMAT(1X, ' MAXIMUM DISCRETIZATION ERROR [(COMPUTED - ANALYTIC',
1 ' PHI)/MAX ANALYTIC PHI] = ',1PE12.4)
C
600 CONTINUE
    END

```

## **APPENDIX G**

### **A Numerical Study of the Structure of the Outflow Layer of a Tropical Cyclone Using a Primitive Equation Model**

**A Numerical Study of the Structure of the  
Outflow Layer of a Tropical Cyclone  
Using a Primitive Equation Model**

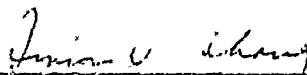
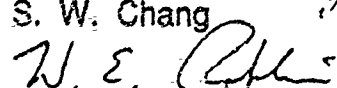
by  
**Jainn-Jong Shi**


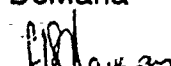
A thesis submitted to the Graduate Faculty of  
North Carolina State University  
in partial fulfillment of the  
requirements for the Degree of  
Master of Science

**Department of Marine, Earth and Atmospheric Sciences**

Raleigh  
1987

**Approved By:**

  
\_\_\_\_\_  
S. W. Chang  
  
\_\_\_\_\_  
W. E. Robbins

  
\_\_\_\_\_  
M. DeMaria  
  
\_\_\_\_\_  
S. Raman ---- Chairman

## ABSTRACT

SHI, JAINN-JONG. A Numerical Study of the Structure of the Outflow Layer of a Tropical Cyclone Using a Primitive Equation Model. (Under the direction of Dr. Sethu Raman)

A primitive equation numerical model is used to simulate the outflow structure of a tropical cyclone and study how the outflow jet and the cyclone react to the upper tropospheric forcing. The model, which was developed at the Naval Research Laboratory (NRL), is a three-dimensional, meso-scale, primitive equation model incorporating a split-explicit time integration scheme along with cumulus and boundary layer parameterizations. It is also hydrostatic with ten  $\sigma$ -layers and is initialized with a cyclonic vortex in the mean tropical sounding without large scale wind.

The model tropical cyclone reaches a quasi-steady state with a central pressure of 984 mb and a maximum surface wind of 20  $\text{ms}^{-1}$  at 72 hour. The anticyclonic flow is strongest at 150 mb. The outflow is dominated by a narrow, 3000 km long jet originating north of the storm and curving anticyclonically to the southwest with a maximum speed of 33  $\text{ms}^{-1}$ . Angular momentum budget shows that the transport by the outflow jet is twice as compared to that by the mean flow. Analysis of the cross-section perpendicular to the outflow jet shows that there is a circum-jet secondary circulation in the entrance region of the jet. The secondary circulation has an ascending branch on the

anticyclonic shear side of the jet and a descending branch on the cyclonic shear side.

Two numerical experiments were conducted to test the response of the model tropical cyclone to the upper-tropospheric forcing. In Experiment 1, the jet is accelerated artificially to simulate the situation of the joining of the outflow jet with a westerly jet. In Experiment 2, the divergence atop the tropical cyclone is increased to simulate the superposition of a ridge over the tropical cyclone. In Experiment 1, the model tropical cyclone reacts to the forcing only slightly, while it deepens by approximately 10 mb in Experiment 2. These results suggest that the superposition of the upper tropospheric ridge is a favorable condition for the intensification of a mature tropical cyclone. It is also found that imposed upper tropospheric divergence causes an increased deep convection in the first few hours of the simulation. The low level convergence then gets strengthened several additional hours later because of this increased convection.

## ACKNOWLEDGEMENTS

I desire to express my deepest appreciation to Dr. Sethu Raman, Chairman of the advisory Committee for patiently sharing his time to direct this research. He provided many helpful suggestions for the completion of this thesis. Particular thanks is given to Dr. Simon Chang of the Naval Research Laboratory, one of my committee members, for his guidance in this work and his assistances in understanding the NRL numerical weather prediction model and in using the NRL computer facilities. Appreciation is also extended to the other committee members, Dr. Mark DeMaria for giving me valuable suggestions and Dr. W. Robbins for his help in Computer Graphics.

I am very grateful for the time I was able to spend with Drs. Rao Madala and Keith Sashegyi of the Naval Research Laboratory for giving me a lot of technical assistances and suggestions.

I also appreciate to my fellow graduate students for giving me all kinds of assistances I need, especially to Mr. Teddy Holt, Miss Kathy Brehme, Capt. James Kroll and First Lt. John Pickle. I would like to thank Mrs. Susan Templemen for typing this thesis for me.

Finally, I wish to thank my parents, wife, Amy and lovely daughter, Katherine, for their support during the work.

This research was supported by the Naval Research Laboratory, Washington, D.C..

## Table of Contents

	Page
List of Symbols .....	vi
List of Figures .....	ix
List of Tables .....	xii
1. INTRODUCTION .....	1
1.1 Background .....	1
1.2 Literature Review .....	3
1.2.1 General Picture of the Outflow Layer .....	3
1.2.2 Influence of the Environment on the Outflow Layer .....	7
1.3 Research Objectives .....	10
2. BRIEF REVIEW OF THE NRL TROPICAL CYCLONE MODEL ..	12
2.1 Governing Equations .....	12
2.2 Grid System .....	16
2.3 Finite Difference Scheme .....	19
2.3.1 Spatial Differencing .....	19
2.3.2 Time Differencing .....	20
2.4 Parameterization Scheme .....	23
2.4.1 Cumulus Parameterization .....	23
2.4.2 Boundary Layer Parameterization ...	25
2.5 Initial and Boundary Conditions .....	25
3. DISCUSSION OF RESULTS .....	28
3.1 A Quasi-Steady Tropical Cyclone Generated by the NRL Tropical Cyclone Model .....	28
3.2 The Outflow Layer .....	35
3.2.1 Core of the Outflow Jet .....	35
3.2.2 Secondary Circulation .....	40
3.2.3 Angular Momentum Budget .....	45
3.3 Trajectories of the Released Particles .....	50
3.3.1 Purpose and Methodology .....	50
3.3.2 Trajectories .....	53
4. RESPONSES OF A TROPICAL CYCLONE TO LARGE-SCALE FORCING IN THE UPPER TROPOSPHERE .....	61
5. SUMMARY AND CONCLUSIONS .....	74
6. REFERENCES .....	77



## List of Symbols

$f$	Coriolis parameter
$g$	acceleration due to gravity
$h_x$	map factor in the x-direction
$h_y$	map factor in the y-direction
$\underline{k}$	unit vector in the z-direction
$m$	$= rv$ , relative angular momentum
$m_a$	$= rv + fr^2/2$ , absolute angular momentum
$q$	specific humidity
$r$	radius
$r_0$	radius of the maximum tangential wind
$t$	time coordinate
$u$	velocity component in the x-direction; radial wind component in the cylindrical coordinates
$v$	velocity component in the y-direction; tangential wind component in the cylindrical coordinates
$w$	velocity component in the z-direction
$C_D$	$= 1 \times 10^{-3}$ , drag coefficient
$C_E$	$= 2 \times 10^{-3}$ , exchange coefficient of latent heat
$C_H$	$= 2 \times 10^{-3}$ , exchange coefficient of sensible heat
$C_P$	specific heat for dry air at constant pressure
$D$	mass divergence
$F_u$	the friction force in the x-direction
$F_v$	the friction force in the y-direction
$F_T$	source or sink of heat

$F_q$	source or sink of moisture
$H$	total amount of water vapor needed to create a cloud over a unit area
$K$	$= R/C_p$ ; index
$L$	latent heat of condensation
$M$	total angular momentum in a certain volume; the total number of grid points in the x-direction
$N$	the total number of grid points in the y-direction
$P$	pressure
$P_b$	pressure of the bottom of a cumulus cloud
$P_s$	surface pressure
$P_t$	pressure of the top of a cumulus cloud
$R$	gas constant for dry air
$T$	temperature
$V$	velocity
$\delta x$	finite difference operator in the x coordinate
$\delta y$	finite difference operator in the y coordinate
$\delta \sigma$	finite difference operator in the $\sigma$ coordinate
$\Delta x$	half degree longitude distance at equator
$\Delta y$	half degree latitude distance at equator
$\Delta t$	time interval
$\zeta$	$= \mathbf{k} \cdot (\nabla \times \vec{V})$ , vertical component of relative vorticity
$\theta$	potential temperature; latitude
$\lambda$	frequency scale
$\rho$	air density
$\sigma$	$= P/P_s$ , vertical coordinate in the model

$\sigma$      =  $d\sigma/dt$ , vertical velocity in the  $\sigma$  coordinate  
 $\sigma_0$     =  $1000/P_s$   
 $\Delta\sigma$     vertical depth of each layer in the model  
 $\Delta\tau$     subdivided time interval of  $\Delta t$   
 $\phi$        geopotential  
 $\Phi$        longitude  
 $\omega$        =  $dp/dt$ , vertical velocity in P-coordinate

## List of Figures

	page
1.1 Upper-tropospheric outflow layer analysis for Hurricane Camille, 1969. Values of isotachs are in $\text{ms}^{-1}$ . The principal outflow channel is north of the cyclone center. Circle is at radius of $6^\circ$ latitude (666 km). Figure adapted from Black and Anthes (1971) .....	5
1.2 Same as Figure 1.1 but for Hurricane Irene, 1981. The outflow channel is located to the northeast of the cyclone center. Figure adapted from Smith (1975) .....	5
1.3 Outflow channel schematic from Sadler (1976). Note that the cyclone is located to the right rear of the wind speed maximum in the outflow channel .....	9
2.1 Horizontal and vertical grid network utilized in the model for the simple case of $K = 2$ . (Madala, et. al., 1987) .....	17
2.2 Typical vertical distribution of normalized pressure for five vertical layers ( $KK = 5$ ). (Madala, et. al., 1987) .....	18
2.3 Division of time interval $2 \ t$ into $m$ -subintervals for use in the split-explicit time integration scheme (Madala, 1981) .....	22
2.4 Initial condition of surface pressure (solid lines) and 1000 mb wind (vectors) .....	26
3.1 1000 mb temperature (dash lines) pressure (solid lines) and 1000 mb wind (vectors) structure at 96 hour. (from 141 x 91 model) ..	29
3.2 Temperature (dash lines), height (solid lines) and wind (vectors) structure at 150 mb at 96 hour. (from 141 x 91 model) .....	31
3.3 Isotachs at 150 mb at 96 hour. (from 141 x 91 model) .....	32
3.4 Distribution of the precipitable water amount (cm). Shaded area indicates the model eye wall. (from 141 x 91 model) .....	33

	page
3.5 Isotachs (from 81 x 81 model) at 150 mb at 96 hour. <b>A</b> and <b>B</b> mark the two cross-sections ....	36
3.6 Cross-section at the outflow jet entrance region at 96 hour. The contours are the wind normal to the cross section. The vectors are the combination of the vertical motion and the wind tangent to the cross-section .....	37
3.7 Same as Fig. 3.5 but for the cross section intercepting the jet maximum wind .....	38
3.8 Relative humidity (%) at 150 mb at 96 hour ...	41
3.9 Potential vorticity ( $10^{-12} \text{ g } ^\circ\text{k cm}^{-1} \text{ s}^{-3}$ ) at 150 mb at 96 hour .....	42
3.10 Cross-section of the deviation of the potential temperature from the horizontal mean at the jet entrance region at 96 hour .....	44
3.11 Trajectories of the particles released at 950 mb. <b>A</b> and <b>B</b> indicate the trajectories of the particles released at 20 and 50 km, respectively .....	54
3.12 Trajectories of the particles released at 500 mb .....	57
3.13 Trajectories of the particles released at 150 mb .....	58
3.14 Trajectories of all particles .....	60
4.1 Variation of the minimum surface pressure with time. <b>A</b> represents the control model tropical cyclone. <b>B</b> and <b>C</b> represent Experiment 1 and 2, respectively .....	64
4.2 Same as Figure 4.1 but for the maximum convective precipitation rate .....	66
4.3 Same as Figure 4.1 but for the maximum wind speed at sigma = 0.15 .....	67
4.4 Same as Figure 4.1 but for the maximum wind speed at sigma = 0.95 .....	68

	page
4.5 The close region <b>A</b> for equation (4.3). (ICEN, JCEN) is the grid point where the surface pressure is lowest .....	69
4.6 The mass divergent profile at 96 hours. <b>A</b> , <b>B</b> and <b>C</b> represent the same results as in Figure 4.1 .....	71
4.7 Same as Figure 4.6 but for 120 hours .....	72

## List of Tables

	page
3.1 Model and empirical angular momentum budgets in the upper layer of tropical cyclones .....	48
3.2 Distribution of the particles at 0 hour .....	52

## 1. INTRODUCTION

### 1.1 Background

A tropical storm is defined as a warm core low pressure system in which the maximum sustained surface wind is 35 knots ( $17.8 \text{ ms}^{-1}$ ) or greater. Tropical storms with a maximum sustained wind equal or exceeding 65 knots ( $33.0 \text{ ms}^{-1}$ ) are called as tropical cyclones, hurricanes (when they occur over the Atlantic Ocean and over the Eastern Pacific Ocean) or typhoons (over the Western Pacific Ocean).

The horizontal scale of a typical mature tropical cyclone circulation may vary by over a factor of two from storm to storm, but the general value is between 500 and 1000 km. Because the stratosphere above a tropical cyclone is believed to be relatively undisturbed, the vertical scale may be defined by the tropopause height of about 15 km.

An intense tropical cyclone (or hurricane) is one of the most destructive weather phenomena of all natural disasters. A tropical cyclone, with its gale force wind and torrential rainfall, can cause tremendous damage to the coastal zone and the shipping industries (Anthes, 1982). Numerous empirical and theoretical studies during the past 35 years have tremendously increased our understanding of



these destructive storms. Still, the structure of the tropical cyclone is not as fully understood as the mid-latitude systems for the lack of observational data over the vast tropical ocean.

Recent studies (Holland and Merrill, 1984) have demonstrated that the movement and growth of tropical cyclones are partly dependent on the inertial stability of the storm's wind structure. For example, Holland and Merrill (1984) pointed out that the strong cyclonic vorticity in the lower and middle troposphere in an intense tropical cyclone becomes more stable and likely more resistant to environmental forcing, whereas the upper tropospheric anticyclonic, asymmetric outflow is not as stable inertially (Black and Anthes, 1971), and therefore may be less resistant to the environmental forcing. Thus, the movement and intensity of an intense tropical cyclone would probably respond rapidly to an upper tropospheric forcing. Therefore, an improved understanding of the structure of the outflow of the tropical cyclone is important in predicting the tropical cyclones' intensification and tracks.

Real data analysis of the outflow layer of the tropical cyclone is difficult because of the sparsity of the observational data over the tropical ocean. Much of our knowledge has come from composite studies (Holland, 1982 and 1983; Chen and Gray, 1984) or from a few case studies (Black and Anthes, 1971; Sadler, 1976 and 1977; Holland and

Merrill, 1984). For this reason, we choose to study the outflow layer of a numerical model generated tropical cyclone, in the hope that the outflow structure and dynamics can be realistically simulated in a numerical model. With a numerical model, it is easier to isolate various mechanisms that affect the tropical cyclone outflow and to conduct controlled numerical experiments.

## 1.2 Literature Review

### 1.2.1 General Properties of the Outflow Layer of the Tropical Cyclone

The outflow layer of the tropical cyclone is generally anticyclonic and divergent on the synoptic scale. It is considerably more asymmetric than the middle and lower layers (Alaka, 1961, 1962; Miller, 1963). Black and Anthes (1971) noted that the outflow circulation is highly asymmetric, especially beyond 400 km from the storm center where the standard deviation of the radial and tangential wind components exceed the mean value. In their study, the asymmetric part of the circulation is obtained by subtracting the axisymmetric part of the circulation from the total flow. The resultant circulation, defined as the asymmetric wind, reveals that two eddies dominate the outflow struc-

ture. It is suggested that these eddies are organized by the environmental flow streaming around the divergent outflow field. The outflow layer of the tropical cyclone is comparatively shallow, generally confined between 100 and 300 mb (Frank, 1977a). The asymmetric outflow of the tropical cyclone is characterized by outflow jets. Merrill (1984) mentioned that the outflow from a hurricane appears to be concentrated in one or two outflow maxima or channels. The wind maximum in the outflow layer can normally be found to the north or northwest of the storm center. Figure 1.1 and 1.2 show this concept. Chen and Gray (1984) speculated that the outflow jets help to remove mass from the central region and transport the warm and dry air to outer regions, maintaining the convective instability near the eye.

Merrill (1984) noted that the appearance of outflow channels is similar to that of the "jet streaks" which are commonly observed in association with the mid-latitude troughs. He also speculated that the upper-tropospheric, baroclinic processes may be important in the hurricane outflow jet streak. He speculated that there may be a possible secondary circulation around the outflow layer, similar to the jet streak in mid-latitudes. In the classical jet streak theory (Palmen and Newton, 1969), confluence of the synoptic scale flow into the entrance region results in a stronger temperature gradient and the development of a

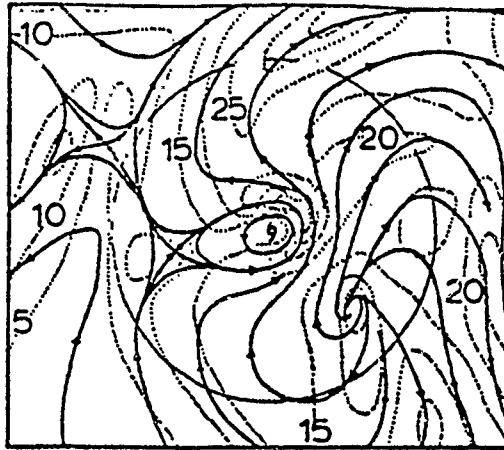


Figure 1.1 Upper-tropospheric outflow layer analysis for Hurricane Camille, 1969. Values of isotachs are in  $\text{ms}^{-1}$ . The principal outflow channel is north of the cyclone center. Circle is at radius of  $6^\circ$  latitude (666 km). Figure adapted from Black and Anthes (1971).

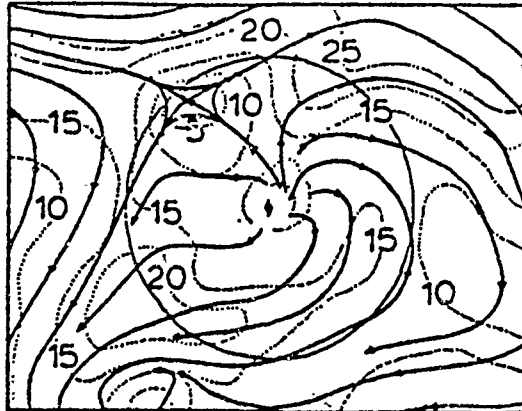


Figure 1.2 Same as Figure 1.1 except for Hurricane Irene, 1981. The outflow channel is located to the northeast of the cyclone center. Figure adapted from Smith (1975).

direct secondary circulation with ascending motion occurring to the warm side of the upper-tropospheric temperature gradient. This circulation acts to reduce the temperature gradient and increase the vertical shear to keep the flow in thermal-wind balance. Therefore the jet streak would increase the upper-tropospheric vertical motion within the convective region of the cyclone. This would then enhance deep convection, and shift the net convective heating upward. The outgoing flux of warm air from the cyclone center acts to further increase the temperature gradient and thus results in a positive feedback.

Merrill (1984) also noticed that there exists a secondary maximum inflow layer at approximately 400 mb level, which could be the return branch of secondary circulation. The existence of jet streaks also helps to explain the existence of cirrus lines oriented radially outward from the cyclone which are sometimes observed in intensifying cyclones.

Ooyama (1987) was able to generate the asymmetric outflow in various environmental flows in a simple two dimensional (in the x- and y- directions) model of the outflow layer using shallow water equations with a prescribed upwelling mass flux. In his model study, two well-defined outflow channels in opposite directions were generated in a two-sided shear environmental flow, while only one well-

defined channel was generated in a one-sided shear environmental flow. He also found that the cyclonic vorticity exists within a radius of 250 km in this simple model.

#### 1.2.2 The Influence of the Environment on the Outflow layer and the Intensification of a Tropical Cyclone

There are many observational studies (e.g. Sadler, 1976 and 1977; Steranka et al., 1986; Rodgers et al., 1987) which link the behavior of tropical cyclones to the strength and position of TUTTs (Tropical Upper Tropospheric Troughs). Sadler showed that in general as a TUTT aligns vertically with the underlying tropical cyclone, the tropical cyclone weakens. If a tropical cyclone is aligned with an upper tropospheric ridge, the cyclone generally intensifies. However, the relationship between the TUTTs and a tropical cyclone is not simple and straightforward. For example, Cnen and Gray (1984) suggested that the outflow jets are formed by the coupling of the storm's outflow with upper- and mid-tropospheric troughs. Rodger et. al.(1987) also observed this phenomenon.

In spite of the evident relationship between TUTTs and the intensity of tropical cyclones, the mechanisms of the intensification still are not fully understood. But, an

outflow to the westerlies has long been recognized as a requirement for tropical storm development. Sadler (1976) suggested that the multi-directional outflow channels to the large scale circulation of the upper troposphere serve to remove the excess heat in the tropical cyclone's central region. Figure 1.3 is a schematic illustrating the relationship between the tropical storm outflow and some common large circulation patterns. In Figure 1.3a, the storm's northern outflow is suppressed when it is located in a region of upper-tropospheric northeasterlies. In Figure 1.3b the east side of deep troughs in the westerlies was a principal outflow channel for each cyclone. In Figure 1.3c, there is an outflow channel to the east of a TUTT into the large-scale westerlies and an outflow into the equatorial easterlies south of the sub-equatorial ridge. This configuration permits vigorous outflow for efficient removal of mass and heat from the tropical cyclone.

According to Sadler(1976), a tropical cyclone is likely to intensify if it is surrounded by concentrated air currents to the east of an upper-tropospheric trough in the upper troposphere or by a strong equatorial outflow channel (see Figure 1.3). Sadler (1977) further conjectured that the strengthening of an outflow channel can extend inward towards the storm center and act as an outflow link to the cyclone's inner region of deep convection.

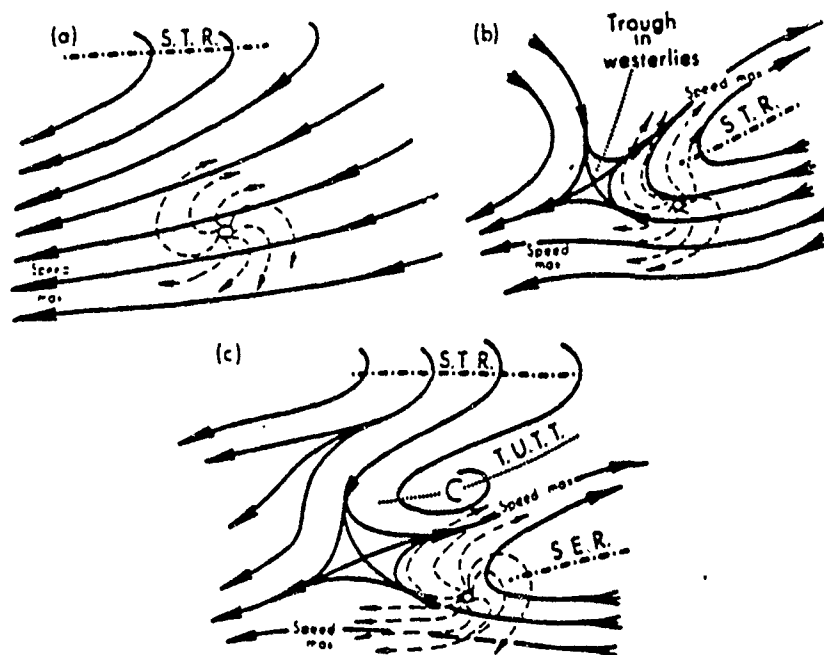


Figure.1.3 Outflow channel schematic from Sadler (1976). Note that the cyclone is located to the right rear of the wind speed maximum in the outflow channel.



Recent study of satellite-measured total ozone amount by Rodgers et al. (1987) suggested that the enhancement of the inner core convection of a tropical cyclone can be related to the upper-tropospheric environment forcing. They found that an increase in the inner core convection in Hurricane Irene (1980) was preceded by the formation of an outflow channel. When the strength of the outflow channel decreased, the inner core convection weakened abruptly. They also found a 33 hour lag between the changes in the inner core convection and Irene's intensity changes.

### 1.3 Research Objective

The objective of this research is to study the structure and sensitivity of the outflow layer of a model generated tropical cyclone. In order to understand the structure of the tropical cyclone outflow, the numerical model starts from an idealized vortex imbedded in a tropical environment with zero large scale winds over a ocean with constant surface temperature. The structure of the outflow, especially the outflow channel (or jet), will be carefully analyzed. The mass divergence, potential vorticity, upper-tropospheric relative humidity(RH), and angular momentum

will be discussed. To help further depict the circulation in the tropical cyclone, trace particles are used to create trajectories.

In addition, the sensitivity of the outflow layer and the cyclone itself to the upper-tropospheric forcing are also examined. In Chapter 2, we will briefly review the NRL Tropical Cyclone Model. In Chapter 3, the simulated structure of the tropical cyclone outflow will be presented. The simulated response of the model generated tropical cyclone under the artificially introduced upper-tropospheric forcing will be discussed in Chapter 4. Finally, in Chapter 5, the summary and conclusions are presented.

## 2. BRIEF REVIEW OF THE NRL TROPICAL CYCLONE MODEL

The Naval Research Laboratory (NRL) tropical cyclone model is a three-dimensional, quasi-hydrostatic, primitive equation model incorporating a split-explicit time integration scheme along with cumulus and boundary layer parameterizations (Madala et al., 1987). The model utilizes the sigma vertical coordinate and time independent boundary conditions. In the following sections more details about this model will be presented.

### 2.1 Governing Equations

The governing primitive equations incorporated in the model are formulated in the flux forms, i.e.,  $P_s u$ ,  $P_s v$ , etc. The system of seven equations (five prognostic and two diagnostic) form a closed system for the seven dependent variables:  $u$ ,  $v$ ,  $T$ ,  $q$ ,  $P_s$ ,  $\phi$  and  $\dot{\sigma}$ , where  $u$  and  $v$  are the velocity components in the x- and y-direction, respectively.  $T$  is the temperature,  $q$  is the specific humidity,  $P_s$  is the surface pressure,  $\phi$  is the geopotential height and  $\dot{\sigma}$  ( $=d\sigma/dt$ ) is the vertical velocity. The equations given below describe the motion of a mesoscale, quasi-hydrostatic, baroclinic atmosphere in a system with  $\sigma$

( $=P/P_s$ ) as the vertical coordinate. The equations are expressed in  $x$ ,  $y$ ,  $\sigma$  and  $t$  coordinates using the generalized expression for curvilinear distance.

1. The momentum equation in  $x$ -direction (east-west):

$$\begin{aligned} \frac{\partial P_s u}{\partial t} + \frac{1}{h_x h_y} \left( \frac{\partial (P_s u h_y u)}{\partial x} + \frac{\partial (P_s v h_x u)}{\partial y} \right) + \frac{\partial (P_s \dot{\sigma} u)}{\partial \sigma} - f P_s v \\ + P_s \frac{uv}{h_x h_y} \frac{\partial h_x}{\partial y} = - \frac{P_s}{h_x} \frac{\partial \phi}{\partial x} - \frac{RT}{h_x} \frac{\partial P_s}{\partial x} + P_s F_u \end{aligned} \quad (2.1)$$

where  $F_u$  is the frictional force and  $h_x$  and  $h_y$  are the map factors in the  $x$ - and  $y$ - direction, respectively.  $R$  is the gas constant for dry air and  $f$  is the Coriolis parameter.

2. The momentum equation in  $y$  direction (north-south):

$$\begin{aligned} \frac{\partial P_s v}{\partial t} + \frac{1}{h_x h_y} \left( \frac{\partial (P_s u h_y v)}{\partial x} + \frac{\partial (P_s v h_x v)}{\partial y} \right) + \frac{\partial (P_s \dot{\sigma} v)}{\partial \sigma} - f P_s u \\ + P_s \frac{u^2}{h_x h_y} \frac{\partial h_x}{\partial y} = - \frac{P_s}{h_y} \frac{\partial \phi}{\partial y} - \frac{RT}{h_y} \frac{\partial P_s}{\partial y} + P_s F_v \end{aligned} \quad (2.2)$$

where  $F_v$  is the frictional force.

3. The thermodynamic equation:

$$\begin{aligned} \frac{\partial P_s T}{\partial t} + \frac{1}{h_x h_y} \left( \frac{\partial (P_s u h_y T)}{\partial x} + \frac{\partial (P_s v h_x T)}{\partial y} \right) + \left( \frac{\sigma}{\sigma_0} \right)^K \frac{\partial (P_s \dot{\sigma} \theta)}{\partial \sigma} - \frac{RT}{C_p} \tilde{D} \\ - \frac{RT}{C_p} \left( \frac{u}{h_x} \frac{\partial P_s}{\partial h_x} + \frac{v}{h_y} \frac{\partial P_s}{\partial h_y} \right) = P_s F_T \end{aligned} \quad (2.3)$$

where  $F_T$  is the source or sink of heat, such as sensible and latent heating,  $\sigma_0 = 1000/p_s$ ,  $K = R/C_p$  and  $\theta$  is the potential temperature.  $C_p$  is the specific heat of dry air at constant pressure.

4. The moisture continuity equation:

$$\frac{\partial P_s q}{\partial t} + \frac{1}{h_x h_y} \left( \frac{\partial (P_s u h_y q)}{\partial x} + \frac{\partial (P_s v h_x q)}{\partial y} \right) + \frac{\partial (P_s \dot{\sigma} q)}{\partial \sigma} = P_s F_q \quad (2.4)$$

where  $F_q$  is the source and sink of moisture, such as condensation and evaporation.

5. The hydrostatic equation:

$$\frac{\partial \phi}{\partial \sigma} = - \frac{RT}{\sigma} \quad (2.5)$$

6. The continuity equation:

$$\frac{\partial P_s \dot{\sigma}}{\partial \sigma} = \tilde{D} - D \quad (2.6)$$

7. The surface pressure tendency equation:

$$\frac{\partial P_s}{\partial t} = - \tilde{D} \quad (2.7)$$

where

$$\tilde{D} = \int_0^1 \nabla \cdot (P_s \mathbf{v}) d\sigma$$

and mass divergence

$$D = \nabla \cdot (P_s \mathbf{v}) = \frac{1}{h_x h_y} \left( \frac{\partial (h_y P_s u)}{\partial x} + \frac{\partial (h_x P_s v)}{\partial y} \right)$$

All the variables have their conventional meteorological meaning and are defined in the list of symbols. Equations 2.1 to 2.7 form a closed set of equations if the functional form of the last terms representing the source and sink in Equations 2.1 to 2.4 (i.e.,  $F_u$ ,  $F_v$ ,  $F_T$ ,  $F_q$ ) are known.

## 2.2 Grid System

The number of grid points of this model is  $(M \times N \times KK)$ , where  $M$ ,  $N$  and  $KK$  are maximum grid points in  $x$ -,  $y$ - and  $\sigma$  directions. The vertical depth of each layer is defined as  $\Delta\sigma(k)$ , where  $k = 1$  to  $KK$ . The horizontal intervals between each two grid points are half degree longitude and latitude distance in  $x$ - and  $y$ - direction, respectively. While the horizontal coordinates are curvilinear with horizontal grid spacing, the actual horizontal interval should be  $h_x\Delta x$  and  $h_y\Delta y$ , where  $h_x$  and  $h_y$  are map scale factors, and  $\Delta x$  and  $\Delta y$  are half degree longitude and latitude distances at the equator.

The horizontal grid network is fully staggered according to Arakawa's C grid (see Figure 2.1) because it accurately simulates the geostrophic adjustment process. For mass field, temperature ( $T$ ), geopotential height ( $\phi$ ) and specific humidity ( $q$ ) are computed at mass points  $(i,j)$ , while the east-west velocity component  $u$  is defined at the midpoint of mass points along the  $x$ -axis and the north-south velocity component  $v$  is computed at the midpoint along the  $y$ -axis.

By definition,  $\sigma$  is equal to unity at the surface and zero at the top of the model. The vertical velocity  $\dot{\sigma}$ , defined as  $d\sigma/dt$ , is evaluated at the  $(K + 1/2)$  levels for  $K = 0$  to  $KK$  (see Figure 2.2), where  $KK$  is the total number

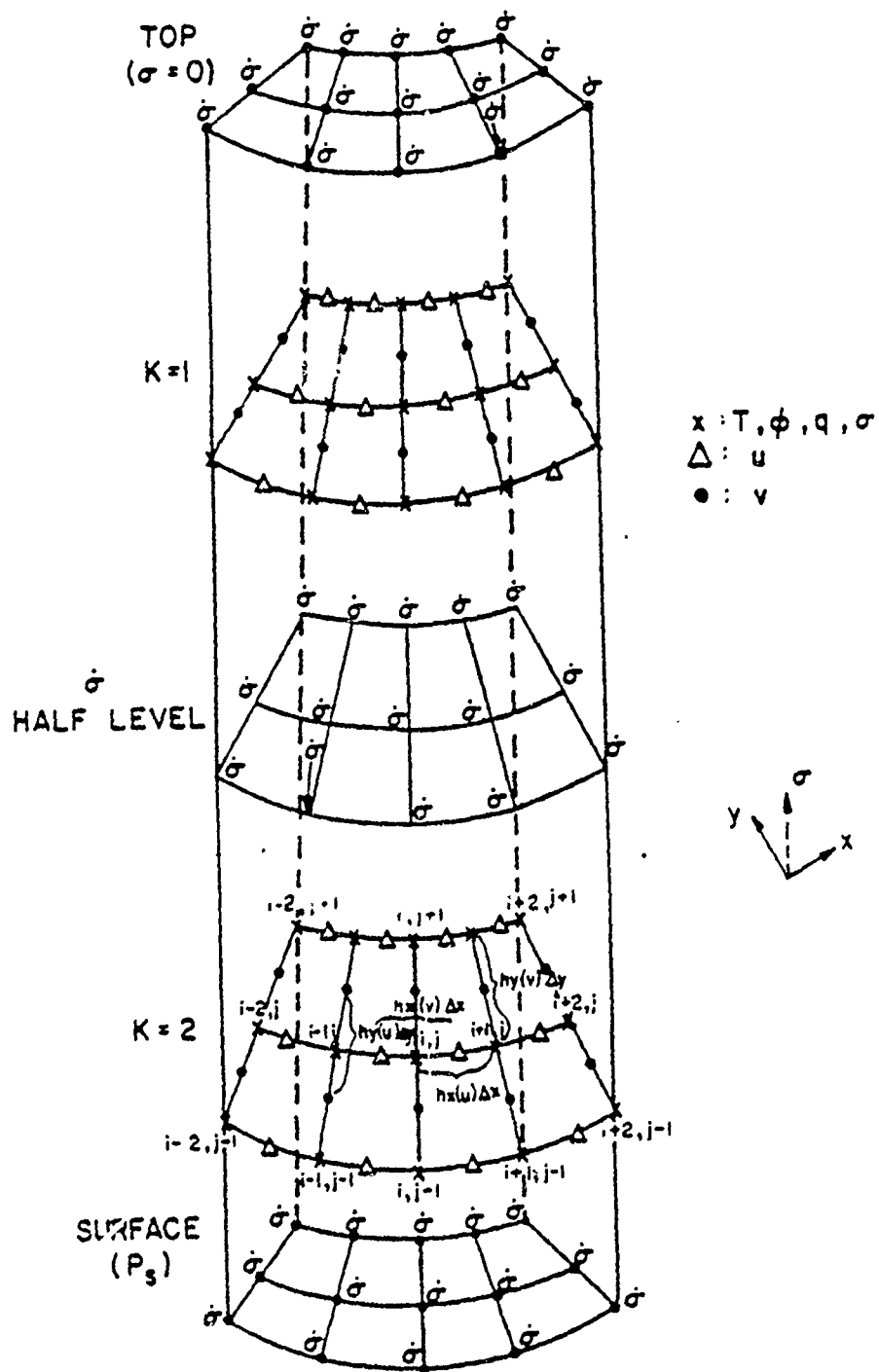


Figure 2.1 Horizontal and vertical grid network utilized in the model for the simple case of  $K = 2$ . (Madala, et. al., 1987)



FOR  $KK = 5$

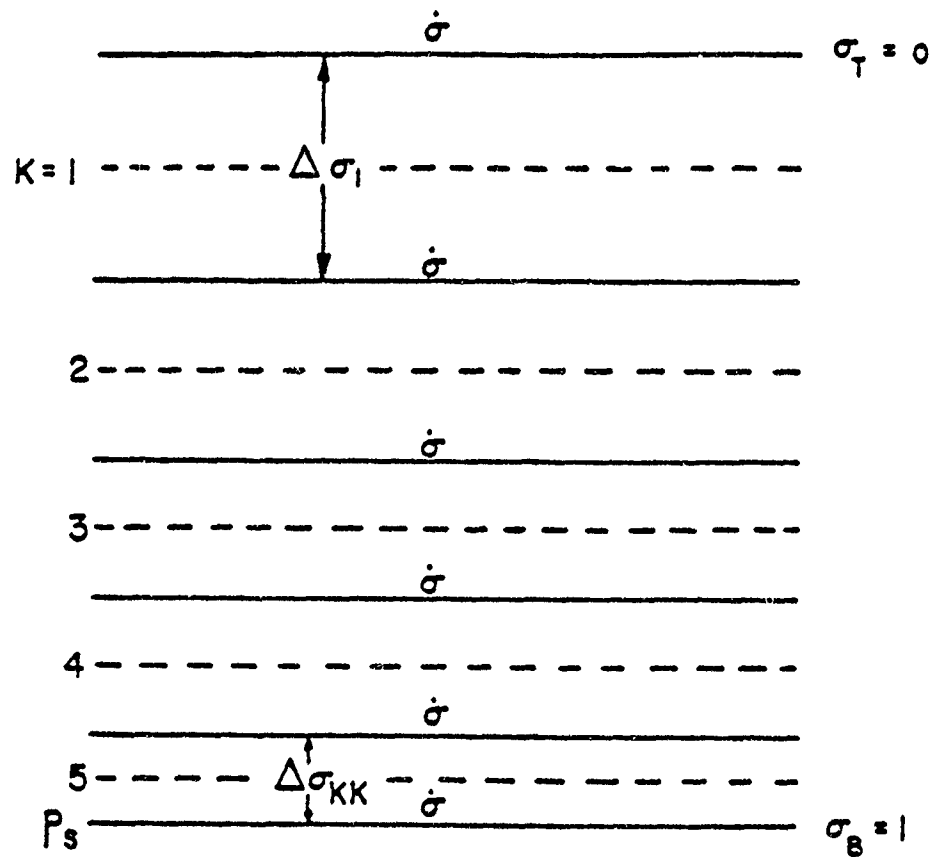


Figure 2.2 Typical vertical distribution of normalized pressure for five vertical layer ( $KK = 5$ ).  
(Madala, et. al., 1987)

of layers. Vertical velocity is equal to zero at surface ( $K = K_K$  and  $\sigma = 1$ ) and at the top ( $K = 0$  and  $\sigma = 0$ ) of the model.

For this study, two different kinds of the grid system were used. One has  $81 \times 81 \times 10$  points (in the  $x$ ,  $y$  and  $\sigma$  direction) and the other has  $141 \times 91 \times 10$  points. Both grid systems had the same horizontal resolution and vertical interval of 0.1 for all layers. For the smaller grid, the model horizontal domain covers a longitudinal span of  $40^\circ$  degrees and the latitudinal borders are on  $1^\circ N$  and  $41^\circ N$ . For the larger grid, the domain covers  $70^\circ$  degrees longitudinal span and the latitudinal borders are on  $0^\circ N$  and  $45^\circ N$ .

## 2.3 Finite Difference Scheme

### 2.3.1 Spatial Differencing Scheme

The spatial finite differencing of the governing equations are second order accurate, quadratic conserving. Let the parameter  $F_{i,j}^k$  represent the value  $F$  (any dependent variable in the model) at the  $(i,j)^{th}$  horizontal grid point on the  $K_{tN}$  level. Then,  $\delta_x$ ,  $\delta_y$  and  $\delta_\sigma$  represent the finite differencing operators in the horizontal and the vertical such that:

$$\delta_x F_{i,j}^k = \frac{(F_{i+\frac{1}{2},j}^k - F_{i-\frac{1}{2},j}^k)}{h_x(i,j) \Delta x} \quad (2.8)$$

$$\delta_y F_{i,j}^k = \frac{(F_{i,j+\frac{1}{2}}^k - F_{i,j-\frac{1}{2}}^k)}{h_y(i,j) \Delta y} \quad (2.9)$$

$$\delta_\sigma F_{i,j}^k = \frac{(F_{i,j}^{k+\frac{1}{2}} - F_{i,j}^{k-\frac{1}{2}})}{\Delta \sigma(k)} \quad (2.10)$$

where  $\Delta x$  and  $\Delta y$  are half degree longitude and latitude distance at equator,  $h_x(i,j)$  and  $h_y(i,j)$  are the map factors in the x-direction and y-direction at the  $(i,j)_{th}$  grid point for  $F$ , respectively.

### 2.3.2 Time Integration Scheme

The time integration scheme in this model is the split-explicit method with the Leapfrog scheme (central differencing scheme). The split-explicit method (Madala, 1981) is utilized to allow for an increase in time step by separating various terms in the prognostic equations into parts governing the slower moving Rossby modes and the faster gravity modes.

The meteorologically relevant Rossby modes move much slower than the gravity modes, especially the external gravity mode. In the split-explicit method, one uses the linearized equations of motion, which can be splitted into KK vertical modes for the model with KK layers. The non-linear terms are then treated as a source for the gravity modes. For example, in the ten layer model used in this study, the external and the first four internal gravity modes have characteristic wave speeds roughly of 300, 100, 30, 15 and 5  $\text{ms}^{-1}$ , respectively. while the Rossby mode moves roughly at 20  $\text{ms}^{-1}$ . Thus, the external and first internal modes, moving much faster than the Rossby mode, require a much smaller time step. Therefore, one simply integrates the faster modes with a sufficiently small time steps, and then integrates the slower modes equations with a larger Rossby time step.

In the split-explicit method, the time interval  $\Delta t$  is subdivided into  $m$  subintervals of length  $\Delta \tau$  (see Figure 2.3). Within these subintervals time step ( $\Delta \tau$ ), the time integration is carried out explicitly. The numerical scheme in the tropical cyclone model subdivides the time interval  $t$  into 8, 4 and 2 subintervals for the external, first and second internal gravity modes, respectively. All the other modes move slowly enough to be incorporated into the large Rossby time step,  $\Delta t$ .

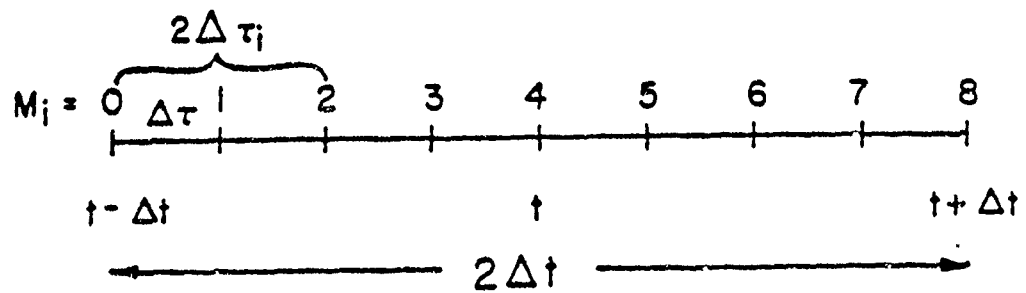


Figure 2.3 Division of time interval  $2\Delta t$  into  $m$ -subintervals for use in the split-explicit time integration scheme (Madala, 1981).

For the first time step of integration for the subinterval  $\Delta\tau$ , the Euler-forward time integration method is used to march from time  $t - \Delta t$  (i.e.,  $M_i = 0$  in Figure 2.3) to  $t - \Delta t + \Delta\tau$  (i.e.,  $M_i = 1$  in Figure 2.3). Then the Leapfrog scheme is used to march each successive time step  $\Delta\tau$  until time  $t + \Delta t$ .

For the  $81 \times 81 \times 10$  model,  $\Delta t$  was equal to 150 seconds and for the  $141 \times 91 \times 10$  model, it was 120 seconds. A smaller time step was required for the  $141 \times 91 \times 10$  model because of the smaller grid distance in the northern part of the model.

## 2.4 Parameterization Schemes

### 2.4.1 Cumulus Parameterization

This tropical cyclone model uses a modified Kuo scheme for parameterizing the effect of cumulus convection. The scheme, introduced by Anthes (1977), is based on the theory of the conditional instability of the second kind (CISK) (Charney and Eliassen, 1964). According to CISK, the convection occurs when there is a low-level moisture convergence in a conditional unstable environment.

Mathematically, the cumulus moisture  $H$  is computed as a function of the difference between the cloud temperature  $T_c$  and the environmental temperature  $T_e$  and the difference between the cloud humidity  $Q_c$  and the environmental humidity  $Q_e$ .  $H$  is then defined by

$$H = g^{-1} \int_{P_b}^{P_t} \left[ \frac{C_p}{L} (T_c - T_e) + (q_c - q_e) \right] dP \quad (2.11)$$

where  $P_b$  and  $P_t$  are the pressures at bottom and top of the cloud and  $L$  is latent heat.  $H$  is also the measure of the total amount of water vapor needed to create a cloud over a unit area. The moist adiabat determines  $T_c$ . Conditional instability is assumed to exist when  $H > 0$ . The new temperature and humidity values are then computed and added to the conservation equations as source or sink. Stable heating is also calculated when there is no cumulus convection and the relative humidity is greater than 96%. If the stable heating is positive, an additional modification of humidity and temperature is required due to the horizontal and vertical advection of moisture (Madala et al., 1987).

#### 2.4.2 Boundary Layer Parameterization

The planetary boundary layer is parameterized in the numerical model to include the effect of friction and the air-sea sensible and latent heat exchanges. The PBL is represented by a single layer with a constant drag coefficient ( $C_D$ ) and constant exchange coefficients for the sensible ( $C_H$ ) and the latent ( $C_E$ ) heat. In the model,  $C_D = 1 \times 10^{-3}$ ,  $C_H = C_E = 2 \times 10^{-3}$ .

#### 2.5 Boundary and Initial Conditions

The boundary condition in the NRL tropical cyclone model is set up as a time independent boundary condition. Because of the size of the model, the boundary regions, which are far away from the center of the model tropical cyclone, are relatively undisturbed. That is the reason why the constant boundary condition is used in this model. For simplicity, it is also assumed that the wind boundary is always zero.

The model tropical cyclone is initialized with a warm core cyclonic vortex in the mean tropical sounding (Sheets, 1968) with no large scale wind. The vortex is initially at  $22.5^\circ$  N and  $50^\circ$  from the model western boundary (see Fig. 2.4). The following function shows the horizontal tangential wind profile.



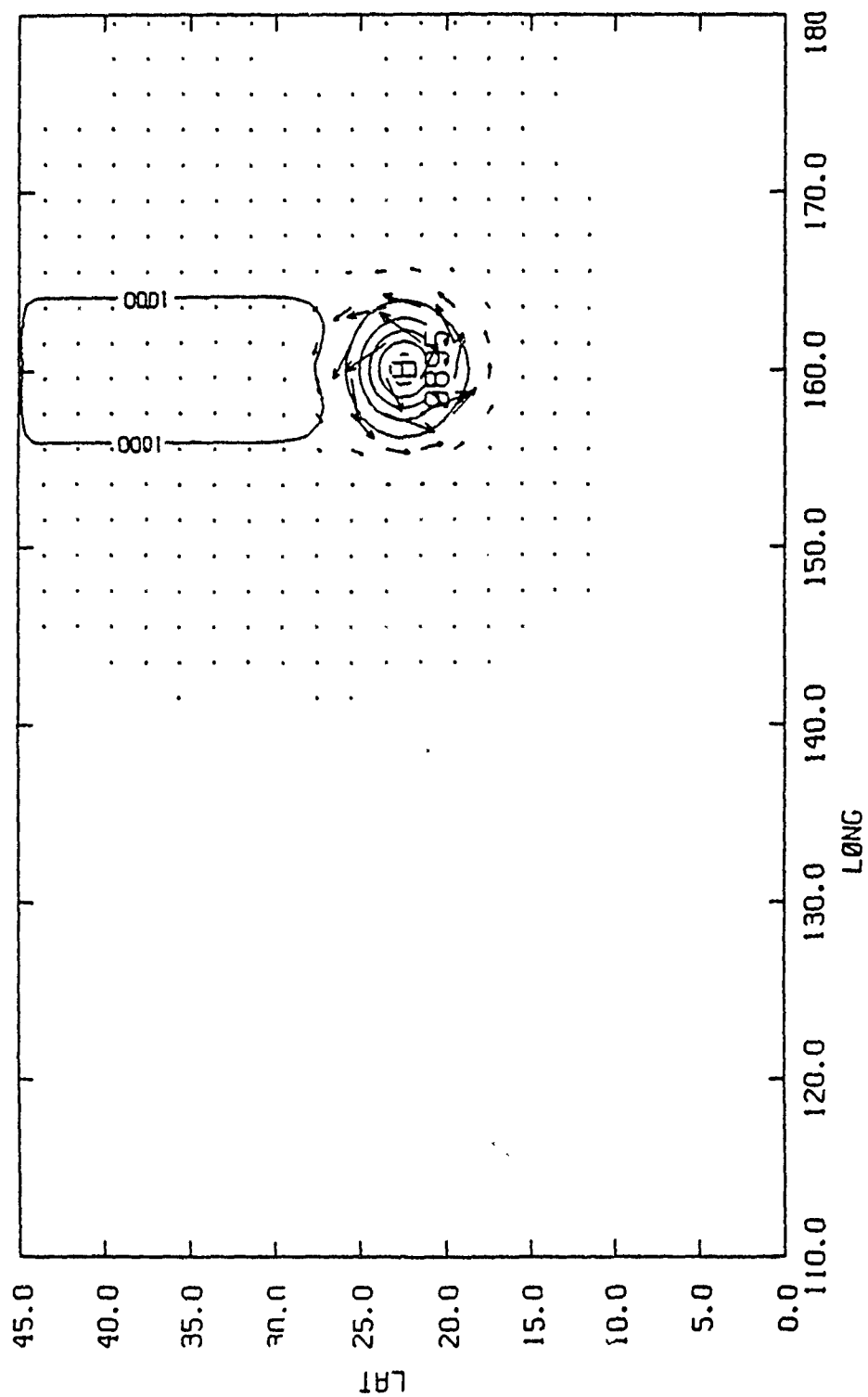


Figure 2.4 Initial condition of surface pressure (solid lines) and 1000 mb wind (vectors).

$$V(r) = V_{\max} * (r/r_0) * \exp((1-(r/r_0)^2)*0.5) \quad (2.12)$$

where  $r$  is radius,  $V_{\max} = 20 \text{ ms}^{-1}$  and  $r_0 = 240 \text{ km}$ . Figure 2.4 shows the surface pressure and circulation structure of the vortex at  $t = 0$  hour.

The sea surface temperature is assumed to be constant at  $302.5^\circ \text{ K}$ . Main purpose of this research is to study the structure of the outflow jet using idealized conditions. It was decided to keep the tropical cyclone environments as simple as possible. This is the reason for assuming constant sea surface temperature and no variations in the boundary.

### 3. DISCUSSION OF RESULTS

#### 3.1 A Quasi-Steady Tropical Cyclone Generated by the NRL Tropical Cyclone Model

The model are integrated for 120 hours. A quasi-steady tropical cyclone developed from the initial vortex at about 72 hour. After 72 hours, the intensity of the tropical cyclone remains relatively unchanged except for its movement toward the northwest and slow expansion of the warm core and the area of low pressure. The tropical cyclone is drifting northwestward approximately at a speed of 9 km/hr (2.5 m/s) due to the latitudinal variation of the Coriolis parameter.

Figure 3.1 shows the surface pressure, the 1000 mb wind vector and the 1000 mb temperature of the model tropical cyclone at 96 hour. The central surface pressure of the tropical cyclone is 984 mb, the maximum surface wind speed is about  $19 \text{ ms}^{-1}$  which occurs at the radius about 150 km. The radius of the farthest closed isobar is about 1300 km. The horizontal pressure gradient in the NE quadrant of the tropical cyclone is greater than it in the SW quadrant of the tropical cyclone in agreement with Chan and Williams (1986). This is because the tangential velocity is stronger in the NE quadrant than in the SW quadrant in order to maintain sufficient transport of the absolute vor-

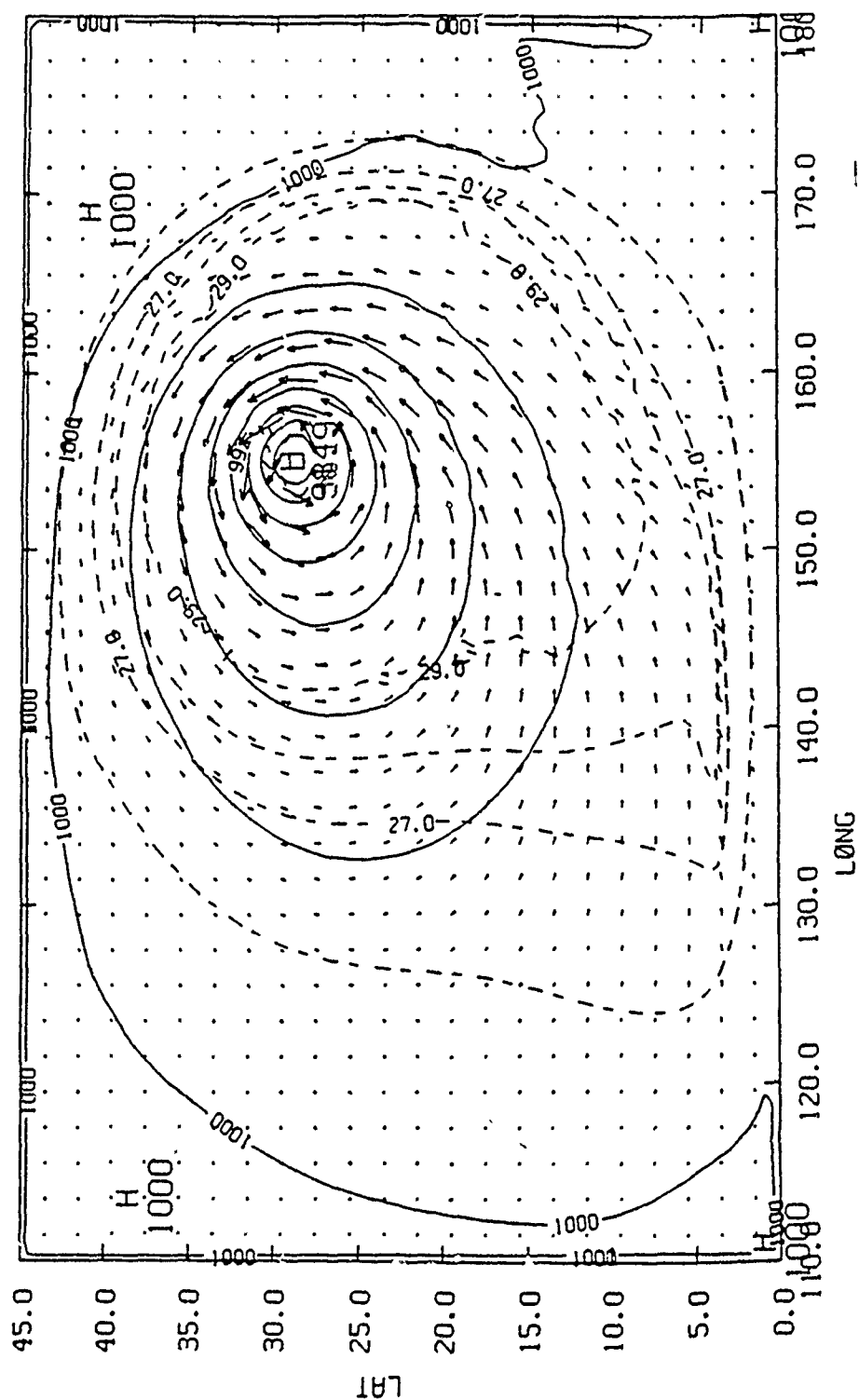


Figure 3.1 1000 mb temperature (dash lines) pressure (solid lines) and 1000 mb wind (vectors) structure at 96 hour. (from 141 x 91 model)

ticity. Therefore, the pressure gradient must be stronger in the NE quadrant as required by the gradient wind balance.

The model tropical cyclone is a warm core system with a region of maximum 1000 mb temperature of  $31.9^{\circ}\text{C}$ , collocating with the center of the low pressure. The temperature surrounding the storm is about  $26^{\circ}\text{C}$ . The warm core results in a geopotential height maximum at the center of the system in the upper layers and provides a pressure gradient force favorable for the development of the anticyclonic flow.

Figure 3.2 shows the outflow structure at 150 mb of the tropical cyclone at 96 hour. There exists a cyclonic flow at the inner radii of a few hundred kilometers surrounded by the general anticyclonic outflow, due to the upward transport of the cyclonic horizontal momentum from the lower troposphere in the center region.

Figure 3.3 shows 150 mb isotachs at 96 hour. The outflow layer wind field is very asymmetric (azimuthally varying about the center of the storm), dominated by an outflow jet with a maximum wind speed about  $33.6 \text{ ms}^{-1}$ .

The structure of the layer between the 850 mb and 300 mb level is basically cyclonic or anticyclonic with little convergence or divergence. The cyclonic motion occurs below 500 mb and the anticyclonic motion occurs above 500 mb in

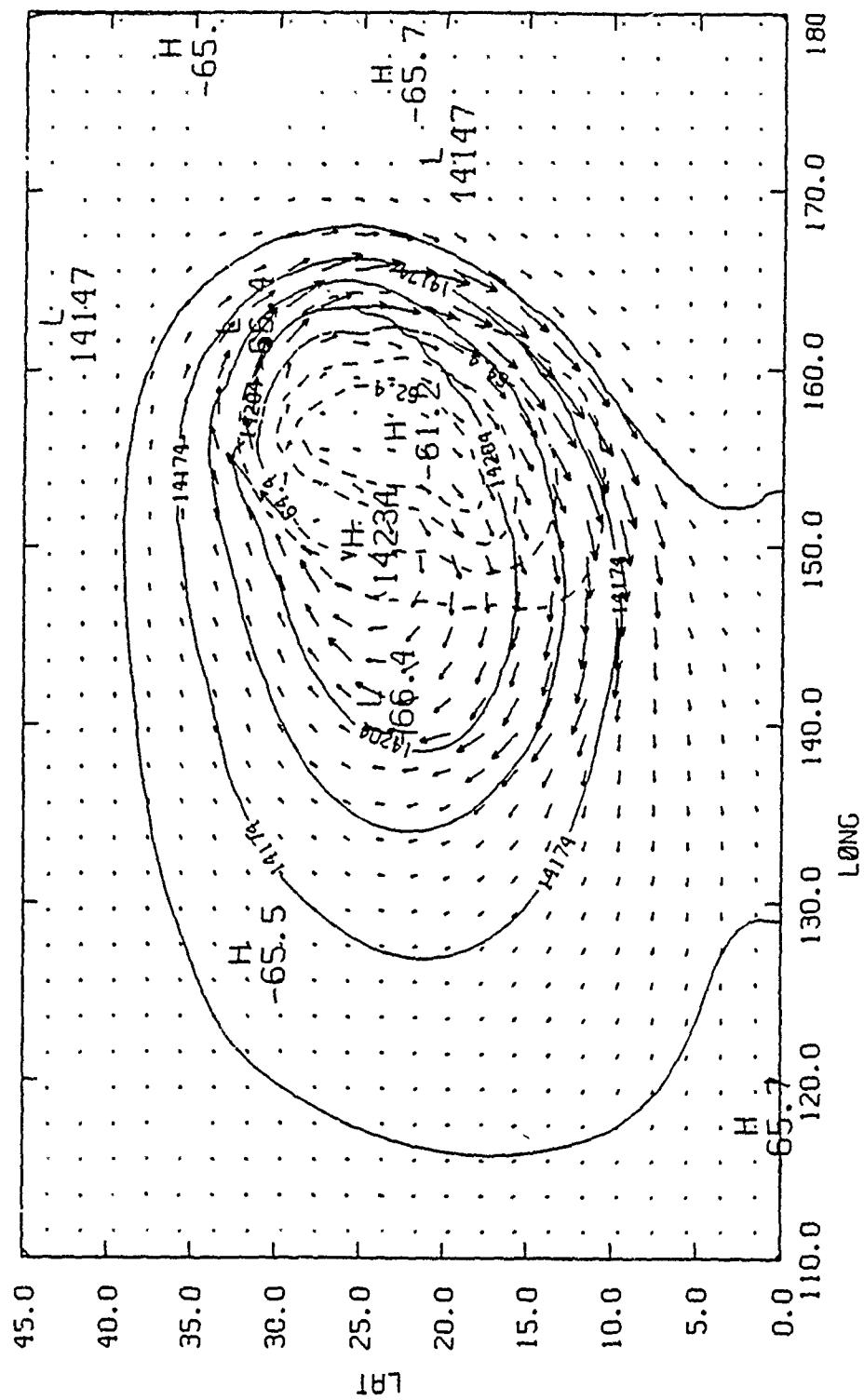


Figure 3.2 Temperature (dash lines), height (solid lines) and wind (vectors) structure at 150 mb at 96 hour. (from 141 x 91 model)

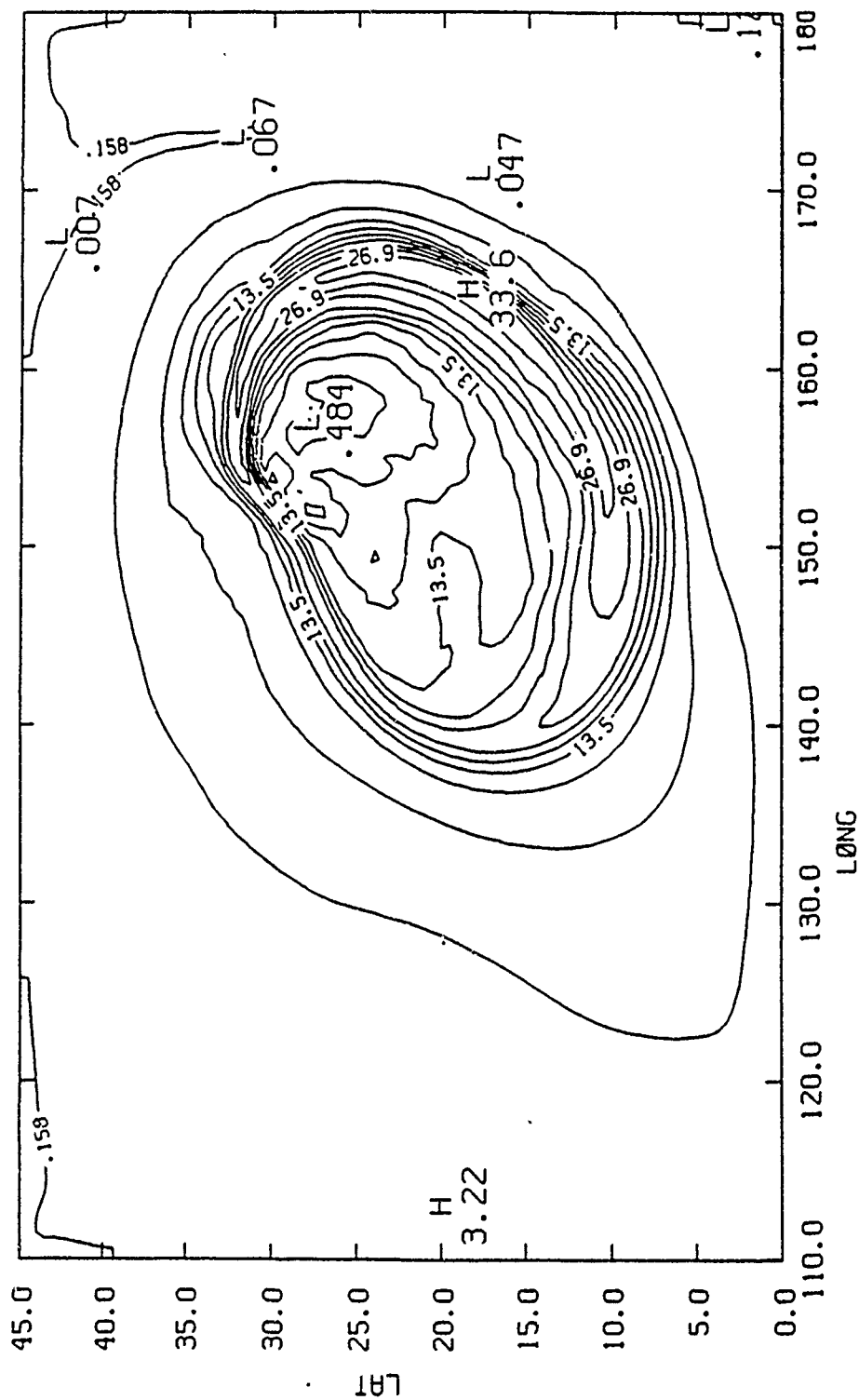


Figure 3.3 Isotachs at 150 mb at 96 hour. (from 141 x 91 model)

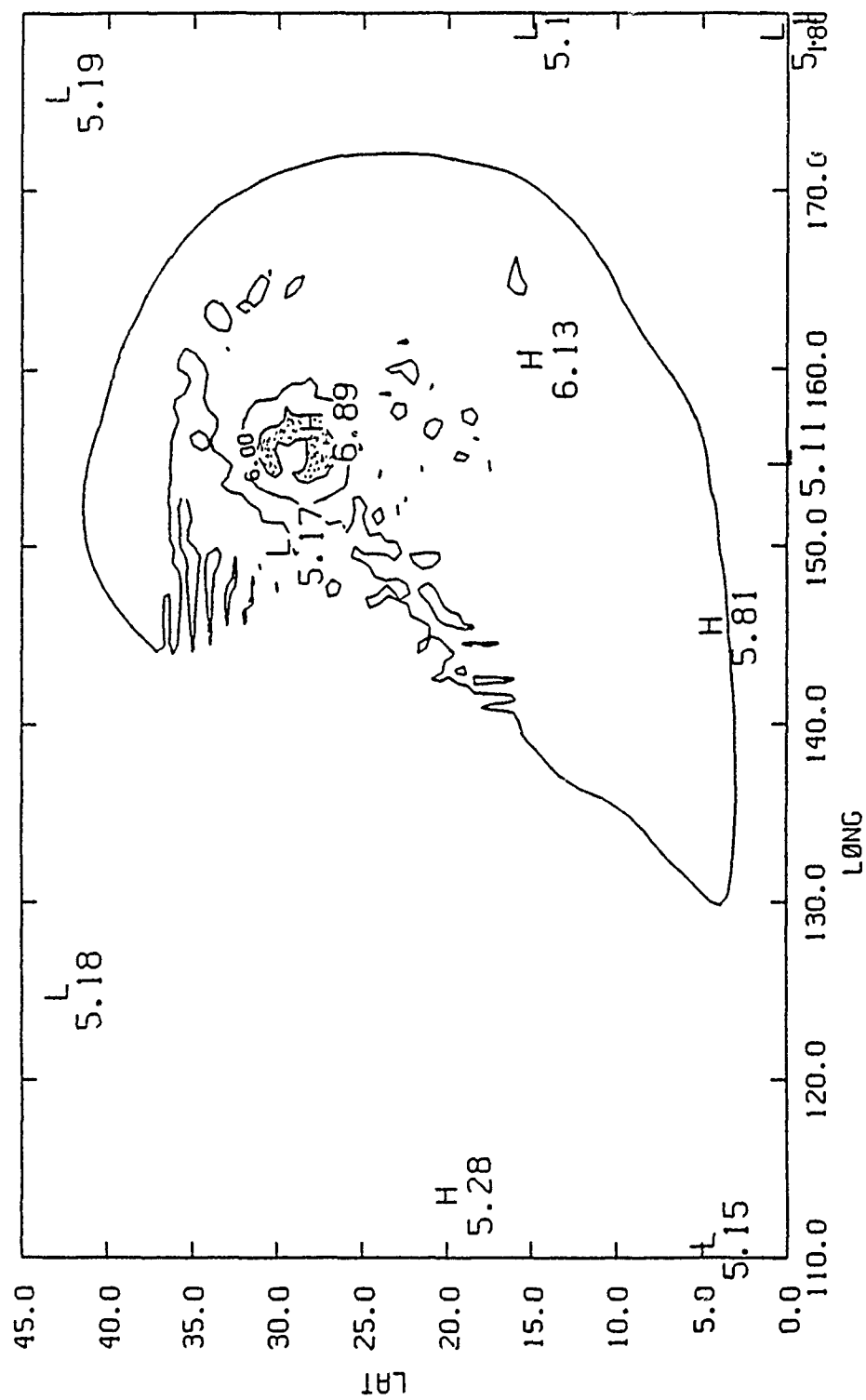


Figure 3.4 Distribution of the precipitable water amount (cm). Shaded area indicates the model eye wall. (from 141 x 91 model)



the middle layer except the inner 100-200 km radii, which area is dominated by the cyclonic motion from surface to the top of the model tropical cyclone.

The eye of the model cyclone is not well defined by the wind field due to the half degree horizontal resolution. The eye region is perhaps better depicted by the precipitable water amount distribution (Figure 3.4). Here, the dry region associated with the downward motion inside the eye wall has a radius of roughly 150 km. The maximum vertical velocity near the eye wall region is about 30 cm/s near 950 mb and about 50 cm/s near 500 mb.

In spite of no environmental wind, this tropical cyclone still has many realistic features of actual tropical cyclones, including asymmetry in the outflow layer, northwest drifting, the warm core and surface wind maximum in the NE quadrant. The model tropical cyclone structure is similar to other model studies, (e.g., Anthes 1972) in the development of the symmetric inflow layer and the asymmetric outflow layer. It has a northwest drift due to the  $\beta$ -effect (Madala and Piacsek, 1975; Anthes and Hoke, 1975).

## 3.2 Outflow Layer

### 3.2.1 Core of the Outflow Jet

The outflow jet (or channel) is a unique feature of tropical cyclones as depicted in Figure 3.3. Ooyama (1987) was able to obtain two jets with prescribed circular upward mass source in the sheared zonal flow. The formation of various jets in different environments is outside the scope of this study. But, a detailed analysis of the well defined and organized jet shown in Figure 3.3 will help us to understand the structure of outflow jets of real tropical cyclones.

In Figure 3.3, it appears that the entrance region of the jet is located at about  $5^{\circ}$  latitude north of the center of the tropical cyclone (at about  $32^{\circ}\text{N}$ ,  $155^{\circ}$ ). The jet extends anticyclonically to the east and then south of the tropical cyclone. In the exit region of the jet, it becomes broader and more diffused and finally diminishes at about  $20^{\circ}$  latitude south of the tropical cyclone (at about  $10^{\circ}\text{N}$ ,  $150^{\circ}$ ).

Figure 3.5 shows the relative positions of the cross-sections A and B at 150 mb isobaric surface at 96 hours. Cross-section A cuts approximately across the jet entrance region and Cross-section B intercepts the region of the maximum wind of the jet. Figures 3.6 and 3.7 show the 96

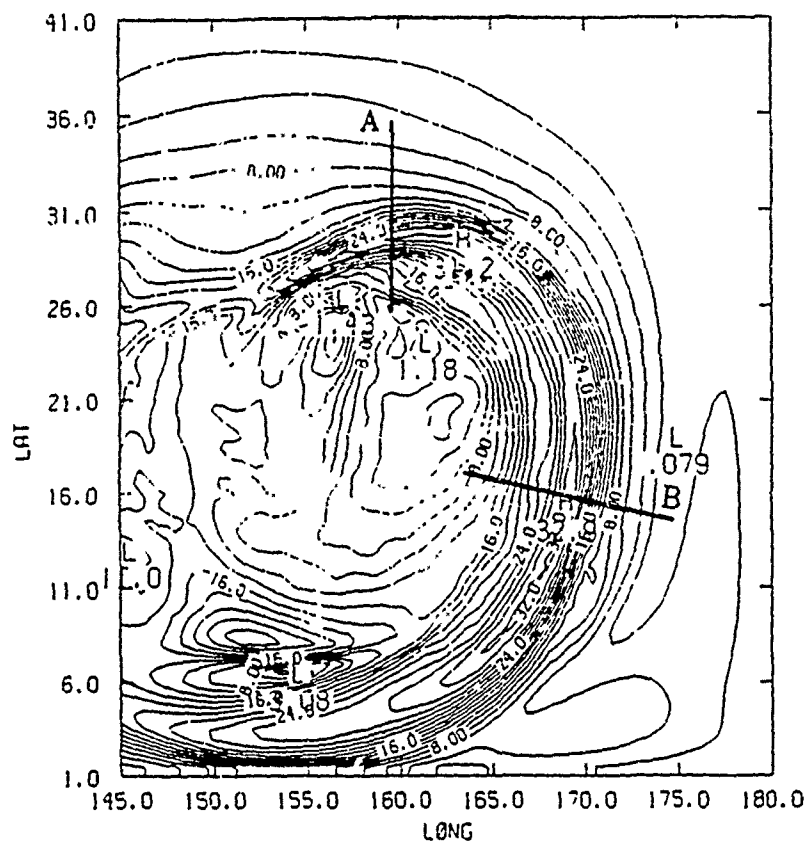


Figure 3.5 Isotachs (from 81 x 81 model) at 150 mb at 96 hour. A and B mark the two cross-sections.

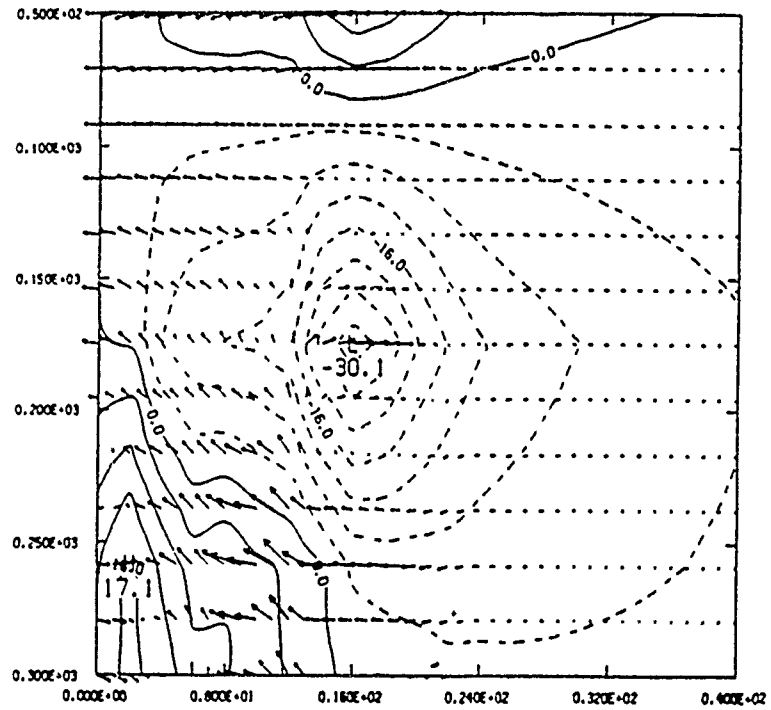


Figure 3.6 Cross-section at the outflow jet entrance region at 96 hour. The contours are the wind which normals to the cross section. The vectors are the combination of the vertical motion and the wind which is tangent to the cross-section.

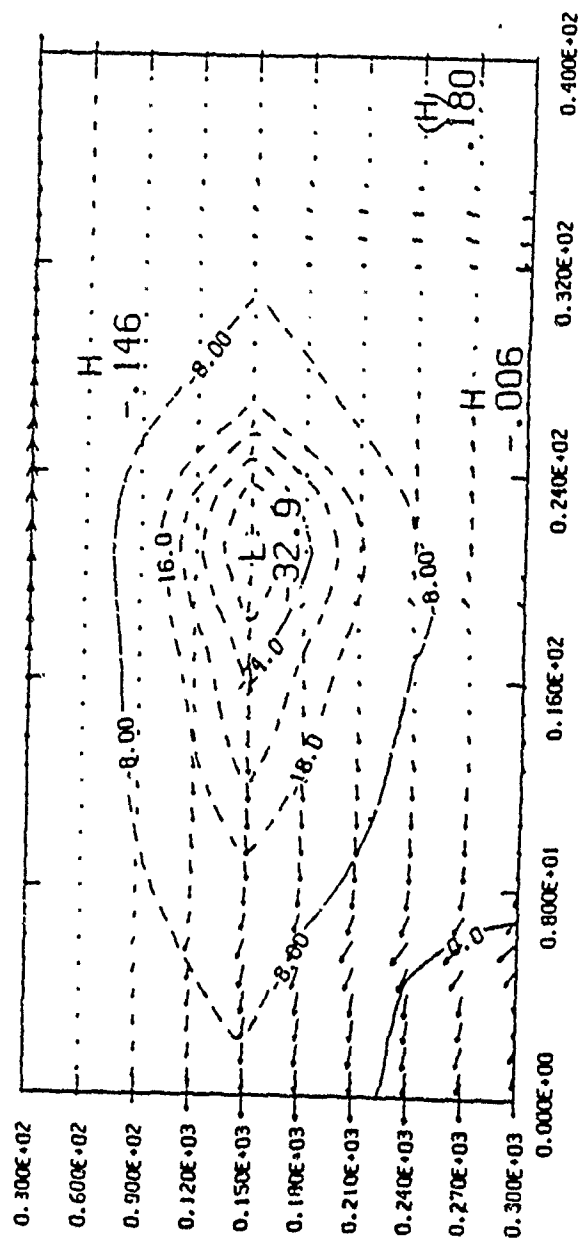


Figure 3.7 Same as Fig. 3.5 except for the cross section intercepting the jet maximum wind.

hour wind structure on Cross-section A and B, respectively. The contours in these two figures represents the normal wind to the cross-sections and the negative value represents the anticyclonic wind. The vectors represent the combination of the vertical velocity ( $\text{mb hr}^{-1}$ ) and the horizontal wind ( $\text{ms}^{-1}$ ) tangent to the cross sections. The vertical axis is from 300 to 100 mb. The horizontal axis is from 0 to 40 points and the interval between the points is roughly  $0.5^\circ$  latitude.

As shown in Figures 3.6 and 3.7, the jet core is mostly confined between 100 and 250 mb judging from the  $16 \text{ ms}^{-1}$  close normal wind contour. The horizontal extent of the jet core is wider in Cross-section B (about  $8.5^\circ$ ) than in Cross section A (about  $4^\circ$ ). These two plots also show two different kinds of wind shear at both sides of the jet core. In Cross-section A, the wind shear is stronger on the side closer to the cyclone center than on the side further away from the cyclone center, while the weaker wind shear is on the side closer to the cyclone center in Cross-section B. In Cross-section A (see Figure 3.6), which cuts across the entrance region, there is a secondary circulation around the jet in the entrance region, while the secondary circulation is absent on Cross-section B across the jet maximum (see Figure 3.7).

### 3.2.2 The Secondary Circulation

As discussed before, there is a circum-jet secondary circulation in the entrance region of the outflow jet (see Figure 3.6). The secondary circulation has an ascending branch on the anticyclonic shear side (facing toward the center) and a descending branch on the cyclonic shear side (facing away from the cyclone center). It also has an outward branch above the jet and an inward branch below the jet.

The relative humidity field and potential vorticity field at 150 mb have been analyzed and shown in Figure 3.8 and Figure 3.9, respectively. Comparing both sides of the outflow jet, it is clear that the higher RH (more than 80%) occurs on the side closer to the cyclone center and the lower RH (less than 40%) occurs on the outer side. This suggests that the ascending motion, which brings moisture from the lower levels through the vertical transport or convection, occurs on the side closer to the cyclone center. Conversely, the sinking motion on the outer side creates a dry region with  $RH < 40\%$ . The potential vorticity in Figure 3.9 is defined as:

$$\frac{1}{\theta} (\zeta + f) \frac{\partial \theta}{\partial p} \quad (3.1)$$

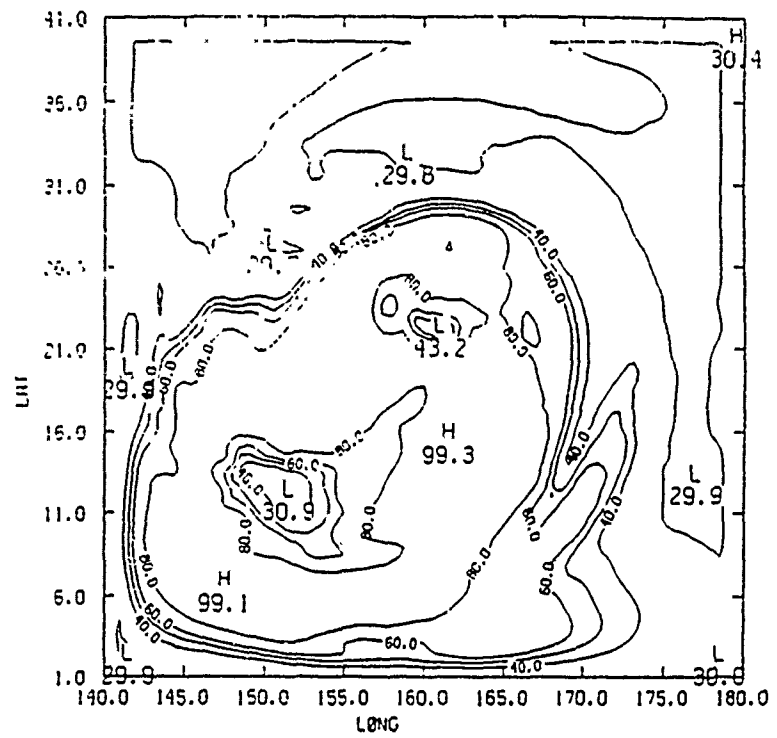


Figure 3.8 Relative Humidity (%) at 150 mb at 96 hour.



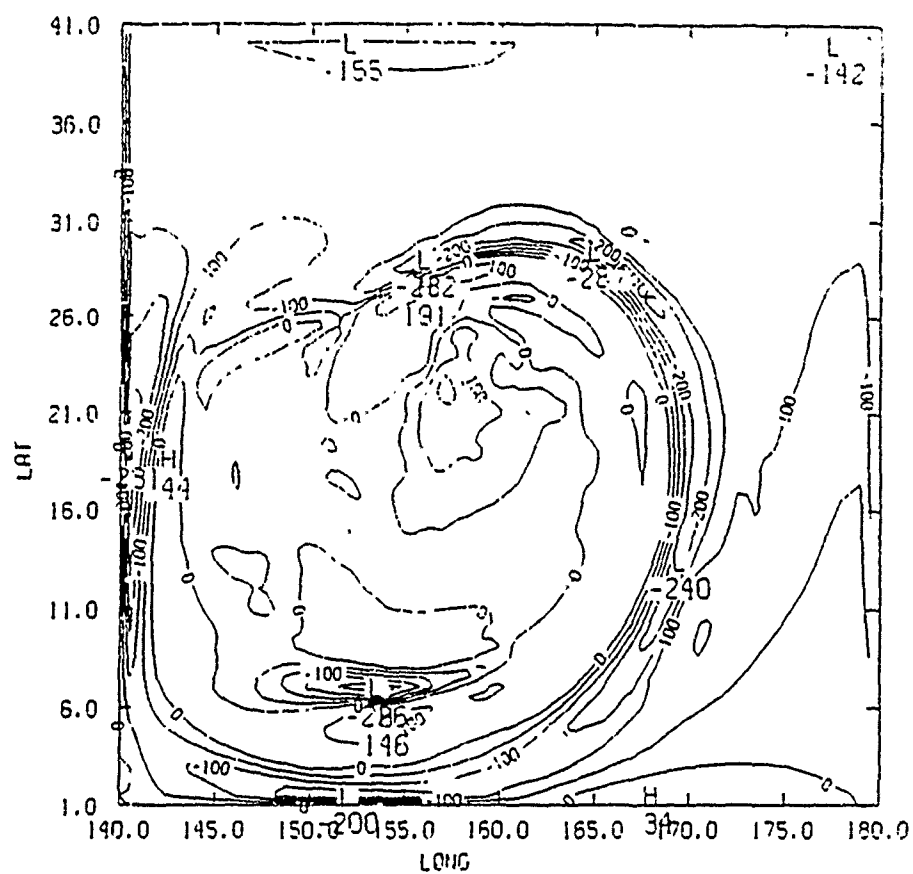


Figure 3.9 Potential vorticity ( $10^{-12} \text{ g } ^\circ\text{k cm}^{-1} \text{ s}^{-3}$ ) at 150 mb at 96 hour.

Because the static stability  $d\theta/dp$  is always negative in the upper layers, the negative value of the potential vorticity defined by (3.1) implies cyclonic vorticity. The region with cyclonic vorticity coincides with the convergence and downward motion. The region of the positive value of the potential vorticity implies the upward motion. As it can be seen in Figure 3.9, the positive value occurs on the side closer to the cyclone center, and thus upward motion occurs below. On the other side of the outflow jet, the potential vorticity is negative, and thus the downward motion occurs below. This is consistent with the vertical motion field shown in Figure 3.6.

Figure 3.10 shows the potential temperature deviation from the horizontal mean on Cross-section A in the entrance region of the outflow jet. The maximum temperature gradient is roughly located at the 150 mb level, where the outflow jet is located. Merrill (1984) suggested that the theory for mid-latitude jet stream can be applied to explain the secondary circulation around the tropical cyclone outflow jet. From the classical jet stream theory (Palmen and Newton, 1969), the confluence of the synoptic scale flow into the entrance region of the jet results in a stronger temperature gradient and a thermally direct circum-jet secondary circulation. In Figure 3.10, the direction of the secondary circulation is indicated by the arrows. It is apparent that the secondary circulation is

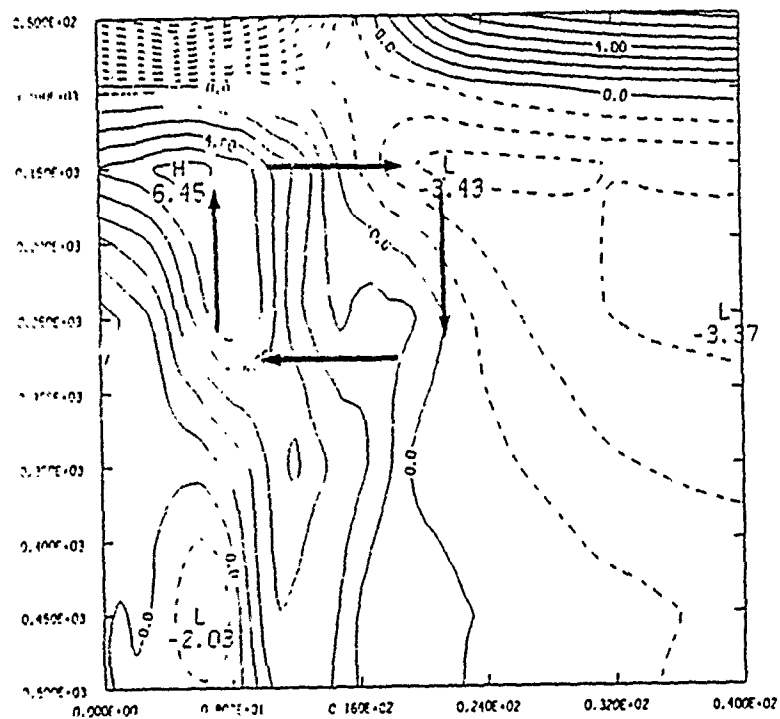


Figure 3.10 Cross section of the deviation of the potential temperature from the horizontal mean at the jet entrance region at 96 hour.

thermally induced and acts to decrease the temperature gradient. In the mean time, the secondary circulation may also cause an enhanced convection at the ascending branch to bring up the moisture and latent heat to maintain the higher temperature in the ascending region.

The structure of the secondary circulation around the outflow jet generated by the model is very similar to the classical description of its counterpart in the mid-latitude jet streams in terms of wind distribution, relative humidity, potential vorticity field and temperature deviation.

### 3.2.3 The Angular Momentum Budget

The observational, theoretical and model studies (Pfeffer, 1956; Palmen and Riehl, 1957; Holland, 1983) have demonstrated the importance of the outflow jet in maintaining the angular momentum budget mainly by means of the eddy momentum flux. From the mass continuity point of view, the upper layer of a tropical cyclone must be a divergent layer while the lower layer of a tropical cyclone is a convergent layer. From the conservation of angular momentum, when a particle moves adiabatically, the absolute angular momentum of the particle must be conserved. A momentum budget study with the model result will be elucidating, especially in

view of the high resolution of the model data as compared to the observational data density. The absolute angular momentum  $m_a$  is defined by

$$m_a = vr + fr^2/2 \quad (3.2)$$

where  $v$  is the tangential velocity related to the cyclone center (in cylindrical coordinates),  $f$ , the Coriolis parameter and  $r$ , the radius. Equation (3.2) indicates that when a particle moves outward in the outflow layer,  $fr^2/2$  gets larger faster than  $r$ , therefore  $v$  must decrease. For negative  $v$  (anticyclonic flow in the outflow layer),  $|v|$  must become significantly large to maintain the conservation of the angular momentum. But, from the conservation of the kinetic energy consideration,  $|v|$  cannot increase infinitely and symmetrically, therefore a symmetric outflow cannot exist (Anthes, 1974). Anthes (1974) suggested that the outflow jet seems to satisfy both the angular momentum and the kinetic energy conservations.

The conservation equation for the angular momentum in a cylindrical coordinate system (Anthes, 1974) is

$$\begin{aligned} \frac{\partial M}{\partial t} = & -2\pi \int_{h_1}^{h_2} \int_{r_0}^{r_1} r^2 \rho(z) (\langle f \rangle^\lambda \langle u \rangle^\lambda + \langle f'u' \rangle^\lambda) dr dz \\ & (A) \quad (B) \\ & -2\pi \int_{h_1}^{h_2} (r_1 \rho(z) \langle m \rangle^\lambda \langle u \rangle^\lambda)_{r_1} - r_0 \rho(z) (\langle m \rangle^\lambda \langle u \rangle^\lambda)_{r_0} dz \\ & (C) \end{aligned}$$

$$\begin{aligned}
& -2\pi \int_{h_1}^{h_2} (r_1 \rho(z) (\langle m'u' \rangle_{r_1}^\lambda - r_0 \rho(z) (\langle m'u' \rangle_{r_0}^\lambda)) dz \\
& \quad (D) \\
& -2\pi \int_{r_0}^{r_1} r (\rho(h_2) \langle w \rangle_{h_2}^\lambda \langle m \rangle_{h_2}^\lambda - \rho(h_1) \langle w \rangle_{h_1}^\lambda \langle m \rangle_{h_1}^\lambda) dr \\
& \quad (E) \\
& -2\pi \int_{r_0}^{r_1} r (\rho(h_2) \langle w'm' \rangle_{h_2}^\lambda - \rho(h_1) \langle w'm' \rangle_{h_1}^\lambda) dr \\
& \quad (F)
\end{aligned} \tag{3.3}$$

and

$$M = \int_{h_1}^{h_2} \int_{r_0}^{r_1} \int_0^{2\pi} r \rho m d\lambda dr dz \tag{3.4}$$

where  $u$  and  $v$  are the radial and tangential components of the velocity, respectively,  $m = rv$ ,  $\langle \rangle$  represents the circular mean and  $\langle \rangle'$  denotes the deviation. Here (A) and (B) represent the mean and eddy Coriolis torque, respectively; (C) and (D) represent the mean and eddy horizontal flux of the angular momentum and (E) and (F) represent the mean and eddy vertical flux of the angular momentum. In the present model study,  $h_1$  (=13700 m) and  $h_2$  (=14700 m) are approximately the height of the bottom and top of the outflow layer. Using Equation 3.3, the angular momentum budget for the model tropical cyclone at 96 hour is computed and shown in Table 3.1, along with the mean storm value given by Palmen and Riehl (1957) and Pfeffer (1958). The eddy Coriolis torque makes a positive contribution in

Table 3.1 Model and empirical angular momentum budget in the outflow layer of tropical cyclone

storm	radial domain $r_0 - r_1$	Coriolis torque	horizon. mean momen. flux	horizon. eddy momen. flux	vertical mean momen. flux	vertical eddy momen. flux
model <sup>1</sup> tropical cyclone	0 - 300 300 - 1000	mean eddy -1.8 0.018 -69.4 10.7	3.6 17.9	-0.7 29.8	0.3 -2.5	0.1 0.3
mean storm <sup>2</sup> (Palmen and Riehl, 1957)	0 - 333 333 - 666	-48.0 -143.0	-20.0 76.0	8.0 23.0	40.0 ----	20.0 44.0
mean storm <sup>2</sup> (Pfeffer, 1958)	222 - 444 444 - 666	-54.0 -78.0	46.0 -11.0	20.0 13.0	5.0 -4.0	---- ----

unit —  $10^{22} \text{ g cm}^{-2} \text{ s}^{-2}$

1. integration depth = 1000 m (13700 m — 14700 m)
2. integration depth = whole upper layer

the present budget study, reflecting that the strongest radial velocity occurs to the north of the tropical cyclone where  $f$  is large. This means that the strongest outflow occurs north of the tropical cyclone where the entrance region of the outflow jet is. The mean Coriolis torque make a negative contribution which shows the fact that mean radial velocity is positive (outward) in the outflow layer.

For the outer region ( $r > 300$  km) in the outflow layer, the horizontal eddy momentum flux becomes more important, as compared to the inner region ( $r < 300$  km). This is because of the existence of asymmetric outflow in the outer region. The eddy momentum flux in the model contributes  $29.8 \times 10^{22} \text{ g cm}^{-2} \text{ s}^{-2}$  as compared to  $17.9 \times 10^{22} \text{ g cm}^{-2} \text{ s}^{-2}$  contributed by the mean momentum flux. This again underscores the highly asymmetric nature and the dominance of the jet in the outflow layer. In the present study, it shows that the vertical momentum flux is relatively unimportant in the momentum budget of the outflow layer. The difference of the vertical eddy and mean momentum flux between the present and the previous budget studies probably because the difference of the integration depth. The integration depth in Palmen and Riehl (1957) and Pfeffer (1958) studies was roughly from 500 mb to the tropopause, while is only 1000 m (from 13700 m to 14700 m) in the present study.



### 3.3 Trajectories of the Released Particles

#### 3.3.1 Purpose and Methodology

The purpose of generating trajectories by tracing the released particles is to figuratively and qualitatively illustrate the air motion and the circulation patterns in the tropical cyclone. In particular, for this study, the trace trajectories may help to elucidate the origin of the air in the outflow jet in a three dimensional space. By tracing the trajectories, we may also be able to isolate the physical processes in the development of the outflow jet. For example, the trajectories may be able to indicate whether the air in the outflow jet is mainly originated from the lower troposphere and transported upward by the eye wall convection, or formed by the entrainment of the air parcels from the upper troposphere.

More than 200 air particles are released at the initial time. All particles are initially located at three pressure levels: 950 mb, 500 mb and 150 mb. At the 950 mb and 150 mb level, the particles are distributed on six rings concentric with the center of the the initial vortex with the radii of 20, 100, 300, 500, 1000 and 1500 km. At the 500 mb level, the particles are distributed on three rings with the radii of 200, 300 and 500 km. The details of the initial distribution of the particles are listed in

Table 3.2. Choice of the radius of each ring is based on the size of the model tropical cyclone and the eye wall and to provide a desirable distribution of the particles inside the eye wall, the outer region of the tropical cyclone and the intermediate region. As listed in Table 3.2, the 20 and 100 km rings are inside the eye wall, because the radius of the eye wall of the model tropical cyclone is roughly 150 km. The 300, 500 and 1000 km are in the intermediate region. The 1500 km ring is in the outer region of the tropical cyclone. The pressure levels of 950 mb, 500 mb and 150 mb can approximately represent the inflow, non-divergent and outflow layer, respectively.

Since the position of each particle is not exactly on the grid point, a bi-linear and a linear interpolation techniques are used to interpolate the horizontal and vertical velocity for each particle, respectively. The position of each particle ( $\phi_n(i)$ ,  $\theta_n(i)$ ,  $P_n(i)$ ) are then used along with the interpolated velocity ( $u_n(i)$ ,  $v_n(i)$ ,  $w_n(i)$ ) and the Euler-forward scheme to calculate the new position of each particle at the next time step. Here,  $\phi$  and  $\theta$  are the longitude and latitude, respectively,  $P$ , the pressure,  $n$ , the  $n$ -th time step and  $i = 1, 2, 3, \dots$  representing each particle. The displacement of each particle at each time step is given by

### 3.2 The Distribution of Particles at 0 hour.

No. of particles radius level	20 km	100 km	300 km	500 km	1000 km	1500 km
950 mb	10	16	16	16	16	8 <sup>1</sup>
500 mb	10	—	16	16	—	—
150 mb	10	16	16	16	16	8 <sup>1</sup>

Note: The particles at each ring are equally distributed.

1. The particles are only in the NW quadrant.

$$\begin{aligned}
\Delta x &= u_n(i) \Delta t \\
\Delta y &= v_n(i) \Delta t \\
\Delta P &= \omega_n(i) \Delta t
\end{aligned}
\tag{3.5}$$

and the new location of each particle by

$$\begin{aligned}
\Phi_{n+1}(i) &= \Phi_n(i) + \frac{\Delta x(i)}{h_x(\theta_n(i)) \Delta x} \\
\theta_{n+1}(i) &= \theta_n(i) + \frac{\Delta y(i)}{h_y(\theta_n(i)) \Delta y} \\
P_{n+1}(i) &= P_n(i) + \Delta P(i)
\end{aligned}
\tag{3.6}$$

where  $h_x$  and  $h_y$  are map factors,  $\Delta x$  and  $\Delta y$  are one half degree longitude and latitude distance at equator, respectively. The particle positions are stored every three time steps.

### 3.3.2 Trajectories

Figure 3.11 shows the trajectories at 96 hour of the particles released at 950 mb level. All the particles released at the 20 km radius are trapped inside the cyclone center, moving up slowly and following the cyclone's northwest drift. Their trajectories form a group pointed by arrow A in Figure 3.11. For the particles released at the 100 km radius, the trajectories are similar to those formed

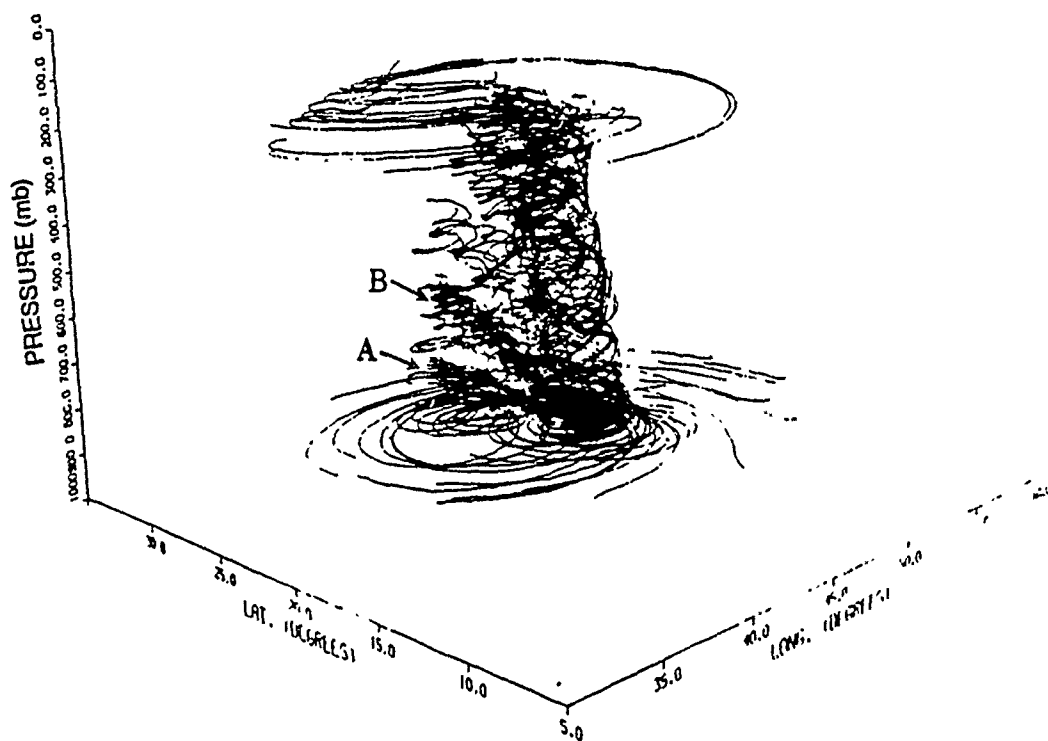


Figure 3.11 Trajectories of the particles released at 950 mb. A and B indicate the trajectories of the particles released at 20 and 50 km, respectively.

by the particles released at 20 km radius except they reach higher altitudes (see arrow B in Figure 3.11). This is because these particles are closer to the eye wall convection where the vertical velocities are stronger. As discussed before, the radius of the eye wall is about 150 km in this model tropical cyclone. Although the eye of the tropical cyclone is poorly resolved due to the coarse horizontal resolution of the model, these particles released at this two radii (20 and 100 km) are generally inside a region with slow updraft or downdraft in the middle of the convection surrounding the storm center.

Particles released at the radii of 300 and 500 km are inside the influence of the cyclone and produce very different trajectories. At first, they move horizontally and cyclonically toward the eye wall region, where they begin to rise. Once they reach the outflow layer, at about 150 mb, they turn anticyclonically and move outward. Some of the particles join the outflow jet.

The particles released at 950 mb level at radii of 1000 and 1500 km are far away from the cyclone center and show little movement. The particles released northwest of the cyclone, which are originally ahead of the cyclone, eventually converge into the central region and move upward. Conversely, the particles to southeast, originally behind the cyclone, slowly move cyclonically around cyclone and fail to move into the central region.

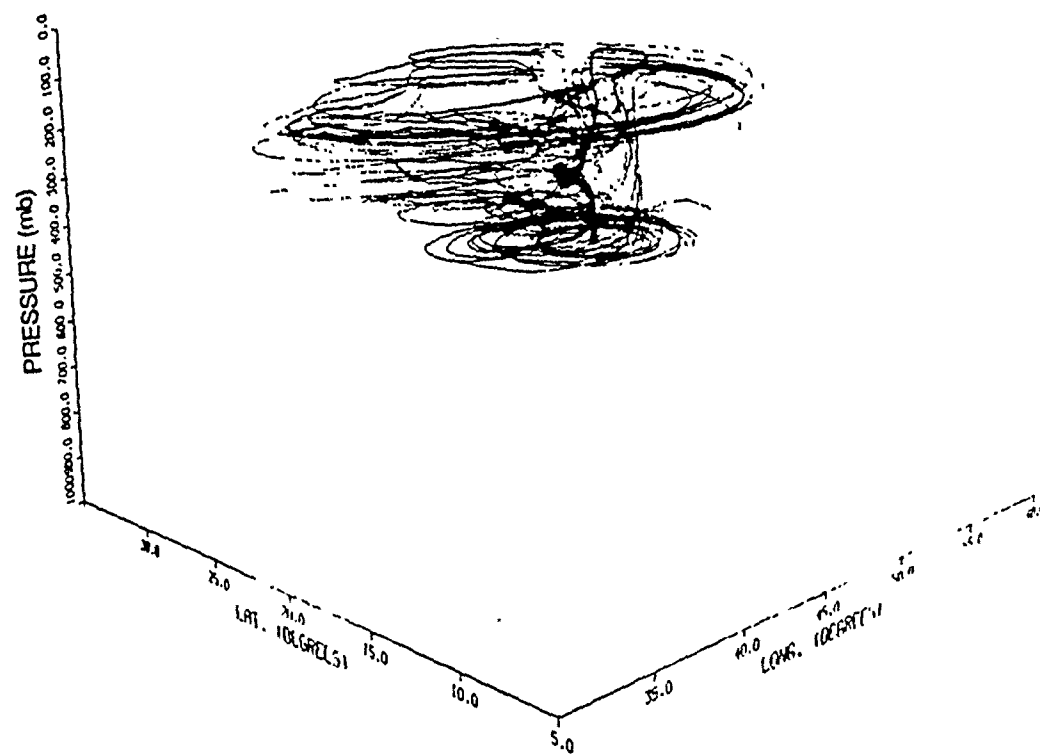


Figure 3.12 Trajectories of the particles released at 500mb.

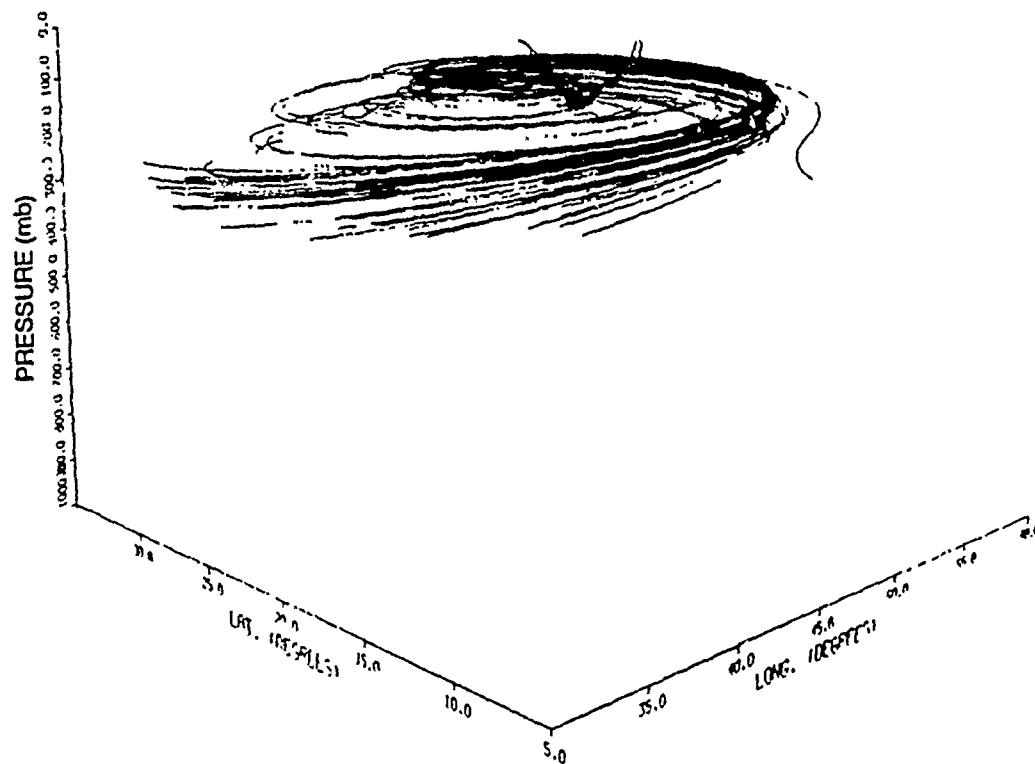


Figure 3.13 Trajectories of the particles released at 150mb.



As shown in Figure 3.13, there is a sinking motion in the outflow jet. For example, the pressure level of a particle, which is included in the jet, is 100 mb at the entrance region and sinks to 300 mb at the exit region.

Figure 3.14 shows the combined trajectory plot of all the particles. This plot gives us a general picture of the circulation in and around a tropical cyclone system. The converging air moves around the inner convective region cyclonically and moves upward in the strong convection. Once the air reaches the outflow layer (about 150 mb height), it starts to diverge in an anticyclonic motion. The trajectories also illustrate that the outflow layer is confined between 100 and 300 mb. In the outflow layer, a outflow jet dominates the outflow and most of the particles are transported outward by this outflow jet. It is also apparent from these trajectories that the flow in the inner radii of a few hundred kilometers is cyclonic, in agreement with the previous observations (Black and Anthes, 1971; Merrill, 1984).

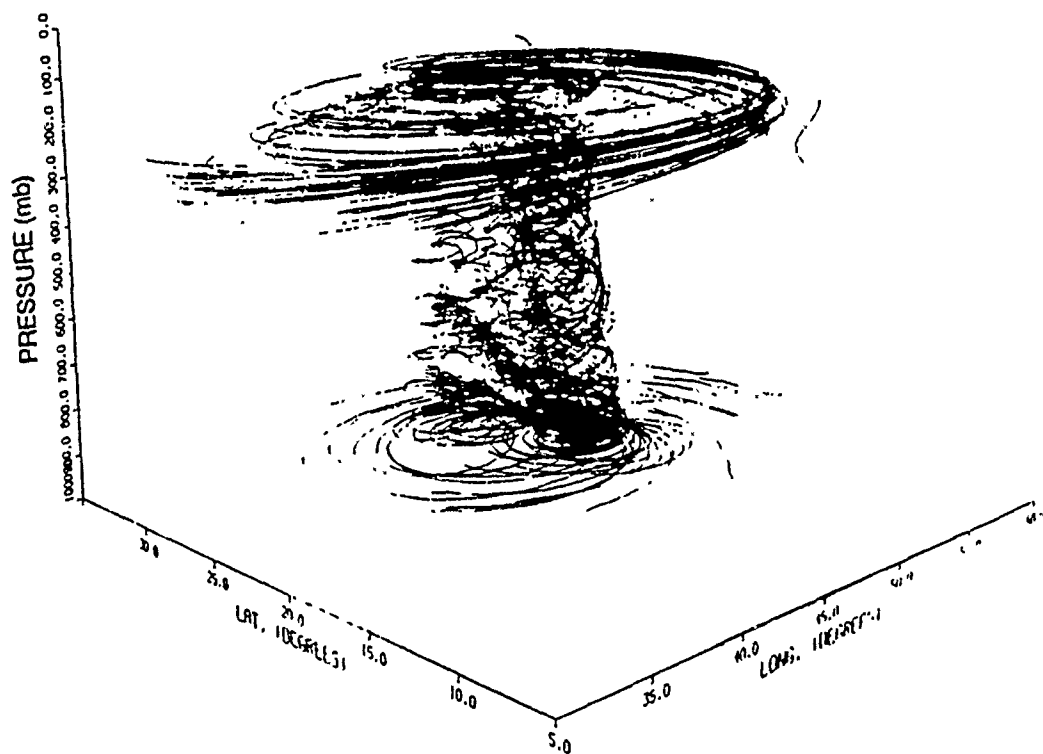


Figure 3.14 Trajectories of all particles.

#### 4. Response of a Tropical Cyclone to Large-Scale Forcing in the Upper Troposphere

As discussed in Chapter 1, there are several favorable situations for the intensification of a tropical cyclone. The first one is when the outflow jet joins a westerly jet (Chen and Gray, 1984; Merrill, 1984). The second is when a tropical cyclone moves below an upper-tropospheric ridge. The third situation is when a tropical cyclone approaches a TUTT (Tropical Upper-Tropospheric Trough) from a location east of the TUTT (Sadler, 1976, 1977; Steranka et al., 1986; Rodgers et al., 1987).

For the first situation, it is observed that the joining of the outflow jet with a westerly jet serves to increase the efficiency of moving the air mass from the central region of a tropical cyclone to the westerly jet. This appears to intensify the deep convection in the central region of a tropical cyclone (Merrill, 1984). For the second situation, the effect of the overlapping of the upper-tropospheric ridge and the tropical cyclone is to furnish a large-scale divergent flow pattern on the top of a tropical cyclone. This would increase the mass divergence in the upper layer of a tropical cyclone. Increase of the mass divergence in the upper layers would act to increase the mass convergence in the lower layers resulting

in the increase of the deep convection in the central region of a tropical cyclone. This process would then result in the intensification of the tropical cyclone.

Two numerical experiments have been conducted to test the response of the model tropical cyclone to the upper-tropospheric forcing. In Experiment 1 of this numerical study, the jet is accelerated by a relaxation method to simulate the situation of the joining of the outflow jet with a westerly jet. In Experiment 2, the total wind at the top of the model tropical cyclone is increased to simulate the superposition of a ridge over the tropical cyclone.

For both the experiments, one more term is added to each of the x- and y-direction momentum equations. The momentum equations (2.1) and (2.2) then become:

$$\frac{dP_s u}{dt} = \dots + \lambda P_s (u_{ref} - u) \quad (4.1)$$

$$\frac{dP_s v}{dt} = \dots + \lambda P_s (v_{ref} - v) \quad (4.2)$$

where  $1/\lambda$  is the e-folding time and the  $u_{ref}$  and  $v_{ref}$  are the speeds which the  $u$  and  $v$  are nudged to. The forcing starts from 72 hour for 48 hours.

For Experiment 1,  $\lambda$  is taken to be equal to  $0.5f$  and the  $u_{ref}$  and  $v_{ref}$  are equal to twice of their respective values at 72 hour (i.e.  $2u(t = 72 \text{ hr})$  and  $2v(t = 72 \text{ hr})$ ), respectively. The region of the forcing is restricted at the second level ( $\sigma = 0.15$ ) of the model and only where the wind speed is greater than  $20 \text{ ms}^{-1}$ .

For Experiment 2,  $\lambda$  is also equal to  $0.5f$  and the  $u_{ref}$  and  $v_{ref}$  are equal to  $2u(t - \Delta t)$  and  $2v(t - \Delta t)$ , respectively. That is the  $u_{ref}$  and  $v_{ref}$  are equal to  $u$  and  $v$  at the previous time step. So, the  $u_{ref}$  and  $v_{ref}$  are time dependent in Experiment 2, while they are time independent in Experiment 1. For simulating the superposition of an upper-tropospheric ridge over the tropical cyclone, the Equations 4.1 and 4.2 are used only at  $\sigma = 0.15, 0.25$  and  $0.35$ , respectively, and in the region inside a  $5^\circ$  latitude radius ring which is concentric with the cyclone center.

The models in both the experiments are integrated for 48 hours starting from 72 hour. Figure 4.1 shows the minimum pressure change with time for (a) the control tropical cyclone (line A); (b) the tropical cyclone in Experiment 1 (line B); and (c) the tropical cyclone in Experiment 2 (line C). It shows that the tropical cyclone in Experiment 1 just deepens slightly more than the control experiment and the tropical cyclone in Experiment 2 deepens by as much as 10 mb at 120 hour.

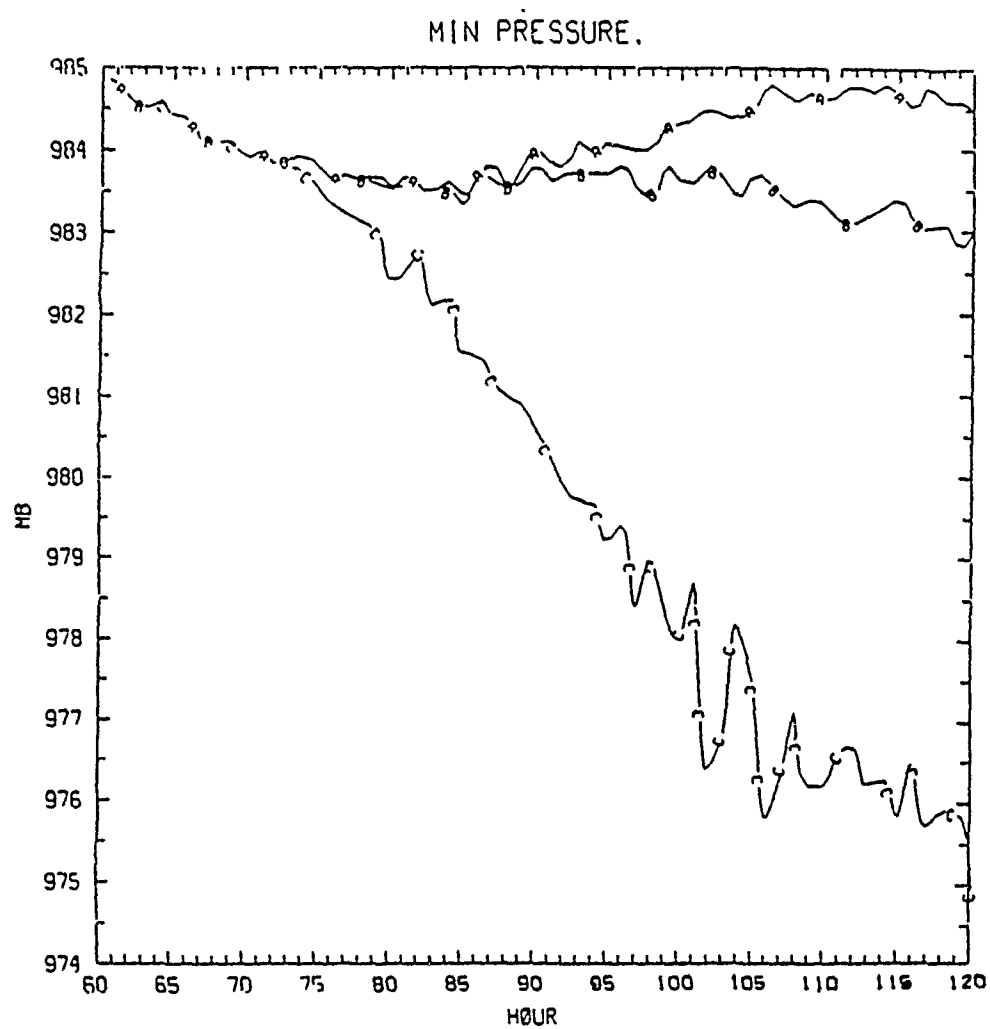


Figure 4.1 Variation of the minimum surface pressure with time. A represents the control model tropical cyclone. B and C represent Experiment 1 and 2, respectively.

Figures 4.2, 4.3 and 4.4 show the time variation of the maximum precipitation rate and the maximum wind speed at  $\sigma = 0.15$  (level of outflow layer) and at  $\sigma = 0.95$ , respectively. Figure 4.2 shows that the deep convection increases by a significant amount in Experiment 2, while only a slight increase is noticed in Experiment 1. The maximum wind speed at  $\sigma = 0.15$  (Figure 4.3), which always occurs in the outflow jet, increased in both experiments, while the maximum speed at  $\sigma = 0.95$  (Figure 4.4) increased only in Experiment 2.

The result, that the maximum wind speed increases near the surface, can always indicate the intensification of the tropical cyclone. So, these four figures (Figures 4.1, 4.2, 4.3 and 4.4) indicate that the tropical cyclone is only intensified in Experiment 2.

The mass divergence pattern in both the experiments can provide more evidence. The total mass divergence in each layer (for  $K = 1$  to 10) is calculated using

$$\Delta\sigma(k) \int_A \int -\frac{P_s}{g} (\nabla \cdot \vec{V})_o dA \quad (4.3)$$

where  $A$  is a closed region (see Figure 4.5).

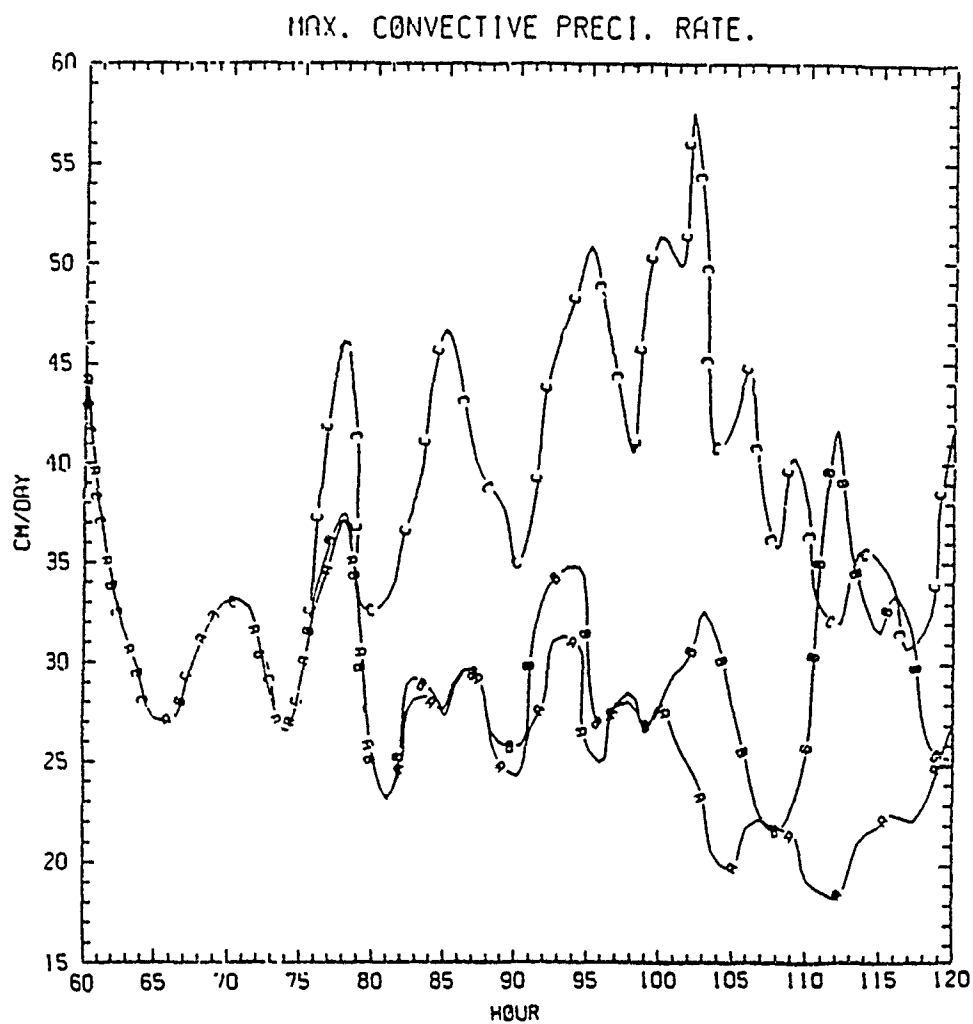


Figure 4.2 Same as Figure 4.1 except for the maximum convective precipitation rate.



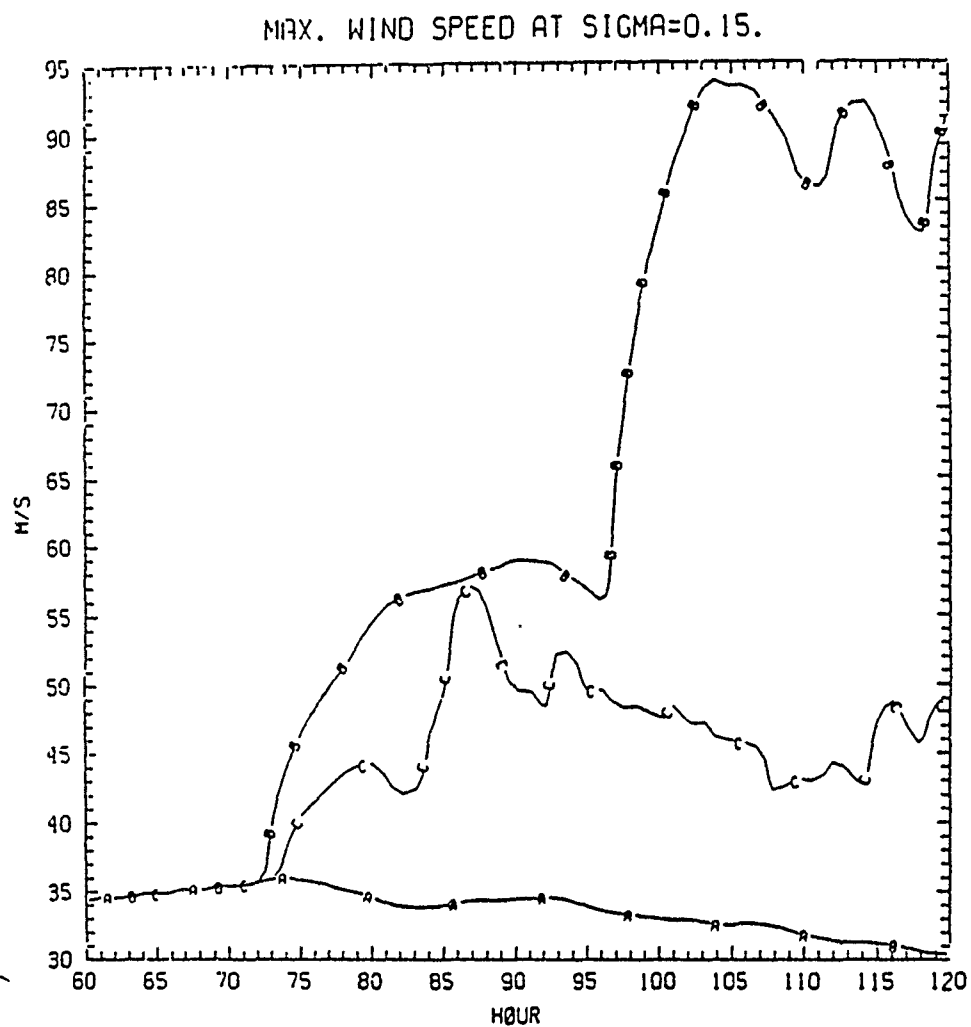


Figure 4.3 Same as Figure 4.1 but for the maximum wind speed at sigma = 0.15.

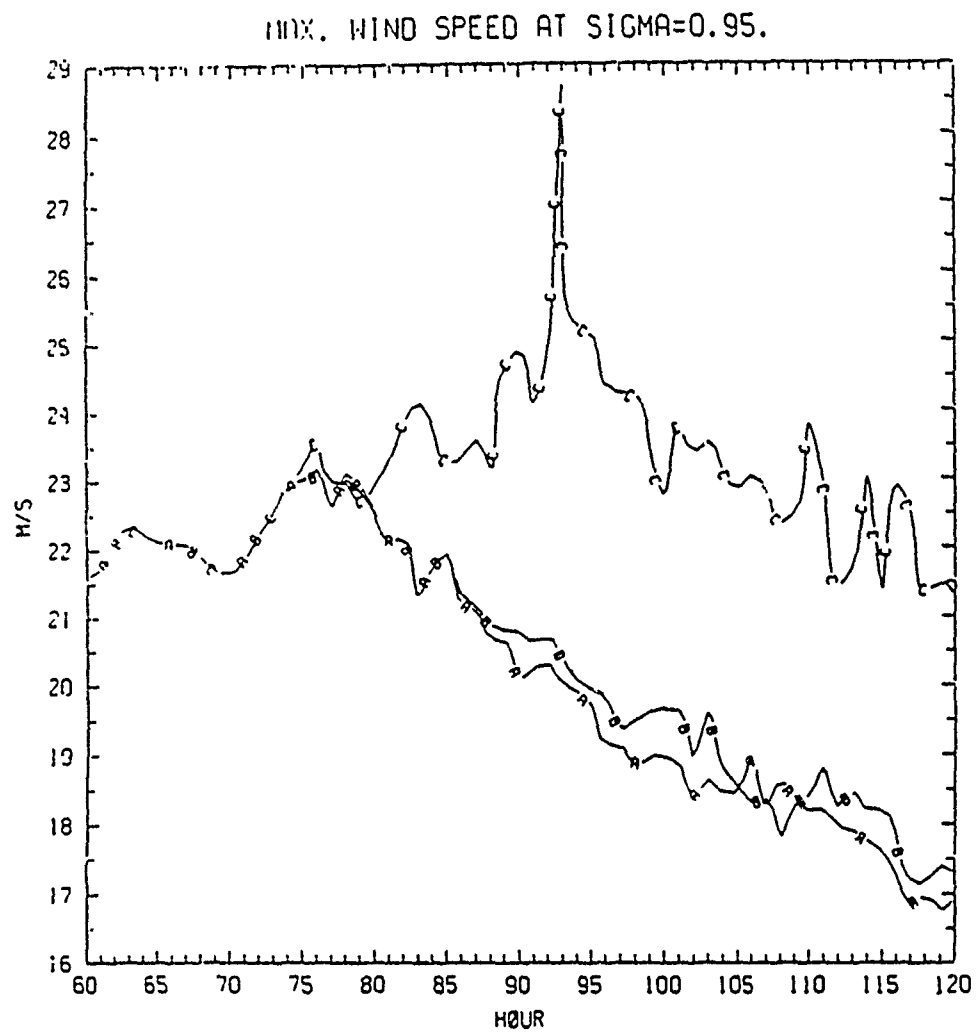
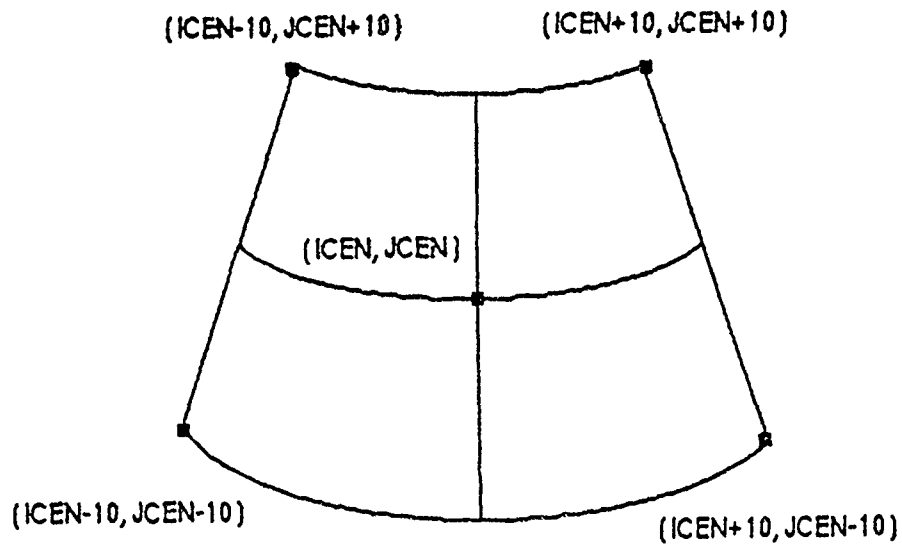


Figure 4.4 Same as Figure 4.1 but for the maximum wind speed at sigma = 0.95.



Region A

Figure 4.5 The close region A for equation 4.3.  $(ICEN, JCEN)$  is the grid point which is closest to the cyclone center.

Figures 4.6 and 4.7 show the mass divergence profiles at 96 and 120 hours, respectively. At 96 hours, the mass divergence in the upper layer and the mass convergence in the lower layer both increased to about  $6-7 \times 10^{12} \text{ gs}^{-1}$  in Experiment 2, while the mass divergence in the upper layer is slightly decreased and the mass convergence did not increase in Experiment 1. At 120 hours, for Experiment 2, the mass divergence in the upper layer and the mass convergence in the lower layer remains greater than those in the control tropical cyclone, but the difference is slightly smaller than that at 96 hours. For Experiment 1 at 120 hours, the maximum mass convergence occurs at  $\sigma = 0.15$  in addition to the low level convergence ( $\sigma = 0.95$ ), while the maximum mass divergence occurs at  $\sigma = 0.25$ . This may indicate that the outflow jet has its part of origin from its surrounding area instead of from the lower levels of the tropical cyclone. This may also be a numerical problem due to the single layer nudging in Experiment 1.

Results from both experiments suggest that the superposition of a tropical upper-tropospheric ridge over a tropical cyclone is a favorable situation for the intensification of a tropical cyclone. Model results suggest that the imposed upper-tropospheric divergence causes an increased mass divergence in the upper layer and an increased deep convection in the central region, and thus increase the mass convergence in the lower layers of the

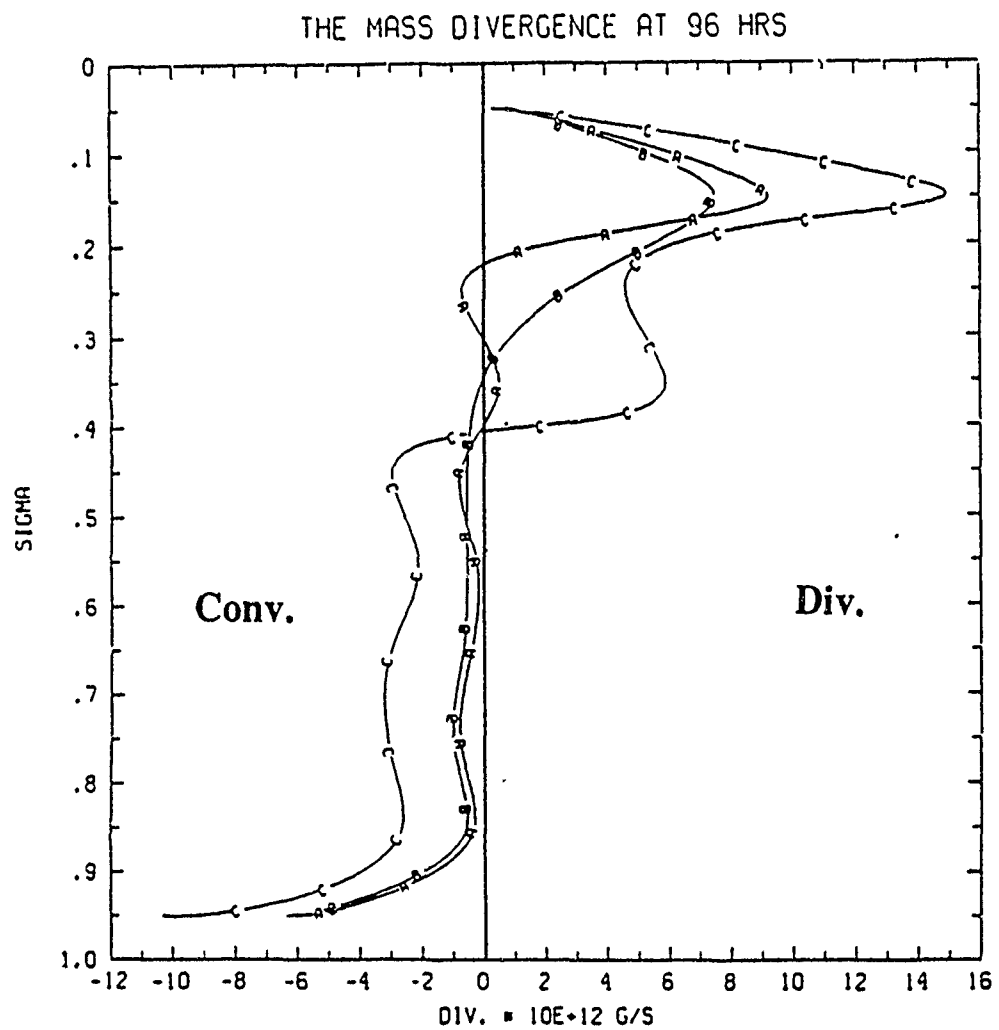


Figure 4.6 The mass divergent profile at 96 hours. A, B and C represent the same results as in Figure 4.1.

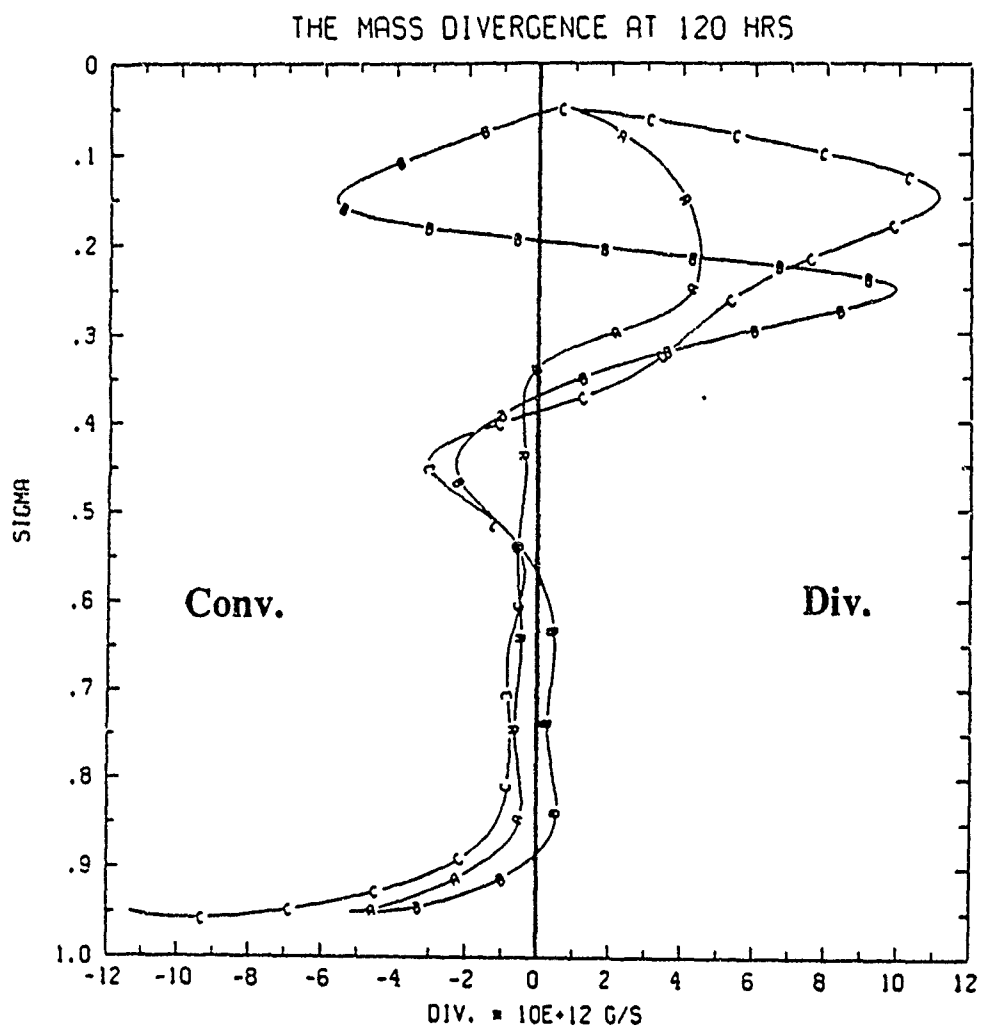


Figure 4.7 Same as Figure 4.6 except for 120 hours.

tropical cyclone. This study also indicates that the maximum intensity change (based on the decrease of the minimum surface pressure) of the tropical cyclone is found to occur at about 33 hours after the upper-tropospheric ridge has been superimposed over the tropical cyclone (see Figure 4.1). This result agrees well with a previous satellite observational study by Rodgers et al. (1987).

## 5. Summary and Conclusion.

A model tropical cyclone is generated to study the outflow structure of a tropical cyclone. The model tropical cyclone reaches a quasi-steady state with a central pressure at 984 mb and a maximum surface wind of  $20 \text{ ms}^{-1}$ . The anticyclonic outflow is strongest at about 150 mb. The outflow is dominated by a narrow and 3000 km long jet, which is well defined and organized, originating from an area north of the storm and extending to the southwest of the storm with a maximum wind speed of  $33 \text{ ms}^{-1}$ . The cross-section analyses of the outflow jet show that there is a secondary circulation around the outflow jet in the jet's entrance region. This secondary circulation has an ascending branch inside the jet (i.e. closer to the cyclone center) and a descending branch outside the jet. The secondary circulation appears to be thermally direct, and it acts to decrease the temperature gradient across the outflow jet.

The angular momentum budget study shows that the horizontal eddy momentum flux associated with the jet is more important in the outer region ( $r > 300 \text{ km}$ ) than in the inner region ( $r < 300 \text{ km}$ ) of the outflow layer. The contribution of the horizontal eddy transport of angular momentum is approximately twice of the mean transport. This underscores the highly asymmetric nature and the



dominance of the jet in the outflow layer. This result agrees with the previous observations (Palmen and Riehl, 1957; Pfeffer, 1958; Black and Anthes, 1971).

To study how the upper tropospheric forcings affect the tropical cyclone intensification, two numerical experiments have been conducted. In Experiment 1, the outflow jet is accelerated artificially to simulate the situation when the outflow jet joins with a westerly jet. In Experiment 2, the total circulation including the rotational and divergent component of the tropical cyclone in the upper levels is increased to simulate the superposition of an upper tropospheric ridge over the tropical cyclone. In Experiment 1, the response of the model tropical cyclone is small. In Experiment 2, the model tropical cyclone deepens by 10 mb in 24 hours. These results suggest that the superposition of an upper tropospheric ridge over a tropical cyclone is a favorable condition for the intensification of a mature tropical cyclone. Further numerical experiments are needed to determine more detail mechanisms of how the upper tropospheric forcings affect the tropical cyclone.

This numerical study focus on the outflow layer and the outflow jet of an idealized tropical cyclone. It also shows the ability of the mesoscale numerical model in simulating the outflow jet with some realistic features. Future studies can be done by adding the two-sided shear

environment into the model. Simulation of an actual cyclone and its outflow jet interacting with synoptic scale features will also be of interest in the future.

## References

- Alaka, M. A., 1961: The occurrence of anomalous winds and their significance. Mon. Wea. Rev., 89, 482-494.
- , 1962: On the occurrence of dynamic instability in incipient and developing hurricanes. National Hurricanes Research Projects, Rept. No. 50, U. S. Weather Bureau, Washington, D. C., 51-56.
- Anthes, R.A, 1974: The Dynamics and Energetics of Mature Tropical Cyclones. Reviews of Geophysics and Space Physics, Vol. 12, No. 3, 495-522.
- , and J. E. Hoke, 1975: The effect of horizontal divergence and the latitude variation of the Coriolis parameter on the drift of a model hurricane. Mon. Wea. Rev., 103, 757-763.
- , 1977: Hurricane Model Experiments with a New Cumulus Parameterization Scheme, Mon. Wea. Rev., 105, 287-300.
- , 1982: TROPICAL CYCLONES: Their Evolution, Structure and Effects. American Meteorological Society. Vol. 19, No. 41, 208 pp.
- Black, P.G. and R.A. Anthes, 1971: On the Asymmetric Structure of the Tropical Cyclone Outflow Layer. J. Atmos. Sci., 28, 1348-1366.
- Chan, J.C. and R.T. Williams, 1986: Analytical and Numerical Studies of the Beta-Effect in Tropical Cyclone Motion, Part I: Zero Mean Flow. J. Atmos. Sci., 44, 1257-1265.
- Charney, J. G. and Eliassen, A., 1964: On the growth of the hurricane depression. J. Atmos. Sci., 21, 68-75.
- Chen, L. and W.M. Gray, 1984: Global View of the Upper Level Outflow Patterns Associated with Tropical Cyclone Intensity Changes during FGGE. Paper presented at the 15th Technical Conference on Hurricanes and Tropical Meteorology, AMS, January 9-13, Miami, Florida.
- Frank, W.M., 1977a: The Structure and Energetics of the Tropical Cyclone, Part I: Storm Structure. Mon. Wea. Rev., 105, 1119-1135.

Hebert, P.J., 1978: Intensification Criteria for Tropical Depressions of the Western North Atlantic. Mon. Wea. Rev., 106, 831-840.

Holland, G. J., 1982: Tropical cyclone motion: Environmental interaction plus a beta effect. Atmos. Sci. Paper No. 348, Colorado State University, Fort Collins, CO, US ISSN0067-0340, 47 pp.

-----, 1983: Angular Momentum Transports in Tropical Cyclones., Quart. J. R. Met. Soc., 109, 187-209.

-----, and R.T. Merrill, 1984: On the Dynamics of Tropical Cyclone Structural Changes. Quart. J. R. Met. Soc., 110, 723-745.

Kuo, H.L, 1974: Further Studies of the Parameterization on the Influence of Cumulus Convection on Large-Scale Flow. Atmos. Sci., 31, 1232-1240.

Madala, R. V. and S. A. Mccsek, 1975: Numerical simulation of asymmetric hurricanes c, a beta-plane with vertical shear, Tellus, 27, 453-468.

-----, 1981: Efficient time integration schemes for atmospheric and ocean models. Chpt. 4, Finite Difference Techniques for Vectorized Fluid Dynamic Calculations. Springer-Verlag, pp 56-74.

-----, S. W. Chang, U. C. Mohanty, S. C. Madan, R. K., Paliwal, V. B. Sarin, T. Holt and S. Raman, 1987: Description of the Naval Research Laboratory Limited Area dynamical Weather Prediction Model. NRL Technical Report No. 5992, Washington, D.C., 131pp.

Merrill, R.T., 1984: Structure of the Tropical Cyclone Outflow Layer. Proceedings of the 15th Technical Conference on Hurricanes and Tropical Meteorology, AMS, January 9-13, Miami, Florida.

Miller, B. I., 1963: The three-dimensional wind structure around a tropical cyclone. National Hurricane Research Project, Rept. No. 15, 41 pp.

Ooyama, K.V., 1987: Numerical Experiments of Study and Transient Jets with a Simple Model of the Hurricane Outflow Layer. Preprints, the 17th Conference on Hurricanes and Tropical Meteorology, AMS, April 7-10, Miami, Florida.

- Palmen, E. and H. Riehl, 1957: Budget of Angular Momentum and Kinetic Energy in Tropical Cyclones. J. Meteor., 14, 150-159.
- Palmen, E. and C.W. Newton, 1969: Atmospheric Circulation Systems. Academic Press, 111 Fifth Ave., New York, NY, 603pp.
- Pfeffer, R.L., 1958: Concerning the Mechanisms of Hurricanes. J. Meteor., 15, 113-119.
- Rodgers, E.B., J. Stout and J. Steranka, 1986: Upper-Tropospheric and Lower-Stratospheric Dynamics Associated with Tropical Cyclones as Inferred from Total Ozone Measurements. Postprints, The Second Conference on Satellite Meteorology/Remote Sensing and Applications, AMS, Williamsburg, Virginia.
- , 1987: Evidence of Upper-Tropospheric Influence on Tropical Cyclone Intensity Change using Satellite Observations. Preprint, the 17th Conference on Hurricanes and Tropical Meteorology, AMS, April 7-10, Miami, Florida.
- Sadler, J.C., 1976: The Role of the Tropical Upper-Tropospheric Trough in Early Season Typhoon Development. Mon. Wea. Rev., 104, 1266-1278.
- , 1977: Mid-Season Typhoon Development and Intensity Changes and the Tropical Upper-Tropospheric Trough. Mon. Wea. Rev., 106, 1137-1152.
- Sheets, R.C., 1968: Some Mean Hurricane Soundings. J. Appl. Meteor., 8, 134-146.
- Smith, C. L., 1975: On the intensification of Hurricane of Celica (1970). Mon. Wea. Rev., 103, 131-148.
- Steranka, J., E.B. Rodgers and R.C. Gentry, 1986: The Relationship Between Satellite Measured Convection Burst and Tropical Cyclone Intensification. Mon. Wea. Rev., 114, 1539-1546.

## **APPENDIX H**

### **A Review and Comparative Evaluation of Multilevel Boundary Layer Parameterizations for First-Order and Turbulent Kinetic Energy Closure Schemes**

# A Review and Comparative Evaluation of Multilevel Boundary Layer Parameterizations for First-Order and Turbulent Kinetic Energy Closure Schemes

TEDDY HOLT AND SETHU RAMAN

*Department of Marine, Earth and Atmospheric Sciences, North Carolina State University, Raleigh*

Multilevel parameterizations of the atmospheric boundary layer using first-order and turbulent kinetic energy (TKE) closure schemes are reviewed. Eleven schemes, chosen as representative of both first-order and TKE closure, are then used for comparison in a one-dimensional barotropic planetary boundary layer model. TKE closure schemes evaluated are the  $E-\epsilon$  schemes in which eddy viscosity  $K_m$  is determined from turbulent kinetic energy and energy dissipation  $\epsilon$  and the  $l$  model schemes in which  $K_m$  is determined from TKE and mixing length  $l$ . Comparison of model simulations of mean and turbulence structure for first-order closure and TKE closure schemes to observational data (MONEX79) is given. The two main conclusions drawn from this comparison are that (1) the mean structure of the boundary layer is fairly insensitive to the type of closure scheme, given that the scheme properly accounts for turbulent boundary layer mixing, and (2) TKE closure is preferable to first-order closure in predicting the overall turbulence structure of the boundary layer. Among the TKE schemes compared in this paper, the modified Detering and Etling (1985) scheme is preferred.

## 1. INTRODUCTION

Much has been written in recent years concerning modeling and parameterizations of the planetary boundary layer (PBL), particularly in review works [e.g., Blackadar, 1979, McBean *et al.*, 1979, Wyngaard, 1982, Panofsky and Dutton, 1984]. However, little has been resolved in terms of development of improved parameterizations or the direction and future progress of PBL parameterization schemes as they relate to numerical weather prediction. The effects of the boundary layer can be incorporated into a large-scale model in two ways, as first discussed by Clark [1970] and Deardorff [1972]. One way is to parameterize the entire PBL as one layer. This involves identifying and relating unresolvable processes in the PBL with resolvable ones. The complexity of this single-layer PBL parameterization lies in the variety and interdependence of atmospheric processes acting on different scales. The second approach, and the one discussed in this paper, is to include several computational levels in the PBL in order to resolve the boundary layer structure effectively and explicitly. Such multilevel-PBL formulations require turbulent fluxes of momentum, heat, and moisture at several levels within the PBL. Thus they require some type of closure scheme to relate turbulent fluxes to mean quantities.

Basic closure schemes are presently limited to first,  $1\frac{1}{2}$  (or turbulent kinetic energy), second, and to a lesser extent, third order. Second- and third-order schemes involve more of the physics of the boundary layer through increased formulation and numerical complexity. The intent here is to concentrate only on multilevel PBL parameterizations as they pertain to first-order and turbulent kinetic energy (TKE) closure. First-order closure is well documented, but there has not been a good review of TKE closure. In section 2 we present a review of past work on various multilevel parameterizations. Representative parameterizations of the first-order and TKE closure

schemes are then selected for comparison using a one-dimensional model.

Observational data of the mean and turbulent structure of the marine boundary layer will be compared to model results in section 3. The data set used is from the Monsoon Experiment (MONEX79). It represents a unique opportunity to study turbulent structure of a marine boundary layer in a region in which relatively weak sea surface temperature gradients existed. The baroclinicity of the region and the effects of the barotropic assumption in the one-dimensional (1-D) model are important and will also be considered in section 3.

## 2. REVIEW OF CLOSURE SCHEMES

### 2.1. First-Order Closure

The closure problem arises from representing the total turbulent flow in the atmosphere in terms of the mean flow. The fundamental concern is not to introduce more unknowns into the equations describing the atmosphere such that the number of unknowns exceeds the number of equations. The principle behind the simplest way of closing the system of equations, first-order closure, as originally proposed by Boussinesq [1877], is to model turbulent transfer as molecular transport as follows:

$$\begin{aligned} -(\overline{uw}, \overline{vw}) &= K_m (\partial U / \partial z, \partial V / \partial z) \\ -(\overline{w\theta}) &= K_h (\partial \Theta / \partial z) \\ -(\overline{wq}) &= K_q (\partial Q / \partial z) \end{aligned} \quad (1)$$

where  $\overline{uw}$ ,  $\overline{vw}$ ,  $\overline{w\theta}$ , and  $\overline{wq}$  represent vertical turbulent fluxes and  $K_m$ ,  $K_h$ , and  $K_q$  are eddy viscosity coefficients of momentum, heat, and moisture, respectively. This is the fundamental premise of first-order closure, that these unknowns, turbulent fluxes  $\overline{uw}$ ,  $\overline{vw}$ , etc. (for first-order closure) are related to mean vertical gradients by an eddy viscosity coefficient  $K$  which is a property of the turbulent flow. It is this eddy viscosity coefficient which must account for the complexities of turbulence. The problem of first-order closure is then effectively reduced to the problem of resolving  $K$ , and this is the problem addressed here.

Copyright 1988 by the American Geophysical Union.

Paper 88RG03114.  
8755-1209/88/88RG-03114\$05.00

TABLE 1.  $K$  Profiles

Author	$K$ Profile	Range of Validity	Constants
O'Brien [1970]	$K_m = K(h) + [(z-h)^2/(h-z_s)^2]\{K(z_s) - K(h)\}$ $+ (z-z_s)[\partial K/\partial z_s + \{2(K(z_s) - K(h))/(h-z_s)\}]$	all $Ri$ $z_s < z < h$	$S^2 = \{(\partial U/\partial z)^2 + (\partial V/\partial z)^2\}$ $\sigma = 15$
Yamamoto et al. [1973]	$K_m = k^2 z^2 [S + (g/\theta)(\partial\theta/\partial z)^{1/2}]$	$\partial\theta/\partial z < 0$ $\partial\theta/\partial z > 0$	$K_0 = 0.0093 \text{ m}^2 \text{ s}^{-1}$ $C = 0.1$
Orlanski et al. [1974]	$K_m = k^2 z^2 [S - (L/2z)(\sigma g/\theta \partial\theta/\partial z)^{1/2}]$ $K_m = K_0 [1 + C(-g\Delta\theta(\Delta z)^{1/2}/\theta K_0 \nu_0)^{1/3}]$ $K_m = K_0$	$\Delta\theta < 0$ $\Delta\theta \geq 0$	$\Delta z$ is local vertical grid size: $\Delta\theta$ is local $\theta$ difference $\nu_0 = 0.0093 \text{ m}^2 \text{ s}^{-1}$ $\beta = 4.7$
Businger and Arya [1974]	$K_m = kzu_* \exp(-fz/V_*^2)(1 + \beta z/L)$	stable	$\beta = 4.7$
Pielke and Mahrer [1975]	$K_m = K(h) + [(z-h)^2/(h-z_s)^2]\{K(z_s) - K(h)\}$ $+ (z-z_s)[\partial K/\partial z_s + \{2(K(z_s) - K(h))/(h-z_s)\}]$ $K_m = K(h)$ $K_m = (z/h)K(z_s)$	$z_s < z < h$ $z > h$ $z < z_s$	
Brost and Wyngaard [1978]	$K_m = kzu_* (1 - z/h)^{1/2} (1 + \beta z/L)^{-1}$	stable	$\beta = 4.7$

For completeness we include simplified equations of the one-dimensional PBL, neglecting horizontal advection terms and considering only vertical turbulent exchange:

$$\begin{aligned}\frac{\partial U}{\partial t} - fV &= -\frac{\partial}{\partial z}(\overline{uw}) - \frac{1}{\rho} \frac{\partial P}{\partial x} \\ \frac{\partial V}{\partial t} + fU &= -\frac{\partial}{\partial z}(\overline{vw}) - \frac{1}{\rho} \frac{\partial P}{\partial y} \\ \frac{\partial \Theta}{\partial t} &= -\frac{\partial}{\partial z}(\overline{w\theta}) \quad \frac{\partial Q}{\partial t} = -\frac{\partial}{\partial z}(\overline{wq})\end{aligned}\quad (2)$$

where uppercase values  $U$ ,  $V$ ,  $\Theta$ , and  $Q$  represent mean values of east-west and north-south wind, potential temperature, and humidity, respectively. Lowercase values denote deviations from the mean. Incorporating the eddy viscosity concept ( $f$ ) along with geostrophic winds ( $U_g$ ,  $V_g$ ) yields a set of more easily modeled equations:

$$\begin{aligned}\frac{\partial U}{\partial t} - f(V - V_g) &= \frac{\partial}{\partial z} \left( K_m \frac{\partial U}{\partial z} \right) \\ \frac{\partial V}{\partial t} + f(U - U_g) &= \frac{\partial}{\partial z} \left( K_m \frac{\partial V}{\partial z} \right) \\ \frac{\partial \Theta}{\partial t} &= \frac{\partial}{\partial z} \left( K_h \frac{\partial \Theta}{\partial z} \right) \quad \frac{\partial Q}{\partial t} = \frac{\partial}{\partial z} \left( K_q \frac{\partial Q}{\partial z} \right)\end{aligned}\quad (3)$$

where  $K_q$  is assumed equal to  $K_h$ .

Modeling of the lowest 100 m of the atmosphere is best accomplished by making use of surface layer theory. Effective and efficient parameterization schemes based on Monin-Obukhov similarity are widely used for the surface layer (see, for example, Panofsky and Dutton [1984], Pielke [1984], and Arya [1977]) and will not be expounded upon here. Instead we focus only on the bulk of the boundary layer away from the surface. It is this region in which nonstationarity and inhomogeneity often dominate that is most difficult to model. In this region, first-order closure schemes can be divided into two groups: one in which mixing length ( $l$ ) parameterizations are used to determine  $K$  and one in which mixing length is not used. We first consider those parameterizations which do not utilize the mixing length approach but instead describe a  $K$  profile.

**2.1.1.  $K$  profile approach.** The simplest and oldest approach to first-order closure is to specify a  $K$  profile in which  $K$  is a constant. These constant  $K$  models are easily solved analytically [Ekman, 1905], but physically they are not well representative of the boundary layer as could be expected from their simplicity [Krishna, 1980]. A more physically realistic approach is to prescribe a  $K$  profile which varies with height. Thus  $K$  is allowed to depend on height, thermal stability, local gradients of potential temperature, etc. Numerous authors including O'Brien [1970], Yamamoto et al. [1973], Businger and Arya [1974], Orlanski et al. [1974], Pielke and Mahrer [1975], Deardorff [1975], Brost and Wyngaard [1978], and Bodin [1980] have considered this approach to study a variety of atmospheric conditions.

In the steady, horizontally homogeneous stable boundary layer, Brost and Wyngaard [1978] parameterized  $K$  based on surface layer and mixed layer scaling, while Businger and Arya [1974] used a scheme in which  $K$  adjusts asymptotically throughout the boundary layer (see Table 1 for a description of  $K$  profile schemes). For more general atmospheric conditions, O'Brien [1970] suggested a scheme, still used by some [see Tapp and White, 1976], in which  $K$  is obtained from a third-order polynomial determined by specified boundary conditions at the top of the boundary layer ( $h$ ) and at the top of the surface layer ( $z_s$ ).

Others have used schemes which utilized different subgrid scale parameterizations, such as that given by Deardorff [1974]. Orlanski et al. [1974] used a simplified two-dimensional (2-D) version of Deardorff's [1974] three-dimensional (3-D) numerical model and specified  $K$  proportional only to local vertical gradients of potential temperature. Deardorff [1975] used a similar approach but with  $K$  proportional to the local turbulent energy. Yamamoto et al. [1973] assumed  $K$  proportional to both vertical wind shear and vertical gradients of potential temperature. Pielke and Mahrer [1975] combined O'Brien's [1970] formulation with Deardorff's [1974] prognostic equation for PBL height  $h$  to better resolve boundary layer growth.

All of these first-order schemes are relatively simple in that they require only routinely measured or model resolvable meteorological variables to explicitly determine  $K$ . Thus  $K$  profiles are specifically determined by parameters such as



$\partial\Theta/\partial z, z:L, z/h$ , etc., where  $L$  is Monin-Obukhov length. This is a drawback in that these parameters are often not good indicators of the total turbulent flow. A slightly different approach to this type of determination of  $K$  is an approach in which  $K$  is expressed in terms of a mixing length  $l$  such that

$$K_m = l^2[(\partial U/\partial z)^2 + (\partial V/\partial z)^2]^{1/2} \quad (4)$$

and one must determine  $l$  instead of  $K$ . This mixing length approach will now be considered.

**2.1.2. Mixing length approach.** The principle of a mixing length in terms of atmospheric turbulence dates back to the work of Prandtl [1932]. He reasoned, from considerations of eddy transfer, that in the surface layer, eddies move vertically at velocity  $w$  and over a distance  $l$  (or mixing length) in the process of adjusting their momentum to that of the surrounding fluid. Blackadar [1962], extending Prandtl's mixing length hypothesis, reasoned that  $l$  varied as  $kz$  close to the ground (where  $k$  is von Kármán's constant) but approached some constant value  $\lambda$  at greater heights, i.e.,

$$l = kz(1 + kz\lambda) \quad (5)$$

Blackadar suggested  $\lambda$  equal to  $2.7 \times 10^{-4} |G|/|f|$  where  $G$  is the geostrophic wind and  $f$  is the Coriolis parameter. Others have used Blackadar's parameterization, or slight modifications of it, in their own schemes for determining  $K$  (see Table 2). For example, Carlson and Foster [1986] used an eddy viscosity turbulence model in a 2-D simulation of unstable boundary layer flow over valleys in which mixing length was Blackadar's formulation modified to include stability effects. Earlier works [Karlsson, 1972; Clarke, 1974; Estoque and Bhumralkar, 1970] used Blackadar's parameterization with modifications included in  $K$  profiles to account for stability (Table 2). Djolov [1973] utilized a modified Blackadar formulation by including the stability function  $\phi_m$ :

$$l = kz(\phi_m + kz\lambda) \quad (6)$$

where  $\lambda = 4.0 \times 10^{-4} |G|/|f|$  and  $\phi_m$  is determined by the usual Businger-Dyer relationships. Delage [1974] used a local Monin-Obukhov length approach and Bodin [1976] a "neutral" mixing length approach modified by the depth of the boundary layer to extend Djolov's work to the stable boundary layer. Lacser and Arya [1986] summarized many of these works and provided a review of mixing length parameterizations in the stably stratified nocturnal boundary layer.

Other parameterizations of mixing length  $l$  exist. For simulating a horizontally homogeneous stratus-filled boundary layer, Tag and Payne [1987] used a 3-D PBL model that incorporated the mixing length parameterization first proposed by Rossby and Montgomery [1935]. In this scheme,  $l$  is separated into a region within the surface layer and a region above it. Mixing length is then a function of distance from the surface, as well as stability, in both regions. A scheme developed to account for stability similar to that of earlier authors [Estoque and Bhumralkar, 1970; Karlsson, 1972] is a modified Djolov [1973] scheme. In this scheme,  $l$  is a function of  $\phi_m$  as earlier, but now  $K_m$  is also a function of Richardson number (see Table 2).

## 2.2. Turbulent Kinetic Energy Closure

An improvement to the simplicity of first-order closure would be a closure scheme in which more of the physics of the atmosphere is taken into account in the formulation of the eddy viscosity coefficient  $K$ . Such a scheme is the turbulent

kinetic energy closure. It is essentially a first-order scheme in that closure is accomplished by means of (1), but the  $K$  coefficient is determined from more involved and hopefully more physically realistic relationships given by prognostic equations for turbulent kinetic energy and energy dissipation or mixing length. This type of closure is also more economical as compared to higher-order closure schemes. For example, second-order closure requires the integration of at least 15 partial differential equations when moisture is included. Simple first-order closure generally requires only the four equations given in (3). TKE closure requires only two additional equations, a total of six, and thus provide a more physically realistic solution to the closure problem than does first-order closure, without the involved numerical complexity of second-order closure. Thus it is often termed  $1\frac{1}{2}$ -order closure [Mellor and Yamada, 1974].

The foundation of TKE closure is the budget of turbulent kinetic energy. It is essentially a first-order closure scheme, so it does involve the same parameterization of  $K$  given in section 2.1. Here we also consider the same basic equations for the description of the atmosphere as in section 2.1 for consistency. However, an additional equation is introduced which computes the turbulent kinetic energy budget in the boundary layer. For turbulent kinetic energy  $E$  expressed as  $(\bar{u}^2 + \bar{v}^2 + \bar{w}^2)/2$ , the prognostic equation for TKE over a horizontally homogeneous surface is derived as (see, for example, Monin and Yaglom [1971])

$$\frac{\partial E}{\partial t} = -\overline{uw} \frac{\partial U}{\partial z} - \overline{vw} \frac{\partial V}{\partial z} + \frac{g}{\Theta} \overline{w\theta} - \frac{\partial}{\partial z} \left( \overline{wE} + \frac{\overline{pw}}{\rho} \right) - \epsilon \quad (7)$$

where the first two terms on the right-hand side (r.h.s.) represent shear production, the third term represents buoyancy production, the fourth turbulent transport, and the fifth dissipation of turbulent energy. In this closure scheme, several terms on the r.h.s. must be parameterized. The shear terms, of course, are related to mean gradients by (1). Similarly, heat flux  $\overline{w\theta}$  in the buoyancy term is generally expressed as

$$-\overline{w\theta} = K_h(\partial\Theta/\partial z - \gamma_{eq}) = K_h(\partial\Theta_{eq}/\partial z) \quad (8)$$

where  $\gamma_{eq}$  ( $= 7.0 \times 10^{-4}$  K/m) incorporates countergradient heat flux [Deardorff, 1966]. The turbulent transport term is composed of vertical turbulent transport  $\partial/\partial z (\overline{wE})$  and pressure transport  $\partial/\partial z (\overline{pw}/\rho)$ . The two terms are generally included as one and modeled as [Monin and Yaglom, 1971; Shur, 1973; Rodi, 1980]

$$-(\overline{wE} + \overline{pw}/\rho) = C(K_m \partial E/\partial z) \quad (9)$$

where  $C$  is a constant. Substitution of these parameterizations into (7) yields

$$\frac{\partial E}{\partial t} = K_m \left[ \left( \frac{\partial U}{\partial z} \right)^2 + \left( \frac{\partial V}{\partial z} \right)^2 \right] + \frac{g}{\Theta} K_h \frac{\partial \Theta_{eq}}{\partial z} + C \frac{\partial}{\partial z} \left( K_m \frac{\partial E}{\partial z} \right) - \epsilon \quad (10)$$

Parameterization of the final term, energy dissipation  $\epsilon$ , can be achieved either diagnostically or prognostically and will be considered in the following sections.

To organize and to clarify the different TKE closure schemes, we now separate them into three basic model schemes based on the prognostic variables considered. Basic equations, assumptions, and recent work on each parameterization will then be evaluated.

TABLE 2. Mixing Length Parameterizations

Author	$K$	$l$	Range of Validity	Constants
Blackadar [1962]	$K_m = f^2 S$	$l = kz/(1 + kz/\lambda)$	all $Ri$	$\lambda = 2.7 \times 10^{-4} (G/f)$
Estoque and Blumvalke [1970]	$K_m = f^2 S(1 + Ri)$	$l = kz/(1 + kz/\lambda)$	$Ri > 0$	$\lambda = 2.7 \times 10^{-4} (G/f)$
Karlsun [1972]	$K_m = f^2 S(1 - \alpha Ri)$	$l = kz/(1 + kz/\lambda)$	$Ri < 0$	$\alpha = 3.0$
	$K_m = f^2 S(1 + \alpha Ri)$		$\partial\theta/\partial z \geq 0$	$\lambda = 2.7 \times 10^{-4} (G/f)$
	$K_m = K_m(1 + \alpha Ri)$			$\alpha = 3.0$
Clarke [1974]	$K_m = f^2 S(1 - \gamma \sigma)$	$l = kz/(1 + kz/\lambda)$	$\partial\theta/\partial z < 0$	$\lambda = 2.7 \times 10^{-4} (G/f)$
	$K_m = f^2 S(1 - \sigma)$		$\partial\theta/\partial z > 0$	$\gamma = 18$
				$\sigma = \frac{(g\theta)^{1/2}}{\theta} \frac{\partial\theta}{\partial z} S^{-1}$
Djorlov [1973]	$K_m = f^2 S$	$l = kz(\phi_m + kz/\lambda)$	$\partial\theta/\partial z \geq 0$	$\phi_m = 1 + 4.7(z/L)$
Modified Djorlov [1973]	$K_m = f^2 S(1 - R_3)^{1/2}$	Djorlov [1973]	$\partial\theta/\partial z < 0$	$\phi_m = [1 - 15(z/L)]^{-1/4}$
	$K_m = 0$		$Ri < 1$	
Deloge [1974]	$K_m = f^2 S$	$\frac{1}{l} = \frac{1}{kz} + \frac{1}{\lambda} + \frac{\beta}{kL}$	$Ri \geq 1$	$\beta = 4.7$
			$\partial\theta/\partial z \geq 0$	$\lambda = 4.0 \times 10^{-4} (G/f)$
Bedin [1976]	$K_m = f^2 S$	$\frac{1}{l} = \frac{1}{L_m} - \left[ \frac{1}{h} \left( \frac{1 + 1.32zh}{0.601 + (kzh)} \right) \cdot \left( \frac{1}{1 - 50L_p h} \right) \right]$	$\partial\theta/\partial z < 0$	$L_m$ is surface $M-O$ length
				$L_p = \frac{1}{kz} + \frac{1}{0.2h}$ ; stable
				$h = 0.1u_* f$
				$\phi_m = (1 - 16z/L)^{-1/4}$
Cunha and Foster [1986]	$K_m = f^2 S$	$l = \frac{kL + z_0 \phi_m}{1 + [k(z - z_0) \phi_m]}$	$z > z_S$	$\lambda = 100$ m
			$z \geq z_S$	
			$L \leq 0$	
			$z \leq z_S$	
Tag and Payne [1987]	$K_m = f^2 \left[ \frac{(DEF)^2}{2} - \frac{g}{u_*} \frac{K_m}{K_m} \frac{\partial\theta}{\partial z} \right]^{1/2}$	$l = \frac{k}{\phi_m} \left[ (z_S + z) \left( \frac{h - z}{h - z_S} \right) \right]$	$z_S < z \leq h$	$DEF = \left[ 2 \left( \frac{\partial u}{\partial z} \right)^2 + 2 \left( \frac{u_*}{\partial z} \right)^2 + 4 \left( \frac{\partial u}{\partial z} \right)^2 \right]$
				$z_S = 0.062 u_* f$
				$h = 16.0 z_S$

$$S^2 = \{(\partial\theta/\partial z)^2 + (\partial\theta/\partial z)^2\}.$$

## TURBULENT KINETIC ENERGY (TKE) CLOSURE

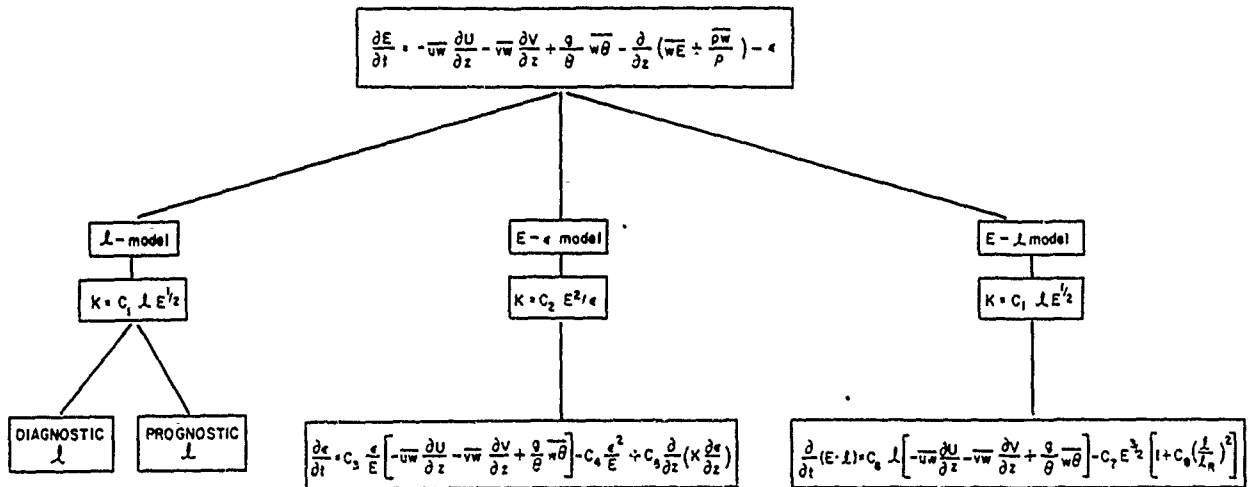


Fig. 1. Model parameterizations based on turbulent kinetic energy closure.

The first TKE parameterization considered is the "l model," in which mixing length  $l$  is modeled either diagnostically or prognostically. The second is the "E- $\epsilon$  model," in which a prognostic equation for  $\epsilon$  is developed. The final approach considered is the "E-l model," in which a prognostic equation for the product  $E \cdot l$  is used. This scheme is often referred to as  $q^2$ -l closure (or a level 2.5 model), where  $(q^2/2)$  is the TKE [Mellor and Yamada, 1974] (see Figure 1).

2.2.1. *The l model.* The basis of the l model is derived from the Prandtl-Kolmogorov hypothesis [see Monin and Yaglom, 1971] relating eddy viscosity to turbulent kinetic energy:

$$K_m = C_l E^{1/2} \quad (11)$$

Constant  $C_l$  is taken as 0.4. With turbulent energy  $E$  evaluated by a prognostic equation (7), the determination of  $K$  is again, as in the mixing length approach, determined by  $l$ . Research in l models has been divided into prognostic versus diagnostic determination of the mixing length.

2.2.1.1. *Diagnostic determination of l:* A diagnostic determination of  $l$  by simple means was given in section 2.1.2 for mixing length parameterization schemes such as Blackadar's [1962] (Table 2). However, recent work has sought to develop diagnostic relationships for  $l$  to be utilized in TKE closure schemes which incorporate more of the complexities of atmospheric flow. Duynkerke and Driedonks [1987] distinguish three different length scales and use an interpolation between the three as the diagnostic length scale. In the surface layer the length scale  $l_B$  is obtained from the modified Blackadar formulation (6) proposed by Djolov [1973]. The limiting value  $\lambda$  in that formulation is the second length scale. It is used in scaling the bulk of the boundary layer [Mellor and Yamada, 1974]:

$$\lambda = C_\lambda \frac{\int_0^h E^{1/2} dz}{\int_0^h E^{3/2} dz} \quad C_\lambda = 0.25 \quad (12)$$

The third length scale ( $l_s$ ) is that for the stable layer, where

$$l_s = C_s E^{1/2} / N_m \quad (13)$$

and  $C_s = 0.36$  and  $N_m$  is the Brunt-Väisälä frequency. The mixing length ultimately used by Duynkerke and Driedonks [1987] is given as

$$l = \text{Min}(l_B, l_s) \quad (14)$$

Beljaars *et al.* [1987] used a simple mixing length closure in a spectral finite difference model to simulate neutral surface layer flow over complex terrain. They prescribed  $l$  in their TKE closure scheme as

$$l = \lambda(z + z_0) \quad (15)$$

where  $z_0$  is the roughness length for undisturbed flow. They concluded that such a simple mixing length parameterization was not valid in attempting to simulate turbulent flow under inhomogeneous conditions. Therry and Lacarrere [1983] prescribed an expression for  $l$  in terms of altitude and stratification based on the third-order closure scheme of Andre *et al.* [1978] as well as experimental data in convective conditions.

$$\frac{1}{l} = \frac{1}{kz} + \frac{\text{CLK1}}{h} - \left( \frac{1}{kz} + \frac{\text{CLK2}}{h} \right) m_1 m_2 + \frac{\text{CLK5}}{l_s} \quad (16)$$

where CLK1, CLK2, and CLK5 are constants and  $l_s$  is the mixing length for stable conditions (see Table 3). Russell and Takle [1985] used a modification of Therry and Lacarrere's [1983] formulation for  $l$  in the evolution of the stable boundary layer:

$$\frac{1}{l} = \frac{1}{kz} + \frac{1}{l_s} + \frac{1}{\lambda(1 - z/h)} \quad (17)$$

The parameterization of energy dissipation  $\epsilon$  in the TKE budget plays an important role in the determination of mixing length. If one chooses to use a diagnostic determination of  $l$  as illustrated here (Table 3), then  $\epsilon$  in the TKE budget (7) is an unknown and must be modeled. The problem is circumvented by using the generally accepted relationship of Kolmogorov [1942]:

$$\epsilon = C_\epsilon E^{3/2} / l_s \quad (18)$$

TABLE 3. The  $I$  Model

Author	$I$	Range of Validity	Constants
Dwyer and Prichard [1987]	$I = \min(L, l_0)$ $L = C_p E^{1/3} N_m$ $l_0 = k_z (\phi_m + k_z \lambda)$ $\lambda = C_p \left[ \int_0^h E^{1/3} dz \int_0^h E^{1/3} dz \right]$	Diagnostic Determination of $I$ $\partial I / \partial z > 0$ $\partial I / \partial z \leq 0$	$C_p = 0.36$ $C_p = 0.25$ $N_m^2 = g \left[ \frac{C_p \partial \theta_p}{\partial p \partial z} - C_p \frac{\partial \theta_p}{\partial z} \right]$ $C_p = 1$ unsaturated $C_p = (1 + l_0 q_{\text{sat}}) / (1 + q_{\text{sat}} l_0^2) (C_p R_p T^2)$ saturated $C_p = (l_0 q_{\text{sat}} T) / (1 - q_{\text{sat}})$ unsaturated $C_p = 1$ saturated $k = 0.4$
Bedaux et al. [1987]	$I = k(z + r_0)$	neutral surface layer	$m_1 = (1 + \text{CLK3 } h / k_z)$ $m_2 = [1 - \text{CLK4}(L, h)]^{1/2}$ $m_2 \leq 0$ $L \geq 0$
Therry and Lacarrere [1983]	$\frac{1}{L} = \frac{1}{k_z} + \frac{1}{h} \left( \frac{\text{CLK1}}{k_z} - \left( \frac{1}{k_z} + \frac{\text{CLK2}}{h} \right) m_1 m_2 + \frac{\text{CLK5}}{L} \right)$ $\frac{1}{L} = \left( \frac{g}{\theta} \frac{\partial \theta}{\partial z} / E \right)^{1/2}$	unstable stable	$\text{CLK1} = 15$ ; $\text{CLK2} = 11$ ; $\text{CLK3} = 2.5 \times 10^{-3}$ $\text{CLK4} = 1$ ; $\text{CLK5} = 3$
Russell and Tiele [1985]	$\frac{1}{L} = \frac{1}{k_z} + \frac{1}{L_c} + \frac{1}{\lambda(1 - z/h)}$ $L_c = k_L \beta$	$\partial I / \partial z > 0$	$\lambda = \frac{C_p}{h} \int_0^h (q_r f)^{1/2} dz$ ; $q = (2E)^{1/2}$ $C_p = 0.0593$ $k = 0.4$ $\beta = 4.7$ see Table 2
Bodin [1979]	$\frac{1}{L} = \frac{1}{k_z} + \frac{1}{0.2h} - \frac{1}{h} \left[ \frac{(1 + 1.32z/h)}{0.001 + k_z/h} \right] \left( \frac{1}{1 - 50L/h} \right)$	all $Ri$	
Yu [1976]	$L = k_z (\phi_m + k_z \lambda)$	all $Ri$	$\lambda = 25m$ $k_z \frac{\partial u}{\partial z} = \frac{u}{h} \frac{\partial u}{\partial z}$
Therry and Lacarrere [1983]	$\frac{1}{L} = \frac{1}{k_z} + \frac{\text{CLE1}}{h} - \left( \frac{1}{k_z} + \frac{\text{CLE2}}{h} \right) m_1 m_2 + \frac{\text{CLE5}}{L}$ $0/L_c = 0$ $L_c = \left( \frac{g}{\theta} \frac{\partial \theta}{\partial z} / E \right)^{1/2}$	unstable stable	$m_1 = (1 + \text{CLE3 } h / k_z)$ $m_2 = [1 - \text{CLE4}(L, h)]^{1/2}$ $m_2 \leq 0$ $L \geq 0$ $\text{CLE1} = 15$ ; $\text{CLE2} = 5$ ; $\text{CLE3} = 5 \times 10^{-3}$ $\text{CLE4} = 1$ ; $\text{CLE5} = 1.5$

Prognostic Determination of  $l$  $h'$  is the height at which  $l$  equals  $l_b$ 

$$u_*^2 = l^2 \left[ \left( \frac{\partial U}{\partial z} \right)^2 + \left( \frac{\partial V}{\partial z} \right)^2 \right]$$

$$w_* = \left( \frac{\xi}{\theta} \frac{w \partial \theta}{\partial z} \right)^{1/2}$$

$$\xi = \min(z/h, 1)$$

$$z \leq h'$$

$$z > h'$$

$$\partial \theta / \partial z > 0$$

$$\partial \theta / \partial z < 0$$

Busch *et al.*  
[1976]

$$\frac{\partial l}{\partial t} = \frac{l_* - l}{l(u_*^2 + w_*^2)^{1/2}}$$

$$l_* = (kz \phi_m)(1 - z/h)$$

Mailhot and Benoit  
[1982]

$$\frac{\partial l}{\partial t} = \frac{l_* - l}{l(u_*^2 + w_*^2)^{1/2}}$$

$$l_* = h(0.35\xi + 2.5\xi)$$

$$l_* = h(0.35\xi + 5.1\xi^2 - 5.35\xi^3)$$

where  $l_e$  is termed the dissipation mixing length. Therefore if one chooses to use a prognostic equation for mixing length,  $z$  is no longer an unknown and need not be modeled.

Implementing (18) into the TKE budget raises an interesting question. Examination of (11) and (18) indicates separate length scales for eddy mixing and dissipation. There has been much discussion concerning the relationship between these mixing lengths [see *Therry and Lacarrere*, 1983; *Detering and Elling*, 1985]. Which length scale should be used, and what is the relationship between the two? The common assumption is that the length scales  $l$  and  $l_e$  are equal. *Therry and Lacarrere* [1983] examined several formulations of  $l_e$  and compared them to experimental observations from the Air Mass Transformation Experiment (AMTEX) as well as model and laboratory simulations. They considered the well-known formulation of *Blackadar* [1962] as well as formulations by *Yu* [1976] and *Bodin* [1979] and concluded that none of the formulations account for the wide range of stability encountered in the atmosphere. Instead they proposed an expression for  $l_e$  which agreed better with experimental results:

$$\frac{1}{l_e} = \frac{1}{kz} + \frac{\text{CLE1}}{h} - \left( \frac{1}{kz} + \frac{\text{CLE2}}{h} \right) m_1' m_2' + \frac{\text{CLE5}}{l_s} \quad (19)$$

where CLE1, CLE2, and CLE5 are constants and  $l_s$  is the mixing length for stable conditions. We include in Table 3 formulations for both  $l$  and  $l_e$ . Using a simplified rate equation for  $w^2$  to obtain an explicit relationship for  $w^2/E$ , *Therry and Lacarrere* [1983] derived a relationship between  $l$  and  $l_e$ :

$$l = \left( 1 + \frac{g}{\Theta} \frac{l_e}{C_e E^{3/2}} \right) l_e \quad (20)$$

Thus, for convective conditions,  $l$  is larger than  $l_e$  [*Therry and Lacarrere*, 1983].

The range of application using a diagnostic determination of  $l$  emphasizes the importance of properly specifying mixing length. However, it is easy to see that many of these parameterizations are dependent on atmospheric stability conditions and are not applicable for a wide variety of cases. This, of course, is a drawback in the formulation of a diagnostic relationship.

**2.2.1.2. Prognostic determination of  $l$ :** An alternative approach in the  $l$  model to determining mixing length by diagnostic formulation is to allow  $l$  to be time dependent. Such a prognostic equation of mixing length was first formulated by *Shir* [1973] and *Lewellen and Teske* [1973] for second-order modeling. *Busch et al.* [1976] extended the prognostic concept to a simple PBL model. Similarity theory is used in the surface layer, but above the surface layer, *Busch et al.* [1976] reasoned that the evolution of mixing length should depend on two parameters: (1) the strength of boundary layer mixing (characterized by friction velocity  $u_*$  and convective velocity  $w_*$ ) and (2) the difference between actual mixing length  $l$  and the value of the mixing length for boundary conditions kept constant at any given time ( $l_*$ ):

$$\frac{\partial l}{\partial t} = \frac{(l_* - l)}{[l/(u_*^2 + w_*^2)^{1/2}]} \quad (21)$$

where

$$\begin{aligned} l_* &= (kz/\phi_m)(1 - z/h) & z \leq h' \\ l_* &= l_s & z > h' \end{aligned} \quad (22)$$

TABLE 4. The  $E$ - $\epsilon$  Model

Author	Constants			
	$C_2$	$C_3$	$C_4$	$C_5$
Duynkerke and Driedonks [1987]	0.09	1.44	1.92	0.77
Beljaars et al. [1987]	0.032	1.44	1.92	0.54
Stubley and Rooney [1986]	0.09	1.44	1.92	0.77
Detering and Etling [1985]	0.026	1.13	1.90	0.77
Modified Detering and Etling [1985]	0.026		1.90	0.77
Marchuk et al. [1977]	0.08	1.38	1.40	1.0

For the modified Detering and Etling [1985] model  $C_3$  is 1.13/ $h$ .

and  $h'$  is the height at which  $l_z$  equals the residual mixing length  $l_b$  ( $h'$  is taken as roughly  $h$ ).

Mailhot and Benoit [1982] used the Busch et al. [1976] parameterization in a 1-D finite element model but determined  $l_z$  from Blackadar [1962] and J. W. Deardorff (unpublished manuscript, 1977) formulae for stable and unstable boundary layers, respectively:

$$l_z = h[0.35\zeta/(1 + 2.5\zeta)] \quad \text{stable} \quad (23)$$

$$l_z = h(0.35\zeta + 5.1\zeta^2 - 5.35\zeta^3) \quad \text{unstable}$$

where  $\zeta = \min(z/h, 1)$ .

There exist relatively few prognostic relationships for mixing length used in TKE closure schemes because the prognostic equation for  $l$  is better expressed as a prognostic equation for energy dissipation  $\epsilon$ . An equation for  $\epsilon$  is more common because the concept of energy dissipation is easier to grasp than that of a mixing length. In addition, using the dissipation equation as an additional prognostic equation eliminates the need for parameterizing  $\epsilon$  in the TKE budget. This type of formulation is referred to as an  $E$ - $\epsilon$  model and will be considered next.

**2.2.2.  $E$ - $\epsilon$  model.** The concept of using a prognostic equation for energy dissipation  $\epsilon$  instead of a length scale formulation in the turbulent kinetic energy budget was first proposed among others by Harlow and Nakayama [1967], Daly and Harlow [1970], and Hanjalic and Launder [1972] for fluid engineering applications. The relationship for eddy viscosity in terms of  $\epsilon$  can be derived easily from (11) and (18):

$$K_m = C_2 E^2 / \epsilon \quad (24)$$

Therefore calculating  $\epsilon$  by means of a prognostic equation is analogous to using a prognostic equation for  $l$ . The derivation of the dissipation equation from the equation of motion is quite involved and will not be considered here (see Lumley [1980], Marchuk et al. [1977], or Wyngaard [1975]). Several approximations and parameterizations must be made to obtain the resulting popular form of the simplified equation used in the  $E$ - $\epsilon$  model:

$$\frac{\partial \epsilon}{\partial t} = C_3 \frac{\epsilon}{E} \left[ -\overline{uw} \frac{\partial U}{\partial z} - \overline{vw} \frac{\partial V}{\partial z} + \frac{g}{\Theta} \overline{w\theta} \right] - C_4 \frac{\epsilon^2}{E} + C_5 \frac{\partial}{\partial z} \left( K_m \frac{\partial \epsilon}{\partial z} \right) \quad (25)$$

where the first term on the r.h.s. represents the generation of  $\epsilon$ . For modeling purposes the bracketed portion of this generation term is taken in the  $E$ - $\epsilon$  model as the maximum of shear production versus shear and buoyancy production, i.e., max

(shear, shear + buoyancy) [Duynkerke and Driedonks, 1987]. The second term on the r.h.s. represents destruction of  $\epsilon$ , and the third term represents the turbulent transport. The constant  $C_3$  is somewhat like an inverse Prandtl number and links eddy viscosity for dissipation to that of momentum, i.e.,  $K_t = C_3 K_m$ .

Several researchers have used the  $E$ - $\epsilon$  model to describe a variety of atmospheric conditions. There is general agreement on the simplified equation (25) used in the  $E$ - $\epsilon$  model but some differences in the constants (as discussed by Rodi [1980]). This could be expected because it is through these constants that each modeler strives to "fine tune" his results to those of experimental observations or other model results. Most  $E$ - $\epsilon$  models have been used with a standard set of constants derived from engineering applications (see, for example, Launder and Spalding [1974]):

$$C_3 = 1.44 \quad C_4 = 1.92 \quad C_5 = 0.77 \quad (26)$$

Duynkerke and Driedonks [1987], Beljaars et al. [1987], and Stubley and Rooney [1986] all used the above constants in  $E$ - $\epsilon$  models for boundary layer flow over various terrains and under a variety of stability conditions. The only exception was Beljaars et al. [1987], who modified  $C_3$  to 0.54. Marchuk et al. [1977] modified the standard  $E$ - $\epsilon$  model slightly for the simulation of the oceanic mixed layer and used constants  $C_3 = 1.38$ ,  $C_4 = 1.40$ , and  $C_5 = 1.0$ . Table 4 gives a summary of the various constants used in the  $E$ - $\epsilon$  models.

A different approach to the determination of constants in the  $E$ - $\epsilon$  model was made by Detering and Etling [1985]. They considered the  $E$ - $\epsilon$  model and its application to neutrally stratified flows in idealized nonrotating boundary layers as opposed to atmospheric boundary layers. Their aim was to develop an  $E$ - $\epsilon$  model suitable for atmospheric applications which compared well with atmospheric data. They reasoned that the constants derived from engineering applications for flows in nonrotating boundary layers (equation (26)) were not representative of atmospheric flow in which processes throughout the depth of the boundary layer have an effect on turbulent structure. They applied the standard  $E$ - $\epsilon$  model to the atmospheric boundary layer for comparison with observations and a simple mixing length model. Their conclusion from thin shear laboratory flows was that the model with the standard set of constants (26) produced much larger values of  $u_*$  and  $K$  compared to observations. Lee and Kao [1979] in a finite element model of the neutral PBL and Mason and Sykes [1980] in a 2-D model simulating vortex roll development also presented similar discrepancies between modeled values of  $u_*$  and  $K$  and observations. Detering and Etling [1985] explained that the difference in values could be the result of the differences in the underlying assumptions and principles upon which the constants in the closure scheme are determined. So instead of the values given in (26), Detering and Etling [1985] proposed values for the constants, specifically  $C_3$ , which adjust the  $E$ - $\epsilon$  model to better simulate the observed structure of the atmospheric boundary layer. Constants  $C_4$  and  $C_5$ , equal to 1.90 and 0.77, respectively, are roughly those determined from engineering flows. However, Detering and Etling [1985] provide a correction for  $C_3$ . It is based on the assumption that  $C_3$  should depend on characteristic length scales of turbulent flow considered. The modification for  $C_3$  is then

$$C_3' = C_3 / h \quad (27)$$

where  $l$  is given by (18) and  $h$  is the depth of the boundary layer. This modification is not based on stringent arguments but is proposed simply because it models the observed structure of the boundary layer.

2.2.3. *The E-l model.* A scheme similar to that for the E- $\epsilon$  model is a scheme in which a prognostic equation for the product  $E \cdot l$  is used in conjunction with the prognostic equation for turbulent kinetic energy (7). Termed the E-l (or  $q^2$ -l) model, it was proposed by Mellor and Yamada [1974] as a "model of compromise" between their level 2 and 3 models (hence level 2.5 model). The advantage of the E-l model is that it retains most of the features of a full second-order closure model without the associated complexity. All second-moment equations besides the two prognostic ones are reduced to algebraic equations. It is similar to an E- $\epsilon$  model in that a prognostic equation for  $l$  (or  $\epsilon$ ) is used, but it involves much more of the structure of a second-order model. In this section we consider together the models termed E-l ( $q^2$ -l) and level 2.5. E-l models are actually level 2.5 models in which a simplified expression for  $K$  has been used [see Yamada, 1983]. However, the same prognostic equations are used in both models, and hence they are considered together.

Expressions for turbulent fluxes in the E-l model are obtained from simplifications of the level 2.5 model:

$$\begin{aligned} -(\overline{uw}, \overline{vw}) &= S_m K_m (\partial U / \partial z, \partial V / \partial z) \\ -(\overline{w\theta}, \overline{wq}) &= \alpha S_m K_m (\partial \Theta / \partial z, \partial Q / \partial z) \end{aligned} \quad (28)$$

The exchange coefficient  $K_m$  is given by (11), and  $S_m$  and  $\alpha$  ( $= K_h / K_m$ ) are functions of the flux Richardson number  $Ri_f$  [Yamada, 1975, 1983] as below:

$$S_m = \frac{1.5}{1 + 0.2231 - Ri_f} \quad \begin{aligned} & - Ri_f(0.2341 - Ri_f) \\ & / (1 + 0.2231 - Ri_f) \end{aligned} \quad Ri_f < 0.16 \quad (29)$$

$$S_m = 0.085 \quad Ri_f \geq 0.16$$

$$\alpha = 1.318(0.2231 - Ri_f) / (0.2341 - Ri_f) \quad Ri_f < 0.16 \quad (30)$$

$$\alpha = 1.12 \quad Ri_f \geq 0.16$$

The prognostic equation for the length scale in the E-l model as given by Yamada and Kao [1986] for horizontally homogeneous flow is

$$\begin{aligned} \frac{\partial(E \cdot l)}{\partial t} &= C_6 l \left[ -\overline{uw} \frac{\partial U}{\partial z} - \overline{vw} \frac{\partial V}{\partial z} + \frac{g}{\Theta} \overline{w\theta} \right] \\ & - C_7 E^{3/2} [1 + C_8 (l/l_R)^2] \end{aligned} \quad (31)$$

where  $l_R$  is a measure of the distance away from the wall [Mellor and Yamada, 1982] and is modified to include stability effects [Yamada and Kao, 1986]:

$$\begin{aligned} l_R &= kz - \mu h [Ri_f / (1 - Ri_f)] \quad Ri_f < 0 \\ l_R &= kz \quad Ri_f \geq 0 \end{aligned} \quad (32)$$

with constant  $\mu$  equal to 0.2. Constants  $C_6$ ,  $C_7$ , and  $C_8$  in (31) are empirically determined from neutrally stratified laboratory experimental data that include channel, pipe, boundary-layer, and homogeneous shear flows [Mellor and Yamada, 1982]:

$$C_6 = 1.8 \quad C_7 = 0.06 \quad C_8 = 1.33 \quad (33)$$

The E-l model generally works well in simulating a wide range of geophysical problems, as shown by Mellor and Yamada [1982]. However, Yamada [1983] emphasized that based on how the constants (33) are determined, the E-l model

might not be as ad hoc as it seems. He considered the complicated closure assumptions originally developed for an E-l equation [Rotta, 1951] along with the determination of constants to be major shortcomings in the E-l model. Comparison with turbulence data and other prognostic length scale equations will be helpful in determining the usefulness and efficiency of the E-l model.

### 3. COMPARISON OF CLOSURE SCHEMES

In this study, 11 parameterization schemes, chosen as representative of both first-order and TKE closure schemes (given in Tables 1-4), are used for comparison in a one-dimensional model. First-order closure schemes are divided into (1)  $K$  profile (O'Brien's [1970] formulation) and (2) mixing length (Blackadar [1962], Djolov [1973], and modified Djolov [1973]) schemes. TKE closure schemes are divided into (1)  $l$  model (Therry and Lacarrere [1983] formulation for  $l$  and  $l_e$ , Bodin [1979], and Duynkerke and Driedonks [1987]) and (2) E- $\epsilon$  model (constants given in Table 4). The E-l model is not considered for the sake of brevity. For each closure scheme, only the formulation of the eddy viscosity coefficient  $K_m$  and associated constants are varied.

#### 3.1. One-Dimensional Model

As a means of testing the first-order and TKE closure schemes, numerical simulations of the boundary layer were made using a one-dimensional time-dependent barotropic PBL model originally developed at the Naval Research Laboratory and modified at North Carolina State University to include TKE parameterization schemes. The model consists of prognostic equations given in (3) for  $U$ ,  $V$ ,  $\Theta$ , and  $Q$ . There are 30 levels in the vertical (to a height of approximately 3 km) with logarithmic resolution. The numerical scheme is a simple centered-difference in space and forward in time. Fluxes, eddy viscosities, mixing length, and vertical gradients are evaluated at levels midway between the levels at which  $U$ ,  $V$ ,  $\Theta$ , and  $Q$  are computed.

Surface layer profiles are assumed valid to the lowest computational level (approximately 45 m) where surface layer similarity is used. Above the surface layer, mixed layer theory based on either first-order or TKE closure is used with eddy coefficient  $K_m$  determined by the appropriate relationships given in section 2. Eddy viscosity for heat  $K_h$  is a function of  $K_m$  and  $z/L$  as given by Businger et al. [1971]. The dependence on  $L$  is a shortcoming of the model because  $L$  is a surface variable. For model calculations, PBL height  $h$  was given as the lowest level at which local Richardson number exceeded 1.

Lower boundary conditions for  $E$  and  $\epsilon$  necessary for TKE closure are given as [Mailhot and Benoit, 1982]

$$E = 3.75 u_*^2 \quad z/L > 0 \quad (34)$$

$$E = 3.75 u_*^2 + 0.2 w_*^2 + (-z/L)^{2/3} u_*^2 \quad z/L < 0$$

$$\epsilon = u_*^3 / kz \quad (35)$$

where  $u_*$  is friction velocity and  $w_*$  is convective velocity given as

$$u_* = [(\overline{uw})_0^2 + (\overline{vw})_0^2]^{1/4} \quad (36)$$

$$w_* = [(g/T)h(\overline{wT})_0]^{1/3} \quad (37)$$

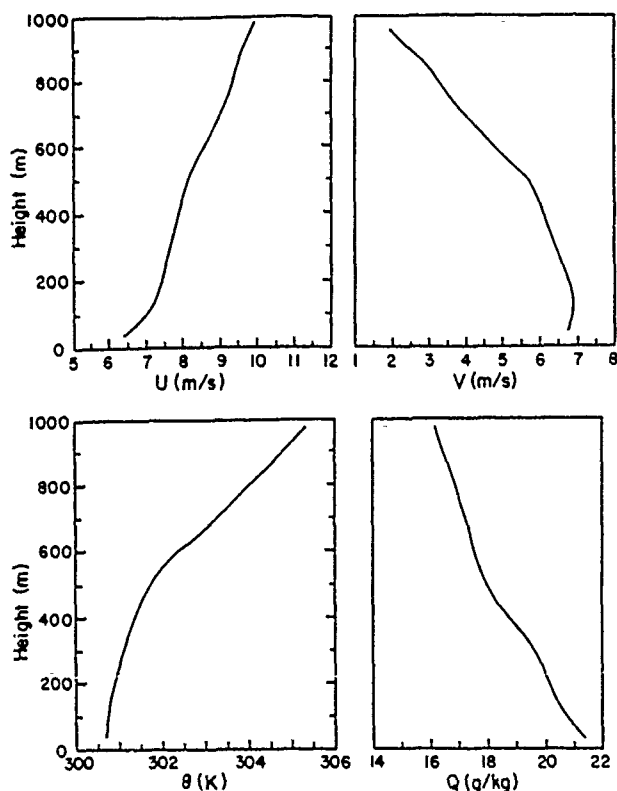


Fig. 2. Profiles used for initialization of the one-dimensional model obtained from MONEX79 radiosonde data.

where subscript zero denotes near-surface values.  $T_v$  is virtual temperature,  $g$  is gravitational acceleration, and virtual temperature flux  $wT_v$  is calculated as

$$\overline{wT_v} = \overline{wT} + 0.61 \overline{T} \overline{wq} \quad (38)$$

Upper boundary conditions require  $E = \epsilon = 0$ .

### 3.2. Data

Data from the Monsoon Experiment were used in the one-dimensional model simulations. Data were collected from aircraft (mean and turbulence), ship, satellite, and towers in the Bay of Bengal and Arabian Sea regions during MONEX79. Because of limited aircraft data, only one observation day, July 14, 1979, over the Bay of Bengal was chosen here for model simulations. The 1-D model discussed in section 3.1 was initialized at 0000 UT using the mean profiles of  $U$ ,  $V$ ,  $\Theta$ , and  $Q$  (Figure 2) obtained from a Soviet ship located in the Bay of Bengal ( $18.0^\circ\text{N}$ ,  $89.5^\circ\text{E}$ ) and was integrated for a 12-hour period. Unfortunately, monsoon conditions in the Bay of Bengal region during this time period were both nonstationary and inhomogeneous. The monsoon trough had begun to shift northward to the foothills of the Himalayas signaling the beginning of break monsoon conditions. Associated with this shift was a recession of the boundary layer jet and a substantial decrease in wind speed from a maximum of 18 m/s at a height of 1 km at 0600 UT July 13 to 8 m/s at 0000 UT July 14 [Holt and Raman, 1987].

To account for the highly variable conditions present on July 14, averaged ship and aircraft data were used to obtain vertical profiles of mean variables  $U$ ,  $V$ ,  $\Theta$ , and  $Q$  used in model verification. The 0600 UT soundings from the polygon of stationary Soviet ships centered near  $16.2^\circ\text{N}$ ,  $89.4^\circ\text{E}$  along

with the 0400 UT low-level mean aircraft data ( $19.9^\circ\text{N}$ ,  $88.9^\circ\text{E}$ ) from the NCAR Electra were averaged to obtain mean profiles up to a height of about 1 km. Verification of flux profiles is from Electra turbulence data only. The Electra research flight of July 14 consisted of a vertical "stack" used to study the vertical structure of the monsoon boundary layer.

Sea surface temperature in the region of observations (obtained from ship data) was taken to be a constant  $29^\circ\text{C}$  ( $\Theta = 301.7\text{ K}$ ) for all model simulations. Geostrophic wind obtained from pressure fields was approximately 16.8 m/s at  $233^\circ$ . The geostrophic wind is an important input parameter in the 1-D model but one which is often difficult to determine accurately. Thus sensitivity of the model to changes in the magnitude of the geostrophic wind is also important and will be considered following the discussion of results.

This monsoon data set was chosen for use in the numerical simulations for two basic reasons: (1) both mean and turbulence structure were readily available and (2) the lack of strong baroclinicity in the boundary layer should make straightforward comparison of different PBL parameterizations to observational data easier to understand. However, the assumption of barotropic conditions in the 1-D model is not entirely representative of the conditions on July 14 as weak horizontal temperature gradients could have existed. Thus, ideally, no closure scheme used in this barotropic 1-D model can be expected to exactly predict the observed structure that would depend on baroclinic effects such as a low-level jet. And as mentioned, the nonstationary monsoon boundary layer also poses problems in determining a representative vertical profile of the region.

For more detailed information on the structure of the boundary layer on this day or the MONEX79 data set, see Holt and Raman [1986].

### 3.3. Model Results for Different PBL Parameterizations

3.3.1. *Mean profiles.* There are a variety of ways to systematically and quantitatively measure the accuracy or skill of a model, including root-mean-square (rms) errors, correlation coefficients, bias or threat scores, etc. However, differing conclusions can be drawn depending on the statistical method chosen. As a means of quantifying the comparison of model simulations to observational data, rms errors have been computed from mean profiles for each of the 11 PBL parameterizations (Table 5). Calculations of deviations are made at nine levels:

$$\text{rms} = [\sum (O_n - P_n)^2 / (n - 1)]^{1/2} \quad (39)$$

where  $O_n$  is observations at level  $n$  and  $P_n$  is predicted model value at level  $n$ , where  $n = 0.1, 0.2, \dots, 0.9$  km. The rms errors provide an overview of the absolute accuracy of a data set. However, they are poor indicators of how well a model predicts the overall structure of a variable [Anthes, 1986]. For example, Figures 3 and 4 show the east-west ( $U$ ) and north-south ( $V$ ) wind components for MONEX79 observations and model simulations. Model results are divided according to parameterization schemes given earlier. The first-order schemes of Blackadar [1962] and Djolov [1973] show no jet structure in either the  $U$  or the  $V$  profiles but generally give the smallest rms errors. This is simply because they approximate a mean fit to the data. The preferable first-order schemes are the modified Djolov [1973] or O'Brien [1970] schemes in



TABLE 5. Root-Mean-Square Errors

	U, m/s	V, m/s	$\Theta$ , K	Q, g/kg
<i>First-Order Model</i>				
Blackadar [1962]	0.99	0.78	1.35	0.99
Djorlov [1973]	0.90	0.80	1.42	1.05
Modified Djorlov [1973]	0.66	1.39	0.33	1.45
O'Brien [1970]	0.55	1.51	0.34	1.64
<i>l Model</i>				
Bodin [1979]	0.94	1.22	0.28	2.25
Therry and Lacarrere [1983]	0.98	1.26	0.29	1.97
Duynkerke and Driedonks [1987]	0.72	1.38	0.24	1.53
<i>E-ε Model</i>				
Beljaars et al. [1987]	1.21	0.99	0.29	2.90
Duynkerke and Driedonks [1987]	1.24	1.05	0.29	2.90
Detering and Etling [1985]	1.15	1.03	0.29	2.74
Modified Detering and Etling [1985]	1.26	1.00	0.26	2.78

which a jet structure is predicted (although largely overestimated in the  $V$  profile).

Among TKE closure models (i.e.,  $E-\epsilon$  and  $l$  models) there is only slight variation from one parameterization to another. For example, all  $E-\epsilon$  and  $l$  model parameterizations overpredict the height of the jet in the  $U$  profile. Model results indicate a weak jet of 6.0–6.5 m/s at roughly 600–700 m. Observed jet height is approximately 400–450 m. Model results show a well-mixed profile from the surface up to approximately 500 m.

TKE closure schemes perform better in simulating the observed  $V$  profile, in which the jet is much less pronounced (Figure 4). Both  $E-\epsilon$  and  $l$  model results are similar, showing little variation among schemes. Each parameterization overpredicts  $V$  by roughly 1.0–1.2 m/s up to the height of the jet maximum. However, the observed  $V$  structure and the height of the jet maximum are simulated well.

Figure 5 shows observations and model simulations of potential temperature  $\Theta$ .  $E-\epsilon$  and  $l$  model parameterizations predict well the potential temperature structure, although slightly underpredicting mixed layer values by roughly 0.3–0.4 K. Observations from MONEX79 data indicate a PBL height  $h$  of approximately 400 m [Holt and Raman, 1986]. However, the vertical resolution of observed  $\Theta$  near the inversion is not as good as near the surface, and thus it is difficult to state definitively that the models overpredict PBL height. All  $E-\epsilon$  parameterizations predict  $h$  equal to approximately 600 m. Parameterizations with the  $l$  model vary in estimating  $h$ . Therry and Lacarrere's [1983] parameterization involving mixing lengths  $l$  and  $l_e$  gives  $h$  equal to 500 m. Schemes of Bodin [1979] and Duynkerke and Driedonks [1987] predict mixed layer depths of 550 and 590 m, respectively. Table 6 gives values of  $h$  for each parameterization as well as other parameters derived from surface variables.

In contrast to the TKE schemes, first-order closure schemes do not model the observed  $\Theta$  structure as well. This is a major shortcoming of the first-order schemes. The Blackadar [1962] and Djorlov [1973] parameterizations show no temperature inversion but rather a much warmer and more stable boundary layer. This is because their parameterizations do not consider the effect of the inversion, such as the reduced turbulent mixing above the boundary layer. The O'Brien [1970] and the modified Djorlov [1973] parameterizations indicate a cooler

and slightly unstable boundary layer. The modeled depth of the boundary layer, as inferred from the potential temperature structure, and the modeled height of maximum winds show a relationship similar to observations. The low-level jet observed during MONEX79 was typically situated at or slightly above the top of the boundary layer. Profiles of resultant wind speed ( $U^2 + V^2$ )<sup>1/2</sup> (not shown here) calculated with both first-order and TKE closure show wind speed maxima located within the transition region between the boundary layer top and the capping stable layer. Strong boundary layer mixing as evident in

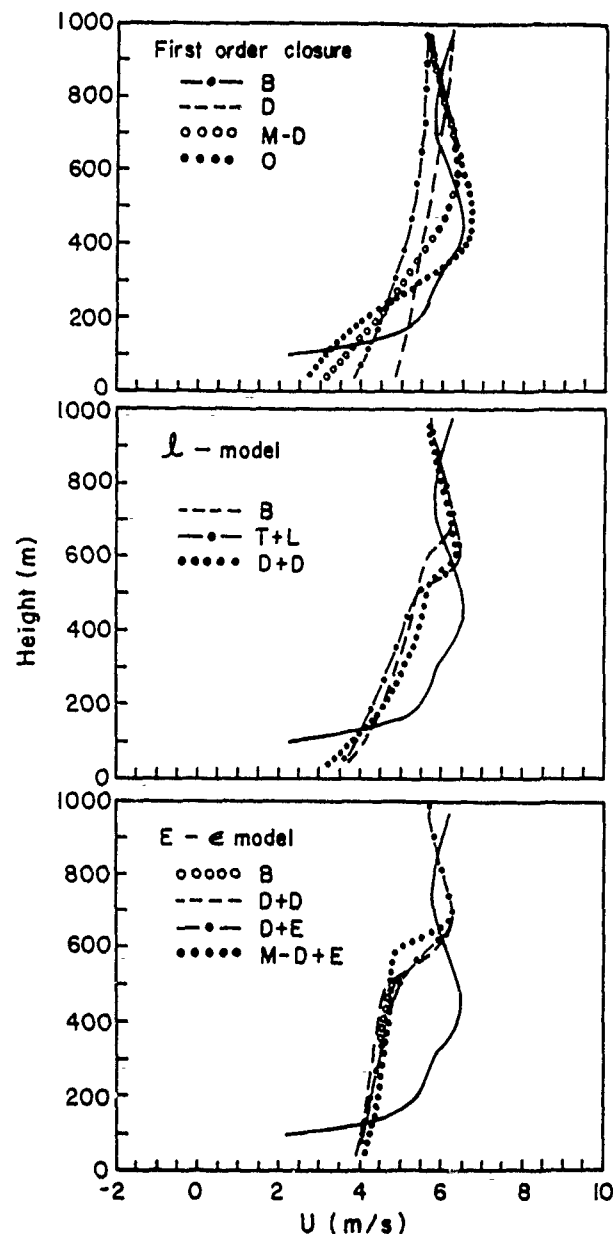


Fig. 3. Vertical profiles of mean east-west wind component  $U$  at roughly 0400 UT on July 14, 1979. Solid curves indicate observations obtained from averaged ship and aircraft data. Model simulations are divided according to (a) first order closure: Djorlov [1973] (D); Blackadar [1962] (B); O'Brien [1970] (O); modified Djorlov [1973] (M-D), (b)  $l$  model: Bodin [1979] (B); Therry and Lacarrere [1983] (T+L); Duynkerke and Driedonks [1987] (D+D) and (c)  $E-\epsilon$  model: Duynkerke and Driedonks [1987] (D+D); Detering and Etling [1985] (D+E); Beljaars et al. [1987] (B); modified Detering and Etling [1985] (M-D+E).

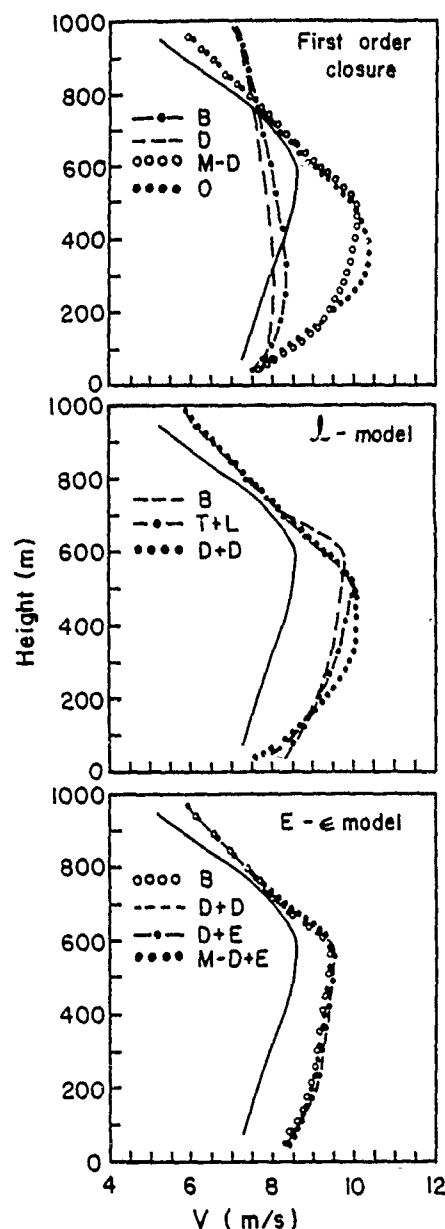


Fig. 4. Same as Figure 3 but for north-south wind component  $V$ .

the profile of the eddy viscosity coefficient  $K_m$  is important in producing the jet structure and will be discussed later.

Model simulations and observations of specific humidity  $Q$  are given in Figure 6. No parameterization does particularly well in predicting the observed  $Q$  magnitudes, although TKE models generally simulate the basic structure better in the boundary layer.  $E-\epsilon$  and  $l$  model parameterizations overpredict  $Q$  by 2.0–2.5 g/kg throughout the depth of the boundary layer. The O'Brien [1970] and modified Djolov [1973] first-order parameterization schemes predict similar values. The large predicted values are probably due to excessive evaporation in the surface layer. Reduction of surface moisture variable  $q_s$  by 5–10% gives magnitudes more comparable with observations. The Blackadar [1962] and Djolov [1973] schemes perform only slightly better near the surface but do not predict the well-mixed profile of  $Q$  observed.

The effect of boundary layer mixing on mean profiles can be

seen in the profile of eddy viscosity coefficient  $K_m$  (Figure 7). Observed values are calculated from (1) and show the well-observed boundary layer maximum at a height between  $h/3$  to  $h/2$ . However, model predictions based on TKE closure, while approximating the basic parabolic structure of  $K_m$ , generally do not predict the observed magnitude or height of this maximum. Given the simulated wind profiles, however,  $K_m$  is as good as could be expected.

Thus  $E-\epsilon$  model parameterizations as well as Dyer and Driedonks [1987]  $l$  model parameterization generate large boundary layer mixing. This is evident in the observed mean profiles, particularly wind profiles in which the jet is situated just above the height of maximum  $K_m$ . First-order closure schemes do not predict  $K_m$  as well. The Blackadar [1962] and Djolov [1973] parameterizations show large mixing throughout the depth of the model, as evidenced in the large values of  $K_m$  above the boundary layer. The modified Djolov [1973]

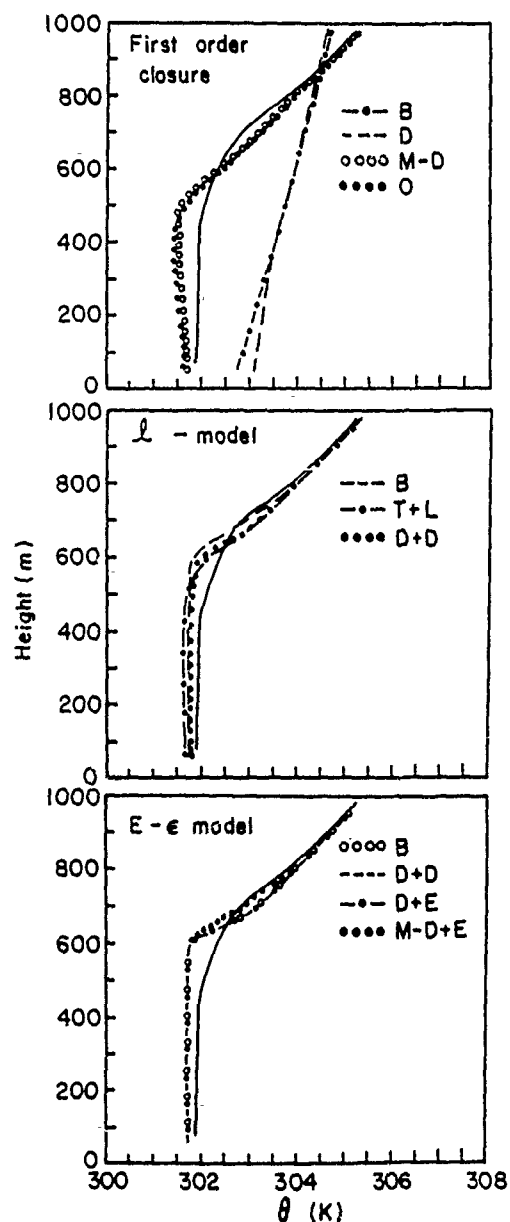


Fig. 5. Same as Figure 3 but for potential temperature.

TABLE 6. Observed and Modeled Boundary Layer Parameters

	$h$ , m	$L$ , m	$w_*$ , m/s	$u_*$ , m/s	$\theta_*$ , K
Observed values	400	-255	0.57	0.36	0.025
<i>First-Order Model</i>					
<i>Blackadar</i> [1962]	...	-570	...	0.247	...
<i>O'Brien</i> [1970]	420	-110	0.628	0.295	0.0289
<i>Djorlov</i> [1973]	...	-1050	...	0.240	...
Modified <i>Djorlov</i> [1973]	480	-95	0.724	0.309	0.0336
<i>l Model</i>					
<i>Therry and Lacarrere</i> [1983]	500	-106	0.751	0.329	0.0348
<i>Bodin</i> [1979]	590	-108	0.784	0.326	0.0321
<i>Duykerke and Driedonks</i> [1987]	550	-93	0.749	0.304	0.0314
<i>E-ε Model</i>					
<i>Duykerke and Driedonks</i> [1987]	600	-119	0.809	0.346	0.0336
<i>Beljaars et al.</i> [1987]	600	-111	0.808	0.338	0.0335
<i>Detering and Etling</i> [1985]	600	-112	0.808	0.339	0.0335
Modified <i>Detering and Etling</i> [1985]	600	-119	0.821	0.351	0.0345

scheme is an improvement in that  $K_m$  approaches zero at the top of the boundary layer.

From the comparison of parameterizations for mean values, two main conclusions can be drawn. First, among first-order closure schemes, mixing length parameterizations such as those of *Blackadar* [1962] or *Djorlov* [1973], which do not account for effects of the capping boundary layer inversion, do not perform well as compared to schemes which include the effects of reduced mixing above the boundary layer. These mixing length schemes show little agreement with observed mean boundary layer structure. The second conclusion is that among the remaining parameterizations, both first-order and TKE closure, mean variables are relatively insensitive to the closure scheme. Judging from rms errors and the overall predicted mean boundary layer structure, the first-order schemes of *O'Brien* [1970] or modified *Djorlov* [1973] or the *l* model or *E-ε* model schemes perform equally well. First-order schemes show smaller rms errors and a closer approximation to the structure in the  $U$  and  $Q$  profiles, but TKE closure schemes perform better for  $V$  and  $\Theta$ . Other studies [*Duykerke and Driedonks*, 1987; *Beljaars et al.*, 1987; *Hunt and Simpson*, 1982] have also shown the insensitivity of mean variables to the type of closure scheme.

**3.3.2. Turbulence profiles.** In contrast to mean profiles, turbulence profiles show significant differences among all closure schemes. Figure 8 gives model simulations and MONEX79 observations of the vertical variation of momentum flux for various parameterizations. In general, the *E-ε* model performs best, particularly the modified *Detering and Etling* [1985] parameterization in which constant  $C_3$  is modified to vary with height. All *E-ε* parameterizations do well in predicting near-surface values and the general structure of momentum flux but underestimate throughout the boundary layer. Parameterizations using the *l* model do not predict near-surface values as well as the *E-ε* model (as seen from  $u_*$  values in Table 6). Observed values of momentum flux above the top of the boundary layer (about 400 m) show an increase which is not modeled by any parameterization. This increase is probably due to penetrative convection. Both first-order and TKE closure schemes predict momentum flux decreasing to zero at the top of the boundary layer, with the exception of the *Blackadar* [1962] and *Djorlov* [1973] mixing length parameterizations which have unrealistic  $K_m$  profiles above  $h$ .

Observations and model simulations of sensible heat flux  $w\theta$  are given in Figure 9. Observed heat flux decreases with height from a near-surface value of approximately  $0.008 \text{ m s}^{-1} \text{ K}$ , becoming negative in the upper part of the boundary layer. First-order closure has difficulty in simulating the observed heat flux structure, particularly the parameterizations of *Blackadar* [1962] and *Djorlov* [1973]. These mixing length parameterizations erroneously predict negative heat flux throughout the boundary layer evident from  $\Theta$  profiles (Figure 5). Of the TKE schemes, the *E-ε* model performs best in modeling the positive heat flux in the lower half of the boundary layer and the negative flux aloft. The modified *Detering and Etling* [1985] parameterization most closely models the observed structure in the lower boundary layer but surprisingly does worst in predicting the negative heat flux maximum. The *Duykerke and Driedonks* [1987] *E-ε* parameterization models the negative heat flux well, overestimating by approximately 30% at the top of the boundary layer. The *l* model generally does well in predicting positive heat flux from the surface up to mid-boundary layer depth but as in first-order closure has difficulty modeling the negative flux. *Bodin's* [1979] parameterization, in which  $l$  is diagnostically determined as a function of  $z/h$ , has particular difficulty near  $z = h$ . It greatly overestimates heat flux near the inversion. *Therry and Lacarrere's* [1983] parameterization is comparable to *E-ε* parameterizations near  $z = h$ .

Convective temperature  $\theta_*$  and Monin-Obukhov length  $L$  given in Table 6 were calculated as

$$\theta_* = (\overline{wT_e})_0 / w_* \quad (40)$$

$$L = -T_e u_*^3 / (kg(\overline{wT_e})_0) \quad (41)$$

where  $u_*$  and  $w_*$  were calculated from (36) and (37). Model simulations of friction velocity  $u_*$  using TKE closure agree well with MONEX79 observations. First-order closure generally underpredicts  $u_*$ , as mentioned earlier. However, first-order closure does better in predicting convective velocity  $w_*$  and convective temperature  $\theta_*$ . This is believed to be due primarily to the inclusion of moisture flux  $\overline{wq}$ . Figure 10 shows model results and observations of the moisture flux profile. No parameterization does particularly well in predicting the observed magnitude of moisture flux, but near the surface, first-order closure gives the best prediction. *E-ε* and *l*

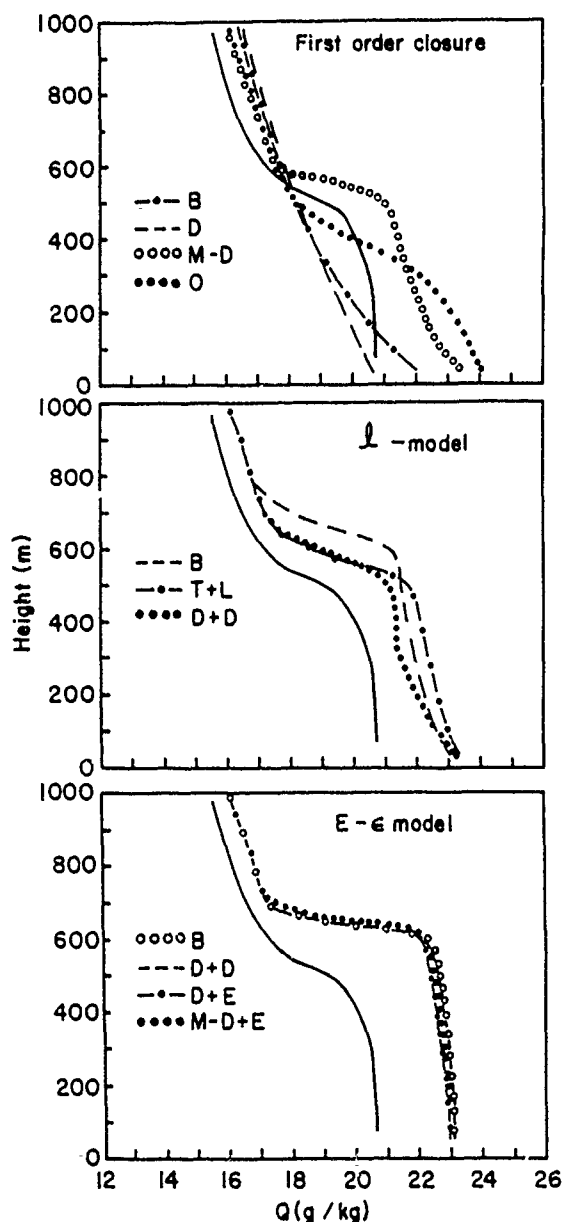


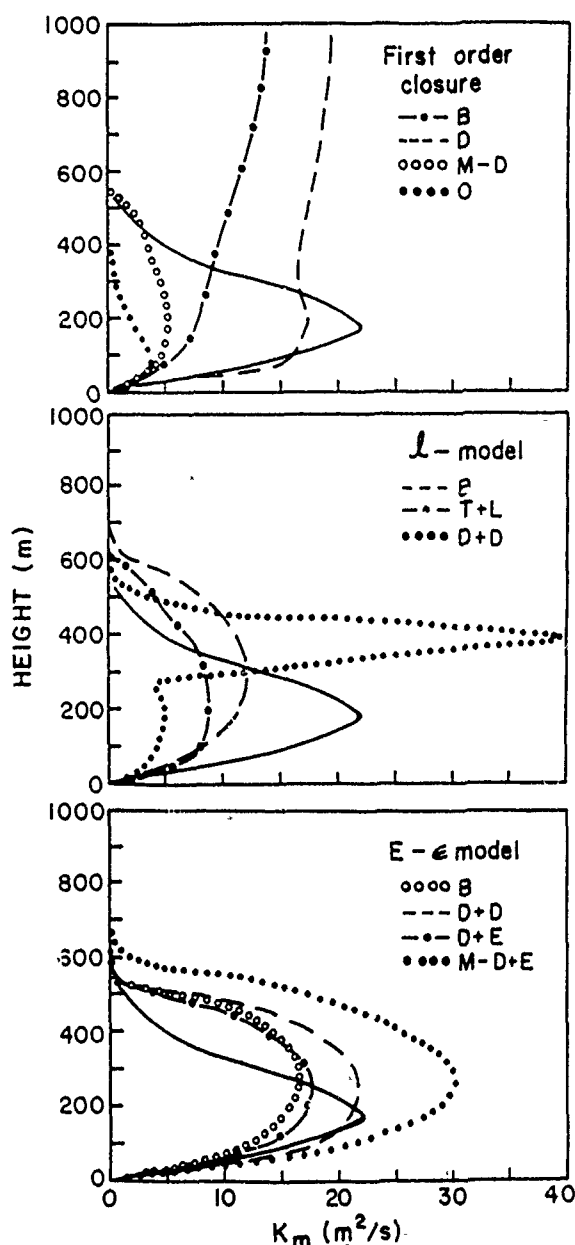
Fig. 6. Same as Figure 3 but for specific humidity.

model parameterizations perform better near the inversion base but generally overpredict in the lower half of the boundary layer. Thus larger  $(\overline{wq})_0$  values from TKE parameterizations, as well as deeper boundary layer depth  $h$ , result in overprediction of  $w_s$ . If one simply considers heat flux with no moisture, TKE parameterizations provide much closer approximations of  $w_s$ ,  $\theta_s$ , and Monin-Obukhov length  $L$  than first order. This is seen in the heat flux profiles of Figure 9.

Figure 11 shows model simulations and observations of turbulent energy  $E$  for  $E-\epsilon$  and  $l$  model parameterizations. The vertical structure is typical of convective boundary layers [Deardorff, 1974]. All parameterizations underpredict near the surface up to approximately 200 m but generally do well above 200 m. The Duynkerke and Driedonks [1987] parameterizations for both  $E-\epsilon$  and  $l$  models show the greatest deviation from other models and from observations.

3.3.3. *Turbulent kinetic energy budget.* Figures 12 and 13 give observations and model simulations of the vertical profile

of the budget of turbulent kinetic energy as given by (7). The  $l$  model simulations are presented in Figure 12, and  $E-\epsilon$  results are given in Figure 13. Solid lines represent MONEX79 observations of buoyancy production ( $B$ ), shear production ( $S$ ), dissipation ( $D$ ), and turbulent transport ( $T$ ). Similarly, dashed lines represent model simulations. Comparison of the three  $l$  model parameterizations given in Figure 12 shows interesting differences. In the lowest 300 m of the boundary layer, all parameterizations indicate shear and dissipation as the dominant source and sink terms, respectively. However, each parameterization greatly overestimates these terms, showing an approximate balance between the two. In contrast, the observed TKE budget shows turbulent transport and dissipation as equally dominant sink terms in the lowest 300 m, balanced by shear and buoyancy near the surface but primarily by shear in the middle of the boundary layer. Buoyancy production is simulated well near the surface, as shown in the discussion of

Fig. 7. Same as Figure 3 but for eddy viscosity  $K_m$ .

heat flux earlier, but negative fluxes near the inversion are largely overestimated, particularly by *Bodin* [1979]. All three *l* model parameterizations predict transport of TKE from the lower to the upper half of the boundary layer as shown by observations but underestimate the strength of this transport. The height at which turbulent transport changes from upward to downward is modeled well by *Bodin* [1979] and *Duynderke and Driedonks* [1987] but is underestimated by *Therry and Lacarrere* [1983]. *Therry and Lacarrere* proposed a correction term for the parameterization of  $w\bar{E}$  to account for the upward transport in the lower part of the convective boundary layer:

$$\overline{wE} = -C_k K_m (\partial \bar{E} / \partial z) + C_E w_* (l_v E^{1/2} \chi g / \Theta \bar{w} \theta) \quad (42)$$

where  $C_k$  and  $C_E$  are constants. They showed that this improved parameterization, which included an additional buoy-

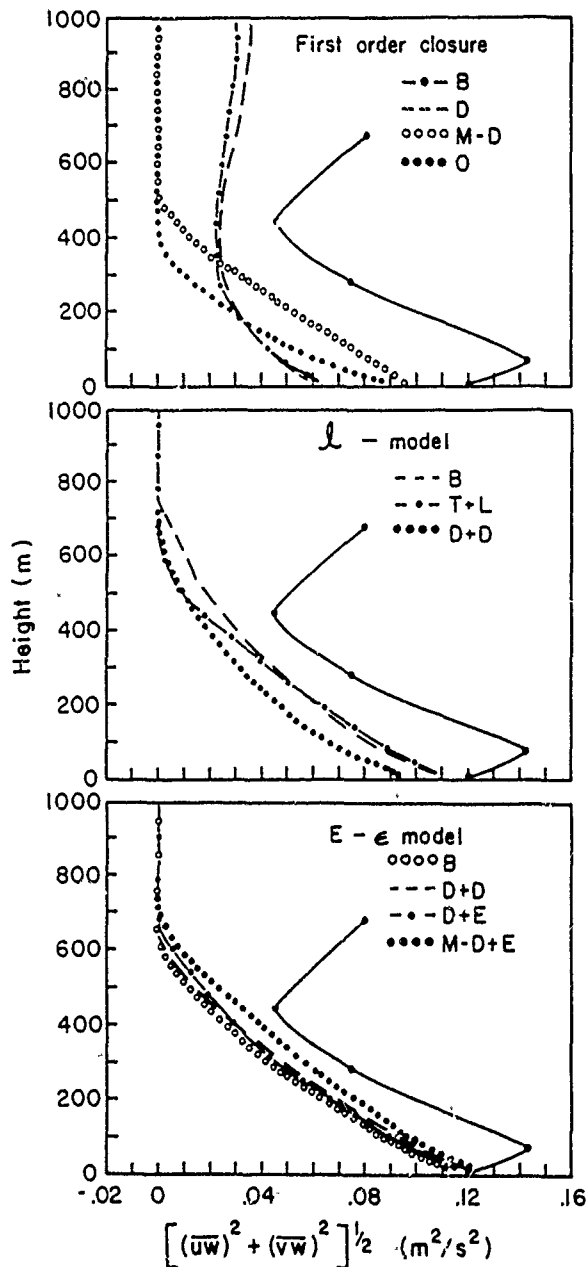


Fig. 8. Same as Figure 3 but for momentum flux. Observational data are from NCAR Electra aircraft data only.

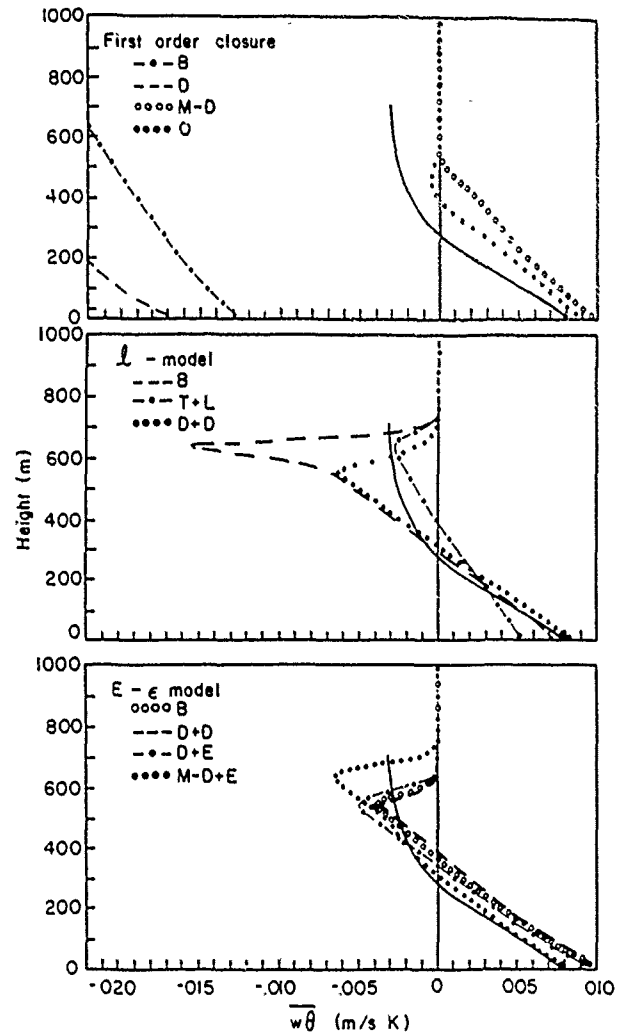


Fig. 9. Same as Figure 8 but for heat flux.

ancy production term in comparison to (9), modeled the flux of TKE better and effectively raised the height at which turbulent transport changed sign. This modification was incorporated into *Therry and Lacarrere's* [1983] original parameterization. Results indicate better agreement with observations for the height at which turbulent transport changes from positive to negative but show only small changes in the magnitude of source and sink terms in the TKE budget. Closer examination of the observed  $w\bar{\theta}$  profile indicates that buoyancy flux becomes negative at such a low altitude that it does not strongly influence  $w\bar{E}$  for this monsoon boundary layer.

The vertical profiles of dissipation predicted by the *l* model parameterizations (Figure 12) are indications of the sensitivity to mixing length determination. *Therry and Lacarrere's* [1983] parameterization involving a dissipation mixing length  $l_i$  overpredicts dissipation throughout the boundary layer. *Bodin's* [1979] parameterization is similar to that of *Therry and Lacarrere* but does better in predicting the vertical structure of  $\epsilon$  except near the inversion. Of all parameterizations, *Duynderke and Driedonks'* [1987] simulation of dissipation shows the largest values near the surface. Interestingly,  $\epsilon$  decreases to zero near 400 m, much lower than observed or predicted by other *l* model parameterizations. Examination of the vertical structure of mixing length (or  $K_m$  given in Figure 7) reveals the

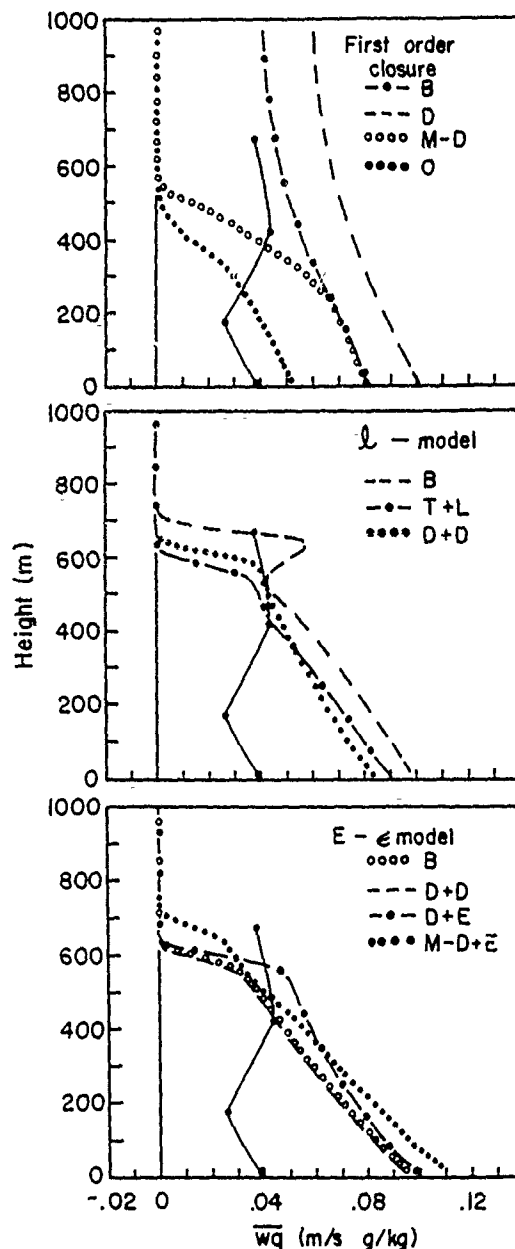


Fig. 10. Same as Figure 8 but for moisture flux.

possible reason. Anomalous large values of  $K_m$  and hence  $l$  at approximately 400 m in *Duynkerke and Driedonks*' [1987] parameterization cause  $\epsilon$  to approach zero. The large mixing length is directly affected by the determination of  $\lambda$  in (12), which *Duynkerke and Driedonks* assumed to be approximately equal to  $h/8$  (about 70 m) for the bulk of the boundary layer. Thus proper determination of mixing length is the major problem in  $l$  model parameterizations. One length scale is obviously not suitable either for momentum and dissipation or for an unstable versus stable boundary layer. The inclusion of a prognostic equation for dissipation to replace mixing length appears to be an improvement.

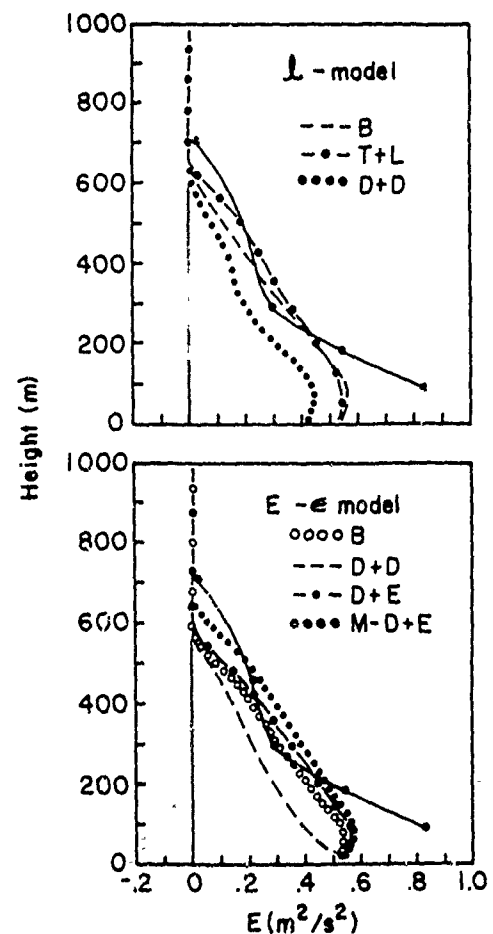
Figure 13 shows the TKE budget for the  $E-\epsilon$  model. In comparison to the  $l$  model parameterizations shown in Figure 12, profiles predicted by the  $E-\epsilon$  model generally show less variation among individual parameterizations. They also show better agreement with observations. This is particularly true

for shear and dissipation. All  $E-\epsilon$  parameterizations predict the general structure of  $\epsilon$  much better than the  $l$  model. The modified *Detering and Etling* [1985] parameterization performs best overall, showing the smallest overprediction in both shear production and dissipation. Each  $E-\epsilon$  model parameterization underpredicts turbulent transport but does show the general vertical structure, with the exception of *Duynkerke and Driedonks*' [1987] scheme. Their parameterization yields turbulent transport as a source term throughout the boundary layer to compensate for the smaller shear production than that given by other  $E-\epsilon$  parameterizations.

#### 4. MODEL SENSITIVITY TO INITIAL CONDITIONS

Some mention should be made of the uncertainty or sensitivity of the modeled mean and turbulence profiles. Using the modified *Detering and Etling* [1985]  $E-\epsilon$  parameterization, additional simulations were done with the initial geostrophic wind ( $G$ ) increased and decreased by 25%. Thus simulations were carried out for  $0.75G$ ,  $G$ , and  $1.25G$ . In the 1-D case considered here, the geostrophic wind was the most difficult input parameter to determine. Limited data in the region also made it difficult to accurately predict horizontal and vertical temperature distribution. The  $\pm 25\%$  changes were chosen as the maximum and minimum deviations expected in the magnitude of  $G$ .

Compared to original model simulations (geostrophic wind

Fig. 11. Same as Figure 8 but for turbulent kinetic energy of  $l$  and  $E-\epsilon$  models.

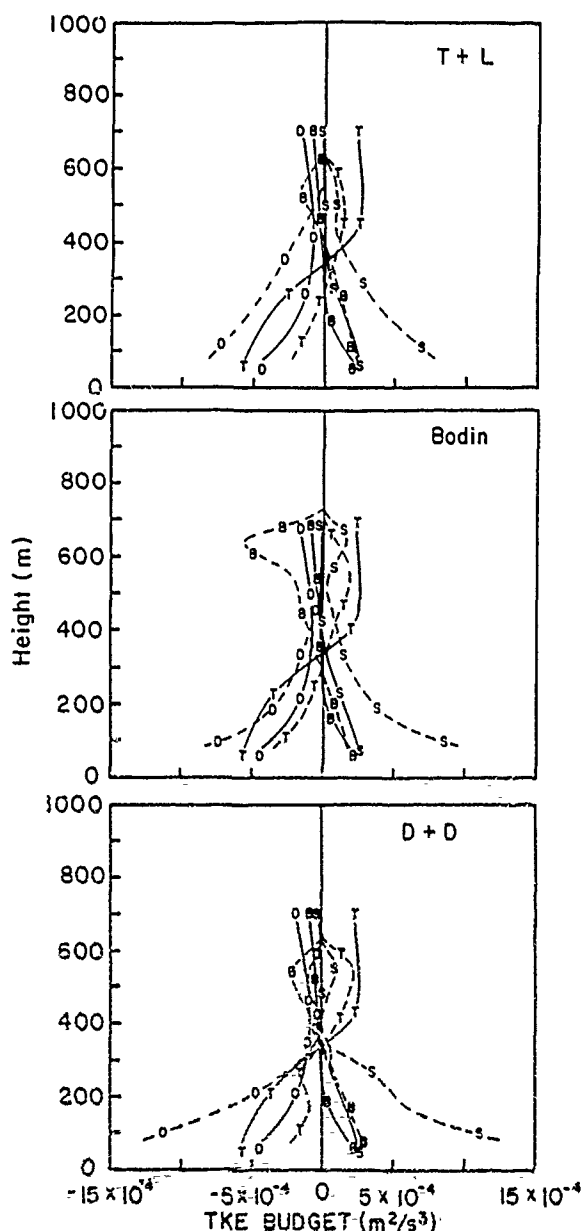


Fig. 12. Vertical profile of the budget of turbulent kinetic energy for the three  $l$ -model parameterizations given by (top) *Therry and Lacarrere* [1983], (middle) *Bodin* [1979], and (bottom) *Duykerke and Driedinks* [1987]. Solid curves represent observations of shear production (S), buoyancy production (B), dissipation (D), and turbulent transport (T). Dashed curves similarly represent model simulations.

of 1.0  $G$ ). model results at 0400 UT for  $\pm 25\%$  changes in  $G$  indicated that wind components  $U$  and  $V$ , turbulent kinetic energy  $E$ , and momentum flux showed the largest deviations. Near the surface (up to about 100 m),  $\pm 25\%$  changes in  $G$  resulted in  $\pm 20$ – $22\%$  changes in the magnitude of  $U$  and  $V$  and  $\pm 28\%$  changes in  $E$ . Momentum flux changed by approximately  $\pm 32\%$ . Near the height of the wind speed maximum (about 600–700 m), changes in  $U$  had reduced to  $\pm 14\%$ , and changes in  $E$  had reduced to  $\pm 21\%$ , while changes in  $V$  and momentum flux had remained approximately constant at  $\pm 23\%$  and  $\pm 29\%$ , respectively. Temperature and moisture variables indicated much smaller variations in both mean (about  $\pm 0.1$ – $0.2\%$ ) and turbulence ( $\pm 7$ – $11\%$ ) throughout the

boundary layer. Thermodynamic variables are less directly affected by  $G$  as evidenced from the PBL equations (3). Variation of mean and turbulent quantities of potential temperature and moisture is dependent primarily on  $K$ . Variations in  $K$  for  $\pm 25\%$  changes in  $G$  were approximately  $\pm 9\%$ , throughout the boundary layer.

The conclusion drawn from these simulations is that reasonable model results are dependent on the accuracy of the initial conditions, such as the geostrophic wind. For  $\pm 25\%$  changes in  $G$ , differences in model simulations are larger than differences between model versions in the  $l$  model or  $E$ - $\epsilon$  groups. This dependency of accuracy on initial conditions is not a new result (see, for example, *Anthes* [1986]). We have sought here only to quantify the uncertainty for this 1-D model. However, the profiles of mean and turbulent parameters showed similar structure, and performance of different parameterization schemes was judged from their ability to predict the known physical mean and turbulent structure of the boundary layer.

We can hypothesize on possible sources of model error. Initial profile data were available only from radiosondes launched from ships (Figure 2). These profiles had a vertical resolution of only 50 mbar (approximately 500 m). In contrast, the vertical resolution of averaged ship and aircraft observations shown in Figures 3–6 was of the order of 100–150 m in the boundary layer. Thus because of poor resolution in the initial profiles, small-scale structures apparent in the observations may be difficult to simulate. This could explain the general overprediction of boundary layer depth  $h$  from the potential temperature profiles. Factors not accounted for in the model, such as inhomogeneity, baroclinicity, and intermittent clouds present in the Bay of Bengal, would also cause errors when verifying model profiles against observations.

## 5. CONCLUSIONS

Comparison of observations and 1-D model simulations of mean and turbulence profiles in the monsoon boundary layer using various parameterization schemes provides two general conclusions. First, mean profiles such as potential temperature, humidity, and horizontal wind components show little sensitivity to the type of closure parameterization as long as the effects of turbulent mixing in the boundary layer are properly handled. Thus, for mean profiles of  $U$ ,  $V$ ,  $\Theta$ , and  $Q$ , determination of  $K_m$  using a diagnostic formulation of  $l$  or a prognostic determination of  $\epsilon$  makes little difference. However, first-order schemes are sensitive to the atmospheric stability and turbulent mixing in the boundary layer. A fundamental weakness of  $K$  profile parameterizations is that they typically must be specified as a function of stability. Thus profiles are given on the basis of stable or unstable conditions, as seen in the work by *Yamamoto et al.* [1973] or *Orlanski et al.* [1974]. Mixing length parameterizations were developed to avoid this stability dependence by specifying a parameterization independent of stability. This was attempted through the concept of a mixing length best illustrated in *Blackadar's* [1962] parameterization. The problem in formulations such as *Blackadar's* and *Djorlov's* [1973] lies in the failure of the mixing length to properly include stability effects, particularly at the inversion and above the boundary layer. Thus to properly model boundary layer structure, mixing length parameterizations must include some function of stability in the determination of  $K_m$ . This is evident upon comparison of results of

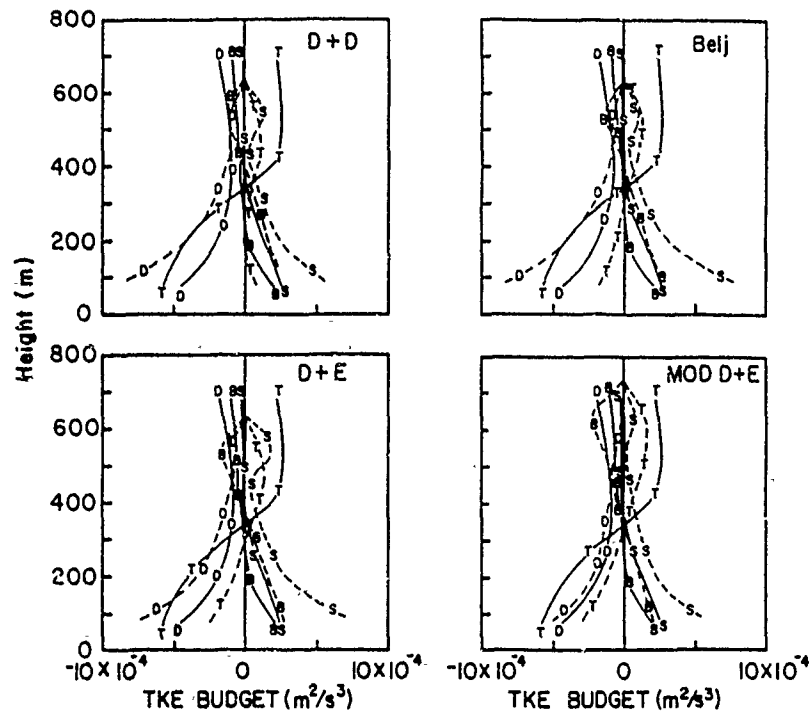


Fig. 13. Same as Figure 12 but for the  $E$ - $\epsilon$  model parameterizations of (top left) Duykerke and Driedonks [1987], (top right) Beljaars et al. [1987], (bottom left) Detering and Etling [1985], and (bottom right) modified Detering and Etling [1985].

the Djolov [1973] and modified Djolov [1973] schemes, which differ only by a factor equal to  $(1 - Ri)^{1/2}$ . Above the boundary layer,  $K_m$  is reduced to zero in the modified Djolov scheme, as seen in observations, but approaches large positive values for Djolov's original parameterization. Mixing length parameterizations which include stability, such as the modified Djolov scheme or the ones given by Karlsson [1972] or Estoque and Bhunralkar [1970] show better agreement with observations. Lack of such stability dependence tends to create well-mixed profiles even above the boundary layer.

The second conclusion derived from comparison of model simulations with observations is that TKE closure shows closer agreement with the observed turbulence structure in the boundary layer than first-order closure. Both the magnitude and the vertical structure of momentum and heat fluxes obtained from TKE closure agree better with observations. Among TKE schemes, comparison of vertical flux structures as well as budgets of TKE indicates that, as a group,  $E$ - $\epsilon$  parameterizations perform better than  $l$  model schemes. Intuitively, this should be true because the  $E$ - $\epsilon$  scheme contains more physics of the boundary layer. Also, the  $E$ - $\epsilon$  scheme should be able to more accurately predict boundary layer structure from a wider variety of atmospheric cases. This is because it is based on a more physically realistic determination of energy dissipation as opposed to the mixing length determination of the  $l$  model schemes. It would be of interest to test PBL parameterizations for differing atmospheric stabilities, not just the convective conditions considered here.

Among  $E$ - $\epsilon$  parameterizations the modified Detering and Etling [1985] scheme performs best overall. This parameterization differs from other  $E$ - $\epsilon$  parameterizations only in the formulation of constant  $C_3$  (dissipation production). The modified constant  $C_3'$  given by (27) is generally less than  $C_3$  because  $l$  is less than  $h$  throughout the boundary layer. Thus

production of dissipation in (25) as calculated from the modified Detering and Etling scheme is less than that for the original Detering and Etling [1985] parameterization or other  $E$ - $\epsilon$  parameterizations given in Table 4. The TKE budget given in Figure 13 reflects this conclusion. Dissipation calculated using the modified Detering and Etling scheme is less than the values for other schemes given and generally shows the closest agreement with observations, but only in the lower part of the boundary layer. The conclusion presented in section 3.3.2 that the modified Detering and Etling scheme has the largest overprediction of negative heat flux near the inversion could also be explained by the dissipation profile. Dissipation near the top of the boundary layer as calculated by modified Detering and Etling approaches zero and is much smaller than the dissipation calculated by other  $E$ - $\epsilon$  parameterizations. Thus a larger negative buoyancy production near the top of the boundary layer is required to balance the shear production and the turbulent transport.

It is interesting to note that the modified Detering and Etling [1985] parameterization was originally proposed because modeled values of  $K_m$  and  $u_*$  using the standard  $E$ - $\epsilon$  model were larger than observations. Comparison here between  $E$ - $\epsilon$  parameterization schemes shows an increase in  $K_m$  and  $u_*$  for the modified Detering and Etling parameterization. The larger  $K_m$  values partly compensate for underprediction of wind shear and generally provide closer agreement with flux observations.

This study has been an attempt to evaluate multilevel PBL parameterizations in a simple 1-D barotropic model. Future research will focus on implementing the improved TKE closure parameterization into a 3-D mesoscale model. Using the Genesis of Atlantic Lows Experiment (GALE) data set, model forecasts will be compared for different boundary-layer physics.



**Acknowledgments.** The one-dimensional model using first-order closure was originally developed at the Naval Research Laboratory by Simon Chang. The authors would like to thank S. Chang for reviewing the manuscript and for useful discussions. This work was supported by the National Science Foundation under grant ATM-83-11812, by the Office of Naval Research under contract N00014-84-K-0620, and by the Naval Research Laboratory, Washington, D. C.

## REFERENCES

- Andre, J. C., G. DeMoor, P. Lacarrere, G. Therry, and R. Du Vachat, Modeling the 24-hour evolution of the mean and turbulent structures of the planetary boundary layer, *J. Atmos. Sci.*, **35**, 1861-1883, 1978.
- Anthes, R. A., Estimating sensitivity and uncertainty in mesoscale numerical models, paper presented at International Conference on Monsoon and Mesoscale Meteorology, Taipei, Taiwan, Nov. 9-14, 1986.
- Arya, S. P. S., Suggested revisions to certain boundary layer parameterization schemes used in atmospheric circulation models, *Mon. Weather Rev.*, **105**, 215-227, 1977.
- Beljaars, A. C. M., J. L. Walmsley, and P. A. Taylor, A mixed spectral finite-difference model for neutrally stratified boundary layer flow over roughness changes and topography, *Boundary Layer Meteorol.*, **38**, 273-303, 1987.
- Blackadar, A. K., The vertical distribution of wind and turbulent exchanges in neutral atmosphere, *J. Geophys. Res.*, **67**, 3095-3102, 1962.
- Blackadar, A. K., High resolution models of the planetary boundary layer, *Adv. Environ. Sci. Eng.*, **1**, 50-85, 1979.
- Bodin, S., An unsteady one-dimensional atmospheric boundary layer model, Proceedings From the WMO Symposium on the Interpretation of Broad-scale NWP Products for Local Forecasting Purposes, Warsaw, October 1976, *Rep. WMO 450*, World Meteorol. Organ., Geneva, 1976.
- Bodin, S., A predictive numerical model of the atmospheric boundary layer based on the turbulent energy equation, *SMHI Rep.*, **13**, Norrköping, Sweden, 1979.
- Bodin, S., Applied numerical modeling of the atmospheric boundary layer, in *Atmospheric Planetary Boundary Layer Physics*, edited by A. Longhetto, pp. 1-76, Elsevier, New York, 1980.
- Boussinesq, J., Essai sur la théorie des courantes, *Mem. Pres. Divers Savant Acad. Sci. Paris*, **23**, 46, 1877.
- Brost, R. A., and J. C. Wyngaard, A model study of the stably stratified planetary boundary layer, *J. Atmos. Sci.*, **35**, 1427-1440, 1978.
- Busch, N. E., S. W. Chang, and R. A. Anthes, A multi-level model of the planetary boundary layer suitable for use with mesoscale dynamic models, *J. Appl. Meteorol.*, **15**, 909-919, 1976.
- Businger, J. A., and S. P. S. Arya, Height of the mixed layer in a stably stratified planetary boundary layer, *Adv. Geophys.*, **18A**, 73-92, 1974.
- Businger, J. A., J. C. Wyngaard, Y. Izumi, and E. F. Bradley, Flux-profile relationship in the atmospheric surface layer, *J. Atmos. Sci.*, **28**, 181-189, 1971.
- Carlson, J. D., and M. R. Foster, Numerical study of some unstably stratified boundary layer flows over a valley at moderate Richardson number, *J. Clim. Appl. Meteorol.*, **25**, 203-213, 1986.
- Clarke, R. H., Recommended methods for the treatment of the boundary layer in numerical models of the atmosphere, *Aust. Meteorol. Mag.*, **18**, 51-73, 1970.
- Clarke, R. H., Attempts to simulate the diurnal cycle of meteorological variables in the boundary layer, *Izv. Acad. Sci. USSR Atmos. Oceanic Phys. Engl. Transl.*, **10**, 360-374, 1974.
- Daly, B. J., and F. H. Harlow, Transport equations in turbulence, *Phys. Fluids*, **13**, 2634-2649, 1970.
- Deardorff, J. W., The countergradient heat flux in the lower atmosphere and in the laboratory, *J. Atmos. Sci.*, **23**, 503-506, 1966.
- Deardorff, J. W., Parameterization of the planetary boundary layer for use in general circulation models, *Mon. Weather Rev.*, **100**, 93-106, 1972.
- Deardorff, J. W., Three-dimensional numerical study of turbulence in an entraining mixed layer, *Boundary Layer Meteorol.*, **7**, 199-206, 1974.
- Deardorff, J. W., The development of boundary layer turbulence models for use in studying the severe storm environment, Open Sesame, in *Proceedings of the Opening Meeting, Boulder, CO, Sept. 4-6, 1974*, edited by D. K. Lilly, pp. 251-264, NOAA, ERL, Boulder, Colo., 1975.
- Delage, Y., A numerical study of the nocturnal atmospheric boundary layer, *Q. J. R. Meteorol. Soc.*, **100**, 351-364, 1974.
- Detering, H. W., and D. Etling, Application of the  $E-\epsilon$  turbulence model to the atmospheric boundary layer, *Boundary Layer Meteorol.*, **33**, 113-133, 1985.
- Djilov, G. D., Modeling of the interdependent diurnal variation of meteorological elements in the boundary layer, Ph.D. thesis, Univ. of Waterloo, Waterloo, Ont., Canada, 1973.
- Duynkerke, P. G., and G. M. Driedonks, A model for the turbulent structure of stratocumulus-topped atmospheric boundary layer, *J. Atmos. Sci.*, **44**, 43-64, 1987.
- Ekman, V. W., On the influence of the Earth's rotation on ocean currents, *Ark. Mat. Astron. Fys.*, **12**, 1-52, 1905.
- Estoque, M. A., and C. M. Bhumralkar, A method for solving the planetary boundary layer equations, *Boundary Layer Meteorol.*, **1**, 169-194, 1970.
- Hanjalic, K., and B. E. Launder, A Reynolds stress model of turbulence and its application to thin shear flows, *J. Fluid Mech.*, **52**, 609-638, 1972.
- Harlow, F. H., and P. I. Nakayama, Turbulence transport equations, *Phys. Fluids*, **10**, 2323-2332, 1967.
- Holt, T., and S. Raman, Observations of the mean and turbulence structure of the marine boundary layer over the Bay of Bengal during MONEX 79, *Mon. Weather Rev.*, **114**, 2176-2190, 1986.
- Holt, T., and S. Raman, A study of mean boundary-layer structures over the Arabian Sea and the Bay of Bengal during active and break monsoon periods, *Boundary Layer Meteorol.*, **38**, 73-94, 1987.
- Hunt, J. C. R., and J. E. Simpson, Atmospheric boundary layers over non-homogeneous terrain, in *Engineering Meteorology*, edited by E. J. Plate, Elsevier, New York, 1982.
- Karlsson, E., A numerical model for the boundary layer of the atmosphere at neutral and stable stratification, *Rep. DM-7*, Inst. of Meteorol., Univ. of Stockholm, Stockholm, Sweden, 1972.
- Kolmogorov, A. N., The equation of turbulent motion in an incompressible fluid (in Russian), *Izv. Akad. Nauk SSSR, Ser. Fiz.*, **6**(1, 2), 56-58, 1942.
- Krishna, K., The planetary boundary layer model of Ellison (1956)—A retrospect, *Boundary Layer Meteorol.*, **19**, 293-301, 1980.
- Lacser, A., and S. P. S. Arya, A comparative assessment of mixing-length parameterizations in the stably stratified nocturnal boundary layer (NBL), *Boundary Layer Meteorol.*, **36**, 53-70, 1986.
- Launder, B. E., and D. B. Spalding, The numerical computations of turbulent flows, *Comput. Methods Appl. Mech. Eng.*, **3**, 269-289, 1974.
- Lee, N. H., and S. U. Kao, Finite-element numerical modeling of atmospheric turbulent boundary layer, *J. Appl. Meteorol.*, **18**, 1287-1295, 1979.
- Lewellen, W. S., and M. Teske, Prediction of the Monin-Obukhov similarity functions from an invariant model of turbulence, *J. Atmos. Sci.*, **30**, 1340-1345, 1973.
- Lumley, J. L., Second order modeling of turbulent flows, in *Prediction Methods for Turbulent Flows*, edited by W. Kolmann, pp. 1-31, Hemisphere, London, 1980.
- Mailhot, J., and R. Benoit, A finite-element model of the atmospheric boundary layer suitable for use with numerical weather prediction, *J. Atmos. Sci.*, **39**, 2249-2266, 1982.
- Marchuk, G. I., V. P. Kochergin, V. I. Klimok, and V. A. Sukhorukov, On the dynamics of the ocean surface mixed layer, *J. Phys. Oceanogr.*, **7**, 865-875, 1977.
- Mason, R. J., and I. ... , A two-dimensional numerical study of horizontal roll vortices in the neutral atmospheric boundary layer, *Q. J. R. Meteorol. Soc.*, **106**, 351-366, 1980.
- McBean, G. A., K. Bernhardt, S. Bodin, Z. Litynska, A. P. van Ulden, and J. C. Wyngaard, The planetary boundary layer, *WMO Tech. Note 165*, World Meteorol. Organ., Geneva, 1979.
- Mellor, C. L., and T. Yamada, A hierarchy of turbulence closure models for planetary boundary layers, *J. Atmos. Sci.*, **31**, 1791-1806, 1974.
- Mellor, C. L., and T. Yamada, Development of a turbulence closure model for geophysical fluid problems, *Rev. Geophys.*, **20**, 851-875, 1982.
- Monin, A. S., and A. M. Yaglom, *Statistical Fluid Mechanics*, vol. 1, MIT Press, Cambridge, Mass., 1971.
- O'Brien, J. J., A note on the vertical structure of the eddy exchange

- coefficient in the planetary boundary layer, *J. Atmos. Sci.*, 27, 1213-1215, 1970.
- Orlanski, I., B. B. Ross, and L. J. Polinsky, Diurnal variation of the planetary boundary layer in a mesoscale model, *J. Atmos. Sci.*, 31, 965-989, 1974.
- Panofsky, H. A., and J. A. Dutton, *Atmospheric Turbulence*, 397 pp., John Wiley, New York, 1984.
- Pielke, R. A., *Mesoscale Meteorological Modeling*, 612 pp., Academic, New York, 1984.
- Pielke, R. A., and Y. Mahrer, Representation of the heated planetary boundary layer in mesoscale models with coarse vertical resolution, *J. Atmos. Sci.*, 32, 2288-2308, 1975.
- Prandtl, L., *Meteorologische Anwendungen der Stromungslehre*, *Beitr. Phys. Atmos.*, 19, 188-202, 1932.
- Rodi, W., *Turbulence Models and Their Application in Hydraulics*, International Delft, Association for Hydraulic Research, Delft, Netherlands, 1980.
- Rossby, C. G., and R. B. Montgomery, The layer of frictional influence of wind and ocean currents, *Pap. Phys. Oceanogr. Meteorol.*, 3, 101 pp., 1935.
- Rotta, J., Statistische Theorie nichthomogener Turbulenz, *Z. Phys.*, 129, 547-572, 1951.
- Russell, R. D., and E. S. Takle, A numerical study of the effects of synoptic baroclinicity on stable boundary layer evolution, *Boundary Layer Meteorol.*, 31, 385-418, 1985.
- Shir, C. C., A preliminary numerical study of atmospheric turbulent flows in the idealized planetary boundary layer, *J. Atmos. Sci.*, 30, 1327-1339, 1973.
- Stubley, G. D., and D. R. Rooney, The sensitivity of  $k-\epsilon$  model computations of the neutral planetary boundary layer to baroclinicity, *Boundary Layer Meteorol.*, 37, 53-70, 1986.
- Tag, P. M., and S. W. Payne, Examination of the breakup of marine stratus—A three-dimensional numerical investigation, *J. Atmos. Sci.*, 44, 208-223, 1987.
- Tapp, M. C., and P. W. White, A non-hydrostatic mesoscale model, *Q. J. R. Meteorol. Soc.*, 102, 277-296, 1976.
- Therry, G., and P. Lacarrere, Improving the eddy kinetic energy model for planetary boundary layer description, *Boundary Layer Meteorol.*, 25, 65-88, 1983.
- Wyngaard, J. C., Modeling the planetary boundary layer—Extension to the stable case, *Boundary Layer Meteorol.*, 9, 441-460, 1975.
- Wyngaard, J. C., Boundary layer modeling, in *Atmospheric Turbulence and Air Pollution Modelling*, edited by F. T. M. Nieuwstadt and H. van Dop, pp. 69-106, D. Reidel, Hingham, Mass., 1982.
- Yamada, T., The critical Richardson number and the ratio of the eddy transport coefficients obtained from a turbulence closure model, *J. Atmos. Sci.*, 32, 926-933, 1975.
- Yamada, T., Simulations of nocturnal drainage flows by a  $q^2l$  turbulence closure model, *J. Atmos. Sci.*, 40, 91-106, 1983.
- Yamada, T., and C.-Y. J. Kao, A modeling study on the fair weather marine boundary layer of the GATE, *J. Atmos. Sci.*, 43, 3186-3199, 1986.
- Yamamoto, G., A. Shimanuki, M. Aida, and N. Yasuda, Diurnal variation of wind and temperature fields in the Ekman layer, *J. Meteorol. Soc. Jpn.*, 51, 377-387, 1973.
- Yu, T. W., Numerical studies of the atmospheric boundary layer with a turbulent energy closure scheme, paper presented at Third Symposium on Atmospheric Turbulence, Diffusion and Air Quality, Am. Meteorol. Soc., Raleigh, N.C., Oct. 1976.

T. Holt and S. Raman, Department of Marine, Earth and Atmospheric Sciences, North Carolina State University, Raleigh, NC 27695.

(Received February 10, 1988;  
accepted June 20, 1988.)

## **APPENDIX I**

### **Evolution of a Marine Boundary-Layer Jet**

## Evolution of a Marine Boundary-Layer Jet

H. GERBER, SIMON CHANG AND TEDDY HOLT\*

*Naval Research Laboratory, Washington, DC*

(Manuscript received 11 April 1988, in final form 26 September 1988)

### ABSTRACT

High-resolution profiles of temperature and wind-speed measurements were made with a tethered balloon in and above the marine boundary layer at San Nicolas Island (SNI) during a period when the cloud-free boundary layer grew from near the sea surface to 450 m in approximately 12 h. Measurements showed the formation of a low-level jet which remained centered at the temperature inversion as the boundary layer grew. The upper limit of the jet coincided with the top of a temperature transition layer that extended from the sharp temperature jump at the inversion to the free atmosphere above.

The experimental evidence suggested that the jet was caused by thermal wind resulting from a specific sea surface temperature gradient, and from horizontal temperature gradients caused by a sloped inversion and the transition layer. Production of mechanical turbulence by wind shear in the jet caused rapid entrainment into the mixed layer of warmer air from above, and the fast growth of the boundary layer.

A quasi-two dimensional (2D) model including turbulence parameterized in terms of turbulent kinetic energy (TKE) and dissipation rate was able to reproduce the main features of the evolving boundary-layer jet and temperature field. The predicted shape, location, and intensity of the jet, and the growth of the boundary layer were similar to the observations. The model also predicted realistic heat and momentum fluxes and TKE budgets as judged by comparisons with aircraft measurements by Brost et al. in a similar case off the West Coast. Using a variety of initial conditions, the model further showed that the jet was likely caused by the combined effects of the inertial acceleration of the wind field, the specific temperature gradients, and the sloping inversion.

### 1. Introduction

In October 1984 a tethered balloon was used to obtain vertical profiles of meteorological parameters in and above the marine boundary layer on SNI off the West Coast of the United States (Gerber 1986); see Fig. 1. In this paper we analyzed several profiles which were obtained on 24 October following an unusual 48-h period of Santa Ana wind conditions at the island. Those conditions were characterized by low wind speeds from the mainland, dry and subsiding air, and a boundary-layer depth over the ocean of only about 30 m. When the continental high pressure which caused the Santa Ana conditions weakened in the local area, westerlies reestablished themselves at the island. This provided a unique opportunity to observe closely the growth of the boundary layer, which increased rapidly to a depth of 450 m in 12 h. During this period a wind jet was observed near the inversion, which separated the mixed layer from the warmer and dryer air aloft. Towards the end of the period, stratocumulus clouds formed just below the inversion.

Jet-shaped wind profiles have been observed previously in the marine atmosphere; see the review by Zemba and Friehe (1987). Most of those observations (e.g., Johnson and O'Brian 1973; Enfield 1981; and Zemba and Friehe 1987) were made off western margins of continents where upwelling of cold water occurring just offshore causes strong horizontal temperature gradients. According to the usual explanation (Enfield 1981; Lydolph 1985; Lester 1985; and Zemba and Friehe 1987), these wind jets are caused by thermal winds due to strong local baroclinic conditions. Other regions which meet this criterion, such as, for example, other coastal regions, the boundary of the Gulf Stream, and the marginal ice zone (Overland et al. 1983) often show strong vertical wind shears for the same reason.

The wind jet observed at SNI is most similar in appearance to the jet observed also off the West Coast by Zemba and Friehe (1987). They concluded that the strong horizontal temperature contrast between the ocean and the land in the atmosphere above the inversion resulted in the baroclinity that caused their jet. The SNI jet formed for other reasons that will be detailed in the following. We describe three sets of meteorological profiles that show the growth of the boundary layer and the evolution of the jet. Also, this episode is modeled with a quasi-2D boundary layer model with turbulence described in terms of sources and dissipation of TKE. The model predictions are

\* Affiliated with: North Carolina State University, Raleigh, North Carolina.

Corresponding author address: Dr. Hermann E. Gerber, Naval Research Laboratory, Code 4112, Washington, DC 20375.

compared with the measurements, and results are given for sensitivity runs of the model where meteorological parameters are changed from the ones observed. Finally, several methods for parameterizing the entrainment rate are compared to the growth of the mixed layer for the SNI case.

## 2. Observations

Buoys located in places shown in Fig. 1 provided the mean daily temperatures which were used in part to construct a rough estimate of the sea surface isotherms for 24 October. Another part consisted of the monthly mean isotherms (U.S. Dept. of Commerce 1984) which run generally SW to NE in the Channel Islands area, with warmest temperatures towards the SE. The surface temperature gradients were estimated to be  $(\partial T/\partial x)_0 = 0.02^\circ\text{C km}^{-1}$  in the easterly direction and  $(\partial T/\partial y)_0 = -0.02^\circ\text{C km}^{-1}$  in the northerly direction in the vicinity of SNI.

The tethered balloon was deployed at Vizcaino Point on the NW tip of SNI. The  $170\text{ m}^3$  balloon belonging to LTA International, Inc., carried sensors to measure wet- and dry-bulb temperature, wind speed, and aerosol scattering coefficient. In addition, an altimeter with an accuracy of  $\pm 1\text{ m}$ , a clock, and a telemetry system for real-time down-linking of the data were onboard. The data was collected at the rate of one scan of all channels every 6 sec. The balloon tether was payed out and retrieved at  $0.5\text{ m s}^{-1}$ .

### a. Temperature and wind profiles

The temperature sensor consisted of a YSI Thermoliner thermistor (accuracy of  $\pm 0.15^\circ\text{C}$  with a  $1/e$  time constant of 3 sec). The thermistor was mounted in a self-aspirated thermally thin radiation shield facing into the wind. Under those conditions negligible temperature lag was expected between sensor and ambient temperatures at the slow ascent and descent rates of the balloon.

The profiles from the three flights on 24 October show how the temperature structure of the boundary layer changed after the Santa Ana conditions were replaced by the more typical westerly flow (see Fig. 2). All profiles were constructed from five-point running means of the raw data. Each of the first two pairs of profiles correspond to the ascent and descent of a flight, while the last profile is for the ascent of the third flight for which the descent changed little. The dotted profiles show the temperature structure on the previous afternoon (1500 LST on 23 October when the Santa Ana conditions were still in effect. The dotted profile indicates a slightly stable atmosphere with a potential temperature increase of  $1^\circ\text{C}$  between 100 and 800 m. The profiles show that between 0900 and 2043 LST 24 October, the surface layer cooled by about  $4^\circ\text{C}$ , while at 500 m a decrease of almost  $10^\circ\text{C}$  occurred. This large cooling is indicative of cold advection into the local area. Above 550 m the temperature changed very little during this period, showing a change of only  $\pm 0.25^\circ\text{C}$  at 600 m. The general shape of the temperature profiles includes a nearly adiabatic lapse rate in the mixed layer

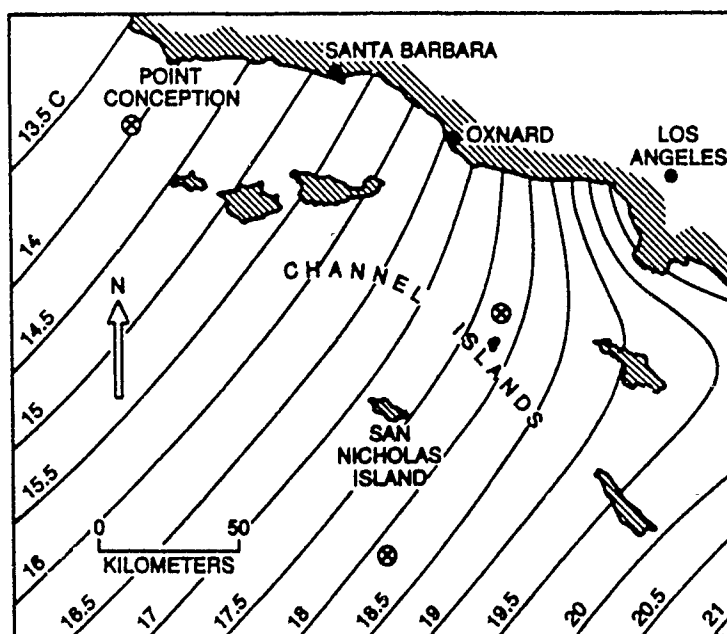


FIG. 1. Sketch of the Channel Islands area off the West Coast. Shown is the location of San Nicolas Island (SNI), and surface isotherms estimated from monthly-mean isotherms and buoys located at X.

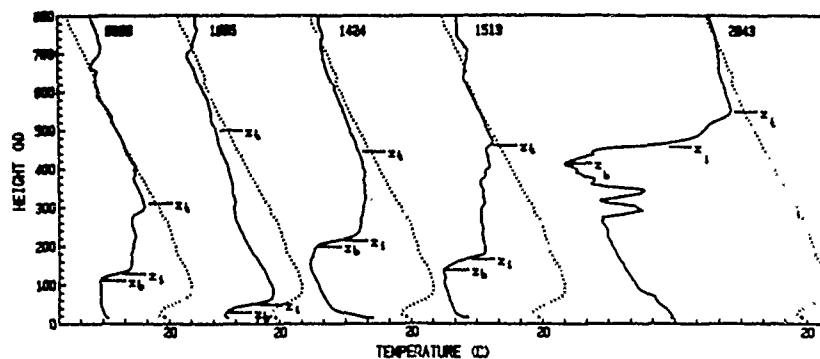


FIG. 2. Temperature profiles measured at the NW tip of SNI on 24 October 1984. Horizontal scale is in  $1^{\circ}\text{C}$  increments. Times indicated at the top of each profile are when the tethered balloon passed through the 400-m level; the significance of the  $z$  levels are described in the text. The dotted temperature profile is for 1500 on the preceding afternoon.

adjacent to the surface. Above the mixed layer is the approximately 30-m thick interfacial layer with a temperature jump of several degrees. The base of the interfacial layer is labeled  $z_b$ , and the center of the layer, labeled  $z_i$ , is the inversion height. Above the interfacial layer is a region of stable lapse rate defined as the transition layer. The top of the transition layer, labeled  $z_t$ , was arbitrarily defined as the height where the dotted and other profiles differed by  $0.5^{\circ}\text{C}$ .

The ocean surface water temperature at SNI decreased by  $4^{\circ}\text{C}$  between 0900 and 2100 LST. This cooling is unusually large for such a short period of time. We speculate that due to the 48 h of Santa Ana conditions prior to the jet event, the water near the surface was warmed by a combination of strong solar insolation and the near-calm wind conditions. The freshening of the westerly wind may have caused mixing of the surface water with the thermocline, and may also have generated upwelling of cold water which occurs in the general area.

The wind measurements were made with a miniature multicup anemometer provided by LTA and calibrated with a Simerl model 55 anemometer. The min-

iature anemometer was mounted on one of the balloon's fins about 2 m from the body of the balloon. This position undoubtedly caused the balloon to influence the wind measurements to some degree. The wind direction, estimated from the orientation of the balloon during flight, was westerly for all profiles on 24 October.

Wind profiles are shown in Fig. 3. In the free atmosphere wind speed increased slightly with height, but remained nearly constant with time. At 600 m the wind speed remained near  $7\text{ m s}^{-1}$ . In the lower atmosphere the evolution of a wind jet is clearly seen. The heights  $z_i$  and  $z_b$  are located in Fig. 3 at the same heights as determined for the temperature profiles in Fig. 2. As shown,  $z_i$  correlates well with the peak in the wind jet, and  $z_b$  correlates to a reasonable degree with the top of the jet for the 0900, 1424, and 1513 profiles. For the 1005 profile, a lack of correlation exists, because the atmosphere appears to have mixed through a deeper layer. In the 2043 profile the jet has nearly disappeared. This last profile is different from all the others, because by that time a stratocumulus deck with 5/10 coverage had formed with cloud base at 275 m and cloud top at 400 m.

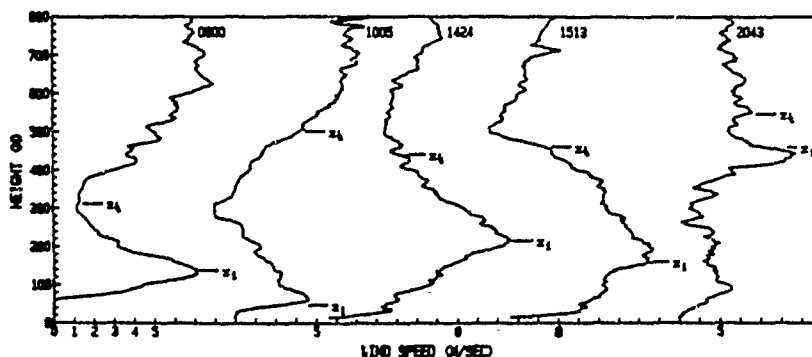


FIG. 3. Wind-speed profiles at the NW tip of SNI on 24 October 1984.

### b. Three-dimensional boundary layer structure

Unfortunately, no along-stream or cross-stream profiles were measured during the SNI experiment to firmly establish the 3D structure of the boundary layer in the vicinity of SNI on 24 October. The sketch of the thermal structure shown in Fig. 4 is based on indirect evidence and some speculation. The indicated N-S slope of the inversion is assumed to be a result of the westerly wind acting on the initially very shallow boundary layer which has more resistance to growth north of SNI than south of it, because of the greater temperature difference between the surface and the free atmosphere in the north. This hypothesis requires the assumptions that the initial surface isotherms are given by Fig. 1, that Santa Ana conditions resulted in a low boundary layer over the entire area, and that the free atmosphere was essentially horizontally homogeneous. The existence of the inversion slope is supported by the observation that the line separating the cloudy area from the clear area late on 24 October was oriented E-W, and moved gradually northward.

The evolution of the wind jet can be qualitatively explained by applying the definition of thermal wind to the estimated N-S temperature field. The westerly wind increases with height ( $\partial u / \partial z > 0$ ) in the mixed layer, because  $\partial T / \partial y < 0$ . In the interfacial and transition layers  $\partial u / \partial z$  decreases and  $\partial T / \partial y > 0$ , because of the sloped inversion. This pattern persisted during the growth of the boundary layer as shown by the good correlations between the position of the wind-jet maximum and  $z_i$ , and between the vertical extent of the jet and the  $z_i$ . Thus, the SNI wind jet appears to be a result of horizontal temperature gradients found at the sea surface and within the growing boundary layer, rather than due to an ocean-land temperature gradient above the inversion as for the wind-jet case described by Zemba and Friehe (1987).

### c. Boundary-layer growth

The boundary layer grew at the average rate of  $\partial z_i / \partial t = 1.04 \text{ cm s}^{-1}$  over the time interval shown in Figs.

2 and 3. This rate depends on the effects of subsidence, advection, and entrainment (Deardorff and Peterson 1980). Unfortunately, these effects cannot be separated for the SNI case, given the available measurements. It is only possible to say that the value of  $\partial z_i / \partial t$  is opposite in sign and much larger than the climatologically expected subsidence in the area due to the subtropical high, which can be estimated as  $-0.25 \text{ cm s}^{-1}$  at 500 m (Lilly 1968). This does not rule out that mesoscale convergence was a major contribution of  $\partial z_i / \partial t$  on 24 October, and the contribution due to the advection of inversion slope is unknown.

Values of  $\partial z_i / \partial t$  similar to the present case were found by Brost et al. (1982a) (hereafter referred to as BWL) in cloud-topped boundary-layer measurements off the California coast. They attributed the growth primarily to shear-induced entrainment in their 17 June case (mean shear of  $0.014 \text{ s}^{-1}$ ), which like the SNI case had a sloped inversion. Brost et al. suggested that in such cases, the inversion rise becomes a local problem decoupled from the mixed layer so that it is much less affected by the friction velocity  $u_*$  and buoyancy velocity scale  $W_b$ . The wind shear in the SNI case was larger than measured by BWL. The shear was  $0.05 \text{ s}^{-1}$  over the depth of the jet for the 1424 LST profile, and as much as  $0.1 \text{ s}^{-1}$  for the 0900 profile. This suggests that shear-generated turbulence was also a major contribution to the entrainment rate and boundary layer growth in the SNI case.

Additional insight on the physical mechanisms involved in the SNI boundary-layer growth is gained by comparing the temperature and wind profiles with profiles of the gradient Richardson number

$$Ri = \frac{g}{\theta_v} \frac{\partial \theta_v}{\partial z} \left[ \left( \frac{\partial u}{\partial z} \right)^2 + \left( \frac{\partial v}{\partial z} \right)^2 \right]^{-1/2}$$

where  $\theta_v$  is the mean virtual potential temperature,  $u$  and  $v$  are mean horizontal velocities,  $g$  is gravity, and the critical  $Ri$  number of 0.25 (Lyons et al. 1965) is shown by the dashed lines in Fig. 5. The profiles in

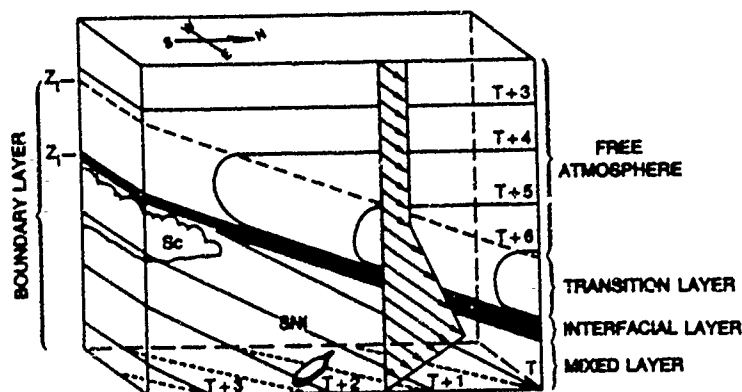


FIG. 4. Sketch of the position of the westerly wind jet with respect to the thermal structure of the atmosphere in the vicinity of SNI.

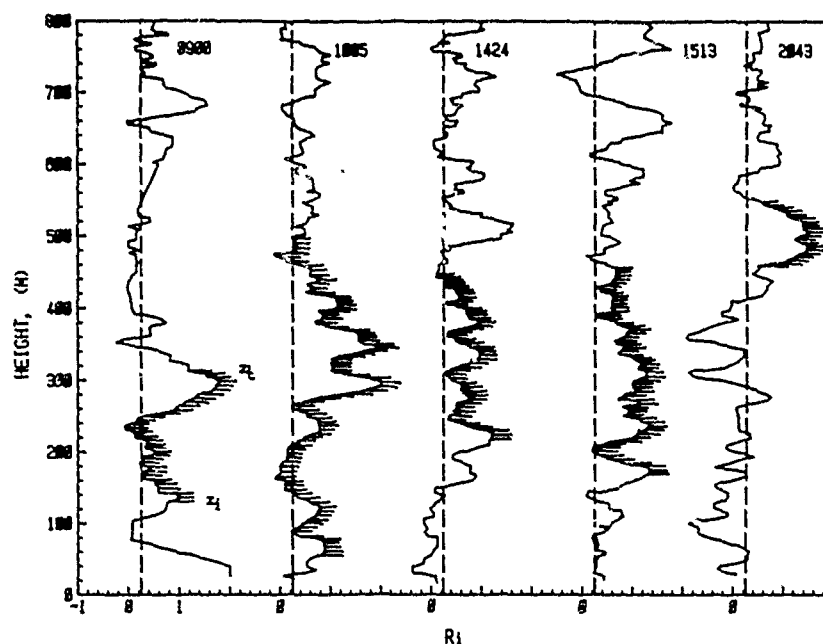


FIG. 5. Profiles of the gradient Richardson number calculated from the observed temperature and wind profiles shown in Figs. 2 and 3. Dashed lines show the critical Richardson number  $Ri = 0.25$ . The hatched areas show the portion of each profile bounded by the inversion height  $z_i$  and by the top of the transition layer  $z_t$ .

Fig. 5 are 2-min running averages, which require careful interpretation, since longer averaging periods are usually called for. The layers in the profiles of Fig. 5 where  $Ri < 0.25$  are areas of increasing turbulence and mixing. The consequence of such a layer, found for example between 350 and 550 m in the  $Ri$  profile for 0900, is seen by comparing the 0900 and 1005 profiles. By 1005 the atmosphere shows  $Ri > 0.25$  over this layer, indicating that turbulence is decreasing and that the atmosphere is in a relaxed state following mixing. Other layers where  $Ri < 0.25$  exist in all the profiles below  $z_i$ , and in some of the profiles in the transition layer. Because there are no superadiabatic lapse rates in those layers (excluding the shallow surface layer, which shows the effects of afternoon solar heating of the ground in the vicinity of the balloon site located 200 m from the ocean), it must be the wind shear that causes the increasing turbulence. Although the nearly adiabatic lapse rate in the mixed layer indicates continuous and strong mixing due to shear-induced turbulence, the upward growth of the mixed layer must be constrained by the temperature jump in the interfacial layer. This constraint is shown by positive values of  $Ri$  at the inversion height  $z_i$  for all profiles, indicating that here thermal stratification overpowers turbulence production by wind shear, and that a sink for turbulence exists. In the transition layer, however, shear-induced mixing appears to be sporadic as demonstrated by the first two sets of profiles in Fig. 5. In each case the transition layer has deepened by the descent of each balloon flight, and has mixed with adjacent portions

of the free atmosphere and the interfacial and mixed layers. The transition layer decreases the temperature jump at the inversion and thus must affect the upward growth of the mixed layer.

### 3. Model simulations

To test the hypothesis that the formation and evolution of the SNI boundary layer jet is mainly caused by the horizontal temperature gradients of a particular type and magnitude, a model simulation study was done. The following sections describe the quasi-2D model used in the modeling, the temperature distributions which must be prescribed for the model, and the results of the modeling.

#### a. Quasi-2D boundary layer model

The surface isotherms in Fig. 1, and the strong cooling seen in the evolving boundary layer in Fig. 2 suggest that cold air advection played an important role in the local meteorology on 24 October. Therefore, a purely one-dimensional model may preclude crucial factors in the observed boundary-layer evolution. Inclusion of the linearized advection of temperature gives the model the partial two-dimensionality. In addition, the horizontal temperature gradient will affect the pressure gradient force through the thermal-wind relationship. There is no horizontal advection of momentum in the model to make it fully 2D, mainly due to the lack of



information about the upstream wind profiles. Obviously, some aspects of the observed PBL behavior, such as the collapse episode at 1005 LST need a full 2D or even 3D model for realistic simulation. But, given the single point nature of our observation, this quasi-2D model is thought to be most suitable.

The equations of motion, and the thermal equation of the model are

$$\frac{\partial u}{\partial t} = f(v - v_g) + \frac{1}{\rho_0} \frac{\partial}{\partial z} \tau_x \quad (1)$$

$$\frac{\partial v}{\partial t} = -f(u - u_g) + \frac{1}{\rho_0} \frac{\partial}{\partial z} \tau_y \quad (2)$$

$$\frac{\partial T}{\partial t} = -u \left( \frac{\partial T}{\partial x} \right)_p - v \left( \frac{\partial T}{\partial y} \right)_p - \frac{1}{\rho_0 c_p} \frac{\partial}{\partial z} H \quad (3)$$

where the last terms represent vertical convergences of turbulent stresses and heat flux.

The horizontal pressure gradient forces  $-fv_g$  and  $fu_g$  are computed from top-down vertical integration of the thermal wind equations:

$$u_g(z) = u_g^T - \int_z^{z_T} \frac{g}{fT} \left( \frac{\partial T}{\partial y} \right)_p dz \quad (4)$$

$$v_g(z) = v_g^T + \int_z^{z_T} \frac{g}{fT} \left( \frac{\partial T}{\partial x} \right)_p dx. \quad (5)$$

The geostrophic wind at the top of the model is assumed to be the prevailing wind-observed above the boundary layer:  $u_g^T = 7 \text{ m s}^{-1}$  and  $v_g^T = 0$ . The horizontal temperature gradients  $(\partial T/\partial x)_p$  and  $(\partial T/\partial y)_p$  are prescribed as shown in section 3b ( $p = \text{prescribed}$ ). Note that those gradients are also used for the horizontal thermal advection in (3).

The model has 30 grid points extending from the surface to 900 m with a uniform grid distance of 30 m. At the lowest grid point, 15 m above the surface,  $u$ ,  $v$ , and  $T$  represent the mean velocity components and the temperature in the surface layer. All momentum and heat fluxes are defined at the surface and at midpoints between adjacent grid points for computational convenience.

For the surface layer, Businger's (1973) formulas are used to compute the surface fluxes based on the Monin-Obukhov stability and potential temperature in the surface layer. The nondimensional equations for the friction velocity and potential temperature are

$$\frac{V_s}{u_*} = \frac{1}{\kappa} \left[ \ln \left( \frac{z_s}{z_0} \right) - \psi_m \left( \frac{z_s}{L} \right) \right] \quad (6)$$

$$\frac{\theta_s - \theta_0}{\theta_*} = 0.74 \left[ \ln \left( \frac{z_s}{z_0} \right) - \psi_h \left( \frac{z_s}{L} \right) \right] \quad (7)$$

where  $V_s = (u_s^2 + v_s^2)^{1/2}$ ,  $z_s = 15 \text{ m}$ , and the stability functions  $\psi_m(z_s/L)$  and  $\psi_h(z_s/L)$  are given in the integral form of Businger's  $\phi_m$  and  $\phi_h$  stability functions

(Businger 1973; Paulson 1970). The Monin-Obukhov stability parameter  $L$  is defined as

$$L = \frac{\rho_0 T u_*^2}{g k \theta_*}, \quad (8)$$

and Charnock's equation (Delsol et al. 1971),

$$z_0 = 0.032 \frac{u_*^2}{g}, \quad (9)$$

is used to compute the ocean's surface roughness.

The surface momentum and heat fluxes are then

$$\tau_x = \rho_0 u_*^2 \frac{u_s}{|V_s|} \quad (10)$$

$$\tau_y = \rho_0 u_*^2 \frac{v_s}{|V_s|} \quad (11)$$

$$H = -\rho_0 c_p u_* \theta_*. \quad (12)$$

Above the surface layer, turbulent mixing is described by a turbulent kinetic energy (TKE) equation and an equation for the rate of dissipation. The eddy viscosity is expressed in the model in terms of TKE and dissipation rate as (Kolmogorov 1942; Monin and Yaglom 1971)

$$K_m = c_2 \frac{E^2}{\epsilon} \quad (13)$$

where  $c_2 = 0.026$ .

The prognostic equation for TKE is (e.g., Monin and Yaglom 1971)

$$\frac{\partial E}{\partial t} = -\overline{u'w'} \frac{\partial u}{\partial z} - \overline{v'w'} \frac{\partial v}{\partial z} + \frac{g}{\theta} \overline{w'\theta'} - \frac{\partial}{\partial z} \left[ \overline{w'E'} + \frac{\overline{p'w'}}{\rho} \right] - \epsilon \quad (14)$$

where the fourth term on the right can be modeled by the  $K_m$  coefficient following Rodi (1980). Thus (14) becomes

$$\frac{\partial E}{\partial t} = -\left[ \overline{u'w'} \frac{\partial u}{\partial z} + \overline{v'w'} \frac{\partial v}{\partial z} \right] + \frac{g}{\theta} \overline{w'\theta'} - \frac{\partial}{\partial z} \left( K_m \frac{\partial E}{\partial z} \right) - \epsilon \quad (15)$$

where the terms on the right are, respectively, the shear production rate, the buoyancy production rate, the turbulent transport rate, and the dissipation rate. The prognostic equation for the dissipation is (Wyngaard 1975; Marchuk et al. 1977; Lumley 1980)

$$\frac{\partial \epsilon}{\partial t} = -C_3 \frac{\epsilon}{E} \left( \overline{u'w'} \frac{\partial u}{\partial z} + \overline{v'w'} \frac{\partial v}{\partial z} \right) - C_4 \frac{\epsilon^2}{E} + C_5 \frac{\partial}{\partial z} \left( K_m \frac{\partial \epsilon}{\partial z} \right) \quad (16)$$

where the terms on the right represent respectively the generation of  $\epsilon$ , the destruction of  $\epsilon$ , and the turbulent transport. The constants in (16) are (Detering and Etling 1985)

$$C_3 = 1.38, \quad C_4 = 1.90, \quad \text{and} \quad C_5 = 0.77.$$

The fluxes of momentum and heat above the surface layer are then

$$\tau_x = -\rho \overline{u'w'} = \rho K_m \frac{\partial u}{\partial z} \quad (17)$$

$$\tau_y = -\rho \overline{v'w'} = \rho K_m \frac{\partial v}{\partial z} \quad (18)$$

$$H = \rho c_p \overline{\theta'w'} = \rho c_p K_h \frac{\partial \theta}{\partial z} \quad (19)$$

where  $K_h$  is related to  $K_m$  by the turbulent Prandtl number  $\phi_m/\phi_h$  (Businger 1973).

#### b. Prescribed temperature gradients

The gradients  $(\partial T/\partial x)_p$  and  $(\partial T/\partial y)_p$ , required in (3)–(5), are estimated from Figs. 1–3. For the surface and mixed layers ( $0 \leq z < z_i$ )

$$\left(\frac{\partial T}{\partial x}\right)_p = 0.02^\circ\text{C km}^{-1} \quad (20)$$

which is the same as the sea surface gradient  $(\partial T/\partial x)_0$  estimated from Fig. 1. The sea surface temperature is cooled linearly by  $4^\circ\text{C}$  over 12 h, an amount consistent with observation.

Above the inversion ( $z > z_i$ ) it is assumed that

$$\left(\frac{\partial T}{\partial x}\right)_p = 0 \quad (21)$$

and that both (20) and (21) are independent of time.

At the sharpest part of the inversion

$$\left(\frac{\partial T}{\partial y}\right)_i = \left(\frac{\partial T}{\partial z}\right)_i \tan \theta \quad (22)$$

where  $\tan \theta = \partial z_i/\partial y$  is the slope of the inversion, and  $(\partial T/\partial z)_i = 0.067^\circ\text{C m}^{-1}$  is the largest vertical temperature gradient seen in the measured temperature profiles. It is speculated that by late on 24 October the slope had become small, since only remnants of the thermal-wind jet remained, and the growth of the boundary layer had slowed. To account for those changes in a simple way, the assumptions are made that  $\partial z_i/\partial y$  depends linearly on height, and that  $\partial z_i/\partial y = 0$  when the boundary layer has grown to a maximum height of  $z_m = 700$  m. This gives

$$\frac{\partial z_i}{\partial y} = \left(\frac{\partial z}{\partial y}\right)_0 \left(1 - \frac{z_i}{z_m}\right) \quad (23)$$

where  $(\partial z/\partial y)_0$  was assumed to equal  $-0.004$ . With these values of  $z_m$  and  $(\partial z/\partial y)_0$ , and for  $z_i = 350$  m,

(23) yields  $\partial z_i/\partial y = -0.002$  which is about the same as the inversion slope of a cloud-topped boundary layer off the California coast observed by Brost et al. (1982b).

In the transition layer,  $(\partial T/\partial y)_p$  is complex as shown in the sketch of Fig. 6 which was constructed by using (22), (23) and the typical shape of this layer estimated from the temperature profiles. The dashed curve in Fig. 6 is the approximate relationship between  $(\partial T/\partial y)_p$  and  $z$  used in the modeling. Between  $z_i$  and the top  $z_t$  of the transition layer,  $(\partial T/\partial y)_p$  and  $z$  are linearly related so that

$$z = \frac{-z_i}{(\partial T/\partial y)_i} \left(\frac{\partial T}{\partial y}\right)_p + z_i + z_t. \quad (24)$$

Combining (22)–(24) gives

$$\left(\frac{\partial T}{\partial y}\right)_p = \left(\frac{\partial T}{\partial z}\right)_i \left(\frac{\partial z}{\partial y}\right)_0 \left(1 - \frac{z_i}{z_m}\right) \left(\frac{z_i}{z_t} - \frac{z}{z_t} + 1\right) \quad (25)$$

for the transition layer ( $z_i \leq z \leq z_t$ ).

Above the transition layer ( $z > z_t$ ),

$$\left(\frac{\partial T}{\partial y}\right)_p = 0. \quad (26)$$

Below the inversion ( $0 \leq z < z_i$ ),

$$\left(\frac{\partial T}{\partial y}\right)_p = \left(\frac{\partial T}{\partial y}\right)_0 \left(1 - \frac{z_i}{z_m}\right) \quad (27)$$

where  $(\partial T/\partial y)_0 = -0.02^\circ\text{C km}^{-1}$  is the sea surface gradient, and  $(1 - z_i/z_m)$  gives the same evolution of  $(\partial T/\partial y)_0$  as  $\partial z_i/\partial y$  in (23). This is used, because advection from the large pool of cool water west of SNI as seen in the monthly mean isotherms will cool the sea surface near SNI more rapidly than areas north of

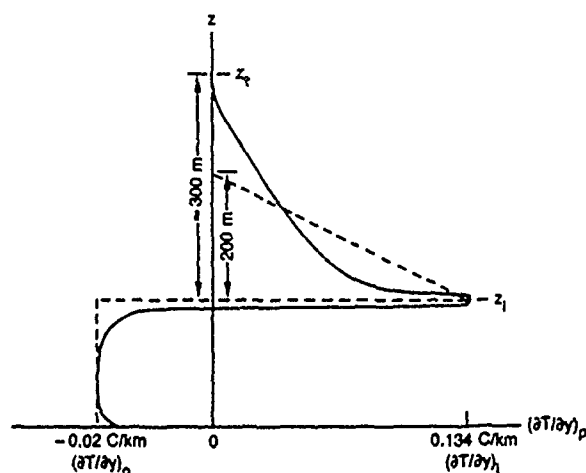


FIG. 6. Sketch of the height dependence of the horizontal temperature gradient in the northerly direction deduced from observations (solid line), and used in the model (dashed line). Not drawn to scale.

the island, so that the N-S temperature gradient will tend to decrease.

### c. Control experiment

The control experiment consisted of using the quasi-2D model with the prescribed temperature gradients given in subsection 3b, and with the measured temperature and wind profiles at 0900 LST (Figs. 2 and 3) as initial conditions. The initial wind direction was assigned to be westerly which was the estimated orientation of the balloon during its ascent at 0900.

The vertical profiles of temperature and wind speed predicted by the model for this experiment are shown in Figs. 7 and 8, respectively. A comparison of those profiles with the measured profiles in Figs. 2 and 3 shows that the model reproduced the main features of the measured profiles with good accuracy. Similarities between the predicted and measured evolution of the profiles include the following: The temperature profiles show a well-mixed layer below the interfacial layer, and a transition layer between the interfacial layer and the free atmosphere. Cooling near the surface is about  $4^{\circ}\text{C}$ , and just below  $z_b$  it is much greater. The inversion height, initially at 125 m at 0900 LST, rises to  $\sim 450$  m 12 h later, and the rate of its rise slows at the end of the period. The good agreement in inversion rise is partly a result of tuning the model by varying the value of  $z_m$  in (23). The initial value of  $z_m = 500$  m gave a total inversion rise of 100 m less than found in the control experiment, where  $z_m = 700$  m was used. This result suggests that at 2100 LST, the inversion still had some slope, and that the inversion rise is very sensitive to the magnitude of the slope. The wind profiles show an evolving wind jet of similar strength and of ap-

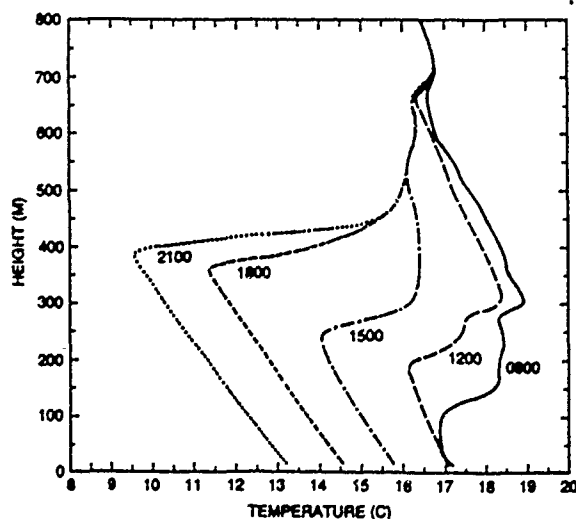


FIG. 7. Time evolution of temperature profiles predicted by the control run of the quasi-2D model using the observed temperature and wind profiles at 0900 LST and the prescribed horizontal temperature gradients as the initial conditions.

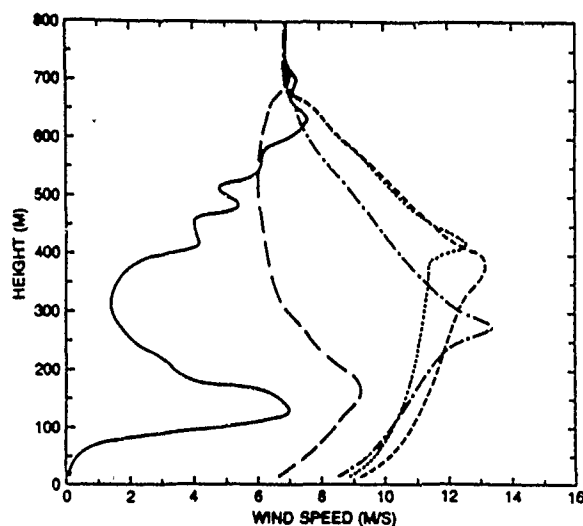


FIG. 8. As in Fig. 7, but for predicted wind-speed profiles.

proximately symmetrical shape whose peak is found within the rising interfacial layer (except profile 1200 LST).

The major difference between the modeled and measured temperature and wind profiles is that the model results do not reproduce the same sporadic rise of the interfacial layer as seen in the measurements. Some sporadicity in the modeled temperature profiles is seen where the heat loss from the transition layer is unsteady (see profiles at 0900, 1200, and 1500 LST); however, differences exist in the shape of the transition layer, and in the vertical extent of the modeled jet which was 150 m too high. As discussed before, these differences may be caused by the essentially 1D nature of the model which precludes the proper behavior of larger eddies, and by the assumptions used in the prescribed temperature gradients. Another difference is that modeled wind speeds in the lower mixed layer are  $2\text{--}3\text{ m s}^{-1}$  too high. This may be a result of the surface roughness given by (9) being too small for the ocean/beach interface of the observing site. The modeled wind direction was WSW rather than the westerly direction estimated from the orientation of the balloon. Finally, the temperature just below  $z_b$  for 2100 is about  $1^{\circ}\text{C}$  warmer than the measured temperature. This difference combined with the wind overestimate suggests that  $(\partial T/\partial x)_0 = 0.02^{\circ}\text{C km}^{-1}$  used in the model is too small.

Energy fluxes and turbulence budgets were calculated with the model and are described next. Figures 9 and 10 show, respectively, the heat and momentum fluxes evaluated for the same times as shown in Figs. 7 and 8. The heat-flux profiles after 1200 LST show a negative peak which coincides with  $z_b$ , an increasingly negative gradient below the peak indicating the effects of cold advection, and a decrease to zero just above the peak of the jet located in the interfacial layer. The downward heat flux peaked at  $z_b$  shows that warmer

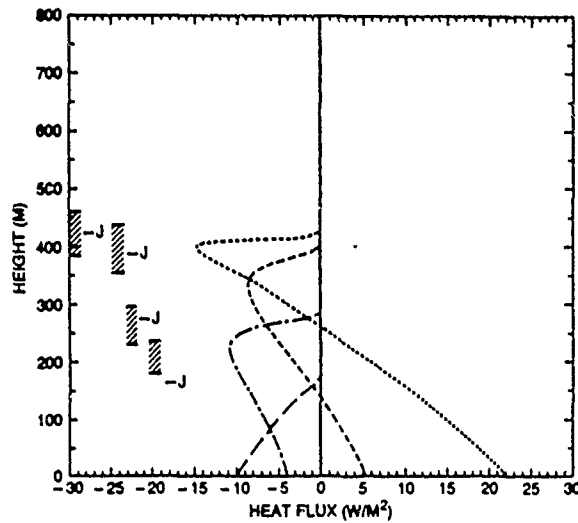


FIG. 9. As in Fig. 7, but for predicted heat-flux profiles. For each profile the hatched area gives the location of the interfacial layer determined from Fig. 7, and  $J$  indicates the height of the wind-jet peak found from Fig. 8. The times corresponding to the hatched areas and positions of  $J$  are, respectively, 2100, 1800, 1500, 1200 LST from top to bottom.

air from the interfacial layer is being entrained into the mixed layer. The profile for 1200 LST does not show evidence of such entrainment. This difference appears to be a result of the location of the peak of the jet. When it peaks within the interfacial layer strong entrainment occurs at  $z_b$ ; when it peaks below  $z_b$  as in 1200 LST no entrainment is evident. The profile for 1200 LST differs because early in the modeling period the mixed layer cooled at a slower rate than the prescribed linear cooling rate of the surface, thus creating temporary warm advection in the mixed layer. The instantaneous heat flux profiles in Fig. 9 cannot be considered to be quasi-steady, because the profiles in

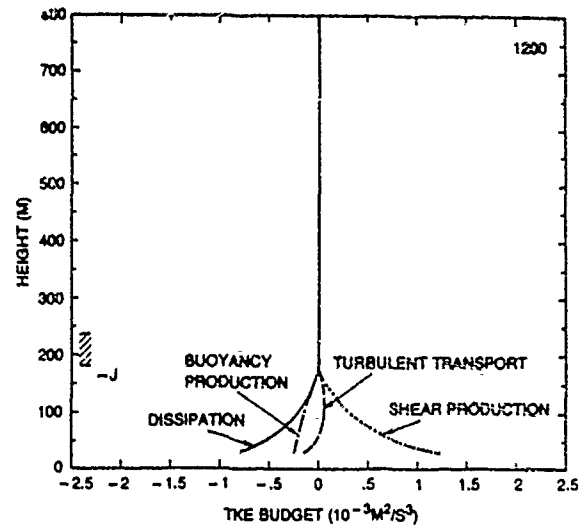


FIG. 11. Turbulent kinetic energy budget predicted by the control run of the quasi-2D model for 1200. Shear production: dotted curve; turbulent transport: dashed curve; buoyancy production: dot-dashed curve; and dissipation: solid line curve.

Fig. 9 do not show heat flux through the top of the interfacial layer, which must occur sporadically as indicated by the heat loss in the transition layer (see Fig. 7) where there is no temperature advection. The momentum fluxes in Fig. 10 decrease linearly with height, and also become zero at the same levels as the heat fluxes.

Figures 11–14 show the calculated TKE budgets. All profiles after 1200 LST show shear production has a maximum near the surface, decreases upward, and then increases to a local maximum at  $z_b$ . Above this level it decreases to 0 near the peak of the jet. The buoyant production has a negative peak at  $z_b$ , and its surface value reflects the effect of cold advection. Dissipation

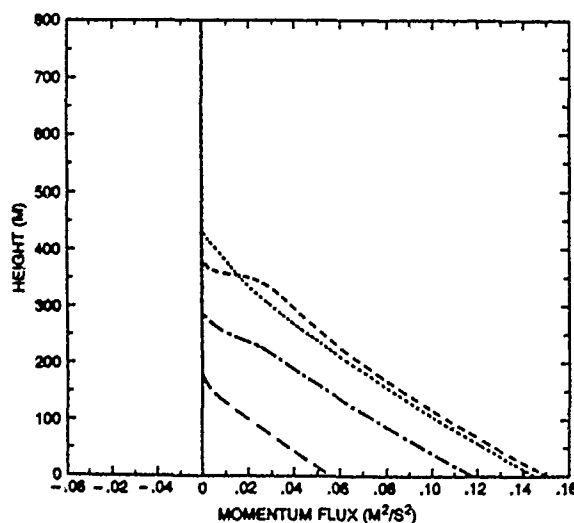


FIG. 10. As in Fig. 7, but for predicted momentum flux.

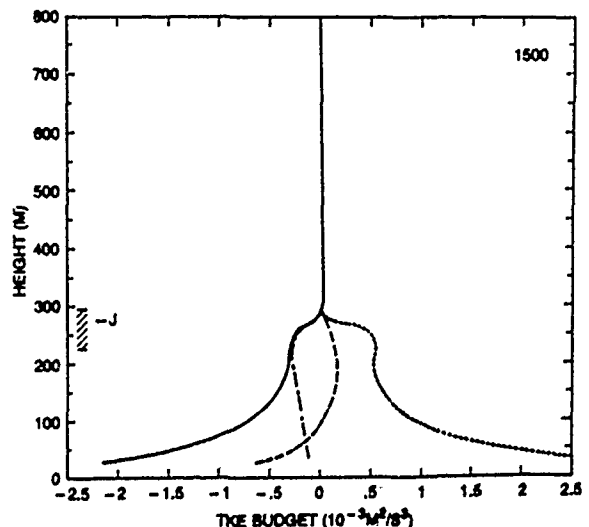


FIG. 12. As in Fig. 11, but for 1500 LST.

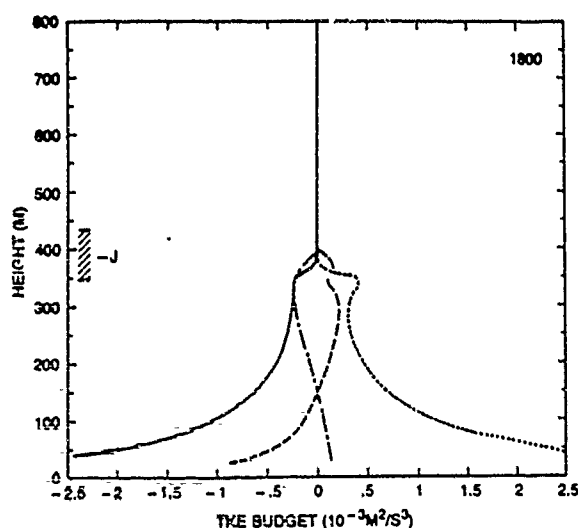


FIG. 13. As in Fig. 11, but for 1800 LST.

is nearly a mirror image of the shear production, but its magnitude is slightly less; the turbulent transport of TKE suggests an upward transport from the lower to the upper portion of the mixed layer.

The peaks of shear and negative buoyancy production at  $z_b$  are consistent with the peaks of downward heat flux found at  $z_b$ , and indicate that shear-generated TKE just under the peak of the jet is causing entrainment of stable interfacial-layer air into the top of the mixed layer. The existence of this entrainment region is indirectly confirmed by the location of the peak of the jet in the interfacial layer. The prescribed temperature gradients that correspond to a capped mixed layer, cooler and lower in the northerly direction, should cause  $\partial T/\partial y$  to change its sign at  $z_b$ . The thermal wind should thus also change the sign of its vertical gradient and show a peak at  $z_b$ . The fact that the peak of the jet is found higher in the interfacial layer indicates that the air near the base of this layer has lost momentum by mixing with slower moving air just below. This effect also appears to apply to the SNI observations, because the wind jet is found within the interfacial layer, rather than at  $z_b$ .

The TKE budget profiles for 1200 in Fig. 11 again differ from the subsequent profiles, because the peak of the jet is found below  $z_b$  at 1200. In this case the growth may have been more dependent on convection due to buoyancy and shear production at the surface. This raises the question, addressed in subsequent sections, on the relative importance of surface convection vs shear production by the jet on the growth of the mixed layer.

The modeled heat flux and TKE budgets resemble those measured by BWL (case 17-2). This may not be a coincidence, because of the similarities between the environmental conditions for their case 17-2 and the SNI episode described here. Both cases have cold air advection over surface isotherms turned about 45 deg

to the surface wind. The warm air is to the right of the wind direction, which is also the direction of the increasing height of a sloped inversion, and strong wind shears exist near the inversion. Case 17-2 has no wind jet, because in this case the thermal wind causes a different vertical wind gradient, since a northerly wind is crossing isotherms oriented NW-SE. The most obvious difference between the 17-2 and SNI cases is that the former corresponds to a marine boundary layer topped with stratocumulus clouds while the latter is a clear-air case. The evidence found by BWL that buoyancy production by convection and by cloud-top radiative cooling in the clouds was small compared to shear production in case 17-2, may be the reason that the 17-2 and SNI cases agree as well as they do. It is tempting to apply the entrainment situation predicted by the present model to the 17-2 case. This application unfortunately cannot be tested with the BWL data, because of the poor resolution of their profiles near the inversion, and because of possible "aircraft bias error" which is a symptom of fast aircraft penetrations through shallow and undulating features such as an interfacial layer.

#### d. Sensitivity experiments

A series of experiments were run in which the initial conditions of the control experiment were changed in a systematic way to test the sensitivities of the jet to external factors such as the horizontal temperature gradients, the slope of inversion, and the initial wind profile.

In the first experiment we changed the control by giving the inversion a slope in the  $x$  direction equal to and opposite in sign to the slope in the  $y$  direction, and by describing  $(\partial T/\partial x)_p$  by equations similar to (25)–(27), but in terms of  $x$ . Thus for this experiment the inversion rises towards the SE where the warmest

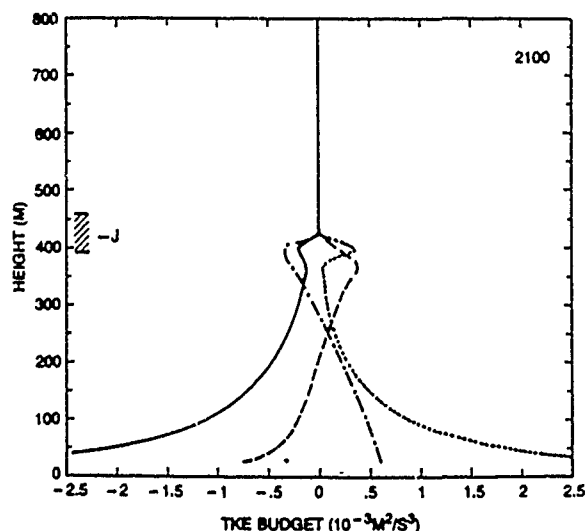


FIG. 14. As in Fig. 11, but for 2100 LST.

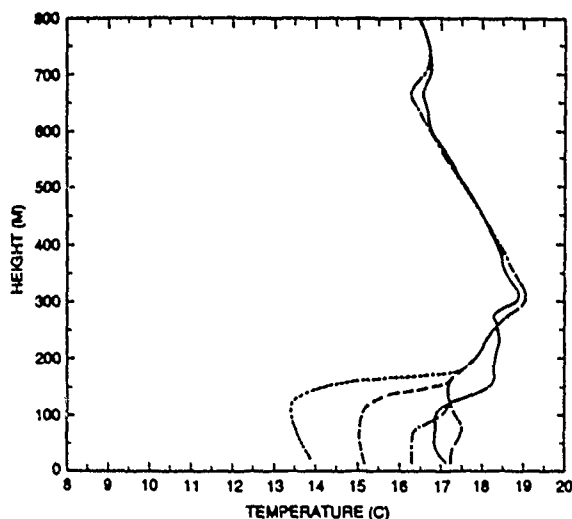


FIG. 15. Time evolution of temperature profiles predicted by a sensitivity run of the quasi-2D model for which there was no slope to the inversion. Curves correspond to the same times used in Fig. 7.

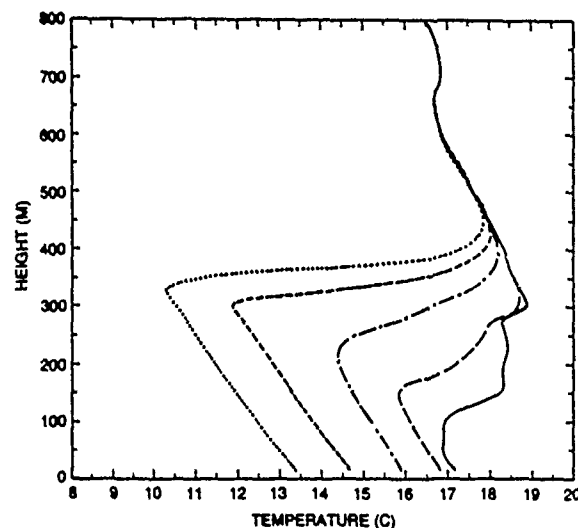


FIG. 17. Temperature profiles for a sensitivity run of the model for which the initial wind-speed profile was constant with height. Curves correspond to the same times as in Fig. 7.

sea surface temperatures are thought to exist. The results (not shown) resemble the control run, in that the mixed layer grows as a result of shear-induced entrainment at the base of the interfacial layer. However, those results do not compare as well to the experimental observations as does the control, because the jet is weaker. This suggests that the inversion rises more towards the S rather than the SE, as supported by the observed E-W orientation of the line separating the Sc layer from the clear area.

In the second experiment the only change from the control was to keep the inversion horizontal. The predicted temperature and wind profiles are shown in Figs. 15 and 16; the mixed layer only grew about 50 m, but

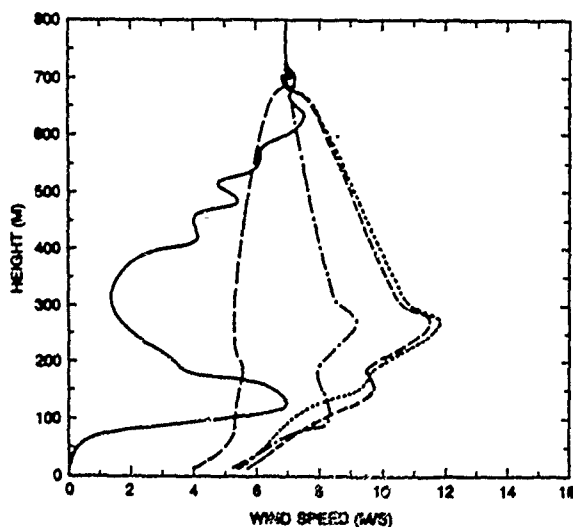


FIG. 16. As in Fig. 15, but for wind profiles.

a jet is again evident. Comparing the jet in Fig. 16 with the wind profiles of the control (Fig. 8) shows that the jet does not coincide with the interfacial layer, and it is weaker. This experiment shows that the sloped inversion and a properly positioned jet are necessary for rapid mixed-layer growth.

In the third experiment the only change from the control was to make the atmosphere horizontally isothermal. The predicted wind profiles (not shown) showed a jet very similar to that of Fig. 16. This result, and the fact that this jet has a maximum which is collocated with the wind minimum in the initial wind profiles, suggests that the inertial acceleration of wind field also contributes to the formation of the jet.

The effect of the wind deficit was removed for the fourth experiment by including in the control a wind profile with a constant  $7 \text{ m s}^{-1}$  wind speed at all heights as the initial condition. The predicted profiles are shown in Figs. 17–19. The strength of the jet is less, the upper limit of the jet is lower, and the mixed layer is about 15% lower than in the control experiment. Those results indicate that the wind shear located above the interfacial layer (see 0900 LST in Fig. 8) enhances the growth rate of the mixed layer as also deduced from the Ri analysis in Fig. 5. With no shear in this sensitivity experiment, the temperature jump and gradient in the interfacial layer increase, and the vertical extent of the transition layer is smaller. The effect of those changes on the TKE budget at 1800 LST are shown in Fig. 19, which should be compared with Fig. 13. While the positions of the jet and the peaks in shear, buoyancy, and dissipation remain the same relative to  $z_i$  in this experiment and in the control, the TKE peaks are much sharper and are found over a more shallow layer in this experiment. The shear production peak as well as the temperature jump for this experiment are now

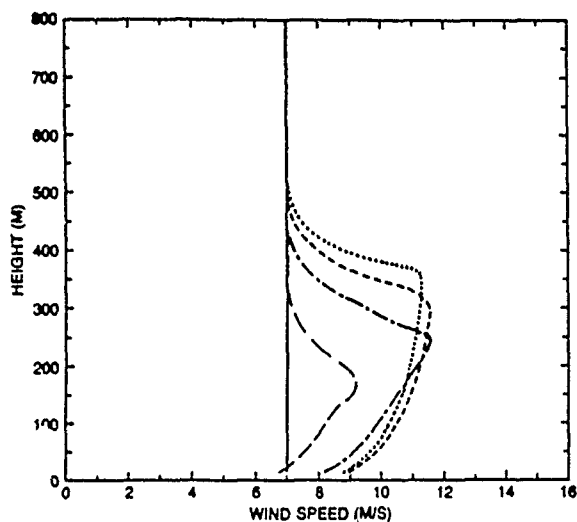


FIG. 18. As in Fig. 17, but for predicted wind-speed profiles.

closer in appearance to the same quantities in case 17-2 of BWL.

In the fifth experiment  $(\partial T / \partial y)_0$  is set to 0 to represent a sea surface temperature distribution that has no N-S gradient. With everything else remaining the same, the model predicts wind and temperature profiles similar to those in Figs. 15 and 16. In this case the westerly component of the geostrophic wind shear is much weaker than the control, so that shear production near the interfacial area is smaller and limits the growth of the mixed layer.

In the final experiment the only change in the control is the sign of  $(\partial T / \partial y)_0$  which is now positive. This places the cooler air to the SW and the warmer air to the NE so that initially the westerly wind produces warm advection. The model results, shown in Figs. 20

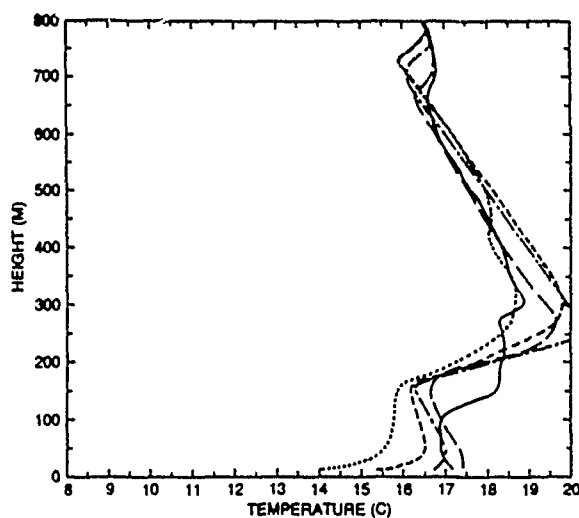


FIG. 20. Temperature profiles for a sensitivity run of the model for which the sign of the surface temperature gradient in the easterly direction was changed. Curves correspond to the same times as in Fig. 7.

and 21, are very different from the control. The imposed temperature distribution causes temperatures to remain relatively unchanged in the boundary layer, except for the surface cooling and some advection modulated changes above the inversion. The effects of advection are generally weaker in this experiment, because the northerly mixed layer winds are at small angles to the NW-SE oriented isotherms.

These modeling results support the hypothesis offered in section 2 that the SNI boundary layer jet was forced by the specified mesoscale temperature field and the sloping inversion, and that entrainment caused by wind shear associated with the jet was crucial in the rapid growth of the mixed layer. They further suggest

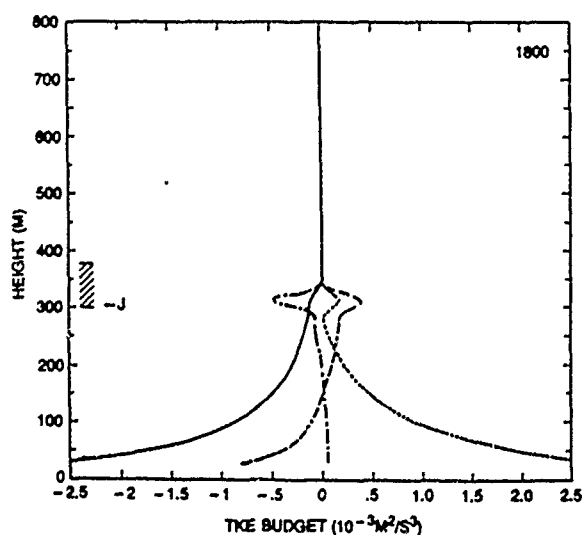


FIG. 19. As in Fig. 17, but for predicted kinetic energy budget. Curves correspond to the same quantities as in Fig. 11.

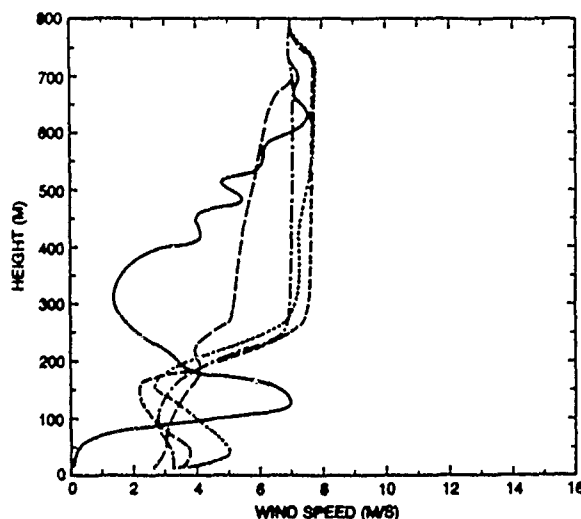


FIG. 21. As in Fig. 20, but for predicted wind-speed profiles.

that thermal advection over sea surface isotherms oriented differently than the specified field will result in different boundary layer behavior.

#### 4. Entrainment

Previous methods of parameterizing entrainment can be compared to the observed rise of the SNI boundary layer under the assumption that advection and divergence did not affect the entrainment. The first method is a traditional convective entrainment parameterization, where the entrainment velocity is given by (Stull 1976)

$$W_{\epsilon} = 0.2 W_m / R, \quad (28)$$

where

$$W_m^3 = W_*^3 + 8u_*^3 \quad (29)$$

is the mixed-layer scaling velocity suggested by Tennekes and Driedonks (1981),  $R$  is a bulk stability parameter given by

$$R = g \Delta \theta_v z_1 / (W_m^2 T) \quad (30)$$

and  $\Delta \theta_v$  is the virtual potential temperature jump across the interfacial layer.

The buoyancy velocity scale  $W_*$  and friction velocity  $u_*$  are given by the usual expressions:

$$W_*^3 = g z_1 w' \theta'_{v1} / T = g H z_1 / (c_p \rho T_0) \quad (31)$$

$$u_* = u k / \ln(z/z_1) \quad (32)$$

where  $z_1 = 4 \times 10^{-4}$  m is an average value of the roughness length measured by Blanc (1982) at the SNI experimental site,  $H$  is the surface heat flux, and the other parameters have the usual meaning.

The profiles in Figs. 2 and 4, and  $H = 10 \text{ W m}^{-2}$  taken from the modeling results in Fig. 9 were used to roughly estimate that  $W_* = 0.33 \text{ m s}^{-1}$  and  $u_* = 0.31 \text{ m s}^{-1}$  were mean values of those quantities during the 12-h observation period; furthermore,  $R = 29.7$ ,  $W_m = 0.65 \text{ m s}^{-1}$ , and  $W_{\epsilon} = 0.44 \text{ cm s}^{-1}$ . The value of  $W_{\epsilon}$  is less than half of the observed entrainment value of  $1.04 \text{ cm s}^{-1}$ . This comes as no surprise, because the traditional entrainment parameterization does not include the effects of wind shear. The value of  $W_{\epsilon}$  is somewhat larger than expected in light of the sensitivity experiments (2, 3, and 5) for which the lack of a proper jet suggested that the growth of the mixed layer was primarily due to forced convection from surface-generated wind shear. The 12-h 50-m growth of the mixed layer, and a surface layer wind of  $6 \text{ m s}^{-1}$  for those sensitivity experiments, translates to an expected growth of about 100 m for the control run when only convective entrainment is considered, rather than to about 200 m which corresponds to  $W_{\epsilon} = 0.44 \text{ cm s}^{-1}$ .

The second comparison is made between the SNI observations and the more recent work of Fairall (1984) which includes wind shear in the entrainment parameterization. He essentially combines the ap-

proach of Wyngaard and LeMone (1980) for calculating structure function parameters in terms of the scalar variance budget equations in the interfacial layer with the conceptual model of Deardorff (1979) for the vertical distribution of the scalar in the layer, to arrive at the dissipation rate of shear produced in the layer. The dissipation rate is then combined with Deardorff's (1980) parameterization of vertical velocity variance in the layer to yield a nondimensional entrainment velocity  $X$  given by

$$X = \frac{W_{\epsilon}}{W_{\epsilon c}} = 1 + \frac{r R_f^{-1} (2 + r R_f^{-1})}{1 + 2(1 + r R_f^{-1})(s - r R_f^{-1})} \quad (33)$$

where  $W_{\epsilon}$  is the entrainment velocity including shear in the interfacial layer,  $W_{\epsilon c}$  is the same as defined in (28),  $r$  and  $s$  are quasi-constants which depend on  $c1 = 11$  and  $c2 = 0.214$  [see Fairall (1984) for an explanation], and  $R_f^{-1}$  is the reciprocal of the flux Richardson number for the interfacial layer given by

$$R_f^{-1} = \frac{7(\Delta S_h)^2 \Gamma}{6(g/T)(\Delta \theta_v)^2} \quad (34)$$

where  $\Delta S_h$  is the wind speed jump across the interfacial layer, and  $\Gamma$  is the potential temperature gradient above the layer. From the observed profiles in Figs. 2 and 3, mean values for the quantities in (33) and (34) are estimated to be  $\Delta S_h = 1.22 \text{ m s}^{-1}$ ,  $\Gamma = 0.0099 \text{ C m}^{-1}$ ,  $\Delta \theta_v = 1.6 \text{ K}$ ,  $R_f^{-1} = 0.21$ ,  $X = 1.099$ , and  $W_{\epsilon} = 0.480 \text{ cm s}^{-1}$ .

Thus, Fairall's (1984) approach also does not predict the rapid rise of the SNI mixed layer. In fairness to his approach, the SNI situation is not a good test of his expression for  $W_{\epsilon}$ , because the SNI conditions differ markedly from Deardorff's (1979) generalized inversion structure model on which Fairall's (1984) derivation is based. Deardorff's conceptual model requires the following conditions: buoyancy production due to entrainment has a negative peak in the center of the interfacial layer [with an enhancement due to shear production added by Fairall (1984)], buoyancy production is 0 at the top of the interfacial layer and has a crossover point near  $z_b$ , and except in the surface and mixed layers there is no wind shear. Clearly the SNI case does not meet those requirements.

Tennekes and Driedonks (1981) review other approaches for parameterizing entrainment with shear. Those approaches also correspond to conditions which do not resemble the SNI case, so that an appropriate expression for  $W_{\epsilon}$  most likely does not exist.

A model for parameterizing the entrainment in the SNI case should include the growth mechanisms which, from the observations and modeling of the SNI case, are proposed as follows: The presence of the wind jet associated with the sloped inversion causes the rapid growth of the boundary layer, but in an unexpected way. The forced convection due to shear production at the surface does not directly influence entrainment to a large degree, but steepens the temperature gradient



in the lower portion of the interfacial layer. This in turn strengthens the wind gradient of the jet, located in the sloped layer, according to the thermal wind relationship, and the jet then causes the entrainment at the base of the interfacial layer where mixing requires the least amount of energy. Thus shear-induced entrainment in the SNI case is not decoupled from the mixed layer as suggested by BWL for their similar case, but depends indirectly on surface-generated convection. The wind shear of the jet also results in sporadic breakdowns in the atmosphere above the interfacial layer, forming a temperature transition layer which mixes with the free atmosphere and the interfacial layer. The transition layer decreases the temperature jump of the interfacial layer thus also enhancing mixed layer growth. On the other hand, air mixing with the interfacial layer from below and above also has the opposite effect: mixing decreases the temperature and thermal-wind gradients in the interfacial layer reducing wind shear, thus slowing mixed layer growth. These competing growth mechanisms appear to be in balance, giving a reasonably stable growth rate of the mixed layer. This balance may be reflected in the observed nearly unchanging shape of the temperature profile in the interfacial layers in Fig. 2; all vertical profiles, except for the last, show an interfacial layer about 30 m thick, with a temperature jump of 2°C, and with nearly identical vertical gradients.

A worthwhile future effort is an attempt to parameterize the entrainment in the SNI case and in similar cases along the lines used by Fairall (1984), but with a more appropriate conceptual model. This would hopefully lead to useful  $W_e$  scaling relationships which include all pertinent meteorological parameters discussed here. As a first step in this direction we offer the relationship

$$W_e \text{ (cm s}^{-1}\text{)} = -300\partial z_i/\partial y \quad (35)$$

which is our best estimate of  $W_e$  based on the modeling results which showed an approximately linear relationship between  $W_e$  and the slope of the inversion for the SNI episode.

## 5. Conclusions

We found that the formation and evolution of the SNI boundary layer jet was due to the interaction of an inertial oscillation of the westerly wind with a sea surface temperature gradient that had isotherms angled SW to NE, and with the resulting horizontal temperature gradients formed in the atmosphere by wind shear and a sloped temperature inversion. Measurements of the temperature and wind fields suggested those formation mechanisms, and model simulations supported them. The formation of a similar thermal-wind jet described by Zemba and Friehe (1987) required a land-ocean temperature contrast. The SNI jet differs in that

it could exist elsewhere over the oceans where similar temperature advection and mesoscale gradients exist.

The rapid growth of the boundary layer was a result of the wind jet whose peak was located within the sloped interfacial layer. The mechanism for the rapid growth included weak mixing at the base of the interfacial layer due to turbulence generated by forced convection in the mixed layer. This mixing increased the vertical temperature gradient in the lower portion of the interfacial layer which, in turn, increased thermal-wind shear just below the peak of the jet, and caused a strong mixing at the base of the interfacial layer. Another, but less important, growth mechanism was the formation due to the jet of a vertical temperature transition layer between the interfacial layer and the free atmosphere above. The transition layer enhanced boundary layer growth by reducing the temperature jump at the interfacial layer.

The quasi-2D model, with turbulence given in terms of eddy diffusivity and the TKE budget, successfully reproduced the main features of the evolving boundary layer jet. The boundary layer growth rate and shape, and location and intensity of the jet were similar to the observations, using reasonable model inputs. The model also produced reasonable momentum, heat-flux, and TKE profiles as judged by a comparison with the same profiles measured with an aircraft in a similar episode off California by Brost et al. (1982a, case 17-2).

The model showed a less sporadic growth rate of the boundary layer than the observed growth rate which indicated occasional mixing over deep layers. The essentially one-dimensional nature of the model (given partial two-dimensionality by prescribing advection), precluded the proper treatment of two- or three-dimensional eddies that may have been responsible for the observed sporadicity.

Sensitivity experiments conducted with the model for horizontal temperature gradients other than those established for the SNI episode produced a different and weaker wind maximum associated with the inertial oscillation, and showed other complex boundary-layer behavior. These results support our conjecture that the observed evolution of the jet and the MBL structure are products of the unique temperature distribution and the slope of the inversion that occurred during the observing period at SNI.

A comparison of several methods of parameterizing entrainment velocity with the observed growth rate of the SNI boundary layer showed little agreement. The proper inclusion of shear in entrainment parameterizations for meteorological situations similar to the SNI episode is a topic for future study.

*Acknowledgments.* The help of Stuart Gathman and Jeffrey James of NRL in collecting the SNI balloon data is gratefully acknowledged. We thank Jill Shertzer for typing the original manuscript. This work was par-

tially supported by the NOSC EOMET Program and the NRL Heavy-Weather-at-Sea Program.

## REFERENCES

- Blanc, T., 1982: The data base for the May 1979 Marine Surface Layer Micrometeorological Experiment at SNI, CA. NRL Memo Report 4713, Naval Research Laboratory, Washington, DC., 627 pp.
- Brost, R. A., J. C. Wyngaard and D. H. Lenschow, 1982a: Marine stratocumulus layers. Part II: Turbulence budgets. *J. Atmos. Sci.*, **39**, 818-836.
- , D. H. Lenschow and J. C. Wyngaard, 1982b: Marine stratocumulus layers. Part I: Mean conditions. *J. Atmos. Sci.*, **39**, 800-817.
- Businger, J. A., 1973: Turbulent transfer in the atmospheric surface layer. *Workshop in Micrometeorology*, D. A. Haugen, Ed. Amer. Meteor. Soc., 67-98.
- Deardorff, J. W., 1979: Prediction of convective mixed-layer entrainment for realistic capping inversion structure. *J. Atmos. Sci.*, **36**, 424-436.
- , 1980: Stratocumulus-capped mixed layers derived from a three-dimensional model. *Bound.-Layer Meteor.*, **18**, 495-527.
- , and E. W. Peterson, 1980: The boundary-layer growth equation with Reynolds averaging. *J. Atmos. Sci.*, **37**, 1405-1409.
- Delsol, F., K. Miyakoda and R. H. Clarke, 1971: Parameterized processes in the surface boundary layer of an atmospheric circulation model. *Quart. J. Roy. Meteor. Soc.*, **97**, 181-208.
- Deterling, H. W., and D. Etling, 1985: Application of the  $E - \epsilon$  turbulence model to the atmospheric boundary layer. *Bound.-Layer Meteor.*, **33**, 113-133.
- Enfield, D. B., 1981: Thermally driven wind variability in the planetary boundary layer above Lima, Peru. *J. Geophys. Res.*, **86**, 2005-2016.
- Fairall, C. W., 1984: Wind shear enhancement of entrainment and refractive index structure parameter at the top of a turbulent mixed layer. *J. Atmos. Sci.*, **41**, 3472-3484.
- Gerber, H., 1986: Tethered balloon measurements at San Nicolas Island (Oct. 1984): Instrumentation, data summary, preliminary data interpretation. NRL Report 8972, Naval Research Laboratory, Washington, DC, 77 pp.
- Johnson, A., and J. J. O'Brien, 1973: A study of an Oregon sea breeze event. *J. Phys. Oceanogr.*, **5**, 761-772.
- Kolmogorov, A. N., 1942: The equation of turbulent motion in an incompressible fluid. *Izv. Akad. Nauk USSR, Ser. Fiz.*, **6**(1-2), 56-58.
- Lester, P. F., 1985: Studies of the marine inversion over the San Francisco Bay area: A summary of the work of Albert Miller, 1961-1978. *Bull. Amer. Meteor. Soc.*, **66**(11), 1396-1402.
- Lilly, D. K., 1968: Models of cloud-topped mixed layers under a strong inversion. *Quart. J. Roy. Meteor. Soc.*, **94**, 292-309.
- Lumley, J. L., 1980: Second order modeling of turbulent flows. *Prediction Method for Turbulent Flows*, W. Kollmann, Ed. Hemisphere Publication Company, 1-31.
- Lydolph, P. E., 1985: *The Climate of the Earth*. Rowan and Allanheld, 317 pp.
- Lyons, R., H. A. Panofsky and S. Wollaston, 1965: The critical Richardson number and its implications for forecast problems. *J. Appl. Meteor.*, **3**, 136-142.
- Marchuk, G. I., V. P. Kochergin, V. L. Klimok and V. A. Sukhorukov, 1977: On the dynamics of the ocean surface mixed layer. *J. Phys. Oceanogr.*, **7**, 865-875.
- Monin, A. S., and A. M. Yaglom, 1971: *Statistical Fluid Mechanics*. Vol. I: MIT Press.
- Overland, J. E., R. M. Reynolds and C. H. Pease, 1983: A model of the atmospheric boundary layer over the marginal ice zone. *J. Geophys. Res.*, **88**, 2836-2840.
- Rodi, W., 1980: Turbulence Models and Their Application in Hydraulics. IAH, 119 pp.
- Stull, R. B., 1976: The energetics of entrainment across a density interface. *J. Atmos. Sci.*, **33**, 1260-1267.
- Tennekes, H., and A. G. M. Driedonks, 1981: Basic entrainment equations for the atmospheric boundary layer. *Bound.-Layer Meteor.*, **20**, 515-531.
- U.S. Department of Commerce, 1984: *Oceanographic Monthly Summary*. 4(10), NOAA/NWS/NESDIS, Washington, DC, 48 pp.
- Wyngaard, J. C., 1975: Modeling the planetary boundary layer—extension to the stable case. *Bound.-Layer Meteor.*, **9**, 441-460.
- , and M. A. LeMone, 1980: Behavior of the refractive index structure parameter in the entraining convective boundary layer. *J. Atmos. Sci.*, **35**, 1573-1585.
- Zemba, J., and C. A. Friehe, 1987: The marine atmospheric boundary layer jet in the Coastal Ocean Dynamics Experiment. *J. Geophys. Res.*, **92**, 1489-1496.

## **APPENDIX J**

### **A Numerical Study of the Outflow Layer of Tropical Cyclones**

A Numerical Study of the Outflow Layer of Tropical Cyclones

Jainn-Jong Shi

Department of Marine, Earth and Atmospheric Sciences  
North Carolina State University, Raleigh, NC 27695

Simon Wei-Jen Chang

Naval Research Laboratory, Washington, DC 20375

Sethu Raman

Department of Marine, Earth and Atmospheric Sciences  
North Carolina State University, Raleigh, NC 27695

October 5, 1989

## Abstract

The structure and dynamics of the outflow layer of tropical cyclones are studied by using a three-dimensional numerical model. A weak and a strong tropical cyclones are produced by the numerical model when starting from idealized initial vortices embedded in mean hurricane soundings. The quasi-steady state outflow layers of both the weak and strong tropical cyclones have similar characteristics: (1) the circulations are mainly anticyclonic (except for a small region of cyclonic flow near the center) and highly asymmetric about the center, (2) the outflow layer is dominated by a narrow but elongated outflow jet, which contributes up to 50% of the angular momentum transport, and (3) the air particles in the outflow jet mostly originate from the lower level, following "in-up-and-out" trajectories.

We found there are secondary circulations around the outflow jet, very much like those associated with mid-latitude westerly jet streams. In the jet entrance region, the secondary circulation is thermally direct. That is, the ascending motion is located on the anticyclonic shear side of the jet, and the descending motion on the cyclonic shear side. And there is a radially outward flow above the jet and inflow below it. In the jet exit region, the secondary circulation is weaker and reversed in its direction (thermally indirect). The secondary circulations leave pronounced signatures on the relative humidity, potential vorticity, and tropopause height fields. The secondary circulation is more intense in the stronger tropical cyclone (with a stronger outflow jet) than in the weaker tropical cyclone.

The dynamic instability of the outflow is tested in numerical experiments with prescribed forcings. It is found that the simulated tropical cyclone intensifies when its upper levels within a radius of approximately 500 km are spun up and forced to be more divergent. Convection plays a key role in transforming the upper level divergence into low level convergence. In another experiment, additional regions of convection are initiated in the ascending branches of the circum-jet secondary circulations away from the inner region when the outflow jet between the radii of 500 and 1000 km is accelerated. These regions of convection become competitive with the inner core convection and eventually weaken the tropical cyclone.

## 1. Introduction

The outflow layer of tropical cyclones is generally shallow, anticyclonic, divergent on the synoptic scale, and considerably more asymmetric than the middle and lower layers (Alaka, 1961, 1962; Miller, 1963; Black and Anthes 1971; Frank, 1977; McBride, 1981; Merrill, 1988a). Except for a small region near the center, the outflow of tropical cyclone is normally concentrated in one or two outflow jets (or channels). It is well known that conditions in the low- and mid-tropospheric environment, such as moist instability, and vertical shears and high ocean surface temperatures, can greatly affect the behavior of tropical cyclones. Recently, however, it has been recognized that the outflow layer is also able to control the intensity or even the movement of tropical cyclones. There have been many observational studies (e.g., Sadler, 1976 and 1978; Holland and Merrill, 1984; Steranka et al., 1986; Rodgers et al., 1987 and 1989a,b; Molinari and Vollaro, 1989) which link the behavior of tropical cyclones to the strength and position of upper tropospheric troughs (UTT's). Sadler (1976 and 1978) showed in general that as an UTT aligns vertically with the underlying tropical cyclone, the tropical cyclone weakens. On the other hand, if a tropical cyclone is aligned with an upper tropospheric ridge, it generally intensifies. Rodgers et al (1989b), based on satellite-measured total ozone, suggested that the positioning of upper-level troughs modulated the inner core convection and, therefore, the intensity of some Atlantic hurricanes.

It has been demonstrated that the asymmetric outflow can be responsible for eddy fluxes of angular momentum comparable in magnitude to those of the tropical cyclone's symmetric radial circulation (Pfeffer, 1958; Palmen and Riehl, 1957; Black and Anthes, 1971; Holland, 1983;

Molinari and Vollaro, 1989). Challa and Pfeffer (1980) showed that the angular momentum flux convergence measured from observational data can accelerate the development of a tropical cyclone in an axisymmetric numerical model. On the other hand, Holland and Merrill (1984) argued that as the tropical cyclone's low- and mid-tropospheric cyclonic circulations develop, the storm becomes more inertially stable, and more resistant to environmental forcing at these levels. However, at the outflow level, the anticyclonic asymmetric flow is more inertially unstable and more responsive to upper-level environmental forcing. It is not difficult to imagine then that one of the tropical cyclone's outflow jets can be accelerated by an approaching upper-level trough as suggested by Sadler (1976 and 1978). It follows then that the tropical cyclone would intensify according to either the eddy angular momentum viewpoint or the inertial instability argument.

The physical process or the chain of events that allows the upper tropospheric forcing to influence the tropical cyclone is, however, less apparent. The kinetic energy budget in Challa and Pfeffer (1980) indicates that with added angular momentum flux the stronger development of their model tropical cyclone is accompanied by an excess of kinetic energy production due to the pressure torque (that is, the work done by the cross-isobaric, radial circulation). It is not clear, however, whether this enhanced radial circulation is a cause or effect of the intensification. Sadler (1978) speculated that the outflow channel, when strengthened, can extend inward to the inner-core convection and serve as the outflow of the inner-core convection and, therefore, enhance the convection. This view is supported by Chen and Gray (1984), who conjectured that the enhanced



outflow can remove more mass and heat from the inner region of the tropical cyclone and maintain the convective instability.

Merrill (1984 and 1988b) proposed a different mechanism for the tropical cyclone's intensification under upper-tropospheric forcing. He noted that the outflow jet, similar to the jet streaks in mid- and high-latitudes, has a secondary circulation around it (Palmen and Newton, 1969; Uccellini et al., 1984). He argued that as the jet is enhanced or "channeled" by the jet-stream associated with the upper-tropospheric trough, the secondary circulation would also be enhanced. This in turn would initiate additional convection in the upward branch of the secondary circulation and intensify the storm. However, a necessary condition for this process is that the upward branch of the secondary circulation is located near the inner region.

These hypotheses of course cannot be substantiated without the knowledge of the detailed structure of the outflow jet. Analysis of observational data on the outflow level on a single-case basis may suffer from the lack of data or poor spatial coverage, whereas, composite data may not give a dynamically consistent structure. A numerical simulation with a three-dimensional (3D) model seems to be an expedient way to obtain a comprehensive description of the tropical cyclone outflow layer. In the following sections 2 and 3, a brief review of the numerical model will be given and the simulated outflow layer structure simulated by the model will be presented. The plausibility of the upper-level forcing changing the behavior of tropical cyclones will be discussed and examined by conducting additional numerical experiments. These results will be presented in section 4.

## 2. The Numerical Tropical Cyclone Model

The tropical cyclone model used in this study is essentially the same as the Naval Research Laboratory (NRL) limited-area numerical model described in Chang et al. (1989). The model is a 3D, hydrostatic, primitive equation, finite difference model with physical parameterizations of the boundary layer and cumulus convection. Model equations and the numerical techniques are documented in detail in Madala et al. (1987). Some modifications are made to accommodate the simulation of an idealized tropical cyclone.

This model uses the Arakawa C grid with a uniform resolution of 0.5 degree in longitude and latitude. There are 141 x 91 horizontal points in the model, covering a domain from the equator to 45°N in latitude with a width of 100 degrees in longitude from, say, 110 to 180°E. (The model result is independent of the longitudinal domain). The model domain is assumed to be entirely over the ocean to avoid complications with sea-land contrasts. A variable Coriolis parameter is used. There are ten  $\sigma$  ( $\sigma = p/p_s$ ) layers in the vertical with equal  $\sigma$  thickness. As in Chang et al. (1989), a constant drag coefficient and constant exchange coefficients for the sensible and latent heats are used. The use of a simple boundary layer parameterization is justified because the structure of the outflow layer should be relatively insensitive to boundary layer formulations.

All the simulations presented in this paper are carried out with no initial environmental winds. There are no winds along the lateral boundaries throughout the integration. Although the lateral boundaries remain undisturbed due to the large model domain, a damping scheme is used to reduce any boundary reflection. To avoid the effect of the sea surface

temperature (SST) variations, the SST is set at 302.5 K over the entire model domain. The model is initialized with the mean hurricane sounding from Sheets (1968). The initial vortex is defined by the following function

$$v^\lambda(\sigma, r) = v_{\max}^\lambda W(\sigma) \left(\frac{r}{r_0}\right) \exp\left[\frac{1}{b} \left(1 - \left(\frac{r}{r_0}\right)^b\right)\right] \quad (1)$$

where  $v^\lambda$  is the tangential velocity relative to the center,  $r$  is the radius,  $b = 2$  and  $r_0 = 240$  km. The vertical structure function  $W(\sigma)$  decreases linearly from 1 at  $\sigma=1$  to 0 at  $\sigma=0.4$ , so that the outflow can develop in the model instead of being prescribed by the initial wind profile. The initial position of the vortex is set at 22.5°N and 150°E.

In order to simulate the outflow layer of both a strong and a weak tropical cyclone, two values of  $v_{\max}^\lambda$  are used: 40 ms<sup>-1</sup> for the strong storm and 20 ms<sup>-1</sup> for the weak storm. In addition, at the ocean surface the humidity for the case of the strong storm is assumed to be 100% of the saturation specific humidity at the SST. A 5% reduction in the surface specific humidity is assumed for the case of the weak storm. A non-divergent, nonlinear balanced initialization is carried out to obtain the initial conditions for the model integration.

### 3. The Structure of the Outflow Layer

The model is integrated for 120 and 96 hours for the weak and strong cases, respectively. A quasi-steady tropical cyclone develops from the initial vortex after about 72 hours in the weak case and after 48 hours in the strong case. The quasi-steady strong storm has a central pressure of 960 mb and a maximum surface wind of 40 ms<sup>-1</sup>. For the weak storm, the central pressure is 984 mb and the maximum surface wind is 20 ms<sup>-1</sup>. The

centers of both the strong and weak storms have moved northwest from their initial positions due to the  $\beta$  effect.

#### a. General Structure

The outflow is the strongest at the 150 mb level for both storms. This is probably because that the tropopause in the initial sounding is at 150 mb and the convective heating stops there. As shown in Figs. 1 and 2, the outflow is anticyclonic (except for a small area near the center) and covers a larger area than the cyclonic circulation in the lower and middle troposphere. As shown by the isotachs in Figs 3 and 4, the outflow is dominated by a single jet in each storm. The maximum speed in the outflow reaches  $54.4 \text{ ms}^{-1}$  in the strong case and  $33.6 \text{ ms}^{-1}$  in the weak case. In both cases, the jet is  $\sim 3000 \text{ km}$  long and very narrow with a e-folding width of  $\sim 200 \text{ km}$ . In the direction perpendicular to the jet, there is very strong anticyclonic shear along the jet core facing the storm center and strong cyclonic shear facing away from the center. In both the strong and weak storms, the single jet starts from a position north of the central cyclonic circulation (the entrance region), where the large Coriolis parameter causes the strongest inertial acceleration. In a supplementary experiment where a tropical cyclone is embedded in a zonal flow with westerlies to the north and easterlies to the south of the storm, two jets are formed, in agreement with the result of Ooyama(1987)'s single layer model.

As indicated by the isotachs, the section of the jet between the jet maximum ( $\sim 10^\circ$  to the east of the storm center) and the exit region ( $\sim 20^\circ$  to the south and southwest of the storm center) is more diffused with diminishing horizontal shears. Comparing the two storms, the jet of the

stronger storm is of higher speed, wider and located farther away from the center. In all, the characteristics of these two simulated jets are very similar to those observed (Black and Anthes, 1971; Sadler, 1976; Merrill, 1988a, Rodgers et al., 1989a).

#### b. Secondary Circulation

Figures 5 and 6 show the normal (in isotachs) and tangential wind components (in vectors) for the cross-sections AA' in the entrance and BB' in the exit region, respectively, between the levels of 30 and 300 mb. The normal wind component shows that the jet is very shallow, and confined between 100-250 mb, with very strong surrounding horizontal as well as vertical shears. The tangential components of the wind indicate that there are circum-jet secondary circulations, similar to those associated with mid- and high latitude jet streams (Palmen and Newton, 1969; Uccellini et al., 1984). In the entrance region of the outflow jet, the direction of the secondary circulation is such that there is an ascending branch on the anticyclonic shear side (facing toward the center) and a descending branch on the cyclonic shear side (away from the cyclone center). It also has an outward branch above the jet and an inward branch below the jet. Because of the warm core, the secondary circulation is thermally direct in the entrance region. In the exit region, the direction of the secondary circulation is reversed (thermally indirect). The upward branch is located on the cyclonic shear side of the jet instead, and the downward branch is located on the anticyclonic shear side of the jet. However, the thermally indirect secondary circulation in the exit region is much weaker and more diffuse than its thermally direct counterpart in the entrance region.

Comparing the maximum vertical and horizontal vectors (shown at the corners of Figs 5 and 6), it is also apparent that the secondary circulation associated with the stronger jet is stronger than its counterpart for the weaker jet. The existence of the secondary circulation around the outflow jet is crucial for the hypothesis that the upper-tropospheric forcing can influence the strength of tropical cyclones through the secondary circulation (Merrill, 1988b).

### c. Relative Humidity and Potential Vorticity

Because there is no significant condensation at the outflow level, the relative humidity (RH) field at the 150 mb level of both the weak and strong storms (shown in Fig. 7) is mainly a manifestation of the transport process, reflecting several important features of the outflow momentum field. In general, on the tropical cyclone scale, there is a wet canopy of  $RH > 80\%$ , with however higher values of RH to the south of the storm center. The storm center, in spite of the coarse horizontal resolution, is represented by a drier region of  $RH < 80\%$  embedded in the wet canopy. There is a very sharp RH gradient in the direction perpendicular to the outflow jet. In the jet entrance region, the RH is  $> 80\%$  on the anticyclonic shear side of the jet, coinciding with the ascending branch of the secondary circulation. On the other hand, the RH is  $< 40\%$  on the cyclonic shear side of the jet due to the descending motion there. This confirms the existence of a steady secondary circulation around with the jet.

South of  $25^{\circ}\text{N}$  along the jet core, the secondary circulation reverses direction, and an increase of RH to  $> 60\%$  occurs downwind of the cyclonic shear side of the jet, indicative of the rising motion there. There is a sharp and narrow dry tongue between  $170^{\circ}\text{E}$ ,  $25^{\circ}\text{N}$  and  $160^{\circ}\text{E}$ ,  $15^{\circ}\text{N}$ ,

due to the downwind transport by the jet of dry air that originated in the downward branch of the thermally direct secondary circulation. Because the thermally indirect secondary circulation is weaker than the thermally direct one, the RH gradient normal to the jet in the exit region is also weaker as compared to the entrance region. There is a dry region located near 150°E and 15°N in the weak case (and similar dry region in the strong case), probably formed by the downward branch of the thermally indirect secondary circulation and general subsidence of the tropical cyclone.

The potential vorticity (PV), defined as

$$PV = - \frac{1}{\theta} (\zeta + f) \left( \frac{\delta \theta}{\delta p} \right) \quad (2)$$

where the vorticity  $\zeta = \delta v / \delta x - \delta u / \delta y$  is computed on pressure surfaces, is conserved in adiabatic processes (Hoskins et al., 1985). In general in an undisturbed atmosphere, the PV is high in the stratosphere due to the high static stability and low in the troposphere. Therefore, in studying mid- and high-latitude storms, the PV can sometimes be used as a tracer for stratospheric air. A value of  $2 \times 10^{-7} \text{ mb}^{-1} \text{ s}^{-1}$  is commonly chosen as the lower limit for stratospheric air (Kuo and Reed, 1988; Rodgers et al, 1989b). In tropical cyclones, the generation of PV due to latent heating may become important and the PV may not be conserved as well as in mid- and high-latitude systems. However, at the 150 mb outflow level where the latent heating is negligible, the PV may still be a good indicator of general rising and sinking motions, especially outside of the inner convective region.

Fig. 8 shows the pressure levels at which the  $PV = 2 \times 10^{-7} \text{ mb}^{-1} \text{ s}^{-1}$ . In other words, it is the "tropopause" as defined by the PV. Except for

the high values near the storm center due to the "eye" effect, there are significant variations of the "tropopause" heights near the outflow jet. In general, the "tropopause" is higher (low pressure values) on the anticyclonic side of the jet, extending from the entrance region downstream, and is lower (high pressure values) on the cyclonic side of the jet. The effects of the secondary circulation of the outflow jet on the spatial distribution of the "tropopause" have also been discussed in cross-sectional plots by Rodgers et al (1989, Fig. 5).

#### d. Angular Momentum

The outflow plays an important role in the maintenance of the angular momentum balance of tropical cyclones (Palmen and Riehl, 1957; Pfeffer, 1958; Anthes, 1974). An angular momentum budget is calculated for the simulated tropical cyclones based on the angular momentum budget equation of Anthes (1974):

$$\begin{aligned}
 \frac{\delta M}{\delta t} = & -2\pi \int_{h_1}^{h_2} \int_{r_0}^{r_1} r^2 \rho(z) (\langle f \rangle \langle u \rangle + \langle f' u' \rangle) dr dz \\
 & -2\pi \int_{h_1}^{h_2} [r_1 \rho(z) (\langle m \rangle \langle u \rangle)_{r_1} - r_0 \rho(z) (\langle m \rangle \langle u \rangle)_{r_0}] dz \\
 & -2\pi \int_{h_1}^{h_2} [r_1 \rho(z) (\langle m' u' \rangle)_{r_1} - r_0 \rho(z) (\langle m' u' \rangle)_{r_0}] dz \\
 & -2\pi \int_{r_0}^{r_1} r [(\rho \langle m \rangle \langle w \rangle)_{h_2} - (\rho \langle m \rangle \langle w \rangle)_{h_1}] dr \\
 & -2\pi \int_{r_0}^{r_1} r [(\rho \langle m' w' \rangle)_{h_2} - (\rho \langle m' w' \rangle)_{h_1}] dr , \quad (3)
 \end{aligned}$$

where  $u$  and  $v$  are the radial and tangential velocities in cylindrical coordinates, respectively,  $r$  is the radius from the center as determined by



the lowest surface pressure, and  $m=rv$ . In the above equation,  $\langle \rangle$  represents an azimuthal mean and  $(\ )'$  denotes a deviation from the mean. Vertical integrations are carried out between the geopotential heights of  $h_1=13700$  gpm and  $h_2=14700$  gpm, encompassing most of the outflow. In (3), the first term on the RHS denotes the mean and eddy Coriolis torque, the second and the third terms denote the horizontal convergences of mean and eddy angular momentum fluxes, respectively. And finally, the fourth and fifth terms represent the vertical convergence of mean and eddy angular momentum fluxes, respectively. To evaluate the values of these terms, model results are linearly interpolated to the cylindrical-pressure coordinates.

Table 1 shows the values of each term in (3) for the simulated strong tropical cyclone at 72 h and the weak tropical cyclone at 96 h. For comparison, observed values for mean tropical storms in Palmen and Riehl (1957) and Pfeffer (1958) are also listed. Our model tropical cyclones are larger in size than the mean storm and therefore the 666 km used as the outer radius of the outflow in observational studies is not appropriate for our model result. Instead, we use radii of 1000 km and 1500 km as the outer boundaries for the modeled weak and strong tropical cyclones, respectively.

Table 1 shows that the values of various terms in (3) evaluated from the modeled tropical cyclones compare reasonably with the observed, considering that the simulated strong tropical cyclone is twice as energetic as the mean storm in Palmen and Newton (1969). The angular momentum balance in both the simulated and the observed tropical cyclones is basically maintained by the Coriolis torque and horizontal transports. Both the model and the observations show that the contribution by the eddy momentum flux convergence is ~50% of the mean momentum flux convergence,

except for the weak storm where the eddy flux is larger than mean flux. Although the single outflow jet in the modeled tropical cyclone cannot account for all of the eddy angular momentum, a harmonic decomposition indicates that the azimuthal wave number one has more than 70% of the total eddy angular momentum. The importance of the eddy term again underscores the dominance of the outflow jet in the outflow layer. The only major discrepancy between the model and the observations is that the vertical momentum fluxes for the modeled storm are insignificant.

#### e. Trajectories

Trajectories were generated by releasing trace particles at the initial time and tracing them in an attempt to find the origins of air particles in the outflow layer. A total of 206 trace particles are released at the initial time of the simulated weak tropical cyclone at the 150, 500 and 950 mb levels, and evenly distributed around six concentric rings with respect to the initial vortex center at radii of 20, 100, 300, 500, 1000 and 1500 km. Approximately, for the weak tropical cyclone that develops, the radius of 20 km is in the "eye", radii of 100 and 300 km are within the inner convective region, 500 km is in the intermediate region, and 1000 and 1500 km is at the outskirts of the tropical cyclone. The pressure levels of 150, 500 and 950 mb are roughly in the outflow, non-divergent, and inflow levels, respectively, of the model tropical cyclone. The position of each particle is calculated by a Euler-forward integration, for which linear interpolations are used to obtain the three dimensional velocity components. Particle positions are stored every three model time steps for trajectory plotting.

Figure 9 shows the trajectories at 96 h formed by all of the 206 particles. The trajectories depict a commonly accepted cyclone scale circulation of an idealized tropical cyclone. There is a cyclonic convergent flow in the low levels, strong upward and cyclonic circulation in the inner region, and a divergent anticyclonic outflow at high altitudes. Upon close examination of particle positions and additional trajectory plots (not shown), the following interesting observations can be made:

(a) Most particles released at 500 and 950 mb at radii of 300 and 500 km are caught in the inner region of convection and transported to the outflow level.

(b) Most particles released at or transported into the inner region of the outflow level are transported away from the inner region by the outflow jet. The trajectories are very close together in the entrance region and become more diffused in the exit region. There is a general sinking in the outflow jet, for most particles are at 100-150 mb in the jet entrance region but descend to 300 mb in the exit region.

(c) Particles released at or transported into small radii at low levels are trapped in low levels inside the radius of the maximum updraft. These trapped particles move toward the northwest as the center drifts toward northwest due to the  $\beta$  effect.

#### 4. Response to Upper-Tropospheric Forcing

As discussed in the introduction, there seems to be at least two ostensibly different mechanisms for the upper troposphere to influence the behavior of tropical cyclones. The first theory (e.g. Challa and Pfeffer, 1980; Molinari and Vollaro, 1989) hypothesizes that the inner circulation

of tropical cyclones can be spun up by an influx of eddy angular momentum when the outflow of tropical cyclones is modified by upper-tropospheric ridge/trough systems. The secondary theory, as proposed by McBride (1981) and Merrill (1988b) and others, asserts that when the outflow jet is accelerated by an upper-tropospheric ridge/trough system, the enhanced secondary circulation can initiate additional deep convection in the inner region, and, thus intensify the tropical cyclone. It has been demonstrated in the previous section that there is indeed a secondary circulation associated with the outflow jet of the simulated tropical cyclones. It is also shown that the secondary circulation associated with stronger jet is stronger. It is thus conceivable that as the outflow jet is accelerated, the secondary circulation will become stronger and may eventually trigger the deep convection that may affect the storm's intensity. It is difficult, however, to completely separate the mechanisms inherent in the two theories.

Two different numerical experiments have been conducted to investigate the behavior of the model tropical cyclone in response to the modification of the outflow layer. In these experiments, various parts of the outflow layer are artificially accelerated by a nudging method, i.e., additional tendency terms are added to the equations of motion in x- and y-direction. The tendency terms are of the form:

$$\begin{aligned}\frac{\delta p_s u}{\delta t} &= \dots + \lambda p_s (u_0 - u), \quad \text{and} \\ \frac{\delta p_s v}{\delta t} &= \dots + \lambda p_s (v_0 - v),\end{aligned}\tag{4}$$

where the time scale  $\lambda=f/2$ , and the asymptotic wind speed  $u_0=2u(t)$  and  $v_0=2v(t)$ . These two extra terms will "nudge" the model winds in the forcing region to double their values within the time scale of  $\lambda$ . Note here the total winds, including both the rotational and irrotational components, are accelerated in (4).

It is not the purpose of this paper to theorize how and/or what part of the tropical cyclone is accelerated under certain upper tropospheric forcings. The cause of such acceleration, may it be accomplished by the approach of an upper level ridge/trough system or by angular momentum transport is outside the scope of this paper. Instead, our purpose is to study the response of the tropical cyclone to the acceleration of certain part of the troposphere.

#### a. Spinning-up the Inner Region

In Exp. 1, the inner region in the upper-troposphere of the tropical cyclone is spun up. Specifically, the tendency terms in (4) are applied to all model grid points between 150-450 mb within a  $5^\circ$  lat. radius from the center of the storm, as determined from the minimum sea level pressure. This variational experiment is carried out from 72 h for the weak control case. As the tropical cyclone moves toward northwest, the area subjected to the acceleration also moves. This experiment is conducted to simulate the situation when the entire upper part of the inner tropical cyclone is accelerated. As shown by Fig 10, the central pressure of Exp. 1 deviates gradually from the control experiment right after 72 h, becoming more intense and reaching approximately 976 mb at 105 h, which is 10 mb deeper than the control. The maximum surface wind at this time in Exp. 1 is approximately  $22 \text{ ms}^{-1}$  as compared with  $17 \text{ ms}^{-1}$  in the control.

In this experiment, the upper-tropospheric winds in the inner region of the model tropical cyclone are all accelerated and there could be two direct dynamic responses to this added forcing. First, the cyclonic circulation that exists in the inner region is spun up. This would decrease the warm core, destabilize the inner region, promote inner-core convection, and eventually lead to the intensification (Gray, 1979). However, cumulus convection in the model is likely to quickly stabilize the additional convectively unstable lapse rate and renders the isolation of the effect very difficult.

The second response is caused by the breakdown of the quasi-gradient balance of the outflow layer as the result of the forcing. Consider the gradient balance of

$$\frac{1}{\rho} \frac{\partial p}{\partial r} = \left( f + \frac{v}{r} \right) v \quad (5)$$

where  $r$  is the radius and  $v$ , the tangential velocity. At very small radii where the the circulation is cyclonic (positive  $v$ ), a supergradient circulation causes divergence. At larger radii but within the forced region of radius of  $5^\circ$  lat., the centrifugal acceleration of a  $20 \text{ m s}^{-1}$  wind is at least no smaller in magnitude than the Coriolis acceleration. A supergradient condition then still causes a divergence. Therefore, the forced acceleration in Exp. 1 creates a mean divergence of the outflow layers within the radius of  $5^\circ$  lat. The eddy flux of angular momentum exerted on the upper levels also creates a cyclonic torque and divergence (Eliassen, 1952; Challa and Pfeffer, 1989). The divergence at the outflow level requires a compensating rising motion and convergence at lower levels for mass continuity. It is unclear what the effect may be if the

convergence occurs immediately under the outflow level. However, if the compensating convergence occurs at low levels, the increased convergence would replenish the system with marine boundary layer air of high equivalent potential temperature and could intensify the tropical cyclone. To examine the vertical extent to which the tropical cyclone responds to the upper-level forced divergence, we computed the mass divergence at 96 h with a  $10^\circ \times 10^\circ$  box centered around the storm. As shown in Fig 11., the upper-level mass divergence is approximately  $11 \times 10^{12} \text{ g s}^{-1}$  in Exp. 1, almost twice as strong as the control. The convergence in Exp. 1 is stronger than the control at all levels below  $\sigma=0.45$ . In the boundary layer, the mass convergence of Exp. 1 is also twice that of the control, similar to the difference between developing and nondeveloping tropical storms (Gray, 1979).

In a supplementary numerical experiment, Exp. 1 is duplicated except that the cumulus convection is suppressed. The vertical distribution of the mass divergence for this supplementary experiment clearly shows that compensating convergence does not extend to low levels. These results suggest that the deep cumulus convection is a key factor coupling the upper-level dynamics with the low levels.

In summary, results from this experiment seem to support the hypothesis that the tropical cyclone can be modified by the upper-tropospheric forcing. The forced spinup of the inner region of the tropical cyclone creates a supergradient condition in the outflow layer, which in turn results in an upper-level divergence. The cumulus convection helps to produce a compensating convergence in the low level and, thus, the tropical cyclone intensifies.

b. Acceleration of the outflow jet.

In the second numerical experiment (Exp. 2), the upper level momentum field is forced as in Exp. 1, except that the forced region is restricted to be between the radii of  $5^{\circ}$  and  $10^{\circ}$  from the center and only where the wind speed exceeds  $20 \text{ ms}^{-1}$ . In fact, the forced region in this experiment is restricted to the jet core located from the northeast to the east relative to the center and between  $\sigma=0.1$  to  $0.3$ . The experiment starts from the 48 h of the strong case, which is used as the control for comparison. Accelerations of the radial wind and the tangential wind in the forced region in this experiment have different effects on the mass divergence. Because the circulation in the forced region is divergent, the acceleration in the radial direction causes divergence. The forced anticyclonic acceleration of the jet at the radii of  $5\text{--}10^{\circ}$ , however, would decrease the inertia term in (5),  $fv+u^2/r$ , and cause a convergence toward the inner region (in other words, the magnitude of the Coriolis force is larger than the centrifugal force). This experiment differs from those in Challa and Pfeffer (1980 and 1989) in that the acceleration due to eddy momentum in their experiment are exerted on all points in their model. In addition, the eddy momentum flux convergence in their experiments results in a cyclonic torque causing divergence at large radii, while in this experiment the acceleration of the jet results in a net anticyclonic torque causing convergence beyond the radius of about  $5^{\circ}$  lat.

At 96 h, the maximum speed in the outflow jet has increased almost two fold to  $\sim 90 \text{ ms}^{-1}$ . It is interesting to note that the mass divergence at the outflow level at 72 h (Table 2) changes only slightly from the control for both the  $5 \times 5^{\circ}$  and the  $10 \times 10^{\circ}$  boxes, as compared with the twofold increase in Exp. 1 (Fig. 11). The small decrease of the divergence



for the  $5 \times 5^\circ$  box is due to the converging effect of the supergradient jet discussed previously. The increased divergence for the larger  $10 \times 10^\circ$  box is due to the forced acceleration of the divergent component of the jet. One may infer from this that the intensity of the tropical cyclone would remain relatively unchanged. However, the central pressure at 96 h is 5 mb higher than the control. An examination of the distribution of the convective heating suggests that the convection induced by the accelerated jet away from the core region appears to weaken the tropical cyclone. Fig. 12 shows the 24 h for 48-72 h accumulated precipitation amount for the control, and two 12 hourly accumulated precipitation amounts for 48-60 h and 60-72 h for the experiment. It is clear that additional precipitation of up to 3.8 cm has been produced on the anticyclonic shear side of the entrance region of the jet in the first 12 h of the experiment. The convection is associated with the upward branch of the direct secondary circulation of the jet, which strengthens because of the acceleration of the jet. By 72 h, the region of the additional precipitation has extended upstream (as suggested by Sadler, 1978) and downstream of the jet, but mainly stays with the upward branch of the circum-jet secondary circulation (i.e., the anticyclonic shear side in the jet entrance region and the cyclonic shear side in the jet exit region). The precipitation over the central region in this experiment is less than the control. The convection away from the core associated with the accelerated jet apparently becomes competitive with the inner core convection and, thus, weakens the tropical cyclone.

It has been observed that Hurricane Florence of 1988 in the Gulf of Mexico may have had a significant interaction with an approaching westerly trough resulting in the explosive development of convection near the

outflow jet which grew even stronger than the inner-core convection (Rodgers, et al, 1989a). Although other factors may have affected the intensification and decay of Hurricane Florence, the numerical simulation presented here may be of relevance to Florence's behavior.

## 5. Summary and Conclusions

Numerical simulations of idealized tropical cyclones with special emphasis on the outflow layer have been conducted. Results show that the anticyclonic outflow is strongest at about 150 mb and is dominated by a well-defined, narrow but long (~3000 km) jet. The jet originates from an area to the northwest of the storm, extending in a clockwise direction to the southwest. The angular momentum budget shows that the horizontal eddy momentum flux, mostly representing the effect of the jet, is as important as the mean flux, indicating the dominance of the jet in the outflow layer. These characteristics of the outflow are in agreement with observational studies (Palmen and Riehl, 1957; Pfeffer, 1958; Black and Anthes, 1971).

Cross-sectional analyses of the outflow jet show the existence of a thermally-direct secondary circulation around the jet in the jet entrance region and a thermally-indirect one in the exit region. The thermally-direct secondary circulation has an ascending branch on the anticyclonic shear side of the jet (i.e., closer to the cyclone center). The thermally-indirect secondary circulation, on the other hand, has ascending motion on the cyclonic shear side. The secondary circulations have pronounced effects on the RH and PV fields at the outflow levels. We found that a more intense tropical cyclone has a stronger outflow jet accompanied by a stronger circum-jet secondary circulation.

In an attempt to study the effect of upper tropospheric forcings on the structure and behavior of the model tropical cyclone, two variational numerical experiments were conducted. In Experiment 1, the total wind in the upper levels of the tropical cyclone within the radius of  $5^\circ$  lat. is increased to simulate the possible consequence of superposing an upper tropospheric ridge over the tropical cyclone. In this case, the model tropical cyclone deepens by  $\sim 10$  mb in 24 hours. These results suggest that the superposition of an upper tropospheric ridge over a tropical cyclone is a favorable condition for the intensification of a mature tropical cyclone. It is also evident that the convection plays an important role in linking the upper levels of the tropical cyclone to the lower troposphere.

In the second experiment, the region of the outflow jet with wind speed of greater than  $20 \text{ m s}^{-1}$  and between the radii of  $5$ - $10^\circ$  latitude from the storm center is forced to accelerate to simulate the possible effect of the confluence of the outflow jet with a westerly jet. The results from this experiment show that the convection is produced in the areas of the ascending branch of the secondary circulation. The convection away from the inner core in our simulation is competitive to the inner core convection and can weaken the tropical cyclone.

These results support the thesis of Holland and Merrill (1984) that the outflow layers of tropical cyclones are dynamically unstable and tropical cyclones are susceptible to upper level forcings. As discussed earlier, the forcing of a certain region of the simulated tropical cyclone in our numerical experiments may not realistically reproduce the interaction between real tropical cyclones and the environment. To remedy this, a real case study on the interaction between tropical cyclone and

upper-tropospheric systems is currently in progress and the results will be reported in the future.

Table 1. Model and Empirical Angular Momentum Budgets in the Upper Layer of Tropical Cyclone

Storm	Radius (km)	Coriolis Torque	Horiz. Mean Flux	Horiz. Eddy Flux	Verti. Mean Flux	Verti. Eddy Flux
Mean Storm	0-333	-48.0	-20.0	8.0	40.0	20.0
(Palmen and Newton, 1957)	333-666	-143.0	76.0	23.0	----	44.0
Mean Storm	222-444	-54.0	46.0	20.0	5.0	----
(Pfeffer, 1958)	444-666	-78.0	-11.0	13.0	-4.0	----
Model (Weak)	0-300	-4.3	3.5	-0.7	-0.3	----
	300-1000	-47.6	13.4	35.1	1.1	-0.4
Model (strong)	0-300	-20.2	-4.7	-5.0	7.3	-0.4
	300-1500	287.1	159.8	79.7	0.5	-6.9

(Units are in  $10^{22}$  g cm<sup>-2</sup>s<sup>-2</sup>.)

Table 2. Mass Divergence at  $\sigma=0.15$  for Control and Exp. 2 at 72 h

Exp	5x5° Box	10x10° Box
Control Experiment	39	39
Exp. 2	34	46

(Units are  $10^{12}$  g s<sup>-1</sup>.)

### Acknowledgments

We thank Mr. Edward Rodgers of GSFC/NASA, Dr. Rao Madala of NRL and Dr. Keith Sashegyi of SAIC for many beneficial discussions. The work is supported by the 6.1 Research Program of the Naval Research Laboratory (NRL), a NRL Cray computation Grant, the Tropical Cyclone Motion Initiative of the Office of Naval Research, and a NASA grant to NRL contract no. S-56314-D. Computations were carried out on the Cray X-MP of NRL.

## References

- Alaka, M. A., 1961: The occurrence of anomalous winds and their significance. Mon. Wea. Rev., 89, 482-494.
- \_\_\_\_\_, 1962: On the occurrence of dynamic instability in incipient and developing hurricanes. National Hurricanes Research Projects, Report No. 50, U. S. Weather Bureau, Washington, D. C., 51-56.
- Anthes, R.A., 1974: The dynamics and energetics of mature tropical cyclones. Reviews of Geophysics and Space Physics, Vol. 12, No. 3, 495-522.
- Black, P. G. and R. A. Anthes, 1971: On the asymmetric structure of the tropical cyclone outflow layer. J. Atmos. Sci., 28, 1348-1366.
- Challa, M., and R. Pfeffer, 1980: Effects of eddy fluxes of angular momentum on model hurricane development. J. Atmos. Sci., 37, 1603-1618.
- \_\_\_\_\_, 1989: The formation of Atlantic hurricanes from cloud clusters and depressions. Submitted to J. Atmos. Sci.
- Chang, S, K. Brehme, R. Madala and K. Sashegyi, 1989: A numerical study of the East Coast Snowstorm of 10-12 February 1983. Mon. Wea. Rev., 117, 1766-1776.
- Chen, L. and W. M. Gray, 1984: Global view of the upper level outflow: patterns associated with tropical cyclone intensity changes during FGGE. 15th Technical Conference on Hurricanes and Tropical Meteorology, AMS, January 9-13, Miami, Florida.
- Elisssen, A., 1952: Slow thermally or frictionally controlled meridional circulations in a circular vortex. Astrphys. Norveg., 5, 19-60.
- Frank, W. M., 1977: The structure and energetics of the tropical cyclone, part I: storm structure. Mon. Wea. Rev., 105, 1119-1135.

- Gray, W.M., 1979: Hurricanes: Their formation, structure and likely role in the tropical circulation. Meteorology over the tropical oceans. D.B. Shaw, Editor, Roy. Meteor. Soc., 155-218.
- Holland, G. J., 1983: Angular momentum transports in tropical cyclones, Quart. J. R. Met. Soc., 109, 187-209.
- \_\_\_\_\_ and R. T. Merrill, 1984: On the dynamics of tropical cyclone structural changes, Quart. J. R. Met. Soc., 110, 723-745.
- Hoskins, B.J., M.E. McIntyre and A.W. Robertson, 1985: On the use and significance of isentropic potential vorticity maps. Quart. Jour. Roy. Meteor. Soc., 111, 877-946.
- Kuo, Y.-H., and R. Reed, 1988: Numerical simulation of an explosively deepening cyclone in the Eastern Pacific. Mon. Wea. Rev., 115, 2081-2105.
- Madala, R. V., S. W. Chang, U. C. Mohanty, S. C. Madan, R. K., Paliwal, V. B. Sarin, T. Holt and S. Raman, 1987: Description of the Naval Research Laboratory limited area dynamical weather prediction model. NRL Technical Report No. 5992, Washington, D.C., 131pp.
- McBride, J. L., 1981: Observational analysis of tropical cyclones formation. Part 1: Basic description of data sets. J. Atmos. Sci., 38, 1117-1131.
- Merrill, R. T., 1984: Structure of the tropical cyclone outflow layer. Preceedings of the 15th Technical Conference on Hurricanes and Tropical Meteorology, AMS, January 9-13, Miami, Florida.
- \_\_\_\_\_, 1988a: Characteristics of the upper-tropospheric Environmental flow around hurricanes, J. Atmos. Sci., 45, 1665-1677.
- \_\_\_\_\_, 1988b: Environmental influences on hurricane intensification. J. Atmos. Sci., 45, 1678-1687.



- Miller, B. I., 1963: The three-dimensional wind structure around a tropical cyclone. National Hurricane Research Project, Report No. 15, 41 pp.
- Molinari, J., and D. Vollaro, 1989: External influences on hurricane intensity. Part I: Outflow layer eddy momentum fluxes. J. Atmos. Sci., 46, 1093-1105.
- Ooyama, K. V., 1987: Numerical experiments of study and transient jets with a simple model of the hurricane outflow layer. Preprints, the 17th Conference on Hurricanes and Tropical Meteorology, AMS, April 7-10, Miami, Florida.
- Palmen, E. and H. Riehl, 1957: Budget of angular momentum and kinetic energy in tropical cyclones. J. Meteor., 14, 150-159.
- \_\_\_\_\_ and C.W. Newton, 1969: Atmospheric Circulation Systems. Academic Press, New York, 603pp.
- Pfeffer, R. L., 1958: Concerning the mechanisms of hurricanes. J. Meteor., 15, 113-119.
- Rodgers, E. B., 1987: Evidence of upper-tropospheric influence on tropical cyclone intensity change using satellite observations. Preprint, 17th Conference on Hurricanes and Tropical Meteorology, AMS, April 7-10, Miami, Florida.
- \_\_\_\_\_, S. W. Chang, J. Stout, J. Steranka and J. J. Shi, 1989a: Satellite observed upper-tropospheric influence on tropical cyclone convection, Submitted to Mon. Wea. Rev.
- \_\_\_\_\_, J. Stout and J. Steranka, and S. Chang, 1989b: Tropical cyclone/upper-atmospheric interaction as inferred from satellite total ozone observation. To appear in J. Appl. Meteor. Climate.
- Sadler, J. C., 1976: The role of the tropical upper-tropospheric trough in early season typhoon development. Mon. Wea. Rev., 104, 1266-1278.

- \_\_\_\_\_, 1978: Mid-season typhoon development and intensity changes and the tropical upper-tropospheric trough. Mon. Wea. Rev., 106, 1137-1152.
- Sheets, R. C., 1968: Some mean hurricane soundings. J. Appl. Meteor., 8, 134-146.
- Steranka, J., E. B. Rodgers and R.C. Gentry, 1986: The Relationship Between Satellite Measured Convection Burst and Tropical Cyclone Intensification. Mon. Wea. Rev., 114, 1539-1546.
- Uccellini, L.W., P.J. Kocin, R.A. Petersen, C.H. Wash, and K.F. Brill, 1984: The President's day cyclone of 18-19 February 1979: synoptic overview and analysis of the subsynoptic jet streak influencing the pre-cyclogenetic period. Mon. Wea. Rev., 112, 31-55.

## Figures

1. Geopotential height field (with 15 gpm intervals) and wind vectors at 150 mb level for the strong control case at 72 h. Note locations of cross-sections AA' in entrance region and BB' in exit region. Cross-sectional analyses will be presented in Figs. 5 and 6.
2. Same as Fig. 1 except for the weak control case at 96 h.
3. Isotachs with intervals of  $7.5 \text{ ms}^{-1}$  at 150 mb for the strong case at 72 h.
4. Isotachs with intervals of  $5 \text{ ms}^{-1}$  at 150 mb for the weak case at 96 h.
5. The wind speed perpendicular (shown by isotachs with positive numbers denoting a wind direction outward from the plot) and tangential (shown by vectors) to the cross-section AA' in the jet entrance region (shown in Fig. 1) of (a) the strong case at 72 h and (b) the weak case at 96 h. The vectors are formed by horizontal winds in  $\text{m s}^{-1}$  and vertical velocities in  $\text{mb h}^{-1}$ . The maximum horizontal and vertical velocity component are plotted at the lower and upper right corners, respectively.
6. Same as Fig. 5, except for the jet exit region for cross section BB'.
7. The 150 mb RH field and the wind vectors  $>20 \text{ ms}^{-1}$  for (a) the strong case at 72 h and (b) the weak case at 96 h.
8. (a) A 3D (viewing from E-NE of the storm) view and (b) plane view of the pressure surface where  $PV=2 \times 10^{-7} \text{ mb}^{-1}\text{s}^{-1}$  for the strong case. This PV value is sometimes used to define the tropopause in mid-latitudes.
9. Trajectories formed by particles released at various radii and pressure levels at  $t=0$ . Most particles that reach the outflow level are transported outward by the outflow jet. Most particles released at radii of 20 and 100 km are "trapped" inside the radius of the maximum wind and only rise slowly and drift toward the NW.
10. Variations of the central pressure of the control (weak) and Exp. 1.
11. The vertical distribution of mass divergence/convergence in a  $10^\circ$  long. x  $10^\circ$  lat. box centered around the storm for the weak control case, Exp. 1, and a supplementary experiment (Exp. 1a) in which latent heating is suppressed.
12. The location of the outflow jet and distributions of a 24 h period accumulated precipitation for the control (upper panel) and two 12 h periods accumulated precipitation of Exp. 2.

Interval = 5m

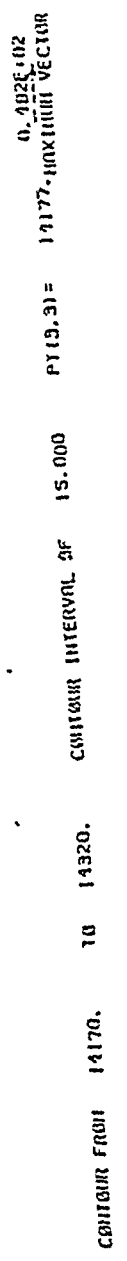
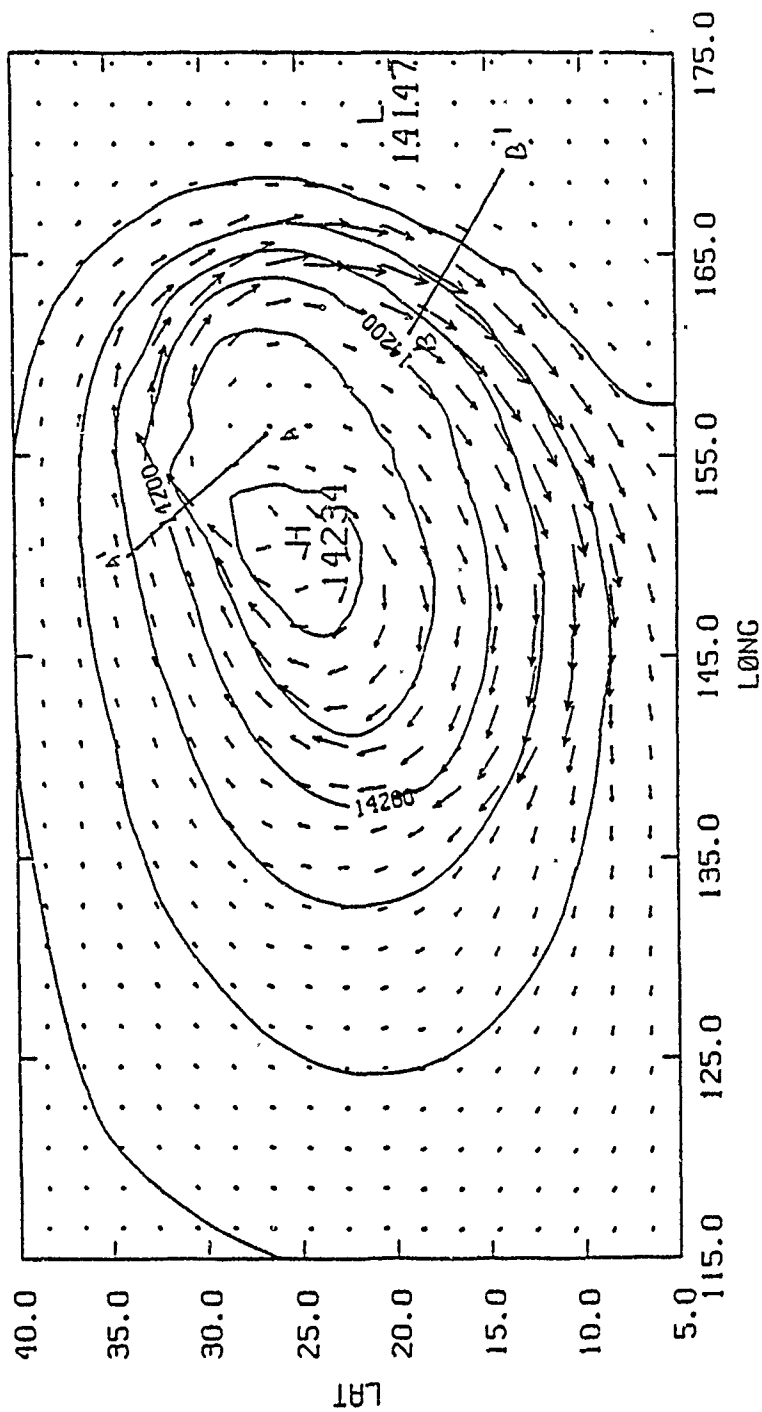


Fig 2.

V. PHI. AT P = 150 MB AT T= 96 HR

interval = 15 m



0.336E+02

PT12.31= 14157

15.000

CONTINUUM INTERVAL OF

14200

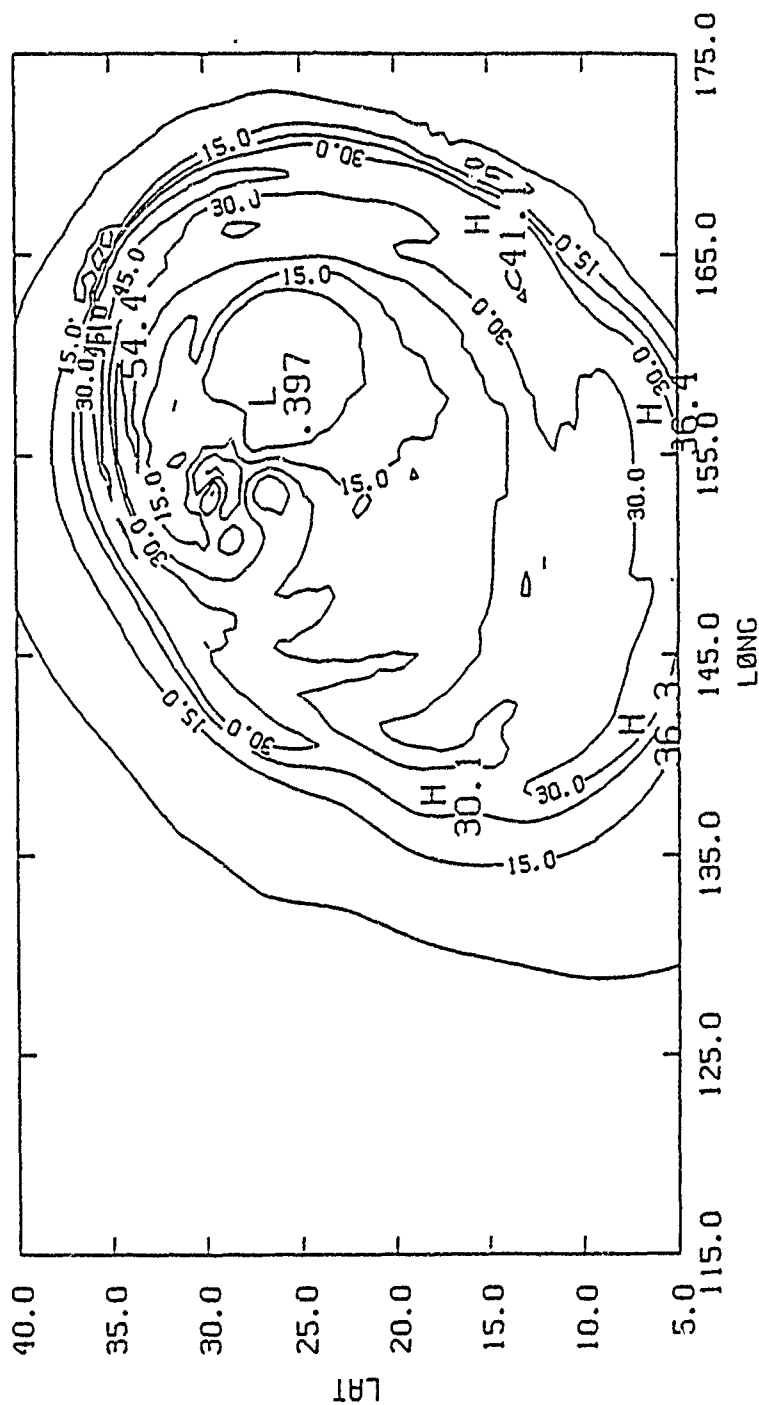
14

14146

CONTINUUM FROM

Fig 3

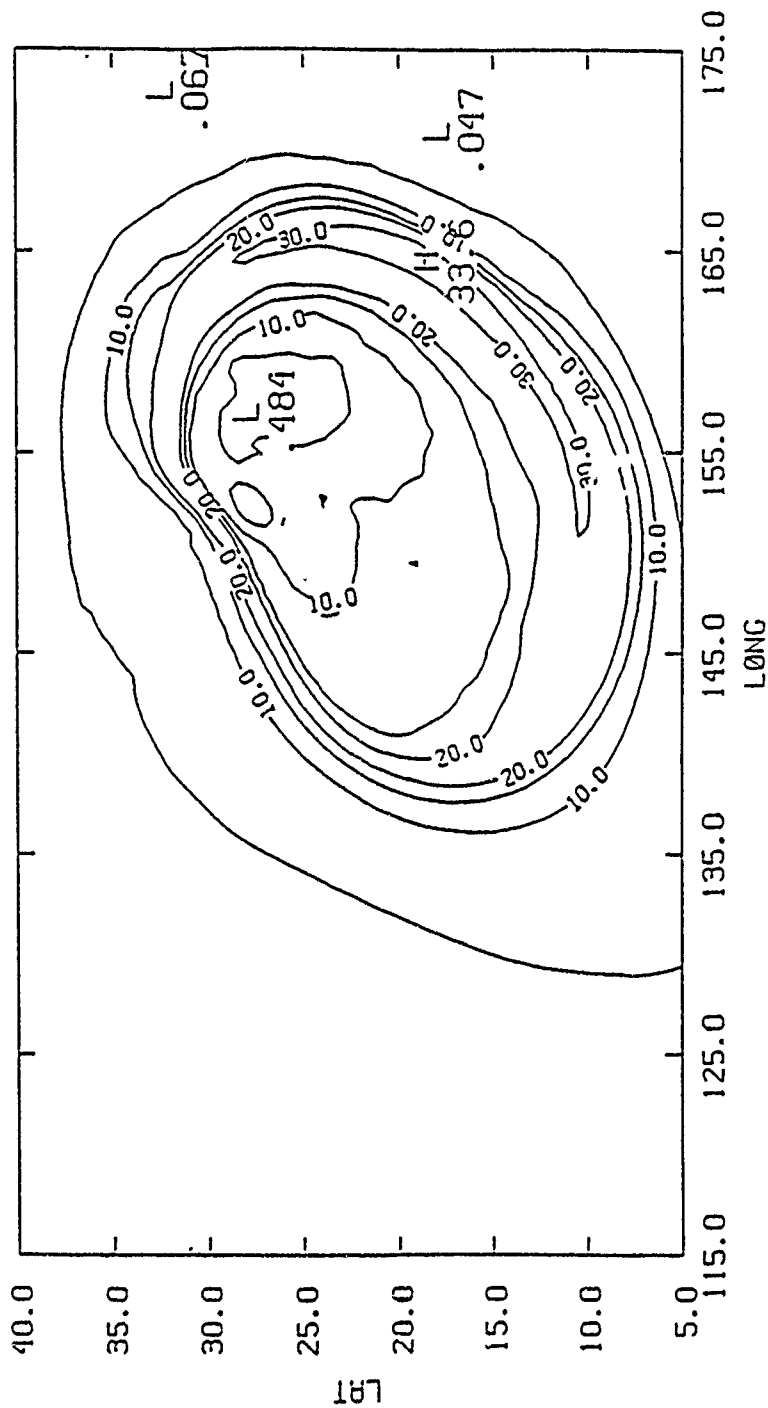
WIND SPEED (M/S) AT P= 150 MB AT T= 72 HR



CONTOUR FROM 0.00000 TO 60.000 CONTOUR INTERVAL OF 7.5000 PT(3.31)= 1.0723

Fig 4

WIND SPEED (M/S) AT P= 150 MB AT T= 96 HR



CONTINUOUS FROM 0.00000 TO 40.00000 CONTINUOUS INTERVAL OF 5.00000 PLOT IS 10.00000

```

CONTOUR FROM -200.00      T0 190.00      CONTOUR INTERVAL OF 10.000      PT(3,31)= 5.5007 MAXIMUM VECTOR 0.212E+02

```



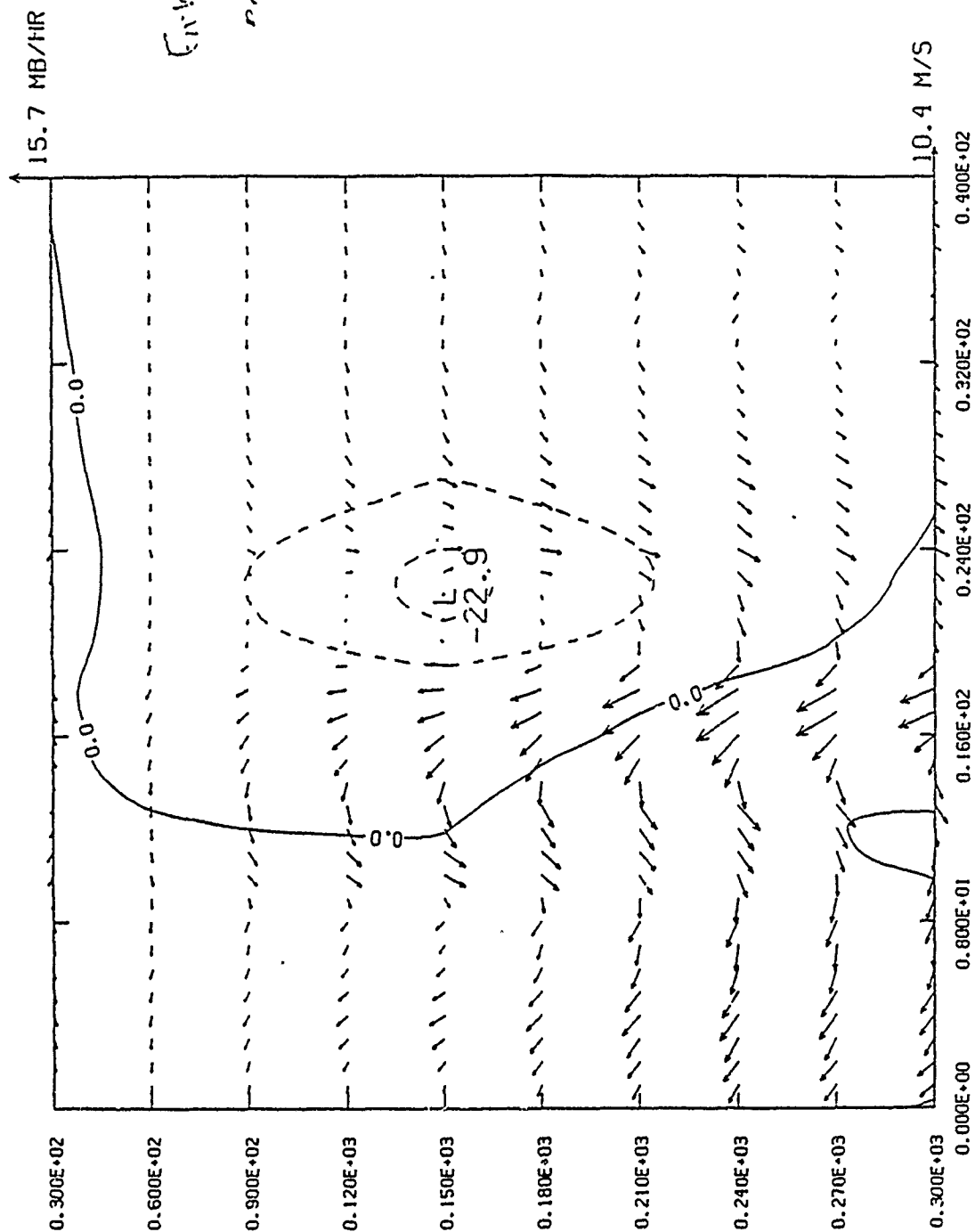
MODEL10 (.5 X .5 GRID)(141X91) START TIME 0000

A (156.0, 26.5N) B (150.0, 34.0N)

CROSS SECTION FROM A TO B FOR CIRCULATION AT 96HR

12

Fig 5-b



Ensemble  
of blends

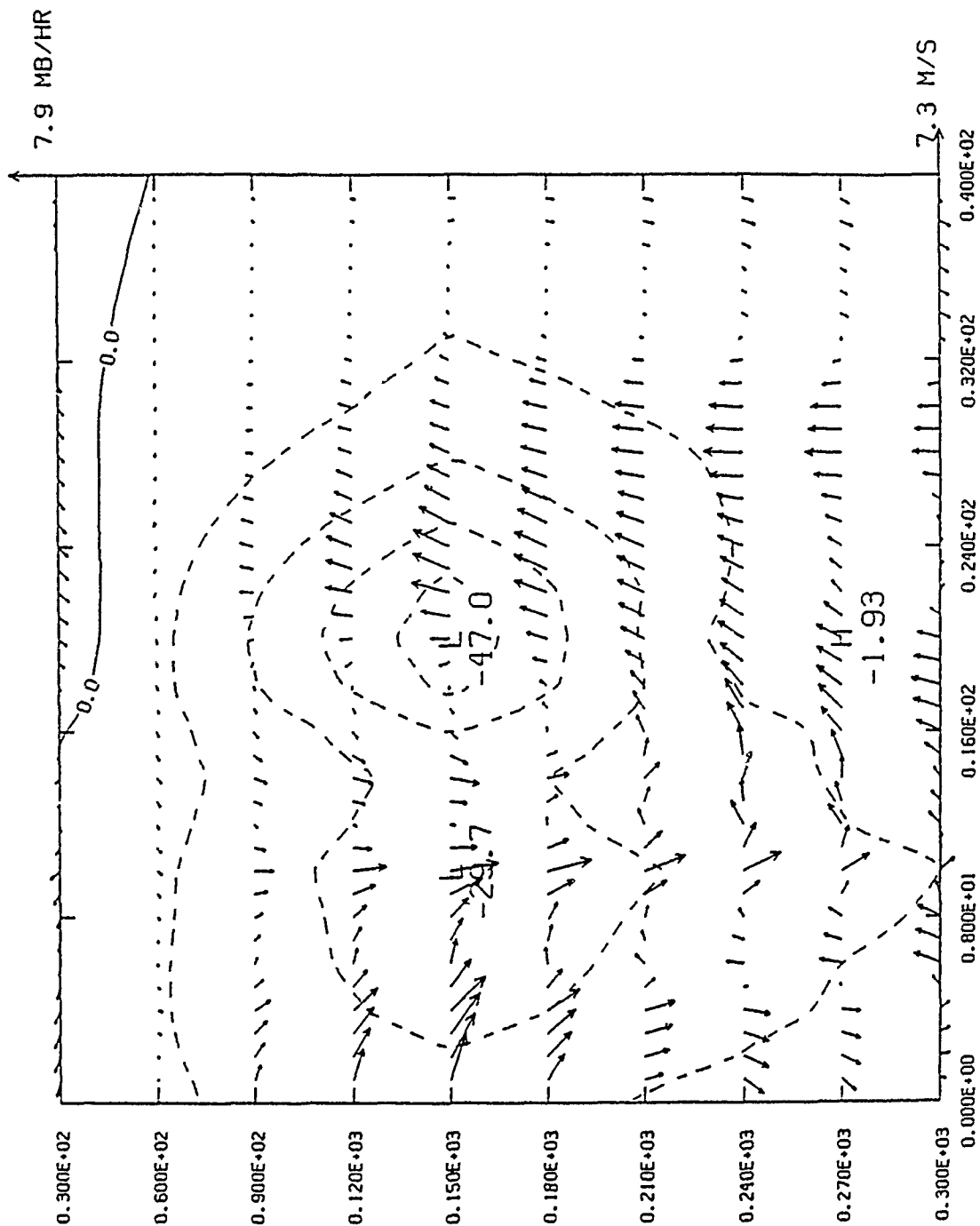
CONTOUR FROM -200.00 TO 190.00 CONTOUR INTERVAL OF 10.000 PT(3.31)= 5.4171 MAXIMUM VECTOR 0.187E+02

MODEL10 (.5 X .5 GRID)(141X91) START TIME 0000

A (164.0, 26.5N) B (174.0, 26.5N)

CROSS SECTION FROM A TO B FOR CIRCULATION AT 72HR

EXIT



CROSS SECTION FROM A TO B FOR CIRCULATION AT 72HR

0.805E+01

PT(3.31) = -9.7188

CROSS SECTION FROM A TO B FOR CIRCULATION AT 72HR

0.805E+01

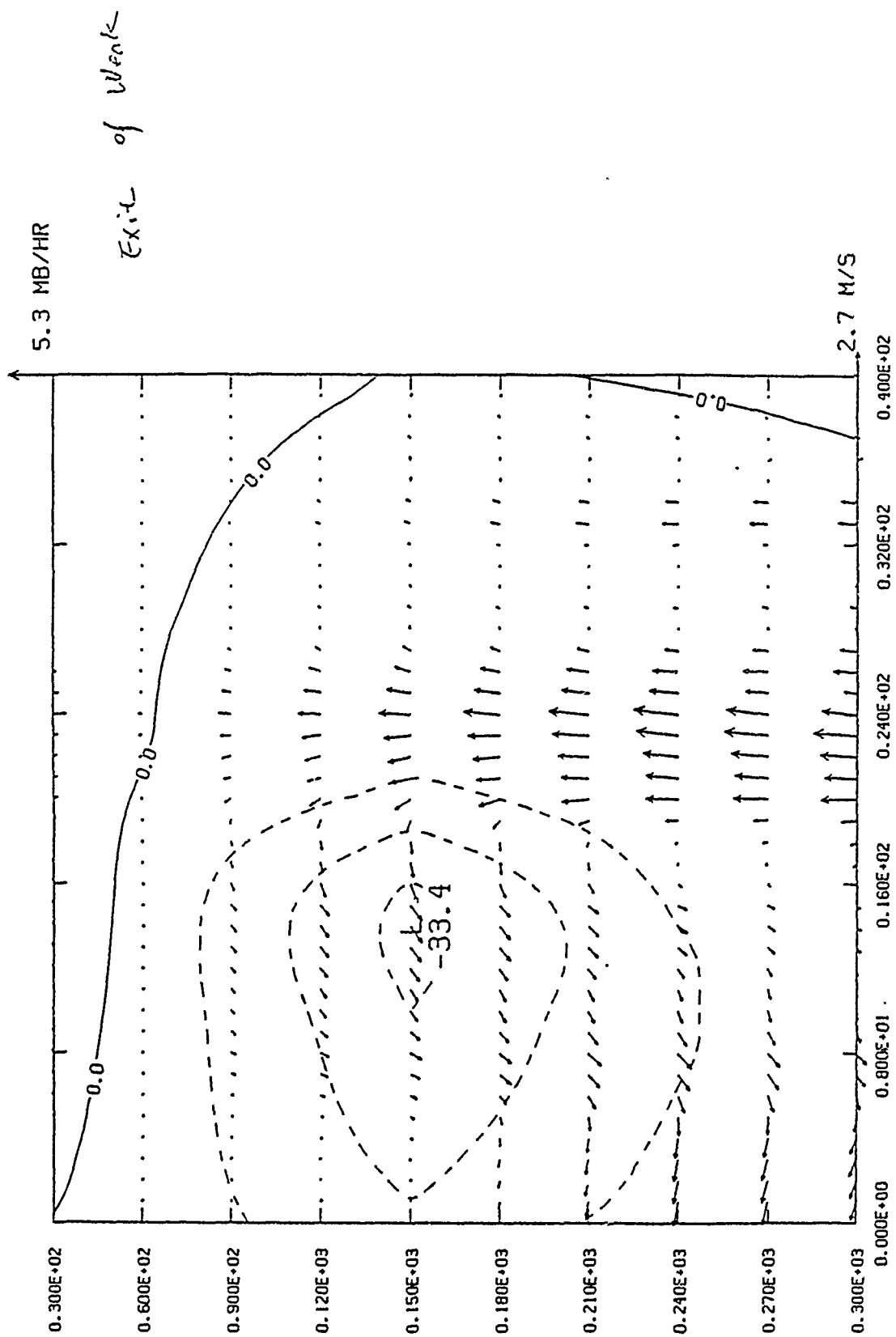
PT(3.31) = -9.7188

CROSS SECTION FROM A TO B FOR CIRCULATION AT 72HR

Fig 66

A (161.0, 19.0N) B (169.0, 14.0N)

CROSS SECTION FROM A TO B FOR CIRCULATION AT 96HR



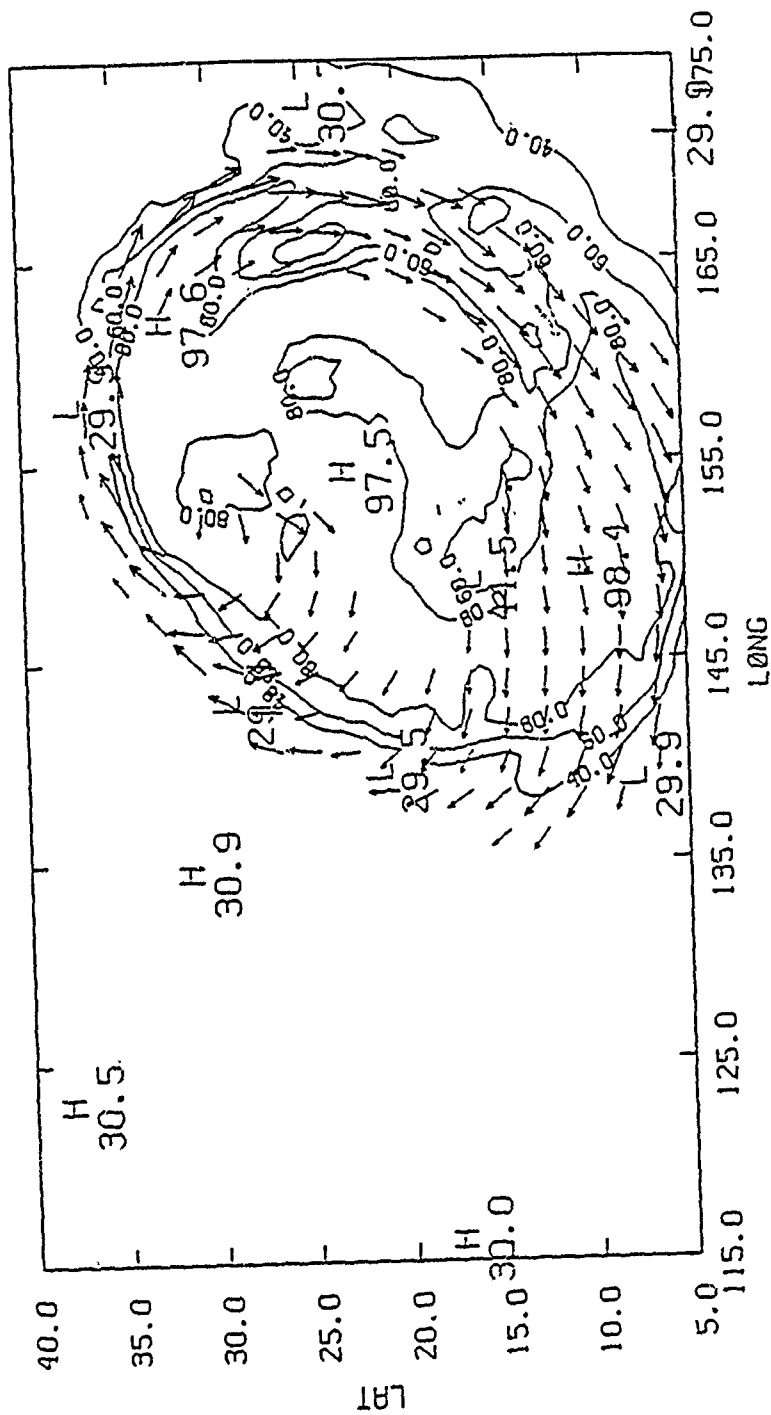
```

CONTOUR FROM -200.00 TO 190.00 CONTOUR INTERVAL OF 10.000
                                P(13.3) = -7.2227 MAXIMUM VECTOR
                                0.533E+01

```

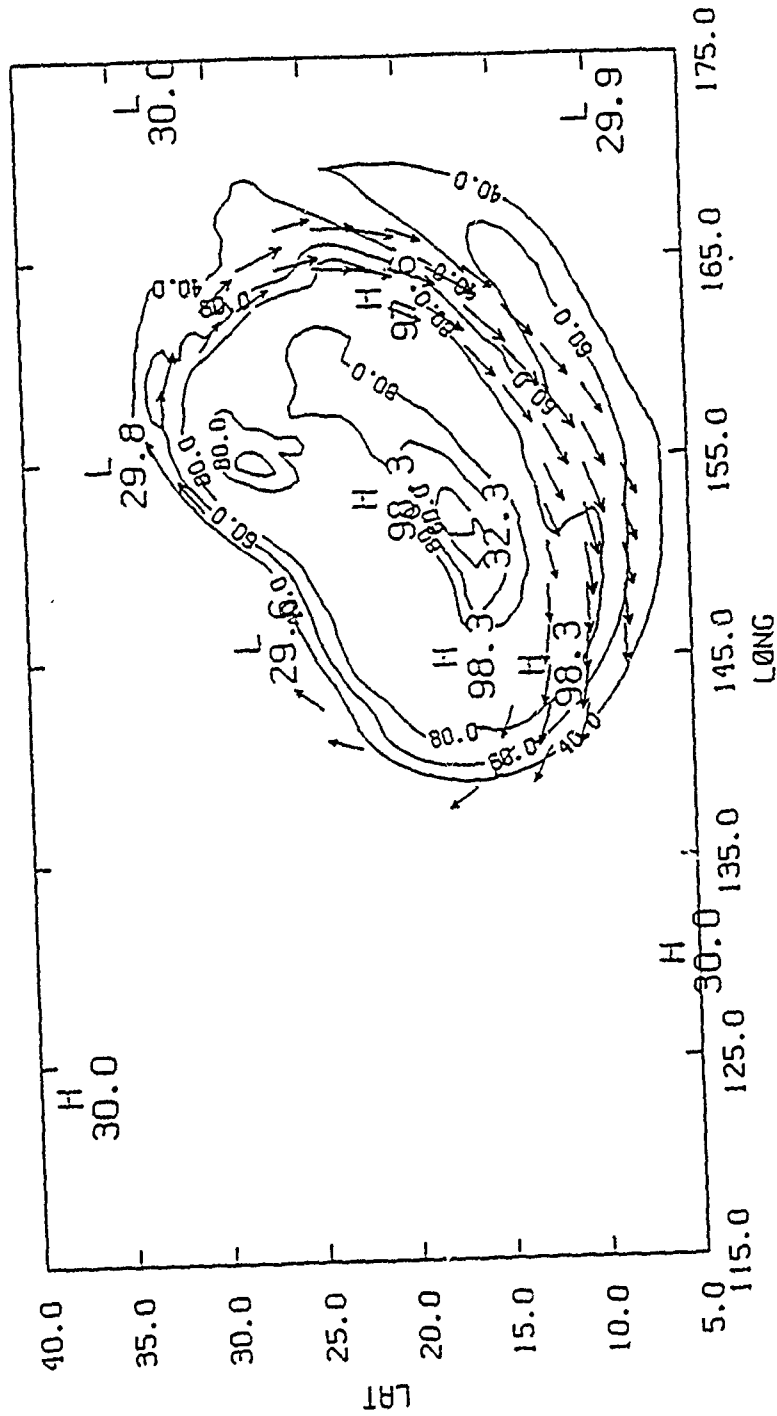
Fig 7.a

RELATIVE HUMIDITY AT P= 150 MB AT T= 72 HR



CONTINUED FROM 40.000 10 00.000 CONTINUED FROM 20.000 P(3.3)= 23.972 INVERTED C'100K 0.492E+02

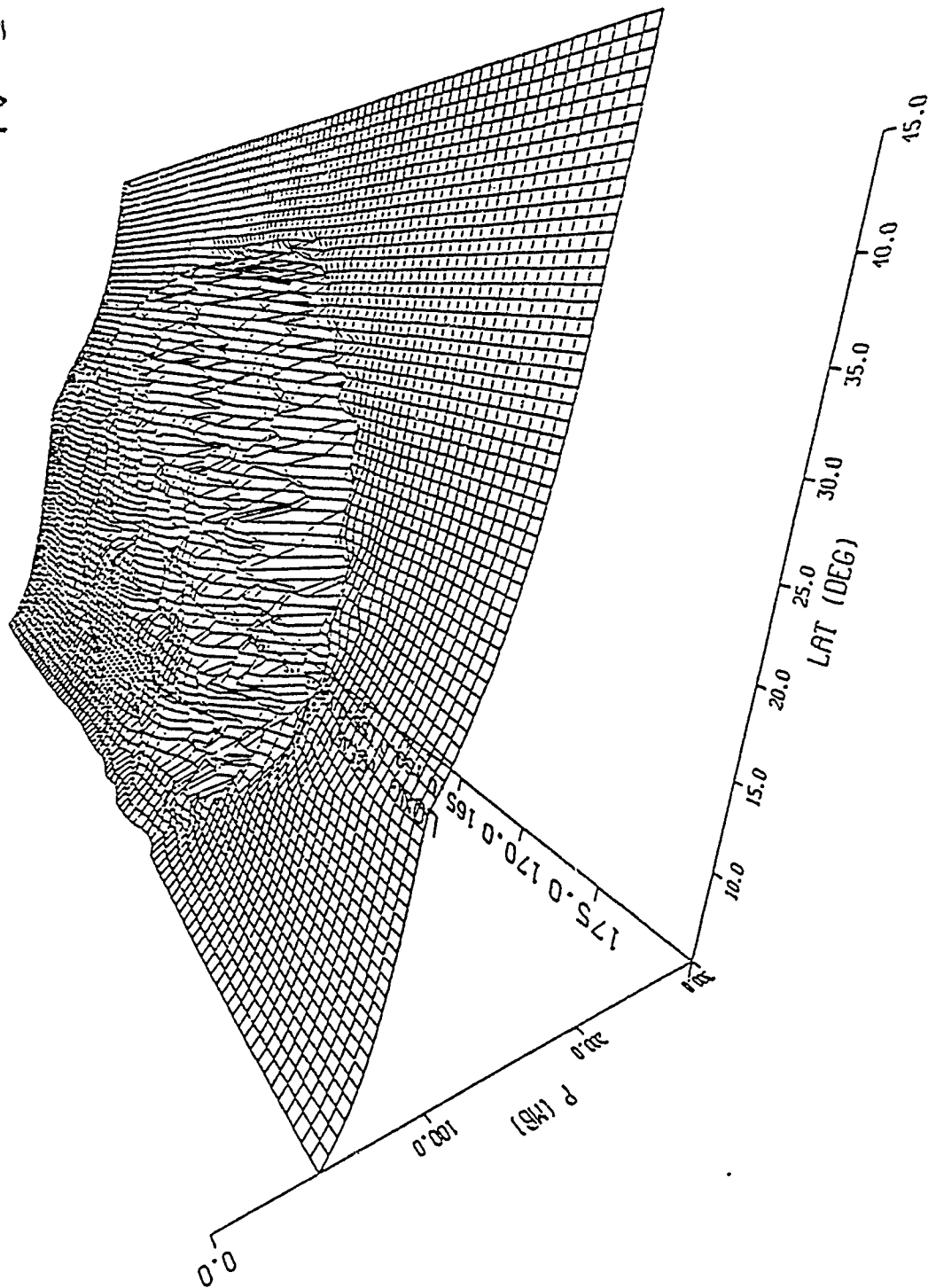
RELATIVE HUMIDITY AT P= 150 MB AT T= 96 HR



CONTOUR FROM 40.000 TO 80.000 CONTOUR INTERVAL OF 20.000 PT(3,9)= 20.950 MAXIMUM VFC10R 0.3300012

Fig. 8

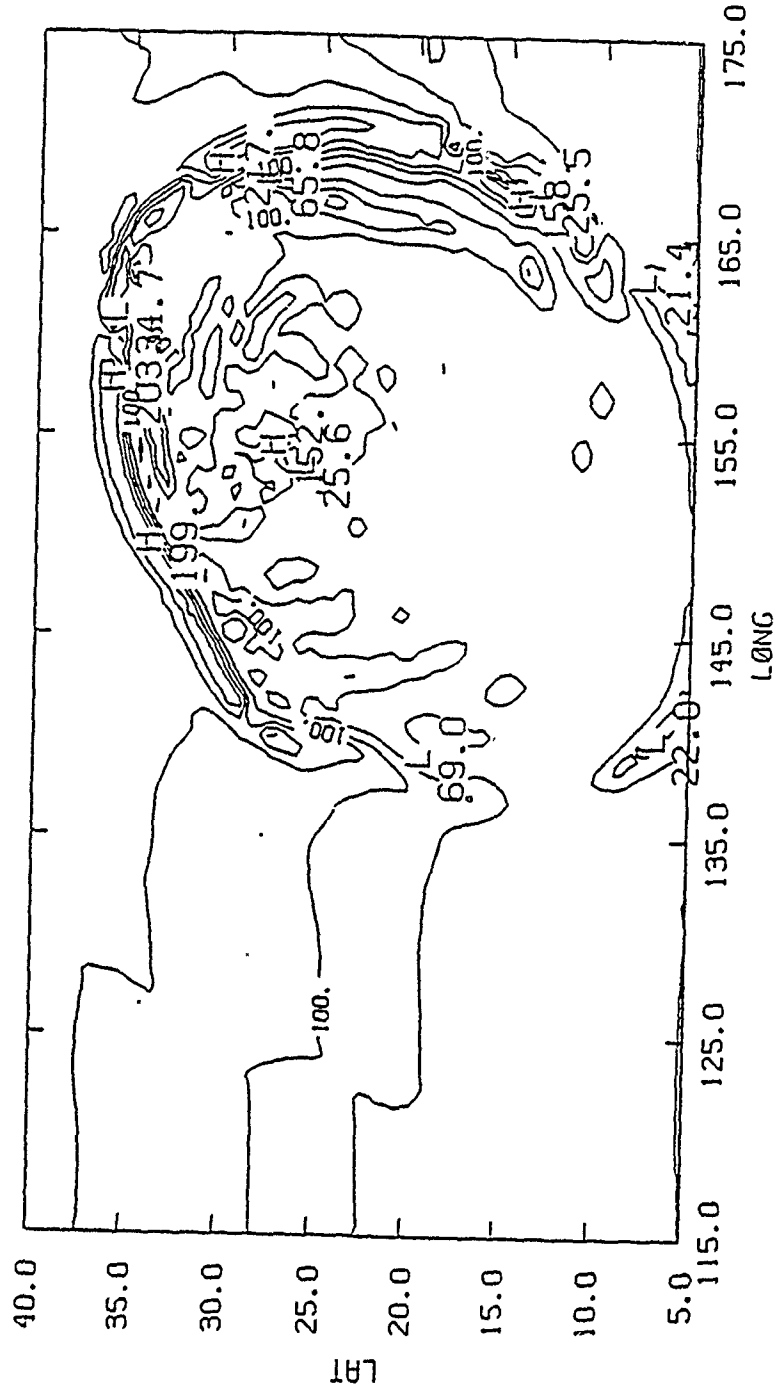
$$PV = 2 \times 10^{-2} \text{ mG}^{-1} \text{ s}^{-1}$$



MODEL91 (1.5 X .5 GRID) (141X91) START TIME 0000

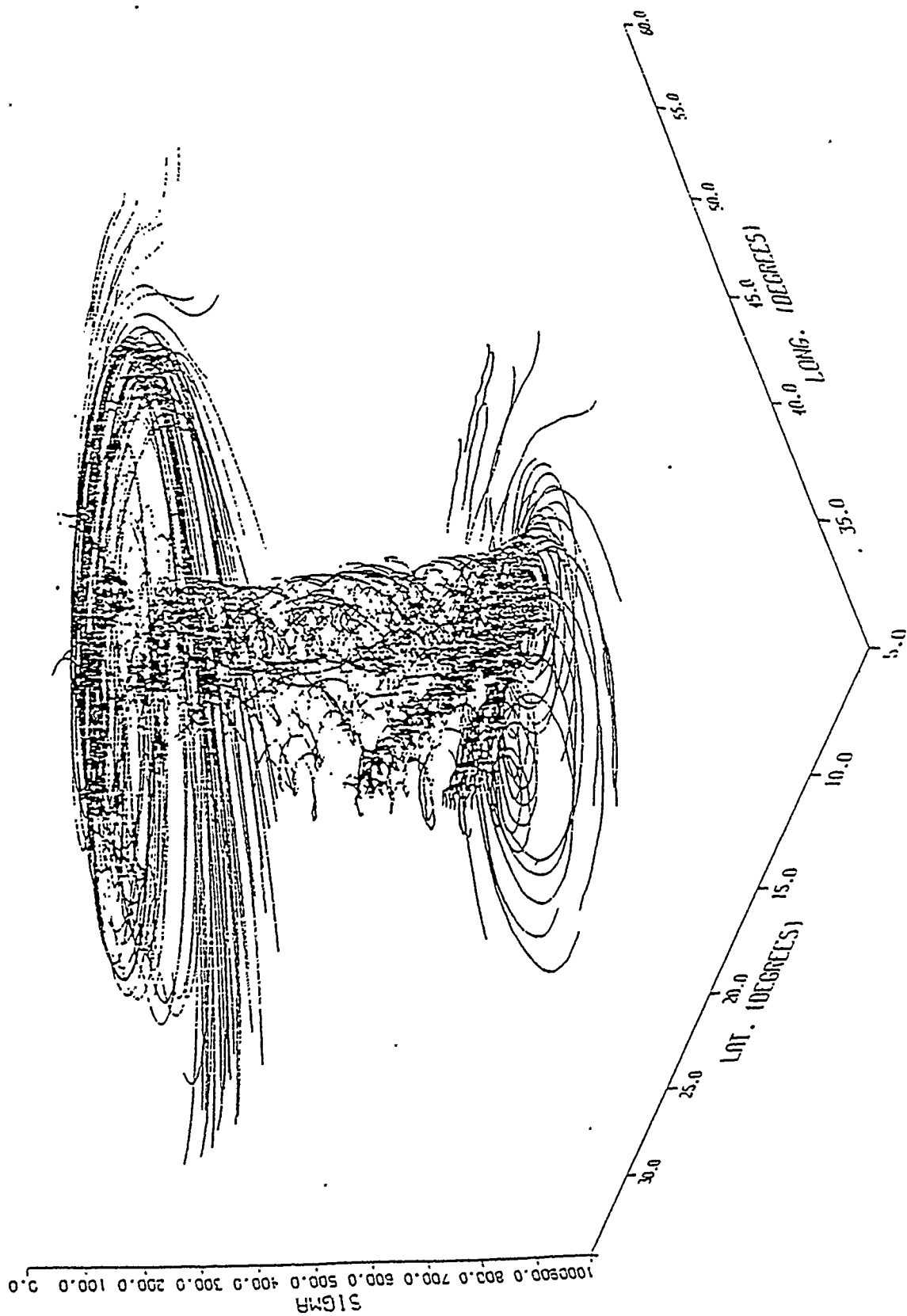
8b

PRES. VALUE (MB) AT PV = 0.2E-06 (IMB\*S)\*\*-1)) AT 72 HR



CONTOUR FROM 25.000 TO 350.00 CONTOUR INTERVAL OF 25.000 P119.314 34.400

Fig 9.





A & C curve

10

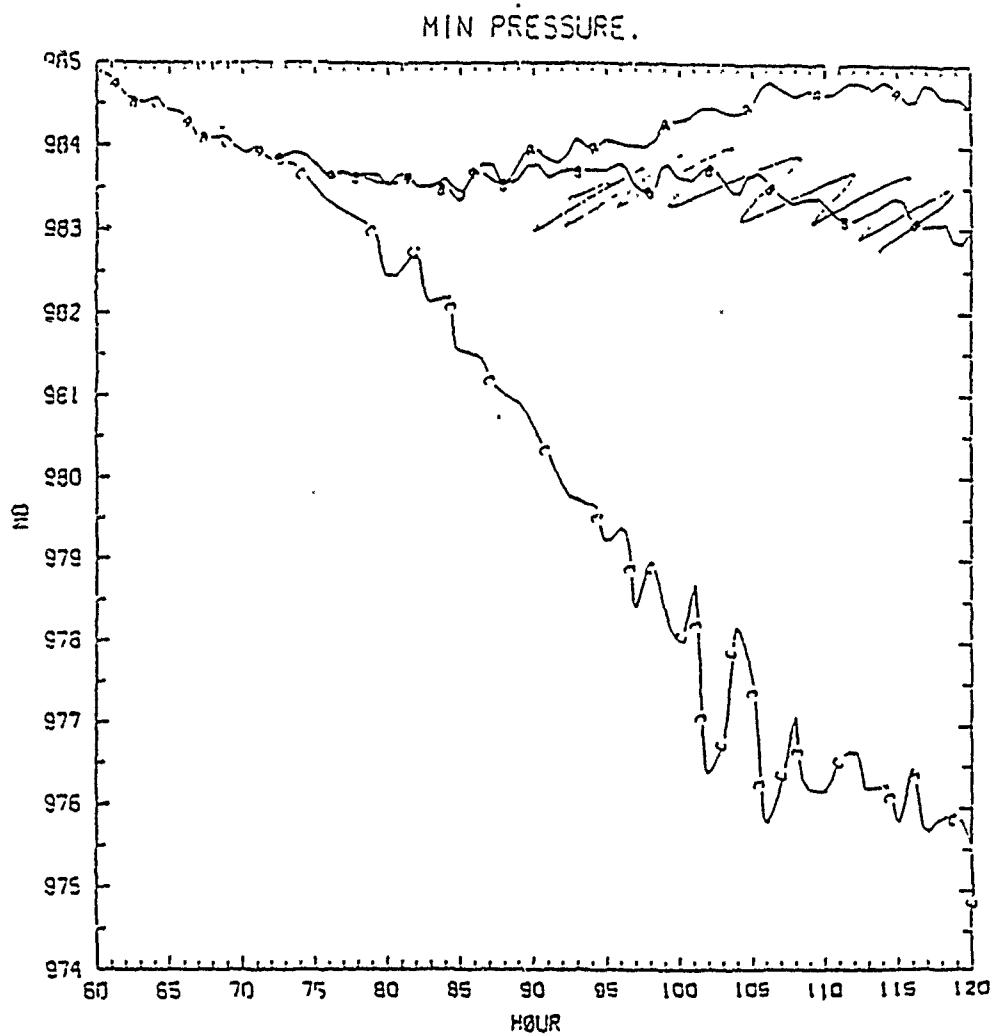


Figure 4.1 Variation of the minimum surface pressure with time. A represents the control model tropical cyclone. B and C represent Experiment 1 and 2, respectively.

Fig 12

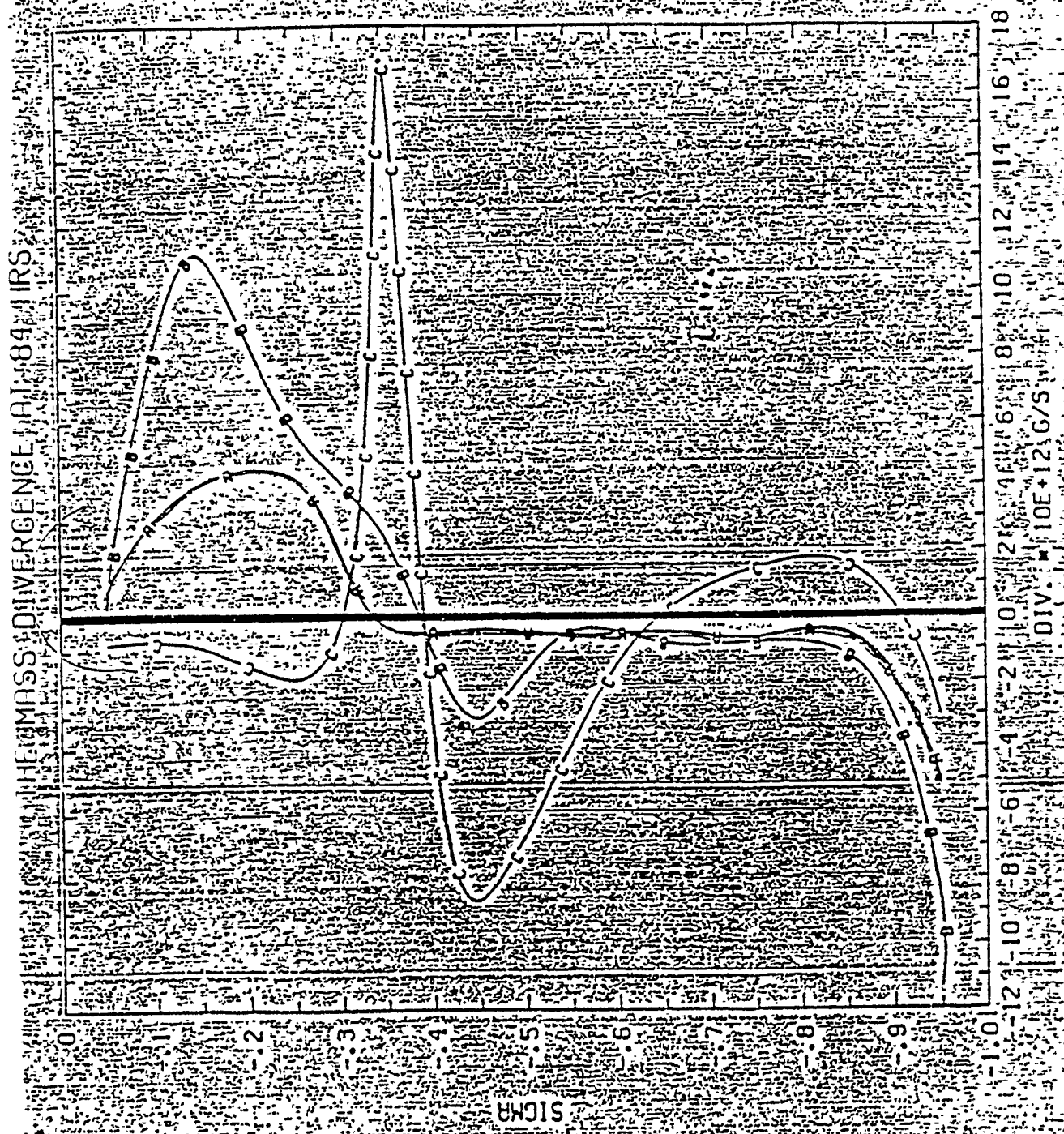
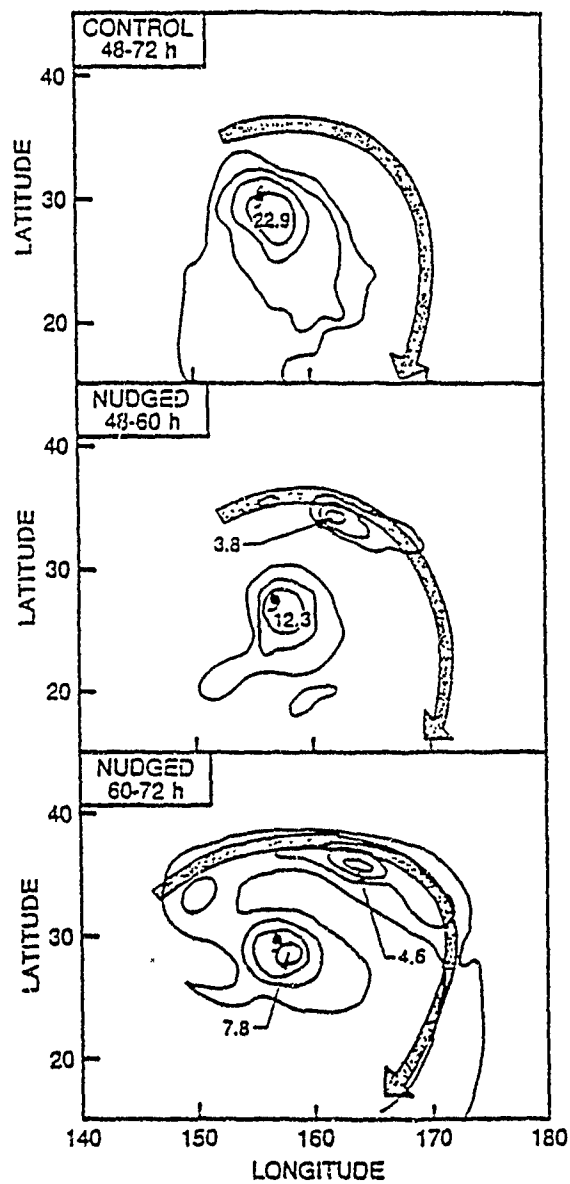


Fig 13.

# ACCUMULATED PRECIPITATION



## **APPENDIX K**

### **Vertical Constituent Transport in the Mesosphere**

## Vertical Constituent Transport in the Mesosphere

DARRELL F. STROBEL,<sup>1,2</sup> MICHAEL E. SUMMERS,<sup>2</sup> RICHARD M. BEVILACQUA,<sup>3</sup>  
MATTHEW T. DELAND,<sup>3,4</sup> AND MARK ALLEN<sup>5,6</sup>

Ground-based microwave spectroscopy measurements of mesospheric CO and H<sub>2</sub>O vertical mixing ratio profiles are used to infer vertical mixing rates in the upper mesosphere. The CO and H<sub>2</sub>O data consistently imply vertical eddy diffusion coefficients in the 70- to 85-km region of  $\lesssim (1-2) \times 10^5 \text{ cm}^2 \text{ s}^{-1}$  during spring through summer at mid-latitudes. Although chemical acceleration of vertical transport is substantial for O and O<sub>3</sub> below the mesopause, the divergences of their associated fluxes are modest, with at most a factor of 2 effect on the concentrations of O and O<sub>3</sub> for measured variability in gravity wave activity. Comparison of Solar Mesosphere Explorer (SME) O<sub>3</sub> data with model results reinforces the conclusions of slow vertical mixing in the upper mesosphere as a consequence of the reduced HO<sub>x</sub> catalytic loss of odd oxygen. The changes in chemical rate constants recommended by Fusch and Eckman (1985), in conjunction with slow vertical mixing, yield good agreement with SME O<sub>3</sub> data. The slow vertical mixing deduced in this study is consistent with upper limits obtained from studies of the mesospheric heat budget and could be construed as evidence for an advectively controlled mesosphere. A comparison of the vertical eddy diffusion coefficients for momentum stresses, constituent transport, and heat transport suggests that the eddy Prandtl number must be of order 10.

## 1. INTRODUCTION

It is now widely agreed that the transport of constituents, heat, and momentum in the mesosphere is generated principally by breaking gravity waves, with an additional contribution from breaking tidal waves [e.g., Lindzen, 1981; Holton, 1982, 1983; Dunkerton, 1982; Schoeberl *et al.*, 1983; Chao and Schoeberl, 1984; Apruzese *et al.*, 1984; Fritts and Dunkerton, 1985; Garcia and Solomon, 1985; Strobel *et al.*, 1985]. In the initial parameterization of turbulence and stress produced by breaking gravity waves, Lindzen [1981] estimated the intensity of the turbulence, as represented by the eddy or turbulent diffusion coefficient of momentum  $D_M$ , to be greater than  $10^6 \text{ cm}^2 \text{ s}^{-1}$  in the mesosphere but noted that this quantity was proportional to  $(\bar{u} - c)^4$ , where  $\bar{u}$  is the mean zonal wind and  $c$  is the phase speed of the gravity wave. This extreme sensitivity of  $D_M$  to  $(\bar{u} - c)$  makes an accurate calculation of its value extremely difficult. Because the mean meridional circulation and associated transport of constituents and heat are also directly dependent on  $D_M/(\bar{u} - c)$ , theoretical prediction of their strengths is also subject to the uncertain magnitude of  $(\bar{u} - c)^3$ .

In a turbulent atmosphere, tracer and potential temperature transport by eddies should be described by the same coefficient,  $D_H$ , in the limit of a chemically inert species and adiabatic motion. Here  $D_H$  is the thermal eddy diffusion coefficient, and the eddy Prandtl number is  $P_r = D_M/D_H$ . The studies of Allen *et al.* [1981, 1984] and Garcia and Solomon

[1985] apparently require  $D_H \sim (1.5-2) \times 10^6 \text{ cm}^2 \text{ s}^{-1}$  for chemically active species in the mesosphere. In contrast, studies of the mesospheric heat budget concluded that  $D_H < 10^6 \text{ cm}^2 \text{ s}^{-1}$ , with a preferred value of, at most,  $6 \times 10^5 \text{ cm}^2 \text{ s}^{-1}$  [Apruzese *et al.*, 1984; Strobel *et al.*, 1985]. In addition, the recent water vapor measurements of Bevilacqua *et al.* [1983, 1985a] and Olivero *et al.* [1986] also appear to require lower  $D_H$  values than those used by Garcia and Solomon [1985] and Allen *et al.* [1981]. Furthermore, the high ozone mixing ratios observed by the Solar Mesosphere Explorer (SME) [Thomas *et al.*, 1984] in the upper mesosphere are also consistent with slow vertical transport and resultant low water vapor mixing ratios.

It should also be noted that the chemical time constant for odd oxygen at 80 km is a factor of  $10^2$  less than the chemical time constant for irreversible loss of H<sub>2</sub>O. Schoeberl *et al.* [1983] parameterized vertical transport and included the effects of breaking gravity waves and a species dependent, vertical eddy diffusion coefficient which, for parameters appropriate for mesospheric conditions, had a linear dependence on the irreversible chemical loss rate. Assuming  $D_H < 6 \times 10^5 \text{ cm}^2 \text{ s}^{-1}$ , they estimated, for chemically active species in the mesosphere and lower thermosphere, that the chemical acceleration term could equal or exceed the thermal eddy diffusion coefficient.

In this study we address three key issues that involve vertical transport: (1) which mesospheric constituent is most diagnostic of vertical transport, (2) what magnitude of mesospheric vertical mixing is implied by this constituent's vertical profile, and (3) to what extent can chemical acceleration of vertical transport for chemically active species alleviate the apparent discrepancy between transport of constituents and heat. Model results are compared with SME ozone measurements, water vapor measurements, and carbon monoxide measurements.

## 2. MODEL

The model adopted for this study is the general one-dimensional, time dependent, photochemical model with vertical transport by eddy and molecular diffusion developed by Allen *et al.* [1981, 1984] and used to study chemistry and transport in the mesosphere and lower thermosphere. It in-

<sup>1</sup> Science Applications International Corporation, McLean, Virginia.

<sup>2</sup> Also at Department of Earth and Planetary Sciences, The Johns Hopkins University, Baltimore, Maryland.

<sup>3</sup> E. O. Hulburt Center for Space Research, Naval Research Laboratory, Washington, D. C.

<sup>4</sup> Bendix Field Engineering Corporation, Oxon Hill, Maryland.

<sup>5</sup> Earth and Space Sciences Division, Jet Propulsion Laboratory, California Institute of Technology, Pasadena.

<sup>6</sup> Also at Division of Geological and Planetary Sciences, California Institute of Technology, Pasadena.

TABLE 1.

Model	$D_H$ Profile	Chemical Acceleration	Comments
A	Allen et al. [1981]	no	DeMore et al. [1985] chemistry
B	initial fit to Bevilacqua et al. [1985a] $H_2O$ data	yes	
C	best overall fit to $H_2O$ and $CO$ data from Bevilacqua et al. [1985a, b]	yes	
D	constant with altitude	yes	
E	same as model C	yes	$CO$ chemistry modified (see text)

All models use the chemistry of Allen et al. [1984], with rate constants given by DeMore et al. [1985].

cludes the chemistry and transport of the major nonnitrogen chemical species in the altitude range 40–130 km: O, O(<sup>1</sup>D), O<sub>2</sub>, O<sub>3</sub>, H, H<sub>2</sub>, OH, H<sub>2</sub>O, HO<sub>2</sub>, H<sub>2</sub>O<sub>2</sub>, CO, CO<sub>2</sub>, CH<sub>4</sub>, and Ar. Because ClO<sub>x</sub> and NO<sub>x</sub> are important in the odd oxygen chemistry below 50 km, we regard our solutions as accurate only somewhat above 50 km.

The chemical model used in our study is essentially Table 1 of Allen et al. [1984], with kinetic rate constants updated in accordance with DeMore et al. [1985]. The solar fluxes, photodissociation cross sections, and radiative transfer calculations are identical to Allen et al. [1984]. The lower and upper boundary conditions are also identical with one exception, at 40 km the H<sub>2</sub>O mixing ratio is set equal to 6.4 parts per million by volume (ppmv). Only diurnally averaged calculations are performed, because Allen et al. [1984] have shown that they are sufficiently accurate for comparison with SME data, which is acquired at a local time of 1500. Table 1 provides a summary of the principal features and differences among the various models used in this study.

The chemical acceleration of vertical transport is also included in the model. Strobel [1981] derived a globally averaged expression for this acceleration by linear gravity waves appropriate for a one-dimensional model as

$$K_{chem}(i) = \frac{(L_i + \sigma)\bar{w}^2}{K^2(\bar{u} - c)^2 + (L_i + \sigma)^2} \quad (1)$$

where  $L_i$  is the net chemical loss rate of species  $i$ ,  $\sigma$  is the growth rate of the wave and represents transience,  $k$  is the horizontal wave number, and  $w'$  is the vertical wave velocity. Schoeberl et al. [1983] extended this parameterization to include the effect of breaking gravity waves and obtained an effective vertical eddy diffusion coefficient of

$$K_{zz}(i) = D_H + \frac{(L_i + \sigma)\bar{w}^2}{k^2(\bar{u} - c)^2 + (L_i + \sigma)^2} \quad (2)$$

for a single gravity wave. The first term represents diffusion by the background turbulence created by the breaking gravity wave for chemically inert species and is equal to the diffusion rate for potential temperature. The second term arises physically because the mixing ratio perturbation,  $\mu'$ , for a chemical species with finite chemical loss ( $L_i \neq 0$ ), undergoes a phase shift relative to the horizontal wave velocity  $v'$  and  $w'$  such that the eddy fluxes  $\mu'v'$  and  $\mu'w'$  are nonzero rather than in quadrature, as in the limit  $L_i \rightarrow 0$ .

Equation (2) must be summed over all gravity waves en-

tering the mesosphere. For long time averages, which are appropriate for our study,  $\sigma \sim 0$  by definition. Only waves with appreciable amplitudes will be important, and they will have amplitudes at or near the saturation limit. Typical mesospheric values for  $|\bar{u} - c|$  and  $k$  are  $\sim 5 \times 10^3$  cm s<sup>-1</sup> and  $2\pi/100$  km, respectively [Vincent and Reid, 1983]. With  $k|\bar{u} - c| \sim 3 \times 10^{-3}$  s<sup>-1</sup>, all chemical species under consideration that undergo significant transport have loss rates such that  $L_i^2 \ll k^2(\bar{u} - c)^2$ . Thus (2) can be written approximately as

$$K_{zz}(i) = D_H + \sum_{\text{waves}} L_i \frac{\bar{w}^2}{k^2(\bar{u} - c)^2} = D_H + \frac{L_i}{N^2} \sum_{\text{waves}} (\bar{u}^2 + \bar{v}^2) \quad (3)$$

with standard gravity wave expressions and the dispersion relation, where  $N$  is the buoyancy frequency. According to Vincent [1984], gravity wave amplitudes are at or near the saturation limit in the mesosphere, and we write (3) in terms of the saturation limit  $A$  ( $=1$ )

$$K_{zz}(i) = D_H + 2 \times 10^{10} L_i A \quad (4)$$

with the numerical value in cgs units derived from Vincent [1984] at saturation, when  $A = 1$ . According to more recent measurements by Vincent [1986], gravity wave amplitudes vary throughout the year in the range  $A = 0.6$ – $2$ . Note that even if a gravity wave breaks, it can still chemically accelerate vertical transport as long as it remains coherent and has a phase relationship between its perturbation mixing ratio and vertical velocity that is comparable to the linear limit.

The only species for which the second term in (4) is important are O and O<sub>3</sub>; all other species have  $L_i A \ll 5 \times 10^{-9} D_H$ . Because of the rapid interchange of O and O<sub>3</sub> by  $O_3 + h\nu \rightarrow O + O_2$  and  $O + O_2 + M \rightarrow O_3 + M$ , the appropriate net chemical loss rate for these two species is the odd oxygen loss rate due principally to  $O + OH \rightarrow O_2 + H$  and  $O + O + M \rightarrow O_2 + M$  [e.g., Figure 4 of Allen et al., 1984].

The thermal eddy diffusion coefficient  $D_H$  can not be calculated directly because we have not established that  $P_e = 1$  and  $D_H = D_M$  [Fritts and Dunkerton, 1985; Strobel et al., 1985]. We do know that  $D_H < 6 \times 10^5$  cm<sup>2</sup> s<sup>-1</sup> [Strobel et al., 1985] and can infer a reasonably accurate mesospheric  $D_H$  profile by fitting a model water vapor mixing ratio profile to measured values, as the time constants for chemistry and transport are comparable, in a manner similar to Allen et al. [1981]. The chemistry of water vapor is also regarded as well known, with reasonably accurate rate constants. In a one-dimensional model the globally averaged mean vertical velocity is, of course, identically zero, but the globally averaged vertical flux of a constituent generated by the mean circulation is not necessarily zero. Based on model results of Garcia and Solomon [1985], a typical maximum amplitude for the mean vertical velocity is  $\bar{w} \sim 0.4$  cm s<sup>-1</sup> at middle and equatorial latitudes during equinox and summer in the 60- to 80-km region. The globally averaged value would be substantially less,  $\sim 0.1$  cm s<sup>-1</sup>. Corresponding mean meridional velocities are typically  $v' \sim 2$  m s<sup>-1</sup>. A typical eddy velocity is  $w' \sim K_{zz}/H$ , where  $H$  is the atmospheric scale height. For H<sub>2</sub>O we find below that  $K_{zz} \sim D_H \sim 10^5$  cm<sup>2</sup> s<sup>-1</sup>, and for O and O<sub>3</sub>,  $K_{zz} \sim 10^6$  cm<sup>2</sup> s<sup>-1</sup>. Thus the respective  $w'$  are 0.2 and 2 cm s<sup>-1</sup>, which are comparable to and significantly larger than  $\bar{w}$ . For the equinox and summer data used in our study, the H<sub>2</sub>O

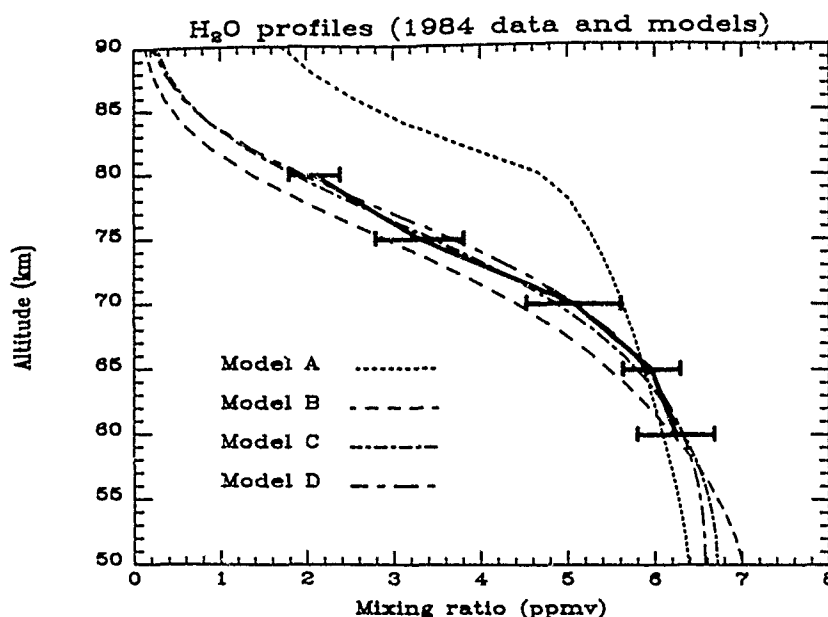


Fig. 1. Comparison of ground-based, observed  $\text{H}_2\text{O}$  mixing ratios with  $1\sigma$  error bars [Bevilacqua *et al.*, 1985a] and model results for the  $D_H$  profiles given in Figure 2 and with chemical acceleration.

eddy and mean circulation fluxes are upward, which implies that the  $D_H$  values deduced from the  $\text{H}_2\text{O}$  profile could be maximum values. Mean meridional  $\text{H}_2\text{O}$  flux divergences are not expected to severely negate this conclusion on the basis of Garcia and Solomon [1985] results.

### 3. DATA

The mesospheric water vapor measurements used in this study were obtained by ground-based microwave spectroscopy from the Propulsion Laboratory (JPL) in Pasadena, California, during the time period from April through June 1984 [Bevilacqua *et al.*, 1985a]. This particular experiment is the longest continuous series of mesospheric water vapor measurements yet published. The profile shown in Figure 1 is an average of the daily measurements taken over the 3-month experiment, with error bars that represent the standard deviation of the individual measurements from the average profile. Thus they include random measurement error as well as any natural atmospheric variation. The absolute error in the measurements is estimated to be about 20% from 60–75 km and more than 30% at 80 km.

The results from the series of measurements are in good agreement with the measurements of Bevilacqua *et al.* [1983], Ackerman *et al.* [1985], and Olivero *et al.* [1986]. The general conclusion of all these experiments is that water vapor mixing ratios in the upper mesosphere are nearly a factor of 2 smaller than calculated by one-dimensional and two-dimensional photochemical models (for example, Allen *et al.*, [1981] (see also Figure 1), and Garcia and Solomon, [1985]).

In order to deduce  $D_H$  we use the JPL water vapor measurements in the 60–80-km altitude range. Below 60 km, transport is not competitive with chemistry in controlling the water vapor abundance, and above 80 km, the measurement sensitivity is not sufficient to permit accurate characterization of  $D_H$ .

As a cross check on the  $D_H$  profile deduced from the water vapor measurements, we use mesospheric CO measurements. For this purpose we adopted the 1-day average measurement

obtained on April 18, 1984, by ground-based spectroscopy of the  $J = 1 \rightarrow 0$  CO line [Bevilacqua *et al.*, 1985b] obtained at the AT&T Bell Laboratories [millimeter wave] Observatory in Holmdel, New Jersey. The resultant CO vertical abundance profile is fairly typical of recent measurements.

The third data set used in this study consists of ozone measurements obtained from the near-infrared spectrometer on board the SME satellite [Thomas *et al.*, 1984]. For consistency with the  $\text{H}_2\text{O}$  and CO measurements we have retrieved, from the SME data base, an effective average profile at  $35^\circ\text{N}$  latitude appropriate for the months of April through June 1984.

### 4. RESULTS

In Figure 2, three vertical profiles of  $D_H$  which produce an acceptable fit to the water vapor data of Bevilacqua *et al.* [1985a], along with the Allen *et al.* [1981, 1984] eddy diffusion coefficient, are illustrated. They generate the rapid fall-off of the observed  $\text{H}_2\text{O}$  mixing ratio above 60 km (Figure 1), in contrast to the Allen *et al.* profile chosen to minimize the  $\text{O}_3$  concentration at the mesopause minimum and satisfy the unpublished H. Trinks' (private communication, 1979)  $\text{H}_2\text{O}$  measurement constraint at 90 km. The water vapor data employed in this study, which are not consistent with the Trinks' measurement, clearly require values of  $D_H \sim 10^5 \text{ cm}^2 \text{ s}^{-1}$  in the critical region of 60–80 km and categorically exclude values of  $\geq 10^6 \text{ cm}^2 \text{ s}^{-1}$ . It should be noted that even with updated chemistry [DeMore *et al.*, 1985] the Trinks' measurement of the  $\text{H}_2\text{O}$  mixing ratio at 90 km still requires the Allen *et al.* eddy diffusion profile. Below 60 km the calculated  $\text{H}_2\text{O}$  mixing ratio is insensitive to the value of  $D_H$  and does not distinguish among the different eddy diffusion profiles of Figure 2.

CO is produced by photolysis of  $\text{CO}_2$  above the mesopause. The mesospheric CO profile reflects the balance between net downward transport and chemical loss [cf. Allen *et al.*, 1981]. Therefore CO is also a useful tracer in our study. In Figure 3 the corresponding, calculated profiles of CO mixing ratio are

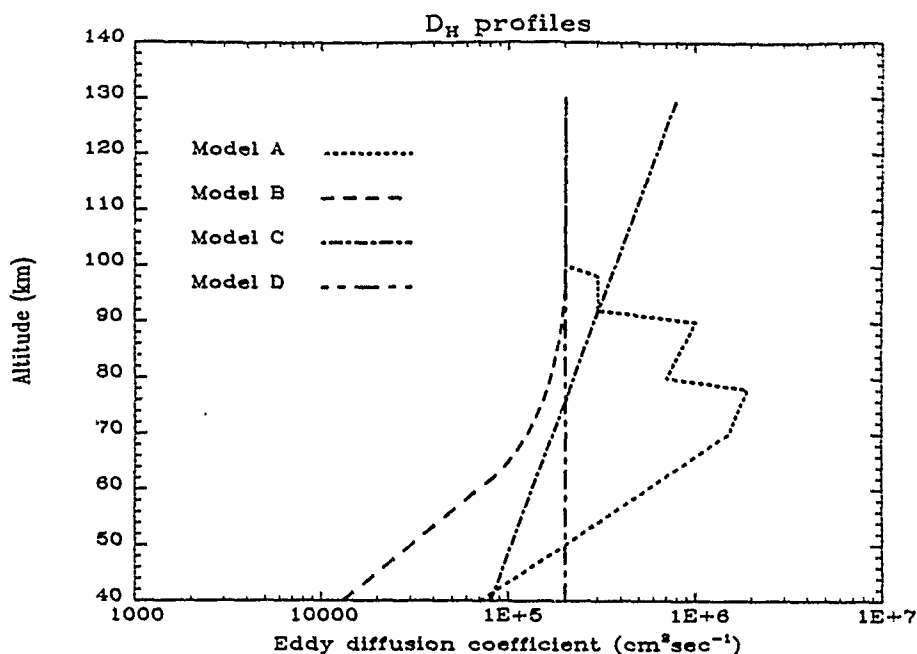


Fig. 2. Vertical eddy diffusion coefficient ( $D_H$ ) profiles for Models A, B, C, and D.

displayed and compared with *Bevilacqua et al.* [1985b] data. Above 70 km the profiles computed with slow vertical mixing (models B, C, D; cf. Figure 2) are clearly more consistent with the CO data than model A, with  $D_H$  an order of magnitude larger. The reader can also use Table 1 to distinguish models A–D. Thus CO measurements confirm the deduction from  $H_2O$  ground-based measurements that vertical mixing is slow in the mesosphere, with  $D_H \sim 10^5 \text{ cm}^2 \text{ s}^{-1}$ . However, neither the new calculations nor the *Allen et al.* [1981] calculation yields an adequate, overall representation of the inferred CO mixing ratio. For the conditions applicable to the adopted CO

data set, it is improbable that the mean circulation would augment the downward transport of CO to increase its predicted mixing ratio by a factor of 5 below 60 km. The two-dimensional model calculations of *Solomon et al.* [1985] with mean circulation and eddy transport had similar problems at mid-latitudes. It should be remembered that  $L_{CO} \lesssim 10^{-6}$  between 40 and 80 km and thus (in equation (4))  $2 \times 10^{10} L_{CO} A < 5 \times 10^4 \text{ cm}^2 \text{ s}^{-1}$ . Also, the chemical and transport time constants are comparable in the 65- to 80-km region, with the chemical time constant shorter below 65 km. Hence we would interpret our underprediction of CO in comparison

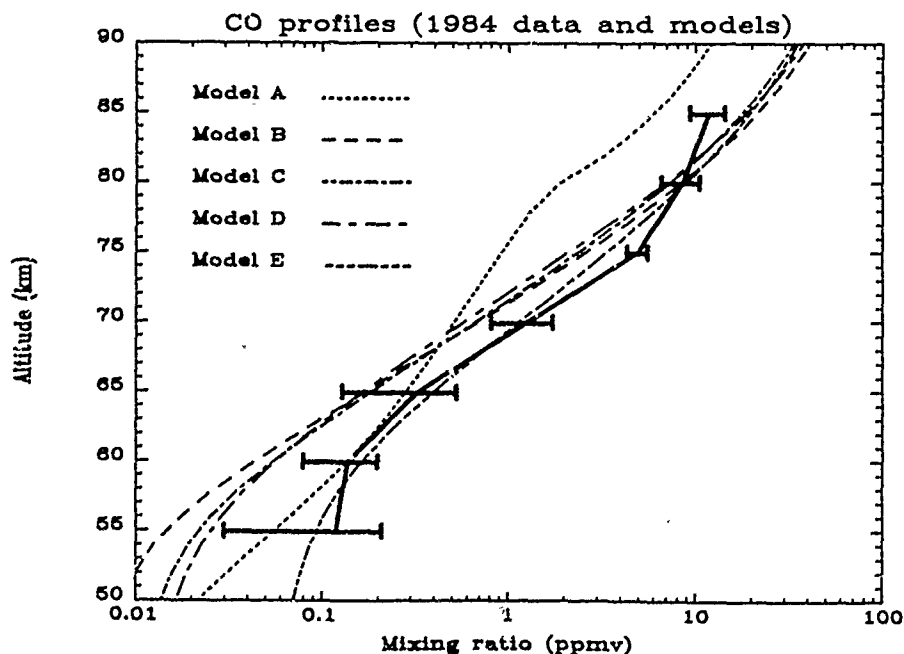


Fig. 3. Comparison of ground-based, observed CO mixing ratios with  $1\sigma$  error bars [*Bevilacqua et al.*, 1985b] and results from Models A, B, C, and D, whose  $D_H$  profiles are given in Figure 2, and Model E, which is the same as Model C but with modified CO chemistry.



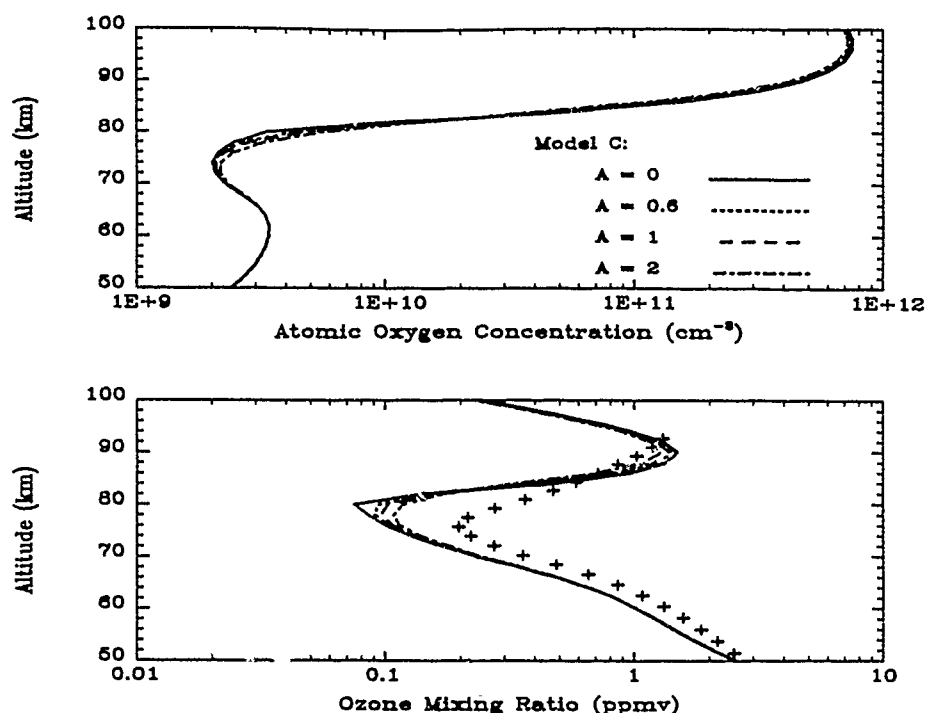


Fig. 4. (a) Model results from O concentration for Model C with indicated value of gravity wave activity,  $\Lambda$ . No chemical acceleration is  $\Lambda = 0$ . (b) Same as Figure 4a, but for O<sub>3</sub> mixing ratio, with comparison of model results and SME data averaged over April 1, to June 30, 1984, at 35°N.

to the microwave measurements below 70 km to inadequate chemistry rather than vertical transport.

Illustrative of the changes required in CO chemistry to produce acceptable agreement with the data are (1) an assumption that O(<sup>1</sup>D) reacts with CO<sub>2</sub> to produce CO with a rate constant of  $1 \times 10^{-12} \text{ cm}^3 \text{ s}^{-1}$ , (2) an increase in the CO mixing ratio at 40 km from 0.01 to 0.03 ppmv, and (3) a temperature dependence for the reaction  $\text{CO} + \text{OH} \rightarrow \text{CO}_2 + \text{H}$

of  $1.35 \times 10^{-13} e^{-100/T}$ . Although the bulk of O(<sup>1</sup>D) collisions with CO<sub>2</sub> result in quenching, it is entirely possible that a small fraction ( $\sim 1\%$ ) result in reaction. DeMore *et al.* [1985] do not recommend a specific temperature dependence for CO + OH, but the above rate is within experimental uncertainty. Calculations with this chemistry are shown in Figure 3, with  $D_H$  for model E identical to  $D_H$  of model C. These calculations are meant to suggest one possible resolution of the

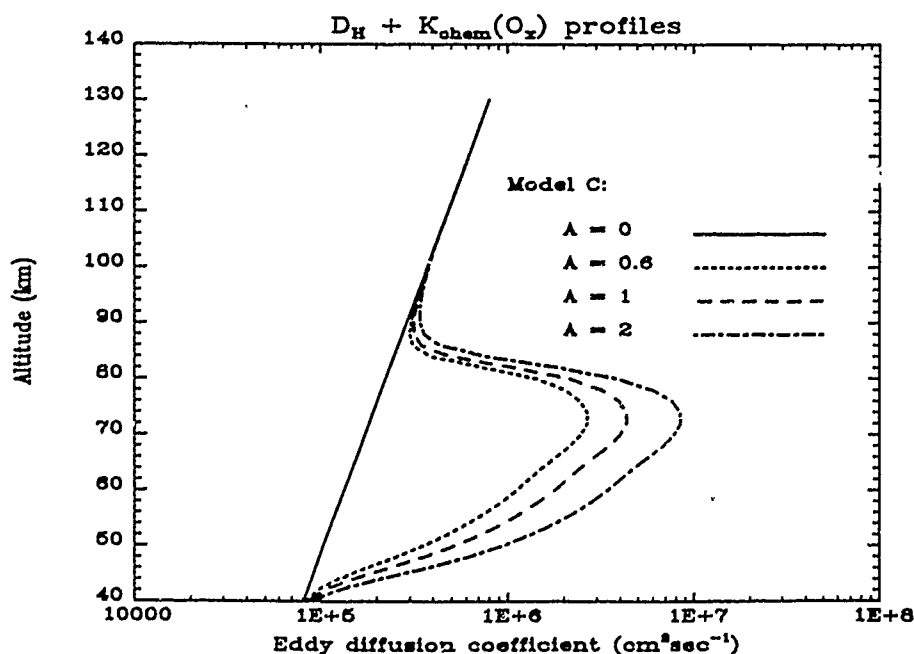


Fig. 5. Vertical eddy diffusion coefficient ( $K_{zz}$ ) profiles for odd oxygen that include chemical acceleration at the indicated value of gravity wave activity  $\Lambda$  for model C.

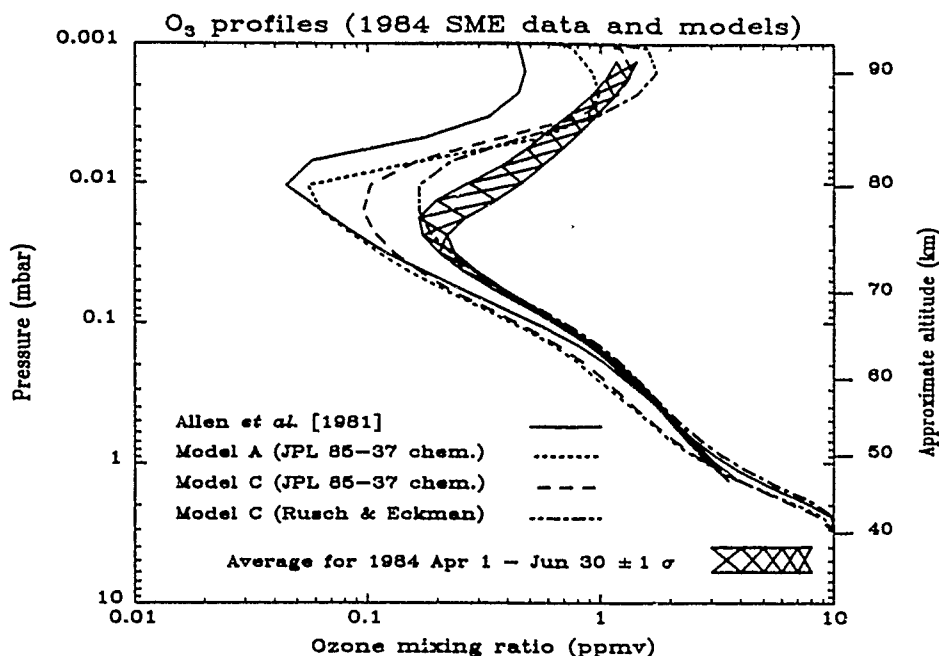


Fig. 6. Comparison of SME  $O_3$  profile obtained from averaged data at  $35^\circ N$ , April 1, to June 30, 1984, with original Allen *et al.* [1981] model result (solid line), with DeMore *et al.* [1985] chemistry substituted (dotted line), Model C (dashed line) and Model C with Rusch and Eckman [1985] modified chemistry (double-dot dash line).

underprediction of CO concentrations. The extra CO source,  $O(^1D) + CO_2$ , is needed below 60 km to account for the quasi-constant mixing ratio, whereas above 60 km the lower mesospheric temperatures and temperature dependence for the  $CO + OH$  reaction result in reduced CO loss rate and hence increased CO mixing ratio. The change in the lower boundary condition for CO results in  $<1\%$  increase in CO above 50 km.

In Figure 4 the effects of slow vertical mixing and chemical acceleration on atomic oxygen and ozone are presented by comparison of model C with  $A = 0$  and  $A \neq 0$ . The chemical acceleration of  $K_{zz}$  is a small effect on the O densities and  $O_3$  mixing ratios,  $<60\%$  in the 76- to 90-km region. Although  $K_{zz}$  increases from  $10^5$  to  $10^7$   $cm^2 s^{-1}$  for odd oxygen with chemical acceleration (Figure 5), the rapid increase in  $L$  with decreasing altitude transforms the O concentration profile from dynamical control above 85 km to chemical control below 75 km. The chemical acceleration of vertical transport is constrained in the limit of large  $L$  because the chemical time constant  $\tau_{chem} \sim L^{-1}$  is always less than the transport time constant  $\tau_{tran} \sim H^2/K_{zz} \rightarrow 5 \times 10^{-11} H^2 L^{-1} \sim 18 L^{-1}$  when  $A = 1$ . Only if  $A$  were large ( $\sim 19$ ) would chemical acceleration of  $K_{zz}$  produce pronounced perturbations in the O and  $O_3$  concentrations. In Figure 4, model results are also compared with SME data and illustrate the usual problem of underprediction of  $O_3$  mixing ratios between 50 and 85 km [Aikin *et al.*, 1984, Rusch and Eckman, 1985, Solomon *et al.*, 1983]. Because of the extremely large variability in the atomic oxygen measurements summarized by Offermann *et al.* [1981], no useful observational constraints exist for our model results displayed in Figure 4.

In Figure 6, model  $O_3$  mixing ratios are compared with the Allen *et al.* [1981] profile and appropriate SME data. Below about 65 km all of the model curves with the same chemistry converge, indicative of the small sensitivity of ozone

to vertical transport below this altitude. Thus the factor of 1.5 disagreement between the models and SME data below 65 km must be the result of inadequacies in mesospheric ozone chemistry, as concluded by Rusch and Eckman [1985]. By adopting their recommended chemistry changes in conjunction with the slow vertical mixing, we obtain good agreement with the SME data. At the ozone minimum near the mesopause, agreement between SME data and model results clearly requires low values of  $D_H$  and  $K_{zz}$ , with the primary effect being the reduced  $HO_x$  catalytic loss of odd oxygen. We also show for completeness the Allen *et al.* [1981, 1984] model results, with DeMore *et al.* [1985] chemistry. mesopause  $O_3$  concentrations are increased, but below 70 km,  $[O_3]$  is reduced by up to 40%. The Allen *et al.* [1984]  $O_3$  profile in Figure 6 reproduced the Aladdin 74 rocket  $O_3$  measurements [Weeks *et al.*, 1978], which are significantly lower than the average SME  $O_3$  profiles in the upper mesosphere. This may reflect the temporal variability in mesospheric  $H_2O$  (as suggested by Allen *et al.* [1984]), possibly as a result of changes in the nondiffusive component of transport.

The structure predicted in the  $O_3$  mixing ratio in all the model results between 75 and 90 km is significantly greater than exhibited in SME data. The near-IR instrument on SME had a field of view which provides a minimum altitude resolution of 3.5 km at the earth's limb when the slit is optimally aligned [Thomas *et al.*, 1984]. This resolution ( $\sim 0.6 H$ ) can result in some smoothing of the predicted factor of 15 change in the  $O_3$  mixing ratio over the 80- to 86-km region (Figure 6). With chemical acceleration the gradient in the  $O_3$  mixing ratio between 80 and 85 km is reduced by a factor of 2.

##### 5. CONCLUDING REMARKS

On the basis of our model calculations we conclude that mesospheric water vapor measurements provide the most definitive signature of vertical mixing in the mesosphere. The

low  $\text{H}_2\text{O}$  mixing ratio and resultant odd hydrogen densities implied by the Bevilacqua et al. [1983, 1985a] measurements lead to substantial reductions in the loss of odd oxygen and CO at the mesopause. As a result, the calculated O,  $\text{O}_3$ , and CO concentrations are in better agreement with mesopause data. Below the mesopause the O and  $\text{O}_3$  density profiles are insensitive to vertical mixing, and the inference of  $K_{zz}$  from their profiles is poorly constrained. Although chemical acceleration of vertical transport is substantial for O and  $\text{O}_3$  below 85 km, it is not sufficient to overcome the chemical control of their density structure. The significance of chemical acceleration is thus subtle; it produces large increases in  $K_{zz}$  for  $\text{O}_x$ , but only modest (at most factor of 2) effects on the concentrations of O and  $\text{O}_3$  unless  $A \sim 10$ , which is precluded on the basis of available data. Our calculations show conclusively with our present understanding of O,  $\text{O}_3$ ,  $\text{H}_2\text{O}$ , and CO chemistry that the vertical  $\text{H}_2\text{O}$  profile is best suited to infer the correct magnitude of vertical mixing in the mesosphere. In the absence of vertical advection,  $D_H$  would be  $\sim(1-2) \times 10^5 \text{ cm}^2 \text{ s}^{-1}$  (cf. Figures 1 and 2) and consistent for early summer in the northern hemisphere at mid-latitudes, with the upper limit deduced from studies of the mesospheric heat budget. Brasseur and Offerman [1986] analyzed O concentration measurements and concluded that the vertical eddy diffusion coefficient is about  $10^5 \text{ cm}^2 \text{ s}^{-1}$  at the mesopause, also consistent with our results. However, a value of  $D_H \sim 10^5 \text{ cm}^2 \text{ s}^{-1}$  is so small that it is impossible to determine whether mesospheric vertical mixing is only diffusive or is dominated by vertical advection. Our analysis could, in fact, be regarded as evidence for an advectively controlled mesosphere.

From Strobel et al. [1985] the associated cooling due to breaking gravity waves is  $\sim 1^\circ\text{K}$  per day, if  $P_r = 1$  and is much less for  $P_r \gg 1$ . Thus to lowest order the mesosphere is in radiative equilibrium. Although it can not be demonstrated from this research, it appears that the consensus is  $D_M \sim 10^6 \text{ cm}^2 \text{ s}^{-1}$  [e.g., Lindzen, 1981; Holton, 1982, 1983; Garcia and Solomon, 1985] and hence the eddy Prandtl number must be of the order 10. With the uncertainties of this estimate considered, the eddy Prandtl number deduced by Justus [1967] of  $3.3^{+1.8}_{-1.1}$  from photographic tracking of rocket-released chemical clouds supports our inference. Fritts and Dunkerton [1985] have analytically demonstrated why, in the wave-breaking process,  $P_r > 1$ . It must be emphasized that our conclusion ( $P_r \sim 10$ ) depends critically on the inference of low  $\text{H}_2\text{O}$  mixing ratios in the upper mesosphere from ground-based microwave spectroscopy, which are consistent with the SME  $\text{O}_3$  data and ground-based CO measurements.

**Acknowledgments.** This research was supported by a grant from the Theory and Data Analysis Branch of the Office of Space Science and Applications Division of NASA and by the Middle Atmosphere Program at the Naval Research Laboratory. A portion of the research was also supported by NASA grants NAGW-826 and NAG 5-796 at Johns Hopkins University.

#### REFERENCES

- Ackerman, M., and A. Girard, Correlation of Spacelab One CO and  $\text{H}_2\text{O}$  and SME  $\text{O}_3$  near the mesopause, *Eos Trans. AGU*, **66**, 999, 1985.
- Aikin, A. C., B. Woodgate, and H. J. P. Smith, Equatorial ozone profiles from the Solar Maximum Mission—A comparison with theory, *Planet. Space Sci.*, **32**, 503–513, 1984.
- Allen, M., Y. L. Yung, and J. M. Waters, Vertical transport and photochemistry in the terrestrial mesosphere and lower thermosphere (50–120 km), *J. Geophys. Res.*, **86**, 3617–3627, 1981.
- Allen, M., J. I. Lunine, and Y. L. Yung, The vertical distribution of ozone in the mesosphere and lower thermosphere, *J. Geophys. Res.*, **89**, 4841–4872, 1984.
- Apruzese, J. P., D. F. Strobel, and M. R. Schoeberl, Parameterization of IR cooling in a middle atmosphere dynamics model. 2. Non-LTE radiative transfer and the globally averaged temperature of the mesosphere and lower thermosphere, *J. Geophys. Res.*, **89**, 4917–4926, 1984.
- Bevilacqua, R. M., J. J. Olivero, P. R. Schwartz, C. J. Gibbins, J. M. Bologna, and D. L. Thacker, An observational study of water vapor in the mid-latitude mesosphere using ground-based microwave techniques, *J. Geophys. Res.*, **88**, 8523–8534, 1983.
- Bevilacqua, R. M., W. J. Wilson, W. B. Ricketts, P. R. Schwartz, and R. J. Howard, Possible seasonal variability of mesospheric water vapor, *Geophys. Res. Lett.*, **12**, 397–400, 1985a.
- Bevilacqua, R. M., A. A. Stark, and P. R. Schwartz, The variability of CO in the terrestrial mesosphere as determined from ground-based observations of the  $J = 1 \rightarrow 0$  emission line, *J. Geophys. Res.*, **90**, 5777–5782, 1985b.
- Brasseur, G., and D. Offerman, Recombination of atomic oxygen near the mesopause: Interpretation of rocket data, *J. Geophys. Res.*, **91**, 10,818–10,824, 1986.
- Caho, W. C., and M. R. Schoeberl, A note on the linear approximation of gravity wave saturation in the mesosphere, *J. Atmos. Sci.*, **41**, 1893–1898, 1984.
- DeMore, W. B., J. J. Margitan, M. J. Molina, R. T. Watson, D. M. Golden, R. F. Hampson, M. J. Kurlyo, C. J. Howard, and A. R. Ravishankara, Chemical kinetics and photochemical data for use in stratospheric modeling, *JPL Publ.*, 85-37, 1985.
- Dunkerton, T. J., Wave transience in a compressible atmosphere. III. The saturation of internal gravity waves in the mesosphere, *J. Atmos. Sci.*, **39**, 1042–1051, 1982.
- Fritts, D. C., and T. J. Dunkerton, Fluxes of heat and constituents due to convectively unstable gravity waves, *J. Atmos. Sci.*, **42**, 549–556, 1985.
- Garcia, R. R., and S. Solomon, The effect of breaking gravity waves on the dynamics and chemical composition of the mesosphere and lower thermosphere, *J. Geophys. Res.*, **90**, 3850–3868, 1985.
- Holton, J. R., The role of gravity wave-induced drag and diffusion in the momentum budget of the mesosphere, *J. Atmos. Sci.*, **39**, 791–799, 1982.
- Holton, J. R., The influence of gravity wave breaking on the general circulation of the middle atmosphere, *J. Atmos. Sci.*, **40**, 2497–2507, 1983.
- Justus, C. G., The eddy diffusivities, energy balance parameters, and heating rate of upper atmospheric turbulence, *J. Geophys. Res.*, **72**, 1035–1039, 1967.
- Lindzen, R. S., Turbulence and stress owing to gravity wave and tidal breakdown, *J. Geophys. Res.*, **86**, 9707–9714, 1981.
- Offermann, D., V. Friedrich, P. Boss, and U. von Zahn, Neutral gas composition measurements between 80 and 120 km, *Planet. Space Sci.*, **29**, 747–764, 1981.
- Olivero, J. J., J. J. Tsou, C. L. Croskey, L. C. Hale, and R. G. Joiner, Solar absorption microwave measurements of upper atmospheric water vapor, *Geophys. Res. Lett.*, **13**, 197–200, 1986.
- Rusch, D. W., and R. S. Eckman, Implications of the comparison of ozone abundance measured by the Solar Mesosphere Explorer to model calculations, *J. Geophys. Res.*, **90**, 12,991–12,998, 1985.
- Schoeberl, M. R., D. F. Strobel, and J. P. Apruzese, A numerical model of gravity wave breaking and stress in the mesosphere, *J. Geophys. Res.*, **83**, 5249–5259, 1983.
- Solomon, S., D. W. Rusch, R. J. Thomas, and R. S. Eckman, Comparison of mesospheric ozone abundances measured by the Solar Mesosphere Explorer and model calculations, *Geophys. Res. Lett.*, **10**, 249–252, 1983.
- Solomon, S., R. R. Garcia, J. J. Olivero, R. M. Bevilacqua, P. R. Schwartz, R. T. Clancy, and D. O. Muhleman, Photochemistry and transport of carbon monoxide in the middle atmosphere, *J. Atmos. Sci.*, **42**, 1072–1083, 1985.
- Strobel, D. F., Parameterization of linear wave chemical transport in planetary atmospheres by eddy diffusion, *J. Geophys. Res.*, **86**, 9806–9810, 1981.
- Strobel, D. F., J. P. Apruzese, and M. R. Schoeberl, Energy balance constraints on gravity wave induced eddy diffusion in the mesosphere and lower thermosphere, *J. Geophys. Res.*, **90**, 13,067–13,072, 1985.

- Thomas, R. J., C. A. Barth, D. W. Rusch, and R. W. Sanders, Solar Mesosphere Explorer near-infrared spectrometer: Measurements of 1.27- $\mu\text{m}$  radiance and the inference of mesospheric ozone, *J. Geophys. Res.*, **89**, 9569-9580, 1984.
- Vincent, R. A., Gravity motions in the mesosphere, *J. Atmos. Terr. Phys.*, **46**, 119-128, 1984.
- Vincent, R. A., Planetary and gravity wave activity in the upper middle atmosphere, paper presented at the 26th Plenary Meeting of the Committee on Space Research (COSPAR), Toulouse, France, 1986.
- Vincent, R. A., and I. M. Reid, HF doppler measurements of mesospheric gravity wave momentum fluxes, *J. Atmos. Sci.*, **40**, 1321-1333, 1983.
- Weeks, L. H., R. E. Good, J. S. Randhawa, and H. Trinks, Ozone measurements in the stratosphere, mesosphere, and lower thermosphere during Aladdin 74, *J. Geophys. Res.*, **83**, 978-982, 1978.
- M. Allen, Earth and Space Sciences Division, Jet Propulsion Laboratory, California Institute of Technology, Pasadena, CA 91125.
- R. M. Bevilacqua and M. T. DeLand, E. O. Hulburt Center for Space Research, Code 4138BE, Naval Research Laboratory, Washington, DC 20375.
- D. F. Strobel and M. E. Summers, Department of Earth and Planetary Sciences, Johns Hopkins University, Baltimore, MD 21218.

(Received December 4, 1986;  
revised March 12, 1987;  
accepted March 13, 1987.)

## **APPENDIX L**

### **The Seasonal Variation of Water Vapor and Ozone in the Upper Mesosphere: Implications for Vertical Transport and Ozone Photochemistry**

The Seasonal Variation of Water Vapor and Ozone in the Upper Mesosphere:  
Implications for Vertical Transport and Ozone Photochemistry

by

Richard M. Bevilacqua<sup>1</sup>, Darrell F. Strobel<sup>2</sup>, Michael E. Summers<sup>1</sup>,  
John J. Olivero<sup>3</sup>, and Mark Allen<sup>4</sup>

<sup>1</sup>E. O. Hulburt Center for Space Research, Naval Research Laboratory,  
Washington, DC. (202) 767-0768

<sup>2</sup>Department of Earth and Planetary Sciences and Department of Physics and  
Astronomy, The Johns Hopkins University, Baltimore, MD.

<sup>3</sup>Department of Meteorology, The Pennsylvania State University, University  
Park, PA.

<sup>4</sup>Earth and Space Sciences Division, Jet Propulsion Laboratory, and Division of  
Geological and Planetary Sciences, California Institute of Technology,  
Pasadena, CA.

Submitted to JGR-Atmospheres: 12 May, 1989

Manuscript revised: 10 August, 1989

### Abstract

Ground-based microwave techniques have supplied the only long-term measurements of water vapor in the mesosphere. We review the entire current data base, which consists of measurements obtained in three separate experiments over an 8-year period. The data from all three experiments indicate that the water vapor seasonal variation at mid-latitudes in the upper mesosphere is dominated by an annual component with low mixing ratios in winter and high mixing ratios in summer. This suggests that the vertical distribution of water vapor in the upper mesosphere (up to 80 km) is controlled by advective rather than diffusive processes. This is consistent with the low mesospheric  $K_{zz}$  values ( $\approx 10^5 \text{ cm}^2 \text{ s}^{-1}$ ) deduced from the vertical gradient of the microwave water vapor measurements in Strobel et al. (1987). However, it is difficult to reconcile the predominantly annual water vapor variation with the semiannual variation in ozone at 78 km observed by SME. We perform a series of 1D photochemical/vertical transport model calculations which verify that (within the context of the hydrogen/oxygen chemistry considered in the model), the seasonal variation of water vapor cannot be the mechanism for the semiannual ozone variation. This variation is either a manifestation of some heretofore unknown ozone photochemical mechanism; or, it could be driven by a seasonal variation in the vertical transport of atomic oxygen from the thermosphere. One possible vertical transport scenario for producing the semiannual ozone variation (while retaining the annual water vapor variation) is described.

## 1. Introduction

It is now well known (Bevilacqua et al., 1983; Brasseur and Solomon, 1984; Remsberg et al., 1984; Strobel et al., 1987) that the photochemical time constant for water vapor in the middle atmosphere is sufficiently long that it serves as a chemical tracer of transport processes. In the stratosphere many water vapor measurements have been made, with the most extensive and complete data base coming from the LIMS (Limb Infrared Monitor of the Stratosphere) experiment. The LIMS data has been used by Remsberg et al. (1984) to infer important properties of the stratospheric general circulation. In the mesosphere, by contrast, the data base is much more sparse. The only long-term measurements of mesospheric water vapor in existence are those made by ground-based microwave techniques. One of the most noteworthy and consistent features of these measurements is that they indicate that the water vapor mixing ratio decreases with altitude above 65 km, in response to photodissociation, at a rate which is far more rapid than that exhibited in many 1- and 2-D photochemical model calculations (e.g. Allen et al., 1981; Garcia and Solomon, 1985). As a result, water vapor mixing ratios in the upper mesosphere are smaller, by as much as a factor of 3, than the model results. Bevilacqua et al. (1983, and 1987) examined this feature of the measurements in a qualitative fashion and concluded that this must imply that vertical transport rates in the mesosphere are significantly slower than that generally assumed in these model calculations.



Strobel et al. (1987) examined this problem in a more quantitative fashion, employing the Cal Tech 1-D photochemical model (Allen et al., 1981, and 1984) and concentrating on the water vapor measurements obtained at the Jet Propulsion Laboratory (JPL) (Bevilacqua et al., 1985, and 1987). In that paper we derived an upper limit, effective eddy diffusion coefficient ( $K_{zz}$ ) value of about  $1-2 \times 10^5 \text{ cm}^2 \text{ s}^{-1}$  in the critical 60 to 80 km region, in comparison to typically adopted values of  $\approx 1 \times 10^6 \text{ cm}^2 \text{ s}^{-1}$ . We showed that adoption of the lower vertical transport rates, and consequent low water vapor abundances near the mesopause, results in better model agreement with both CO measurements obtained by ground-based techniques, and with Solar Mesosphere Explorer (SME)  $\text{O}_3$  measurements.

Since publication of the Strobel et al. (1987) paper, we have completed analysis of the much more extensive set of mesospheric water vapor measurements obtained by ground-based microwave techniques at The Pennsylvania State University (Olivero et al., 1986; Tsou et al., 1988; Bevilacqua et al., 1989). These measurements cover the time period winter through early summer over three successive years. In this paper we review the entire data base of microwave mesospheric water vapor measurements with particular emphasis on the Penn State results. A synopsis of the current data base, which now consists of measurements obtained in three separate experiments over an 8-year period, is contained in Table 1. We reexamine the conclusions reached in our previous papers in light of the large Penn State data set by comparing the average vertical gradient of these measurements to that obtained in our previous experiments. Also, with the addition of the Penn State measurements, a fairly consistent picture of the seasonal variation of water vapor in the upper mesosphere is beginning to emerge for the period winter through summer

(Bevilacqua et al., 1989). We show that this seasonal variation contains additional, independent information concerning vertical transport rates, and the nature of this transport, in the mesosphere. Finally, we compare the observed water vapor seasonal variation with the well documented seasonal variation of ozone in the mesosphere observed by the SME satellite experiment.

## 2. Observations (Vertical Gradient and Seasonal Variation)

In Figure 1 we show average measured water vapor profiles, obtained at Penn State, over the period February through June 1985, 1986, and 1987. The absolute accuracy (1 $\sigma$ -level) of these measurements is estimated to be about 20% up to 75 km, increasing to about 50% at 80 km. Also plotted on this figure are the model A and model C results from Figure 1 of Strobel et al. (1987). The model A water vapor profile was obtained using the  $K_{zz}$  profile derived in Allen et al. (1981), with a value of order  $10^6 \text{ cm}^2 \text{ s}^{-1}$  in the upper mesosphere. Model C is our preferred best-fit to the the spring 1984 JPL water vapor measurements, with  $K_{zz} \approx 1-2 \times 10^5 \text{ cm}^2 \text{ s}^{-1}$  in the critical 60 to 80 km region. Thus, the much more extensive Penn State water vapor measurements confirm the slow vertical transport model C result. In fact, the vertical gradients observed in the average Penn State retrievals are on average even steeper than the JPL measurements (as discussed in the next Section) and confirm that the steep water vapor vertical gradient in the upper mesosphere is a persistent feature at mid-latitudes.

The extensive Penn State data set has allowed us to characterize not only ~~the shape of the vertical water vapor profile,~~ but also its seasonal variation over the period winter through summer (Bevilacqua et al., 1989). This seasonal variation is important because it contains independent information on vertical transport rates and the nature of the dominant transport process in the mesosphere. The importance of the water vapor seasonal variation in this regard is illustrated in a qualitative fashion in Figure 2, and is discussed more quantitatively by Holton and Schoeberl (1988). In the top panel, we show a hypothetical mixing ratio profile of a constituent, which is mainly transport controlled, having a low altitude source and a high altitude sink. Water vapor is a paradigm of such a constituent. Vertical transport occurs either via mean-flow advection or by small-scale diffusive processes (turbulence). The magnitude and orientation of these two transport processes are also illustrated on the top panel.

The mesospheric mean meridional circulation is thought to be dominated at solstice by a single-cell system with rising motions in the summer hemisphere and subsidence in the winter hemisphere (Leovy, 1964). This simple pattern is transformed to a two-cell system at equinox with upward motion at the tropics and downward motion over both poles (cf. Holton and Schoeberl, 1988). Thus, one would expect mean-flow advective transport at mid-latitudes to be dominated by an annual variation with downward transport in winter, little net vertical motion during spring and fall, and upward motion in summer.

Turbulence in the mesosphere is thought to result primarily from the breaking of convectively unstable gravity waves (Lindzen, 1981). His parameterization of the turbulence and stress produced by breaking gravity

waves predicts a semiannual variation in turbulence intensity with maxima at solstice and minima at equinox (Garcia and Solomon, 1985). This seasonal variation results mainly from the fact that (in the Lindzen parameterization)  $K_{zz}$  is proportional to  $(u-c)^4$  at the breaking level, where  $u$  is the mean zonal wind velocity and  $c$  is the gravity wave phase speed. Because of the weak radiative drive, zonal wind speeds are smallest during equinox and, consequently, the turbulence intensity should also be a minimum. Thus, if gravity wave saturation controls turbulence intensity, vertical transport by diffusion should be maximum at solstice and minimum at equinox.

The seasonal variation of a transport-dominated constituent is dependent on the relative magnitudes of the diffusive and advective time constants. These time scales can be estimated by

$$\tau_W \approx H_1/w \qquad \tau_D \approx H_1^2/K_{zz} \quad (1)$$

where  $\tau_W$  and  $\tau_D$  are the time-scales for advective and diffusive vertical transport,

$H_1$  is the constituent concentration scale height,

$w$  is the mean vertical velocity, and

$K_{zz}$  is the vertical eddy diffusion coefficient.

In the lower panel of Figure 2 we consider three limiting cases. In the diffusive case ( $\tau_D \ll \tau_W$ ) the seasonal variation of the constituent is dominated by a semiannual component with maxima at solstice and minima at equinox. When both processes are roughly equal, the winter mixing ratio becomes reduced relative to the diffusive case, because now mean flow and

diffusive transport are oriented in opposite directions. The summer mixing ratio is relatively enhanced, because there they are acting in concert. The net result is that the semiannual variation becomes suppressed. Finally, in an advective atmosphere ( $\tau_D \gg \tau_W$ ) a predominantly annual variation is obtained. We do note, however, that the calculations of Holton and Schoeberl (1988) show that in the advective case at mid-latitudes there is a small semiannual component resulting from the two-cell equinox circulation system. However, this is small compared to the annual component. The essential point of Figure 2 is that, if we assume that we understand the phase of the advective and diffusive transport components, then the water vapor seasonal variation contains qualitative information about the relative magnitudes of these two processes. Furthermore, the winter through spring portion of the water vapor variation is most sensitive to the competition between these two transport mechanisms. In the Penn State measurements this particular part of the seasonal cycle has been sampled during three successive years. In the following, we examine the seasonal variation of the water vapor mixing ratio in the upper mesosphere obtained from the microwave measurements with particular regard to this point.

In Figure 3 we show all the available microwave water vapor observations at 80 km, plotted as a function of calendar month. The error bar indicates the average total absolute error in the retrievals at this altitude, which is about 50% (1 $\sigma$ -level). The measurement precision at this altitude is estimated to be better than 20%. The Penn State measurements, taken from Bevilacqua et al. (1989), represent monthly averages over the three years of observations. These measurements exhibit a relative minimum in mid-winter, with mixing ratios increasing slowly from January to April, then much more rapidly from

April through June. Thus, the Penn State observations indicate that the seasonal variation of water vapor in the upper mesosphere is dominated by an annual component, with high mixing ratios in summer and low mixing ratios in winter. As discussed in Bevilacqua et al. (1989) this seasonal variation was obtained in each of the three successive years of observations.

In the JPL experiment, measurements were obtained in two periods: March-June 1984 (Bevilacqua et al., 1985), and December 1984-April 1985 (Bevilacqua et al., 1987). The monthly average results from those two periods are illustrated in Figure 3. The JPL and Penn State data sets are compared in detail in Bevilacqua et al. (1989). Here we repeat only the most important points of that comparison. In the JPL 1984 data we see a clear increase from April through June, consistent with the Penn State measurements. However, the 1985 measurements do not show the deep mid-winter minimum evident in the Penn State data sets. Rather, the mixing ratio remains essentially constant from January through March, then begins to increase later in the spring. This is perhaps indicative of a larger semiannual component in the JPL measurements. As a result, the JPL winter retrievals are higher by nearly 1 ppmv than the Penn State and Haystack results. However, the summer measurements are in good agreement. As discussed in Bevilacqua et al. (1989), this winter discrepancy may be partially a latitude effect, or it may be the result of zonal asymmetries caused by wave activity.

The Haystack measurement points, taken from Bevilacqua et al. (1983), represent only 4 to 9-day averages. Therefore, data sampling problems make it very problematic to interpret these results in terms of seasonal variation. Nevertheless, the agreement among these measurements and the much more

extensive Penn State data set is encouraging. At Haystack, the winter-spring portion of the seasonal variation was sampled during two successive years. The January 1981 mixing ratio at 80 km is about 50% smaller than the April 1981 result. In December 1981 we measured an anomalously low water vapor profile above 70 km. These were the lowest abundances ever observed in any of our experiments. This measurement period extended from 5 to 11 December, and the low abundances persisted during each of these days. The April 1982 value at 80 km, however, is consistent with the previous year's measurement. Therefore, again we see lower mixing ratios in winter than in spring. Also notice that the highest abundances were obtained in July 1980 with the mixing ratio decreasing monotonically from July through September of 1980 and January 1981, then subsequently increasing in April 1981. In addition, we note that, with the exception of the clearly anomalous December 1981 result, the magnitude of the Haystack mixing ratios are consistent with the Penn State results.

Thus, we find that the entire microwave mesospheric water vapor data base is consistent in indicating that the seasonal variation in the upper mesosphere at mid-latitudes is dominated by an annual component with low values in winter and high values in summer. The measurements, therefore, suggest that advection dominates diffusion in establishing the water vapor vertical distribution. To illustrate this more clearly, in Figure 4 we plot the monthly average Penn State mixing ratios at 80 km, along with a model calculation of the mean vertical velocity field at 80 km and  $40^{\circ}$  N computed by Schoeberl and Chandra (private communication, 1987). The mixing ratio error bars represent the statistical variation (1 $\sigma$ -level) of the individual retrievals from which these grand monthly averages were formed (no error bars

are shown for the months of November through January because during these months data were obtained only in 1985). The vertical velocity field was computed from the net diabatic heating using the model atmosphere temperature/pressure profiles of Barnett and Corney (1985), and the reference ozone profiles of Keating and Young (1985). There appears to be an excellent correlation between the water vapor mixing ratios and model vertical velocity variation. The lowest mixing ratios occur during the time of maximum negative vertical velocity which acts to suppress the upward diffusive transport of water vapor. As the vertical velocity increases so also does the water vapor mixing ratio, reaching high values at the time of maximum positive vertical velocity. Clancy et al. (1984) performed an analysis of the seasonal variation of mesospheric CO, using measurements also obtained by ground-based microwave techniques. They also find predominantly an annual variation, again suggesting advective control. However, for CO this result is expected theoretically, even for large eddy diffusion models, in view of the large CO scale height in the mesosphere relative to that of water vapor (Solomon et al., 1985).

Figures 3 and 4 indicate that there is also a smaller semiannual component suggested by the data, especially in the JPL measurements where the deep mid-winter mixing ratio minimum is not observed. In April, the average Penn State measurements also exhibit a pause in the 80 km general winter to summer mixing ratio increase, perhaps suggestive of a semiannual component. This may be the mid-latitude semiannual advective variation discussed in Holton and Schoeberl (1988), or it may be the signature of the spring  $K_{zz}$  minimum modeled by Garcia and Solomon (1985). However, the semiannual component in the data is significantly suppressed when compared to the annual



component. Furthermore, the clear signature of a diffusive atmosphere is a decrease in the mixing ratios from winter to spring; this is not observed in any of the measurements.

We can use simple scaling arguments to derive an upper limit for  $K_{zz}$  based on the observed seasonal variation of water vapor. First, from the predominant annual variation we know that  $\tau_W \leq \tau_D$ . Using (1), we obtain the result

$$K_{zz} \leq H_1 w. \quad (2)$$

From the measurements, the water vapor scale height ( $H_1$ ) is approximately 4.0 km, and from the model results of Garcia and Solomon (1985), the amplitude of  $w$  at mid-latitudes is not more than  $0.4 \text{ cm s}^{-1}$ , whereas Schoeberl and Chandra (private communication, 1987; Figure 4) calculate  $w \approx 0.25 \text{ cm s}^{-1}$ . This range of estimates lead to the result:

$$K_{zz} \leq (1-1.6) \times 10^5 \text{ cm}^2 \text{ s}^{-1},$$

which is consistent with the  $K_{zz}$  upper limit inferred from the vertical gradient of the measured water vapor profiles in Strobel et al. (1987). As pointed out in Strobel et al. (1987), calculating  $K_{zz}$  using the Lindzen (1981) parameterization (and assuming that the eddy Prandtl number = 1) leads to values of  $K_{zz}$  of approximately  $(1-2) \times 10^6 \text{ cm}^2 \text{ s}^{-1}$ . Thus, we find that the measured water vapor vertical gradient and the seasonal variation are consistent in indicating that diffusive vertical transport time-scales in the mesosphere are much longer than that implied by the Lindzen parameterization.

It is important to point out that the Garcia and Solomon (1985) model results indicate that the diffusive semiannual component in the water vapor profile is present only above about 75 km, and becomes quite prominent at and above 80 km. As discussed in Bevilacqua and Olivero (1988), the vertical resolution (and thus measurement sensitivity) of the microwave technique begins to degrade with increasing altitude fairly rapidly above 75 km (above this altitude the measurement is sensitive to the water vapor column abundance rather than the details of its distribution). Thus, there is some question about the ability of the microwave technique to detect this semiannual component. As discussed in Bevilacqua et al. (1987), in order to explore this point we produced simulated microwave spectra using the Garcia and Solomon (1985) model water vapor profiles for mid-January, April and June, added random noise to the spectra to simulate measurement error, and inverted the resultant spectra to infer the water vapor profile using the same techniques as utilized in the real data analysis (cf. Bevilacqua and Olivero, 1988). As mentioned above, the model profiles show a decrease in the water vapor mixing ratio from January to April at 80 km and  $40^{\circ}$  N of about 33%. The simulated retrievals of the model profile synthetic spectra, with very high spectral signal-to noise ratios (typical of good monthly average spectra), show a decrease at 80 km from January to April of about 7%. For moderate signal-to-noise ratios (typical of daily average spectra), the decrease over this period is only about 1%. Thus, the retrieval degradation of vertical resolution in the upper mesosphere does produce a very significant dampening of the January to April mixing decrease above 75 km present in the Garcia and Solomon model. However, the Penn State and Haystack data retrievals consistently show a water vapor mixing ratio increase from January to April at 80 km of about 70%. The simulations indicate that, even for low spectral signal-to-noise ratios, an

increase in the retrieval mixing ratio of this magnitude would not be obtained if the strong, diffusive semiannual component were present. This appears to be true even for the JPL retrievals where the January to April increase at 80 km is only about 11%. Furthermore, synthetic microwave spectra produced with the Garcia and Solomon (1985) water vapor profiles indicate a decrease in the amplitude of the spectral line near line center of about 8% from January to April, while the 1985 monthly average Penn State measured spectra show an increase of about 8% over the same period. Considering typical values of random error in the monthly average spectra, both the line amplitude decrease in the Garcia and Solomon case, and the increase in the Penn State case are at about the 4- $\sigma$  level. Therefore, the semiannual water vapor variation predicted in the Garcia and Solomon model yields water vapor spectra significantly different from the Penn State retrievals during the period January to April. Thus, while there is evidence for the existence of a semiannual component in the water vapor measurements, these measurements do not support the large semiannual component indicated in the model calculations. This semiannual component is either much more suppressed relative to the annual variation, or is occurring at a higher altitude (above 80 km).

In addition to a discrepancy in the water vapor seasonal variation, the microwave water vapor mixing ratios also have smaller absolute abundances, especially in winter and summer, than the Garcia and Solomon (1985) model calculations (cf. Bevilacqua et al., 1987). For the Penn State and Haystack observations, where we obtained very low mixing ratios in winter, the model results are about a factor of 3 higher than the observations in winter and a factor of 1.4 higher in summer. At JPL, the model results are about a factor

of 1.5 higher in both summer and winter. Garcia (1989) has recently performed a series of calculations with the Garcia and Solomon model in which the effect of an eddy Prandtl number  $> 1$  was explored (this has the effect of decreasing the value of  $K_{zz}$  for constituent transport). The results show that with an eddy Prandtl number of  $\approx 10$  it is possible to bring the modeled and measured water vapor mixing ratios into approximate agreement in winter. However, in summer the model water vapor abundance is mainly advectively controlled, and the magnitude of the water vapor mixing ratio is, thus, insensitive to the value of the Prandtl number. Therefore, a decrease in the strength of the meridional circulation (which drives the vertical velocity field) is required in order to decrease the magnitude of the computed water vapor mixing ratios in summer. In the East Coast Haystack and Penn State observations, the model/measurement discrepancy does maximize in winter. However, the summer discrepancy exhibited in all the measurements is of about the same magnitude as the absolute error level ( $\approx 50\%$  at 80 km) and, therefore, may also be significant. Thus, the water vapor measurements may imply that the eddy Prandtl number is significantly greater than 1 and that the meridional circulation is weaker than that obtained in the Garcia and Solomon (1985) model, which implies that eddy stresses on the zonal wind are less than the Lindzen parameterization yields. It remains to be seen whether it is possible to find a combination of model parameters which matches the water vapor observations, while satisfying the other important 2-D model constraints such as the very cold summer polar mesopause and realistic mesospheric zonal wind speeds.

### 3. Comparison With Ozone Measurements and Model Calculations

The abundance of ozone in the upper mesosphere is expected to be critically dependent on the water vapor abundance because water vapor is the dominant source of odd hydrogen, which controls ozone loss at these altitudes (Allen et al., 1984). Thus, it is instructive to compare the observed seasonal variation of water vapor with similar measurements of mesospheric ozone. In fact, this comparison is an excellent test of our understanding of ozone photochemistry. The most extensive set of measurements of ozone in the upper mesosphere are those obtained from the SME satellite experiment. In particular, the infrared photometer experiment on board SME (Thomas et al., 1984a) has provided daily measurement of ozone in the 1 to 0.001 mb (roughly 50 to 90 km) range from 1982 through 1986. In Strobel et al. (1987), we compared 3-month average vertical profiles of both SME ozone and ground-based water vapor measurements. This analysis showed, first of all, that using up-to-date chemistry and previous vertical transport rates (and thus relatively high upper mesospheric water vapor mixing ratios), SME ozone abundances are more than a factor of 2 larger than the model calculations in the upper mesosphere. A similar conclusion was reached in Rusch and Eckman (1985) and in Clancy et al. (1987). The discrepancy between the measured and modeled ozone profiles is virtually eliminated (in April up to the ozone minimum at 75 km) by adoption of the odd hydrogen reaction rate modifications suggested by Rusch and Eckman (1985), in addition to the much lower water vapor abundances measured in the microwave experiments (Strobel et al., 1987).

One of the most important discoveries of SME was the detection of an apparent semiannual variation in the ozone abundance near the mesopause with a large maximum in spring, smaller maximum in the fall, and relative minima in winter and summer (Thomas et al., 1984b). In order to illustrate this seasonal variation, in Figure 5 we show monthly (and zonally) averaged profiles for the months of January, April, and June 1983 at  $40^{\circ}$  N, obtained by the SME near infrared spectrometer (Thomas et al., 1984a). The seasonal variation exhibited here was repeatable at mid-latitudes over the 5-year lifetime of SME, although the magnitude of the variation was smaller in the last two years of the experiment. Note that the ozone peak in April, which is clearly illustrated in the ozone time series at 0.01 mb plotted in Thomas et al. (1984b), results from a narrow bulge in the profile, centered at about 0.01 mb with a full width of  $\approx 7$  km. Below the April bulge, the January abundances are higher than both the April and June values, whereas above the peak the June abundances are highest. Thus, the observed ozone mixing ratios below and above the peak have an essentially annual variability in contrast to the semiannual variation in the bulge region. At higher latitudes the amplitude of the bulge is increased relative to mid-latitude values. At low latitudes, the April maximum is of smaller amplitude, is centered at a higher altitude ( $\approx 0.005$  mb), and is of much larger vertical extent ( $\approx 14$  km) than the mid-latitude feature.

It has been postulated (Thomas et al., 1984b, and Garcia and Solomon, 1985) that the seasonal ozone variation is driven, at least in part, by a similar variation of opposite phase in water vapor. In other words, what would be required is a semiannual variation in water vapor with minima at the equinoxes and maxima at solstices. This is precisely the type of variation

predicted near the mesopause in a diffusive atmosphere. In fact, the Garcia and Solomon (1985) model approximately reproduces the observed seasonal variation of ozone in the upper mesosphere. The model equinoctal minimum in  $K_{zz}$  produces a water vapor minimum in April above 75 km which, in turn, results in an ozone maximum above this altitude. However, this April maximum is of very narrow vertical extent because above 80 km the variation in the downward transport of atomic oxygen from the thermosphere begins to become important in controlling the ozone distribution (cf. Allen et al., 1981). The low model  $K_{zz}$  values in April also reduce the downward flux and, thus, abundance of atomic oxygen in this region, which acts to decrease ozone. Above 80 km this effect becomes more important than the water vapor variation and, thus, diminishes and finally reverses the April ozone maximum. In addition, the model  $K_{zz}$  seasonal variation produces a semiannual variation in atomic oxygen at 100 km with maxima at equinox, in agreement with green line intensity measurements (Cogger et al., 1981). However, as discussed in Section 2, the model water vapor results are not consistent with the microwave measurements. Specifically, the dominant semiannual water vapor seasonal variation, which drives the ozone variation, is not observed in the measurements. In addition, the predicted water vapor mixing ratios are quite high compared to the measurements, especially in winter.

In order to explore the question of internal consistency between the water vapor and ozone measurements in more detail, we performed a series of ozone seasonal variation calculations using the Cal Tech 1D photochemical model (Allen et al., 1981, and 1984). The model, which contains complete hydrogen/oxygen chemistry, was used as described in Strobel et al. (1987). It was run for the months January, April, and June at  $40^{\circ}\text{N}$ . The background

atmosphere for each monthly run was taken from the Air Force Model Atmosphere (Cole and Kantor, 1978), and we used diurnally averaged photodissociation rates appropriate for the mid-point of each month. The model does not separately handle diffusive and advective transport; rather, it represents all vertical transport as diffusive. The vertical transport rates for each monthly run were determined based on the measured water vapor profiles. That is, the vertical transport was varied to produce model water vapor profiles consistent, in both absolute magnitude and seasonal variation over those three months, with the Penn State observations.

The resultant water vapor profiles for the three model runs are shown in Figures 6a. Note that we did not endeavor to obtain precise fits to the water vapor measurements. Rather, the goal was to reproduce the general character and important features of the seasonal variation, especially in the critical 60 to 80 km region. The water vapor profiles show a more or less monotonic increase from winter to summer, with the more rapid portion of the increase occurring from April through June. The corresponding ozone profiles for the three model runs are shown in Figure 6b. Up to about 80 km we see the expected inverse dependence of ozone on water vapor and decreasing ozone abundance from January to June. Up to 70 km the water vapor forcing is augmented by the zenith angle dependence which also acts to decrease ozone from winter through summer (Allen et al., 1984). Above 80 km atomic oxygen becomes important in controlling the ozone abundance. Atomic oxygen densities maximize in April resulting in an ozone maximum in April above 85 km. Thus, the model constrained by the measured water vapor profiles does produce a semiannuual variation of ozone above about 85 km. However, in the region of the ozone minimum around 78 km the water vapor forcing is most important and a



simple annual variation is obtained, at variance with the SME measurements.

Thus, we obtain the expected result that, with the model vertical transport constrained purely by the water vapor measurements, the ozone semiannual variation is not produced; factors other than water vapor must be generating this ozone variation. In very general terms, there are only two major candidates for this mechanism: local photochemistry (that is local production, local destruction, or change in the  $O_3/O$  partitioning), or variations in the vertical and/or horizontal transport of atomic oxygen into the 78 km region where it can drive the ozone variation. The local production is exceedingly temperature dependent and varies with zenith angle. Both of these effects act to increase ozone above 75 km from winter to summer and produce a predominantly annual variation. However, our model calculations indicate that the observed water vapor seasonal variation in the upper mesosphere is of sufficient magnitude to dominate the local temperature dependence and zenith angle effects on ozone photochemistry. We have performed one other set of model calculations, this time using temperature measurements derived from observations of limb ultraviolet radiances obtained by SME (Clancy and Rusch, 1989). These temperature measurements are significant for our purposes because they show a much larger semiannual component near the mesopause than present in the Air Force Model. For example, from January to April the temperature decrease at 76 km and  $40^\circ$  N is about 12 K in the SME data while it is about half that number in the Air Force Model. There is a small but significant difference in the predicted ozone seasonal variation using the SME temperatures. Whereas in the calculations shown in Figure 6b the ozone abundances are about 20% higher in January than in April in the vicinity of the ozone minimum, in the calculations with the

SME temperatures the January and April abundances are nearly identical in this region. Thus, the use of the SME temperatures produce a stronger semiannual component in the ozone mixing ratios in the upper mesosphere, but an April maximum is still not obtained. The  $O_3/O$  partitioning is dominated by ozone photolysis and production ( $O + O_2 + M \rightarrow O_3 + M$ ) and should be accurately treated in the 1D model. Ozone loss at 78 km is controlled by the odd hydrogen catalytic cycle (Allen et al., 1984). In our model, the  $HO_x$  abundances are determined by the local water vapor abundance, because  $HO_x$  is in approximate photochemical equilibrium at 78 km. Therefore, the water vapor measurements would at least appear to rule out this mechanism for forcing the ozone seasonal variation.

It should be mentioned here, that there is increasing evidence that the simple picture of ozone photochemistry in the upper mesosphere and lower thermosphere, described above, may not be complete. For example, Allen et al. (1984) report that measured ozone abundances in the upper mesosphere and lower thermosphere are consistently higher than model results, and that these observations cannot be accounted for by the present set of known reactions. This finding has prompted a search for an additional chemical source of ozone in the atmosphere (cf. Allen (1986)). In earlier work, Olivero (1974) explored the possibility that heterogeneous chemistry on the surface of meteoric material, or other mesospheric aerosols, may be important in controlling ozone photochemistry near the mesopause. In light of recent findings about the importance of heterogeneous chemistry in the formation of the Antarctic "ozone hole" (cf. Salawitch et al., 1988), perhaps this possibility should be examined in more detail. It is possible that this speculative missing component in ozone photochemistry could be important in

controlling the ozone seasonal variation near the mesopause.

In the absence of some heretofore unknown ozone photochemical or dynamical mechanism, we are left with variations of the transport of atomic oxygen as the only plausible mechanism for the semiannual ozone variation. Furthermore, given the small vertical scale of this variation, it is unlikely to be the result of horizontal transport variations. However, near the mesopause, variations in vertical transport rates (and thus in the flux of atomic oxygen) become important in ozone photochemistry (cf. Allen et al., 1981). The vertical transport of atomic oxygen from the thermosphere has not been properly constrained in the model calculations shown in Figure 6. The water vapor measurements constrain the model vertical transport only up to 80 km, from 80 to 130 km (model upper boundary) the model  $K_{zz}$  profiles were simply extrapolated. It is also important to point out that while our measurements (and vertical transport rates inferred from them) suggest that water vapor is advectively dominated, they clearly do not preclude diffusive control of atomic oxygen. As indicated in (1) and discussed extensively in Holton and Schoeberl (1988), the relative importance of advective and diffusive processes in controlling vertical transport for a particular constituent is dependent on the species scale height, with diffusion being more important for species with small scale heights. The scale height of atomic oxygen near the mesopause is extremely small, of order 1 km, compared with 4 km for water vapor. Thus, it is possible for water vapor to be advectively controlled, and atomic oxygen diffusively controlled. For example, using (1), and our upper limit for  $K_{zz}$  of  $10^5 \text{ cm}^2 \text{ s}^{-1}$ , to calculate  $\tau_w$  and  $\tau_D$  for atomic oxygen, we find values of  $2.5 \times 10^5 \text{ s}$ , and  $1.0 \times 10^5 \text{ s}$  respectively, which would imply diffusive control of atomic oxygen.

The green line intensity variation (which indicates a semiannual variation of atomic oxygen at 100 km in phase with the ozone variation at 80 km) is an important constraint on the seasonal variation of atomic oxygen transport. Thus, the problem is to find a mechanism which produces a semiannual variation in ozone at 78 km and in atomic oxygen at 100 km, while at the same time retaining the annual water vapor variation up to 80 km with a maximum in June. A uniform increase in vertical transport over the entire 80 to 100 km region in April relative to January and June would increase atomic oxygen and, thus, ozone abundances near 78 km. However, as vertical transport is increased the atomic oxygen densities should be enhanced below 90 km and diminished above that altitude because the source region is being depleted (Garcia and Solomon, 1985). Thus, an increase in transport over the entire 80 to 100 km region would enhance ozone abundances in April over a much larger vertical extent than indicated by the SME measurements ( $\approx 11$  km as compared to  $\approx 6$  km), and cause the green line intensity maximum in April to disappear. However, a narrow layer of rapid vertical transport (about an order of magnitude over the value below 80 km, with a full width at half maximum of  $\approx 5$  km) in April centered at about 85 or 90 km, with slower transport both above (to produce the 100 km atomic oxygen maximum) and below (to agree with the water vapor measurements) this altitude, would satisfy the measurement constraints.

This narrow layer of rapid vertical transport could be produced by high phase speed easterly ( $c \approx -20$  to  $-40 \text{ m s}^{-1}$ ) gravity waves which can vertically propagate through the westerly zonal winds of the lower and middle atmosphere at equinox and would break in the vicinity of the mesopause, generating enhanced eddy diffusion and transport. These waves could also

propagate through the mesosphere in the winter, but during winter the mesosphere is more isothermal and the attainment of saturation amplitudes, and accompanying diffusion, may be more difficult. Furthermore, in winter the turbulent layer would have a negligible effect on the water vapor profile because the water vapor mixing ratio vertical gradient in the mesosphere is sufficiently steep that abundances at 85 km are very small. In the summer, the easterly zonal winds in the middle atmosphere would filter out these gravity waves in the vicinity of critical levels. If we assume that these gravity waves saturate in the mesopause region where the mean westerly zonal winds ( $u$ ) are weak ( $u \ll |c|$ ), then during winter and equinox months the wave saturation height and gravity wave induced diffusion coefficient should be essentially a function of  $c$  only (Holton, 1982). Thus, the breakdown of these waves could cause large turbulence in spring, over a narrow layer, despite the weak radiative drive. The essential requirement for enhanced gravity wave induced diffusion at equinox is wave saturation in the vicinity of the mesopause region, where it would be sharply bounded on the topside by the presence of a critical level where the wave amplitude and stresses would vanish. Although the presence of these large phase speed easterly gravity waves (and resultant enhanced turbulence near the mesopause at equinox) is physically plausible, there is no direct evidence for this enhanced turbulence from MST (Mesosphere-Stratosphere-Troposphere) radar measurements. However, because of its narrow vertical extent, the layer (if it were present) may be difficult to detect.

#### 4. Summary and Conclusions

We have reviewed the complete data set of mesospheric water vapor measurements obtained by ground-based microwave techniques. The measurements indicate that the seasonal variation of water vapor in the mesosphere is dominated by an annual component with low values in winter and high values in summer. This suggests that the seasonal variation of water vapor in the mesosphere (below 80 km) is controlled by advective rather than diffusive processes. The predominance of advective over diffusive processes is consistent with the steep vertical gradient persistently observed in the mesospheric water vapor profile, which suggests weak eddy diffusion. Both the seasonal variation and the absolute magnitude of the water vapor mixing ratios obtained in the microwave measurements have been corroborated by measurements obtained in the Spacelab GRILLE and ATMOS experiments (Bevilacqua et al., 1989). In addition, the measurements are also consistent with several recent mesospheric dynamics studies which conclude that the Lindzen parameterization is an overestimate of constituent diffusive vertical transport (cf. Schoeberl (1988)), and with the mesospheric heat budget studies of Apruzese et al. (1984) and Strobel et al. (1985). All these studies suggest that  $K_{zz}$  is about an order of magnitude smaller than the Lindzen values, in agreement with those values inferred from both the seasonal variation and vertical gradient of the water vapor measurements ( $K_{zz} \approx 10^5 \text{ cm}^2 \text{ s}^{-1}$ ). However, recent calculations by Garcia (1989) show that it is not possible to completely reconcile the water vapor measurements with the Garcia and Solomon model calculations simply by increasing the eddy Prandtl number (which has the effect of decreasing the magnitude of  $K_{zz}$ ), because the measured water vapor mixing ratios exhibit

somewhat lower abundances than the model results in summer as well as winter. An increase in the eddy Prandtl number to  $\approx 10$  brings the model results into approximate agreement with the winter measurements, but has little effect in summer where advection is very important in controlling the water vapor abundance.

In addition, it is very difficult to reconcile the predominantly annual water vapor variation obtained from the microwave measurements with the large semianual variation of ozone at 78 km observed by SME. To complicate the picture even further, Thomas (Atomic hydrogen and atomic oxygen density in the mesopause region: global and seasonal variations deduced from SME near-infrared emissions, submitted to the Journal of Geophysical Research, 1989) has recently inferred both atomic hydrogen and oxygen on a global basis in the upper mesosphere and lower thermosphere from SME measurements of  $O_2(^1\Delta_g)$  and Meinel band emission. The atomic hydrogen measurements at 0.01 mb ( $\approx 80$  km) show a very large semianual variation which is well correlated (and apparently consistent) with the SME ozone measurements. On the other hand, atomic oxygen at the same altitude shows a predominantly annual variation which is well correlated with the water vapor measurements, but is not correlated with the ozone and atomic hydrogen measurements. According to current photochemical theory, at 80 km atomic hydrogen is in approximate photochemical equilibrium and, therefore, controlled by the local water vapor abundance. Similarly, atomic oxygen is in approximate photochemical equilibrium there, and its abundance (as well as that of ozone) should be controlled by the local odd hydrogen abundance through the odd hydrogen catalytic cycle. However, this is not observed. For both odd hydrogen and odd oxygen, the photochemical time-scales increase very rapidly with altitude

in the upper mesosphere and lower thermosphere. Both families are predominantly chemically controlled at 80 km, but transport controlled at 90 km (cf. Allen et al., 1984). Thus, the upper mesosphere is a complicated transition region from photochemical to dynamical control. It remains a challenge to the middle atmospheric community to reconcile all these diverse observations and, thereby, develop a consistent picture of the complex interaction of dynamics and photochemistry which produces the observed distribution of chemical tracers in the mesosphere.



### References

Allen, M., A new source of ozone in the terrestrial upper atmosphere, J. Geophys. Res., 91, 2844-2848, 1986.

Allen, M., Y. L. Yung, and J. W. Waters, Vertical transport and photochemistry in the terrestrial mesosphere and lower thermosphere (50-120 km), J. Geophys. Res., 86, 3617-3627, 1981.

Allen, M., J. L. Lunine, and Y. L. Yung, The vertical distribution of ozone in the mesosphere and lower thermosphere, J. Geophys. Res., 89, 4841-4872, 1984.

Apruzese, J. P., D. F. Strobel, and M. R. Schoeberl, Parameterization of IR cooling in a middle atmosphere dynamics model, 2, non-LTE radiative transfer and the globally averaged temperature of the mesosphere and lower thermosphere, J. Geophys. Res., 89, 4917-4926, 1984.

Barnett, J. J., and M. M. Corney, Middle atmosphere reference model derived from satellite data, Handbook for MAP, 16, 47-85, University of Illinois, Urbana, 1985.

Bevilacqua, R. M., J. J. Clivero, P. R. Schwartz, C. J. Gibbins, J. M. Bologna, and D. L. Thacker, An observational study of water vapor in the mid-latitude mesosphere using ground-based microwave techniques, J. Geophys. Res.,

88, 8523-8534, 1983.

Bevilacqua, R. M., W. J. Wilson, W. B. Ricketts, P. R. Schwartz, and R. J. Howard, Possible seasonal variability of mesospheric water vapor, Geophys. Res. Lett., 12, 397-400, 1985.

Bevilacqua, R. M., W. J. Wilson, and P.R. Schwartz, Measurements of mesospheric water vapor in 1984 and 1985: results and implications for middle atmospheric transport, J. Geophys. Res., 92, 6679-6690, 1987.

Bevilacqua, R. M., and J. J. Olivero, The vertical resolution of middle atmospheric measurements by ground-based microwave radiometry, J. Geophys. Res., 93, 9463-9475, 1988.

Bevilacqua, R. M., J. J. Olivero, and C. L. Croskey, Mesospheric water vapor measurements from Penn State: monthly mean observations (1984-1987), J. Geophys. Res., in press, 1989.

Brasseur, G., and S. Solomon, Aeronomy of the middle atmosphere, D. Reidel, Hingham, MS, 1984.

Chapman, S., On ozone and atomic oxygen in the upper atmosphere, Phil. Mag., 10, 369, 1930.

Clancy, R. T., D. O. Muhleman, and M. Allen, Seasonal variability of CO in the terrestrial mesosphere, J. Geophys. Res., 89, 9673-9676, 1984.

Clancy, R. T., D. W. Rusch, R. J. Thomas, M. Allen, and R. S. Eckman, Model ozone photochemistry on the basis of Solar Mesosphere Explorer observations, J. Geophys. Res., 92, 3067-3080, 1987.

Clancy, R. T., and D. W. Rusch, Climatology and trends of mesospheric (58-90 km) temperatures based upon 1982-1986 SME limb scattering profiles, J. Geophys. Res., 94, 3377-3393, 1989.

Cogger, L. L., R. D. Elphinstone, and J. S. Murphree, Temporal and latitudinal 5577 Å airglow variations, Can. J. Phys., 59, 1296-1307, 1981.

Cole, A. E., and A. J. Kantor, Air Force reference atmospheres, AFGL-TR-78-0051, Air Force Geophys. Lab., Cambridge, Mass., 1978.

Garcia, R. R., and S. Solomon, The effect of breaking gravity waves on the dynamics and chemical composition of the mesosphere and lower thermosphere, J. Geophys. Res., 90, 3850-3868, 1985.

Garcia, R. R., Dynamics, radiation, and photochemistry in the mesosphere: implications for the formation of noctilucent clouds, J. Geophys. Res., in press, 1989.

Gibbins, C. J., P. R. Schwartz, D. L. Thacker, and R. M. Bevilacqua, The variability of mesospheric water vapor, Geophys. Res. Lett., 9, 131-134, 1982.

Girard, A., J. Besson, D. Brard, J. Laurent, M. P. Lemaitre, C. Lippens, C. Muller, J. Vercheval, and M. Ackerman, Global results of GRILLE spectrometer

experiment on board Spacelab 1, Planet. Space Sci., 36, 291-300, 1988.

Holton, J. R., The role of gravity wave induced drag and diffusion in the momentum budget of the mesosphere, J. Atmos. Sci., 39, 791-799, 1982.

Holton, J. R., and M. R. Schoeberl, The role of gravity wave generated advection and diffusion in the transport of tracers in the mesosphere, J. Geophys. Res., 93, 11075-11082, 1988.

Keating, G. M. and D. F. Young, Interim ozone reference models for the middle atmosphere, Handbook for MAP, 16, 205-229, University of Illinois, Urbana, 1985.

Leovy, C. B., Simple models of thermally driven mesospheric circulations, J. Atmos. Sci., 21, 327-341, 1964.

Lindzen, R. S., Turbulence and stress owing to gravity wave and tidal breakdown, J. Geophys. Res., 86, 9707-9714, 1981.

Olivero, J. J., Surface (catalytic) reactions on upper atmospheric aerosols, J. Geophys. Res., 79, 1974.

Olivero, J. J., J. J. Tsou, C. L. Croskey, L. C. Hale, and R. G. Joiner, Solar absorption microwave measurements of upper atmospheric water vapor, Geophys. Res. Lett., 13, 197-200, 1986.

Rensberg, E. E., J. M. Russell III, L. L. Gordley, J. C. Gille, and P. L. Bailey, Implications of the stratospheric water vapor distribution as determined from the Nimbus 7 LIMS experiment, J. Atmos. Sci., 41, 2934-2945, 1984.

Rusch, D. W., and R. S. Eckman, Implications of the comparison of ozone abundances measured by the Solar Mesosphere Explorer to model calculations, J. Geophys. Res., 90, 12991-12998, 1985.

Salawitch, R. J., S. C. Wofsy, and M. B. McElroy, Influence of polar stratospheric clouds on the depletion of Antarctic ozone Geophys. Res. Lett., 15, 871-874, 1988.

Schoeberl, M. R., A model of stationary gravity wave breakdown with convective adjustment, J. Atmos. Sci., 45, 980-992, 1988.

Schwartz, P. R., C. L. Croskey, R. M. Bevilacqua, and J. J. Olivero, Microwave spectroscopy of H<sub>2</sub>O in the stratosphere and mesosphere, Nature, 305, 294-295, 1983.

Solomon, S., R. R. Garcia, J. J. Olivero, R. M. Bevilacqua, P. R. Schwartz, R. T. Clancy, and D. O. Muhleman, Photochemistry and transport of carbon monoxide in the middle atmosphere, J. Atmos. Sci., 42, 1072-1083, 1985.

Strobel, D. F., J. P. Apruzese, and M. R. Schoeberl, Energy balance constraints on gravity wave induced eddy diffusion in the mesosphere and lower thermosphere, J. Geophys. Res., 90, 13067-13072, 1985.

Strobel, D. F., M. E. Summers, R. M. Bevilacqua, M. T. DeLand, and M. Allen, Vertical constituent transport in the mesosphere, J. Geophys. Res., 92, 6691-6698, 1987.

Thacker D. L., C. J. Gibbins, P. R. Schwartz, and R. M. Bevilacqua, Ground-based microwave observations of mesospheric H<sub>2</sub>O in January, April, July, and September, 1980, Geophys. Res. Lett., 8, 1059-1062, 1981.

Thomas, R. J., C. A. Barth, D. W. Rusch, and R. W. Sanders, Solar Mesosphere Explorer near-infrared spectrometer: measurements of 1.27  $\mu$ m radiances and the inference of mesospheric ozone, J. Geophys. Res., 89, 9569-9580, 1984a.

Thomas, R. J., C. A. Barth, and S. Solomon, Seasonal variations of ozone in the upper mesosphere and gravity waves, Geophys. Res. Lett., 11, 673-676, 1984b.

Tsou, J. J., J. J. Olivero, and C. L. Croskey, A study of the variability of H<sub>2</sub>O during spring 1984 by ground-based microwave radiometric observations, J. Geophys. Res., 93, 5255-5266, 1988.

### Figure Captions

Figure 1: Average mesospheric water vapor profiles obtained by microwave techniques at Penn State over the period February through June in 1985, 1986, and 1987, plotted with model profiles from Strobel et al. (1987). Model A was obtained with high  $K_{zz}$  values typical of those used in many photochemical models ( $K_{zz} \approx 10^6 \text{ cm}^2 \text{ s}^{-1}$ ). In the Model C profile the  $K_{zz}$  profile was adjusted to fit the water vapor measurements obtained at JPL in the spring of 1984 ( $K_{zz} \approx 10^5 \text{ cm}^2 \text{ s}^{-1}$ ).

Figure 2: Heuristic representation of the influence of diffusive and advective vertical transport processes in producing the seasonal variation of transport dominated constituents in a single hemisphere of the middle atmosphere.

Figure 3: Water vapor mixing ratios at 80 km measured at Penn State, JPL, and the Haystack Observatory, plotted as a function of calendar month. The Penn State observations represent monthly averages obtained over three successive years of observations, each JPL measurement point represents a single monthly average, and the Haystack measurements points are averages over 4 to 9-day observing periods. The error bar represents the average value of the total absolute error in the retrievals (1- $\sigma$  level).

Figure 4: Monthly average mixing ratios at Penn State plotted along with a model calculation of the vertical velocity at  $40^\circ \text{ N}$  and 80 km obtained from Schoeberl and Chandra (private communication, 1987). The water vapor

error bars represent the statistical variation (1 $\sigma$ -level) of the individual monthly averages from which these grand monthly averages were formed (no error bars are shown for November through January because measurements were obtained there only in 1984-85).

Figure 5: Monthly average ozone mixing ratio profiles obtained by SME in January, April and June 1983 (Thomas et al., 1984a).

Figure 6a: Monthly average photochemical model water vapor mixing ratio profiles obtained with the model vertical transport constrained such that the water vapor profiles fit the Penn State water vapor measurements.

Figure 6b: Monthly average ozone profiles obtained in the model runs illustrated in Figure 6a.



# Mesospheric Water Vapor Data Base

## (Ground-based Microwave Techniques)

<u>Measurement Facility</u>	<u>Location (lat.,long.)</u>	<u>Measurement Periods</u>
Haystack Observatory	43°N, 72°W	10 Jul. 1980 - 13 Jul. 1980
		18 Sep. 1980 - 25 Sep. 1980
		28 Jan. 1981 - 4 Feb. 1981
		8 Apr. 1981 - 16 Apr. 1981
		5 Dec. 1981 - 11 Dec. 1981
		1 Apr. 1982 - 8 Apr. 1982
Jet Propulsion Laboratory	34°N, 118°W	27 Mar. 1984 - 1 Jul. 1984
		16 Dec. 1984 - 4 May 1985
Penn State	41°N, 78°W	5 Feb. 1984 - 30 May 1984
		11 Nov. 1984 - 30 Jul. 1985
		22 Feb. 1986 - 30 Jul. 1986
		7 Feb. 1987 - 30 Jun. 1987

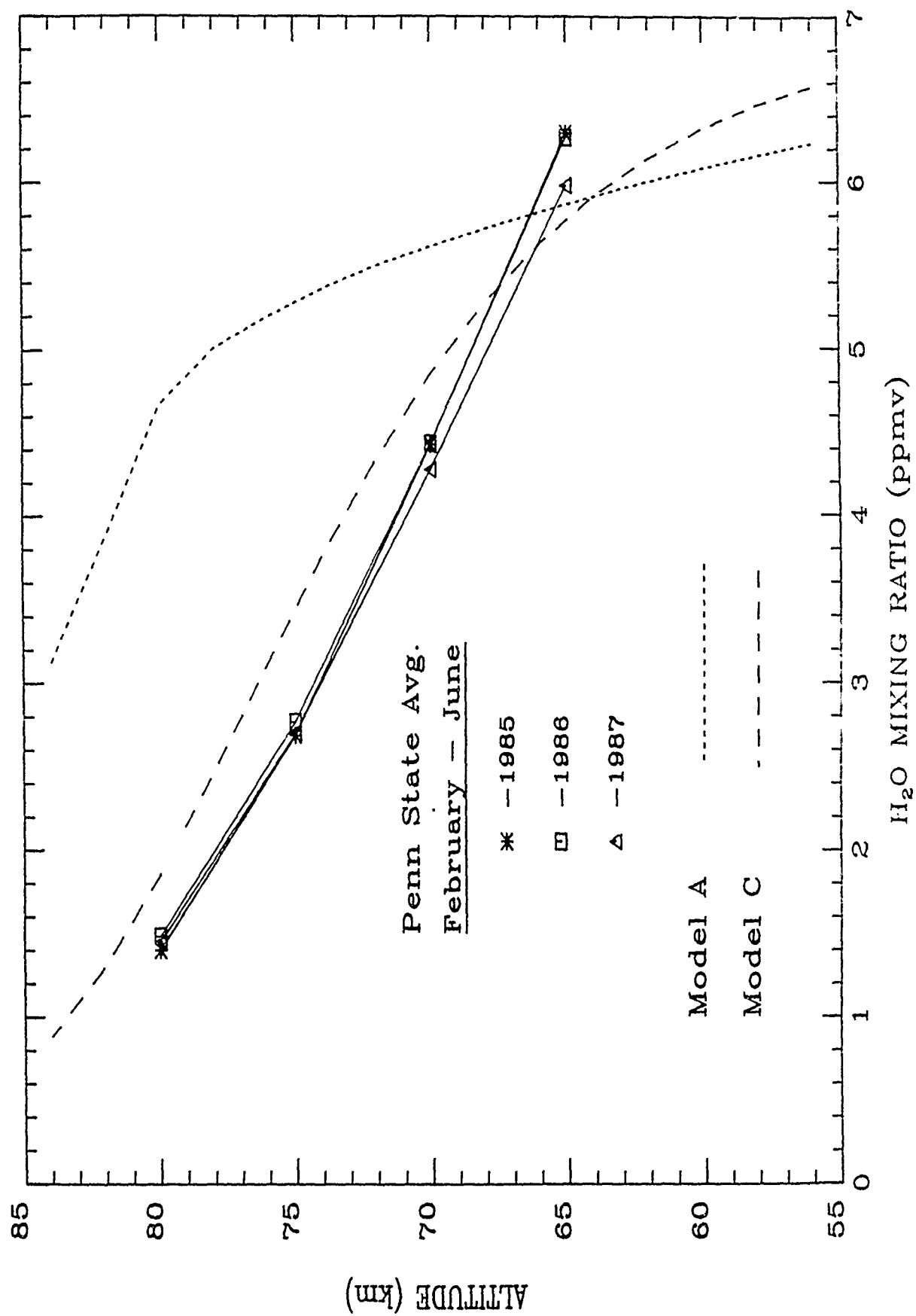
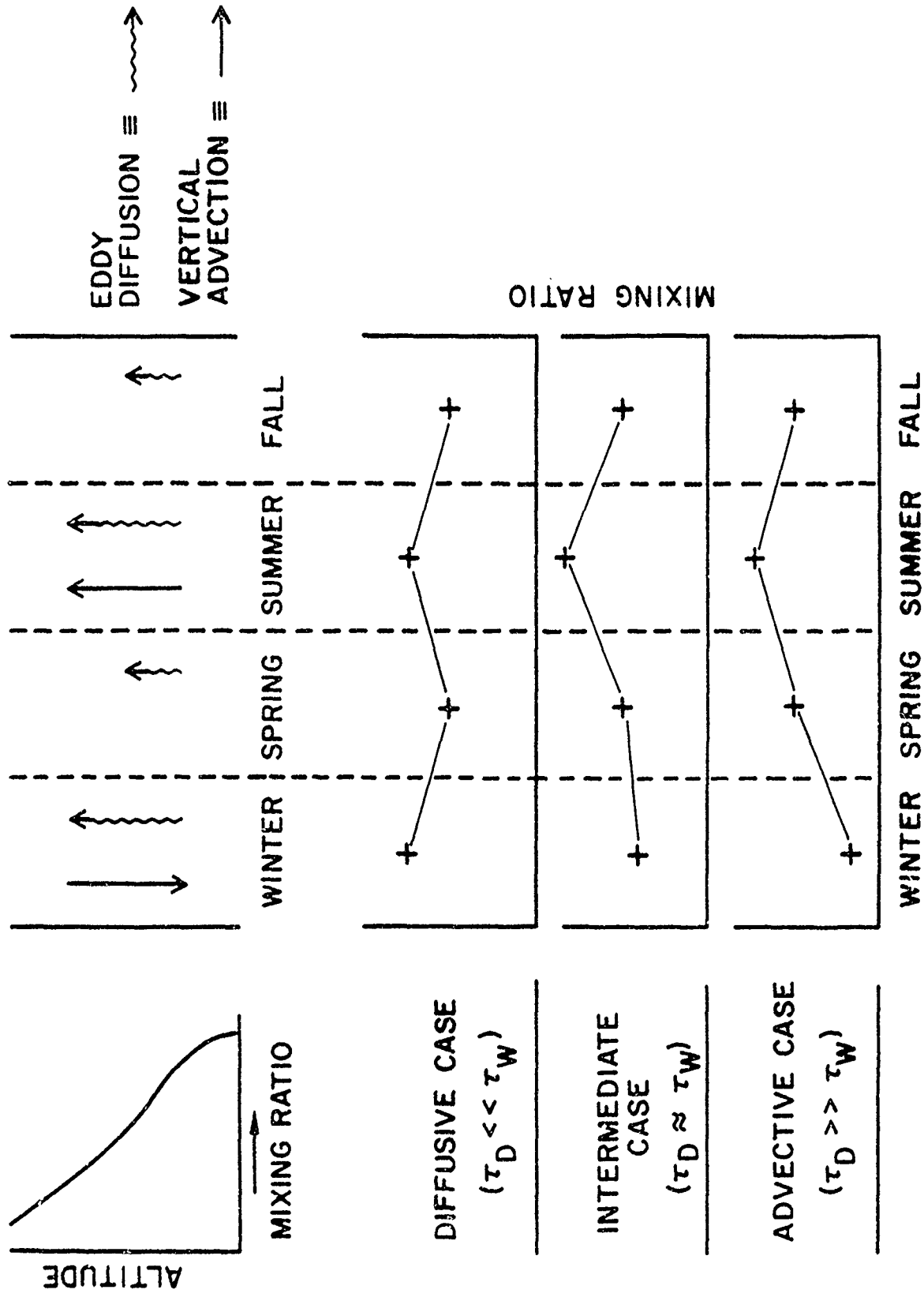


Fig. 1



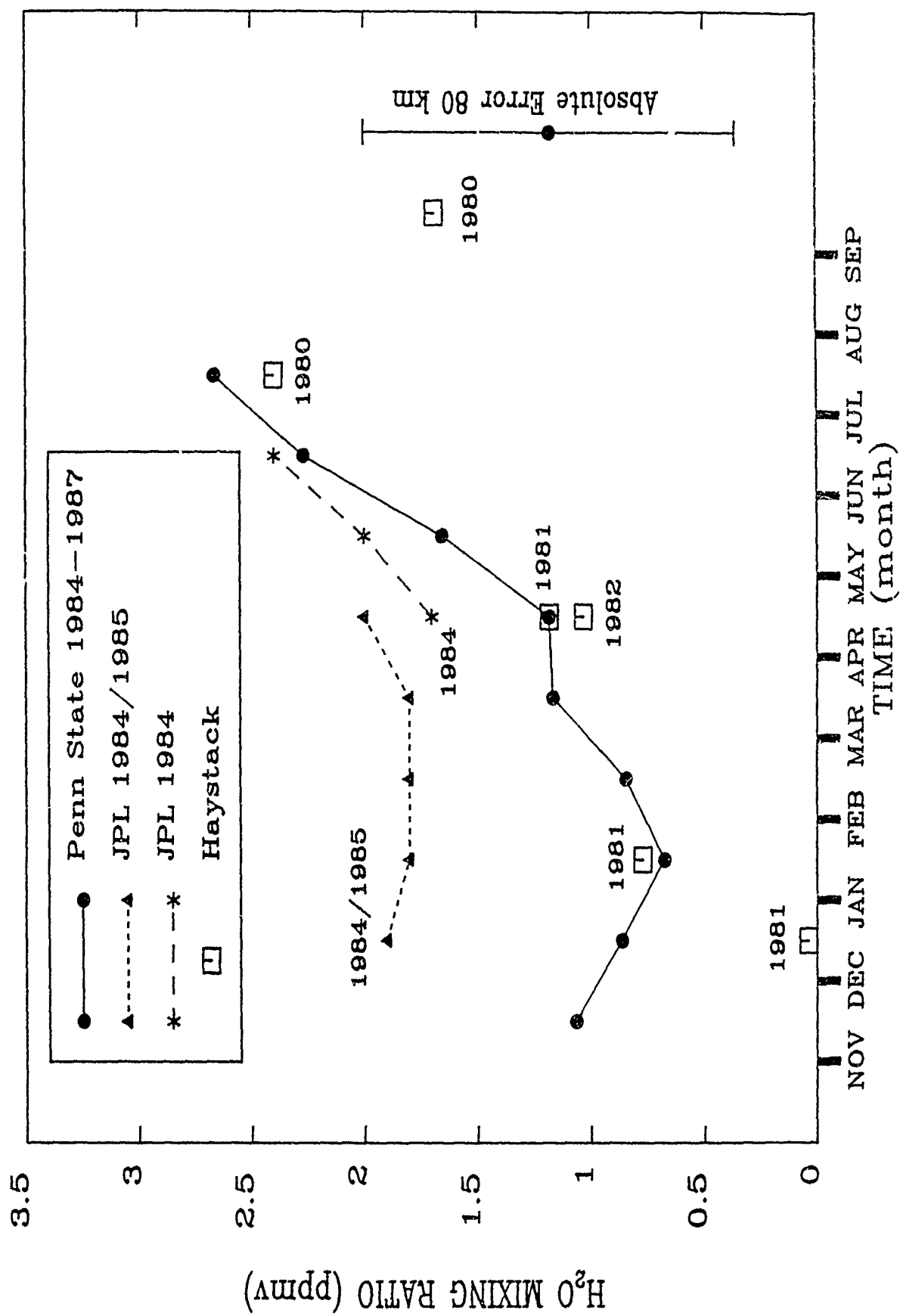
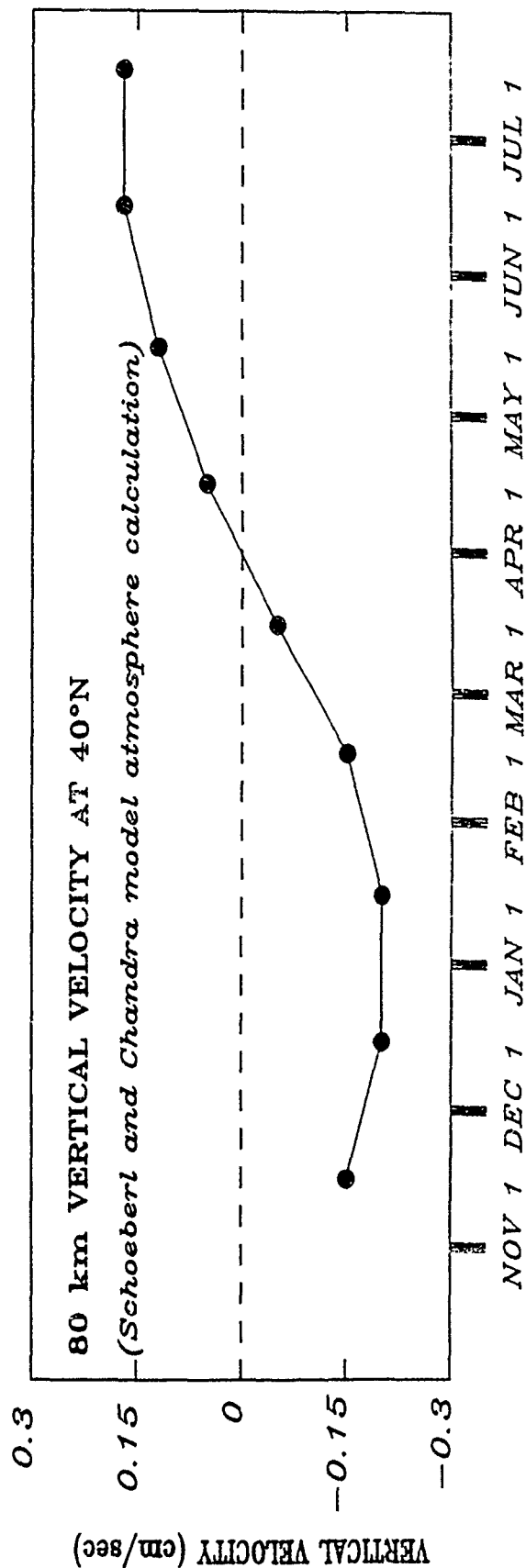
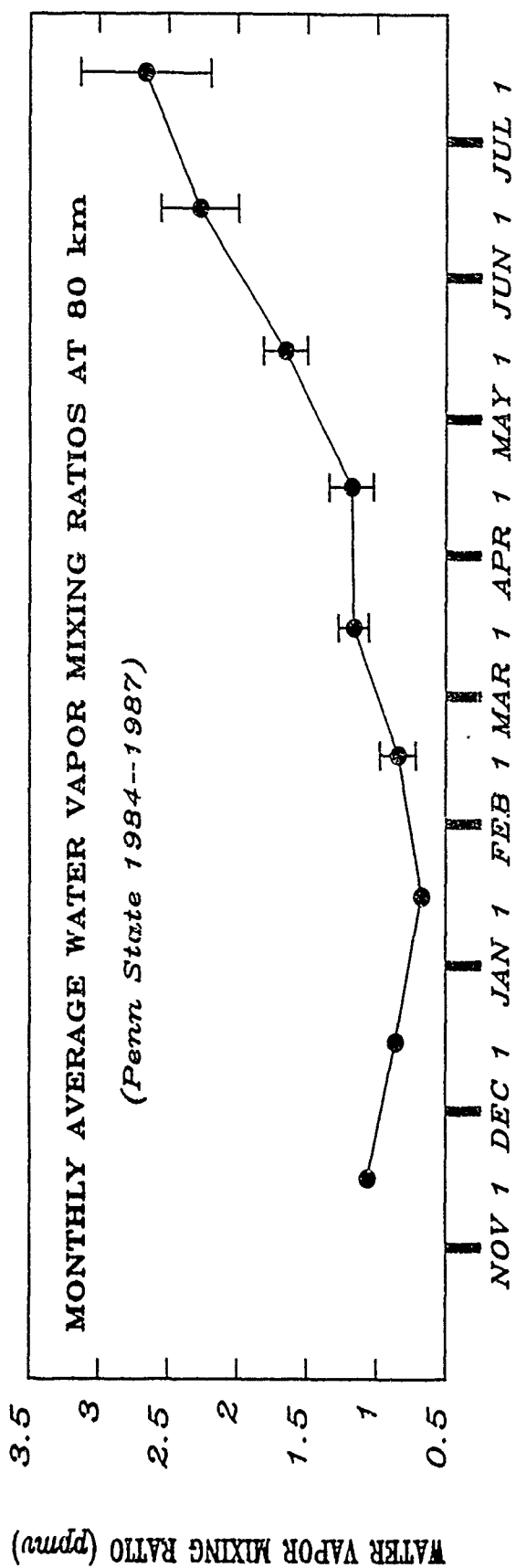


Fig. 3



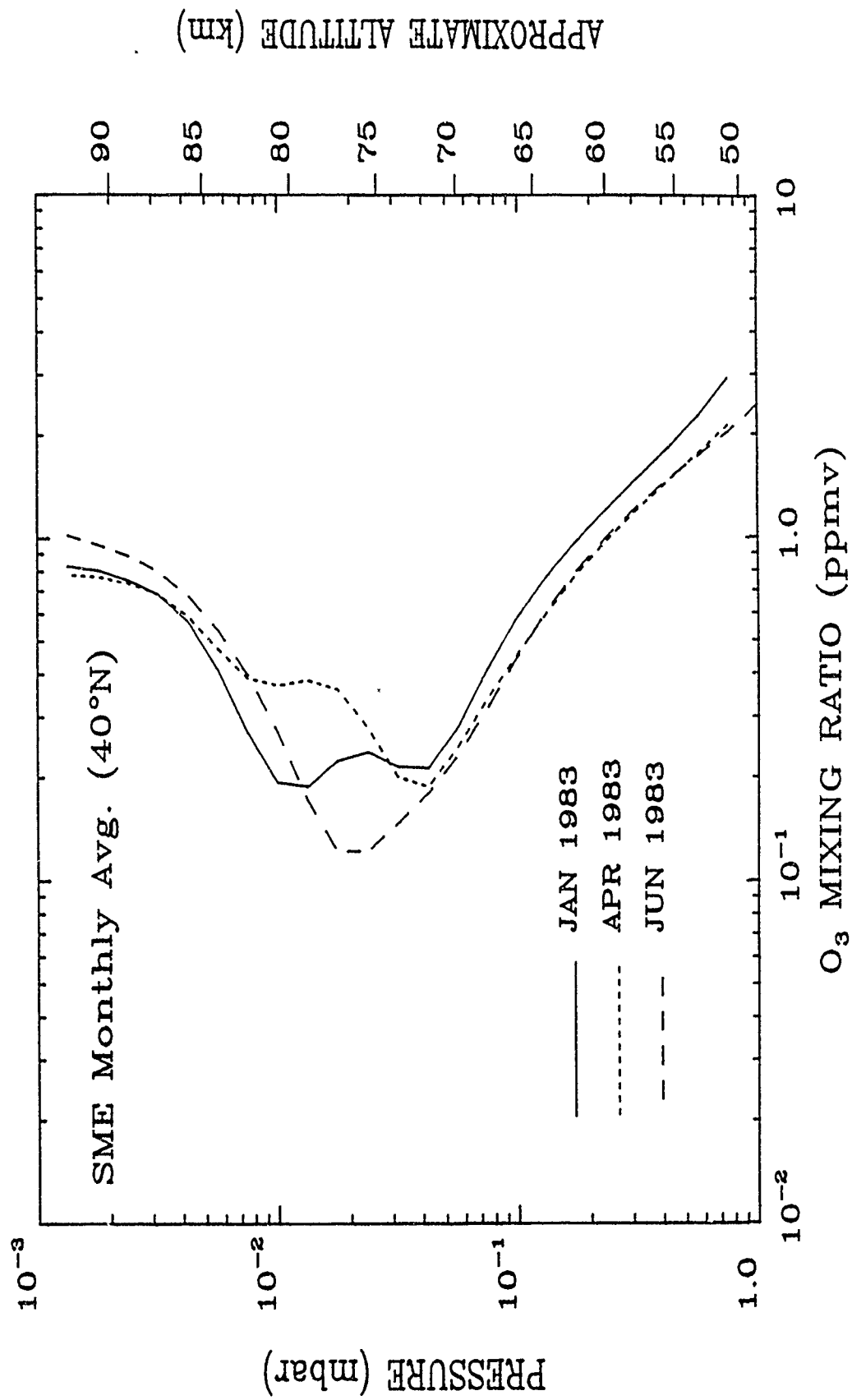


Fig. 5

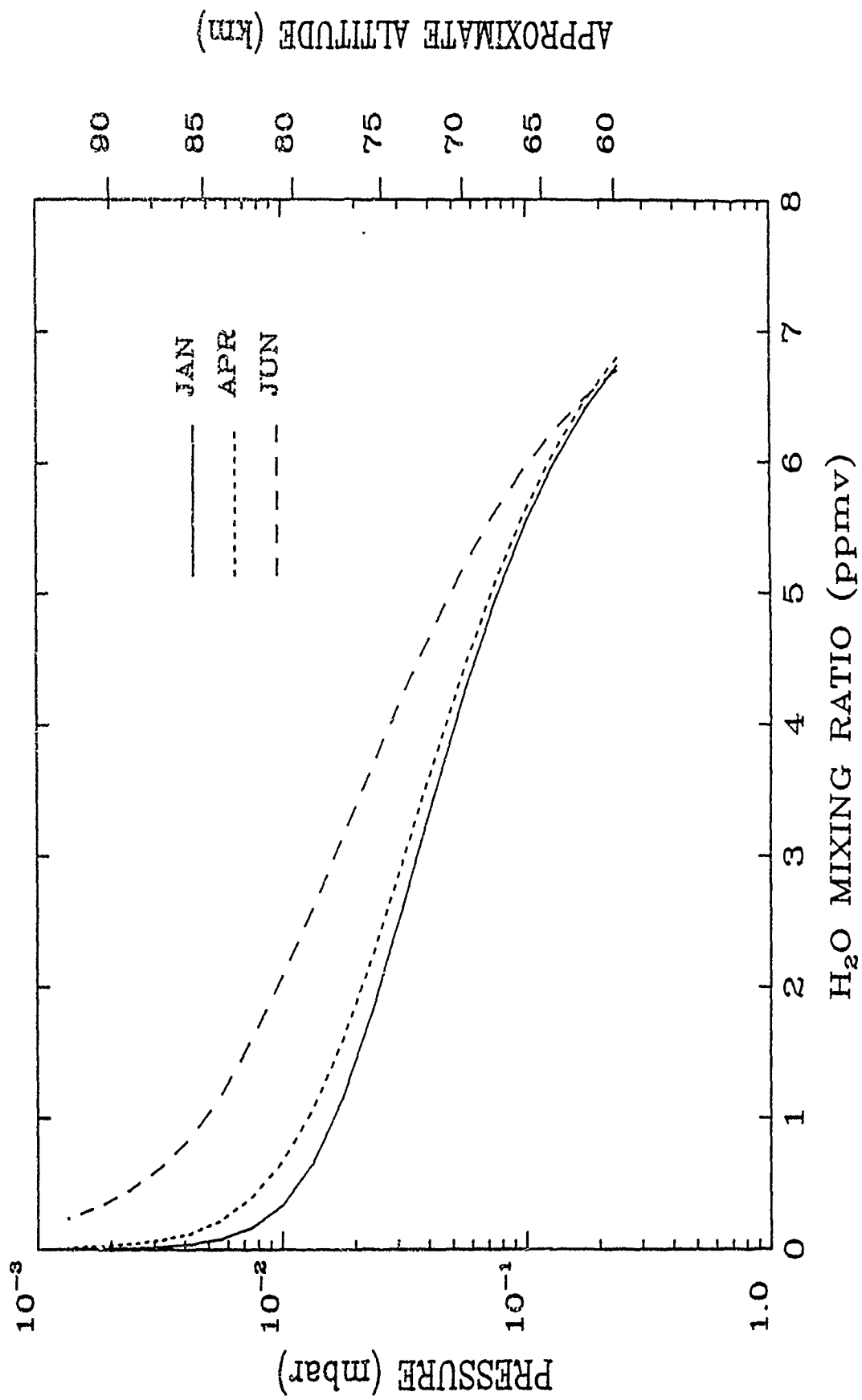


Fig. 6a

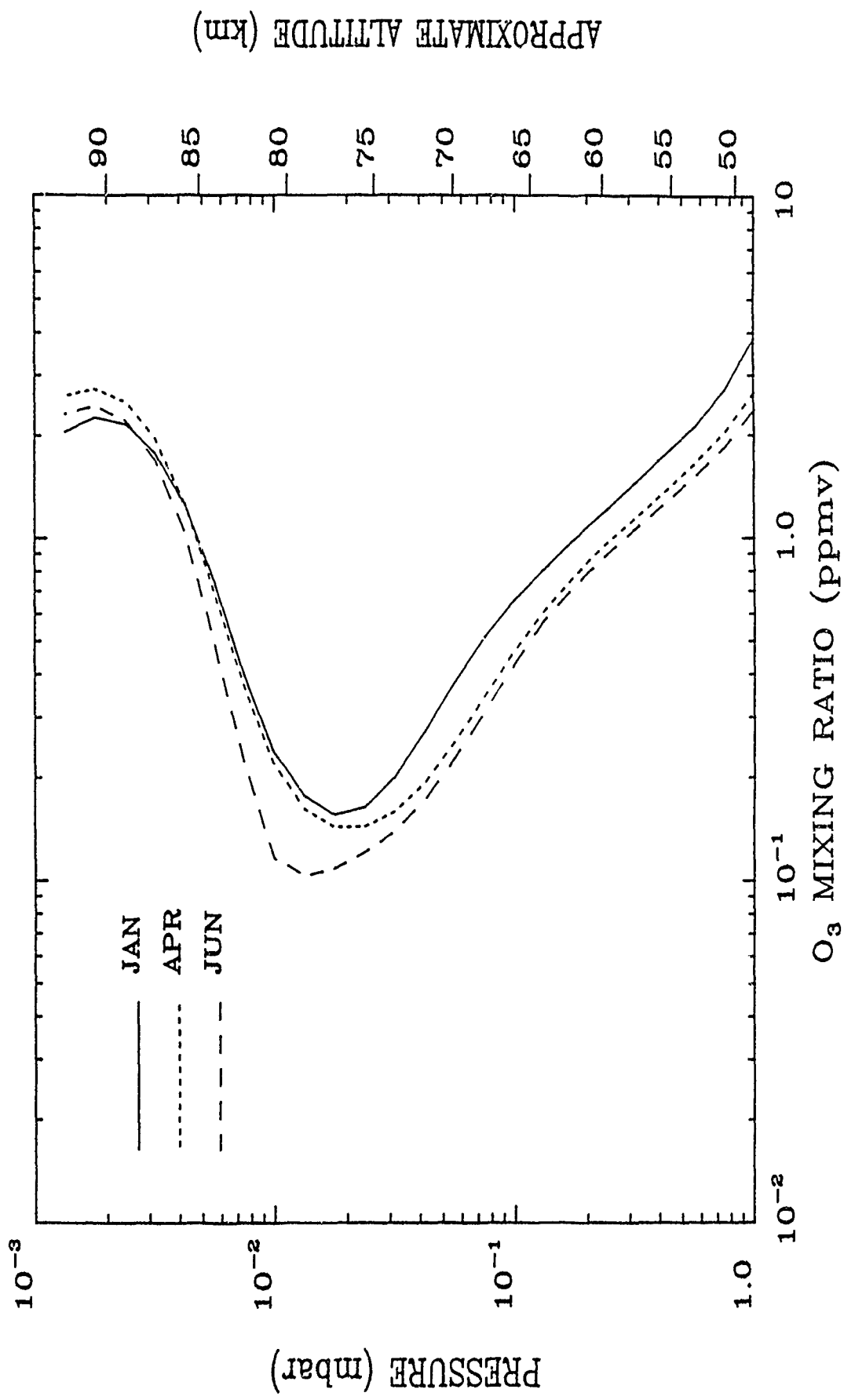


Fig. 6b



## **APPENDIX M**

### **A Model Study of the Response of Mesospheric Ozone To Short-Term Solar Ultraviolet Flux Variations**

4 Dec 89

A MODEL STUDY OF THE RESPONSE OF MESOSPHERIC OZONE  
TO SHORT-TERM SOLAR ULTRAVIOLET FLUX VARIATIONS

by

M. E. Summers and R. M. Bevilacqua

*E. O. Hulburt Center for Space Research, Naval Research Laboratory, Washington, DC*

D. F. Strobel

*Dept. of Earth and Planetary Sciences, and Dept. of Physics and Astronomy*

*The Johns Hopkins University, Baltimore, MD*

M. T. DeLand

*ST Systems Corp. (STX), Lanham, MD*

M. Allen

*Earth and Space Sciences Division, Jet Propulsion Laboratory, and*

*Division of Geological and Planetary Sciences*

*California Institute of Technology, Pasadena, CA*

G. M. Keating

*Atmospheric Sciences Division, NASA Langley Research Center, Hampton, VA*

Submitted to The Journal of Geophysical Research

## ABSTRACT

A one-dimensional photochemical model and a time dependent heat equation are used to study the response of mesospheric ozone concentration to short term solar UV flux variations. We compare our model results with the observed ozone response obtained from a statistical analysis of Solar Mesosphere Explorer data (Keating et al., 1987). Our model with sinusoidal forcing of mesospheric chemistry by solar ultraviolet flux with a period of 27 days, when combined with temperature-chemistry feedback and time dependent atmospheric temperature effects reproduces the major characteristics of the observed ozone response. Below 60 km, the calculated response shows a strong dependence on the magnitude of the assumed flux modulation in the Hartley region of the spectrum. A comparison of the model  $O_3$  response (with temperature feedback included) with the SME observations suggests there is negligible 27 day variation of solar flux longward of 2400 Å, in agreement with Lean (1987). We find that the magnitude of the computed ozone response to increased solar UV flux in the upper mesosphere (above 70 km) is strongly coupled to the water vapor abundance through the  $HO_x$  catalytic cycle that removes ozone, thus the response of the abundances of water vapor and  $HO_x$  species must be calculated self-consistently to accurately model the ozone response. We predict a seasonal dependence of the ozone response to solar UV flux variations as a consequence of the seasonal variation of upper mesospheric water vapor abundances.

## I. INTRODUCTION

It is well known that the solar ultraviolet flux varies in magnitude over the 11 year solar cycle and also on time scales characteristic of the evolution and rotation of solar active regions (see review by Lean, 1987, and references therein). Short-term irradiance variations arise primarily from the enhanced ultraviolet emissions in plage regions on the solar disc. The enhanced flux in  $Ly \alpha$ , for example, can be as much as 40 % higher when an especially active plage region occurs than when the sun is inactive or "quiet". This variation of solar ultraviolet irradiances over time scales of days to months has been observed over the two most recent solar cycles by the AE-C, AE-E, Nimbus 7, SME, and other satellites (Lean, 1987) and perturbs the ozone abundance in the stratosphere and mesosphere, due to a combination of effects resulting from changes in  $O_2$  and  $O_3$  photodissociation rates and changes in atmospheric temperature which affects temperature dependent reaction rates (Frederick, 1977; Allen et al., 1984; Eckman, 1986a,b).

While the response of stratospheric ozone (and in some cases temperature) to solar UV flux variability associated with rotation of active regions in the solar photosphere has been measured in several observational studies (Gille et al., 1984; Chandra, 1986; Hood, 1986), attempts to observationally detect the mesospheric response of ozone have until recently given ambiguous results (Aikin, 1985). Mesospheric ozone is currently believed to respond to solar UV irradiance variations in the wavelength range  $1200 \text{ \AA} < \lambda < 3000 \text{ \AA}$  with a phase lag of less than a day (Brasseur et al., 1987). Over a solar rotation period of  $\sim 27$  days, the solar UV flux variation longward of  $Ly \alpha$  is typically  $< 10$  %. At  $Ly \alpha$  the amplitude of the flux variation may be as large as 20 %. The photochemical time constant for changes in ozone concentration in the mesosphere is short ( $\sim 100$  seconds in the upper mesosphere) and thus ozone there is highly variable. Because of this rapid variability and the small magnitude of the fractional variation of solar UV flux, the fractional change in ozone concentration in the mesosphere is difficult to detect; to unambiguously detect the

response, one must examine large amounts of data.

Two statistical studies of the correlation of Solar Mesosphere Explorer (SME) air-glow observations of mesospheric ozone with solar UV fluxes have reported a statistically significant mesospheric ozone response to solar UV variations with a 27 day period and presumably associated with solar rotation (Aikin and Smith, 1986; Keating et al., 1987). Using a SME data set of 244 days, Aikin and Smith (1986) established a positive correlation between ozone and solar UV flux with a primary period of 27.1 days for the middle atmosphere. In the altitude region between 65 and 70 km and near 50 km, a secondary period of 13.5 days was apparent. Keating et al. (1987), using a larger SME data set of 622 days, detected an ozone response to solar UV variations throughout the 0.5 to 0.05 mbar (approximately 55 to 85 km altitude) region of the mesosphere. Both studies used the magnitude of the solar  $Ly \alpha$  flux as an indicator of solar UV variability.

In the statistical study performed by Keating et al. (1987), ozone concentration, solar flux, and atmospheric temperature were analyzed in terms of "ratios" of averages of these observables, i.e.,

$$R(X) = (X - \bar{X})/\bar{X} \quad (1)$$

where  $X$  is a 5 day running mean of a particular observable (e.g.,  $O_3$  density or solar  $Ly \alpha$  flux), and  $\bar{X}$  is a 27 day running mean of  $X$ . This function represents a statistical filter that enhances variations that occur near the 27 day period and suppresses shorter and longer term variations. The ozone response as defined by Keating et al. (1987) is  $R(O_3)/R(F_{Ly\alpha})$ . The statistically inferred mesospheric ozone response, as shown in Figure 13 of the Keating et al. (1987) paper, clearly shows structure in the 60 to 85 km altitude region. The response is positive below 63 km and above 78 km and negative in the intermediate altitude region.

Previous theoretical work by Frederick (1977) and Garcia et al. (1984) predicted a negative ozone response to an increase in UV solar flux, peaking near 70 km. In Garcia et

al. (1984), who investigated the response to the 11 year solar cycle variation, the region of negative ozone response was limited to the 70 km region, with a strong positive response at higher altitudes peaking at 80 km. In Frederick (1977), however, the response was negative throughout the mesosphere. The key difference between the two studies is that Frederick (1977) had a fixed water vapor profile, while Garcia et al. (1984) allowed the water vapor profile in their model to respond to the solar flux changes. Although the Garcia et al. (1984) results are in better agreement with the Keating et al. (1987) analysis, they do substantially overpredict the magnitude of the observed ozone response maximum near 80 km.

In both the Frederick (1977) and Garcia et al. (1984) studies the response was calculated for effective times much longer than the 27 day flux variation, essentially the asymptotic response. Thus an adjustment of the atmosphere which may occur as a response to the enhanced flux, and which has a characteristic process timescale comparable to 27 days, would not be fully evident in these calculations, e.g., tracer transport by diffusive processes with a timescale of order 2 weeks in the middle mesosphere.

In their study of mesospheric and lower thermospheric ozone, Allen et al. (1984) performed a systematic investigation of the sensitivity of  $O_3$  to changes in various atmospheric parameters, including solar illumination conditions and changes in spectral output of the sun (see Table 3 in Allen et al., 1984). Their steady state results incorporated the response of the abundances of transportable constituents, specifically water vapor, to changes in solar irradiance. For variability in solar illumination for both changes in season and over a 11-year solar cycle, Allen et al. (1984) found a positive correlation between solar flux and ozone above 80 km. At 80 km their calculated change in ozone abundance was 10 % and larger at higher altitudes. Below this altitude their calculated response was less than 1 %. This result above the 80 km altitude level is at variance with Frederick (1977), but is consistent with Garcia et al. (1984), and illustrates the necessity of incorporating the response of transportable constituents to variability in solar illumination in model studies

of the ozone response.

Eckman (1985; 1986a,b) modeled the time-dependent ozone response primarily in the region below 70 km, and obtained results in partial agreement with SME measurements of the ozone response. This theoretical study explicitly included time dependence of photochemical processes in the model of ozone response to solar flux variations. However, the distributions of  $H_2O$  and  $H_2$  were specified rather than calculated in this model, which limits the applicability of the Eckman (1986a) model to middle and upper mesosphere ozone responses since photodissociation of water vapor is the source of odd hydrogen species which catalytically destroy ozone.

Brasseur et al. (1987) also investigated the theoretical response of ozone to solar flux variations with a one-dimensional photochemical-radiative time-dependent model of the upper stratosphere and lower mesosphere and found substantial agreement between model results and the data analysis of Keating (1987). The Brasseur et al. (1987) model also included a specified constant water vapor mixing ratio with altitude and no variation of water vapor abundance with solar irradiance. Above the stratopause the water vapor abundance falls sharply due to photodissociation from solar UV radiation, primarily  $Ly \alpha$ , and a realistic model of the ozone response in this region of the atmosphere must include realistic water vapor abundances.

In the lower mesosphere (below 60 km) and upper stratosphere the observations of the ozone and solar UV correlation are in substantial agreement with simple photochemical models (Hood, 1987; Hood and Douglass, 1988). Both the amplitude and phase of the response in this region of the atmosphere can be accurately described when the observed temperature response is incorporated into such models (Hood and Douglass, 1988).

In light of the recent detection of a 27 day mesospheric ozone periodicity (Keating et al., 1985, 1987), we performed a detailed 1-D modeling study of the mesospheric ozone response to solar UV flux variations to remove some of the deficiencies in previous studies and to specifically examine the importance of solar zenith angle, self consistent calculation

of water vapor abundance and temperature feedback with a simple radiative model. The goal of this paper is to determine the relative importance of several modeled processes in controlling the magnitude and phase of the mesospheric ozone response.

The plan of this paper is as follows. In Section II we describe the photochemical model used to study mesospheric chemistry and the response of chemistry and constituent profiles to solar flux variations. We discuss the assumptions made for the purpose of comparing model results with the Keating et al. (1987) ozone response. Section III contains numerical results for the theoretical ozone response. At the end on section III we show the results of selected time-dependent calculations to illustrate the degree to which a relatively simple model of the mesosphere such as used here is able to capture the major characteristics of the observed response. A summary of the major conclusions and implications of this study is made in Section IV.

## II. THEORETICAL MODEL

The one-dimensional photochemical model developed at Caltech, and described in detail by Allen et al. (1981, 1984), was used in this study. It incorporates vertical transport by eddy and molecular diffusion and updated (JPL-87) kinetic rate constants (Strobel et al., 1987). The lower boundary of the model was selected to be at 40 km altitude due to our neglect of  $ClO_x$  and  $NO_x$  reactions to give reliable solutions above about 55 km. The upper boundary was chosen to be 130 km. The calculations adopted diurnal averaging of atmospheric transmission functions in the UV and visible regions of the solar spectrum. In this paper photochemical reactions will be referred to with the same numbering scheme given in Allen et al. (1981). The baseline reference model (case A) is in all essential respects model C of Strobel et al. (1987). The time-dependent temperature calculation part of the model is described in section III(b).

The background atmosphere was adopted from the AFGL model of Cole and Kantor



(1978), extended to 120 km using the data of Forbes (1985). As mentioned in the Introduction, the statistical study of Keating et al. (1987) includes almost 2 years of data at many latitudes and as such introduces a problem in the choice of an appropriate background atmosphere for our 1-D model calculations. An examination of the atmospheric data base showed that near equinox, the vertical profiles of temperature and total density have a relatively small variation over a wide range of latitudes. Also, atmospheric pressure and temperature fields near equinox are generally midrange between the values at solstices for midlatitude regions. Thus we chose a monthly average temperature and total density profile appropriate for March and 33° N for the background atmosphere in this paper, although in some future study background atmospheric variations may have to be considered. This particular choice of latitude will be discussed below.

The ozone response curve shown in Figure 13 of Keating et al. (1987) incorporates a large amount of data, covering almost 2 years in time and  $\pm 40$  degrees in latitude. Since it would clearly be prohibitive to make enough model runs to even partially reproduce this data set, some simplifying assumptions are necessary. In particular, only the effects of variations in the magnitude of the solar flux and solar zenith angle ( $\chi$ ) are considered. The 1-D model, when used to represent diurnally averaged conditions, has been shown (Allen et al., 1984) to give results which are appropriate for a local time of approximately 3 p.m., the time of SME observations (Thomas et al., 1983). We ran the model under solar illumination conditions that give effective average solar zenith angles ( $\chi$ ) at 3 p.m. of 45°, 55°, 65°, and 75°. In Table 1 we show the probability of the occurrence, in the Keating et al. (1987) data set, of a solar zenith angle ( $\chi$ ) at 3 p.m., within the tabulated 10° bins. More than 98 % of the expected solar zenith angles are less than 80 degrees. For purposes of comparison between the Keating et al. (1987) observed ozone response and the photochemical model, we used a weighted sum of model runs made at the above selected zenith angles, where the weights are obtained from Table 1. We have found that in general, the weighted sum of the model results differs little from a single run at a 55° zenith

angle at 3 p.m. local time. At equinox this zenith angle corresponds to solar illumination conditions at latitude  $33^{\circ}$  N.

The Solar Mesosphere Explorer (SME) instruments measured ozone and solar flux on a daily basis. The solar irradiance spectrometer range covers our region of interest (1200 - 3000 Å) in the solar spectrum. SME solar flux measurements for the time period January 1982 through December 1983 were averaged to form the baseline solar flux profile,  $F_{ref}(\lambda)$ . This is the same time period covered by the SME ozone data analyzed by Keating et al. (1987). We ignore the solar flux variation for wavelengths outside of the above wavelength range, since deposition of solar radiation for wavelengths below 1200 Å is only significant in the thermosphere and solar flux variations over a solar rotation period above 3000 Å are too small (less than 1 %, see Lean, 1987) to be important .

An attempt was made to correlate the SME solar flux at  $Ly \alpha$  with all other wavelengths within the above wavelength range, using the Keating et al. (1987) parameter R as a variable. This provided a variation curve with complex structure. The correlation coefficients of the regression fits become poor for wavelengths longer than about 2000 Å. However, the essential physics associated with this correlation can be represented by a function for the amplitude of the solar flux variation over a solar rotation with monotonic dependence on wavelength

From a statistical study of the solar flux variation with rotation over many solar rotations and using a number of data sets including SME, Lean (1987) deduced the average solar rotational modulation of ultraviolet irradiance within selected wavelength intervals. The solar rotational modulation is simply the maximum percentage variation in irradiance during a solar rotation. The observed rotational modulation of the solar irradiance at selected wavelengths is

$$< 1\% \quad (3000\text{\AA}),$$

$$2.5\% \quad (2500\text{\AA}),$$

6% (2000Å),

16% (1500Å),

40% (1216Å),

60% (1026Å, 304Å),

200% (284Å).

Initially we assume a 1 % variation at 3000 Å, which should represent an upper limit to average solar flux modulation in that spectral region. We have used these values (reduced by a factor of 2 to give an amplitude for the assumed periodic solar flux variation) to which we have fit a smooth curve that represents the amplitude of the periodic solar flux changes in our model calculations. We then scaled the resulting curve by the average fractional variation of solar  $Ly\ \alpha$  flux as observed by SME during the 1982-1984 time period. This gave an amplitude for solar flux variation over a "typical" solar rotation period at  $Ly\ \alpha$  of approximately 10 %. The factor by which the solar flux is multiplied to get the maximum during a solar rotation period is shown as the dashed line in Figure 1. At  $Ly\ \alpha$  the average solar flux over this time period was  $3.23 \times 10^{11} \text{ cm}^{-2} \text{ s}^{-1}$ .

Two solar flux profiles were used for the asymptotic model calculations of the ozone response; the baseline profile,  $F_{ref}(\lambda)$ , and the baseline profile multiplied by one plus the assumed fractional variation given in Figure 1, to give  $F_{max}(\lambda)$ . The fractional variation of solar  $Ly\ \alpha$  flux is defined by

$$\frac{\Delta F_{Ly\alpha}}{F_{Ly\alpha}} = \frac{F_{max}(Ly\alpha) - F_{ref}(Ly\alpha)}{F_{ref}(Ly\alpha)} \quad (2)$$

We define the ozone response to be

$$\frac{\Delta O_3}{O_3} = \frac{[O_3]_{max} - [O_3]_{ref}}{[O_3]_{ref}} \quad (3)$$

where  $[O_3]$  represents the ozone density. As will be shown later, if one scales the ozone response by the assumed fractional solar flux variation at  $Ly \alpha$ , the result is relatively insensitive to both the absolute magnitude of the solar fluxes and to the amplitude of the  $Ly \alpha$  variation adopted in the calculations. In what follows we will calculate the ozone response in this manner, and for comparison with the observations of Keating et al. (1987), we present this response normalized by the fractional variation of solar flux at  $Ly \alpha$ .

### III. MODEL RESULTS

We begin by looking at the steady state ozone response for two reasons. First, this study is aimed at determining which of several processes are most responsible for characterizing the response of ozone to solar flux variations in the mesosphere and are not primarily interested in obtaining a detailed "fit" to observations. Rather, we are exploring the sensitivity of the ozone response to selected parameters, and steady state calculations are adequate for this purpose. Secondly, the steady state response is computationally about two orders of magnitude faster than calculations of the time dependent response.

#### 1. Steady State Response - Sensitivity Analysis

In order to calculate the steady state response, we first calculate the steady state distribution of species with the baseline solar flux profile, and then the steady state profile with the increased solar flux profile. We define the asymptotic ozone response to be the fractional change in ozone concentration between the two cases (eq. 3). In Table 2 we list the model cases considered and the key assumptions for each. The reference model, case A, incorporates standard JPL stratosphere/mesosphere chemistry (JPL-1985), and an eddy diffusion coefficient ( $K_{zz}$ ), shown in Figure , which was found to provide satisfactory agreement between the model  $H_2O$ , shown in Figure , vertical mixing ratio profile and recent microwave measurements of mesospheric water vapor, i.e., model C of Strobel et al.

(1987).

(a) Sensitivity to wavelength dependent UV flux variations.

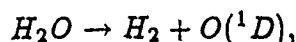
The sensitivity of the calculated ozone response to solar flux variations in individual wavelength intervals is shown in Figure 2 for model A, where we have chosen solar illumination conditions which correspond to a diurnal average solar zenith angle at  $55^\circ$ , and the solar UV flux is increased over the baseline flux by a factor equal to the ratio plotted in Figure 1 within specific wavelength regions. The four wavelength regions are shown at the top of Figure 1 and are labeled SRC (1200 Å - 1750 Å), SRB (1750 Å - 2000 Å), Herzberg (2000 Å - 2425 Å), and Hartley (2425 Å - 3000 Å). In Figure 2 we show the effect of varying the flux within the first three ranges and a case where we have varied the flux only within the  $Ly \alpha$  line. For a much more detailed discussion of mesospheric chemistry and of the atmospheric regions that are most sensitive to the solar UV flux in these regions of the solar spectrum, the reader is referred to the works by Allen et al. (1981; 1984), Clancy et al. (1987), and the standard text by Brasseur and Solomon (1984).

It is clear from Figure 2 that the greatest response above about 63 km is due to the  $Ly \alpha$  flux variation (except for a very narrow region at 75 km). In the region between 65 km and 75 km the increased  $Ly \alpha$  solar flux enhances the photodissociation of water vapor and hence increases the density of odd hydrogen ( $HO_x$ ). This effect peaks near 70 km where unit optical depth for  $Ly \alpha$  penetration through overlying absorbing molecular oxygen occurs. Above 75 km there is insufficient  $HO_x$  production to overcome increased  $Ly \alpha$  photodissociation of molecular oxygen (odd hydrogen still plays a role in determining the ozone density to about 82 km). Thus, at 85 km where increased net production of odd oxygen maximizes, there is a peak in the ozone response.

Above 75 km the ozone response to increased solar flux is complex, with  $Ly \alpha$ , Schumann Runge continuum, and Schumann Runge band regions all contributing in significant amounts, through enhanced odd oxygen production. Below 65 km penetration of solar

photons in the Schumann-Runge bands and Herzberg continuum produces a net positive ozone response, since insignificant water vapor photodissociation occurs that low in the atmosphere. The effect of varying the solar flux in the Hartley region of the solar spectrum by the assumed ratio function produces a negligible ozone response. It should be noted that the magnitudes of the ozone response profiles maxima and minima are similar to those shown by Garcia et al. (1984), both in location and degree.

Figure 3(a) and 3(b) show the fractional change in photodissociation rate coefficients and rates, respectively, for the photodissociation pathways for  $O_2$ ,  $O_3$ , and  $H_2O$ . Note that although the fractional changes may be large ( $\sim 10\%$ ), e.g.,  $Ly\ \alpha$  dissociation of



the reaction may be of minor importance in the photochemistry over an extended altitude range (e.g.  $H_2O$  below 65 km). Note that the net fractional change in the water vapor photodissociation rate coefficient is positive and large throughout the upper mesosphere, and also that the water vapor abundance profile, shown in Figure 3(c), has decreased slightly as a result of the increased solar flux. As a result, the net rate of water vapor photodissociation has decreased above about 81 km altitude. This illustrates the necessity of incorporating the response of the water vapor abundance profile to solar flux changes in order to accurately model the response of ozone to solar flux changes.

(b) Sensitivity to solar illumination conditions.

The calculated ozone response is a function of solar illumination conditions as can be seen in Figure 4, where we have normalized the calculated ozone response by the fractional change in  $Ly\ \alpha$  flux for purposes of comparison with the data analysis of ozone response by Keating et al. (1987) which is plotted on our altitude grid (see Keating et al. (1987), figure 13). The Keating et al. (1987) response is shown for reference only in the following figures, and conclusions regarding a comparison between model results and this observed

response will be discussed later. The negative response maximum increases in altitude from 67 km at a zenith angle of  $45^\circ$  to 72 km at  $75^\circ$ . The variations in the altitude of the ozone negative response maximum with increasing latitude are also in agreement with the Garcia et al. (1984) results. This is a general result for most of our calculated asymptotic responses using spring water vapor concentration profiles (Bevilacqua et al., 1983; 1988). The small positive response below 60 km, roughly constant with altitude is relatively insensitive to the solar zenith angle, i.e., invariant with latitude.

The weighted average (cf. Table 1) response for model A is shown as the solid line in Figure 5(a). Also shown in Figure 5(a) are the responses for different baseline  $Ly \alpha$  flux levels, from  $2.0$  to  $4.0 \times 10^{11} \text{ cm}^{-2} \text{ s}^{-1}$ , representing the variation of solar photon flux in this line over the time period in which SME measurements were considered. The response below 60 km is identical in all cases, within model determinations. Between 60 and 70 km, a factor of two increase in the flux level lowers the altitude of the maximum negative response about 3 km and increases its magnitude by about 30 %. Above 70 km, the response is more sensitive; at the peak in the positive response, the variation is about 40 %. The important point is that the character of the response curve is insensitive below 70 km to the magnitude of the solar UV photon flux.

(c) Sensitivity to baseline  $Ly \alpha$  flux level and variation amplitude.

As noted in the Introduction, the amplitude of variation of solar irradiance depends on the "activity" of the plage regions in the solar atmosphere. Thus the amplitude of irradiance variation will vary from one solar rotation to the next. Figure 5(b) shows the sensitivity of the ozone response to the amplitude of the solar photon flux variation. Based upon the study of Lean (1987), the rotational solar flux amplitude variation at  $Ly \alpha$  ranges between 5% and 30 %. Figure 5(b) shows that over this range of amplitude variation the ozone change is nearly linear, thus there is negligible change in the calculated ozone response when normalized by the flux in  $Ly \alpha$ . This supports the validity of our method

for performing these calculations and comparing with mesospheric data. Normalizing to the solar flux at the  $Ly\ \alpha$  line removes the almost certain variation of solar flux amplitude with wavelength from one solar rotation to another. Only if higher signal to noise data of the ozone response were available for a shorter time series could the difference between a  $Ly\ \alpha$  rotational increase of 5 % and one of 30 % be delineated.

(d) Sensitivity to assumed ozone chemistry.

The ozone density in the mesosphere is a strong function of the kinetic reaction rates for the  $HO_x$  catalytic cycles which remove ozone (Allen et al. 1981, 1984), and various proposals involving modifications of these rates and other key rates involving net odd oxygen production have been put forward as attempts to explain the model/data discrepancies of ozone in the mesosphere and lower thermosphere (Rusch and Eckman, 1985; Strobel et al., 1987; Clancy et al., 1987). We have incorporated the Rusch and Eckman (1985) changes in the calculation of ozone response in model B. As seen in Figure 6, these changes yield only a slight decrease in the magnitude of the calculated ozone response, with a maximum decrease in the positive ozone response at 83 km of less than 20 %. Similar model runs were made with the additional changes recommended by Clancy et al. (1987, in their models A and B). These model runs produced almost identical results as those shown for our model B. Thus we can conclude that these suggested modifications in mesospheric ozone photochemistry may be sufficient to alleviate model/data discrepancies in ozone abundances, but do not affect in a significant way the prediction of the ozone response to solar flux changes expected during a solar rotation.

(e) Sensitivity to water vapor abundance.

The mixing ratio of water vapor at 80 km is 1.6 ppmv for model A and is consistent with ground-based microwave measurements of water vapor which represent an average for the time period April through June, 1984 at JPL (Bevilacqua et al., 1985). More recent



microwave measurements of mid-latitude mesospheric water vapor at Penn State, which encompass the months of November through July, show substantial seasonal variation of upper mesosphere water vapor (Bevilacqua et al., 1988). These measurements are in agreement with the 1984 spring water vapor abundances at 80 km, but the December and June values are 1.0 ppmv and 2.9 ppmv, respectively, at this altitude.

In model C we have increased the magnitude of the background vertical mixing to give 3 ppmv of water vapor at 80 km, with a vertical gradient in water vapor mixing ratio from 60 to 80 km that is similar to that for the June water vapor measurements (Bevilacqua et al., 1987) and is consistent with the water vapor profile used in the model calculations of Allen et al. (1981). The abundance of water vapor in model C is large enough that enhanced  $I_y \propto$  flux produces a sufficient increase in reactive  $\text{HO}_x$  up to 80 km to generate a net catalytic loss of ozone. For completeness, a model run was done to simulate the December water vapor measurements of Bevilacqua et al. (1987) with  $\sim 1$  ppmv at 80 km. Although the water vapor abundance was smaller than the value for model A, the calculated response was almost identical, which indicates that there is an effective threshold value of the water vapor abundance above which there is the onset of negative ozone response in the region above 80 km. This threshold is approximately 1.5 ppmv at 80 km, typical of spring microwave measurements (Bevilacqua et al. 1987). We therefore infer that the ozone response to solar UV flux variations should be seasonally variable through the seasonal variation of water vapor abundances.

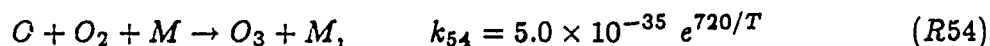
(f) Sensitivity to temperature-chemistry feedback.

Temperature in the stratosphere and mesosphere is intimately connected to the ozone distribution. Variability in ozone concentration and local atmospheric temperature are likewise related with a phase lag which depends on altitude (Brasseur et al., 1987; Keating et al., 1987; Mohanakumar 1985, Hood, 1986, 1987; Hood and Douglass, 1988). Although the phase lag may be as long as weeks in the middle stratosphere the phase lag in the

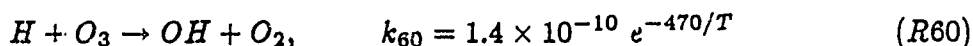
upper mesosphere is much shorter than the solar rotational period (Brasseur et al., 1987).

The inverse temperature dependence of ozone has been observed in the mesosphere and upper stratosphere by Aikin and Smith (1986), and has been investigated with a 1-D radiative and photochemical model (not including transport) by Eckman (1985). For the region above about 75 km where ozone chemistry is relatively simple this negative feedback may be described as follows. A positive ozone response will lead to a local increase in the heating rate, since ozone and molecular oxygen are the primary absorbers of solar UV energy in this region of the atmosphere (Strobel, 1978). Here the atmosphere is in approximate radiative equilibrium on a globally averaged basis; thus an increase in heating leads to an increased temperature, with a time lag of order 1 day at 80 km (Brasseur et al., 1987).

To first order an increase in temperature has two kinetic effects. Increased temperature results in a lower kinetic rate coefficient for 3-body recombination of atomic and molecular oxygen, i.e.,



and a higher rate coefficient for the 2-body reaction of atomic hydrogen and ozone



(see Allen et al., 1981,1984). Both of these effects serve to moderate the effect of an increased production of atomic oxygen by photodissociation of  $O_2$ , thus suppressing ozone density variations due to solar UV flux variations.

Temperature feedback is difficult to model accurately in the mesosphere because of the complexity of IR radiative transfer. We constructed a simple model for temperature where heating is due to absorption of solar energy by  $O_2$  and  $O_3$ , and lost by cooling-to-space in the 15 micron bands of  $CO_2$ . This is expected to be adequate below the mesopause. Energy balance is given by

$$Q_2[O_2] + Q_3[O_3] = C_o[CO_2]e^{-960/T} \quad (4)$$

where  $[O_2]$  and  $Q_2$  represent the density and heating rate due to  $O_2$ ,  $[O_3]$  and  $Q_3$  represent the same for  $O_3$ ,  $[CO_2]$  is the density of  $CO_2$ ,  $C_o$  is the cooling coefficient,  $e^{-960/T}$  is the temperature dependent part of the Planck function and  $T$  is atmospheric temperature. We used the parameterization of Strobel (1978) to calculate the heating rates. The model atmosphere in our calculations is assumed to be in thermal equilibrium between local cooling and heating at the specified temperature profile. This allows us to calculate cooling coefficients which are a function of altitude. These cooling coefficients are assumed independent of small amplitude solar flux variations. In response to variations in the solar UV new oxygen and ozone densities are calculated, then new heating rates and a new temperature profile are calculated. This is done in an iterative manner until convergence of the temperature and ozone profiles is reached.

The ozone response is moderated by the temperature feedback as shown in Figure 7(a) for the asymptotic response (case D). Shown for comparison in Figure 7(a) is the result for model case A. We show the results for model D both with and without an increase in the photon flux in the Hartley region of the spectrum. First we examine the case with an increase in the Hartley region. Above 75 km the normalized ozone response is decreased by about 25 % over case A when temperature feedback is included. Between 65 km and 75 km the temperature feedback has a relatively more dramatic effect on the calculated response. Below 65 km temperature feedback suppresses the calculated ozone response. This is a result of the assumed 1 % increase in solar flux out to 3000 Å. Suppressing this increase in the Hartley region of the spectrum ( $\geq 2425$  Å) has little effect on the ozone response above 73 km, but below 60 km where most atmospheric heating is due to the absorption of solar photons in the Hartley continuum by ozone the positive ozone response is restored with temperature feedback included, albeit at reduced amplitude for  $\Delta T$ . This may also be seen in Figure 7(b), which shows the temperature perturbation with solar flux increase for the

two cases (with and without Hartley region). The difference in temperature perturbations above 68 km is negligible, but increases in magnitude with decreasing altitude and reaches a maximum near 40 km where the ozone becomes optically thick to Hartley photons. The peak in the negative response (near 68 km with no temperature feedback) shifts to higher altitudes with temperature feedback (71 km). Temperature feedback decreases the positive response near 84 km.

(g) Comparison of the steady state response with observations.

Based upon the above sensitivity analysis, some specific deductions can be made on the basis of a comparison of the steady state model ozone response and the SME response (Keating et al., 1987). The steady state response shows the same general character as the observed response, a positive response above about 80 km and below 65 km, and a negative response in the intermediate region. However, the magnitude of the ozone response in each of these regions differs substantially from the observations. The importance of average zenith angle changes, which reflects the latitude dependence of the ozone response, is small below 75 km and in the region where it is most important near 84 km, the changes are not nearly larger enough to reduce the magnitude of the calculated response to match the data. The small positive response below 60 km, roughly constant with altitude, compares favorably with the data but is approximately 20 % smaller and relatively insensitive to the solar zenith angle, i.e., invariant with latitude.

Variations in the baseline flux, as modelled by varying the choice of flux for  $Ly \alpha$ , as well as variations in the amplitude of the variation in solar flux, show little effect on the character and magnitude of the ozone response. The magnitude of the response change is insufficient to substantially change the discrepancy between the calculated response and the Keating et al. (1987) data, especially above 70 km.

Changes in model chemistry, as suggested by various researchers, which can partially alleviate model/data discrepancies on mesospheric ozone abundances, produced little effect

on the calculated ozone response. Thus one can conclude that these suggested modifications in mesospheric ozone photochemistry do not affect in a significant way the prediction of the ozone response to solar flux changes expected during a solar rotation.

The abundance of mesospheric water vapor, on the other hand, has a substantial effect on the calculated ozone response. This increase in water vapor abundance in the upper mesosphere in model C over the reference model A has the effect of raising and deepening the region of negative ozone response to be in close agreement with the Keating et al. (1987) results, as can be seen in Figure 6. The peak in the positive ozone response increases from 84 km (model A) to 90 km (model C), above the region of reliable SME ozone measurements. The calculated response starts to diverge from SME data above 82 km and approaches a factor of two larger at 84 km. This suggests that the ozone response to variations in solar illumination conditions will show a seasonal dependence through the seasonal variation in water vapor abundances (Bevilacqua et al., 1985).

Temperature-chemistry feedback also is significant in determining the ozone response. Above 80 km, the effect is to improve the model/data agreement over case A when temperature feedback was not included. Temperature feedback decreases the positive response near 84 km but not sufficiently to match the Keating et al. (1987) profile. Between 65 km and 75 km the temperature feedback has a relatively more dramatic effect on the calculated response, in the direction to improve the fit to the Keating et al. (1987) data. The peak in the negative response (near 68 km with no temperature feedback) shifts to higher altitudes with temperature feedback (71 km), in better agreement with the Keating et al. (1987) response. Below 65 km temperature feedback suppresses the calculated ozone response, in disagreement with observations. This is a consequence of the assumed 1 % increase in solar flux out to 3000 Å. Suppressing this increase in the Hartley region of the spectrum ( $\geq 2425$  Å) has little effect on the ozone response above 73 km, but below 60 km where most atmospheric heating is due to the absorption of solar photons in the Hartley continuum by ozone, the positive ozone response is restored with temperature feedback

included.

The steady state results presented above illustrate the sensitivity of the calculated ozone response to various model parameters. Of all the above changes, the water vapor abundance and temperature-chemistry feedback appear to dominate the ozone response. Temperature-chemistry feedback is a well defined process and readily modelled. However, the latitudinal and seasonal variation of mesospheric water vapor is unknown, but we suspect that the seasonal variability is large (Bevilacqua et al., 1989). In the absence of more complete information on its variation, we choose to utilize equinox water vapor abundances in the calculations below, and stress that this is an important over-simplification of the mesosphere. However, this choice allows us to study in detail the separate effect of time-dependent atmospheric processes on the ozone response and is therefore useful.

## 2. Time-Dependent Response

The characteristic time scale for changes in the abundances of certain long lived mesospheric constituents can range from days to many months. The photochemical lifetime of CO is of order 1000 days in the upper mesosphere but only of order a few days near the stratopause. Water vapor has the inverse altitude dependence of its chemical lifetime, near 100 days at the stratopause and decreasing to only about 10 days at the mesopause. As identified above in the sensitivity analysis on the ozone response, water vapor plays a key role in ozone loss. Thus the time response of water vapor is at least one reason that the ozone response to changes in solar UV flux variations will show a time dependence. Below we explore this in some detail.

The time evolution of active plage regions in the solar atmosphere is clearly not simple to numerically simulate. Even for plage regions undergoing little changes in the level of activity over a solar rotation, the exact periodicity will depend upon their solar latitude, since the sun does not rotate as a solid body. The study by Lean (1987) found characteristic

periods of solar irradiance variations typically of 27 or 13 days. A single long-lived active region on the solar disc will produce enhanced UV irradiance for about half a rotation period. Thus, ignoring the evolutionary aspects of plages, enhanced UV irradiance may be approximated as either a step function or possibly as a sinusoidally varying function, with a step size or equivalently a wavelength of order half a rotation period. This assumes that only one localized region of the sun is producing the enhanced UV emission. If several plage regions are active, and widely dispersed in solar longitude, then an effective time scale could be much longer than half a rotation period.

We have simulated the time dependent response of mesospheric ozone to solar ultra-violet forcing by time marching the photochemical solution in accord with a time varying solar flux. Based upon the results from model D, we have set the Hartley flux variation to zero in all of our time dependent calculations which we present. We chose time steps of 1 day, and at each time step we calculated the diurnal average concentration profiles for model species. For models E and F we have simulated the ozone response for a step function increase in solar flux, both without and with temperature - chemistry feedback included, respectively. We started the time integration at day 1 with a steady state solution calculated with a baseline solar flux level, and then at each subsequent time used the maximum solar flux level, and allowed the constituent profiles to relax in response to the increased solar flux. In Figures 8 (a) and (b) we show results for models E and F, respectively. We illustrate the response after 7, 14, 27, and 54 days of time integration. The asymptotic response is simply the ratio of the ozone profiles for the steady state enhanced flux solution and the steady state baseline flux solution, and is shown for comparison. From a study of the periodicity of UV solar flux with solar rotation, Lean (1987) found maximum power at time periods of 27 days and 13 days, corresponding to 1 and 2 active plage regions, respectively.

As can be seen from Figure 8(a), at  $t = 54$  days the ozone distribution has very nearly reached its asymptotic value at all altitudes. Below 65 km altitude, the asymptotic

response is reached in much less than 7 days. However, for a time period of 7 to 14 days, characteristic of the time a single active solar plage region is on the visible disk, the ozone response above the 65 km altitude level is far from its asymptotic limit. For  $t = 14$  days, the response is only 0.3 of its limiting value due to the time-dependent response of the water vapor profile (see discussion in the Introduction). An increase in the UV flux which dissociates water vapor will depress the water vapor mixing ratio profile. Depressing the water vapor profile above the 75 km altitude region leads to lower  $HO_x$  and hence lower catalytic destruction of ozone. The time scale over which the local water vapor abundance adjusts to an increase in solar UV flux is the transport time scale, on the order of 10 days at 80 km. The time scale for the entire water vapor vertical profile is somewhat longer since it is an integrated effect down to about 65 km. It is clear that the results for model integrations for 7 and 14 days encompass the mesospheric response as deduced by Keating et al. (1987)

The effect of temperature-chemistry feedback on the time dependent ozone response is similar to that for the asymptotic cases. The temperature increase due to increased ozone densities near 80 km moderates the ozone response, by about 30 %, as is seen in Figure 8(b), for model case F, where we have not time-stepped the heat equation, but calculated the instantaneous solution to eq. 4, thus we are overestimating the temperature-chemistry moderating effect on the ozone response.

The time scale for changes in plage activity is of order half a solar rotation. During this time plages can form and disintegrate. For solar activity of this sort, a more proper description of solar UV flux variation might be of sinusoidal nature. A periodic variation of incident solar flux on the mesosphere will produce a predominantly instantaneous response from ozone and a delayed atmospheric water vapor and temperature response at all altitudes. To accurately simulate this effect one must time step the time-dependent heat equation along with the chemistry continuity equations. For numerical simplicity we assume a sinusoidal forcing of solar ultraviolet flux for model case G. We calculate the



time dependent atmospheric temperature from the equation

$$\rho C_p \frac{dT}{dt} = Q_2[O_2] + Q_3[O_3] - C_o[CO_2]e^{-960/T} \quad (5)$$

where  $\rho$  is the mass density of the atmosphere, and  $C_p$  is the atmospheric heat capacity. The time dependent heat equation is solved for atmospheric temperature in a manner similar to that of the time dependent chemical continuity equations, i.e., we time step eq. 5 forward in time with time steps of length 1 day, in accord with a time varying solar UV flux. Model results for this case (G) are shown in Figure 9.

At all altitudes between about 78 and 83 km the calculated ozone response for model G is in phase with the solar ultraviolet forcing and in excellent agreement with the Keating et al. (1987) results, from the upper stratosphere and throughout the mesosphere. We note that in the mesosphere the water vapor abundance has a strong influence on the magnitude of the ozone response and even better agreement could be obtained with greater water vapor mixing ratios. In this region the temperature has a phase lag of between 5 and 8 days, about one quarter of a forcing period. This is to be expected since an increasing temperature is produced when the ozone is above its average value, i.e., when solar flux is above the average value. We have performed other simulations of this model using larger and smaller amplitudes for the solar flux modulation, with similar results. This model with the most rigorous treatment of the chemistry and physics of ozone variability accounts for the essential aspects of the observed ozone response (Keating et al., 1987), in particular the precise altitudes where the response reverses sign. In general, the results for periodic forcing of solar UV on the ozone response is intermediate between the step function cases for time integrations of 7 and 14 days. This therefore illustrates the fact that the character and magnitude of the ozone response profile is not sensitive to the precise functional form of the time dependence of the solar flux variation.

The calculated phase of the ozone response below 65 km is small ( $\sim 1$  day) but positive, in contrast to the calculated response by Hood and Douglass (1988) who found

large ( $\sim 5$  days) negative responses in the upper stratosphere when observed temperature responses are included in their photochemical model. The negative phase of the ozone response in their model is due to the fact that the observed temperature has a large ( $\sim 5$  day) positive phase lag relative to the solar UV forcing. The positive phase lag of the temperature in our model is less than a day, sufficiently small to eliminate the negative phase lag of ozone. Thus our temperature model is clearly an incomplete description of the thermodynamics of the upper stratosphere and lower mesosphere. In order to accurately describe the ozone response in this region of the atmosphere a better theoretical description of the temperature response due to both chemical and dynamical effects is needed.

#### IV. SUMMARY

In this study we have performed an investigation of the sensitivity of the theoretical ozone response to solar UV flux changes and the dependence of this response on changes in selected model and atmospheric parameters. We have deduced the importance of water vapor abundance and time dependence of the calculated ozone response, and we have confirmed the important effect that temperature-chemistry feedback has upon the calculated response. This study lays the groundwork for more detailed and extensive model studies of the response of mesospheric ozone to solar flux variations, and illustrates the need for more extensive measurements of mesospheric water vapor abundances and for more detailed data analysis of mesospheric ozone data bases.

We have found that water vapor in the upper mesosphere exerts a strong influence on the magnitude of the observed ozone response. The water vapor abundance in the upper mesosphere is critically dependent on the magnitude of vertical transport in that region as demonstrated by Strobel et al. (1987). The microwave measurements of Bevilacqua et al. (1988) indicate a dominant annual variation in upper mesospheric water vapor mixing ratios and by inference annual variations in vertical transport dominate. Hence we expect on the basis of our study that the water vapor seasonal variation produces a corresponding seasonal signature in the ozone response, when the water vapor mixing ratio exceeds a threshold value, which we determined as  $\sim 1.5$  ppmv at 80 km, a typical springtime value (Bevilacqua et al., 1988). This signature is of sufficient amplitude to mask other signatures in seasonally averaged ozone response data, and necessitates organizing ozone data in the future according to common background water vapor concentrations in the upper mesosphere to extract these other signatures.

We have found that the strong sensitivity of the calculated ozone response to water vapor abundances in the mesosphere will mask the smaller changes in ozone response which is produced by suggested modifications to ozone chemistry that have been proposed

to improve model/data agreement on mesospheric ozone abundance. From our study we infer that the solar flux/ozone response measurements in the mesosphere are not likely to be useful in the further refining our understanding of ozone chemistry. This is in agreement with the work of Hood and Douglass (1988) who found that the upper stratosphere and lower mesosphere ozone response is in substantial agreement with current photochemical theories.

As important conclusion of this work is that the response of the water vapor profile must be calculated self-consistently with the ozone response to solar flux variations in order to accurately describe ozone variation on time periods characteristic of solar rotation. The response of the water vapor profile has been neglected in previous studies.

The ozone response in the lower mesosphere, below 70 km, reaches its asymptotic limiting value for enhanced solar ultraviolet flux on a time scale smaller than the solar rotation period, while the response above that region requires increasingly longer times to reach the asymptotic values. In the region near 80 km, the ozone response after half a solar rotation period is only about 30 % of its asymptotic value. Our model with periodic forcing of mesospheric chemistry by solar ultraviolet flux with a period of 27 days, when combined with temperature-chemistry feedback and time dependent atmospheric temperature effects accounts for the observed ozone response of Keating et al. (1987).

Finally we note that the combined effects of water vapor variation, temperature feedback effects, negligible solar flux variation above 2400 Å, and time dependent nature of solar rotation driven ultraviolet flux forcing does reproduce the inferred ozone response profile derived by Keating et al. (1987) from SME data. The corresponding water vapor data base, which is needed to supply the seasonal and latitudinal profiles, is restricted to essentially mid-latitudes in the Northern Hemisphere and hence insufficient to allow more rigorous deductions regarding model data comparisons of the mesospheric ozone response to solar UV flux variations. Thus we suggest that more mesospheric water vapor measurements be made to more accurately describe both the seasonal and latitude dependences.

Also we note the strong need to observationally extract both seasonal and latitude dependences of the mesospheric ozone response to facilitate further progress in understanding the response of ozone to solar flux changes.

#### ACKNOWLEDGEMENTS

The authors are indebted to D. E. Anderson and M. Nicolet for useful discussions, and to W. J. Sawchuck for aid in developing the IDL graphics routines for producing several of the figures.

## REFERENCES

- Aikin, A. C., and H. J. P. Smith, Mesospheric Ozone Changes Associated with 27 Day Solar Ultraviolet Flux Variations, *Geophys. Res. Lett.*, **13**, 427-430, 1986.
- Allen, M., Y. L. Yung, and J. M. Waters, Vertical transport and photochemistry in the terrestrial mesosphere and lower thermosphere (50-120 km), *J. Geophys. Res.*, **86**, 3617-3627, 1981.
- Allen, M., J. I. Lunine, and Y. L. Yung, The vertical distribution of ozone in the mesosphere and lower thermosphere, *J. Geophys. Res.*, **89**, 4841-4872, 1984.
- Bevilacqua, R. M., J. J. Olivero, P. R. Schwartz, C.J. Gibbins, J.M. Bologna, and D.L. Thacker, An observational study of water vapor in the mid-latitude mesosphere using ground-based microwave techniques, *J. Geophys. Res.*, **88**, 8523-8534, 1983.
- Bevilacqua, R. M., W. J. Wilson, W. B. Ricketts, P. R. Schwartz, and R. J. Howard, Possible seasonal variability of mesospheric water vapor. *Geophys. Res. Lett.*, **12**, 397-400, 1985.
- Bevilacqua, R. M., J. J. Olivero, M. E. Summers, D. F. Strobel, M. Allen, Long-Term Measurements of Mesospheric Water Vapor From Penn State, Part B: Implications for Vertical Transport Time-Scales and Processes in the Middle Atmosphere, *EOS*, **68**, 1398, 1987.
- Bevilacqua, R.M., W.J. Wilson, and P.R. Schwartz, Measurements of mesospheric water vapor in 1984 and 1985: Results and implications for middle atmospheric

- transport, J. Geophys. Res., **92**, 6697-6690, 1987.
- Bevilacqua, R. M., J. J. Olivero, and C. L. Craskey, Mesospheric water vapor measurements from Penn State: Observations and Climatology, J. Geophys. Res., submitted, 1988.
- Brasseur, G., A. De Rudder, G. M. Keating, and M. C. Pitts, Response of Middle Atmosphere to Short-Term Solar Ultraviolet Variations: 2. Theory, J. Geophys. Res., **92**, 903-914, 1987.
- Chanin, M. L., N. Smires, and A. Hauchecorne, Long-Term Variation of the Temperature of the Middle Atmosphere at Mid-Latitude: Dynamical and Radiative Causes, J. Geophys. Res., **92**, 10933-10941, 1987.
- Clancy, R. T., D. W. Rusch, R. J. Thomas, M. Allen, and R. S. Eckman, Model Ozone Photochemistry on the Basis of Solar Mesosphere Explorer Mesospheric Observations, J. Geophys. Res., **92**, 3067-3080, 1987.
- Cole A. E., and A. J. Kantor, Air Force Reference Atmospheres, AFGL-TR-78-0051, 1978.
- Eckman, R. S., A Theoretical and Observational Investigation of the Response of Ozone to Short-Term Variations in the Solar Ultraviolet Irradiance, Ph.D. Thesis, University of Colorado, 1985.
- Eckman, R. S., Response of Ozone to Short-Term Variations in the Solar Ultraviolet Irradiance 1. A Theoretical Model, J. Geophys. Res., **91**, 6695-6704, 1986a.
- Eckman, R. S., Response of Ozone to Short-Term Variations in the Solar Ultra-

- violet Irradiance 2. Observations and Interpretation, J. Geophys. Res.,  
91, 6705-6721, 1986b.
- Farmer, C.B., NSSDC Data Center, 1988.
- Forbes, J. M., Thermosphere Structure Variations During High Solar and Magnetic Activity Conditions, Final Technical Report for AF Contract F19628-82-K0031, Boston University, 1985.
- Frederick, J. E., Chemical Response of the Middle Atmosphere to Changes in the Ultraviolet Solar Flux, Planet. Space Sci., 25, 1-4, 1977.
- Froidevaux, L., M. Allen, and Y.L. Yung, A critical analysis of  $ClO$  and  $O_3$  in the mid-latitude stratosphere, J. Geophys. Res., 90, 12,999-13,029, 1985.
- Garcia, R. R., S. Solomon, R. G. Roble, and D. W. Rusch, A Numerical Response of the Middle Atmosphere to the 11-Year Solar Cycle, Planet. Space Sci., 32, 411-423, 1984.
- Garcia R.R. and S. Solomon, The effect of breaking gravity waves on the dynamics and chemical composition of the mesosphere and lower thermosphere, J. Geophys. Res., 90, 3850-3868, 1985.
- Gille, J. C., C. M. Smythe, and D. F. Heath, Observed Ozone Response to Variations in Solar Ultraviolet Radiation, Science, 225, 315-317, 1984.
- Girard, A., J. Besson, D. Brard, J. Laurent, M. P. Lemaitre, C. Lippens, C. Muller, J. Vercheval, and M. Ackerman, Global Results of Grille Spectrometer Experiment on Board Spacelab 1, Planet. Space Sci., 36, 291, 1988.
- Hood, L. L., Solar Ultraviolet Radiation Induced Variations in the



Stratosphere and Mesosphere, J. Geophys. Res., **92**,

876-888, 1987

Hood, L. L., and A. R. Douglas, Stratospheric Responses to Solar

Ultraviolet Variations: Comparisons with Photochemical Models,

J. Geophys. Res., **93**, 3905-3911, 1988.

Keating, G.M., M.C. Pitts, G. Brasseur, and A. De Rudder, Response of middle

atmosphere to short-term solar ultraviolet variations: 1. Observations,

J. Geophys. Res., **92**, 889-902, 1987.

Lean, J., Solar Ultraviolet Irradiance Variations: A Review, J. Geophys. Res.,

**92**, 839-868, 1987

Mohanakumar, M., An Investigation on the Influence of Solar Cycle on Mesospheric

Temperature, Planet. Space Sci., **33**, 795-805, 1985.

Olivero, J.J., J.J. Tsou, C.L. Croskey, L.C. Hale, and R.G. Joiner, Solar absorption

microwave measurements of upper atmospheric water vapor, Geophys. Res. Lett.,

**13**, 197-200, 1986.

Prather, M.J., Ozone in the upper stratosphere and mesosphere, J. Geophys. Res.,

**86**, 5325-5338, 1981.

Rusch, D. W., and R. S. Eckman, Implications of the Comparison of Ozone

Abundances Measured by the Solar Mesosphere Explorer to Model Calculations,

J. Geophys. Res., **90**, 12,991-12,998, 1985.

Schwartz, P.R., C.L. Croskey, R.M. Bevilacqua, and J.J. Olivero, Microwave

spectroscopy of  $H_2O$  in the stratosphere and mesosphere, Science,

305, 294-295, 1983.

Schwartz, P.R., R.M. Bevilacqua, T.A. Pauls, D.L. Thacker, W.B. Waltman,  
Ground-based monitoring of water vapor in the earth's middle atmosphere,  
manuscript in preparation, 1988.

Strobel, D. F., Parameterization of the Atmospheric Heating Rate From 15 to 120 km  
Due to O<sub>2</sub> and O<sub>3</sub> Absorption of Solar Radiation, J. Geophys. Res.,  
83, 6225-6230, 1978.

Strobel, D. F., M. E. Summers, R. M. Bevilacqua, M. T. DeLand, and M. Allen,  
Vertical Constituent Transport in the Mesosphere, J. Geophys. Res., 92, 6691, 1987.

Strobel, D. F., Constraints on gravity wave induced diffusion in the middle atmosphere,  
Pure & Appl. Geophys., in press, 1989.

Thomas, R.J., C.A. Barth, D.W. Rusch, and R.W. Sanders, Solar Mesosphere  
Explorer near-infrared spectrometer: measurements of 1.27  $\mu\text{m}$  radiances and  
the inference of mesospheric ozone, J. Geophys. Res., 89,  
9569-9580, 1984.

Tsou, J.J., J.J. Olivero, and C.L. Croskey, A study of the variability of H<sub>2</sub>O  
during spring 1984 by ground-based microwave radiometric observations,  
J. Geophys. Res., 93, 5255-5266, 1988.

Table 1

Zenith Angle Probability of Occurrence

Range of $\chi$	Probability of occurrence
40 - 50	0.517
50 - 60	0.233
60 - 70	0.144
70 - 80	0.089
80 - 90	0.017

Table 2

Summary of Model Cases

Model Case	Description
A	Reference Case (JPL-85 chemistry)
B	$HO_x$ rate coefficient modifications (Rusch & Eckman, 1985)
C	Bevilacqua et al. (1988) water vapor profile
D	Temperature-Chemistry (T-C) feedback effect
E	Time dependent response, step function in $\Delta F$ , no T-C feedback
F	Time dependent response, step function in $\Delta F$ , T-C feedback
G	Time dependent response, sinusoidal $F_\lambda(t)$ forcing, T-C feedback

## Figure Captions

Figure 1. Ratio of perturbed solar flux profile (dashed line) to baseline SME solar flux profile (averaged from January 1982 to December 1983) between 1200 Å and 3000 Å adopted for the calculations.

Figure 2. Ozone response for changes in solar UV flux within discrete wavelength intervals of the solar spectrum. The change in solar flux within the intervals is equal to the ratio shown in Figure 1. The wavelength intervals are defined in the text. Calculations were made at a zenith angle of 45 degrees.

Figure 3. (a) Fraction change in photodissociation rate constants for a fractional change in the incident solar flux profile shown in Figure 1. (b) Fractional change in photodissociation rates for the fractional increase in solar flux shown in Figure 1. In both (a) and (b) the last two reactions have identical changes. (c) The fractional change in water vapor abundance (ppmv) for the above model.

Figure 4. Ozone response calculated for 4 separate zenith angles with a 10 % change in solar flux at Lyman alpha. The ozone response normalized to the Lyman alpha fractional variation as determined by a statistical analysis of SME data (Keating et al., 1987) is shown for comparison.

Figure 5. (a) Ozone response for baseline solar Lyman alpha photon fluxes shown and 10 % flux increase at Lyman alpha. (b) The response as a function of fractional increases in solar Lyman alpha fluxes. The baseline flux is that obtained from SME for the time period discussed in the text.

Figure 6. Ozone response for the reference model (model A, solid line), for the case where the efficiency of the  $\text{HO}_x$  catalytic loss of ozone has been decreased according to the recommendations of Rusch and Eckman (1985) (model B, short dashed line), and for the case where the water vapor is increased high in the mesosphere to match the June data of Bevilacqua et al. (1988) (model C, long dashed line).

Figure 7. (a) Ozone response without temperature feedback (solid line), with temperature feedback (short dashed line), with temperature feedback but Hartley region variation suppressed (short, long dashed line), and with flux variation affecting atmospheric heating but not dissociation rates (long dashed line), all assuming local radiative equilibrium and temperature response calculated as described in the text. (b) The temperature perturbation produced by solar flux variation. The solid line is the temperature response with flux variation given in Fig. 1. The dashed line is the temperature response when the solar flux variation in the Hartley region is suppressed.

Figure 8. (a) Time dependent ozone response without temperature feedback for a step function increase in solar flux after 7, 14, 27, 54 days and the asymptotic limiting response. (b) The same but including temperature feedback.

Figure 9. (a) Ozone response for a sinusoidal variation of solar UV flux for model G. (b) Phase lag between Ozone maximum and solar flux maximum as a function of altitude for model G.

Figure 1

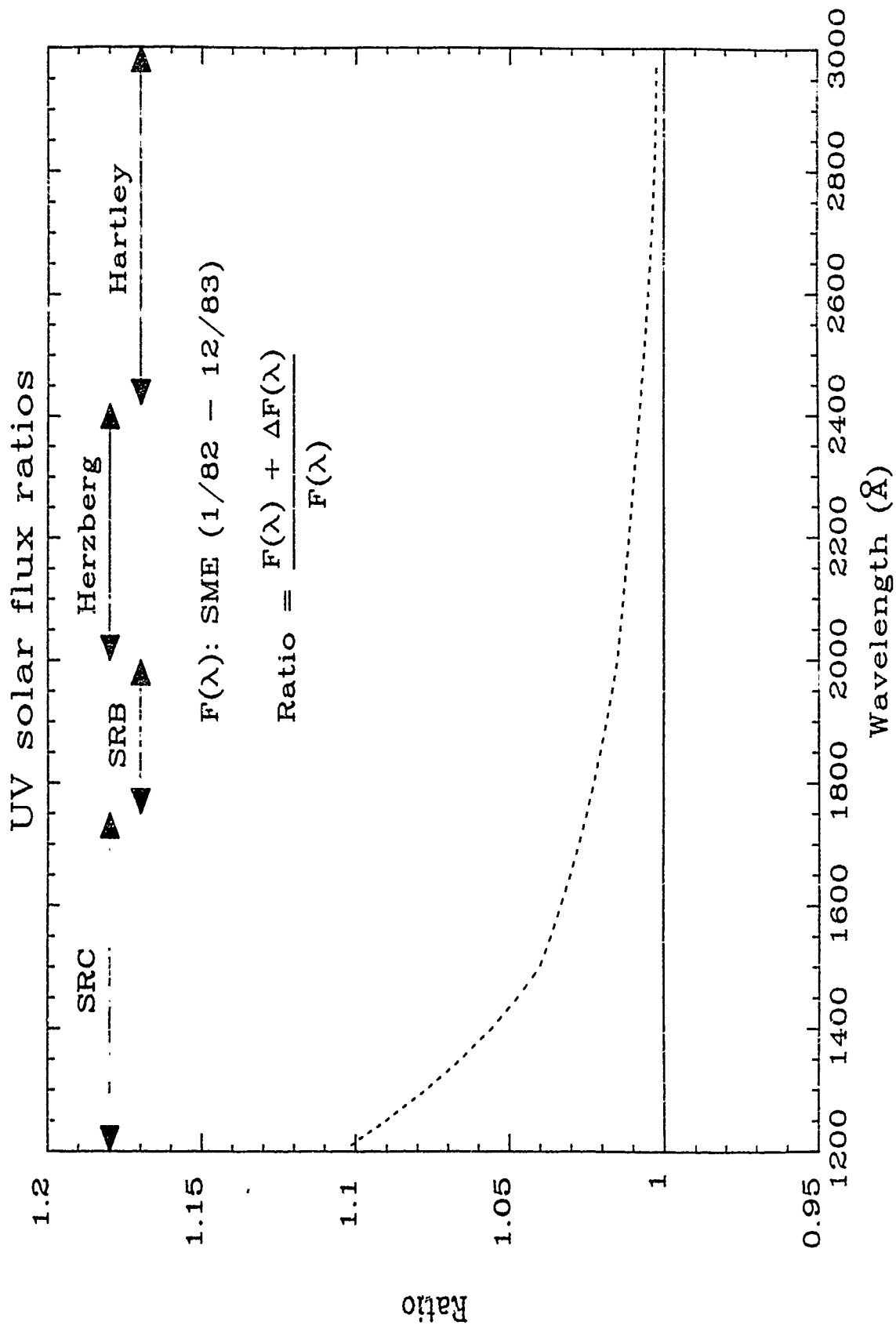


Figure 2

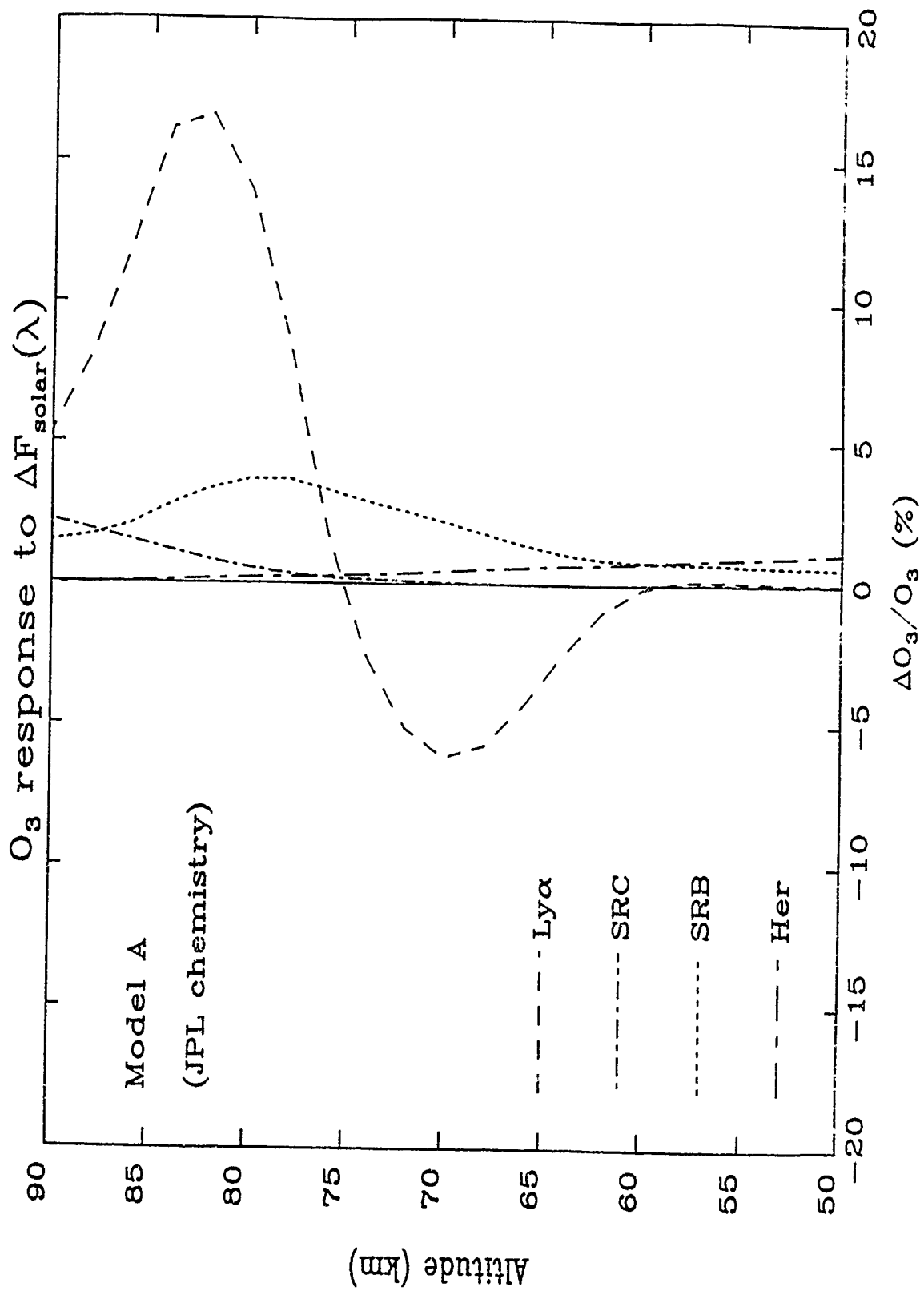




Figure 3(a)

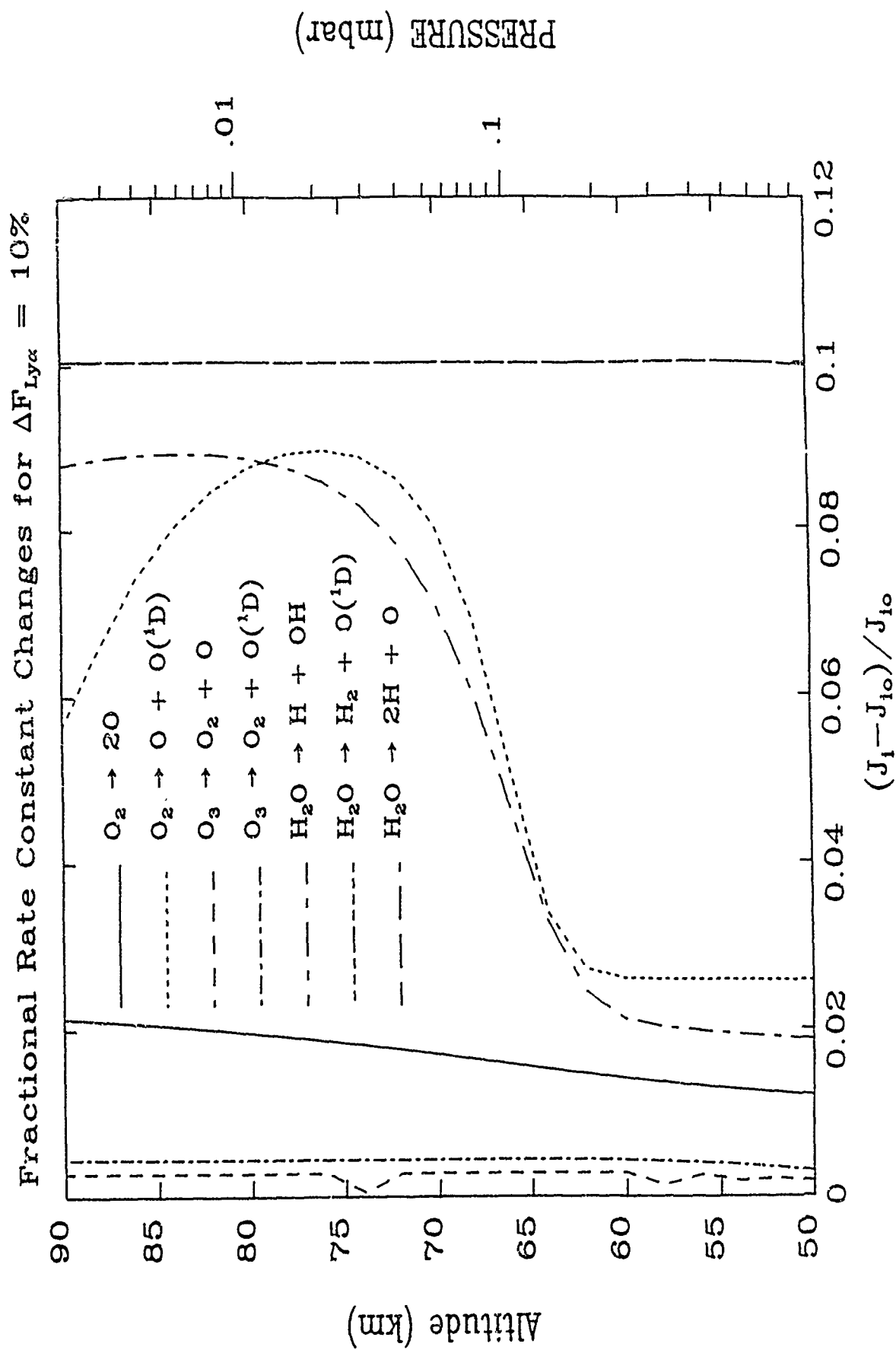


Figure 3(b)

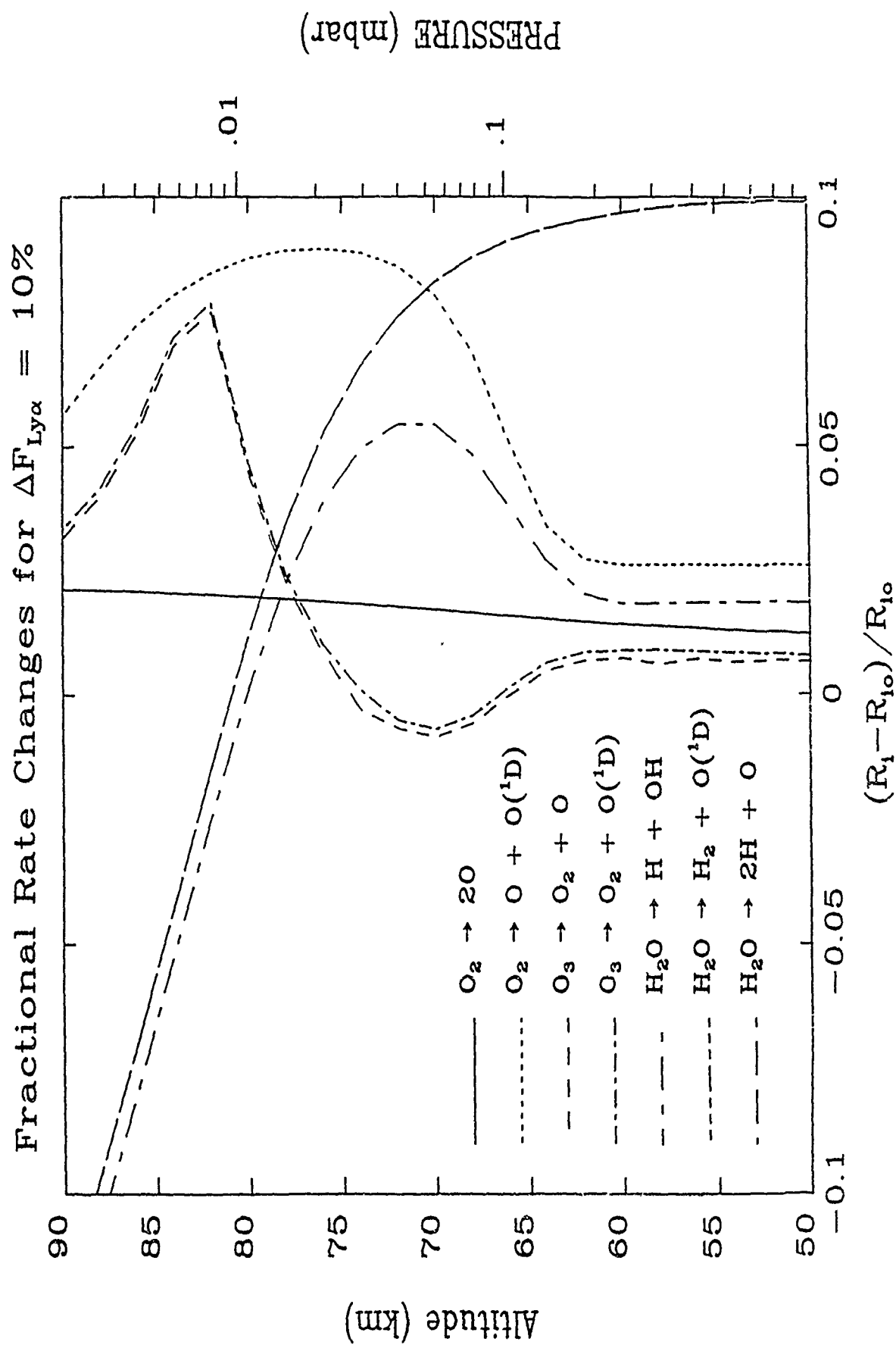


Figure 3(c)

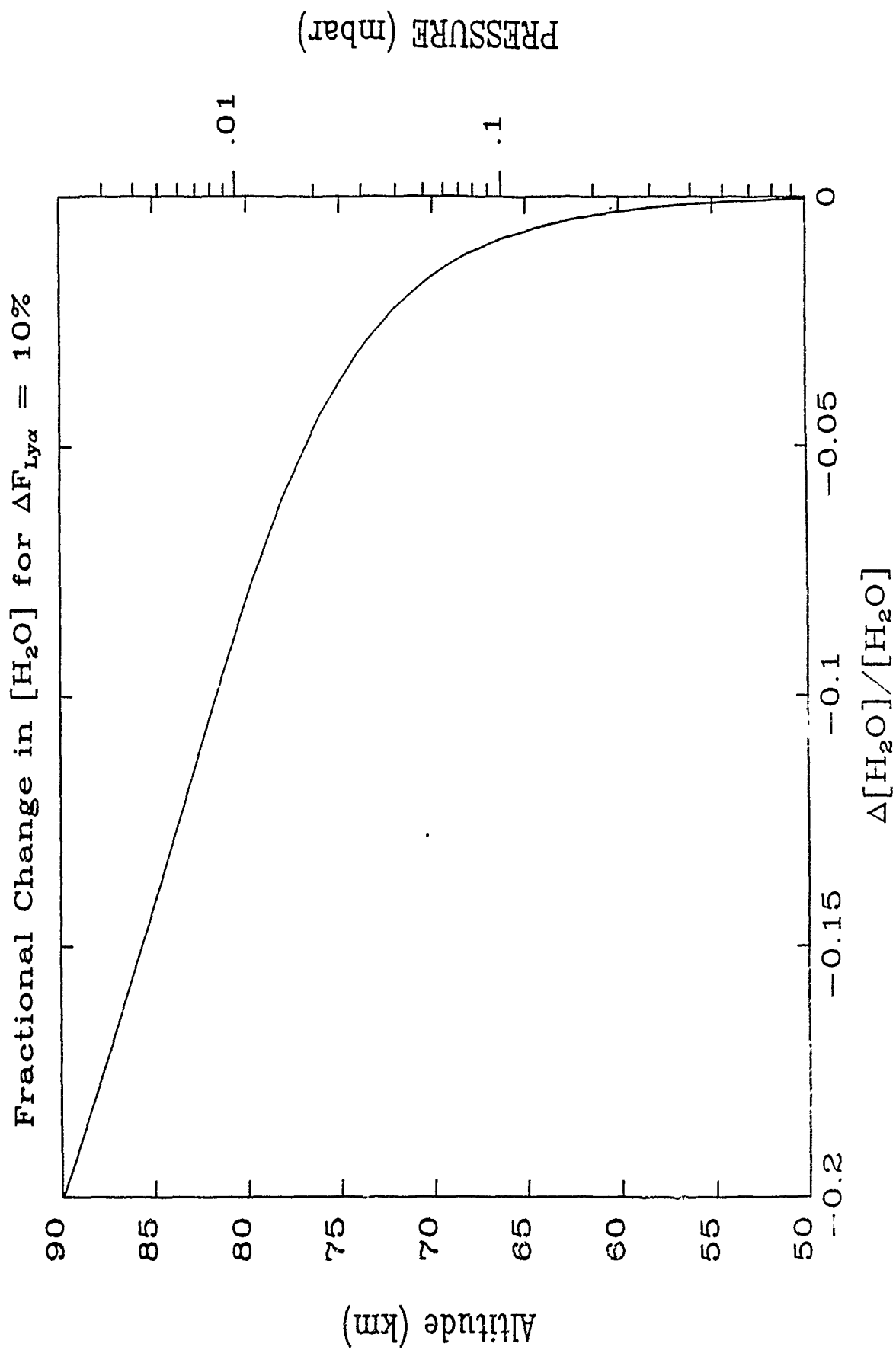


Figure 4

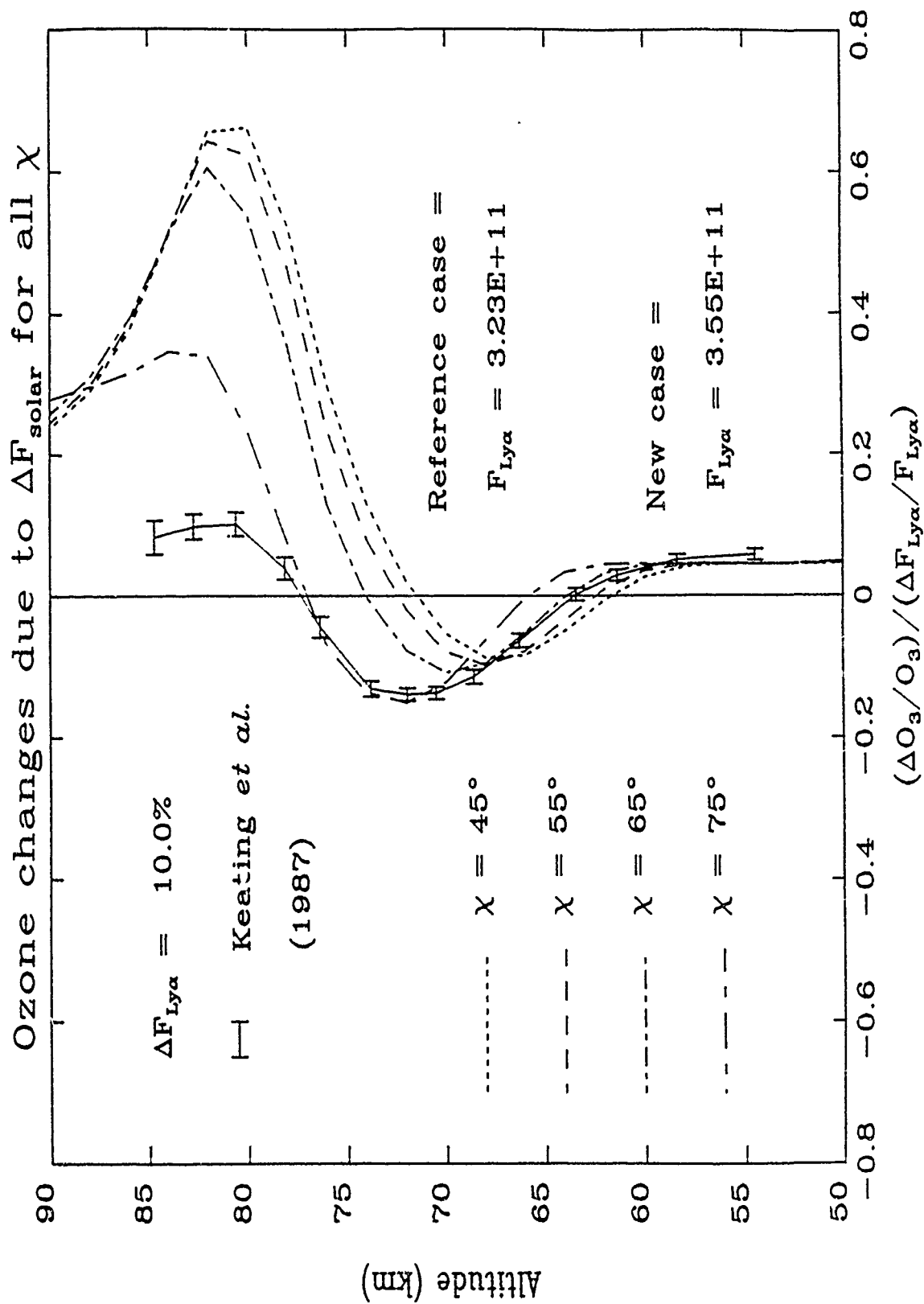


Figure 5(a)

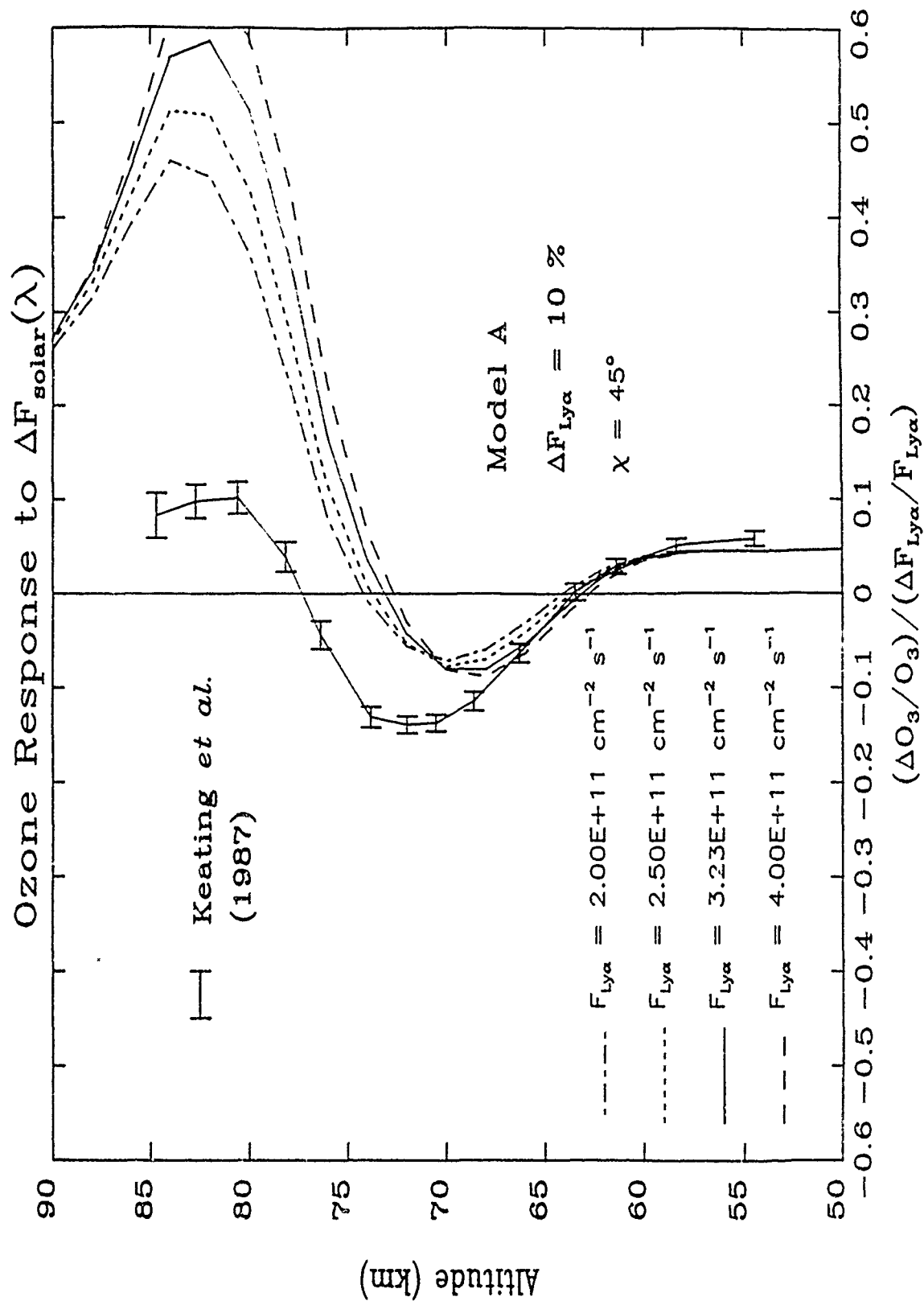


Figure 5(b)

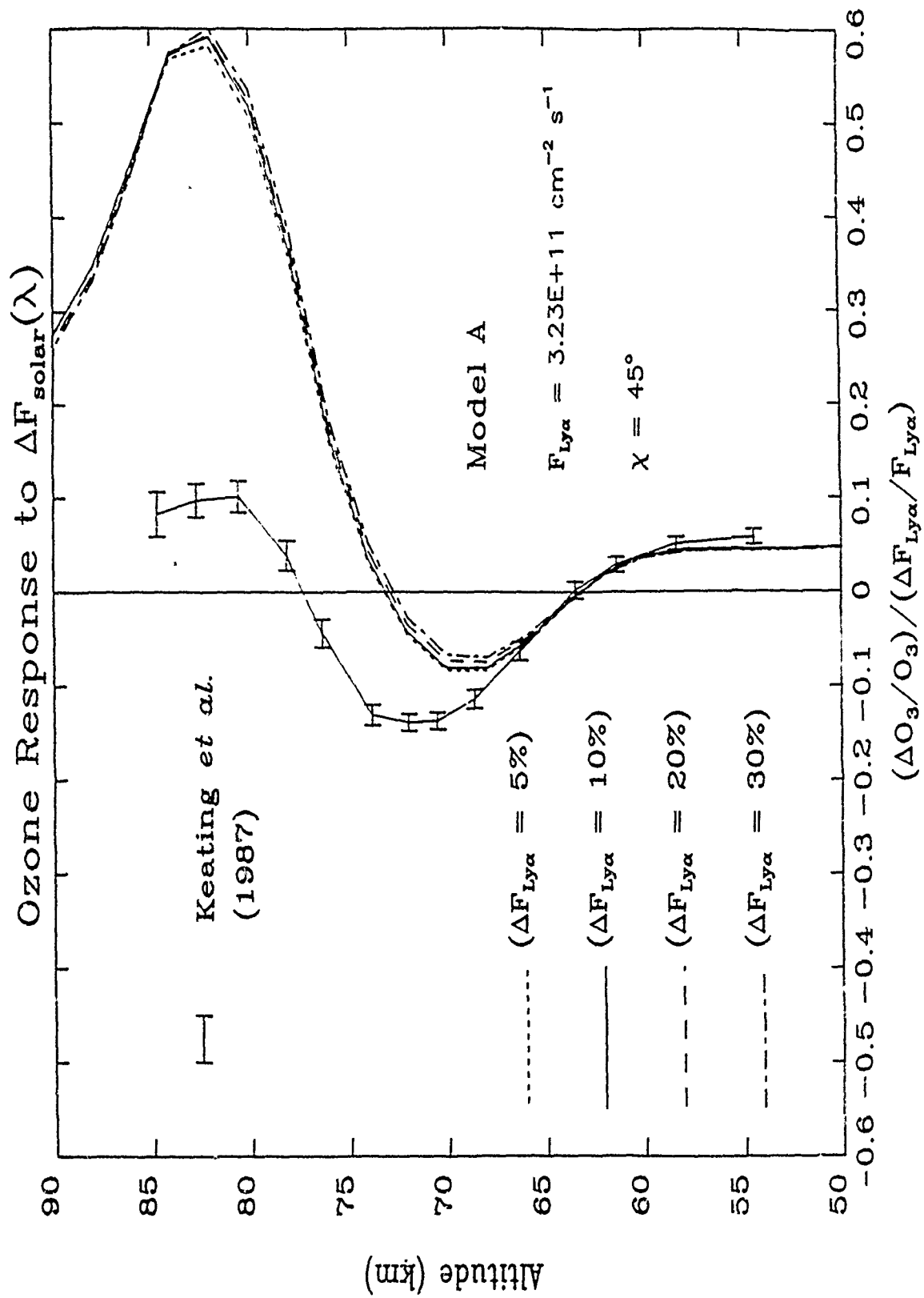


Figure 6

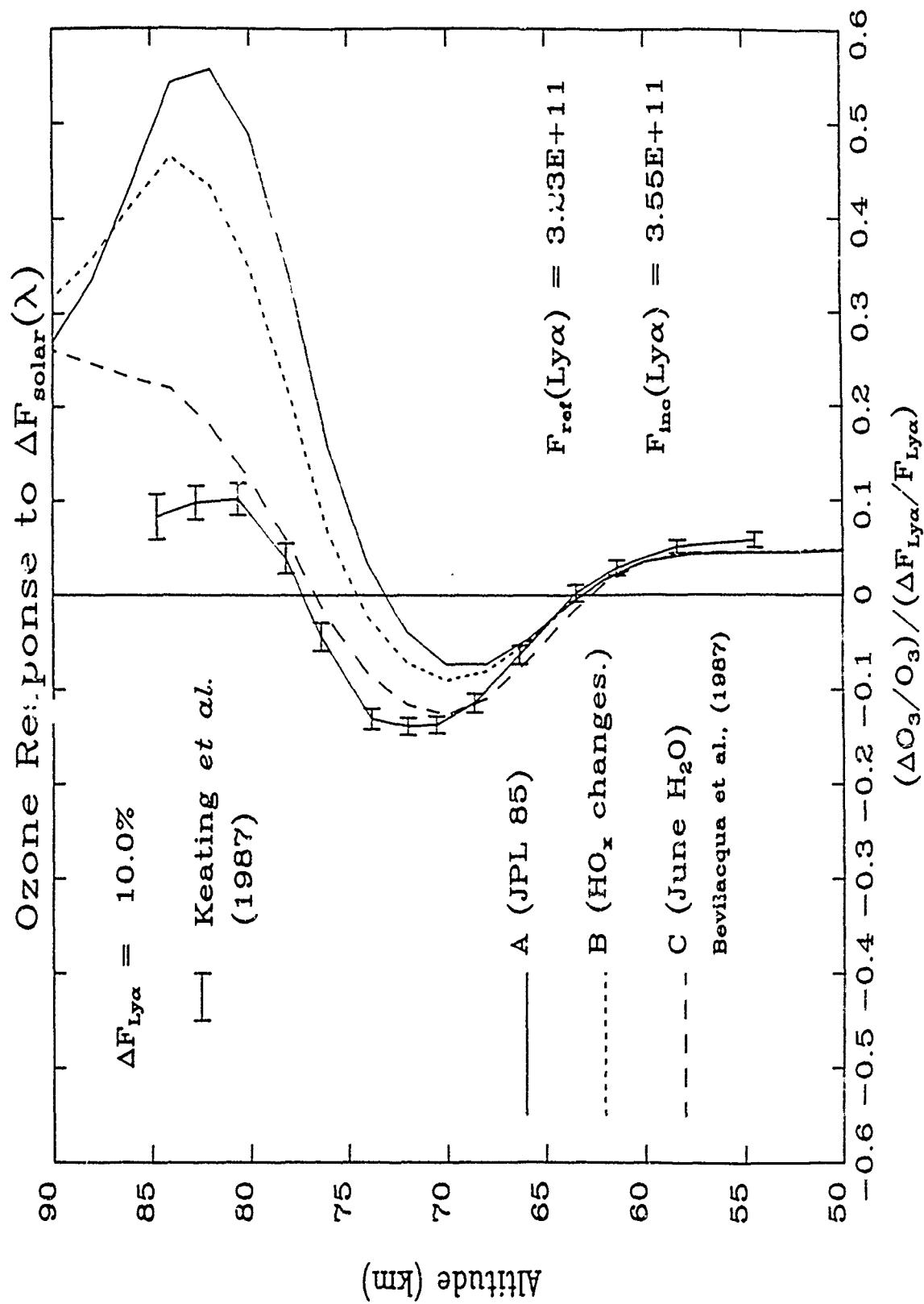


Figure 7(a)

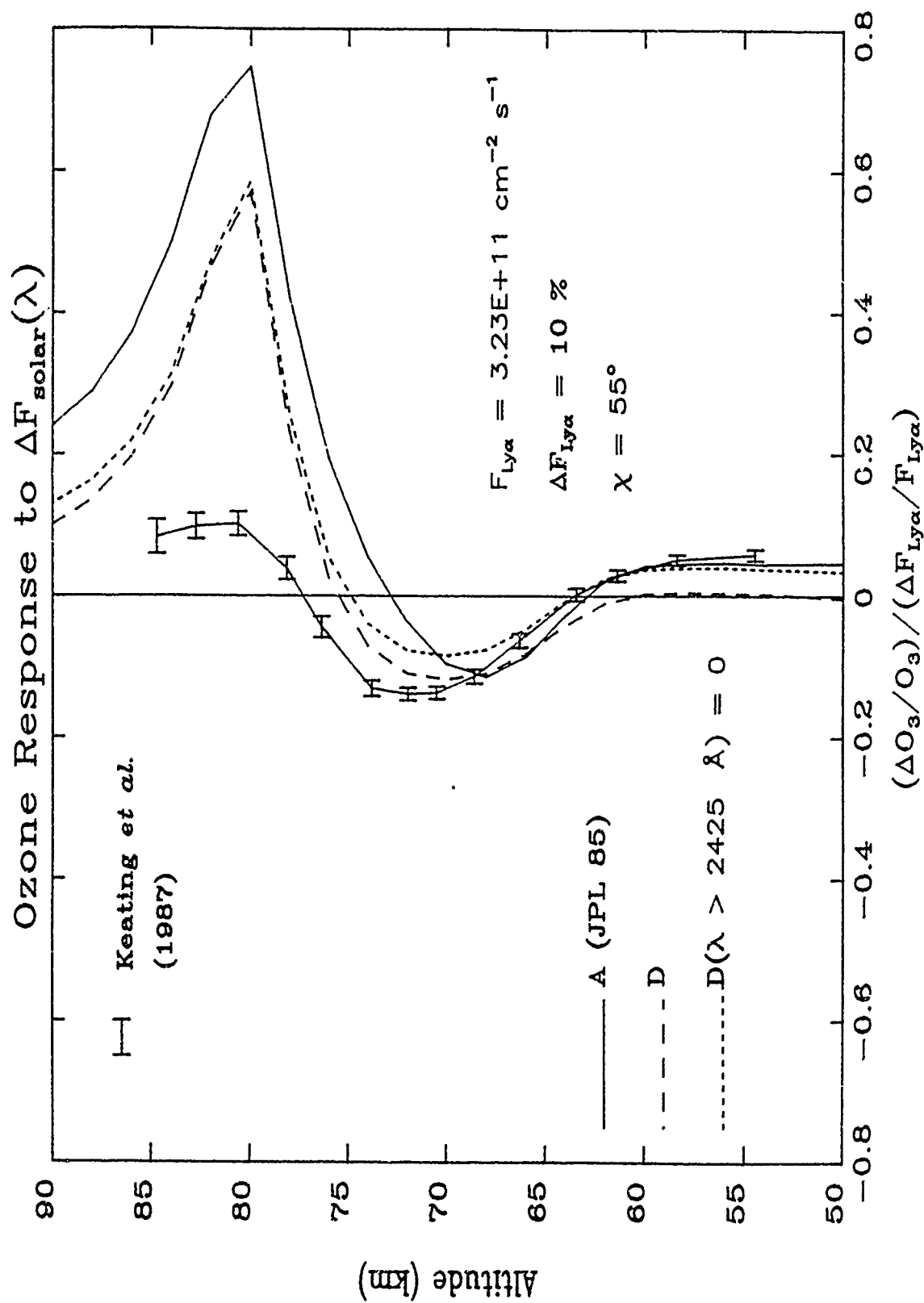




Figure 7(b)

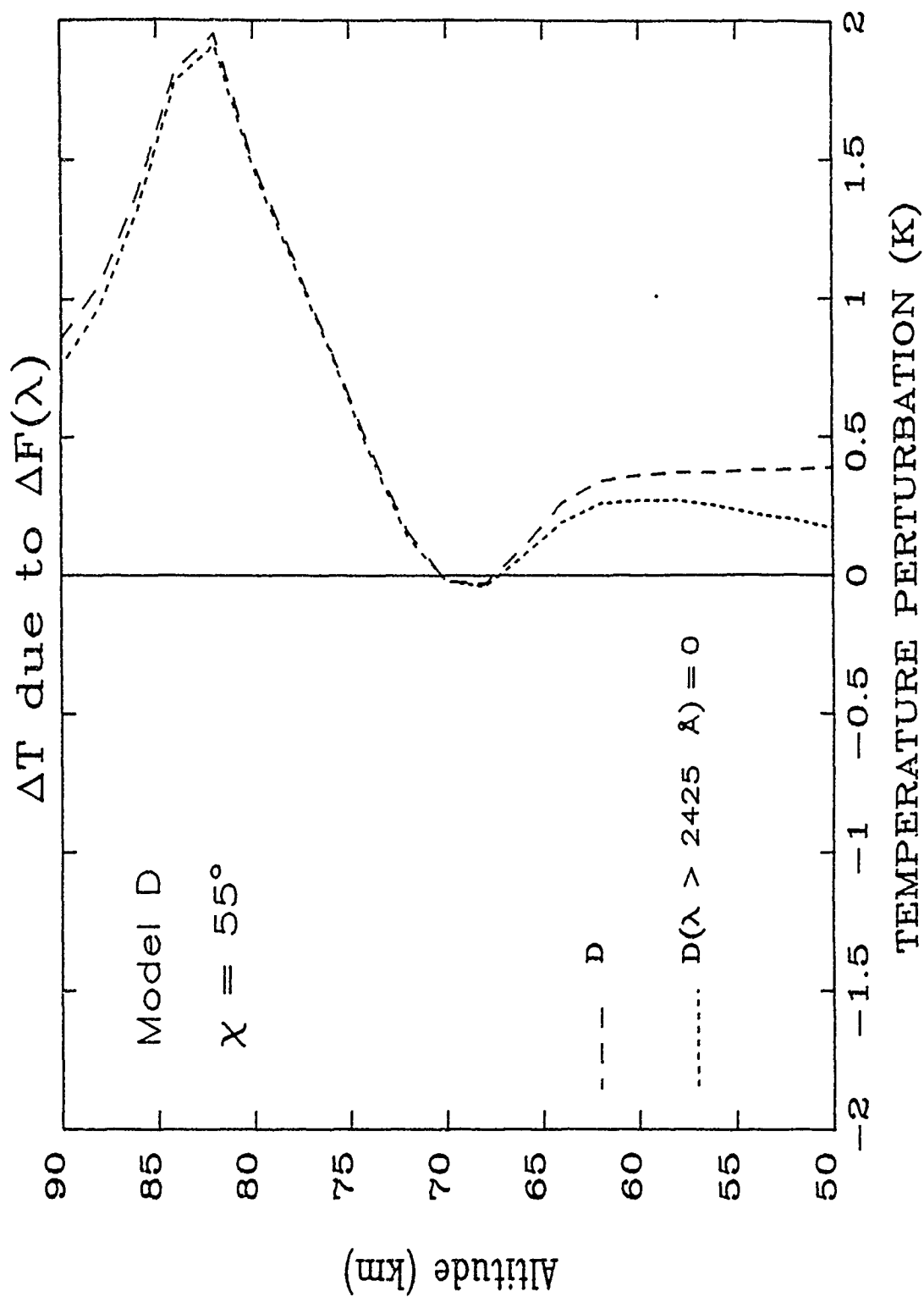


Figure 8(a)

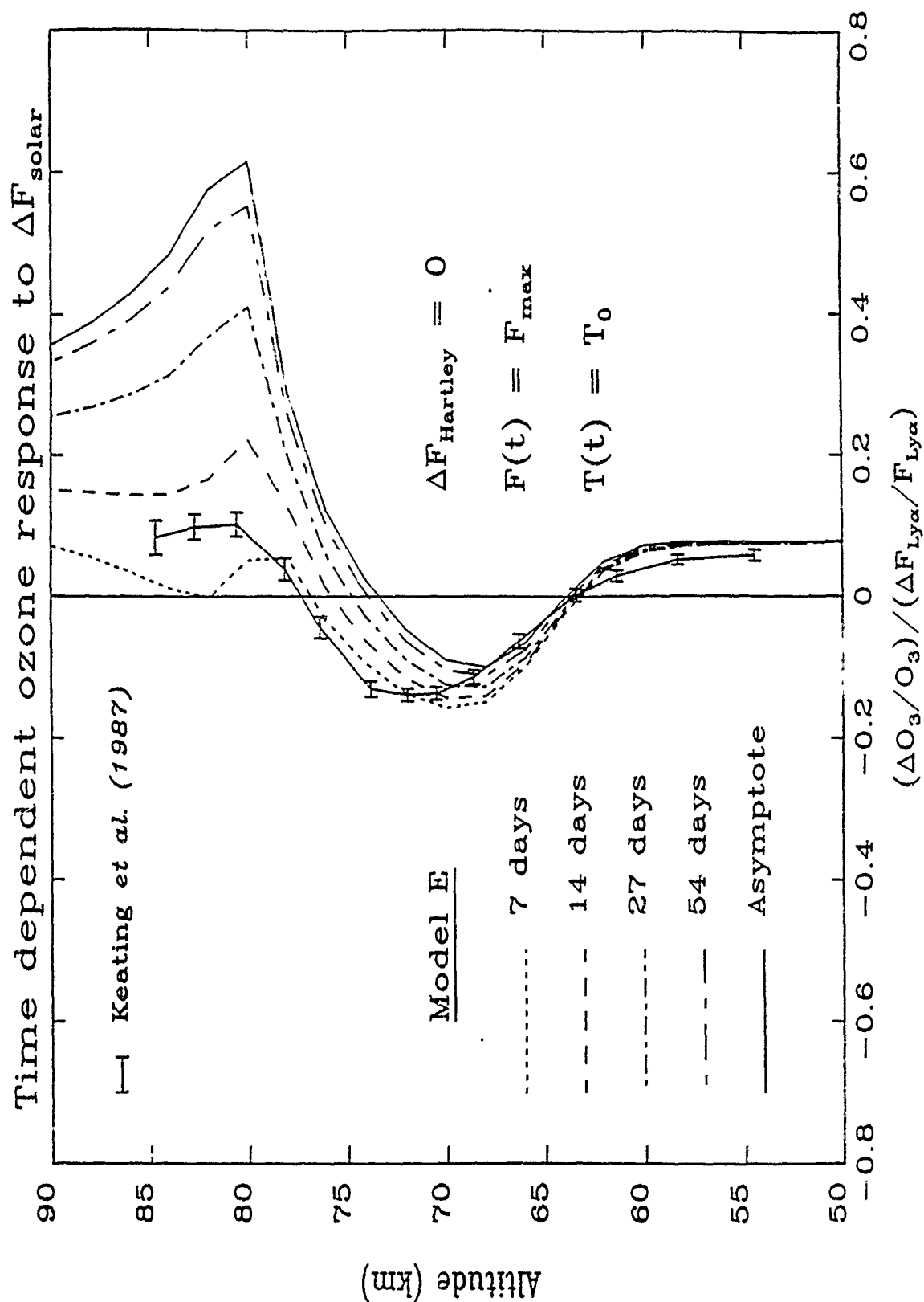


Figure 8(b)

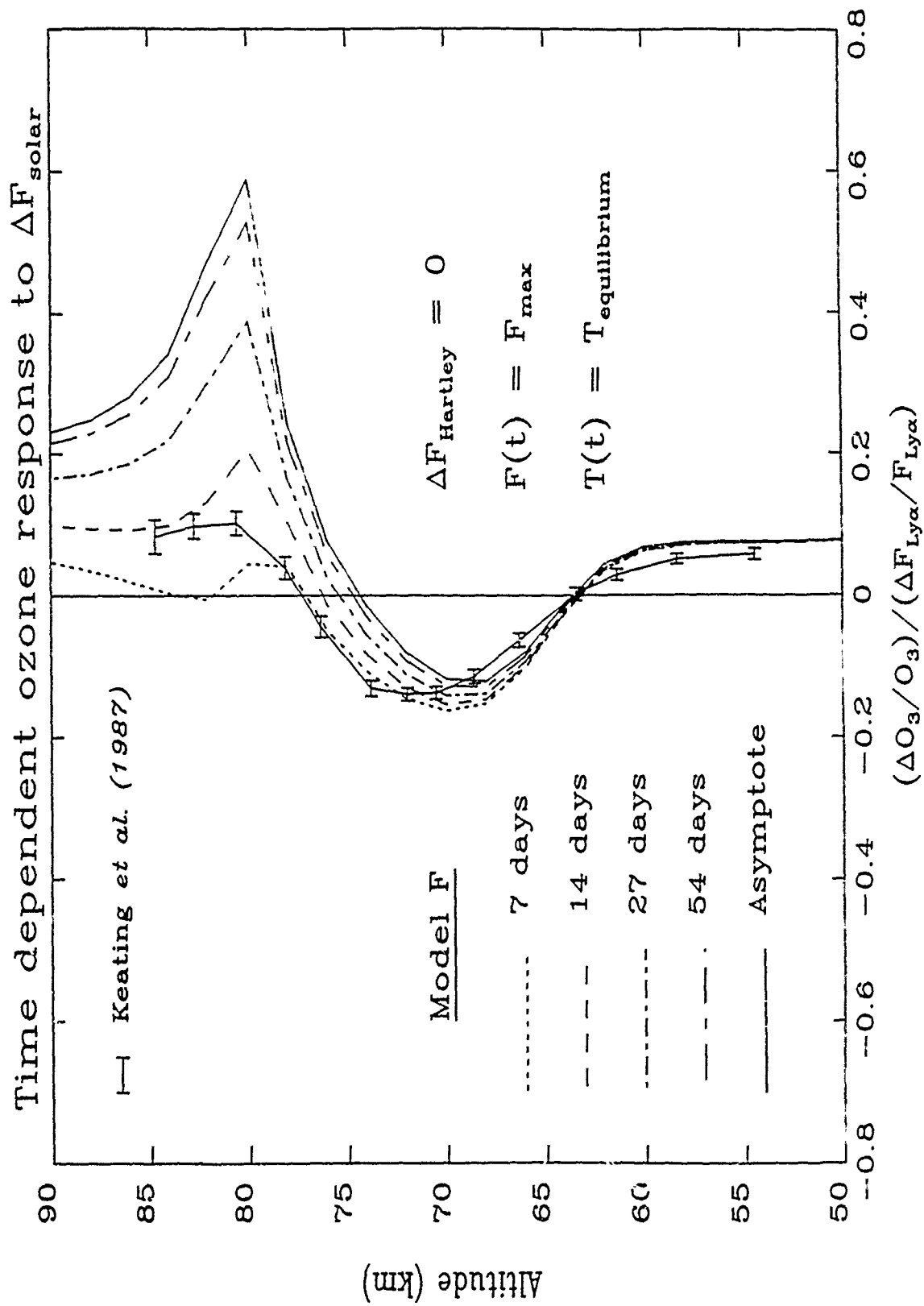


Figure 9(a)

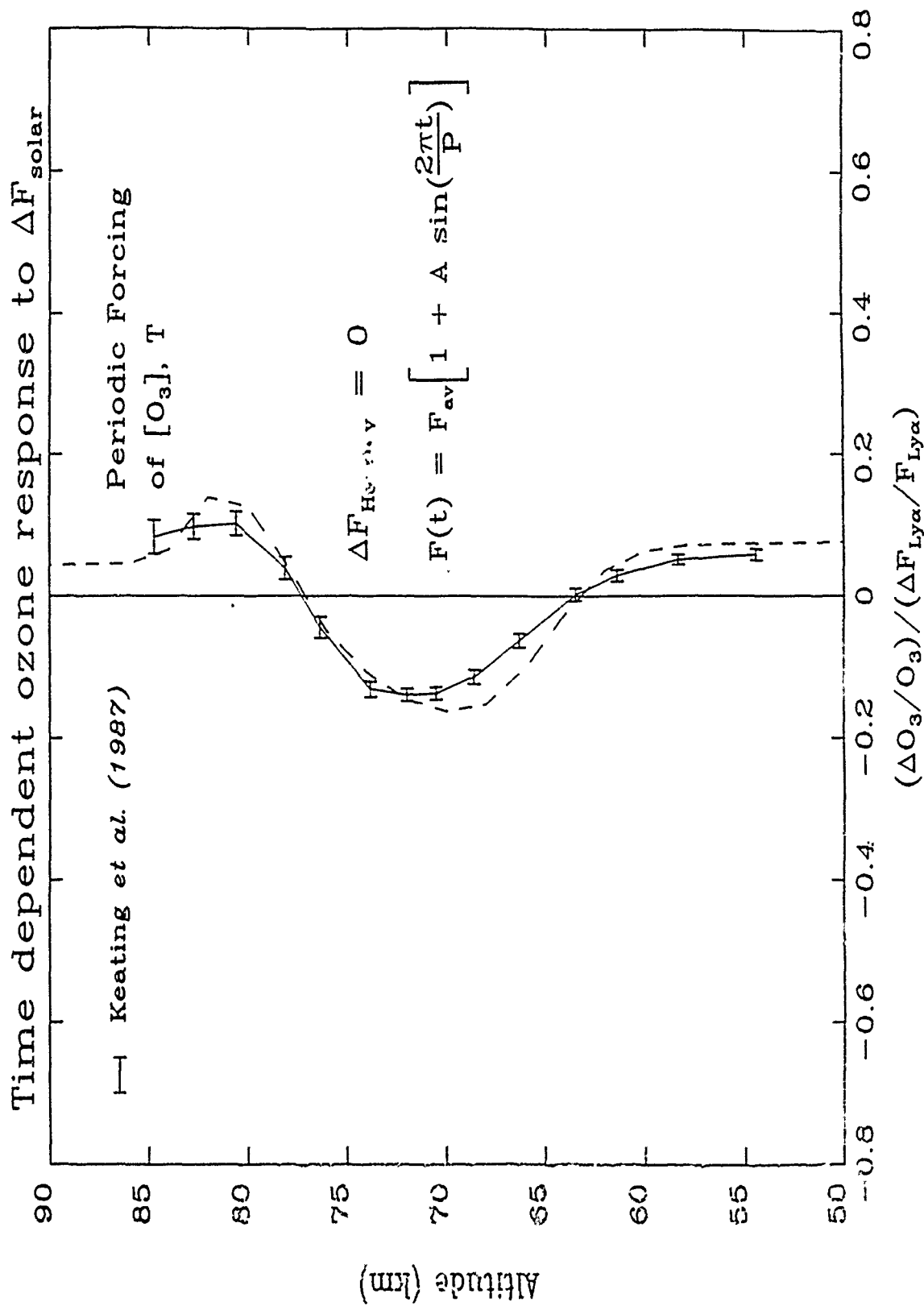
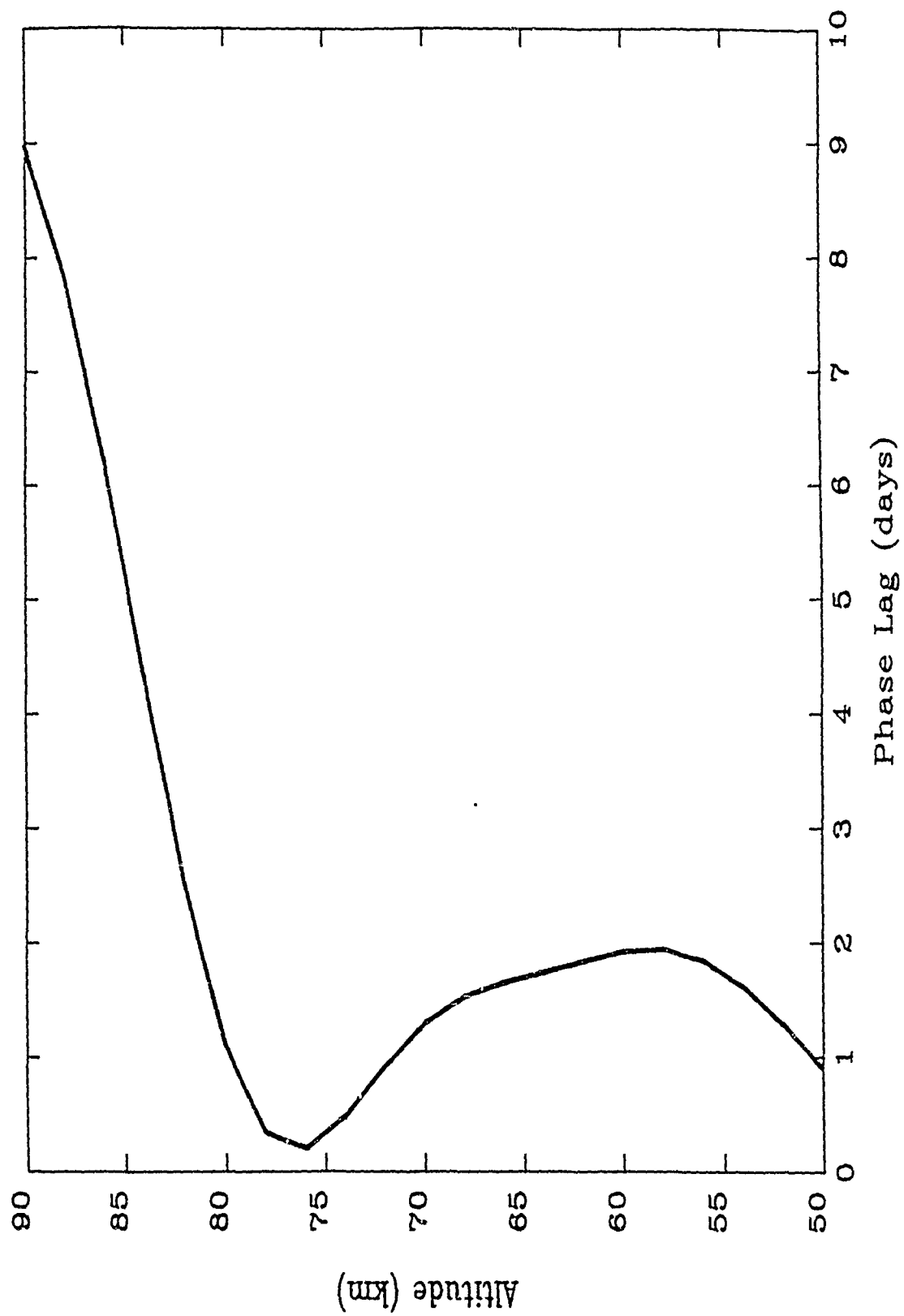


Figure 8(b)



## **APPENDIX N**

### **Diurnal Variations of Mesospheric Ozone Obtained by Ground-Based Microwave Radiometry**

## Diurnal Variations of Mesospheric Ozone Obtained by Ground-Based Microwave Radiometry

W. C. ZOMMERFELDS,<sup>1</sup> K. F. KUNZI,<sup>1</sup> M. E. SUMMERS,<sup>2</sup> R. M. BEVILACQUA,<sup>2</sup> D. F. STROBEL,<sup>3</sup>  
M. ALLEN,<sup>4</sup> AND W. J. SAWCHUCK<sup>5</sup>

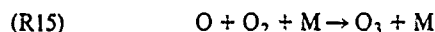
From December 1986 until April 1987 ground-based microwave observations of the diurnal variation of mesospheric ozone were made over Bern, Switzerland. These data were of sufficient quality to define the characteristic diurnal behavior of the ozone mixing ratio during winter and equinoctial conditions. The observed diurnal variation of ozone peaks at ~74 km, where its amplitude is about a factor of 6. At 65 km the observed diurnal variation is a factor of 3, whereas at 55 km it is only a factor of 1.4. One-dimensional model calculations accurately reproduce the relative diurnal variation of ozone at equinox, suggesting that the model value of the ozone photolysis rate coefficient is accurate to better than 10%. For winter conditions, however, the model underpredicts the observed relative diurnal variation by a factor of 2; a major part of this discrepancy is due to an observed postmidnight increase in ozone. Various suggested changes in model parameters to better reproduce the ozone abundance vertical profile result in only small differences in the relative diurnal variation, indicating that these observations do not provide a sensitive test of the mesospheric chemistry controlling the abundance of odd oxygen.

### 1. INTRODUCTION

The diurnal variation of ozone can be remotely sensed by microwave radiometry. This technique has been successfully demonstrated by *Wilson and Schwartz* [1981] and *Lobsiger and Kunzi* [1986]. It has distinct advantages over other measurement techniques, such as Umkehr and Lidar systems, in that clear weather is not required, the results are not dependent on the solar zenith angle, and both day and night measurements can be obtained with a temporal resolution of 15 min.

In order to understand the significance of diurnal mesospheric ozone measurements it is necessary to review the basic photochemistry of molecular oxygen in the Earth's middle atmosphere. For the reader interested in a rigorous discussion with accurate plots of time constants and chemical rates, *Allen et al.* [1984] should be consulted. Dissociation of molecular oxygen is predominantly in the Schumann-Runge bands and Herzberg continuum. Under the most favorable optical thickness conditions the time constant for O<sub>2</sub> dissociation is at least 10<sup>6</sup> s. The resultant O atoms react rapidly with O<sub>2</sub> to form O<sub>3</sub>. The ultimate loss processes for O<sub>3</sub> in the mesosphere are recombination of O<sub>3</sub> with O atoms directly or by catalytic reactions involving odd hydrogen. A typical time constant for removal of odd oxygen throughout the lower mesosphere is ~10<sup>5</sup> s. Consequently the chemical production and loss of odd oxygen can produce only minor diurnal variations in the ozone density.

However, the odd oxygen components O and O<sub>3</sub> undergo rapid interchange reactions in the middle atmosphere, the two most important reactions being



(The reaction numbers are taken from *Allen et al.* [1981].)

The former reaction has an optically thin time constant of ~10<sup>2</sup> s and a maximum time constant of ~2.5 × 10<sup>3</sup> s due to the optically thin Chappius bands. The latter reaction has a time constant which varies from ~10 s at 50 km to ~10<sup>4</sup> s at 80 km. These two reactions essentially control the partitioning of O and O<sub>3</sub> in the middle atmosphere and, as a consequence of their fast rates, the diurnal variation of ozone.

At the stratopause O<sub>3</sub> is at least a factor of 10 more abundant than O atoms in the day, and conversion of all O atoms to O<sub>3</sub> at night is a minor perturbation to the O<sub>3</sub> density. Above the mesopause O exceeds O<sub>3</sub> by more than two orders of magnitude, but (R15) has a time constant of >10<sup>5</sup> s. Hence very little O is converted to O<sub>3</sub> during the night. Similar arguments apply to O<sub>3</sub> photolysis (reaction (R3, R4)). At and above the mesopause, photolysis of O<sub>3</sub> at sunrise adds little to the O density, but establishes the O<sub>3</sub> concentration in chemical equilibrium with the transport-dominated O atoms. Down at the stratopause, photolysis of O<sub>3</sub> is important in reestablishing the O concentration at sunrise but cannot deplete O<sub>3</sub> because of rapid recycling (reaction (R15)). Consequently, the most significant diurnal variation of O<sub>3</sub> occurs in the intermediate region, i.e., the mesosphere, where the O and O<sub>3</sub> densities are comparable in magnitude, and fortunately accessible to ground-based microwave measurements.

In this paper we report ground-based microwave radiometric observations of the diurnal variation of mesospheric ozone abundances for the period of December 1986 to April 1987 over Bern, Switzerland. A one-dimensional photochemical model with parameterized transport is used to analyze and interpret our microwave data. The absolute concentrations of ozone contain relevant information on the chemical production and loss mechanisms of odd oxygen.

<sup>1</sup>Institute of Applied Physics, University of Bern, Bern, Switzerland.

<sup>2</sup>E. O. Hulburt Center for Space Research, Naval Research Laboratory, Washington, D. C.

<sup>3</sup>Department of Earth and Planetary Sciences and Department of Physics and Astronomy, Johns Hopkins University, Baltimore, Maryland.

<sup>4</sup>Earth and Space Sciences Division, Jet Propulsion Laboratory, and Division of Geological and Planetary Sciences, California Institute of Technology, Pasadena.

<sup>5</sup>Computational Physics, Incorporated, Annandale, Virginia.

Copyright 1989 by the American Geophysical Union.

Paper number 89JD01094,  
0148-0227/89/89JD-01094\$05.00

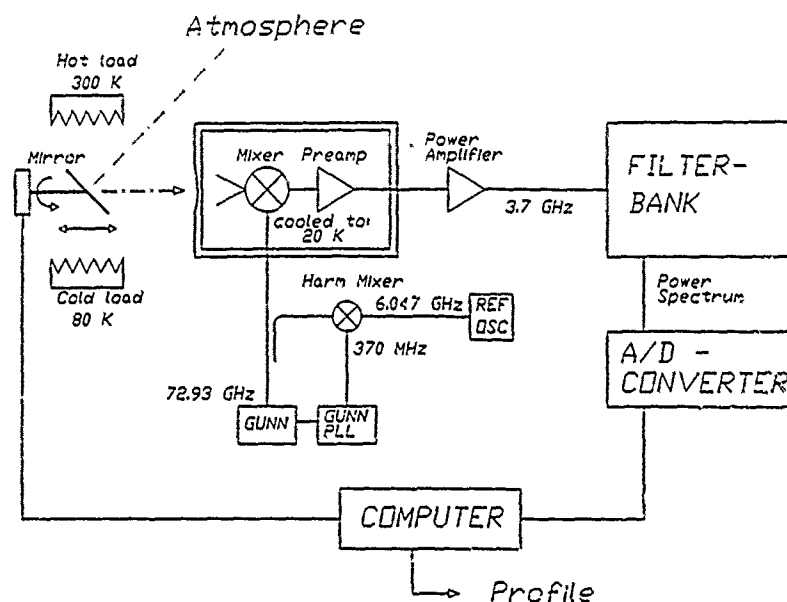


Fig. 1. Schematic diagram of the Bern microwave radiometer.

whereas the relative variation from day to night of  $O_3$  contains information on whether our understanding of the recycling reactions of odd oxygen is correct. In section 2 the observational technique is described. A discussion of sources of error is then given in section 3. Section 4 presents the observations. A brief discussion of the one-dimensional model is given in section 5, followed by the interpretation of observational results in section 6. Section 7 presents our conclusions.

## 2. OBSERVATIONAL METHOD

Our observing technique has been described previously by Lobsiger *et al.* [1984] and Lobsiger [1987]. We observe the thermal emission of an ozone line at 142.175 GHz. The ground-based microwave radiometer is illustrated schematically in Figure 1. A mixer with a horn antenna receives the atmospheric microwave signal and converts it down to an intermediate frequency (IF) at 3.7 GHz, which is then amplified. The system spectrometer is a conventional 36-channel filter bank having a resolution of 30 MHz at the line wings, increasing to 0.2 MHz at the center. Detectors provide a voltage proportional to the power output of the filters that is fed into the computer by an analog to digital converter. The computer controls the radiometer and integrates the measured spectra.

The system is calibrated by measuring the blackbody radiation of a hot and a cold microwave absorber. This calibration is done by switching the antenna beam with a rotating mirror every few seconds between the atmosphere and the two reference absorbers. The mirror is reciprocating to reduce baseline effects caused by standing waves in the quasi-optical part of the microwave front end [Gustine, 1977]. The subharmonic mixer is pumped by a Gunn oscillator at 72.937 GHz, whose frequency is stabilized to better than one part in  $10^7$ , relative to a highly stable reference quartz oscillator in a phase-locked loop (PLL). The mixer was tuned mechanically to single-sideband (SSB) response

with an image band rejection relative to the signal band of better than 17 dB. The receiver is essentially the same as that used in the ozone observations of Lobsiger and Kunzi [1986] except that in the present system both the front end mixer and the first IF field effect transistor (FET) preamplifier are cryogenically cooled to  $\sim 20$  K. Cooling the front end components reduces the SSB receiver noise temperature from  $\sim 1800$  K for the uncooled system down to  $\sim 700$  K for the present, cooled instrument.

The quantity of interest in the observations is the stratospheric  $O_3$  signal ( $T_{Bstr}$ ). However, in the ground-based measurement configuration the stratospheric signal is attenuated by the troposphere, and the measurements also contain the tropospheric emission component. We approximated the troposphere as a homogeneous layer with a temperature  $T_T$  and transmittance  $A$ , which is well correlated to the tropospheric water content. Therefore the ground-based brightness temperature measured in the experiment ( $T_{BG}$ ) can be written:

$$T_{BG} = T_{Bstr}A + T_T(1 - A) \quad (1)$$

From measurements obtained over one year [Lobsiger, 1987] we found that taking the CIRA (1972) temperature at 1 km above the surface is a good approximation for tropospheric temperature if we averaged our data over a whole month. At the line wings the contribution of the  $O_3$  line is relatively small in comparison to tropospheric contributions, and we can determine the tropospheric transmittance  $A$  to a good approximation, from the measured off-line sky brightness temperature and use it to remove the tropospheric contributions from the observed line center. The  $O_3$  line is symmetric, and errors can be reduced by folding the line around the center to calculate a mean-half line. We derived the brightness temperatures at the desired frequencies for the inversion from a cubic spline fit to the spectral line.

The observed stratospheric  $O_3$  line amplitude is proportional to the concentration and is broadened by atmospheric pres-



sure. The ozone volume-mixing ratio (VMR) profile is determined from the observed line spectrum with an iterative inversion algorithm [Twomey, 1977; Randegger, 1980]. We start from an arbitrary initial guess of the  $O_3$  profile of 1 ppm VMR to calculate a brightness temperature spectrum. The resulting iterated profile is practically independent of the initial guess (error <1%). The brightness temperature is calculated by integrating the radiative transfer of the atmosphere in 0.5-km layers from the surface up to 100 km. The observed brightness temperature differences at neighboring filter channels ( $T_{Bsr}(\nu_i) - T_{Bsr}(\nu_{i-1})$ , see Table 1) are then compared with the equivalent brightness temperature differences obtained from the calculated spectrum in order to correct the initial guess  $O_3$  profile. This process is repeated until the difference between calculated and observed data is smaller than the data error. The iterative algorithm modifies the profile at the iteration points using the relaxation formula derived by Chahine [1972] and interpolates the profile linearly for the integration of the radiative transfer equation. The iterated profiles are smoothed, using a Gaussian function with a full width at half maximum (FWHM) of 5 km, to reduce oscillations in the iterated profile which are caused by errors in the observed spectrum. In the radiative transfer calculations we used an  $O_3$ -air collision line width parameter of 2.55 MHz/mbar at 292 K (N. Monnateuil, private communication, 1983) and the CIRA (1972) reference temperature and pressure profiles.

In this manner we determined the ozone profile in the 20- to 76-km altitude range. The lower altitude limit is given by the total frequency bandwidth of the spectrometer of  $\pm 85$  MHz. Above approximately 80 km the line shape is no longer dominated by pressure but by Doppler broadening, and no altitude information can be obtained based on the well-known pressure profile. Table 1 shows the frequency offsets of the brightness temperature differences, and their corresponding measurement weighting function peak altitudes, employed in the mesospheric component of the retrievals (of interest in the diurnal variation measurements). The weighting function peaks denote the altitudes at which the brightness temperature differences are most sensitive to variations in the  $O_3$  profile. These weighting function peak altitudes are the profile iteration points employed in the Chahine inversion. They occur at higher altitudes in spring than in winter because of the seasonal variation of model atmosphere temperature and pressure in the mesosphere. Also indicated in Table 1 are the measurement weighting function widths (half width at half maximum). The weighting function widths give a rough upper limit estimate of the retrieval vertical resolution.

TABLE 1. Frequency Offsets Relative to Line Center of Brightness Temperature Differences ( $T_{Bsr}(\nu_i) - T_{Bsr}(\nu_{i-1})$ ), Corresponding Iteration Altitudes (Weighting Function Peak Altitudes), and Weighting Function Half Width at Half Maximum Values Employed in the Chahine Inversion Procedure

$\nu_i - \nu_{i-1}$ , MHz	$Z_i$ , km		
	December	January	April
0.0-0.2	73 $\pm$ 9.5	74 $\pm$ 9.5	76 $\pm$ 8.5
0.2-0.4	66 $\pm$ 8.0	66 $\pm$ 8.0	68 $\pm$ 7.5
0.4-0.8	60 $\pm$ 7.5	60 $\pm$ 7.5	62 $\pm$ 7.5
0.8-1.6	54 $\pm$ 7.0	54 $\pm$ 7.0	56 $\pm$ 7.5

TABLE 2. Upper Limit on Uncertainty of Scaling Factors

Scaling Factor	Uncertainty, %
Determination of tropospheric attenuation	5
Estimate for tropospheric temperature	4
Measurement of sky temperature	4
Uncertainty of reference blackbodies	5
Influence of image sideband	2
Width of antenna beam	3
Inversion algorithm	10
Total uncertainty limit	13

The total uncertainty limit is the square root of the sum of the squares for all factors.

### 3. ERROR CONSIDERATIONS

We assume that sufficient integration time was available and that the receiver noise, as discussed in the next section, can be neglected. Table 2 gives a list of factors leading to altitude independent errors, which we refer to as scaling factors of the profile. From Lobsiger *et al.* [1984] we estimated the error, introduced by the approximate method for the tropospheric correction, to be 5%. The two reference absorbers used for calibration are not perfect blackbodies and we estimated a calibration error of 3-4%, giving a total calibration error of <5%. The front end mixer is sensitive in the signal band at 142.175 GHz but also in the image band at 149.575 GHz. By mechanical tuning we have reduced the image band sensitivity by more than 17 dB relative to the signal band. The remaining error caused by the influence of the image band is less than 2%. Our retrieval algorithm assumes a pencil beam antenna; the radiometer has, however, an antenna beam width at half power of 30° with a zenith angle of 35°. Contributions from the atmosphere seen by the radiometer at zenith angles lower than the main beam are partially balanced by contributions from higher zenith angles. The error due to the finite beam width was estimated at 3%. Randegger [1980] tested our inversion algorithm with simulated noise, and we estimated the error of the retrieval process to be ~10%. This includes uncertainties introduced by the choice of parameters of the spline function to smooth the spectrum. The total uncertainty of the scaling factor on the retrieved profiles is therefore 13%, assuming statistically independent errors.

Altitude dependent fluctuations and errors on the retrieved profiles are caused by instrumental baseline structure on the measured spectra, which is due to standing waves in the radiometer and nonlinearities of the system. Within the frequency range under consideration ( $\pm 85$  MHz around the line center) the amplitude of any instrumental baseline structure is smaller than 0.1 K. From inversions with simulated spectra we estimate an error of 0.5 ppm VMR on our profiles. The baseline on the measured spectra was constant over periods longer than a week, and the time dependent error on the observed differences between nighttime and daytime profiles is estimated to be smaller than 10%.

Another source of altitude-dependent errors in the retrieved ozone profiles is deviation of the actual middle atmosphere temperature profile from the model atmosphere values. For the 142.175-GHz ozone line the magnitude of this error is such that a 1% ambient temperature error results in about a 1.6% error in the retrieved ozone profile at that altitude. Thus for typical deviations of middle atmosphere

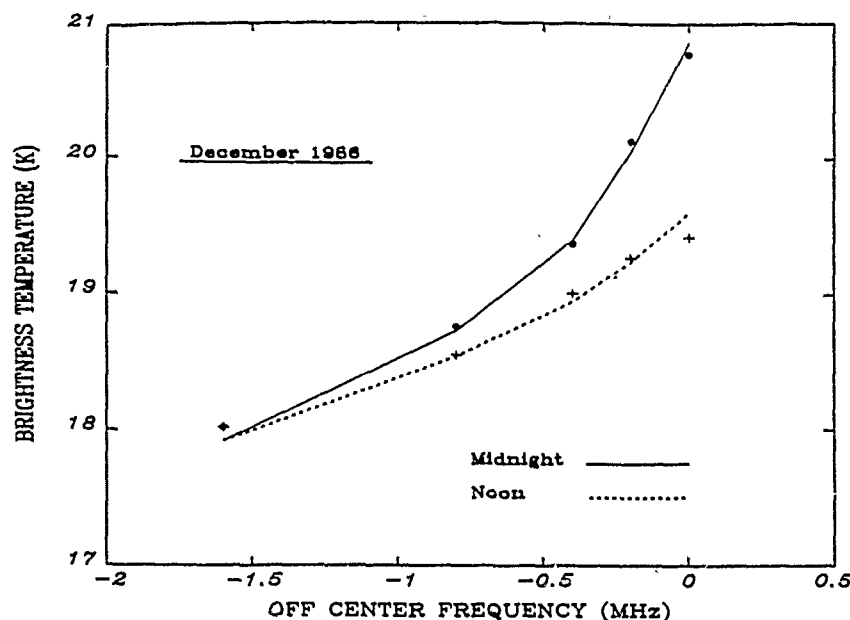


Fig. 2. Observed thermal emission of the stratospheric ozone line without contributions from the troposphere. The line is symmetric; only the lower half of the line, and only the central part of the line relevant for the mesosphere, is shown.

temperature from model profiles of about 4% [Forbes, 1985], the resultant probable error in the ozone retrievals is roughly 6%.

#### 4. OBSERVATIONS

Data were obtained at Bern (46.57°N, 7.26°E) during the period from December 1986 to April 1987 looking in a northeasterly direction with an antenna zenith angle of 35°. The cold and dry winter troposphere permits good observations. During the summer months the tropospheric humidity is frequently too high, and the required integration time cannot be obtained.

To measure the diurnal variations between 50 and 76-km altitude, the ozone line center needs to be measured with a frequency resolution of the order of 0.2 MHz within a bandwidth of 2 MHz. For an accurate inversion the noise on the observed stratospheric brightness temperature ( $\sigma_{T_{str}}$ ) must be less than 0.05 K. The sensitivity of the radiometer is limited by the receiver noise  $T_N$ . From Krauss [1966] we derive the following expression for the required measuring time  $t$ :

$$t = \frac{3}{\Delta\nu} \left[ \frac{T_N}{\sigma_{T_{str}} A} \right]^2 \quad (2)$$

where  $A$  represents the transmittance of the troposphere and  $\Delta\nu$  is the spectral resolution. Samples measured under bad weather conditions with tropospheric transmittance less than 0.5 are not used. The factor 3 in (2) is introduced by the calibration cycle made during the observations. With our microwave radiometer we, therefore, require a measuring time of  $t \geq 3$  hours. Measurements were made 24 hours per day, and the data were recorded in bins of 15-min averages. We integrated the data over a whole month, to determine the  $O_3$  variation of a mean corresponding to day 15 of the month, with a time resolution of 15 min. We integrated

samples of each day having the same time difference relative to the sunrise time, to determine the mean a.m. variation and integrated likewise relative to sunset to get the mean p.m. variation. The time scales were corrected for day 15 of the month. By integrating samples of a whole month with at least 13 days of good observations, mean spectra were obtained with sufficient integration time.

Figure 2 shows the spectrum of the observed December 1986 monthly average  $O_3$  spectral line at noon and midnight as a typical example for all measurements. In Figures 3a and 3b, the Bern, monthly averaged, noontime vertical profiles of  $O_3$  mixing ratio are illustrated for the months of December 1986 and April 1987, respectively, along with error bars which represent the total estimated error from Table 1. For these profiles the data were averaged  $\pm 2$  hours around noon. Shown for comparison are monthly averaged Solar Mesosphere Explorer (SME) [Thomas *et al.*, 1984a] retrievals for April 1985 and December 1983 for latitude 45°N and their corresponding standard deviations. SME data for December 1983 were chosen for the comparison since SME data for December 1985 were not available and data for December 1984 were available only at pressures less than about 0.1 mbar. A direct comparison between the Bern and SME retrievals is not straightforward since the SME data represent averages of observations taken essentially over North America at about 1500 LT. For April, with the exception of the Bern value at the 68-km iteration point, the error bars for the two profiles generally overlap. The 68-km Bern value is, however, about  $2\sigma$  away from the SME profile. The retrievals for December show more substantial disagreement not only in absolute values for mixing ratios but for the general shape of the vertical profiles, especially below 60 km and above 70 km. The discrepancy above 70 km may be instrumental, resulting from the fact that the sensitivity of the microwave measurements decreases rapidly above this altitude. However, the discrepancy below 60 km is unlikely to

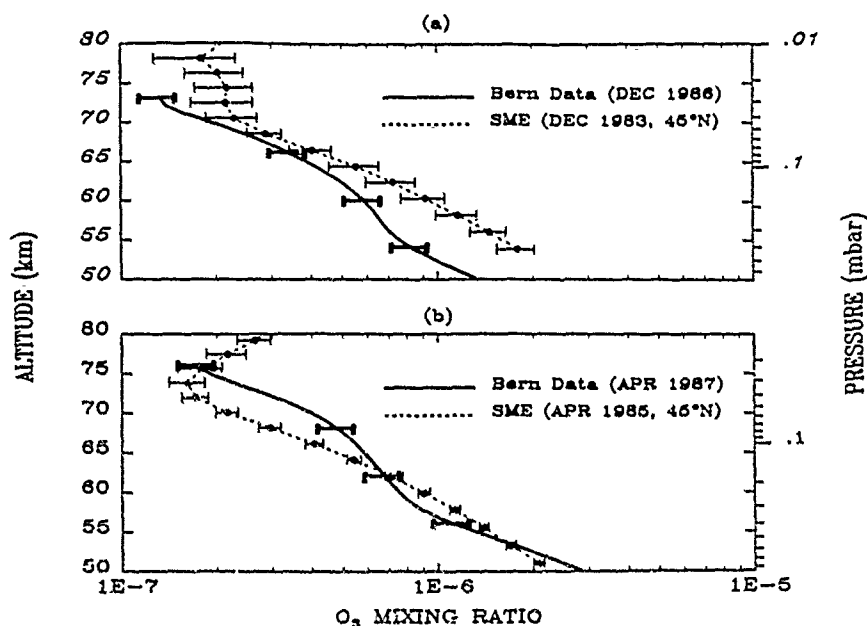


Fig. 3. (a) Average ozone abundance profile at local noon for December 1986. Solid line, microwave measurements; dashed line, SME data. (b) Average noon profile of April 1987. Solid line, microwave measurements; dashed line, SME data.

be an instrumental artifact and probably results from real mixing ratio variations. But even more perplexing in a comparison of Figures 3a and 3b is that our observed mesospheric  $O_3$  mixing ratios increase from winter to spring in disagreement with the SME inferred mixing ratios below 73 km. Note that the  $O_3$  mixing ratio bulge observed by SME which exhibits a semiannual variation with peak values at equinoxes is above 73 km, the maximum height of our observations (see Thomas *et al.* [1984b]; also discussion by Bevilacqua *et al.*, Seasonal variation of water vapor and ozone in the mesosphere: Implications for vertical transport and ozone photochemistry, submitted to *Journal of Geophysical Research* (1989)). With our limited data base it is difficult to interpret this disagreement. The SME data demonstrate consistently over a five-year period that winter  $O_3$  mixing ratios exceed spring values below 73 km. This trend between 65 and 75 km is predicted by most mesospheric models when transport and  $H_2O$  mixing ratios are held fixed. With the observed increase in  $H_2O$  mixing ratios from winter to spring included, the predicted decrease in  $O_3$  mixing ratio is enhanced. Because the SME data pertain to the middle atmosphere over North America, we can only speculate that the difference is a longitudinal effect and/or an unusual winter in the middle atmosphere over Europe during early 1987. This type of zonal asymmetry in ozone is undoubtedly dynamical in origin and thus cannot be simulated with our one-dimensional model. Therefore in this paper we model only the relative diurnal variation of mesospheric ozone inferred from the microwave measurements, rather than absolute mixing ratios. The relative diurnal variation should be largely insensitive to longitudinal variations in absolute ozone abundances and will also minimize the effect of systematic errors in the ozone measurements.

The December, January, and April monthly average diurnal variations of the  $O_3$  VMR at 55, 65 and 74 km altitude are shown in Figures 4-6. Except for the periods  $\pm \frac{1}{2}$  hours

around sunrise and sunset, the data were smoothed in time with a Gaussian function, having a FWHM of 1 hour. Data obtained for the months of February and March 1987 were substantially lower in quality and consequently are not shown.

## 5. MODEL

The model adopted for this study is the one-dimensional, time dependent, photochemical model with vertical transport by eddy and molecular diffusion developed by Allen *et al.* [1981, 1984] and used to study chemistry and transport in the mesosphere and lower thermosphere. It includes the chemistry and transport of the major nonnitrogen chemical species in the altitude range 40-130 km:  $O$ ,  $O(^1D)$ ,  $O_2$ ,  $O_3$ ,  $H$ ,  $H_2$ ,  $OH$ ,  $H_2O$ ,  $HO_2$ ,  $H_2O_2$ ,  $CO$ ,  $CO_2$ ,  $CH_4$ , and  $Ar$ . Because  $ClO_x$  and  $NO_x$  are important in the odd oxygen chemistry below 50 km, we regard our solutions as accurate only above about 55 km. Vertical transport by eddy diffusion and the chemical acceleration of vertical transport as described by Strobel *et al.* [1987] were incorporated in the model since the chemical acceleration term can be potentially significant for  $O$  and  $O_3$ .

The chemical model used in our study is essentially that of Allen *et al.* [1984, Table 1], with kinetic rate constants updated in accordance with DeMore *et al.* [1987]. The solar fluxes, photodissociation cross sections, and radiative transfer calculations are identical to those of Allen *et al.* [1984], with the exception that the background model atmosphere is extended down to the ground to ensure precise calculation of sunrise and sunset at each height grid point in a spherical atmosphere. The lower and upper boundary conditions were also identical with one exception: at 40 km the  $H_2O$  mixing ratio is set equal to 6.4 parts per million by volume (ppmv). We will subsequently refer to theoretical calculations using this assumed chemistry as the Jet Propulsion Laboratory (JPL) model.

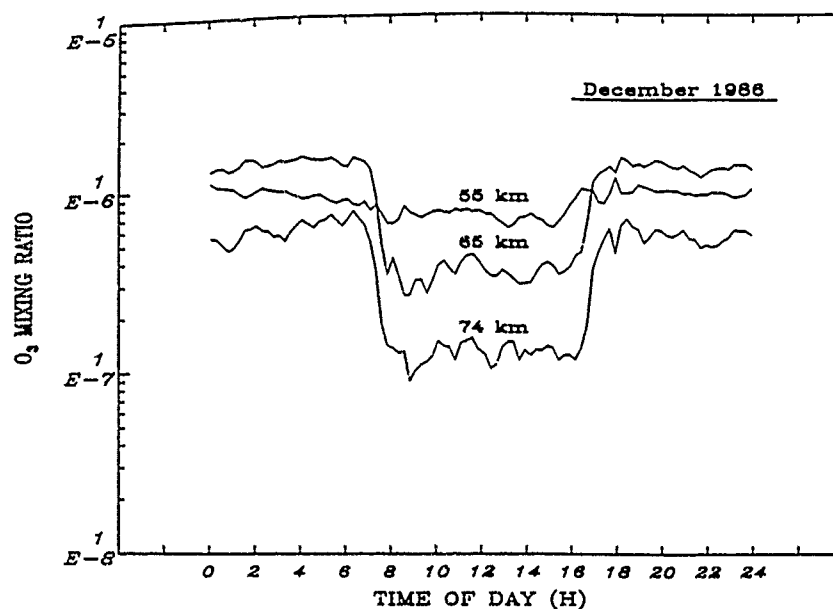


Fig. 4. The deduced variation of the  $O_3$  mixing ratio based upon inversion of the data for altitudes of 55, 65, and 74 km during December 1986.

To generate model results for comparison with the monthly averaged diurnal variations of  $O_3$  mixing ratios as a function of height for the period of December 1986 through June 1987, appropriate model atmospheres for each month at Bern, Switzerland, latitude  $47^\circ N$ , were constructed. For the standard model the eddy diffusion profile,  $K_{zz}$ , was the model C profile of Strobel *et al.* [1987]. Unfortunately, we did not have any data available in addition to the ozone data at Bern which could be used to constrain the eddy diffusion and  $H_2O$  mixing ratio profiles. Our choice of the eddy diffusion profile and, as a consequence, the  $H_2O$  profile, as described by Strobel *et al.* [1987], is governed by mid-

latitude  $H_2O$  data, typically  $34\text{--}43^\circ N$  latitude over the United States, obtained by Bevilacqua *et al.* [1983, 1987, 1989].

#### 6. INTERPRETATION OF RESULTS

The diurnal variation of ozone reflects two chemical phenomena, the diurnal variation of total odd oxygen [ $O + O_3$ ], which is governed by the continuity equation

$$\frac{\partial [O + O_3]}{\partial t} = 2J_2[O_2] - 2(k_{16}[O][O_3] + k_{17}[O][OH] + k_{18}[O][HO_2] + k_{12}[O]^2[M]) \quad (3)$$

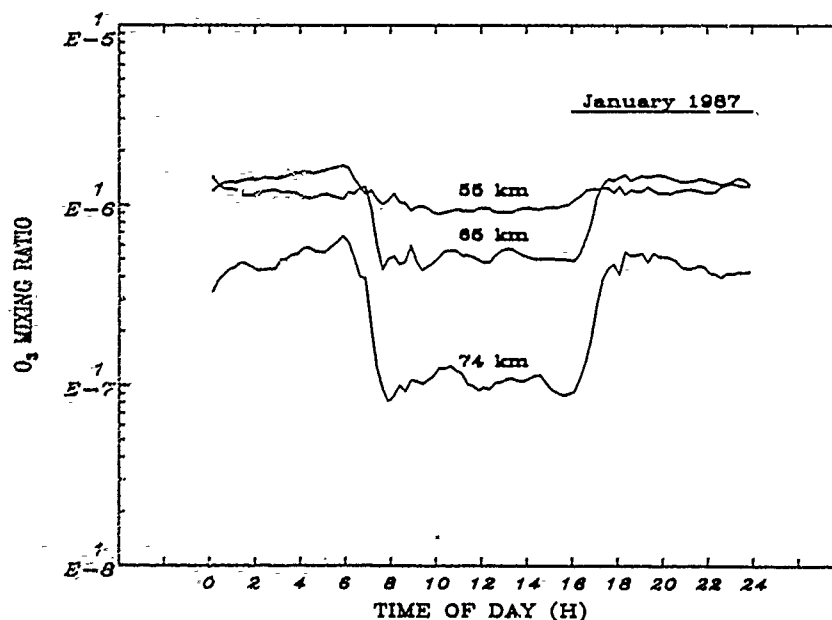


Fig. 5. Same as Figure 4, but for January 1987.

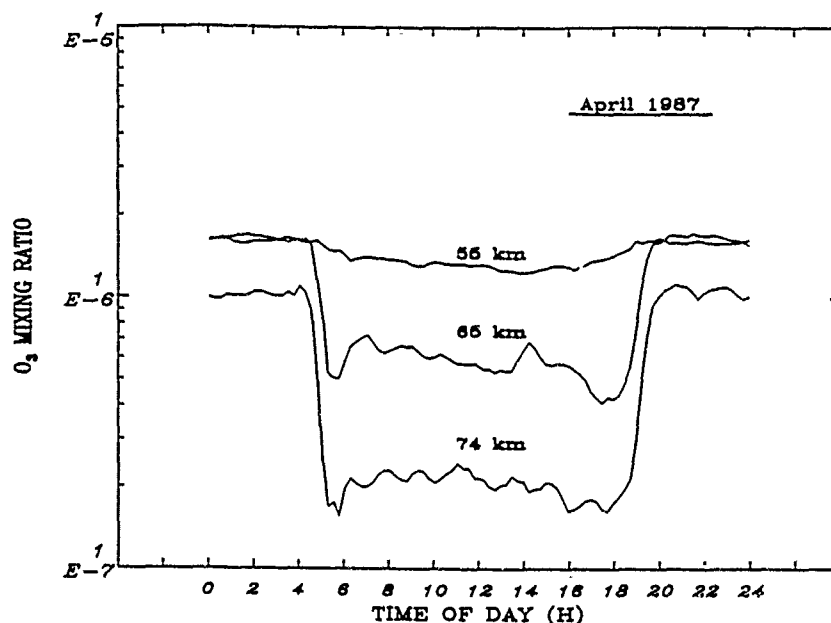


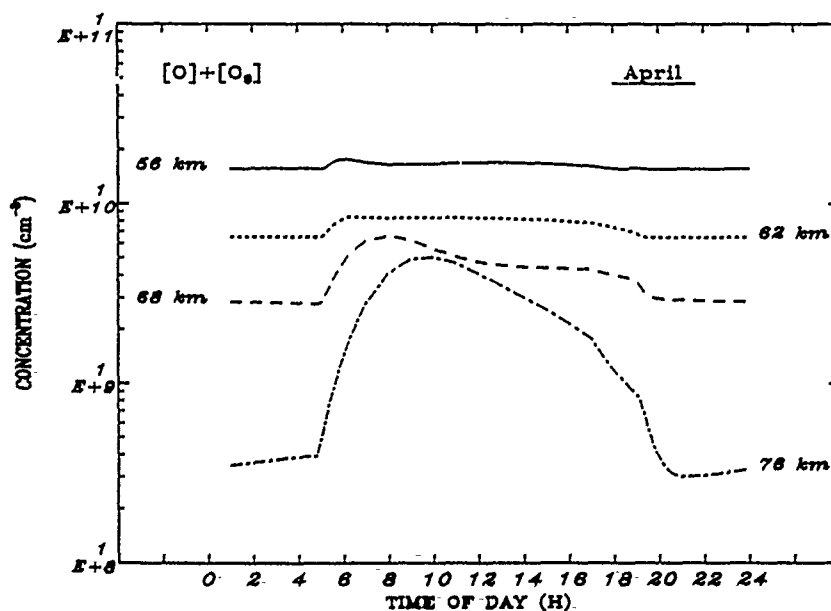
Fig. 6. Same as Figure 4, but for April 1987.

and the diurnal variation of the partitioning between O and O<sub>3</sub> described by

$$\frac{\partial[\text{O}_3]}{\partial t} = k_{13}[\text{O}][\text{O}_2][\text{M}] - (J_3 + J_4)[\text{O}_3] \quad (4)$$

The theoretical diurnal variation for total odd oxygen determined by (3) is shown in Figure 7, and the diurnal variation of ozone from (4) is shown in Figure 8, both for equinoctial conditions (April). Note the small diurnal variation of odd oxygen in the lower mesosphere (~15% at 56 km and 30% at 62 km) characterized by net production in the morning and net loss in the afternoon. In the upper mesosphere where O

is the dominant form of odd oxygen, the day to night variation of the ozone mixing ratio becomes substantial (a factor of ~2 at 68 km and ~17 at 76 km). Near the mesopause the validity of (3) breaks down as the divergence of the downward O atom flux contributes to the diurnal variation of [O<sub>1</sub>]. This is evident at 76 km in Figure 7, where odd oxygen increases throughout the night in the absence of production processes by flux convergence of the downward diffusing O atoms. The most significant diurnal variation of [O<sub>3</sub>] occurs at sunrise and sunset (Figure 8) associated with the onset and termination of O<sub>3</sub> dissociation (reaction (R3, R4)). At sunrise, dissociation destroys O<sub>3</sub> with  $\geq 100$  s time

Fig. 7. Model variation of the total odd oxygen concentration ([O] + [O<sub>3</sub>]) as a function of time for the indicated altitudes.

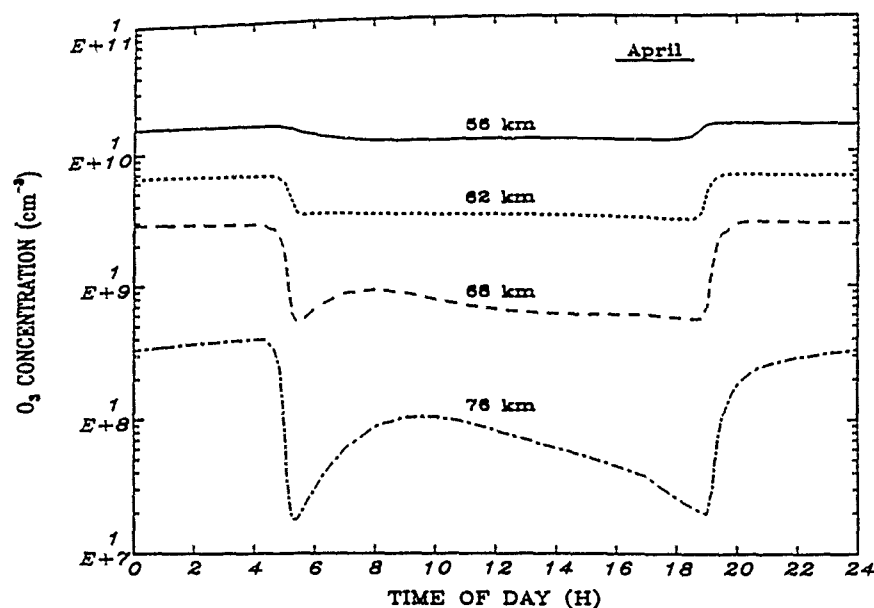


Fig. 8. Model variation of the  $O_3$  concentration as a function of time for the indicated altitudes.

constant followed by a subsequent adjustment and recovery of  $[O_3]$  with a time constant varying from 10 to  $10^4$  s over the range of 50–80 km.

It is tempting to directly compare our theoretical expectations with inferred  $O_3$  density profiles from microwave radiometry. However, it is somewhat misleading to directly compare retrieved  $O_3$  density profiles with model results because the vertical resolution of the  $O_3$  mixing ratio retrievals is fairly coarse ( $\sim 1.5$   $O_3$  scale heights). Note that in Figure 8 model calculations predict a large, localized diurnal variation of  $O_3$  above 70 km which is significantly greater than the variation below 70 km. Given the broad retrieval vertical resolution, this large diurnal variation in  $O_3$  centered at 75 km would be significantly smoothed out in the retrieved profiles. A more accurate method of comparison, which avoids the ambiguity of the varying vertical resolution of the retrieved  $O_3$  profiles, is to directly compare the measured diurnal variation of the brightness temperature differences (hereinafter referred to as DBT for differential brightness temperature). The model values were generated by computing a synthetic spectrum (at the measured frequencies) for the  $O_3$  profile at each photochemical model time step in the diurnal calculation. For the comparison we used the DBT values at the frequency offsets given in Table 1 (we refer to the DBT values by their highest offset, for example, DBT (0.2 MHz) =  $T_{BSR}(0.0) - T_{BSR}(0.2)$ ). Table 1 shows that these DBT values are sensitive to the  $O_3$  profile in the altitude range in which the constraints of model validity, in terms of absolute  $O_3$  concentration and significant diurnal variation, are satisfied.

Our best quality data for equinoctial conditions are the month of April 1987. Figures 9a–9d illustrate the diurnal variation of ozone in terms of the observed quantity, DBT, at the indicated frequency offsets plotted on a relative basis in order to remove the differences in the absolute magnitude of the  $O_3$  mixing ratios, as discussed above. The DBT values are normalized to an average daytime value ( $\pm 2$  hours about local noon), and the relative increase is plotted in these

figures to determine whether the model and observations are in agreement on the fractional change in ozone through a diurnal cycle. As is readily obvious, this agreement between the data and the model with standard JPL chemistry is good ( $\leq \pm 20\%$ ) at altitudes 76, 68, and 56 km. At 62 km, Figure 9c indicates the JPL model overpredicts nighttime DBT values by  $\sim 30\%$ . As discussed above, data at and below this altitude (or equivalent frequency offset) are of lower quality. In Figure 10 the DBT values are normalized to the midnight average (instead of the daytime average), and it is apparent that the model and observations are in excellent agreement from the beginning of sunset to the end of sunrise. The essential problem is the average daytime value of the DBT, as its time variation throughout the day is correctly described by the model.

It is particularly noticeable at the frequency offset of 0.8 MHz that there is significant spectral power in the  $\sim 2$ -hour period even though the sampling time is 15 min. This is evident at other altitudes, although not as pronounced. We cannot account for any analysis procedure which would introduce this 2-hour period. The amplitude of the middle atmosphere signature cannot be understood as the effect of an internal gravity wave propagating through the troposphere and modulating the tropospheric opacity. We are at an impasse in resolving these discrepancies at 62 km in the April data.

Overall, the model accurately describes the relative diurnal variation of ozone in the middle atmosphere during equinox, but we emphasize that models with standard JPL photochemical rate constants underpredict absolute ozone concentrations in the stratosphere and mesosphere as discussed by several authors [Allen *et al.*, 1981, 1984; Froidevaux *et al.*, 1985; Rusch and Eckman, 1985; Strobel *et al.*, 1987; Clancy *et al.*, 1987]. Modifications to the standard chemistry have been suggested to remedy this model underprediction. Rusch and Eckman [1985] decreased the efficiency of the odd hydrogen catalytic cycle which destroys ozone in the mesosphere by modifying the reaction rate

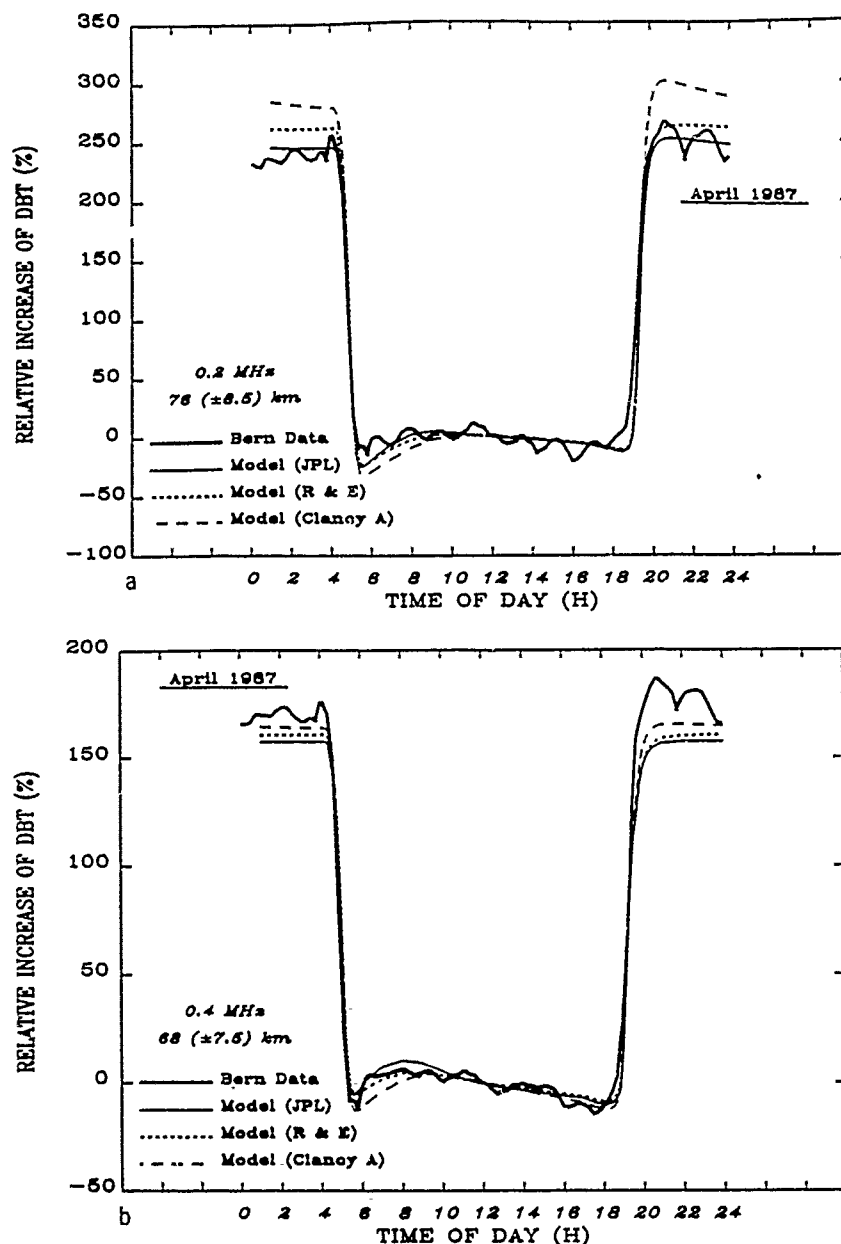


Fig. 9. (a) Relative diurnal variation of the 0.0- to 0.2-MHz brightness temperature difference normalized by the average value over the 1200  $\pm$  2 hour time period. This temperature difference is sensitive to the  $O_3$  mixing ratio in the  $76 \pm 8.5$  km region (see Table 1). The heavy solid line represents the measurements, and the light solid line is the variation of the synthetic spectra (at frequency offsets corresponding to those of the measurements) generated using the diurnal variation of the model  $O_3$  profiles for standard JPL-87 chemistry. The short-dashed line and long-dashed line represent synthetic spectra generated using model chemistry incorporating recommended modifications by *Rusch and Eckman* [1985] and *Clancy et al.* [1987], respectively. (b) Same as Figure 9a for the 0.2- to 0.4-MHz brightness temperature difference ( $68 \pm 7.5$  km). (c) Same as Figure 9a for the 0.4- to 0.8-MHz brightness temperature difference ( $62 \pm 7.5$  km). (d) Same as Figure 9a for the 0.8- to 1.6-MHz brightness temperature difference ( $56 \pm 7.5$  km).

coefficients of certain key  $HO_x$  reactions to the lowest values allowed within experimentally determined uncertainties. This was done to provide photochemical model agreement with mid-latitude SME ozone data. *Strobel et al.* [1987] performed a similar analysis using mid-latitude SME ozone data and ground-based microwave mesospheric water vapor data and found essentially the same result. *Clancy et al.* [1987] used the *Rusch and Eckman* [1985] photochemical model in addition to the Caltech model [Allen et al., 1981,

1984] in a study which examined high-latitude SME P.M. ozone profiles and A.M./P.M. ozone ratios and attempted to determine the possible contributions of uncertainties in  $O_2$  and  $O_3$  absorption cross sections to model/data discrepancies. The *Clancy et al.* [1987] study found that a combination of a 30% increase in the Schumann-Runge band  $O_2$  cross sections, a 30% decrease in the  $(O^1D)$  yield from ozone photolysis, and a decrease in the efficiency of the odd hydrogen catalytic loss of ozone would provide consistency

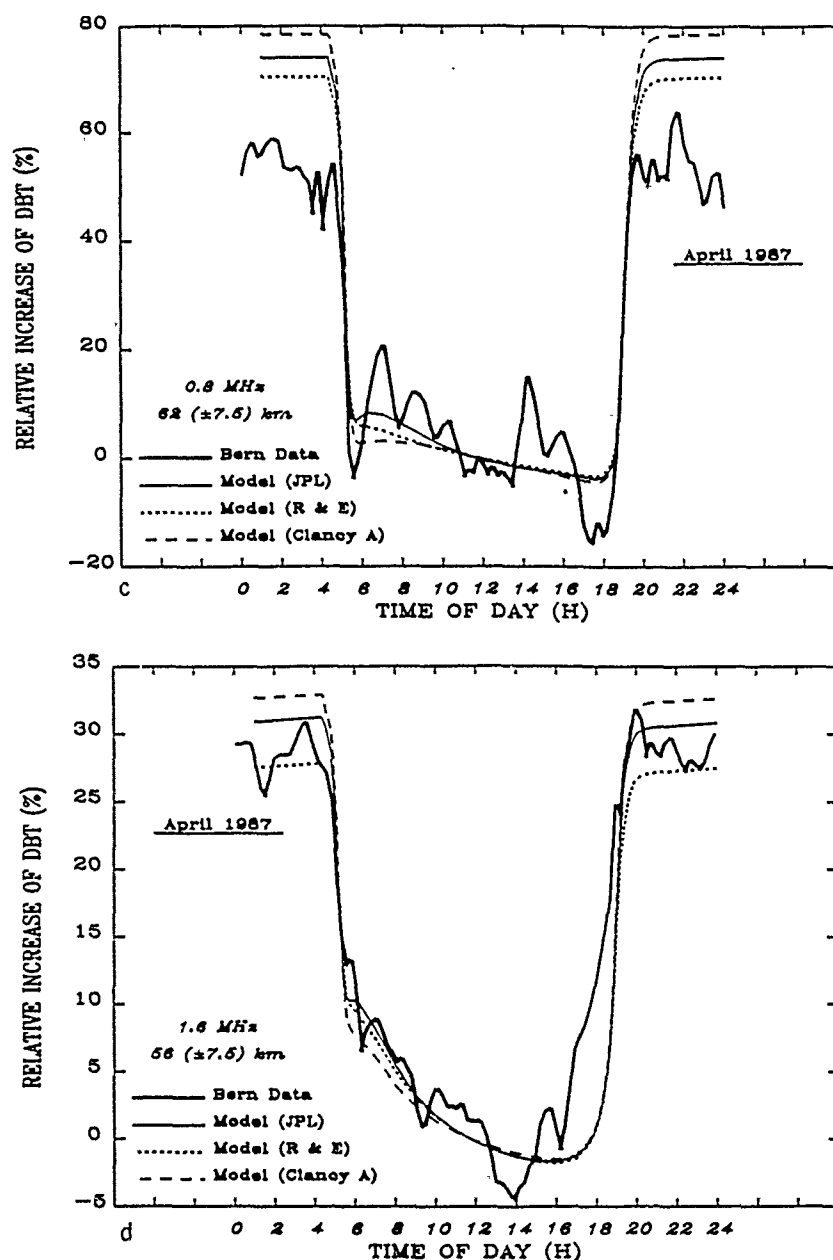


Fig. 9. (continued)

between their model and SME data (see model A of Clancy *et al.* [1987]).

We have performed model simulations of the diurnal ozone variation with both the Rusch and Eckman [1985] suggested changes in odd hydrogen reaction rates, and the changes incorporated in model A of Clancy *et al.* [1987] for comparison with our diurnal ozone data. In both cases the model results were converted to relative increases of DBT and normalized to noontime values to facilitate the comparison with data. The results are plotted along with the standard JPL chemistry model in Figures 9a–9d. In general, the Clancy model A chemistry produces larger diurnal variation of ozone by ~10%. However, all three cases are sufficiently close to preclude unambiguous determination of a "best" case. The reasons for this are threefold. First, the largest effect on the diurnal variation of the ozone abundance

owing to the above changes in photochemistry is primarily above 75 km, above the useful range of our data. Second, the broad weighting functions of our retrievals tend to smooth out small-scale variations with altitude that occur when different combinations of changes in chemistry are incorporated in the model. The third reason is related to the particular choice of chemical reactions in which changes were made. The sharp transition at sunrise between high nighttime and low daytime ozone abundances is due to the short time scale for ozone photolysis, leading to a rapid repartitioning between O and O<sub>3</sub> after sunrise (see (3)). Thus the average day to night ozone abundance ratio at a particular level in the mesosphere is strongly controlled by the magnitude of the ozone photodissociation rate coefficient, which was not changed in the chemical modifications discussed above. On the basis of the reasonable agreement



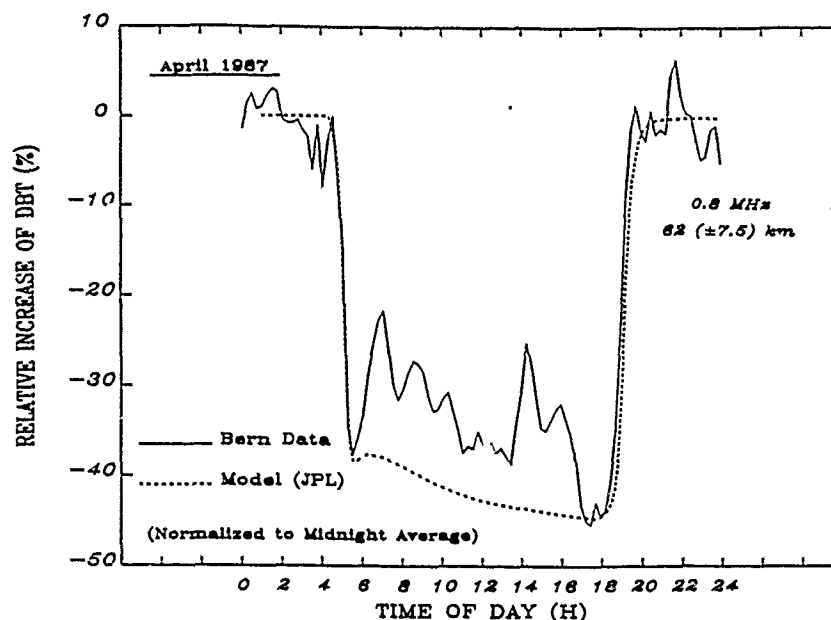


Fig. 10 Relative diurnal variation of the 0.4- to 0.8-MHz brightness temperature difference shown normalized to the midnight  $\pm 2$  hours average.

between the modeled and observed relative day to night variation in ozone mixing ratio, we conclude that the model value of the ozone photolysis rate coefficient is accurate to better than 10%. However, we feel that these observations do not provide sufficient constraints for deducing the correct mesospheric ozone chemistry from among the above suggested models.

The best available data for winter are the months of December 1986 and January 1987. For these months only high-altitude data at frequency offsets of 0.2 and 0.4 MHz (74 and 66 km, respectively) have sufficient signal to noise to merit serious comparison to model calculations. The relative variation of DBT for December 1986 is shown in Figures 11a and 11b, whereas Figures 12a and 12b illustrate a comparison of data and model calculations for January 1987. Note that the model consistently underpredicts the diurnal variation of the relative DBT by as much as a factor of 2. A major part of this underprediction is associated with the postmidnight increase in  $O_3$  mixing ratio. This rise in the  $O_3$  mixing ratio by up to a factor of 2 is a real feature in the data. It is tempting to interpret Figures 11a and 11b in terms of a midnight minimum in  $O_3$  with "excess" amounts at sunset and sunrise which might be due to vertical motions, but in Figures 12a and 12b the sunrise  $O_3$  abundance definitely exceeds the sunset value. The average  $O_3$  vertical mixing ratio profile for midnight in January shows a local maximum at  $\sim 65$  km. Thus conservative vertical displacements of air parcels would lead to decreased  $O_3$  mixing ratios at 65 km at other times during the night in disagreement with Figures 11b and 12b.

It should be emphasized that the January 1987 measurements were made with excellent tropospheric transmittances and that these observed increases in DBT are much too large to be accounted for by temperature errors in tropospheric correction term. Also apparent in the data is a decrease in the relative DBT between sunset and midnight, of smaller amplitude than the postmidnight increase (Figures 12a and 12b). From Lobsiger and Kunzi [1986, Figure 4] an increase

in  $O_3$  concentration of  $\sim 10\%$  after midnight was observed at 74 km. Our data at 74 km for December 1986 and January 1987 show an increase of 30–40% after midnight in the absolute  $O_3$  mixing ratio until sunrise (Figures 4 and 5). At these altitudes the model predicts constant DBT between sunset and sunrise. There are no chemical or transport effects in the model which can create sufficient  $O_3$  or transfer O atoms down from the thermosphere to be converted chemically by (R15) to  $O_3$  in this altitude region which could potentially explain the nighttime behavior of  $O_3$ . The post-midnight increase in  $O_3$  is not present in the equinoctial (April 1987) data. In addition, recent measurements made in Bern during January/February 1988 do not show a significant nighttime variation.

If we assume that the postmidnight increase in  $O_3$  is real, then the most plausible explanation is an enhanced downward flux of O atoms from the lower thermosphere whose convergence in the 65- to 75-km region leads to the observed  $O_3$  increase. This increase must occur in a time short in comparison to the typical time constant for removal of odd oxygen ( $\sim 10^5$  s). Thus the approximate continuity equation is

$$\frac{\partial [O_3]}{\partial t} = -\frac{\partial \phi}{\partial z} \quad (5)$$

which can be integrated with respect to height to yield

$$\frac{\partial N(O_3)}{\partial t} = -[\phi(O, 85 \text{ km}) - \phi(O, 60 \text{ km})] \quad (6)$$

where  $N(O_3)$  is the column density,  $\phi$  is the flux, and  $\phi(O, 60 \text{ km}) \sim 0$  as most of the O atom flux has been converted to  $O_3$ , and note that  $\phi(O, 85 \text{ km})$ , the mesopause flux, is downward and hence negative. The column density of  $O_3$  above 60 km is approximately  $4 \times 10^{15} \text{ cm}^{-2}$ . A 15% increase in the column density over 6 hours or  $2 \times 10^4$  s requires

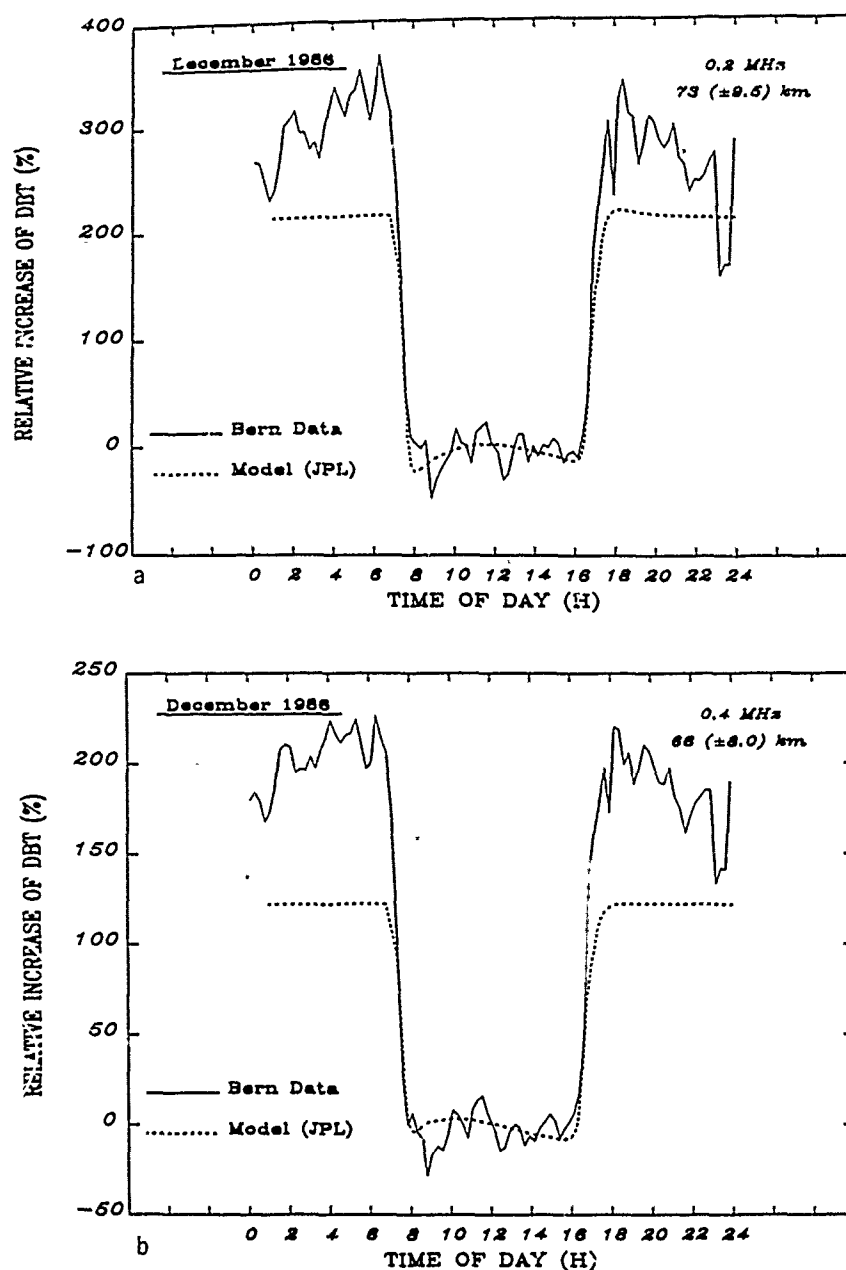


Fig. 11. (a) Same as Figure 9a, except for December (73  $\pm$  9.5 km) and shown only with model results using standard JPL-87 chemistry. (b) December (66  $\pm$  8.0 km) comparison.

downward O atom flux  $\phi(\text{O}, 85 \text{ km})$  or order  $4 \times 10^{10} \text{ atoms cm}^{-2} \text{ s}^{-1}$ . This is a reasonable value for the downward O atom flux at the mesopause, but it must penetrate down to at least 70 km, rather than only 80 km where at night it is typically depleted. To penetrate to a given level, the vertical transport time constant must be shorter than the chemical time for conversion of O atoms to  $\text{O}_3$  by (R15) over the altitude region above that level. The time constant for (R15) varies from  $\sim 300$  to  $1 \times 10^4 \text{ s}$ . The time constant for eddy transport is  $H^2/K_{zz}$ . In the region of strong flux convergence the scale height of atomic oxygen is typically predicted to be  $\sim 1 \text{ km}$ . At 70 km where the postmidnight increase of  $\text{O}_3$  appears to peak, the chemical time constant of (R15) is  $\sim 10^3 \text{ s}$ . If we require the flux convergence to peak there, then the transport and chemical time constant should be comparable

at 70 km, i.e.,  $H^2/K_{zz} \sim 10^3 \text{ s}$ . But  $H \sim 10^5 \text{ cm}$ ; hence  $K_{zz}$  must be  $\sim 10^7 \text{ cm}^2 \text{ s}^{-1}$ . This is two orders of magnitude larger than the baseline  $K_{zz}$  profile used in our diurnal calculations. In terms of a mean vertical velocity ( $\sim K_{zz}/H$ ) this is equivalent to  $\bar{W} \sim -1 \text{ m s}^{-1}$ . An enhancement in either  $K_{zz}$  or  $\bar{W}$  of this magnitude over a 6-hour period seems to be very excessive, especially down to 70 km, and would thus cast suspicion on the reality of the observed postmidnight increase in  $\text{O}_3$ . We do note that Bjarnason *et al.* [1987] suggest that tidal influences on the local zonal wind profile affect the magnitude of gravity wave-induced vertical diffusion. At 86 km in the summer at 70°N they find an order of magnitude variation in  $K_{zz}$  with minimum values between 18 and 24 hours and elevated values from midnight to early afternoon. With chemical acceleration of eddy diffusion

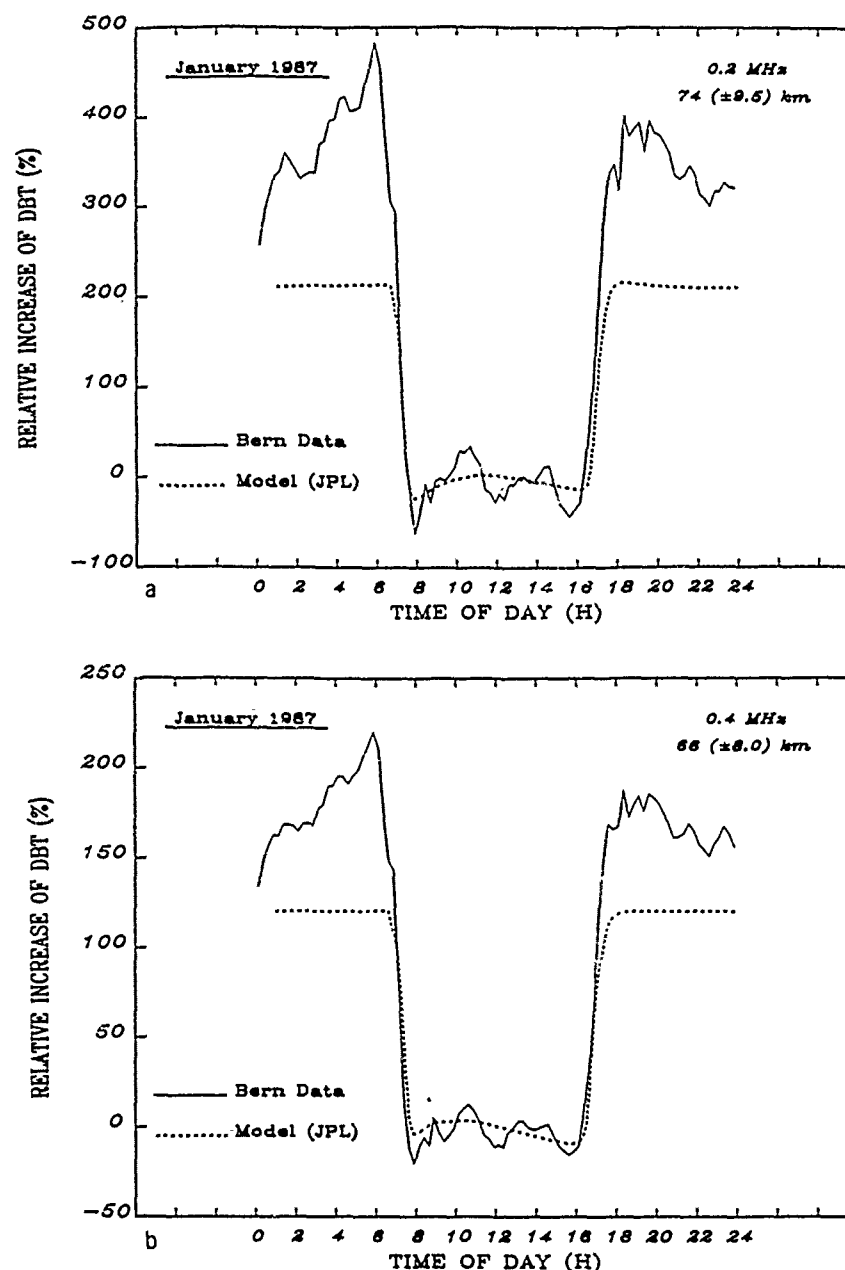


Fig. 12. (a) Same as Figure 11(a) except for January ( $74 \pm 9.5$  km). (b) January ( $66 \pm 8.0$  km) comparison.

included, the magnitude of  $K_{\text{O}_2}$  at 70 km peaks around noon with minimum values around midnight [Bjarnason *et al.*, 1987, Figure 14], but the total variation is only a factor of 2.

#### 7. CONCLUDING REMARKS

The ground-based microwave observations of the diurnal variation of mesospheric ozone presented in this paper are currently the best available measurements of this type. From the data taken from December 1986 to April 1987 over Bern, Switzerland, we obtained monthly averaged results of sufficient quality to define the characteristic diurnal behavior of the ozone mixing ratio in the mesosphere during winter and equinox conditions. One-dimensional photochemical model calculations for equinoctial conditions correctly predict the relative diurnal variation of ozone. This supports the asser-

tion that (4) represents the essential chemistry necessary to understand the diurnal variation of ozone. Furthermore, the reasonable agreement between the model and observations suggest that the model value of the ozone photolysis rate coefficient is accurate to better than 10%. Model simulations incorporating various recently suggested modifications to standard mesospheric odd hydrogen and odd oxygen photochemistry [Rusch and Eckman, 1985; Clancy *et al.*, 1987] show little distinction in the calculated relative diurnal variation of brightness temperature differences. To the extent that these model modifications represent the range of uncertainty in our understanding of ozone photochemistry, we conclude that observations of the diurnal variation of ozone by this technique do not represent a good test for competing photochemical theories.

During the winter months, (4) predicts only about one half the observed diurnal variation of ozone: part of this discrepancy is due to the observed postmidnight increase in ozone. This is strictly a winter phenomenon in our data base, which was not observed in recent measurements during January/February 1988. Clearly, further measurements are required to identify whether this phenomenon is typical and whether special geophysical conditions are required to generate this nighttime increase in mid-latitude ozone. One proposed explanation of this phenomenon in terms of enhanced downward transport of atomic oxygen from the lower thermosphere requires substantially elevated values of  $K_{\infty}$  or  $\bar{v}$  in the postmidnight period which appear to be excessive. It is sufficiently intriguing, though, to merit further research.

**Acknowledgments.** This research was supported by a grant from the Theory and Data Analysis Branch of the Office of Space Science and Applications Division of NASA and by the Middle Atmosphere Program at the Naval Research Laboratory.

#### REFERENCES

- Allen, M., Y. L. Yung, J. Waters, Vertical transport and photochemistry in the terrestrial mesosphere and lower thermosphere (50–120 km). *J. Geophys. Res.*, **86**(A5), 3617–3627, 1981.
- Allen, M., J. I. Lunine, Y. L. Yung, The vertical distribution of ozone in the mesosphere and lower thermosphere. *J. Geophys. Res.*, **89**(D3), 4841–4872, 1984.
- Bevilacqua, R. M., J. J. Olivero, P. R. Schwartz, C. Gibbins, J. M. Bologna, and D. Thacker, An observational study of water vapor in the mid-latitude mesosphere using ground-based microwave techniques. *J. Geophys. Res.*, **88**(C13), 8523–8534, 1983.
- Bevilacqua, R. M., W. J. Wilson, and P. R. Schwartz, Measurement of mesospheric water vapor in 1984 and 1985: Results and implications for middle atmospheric transport. *J. Geophys. Res.*, **92**(D6), 6679–6690, 1987.
- Bevilacqua, R. M., J. J. Olivero, and C. L. Croskey, Mesospheric water vapor measurements from Penn State: Monthly mean observations (1984–1987). *J. Geophys. Res.*, in press, 1989.
- Bjarnason, G. G., S. Solomon, and R. R. Garcia, Tidal influences on vertical diffusion and diurnal variability of ozone in the thermosphere. *J. Geophys. Res.*, **92**(D5), 5609–5620, 1987.
- Chahine, M. T., A general relaxation method for inverse solution of the full radiative transfer equation. *J. Atmos. Sci.*, **29**, 741–747, 1972.
- Clancy, R. T., D. W. Rusch, R. J. Thomas, M. Allen, and R. S. Eckman, Model ozone photochemistry on the basis of Solar Mesosphere Explorer mesospheric observations. *J. Geophys. Res.*, **92**(D3), 3067–3080, 1987.
- DeMore, W. B., M. J. Molina, S. P. Sander, D. M. Golden, R. F. Hampson, M. J. Kurylo, C. J. Howard, and A. R. Ravishandara, Chemical kinetics and photochemical data for use in stratospheric modeling. *Publ. 87-41*, Jet Propul. Lab., Pasadena, Calif., 1987.
- Forbes, J. M., Thermosphere structure variations during high solar and magnetic activity conditions, final technical report for Air Force contract F19628-82-K0031, Boston Univ., Boston, Mass., 1985.
- Froidevaux, L., M. Allen, and Y. L. Yung, A critical analysis of ClO and O<sub>3</sub> in the mid-latitude stratosphere. *J. Geophys. Res.*, **90**, 10,733–10,738, 1985.
- Gustincic, J., A quasi-optical receiver design. *Proceedings of IEEE Conference on Microwave Theory and Techniques*, pp. 99–100. Institute of Electrical and Electronics Engineers, New York, 1977.
- Krauss, J. D., *Radio Astronomy*, McGraw-Hill, New York, 1966.
- Lobsiger, E., Ground based radiometry to determine stratospheric and mesospheric ozone profiles. *J. Atmos. Terr. Phys.*, **49**(5), 493–501, 1987.
- Lobsiger, E., and K. F. Kunzi, Night-time increase of mesospheric ozone measured with a ground-based microwave radiometer. *J. Atmos. Terr. Phys.*, **48**(11–12), 1153–1158, 1986.
- Lobsiger, E., K. F. Kunzi, and H. U. Dutsch, Comparison of stratospheric ozone profiles retrieved from microwave-radiometer and Dobson-spectrometer data. *J. Atmos. Terr. Phys.*, **46**(9), 799–806, 1984.
- Randegger, A., On the determination of atmospheric ozone profile for ground based microwave measurements. *Pure Appl. Geophys.*, **118**, 1052–1065, 1980.
- Rusch, D. W., and R. S. Eckman, Implications of the comparison of ozone abundances measured by the Solar Mesosphere Explorer to model calculations. *J. Geophys. Res.*, **90**(D7), 12,991–12,998, 1985.
- Strobel, D. F., M. E. Summers, R. M. Bevilacqua, M. T. DeLand, and M. Allen, Vertical constituent transport in the mesosphere. *J. Geophys. Res.*, **92**(D6), 6691–6698, 1987.
- Thomas, R. J., C. A. Barth, D. W. Rusch, and R. W. Saunders, Solar Mesosphere Explorer near-infrared spectrometer: Measurements of 1.27- $\mu$ m radiance and the inference of mesospheric ozone. *J. Geophys. Res.*, **89**, 9569–9580, 1984a.
- Thomas, R. J., C. A. Barth, and S. Solomon, Seasonal variations of ozone in the upper mesosphere and gravity waves. *Geophys. Res. Lett.*, **11**, 673–676, 1984b.
- Twomey, S., *Introduction to the Mathematics of Inversion in Remote Sensing and Indirect Measurements*, Elsevier, New York, 1977.
- Wilson, W. J., and P. R. Schwartz, Diurnal variations of mesospheric ozone using millimeter-wave measurements. *J. Geophys. Res.*, **86**(C8), 7385–7388, 1981.
- M. Allen, Earth and Space Sciences Division, Jet Propulsion Laboratory, California Institute of Technology, Pasadena, CA 91109.
- R. M. Bevilacqua and M. E. Summers, E. O. Hulburt Center for Space Research, Naval Research Laboratory, Washington, DC 20375.
- K. F. Kunzi and W. C. Zimmerfelds, Institute of Applied Physics, University of Bern, Bern, Switzerland.
- W. J. Sawchuck, Computational Physics, Inc., 4115 Annandale Road, Annandale, VA 22003.
- D. F. Strobel, Department of Earth and Planetary Sciences, Johns Hopkins University, Baltimore, MD 21218.

(Received November 28, 1988;  
revised May 26, 1989;  
accepted May 26, 1989.)